Nearshore Sediment Dynamics in a Mixed Sand/Mud Environment

A Thesis

submitted in fulfilment

of the requirements for the degree

of

Doctor of Philosophy

in Earth Sciences

by

Brett James Beamsley

The University of Waikato

Te Whare Wānanga o Waikato

The University of Waikato

May 2003

Frontispiece

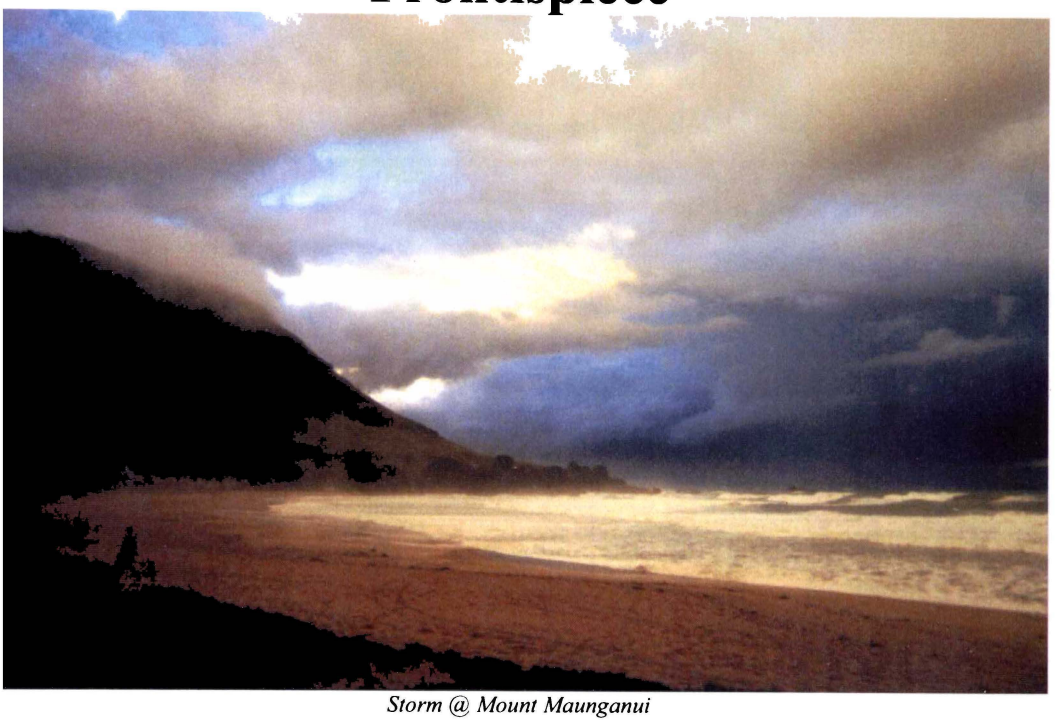

Storm @ Mount Maunganui

There is a pleasure in the pathless woods,
There is a rapture on the lonely shore,
There is society where none intrudes
By the deep sea, and music it roar:
I love not man the less, but nature more,
From these our interviews, in which I steal
From all I may be, or have been before,
To mingle with the universe, and feel
What I can ne'er express, yet cannot all conceal.

Roll on, thou deep and dark blue Ocean, -roll!
Ten thousand fleets sweep over thee in vain;
Man marks the earth with ruin, - his control
Stops with the shore; - upon watery plain
The wrecks are all thy deed, nor doth remain
A shadow of man's ravage, save his own,
When, for a moment, like a drop of rain,
He sinks into thy depths with bubbling groan,
Without a grave, unknelled, uncoffined, and unknown.

His steps are not upon thy paths, - thy fields
Are not a spoil for min, - thou dost arise
And shake him from thee; the vile strength he wields
For earth's destruction thou dost all despise,
Spurning him from thy bosom to the skies,
And send'st him, shivering in thy playful spray
And howling, to his gods, where haply lies
His petty hope in some near port or bay,
And dashest him again to earth: - there let him lay.
The armaments which thunderstrike the walls
Of rock-built cities, bidding nations quake
And Monarchs tremble in their capitals,
The oak leviathans, whose huge ribs make
Their clay creator the vain title take
Of lord of thee and arbiter of war, -
These are thy toys, and, as the snowy flake,
They melt into thy yeast of waves, which mar
Alike the Armada's pride or spoils of Trafalgar

Thy shores are empires, changed in all save thee;
Assyria, Greece, Rome, Carthage, what are they?
Thy waters wasted them while they were free,
And many a tyrant since; their shores obey
The stranger, slave, or savage; their decay
Has dried up realms to deserts: not so thou;
Unchanged save to thy wild waves' play,
Time writes no wrinkles on thine azure brow;
Such as creation's dawn beheld, thou rollest now.

Thou glorious mirror, where the Almighty's form
Classes itself in tempests; in all time,
Clam or convulsed, - in breeze, or gale, or storm,
Icing the pole, or in the torrid clime
Dark-heaving; boundless, endless, and sublime,
The image of Eternity, - the throne
Of the Invisible! even from out thy slime
The monsters of the deep are made; each zone
Obeys thee; thou goest forth, dread, fathomless, alone

Lord Byron

Abstract

Poverty Bay, on the New Zealand's northeast coastline, is a high-energy coastal embayment that receives significant quantities of fine, fluvial sediment from two river systems. Examining seabed geomechanical characteristics, sediment fluxes and morphological features in northern Poverty Bay provided the opportunity to study interactive processes, including sediment entrainment rates over the cohesively bound mixed sand/mud seabeds, and the dispersion of a turbid river plume. Three field experiments and an extensive seabed-sampling programme were undertaken, and a 2-cell numerical model was developed and validated against infilling rates of the port of Gisborne navigation channel. The implications for existing and future operations at the port of Gisborne, including the suitability of capital and maintenance dredged material for use in reclamation, have been evaluated.

Within the study site, near-bed wave orbital velocities and fluvial inputs control the spatial variability in the seabed sediment textural characteristics, with the seabed grain size decreasing with depth and distance from the mouth of the Turanganui River. A hand-held shear vane was used to quantify the in-situ shear strength of the cohesively bonded mud/sand surficial sediment, and the in-situ shear strength has been correlated (R^2 = 0.83) with the cumulative effect of several of the sediment textural and environmental parameters.

Near-bed sediment diffusion and entrainment was examined using an array of micro-scale inline pumps. The effect that cohesive bonding of the mixed sand/mud seabed has on retarding the entrainment rate was examined by considering both the textural and geomechanical characteristics of the seabed. No correlation was found between the ratios of estimated to predicted near bed reference concentration (ζ) and either the median grain size (d_{50}) or the ratio of percent sand to mud of the seabed. However, a good correlation was found between ζ and the normalised in-situ shear strength (χ) of the seabed (adjusted R^2 = 0.99), with the relationship of the form,

$$\ln(\zeta) = -0.51 - 1.30\chi^3$$

The conversion of the downward flux from sediment traps to a time-averaged suspended sediment concentration (*SSC*), and near bed reference concentration (C_0) was found to be critically dependant on the fall velocity statistic (w_f) of the grain size distribution. Due to flocculation of the near-bed suspended sediment, the dispersed equivalent w_f distribution and median w_f of the distribution resulted in poor predictions of C_0. Instead, an in-situ '*effective*' w_f distribution of the suspended sediment was developed using the measured l_s from individual dispersed grain size bins within the *SSC* profile and the predicted sediment diffusivity (ε_s). C_0 predicted using the effective w_f distribution agreed with pumped samples and theory predicted C_0, and provided a robust method of determining the time-averaged *SSC* of mixed sand/mud sediment using sediment traps.

The diffusion of sediment within the near-bed *SSC* profile varied as a function of w_f, with relatively finer sediment exhibiting less diffusion. The mixing length (l_s) profile was well approximated by a linear profile, with l_s varying as a function of elevation (z) and the von Karman constant (κ), i.e. $l_s = \kappa z$. Within 4-8 cm of the bed l_s is constant and equal to 0.06 m.

β is defined as the ratio of sediment diffusivity (ε_s) to eddy viscosity (ε_f), and is commonly used as a correction factor for predictive *SSC* profile equations. By

examining the diffusion of sediment within the near-bed *SSC* profile a new equation for β was obtained,

$$ln(\beta) = -0.95 - \frac{0.4\psi}{ln(\psi)}$$

The horizontal diffusion of sediment within the Turanganui River plume was found to be a function of the distance (x) from the mouth of the Turanganui River and a decay rate factor (D_x), where

$$C_x = C_{ob} e^{(-x/D_x)}$$

The form of the equation is similar to the Nielsen time-averaged gradient diffusion equation. D_x was correlated ($R^2 = 0.92$) with river discharge (φ_{river}), and found to exponentially decrease with increasing φ_{river}, where

$$D_x = 591 + 2850 \exp\left(-\varphi_{river}/2.1\right)$$

The relationship suggests that the effective w_f of the suspended sediment within the plume increases with increasing *SSC*, presumably due to increased flocculated particle size. Based on the developed empirical formulae the Turanganui River is predicted to discharge 7.6×10^7 kg of fluvial derived sediment into Poverty Bay on an annual basis.

The developed relationships and formulae that describe the hydrodynamical processes within northern Poverty Bay have been implemented in a 2-cell numerical model that considers both downward and horizontal sediment fluxes. The port of Gisborne shipping channel infilling rate, as determined from hydrographic surveys and dredging records, was used to validate the model. The 2-cell numerical model accurately predicts channel infilling rates, and provides an insight into the governing hydrodynamical processes in northern Poverty Bay. The developed model represents an alternative to the implementation of a full 3-dimensional hydrodynamic model.

Hydrographic surveys and dredging records show the channel area passes through the beach nearshore zone, and during the monitoring period maintenance dredging only maintained the channel design depth along the channel leads, while significant infilling occurred near the channel edges (Δh = -1 m). Extrapolation of the results suggests an annual channel infilling rate of 171,400 m^3 per year, corresponding to a maintenance dredging cost of approximately $857,000 to $1,200,000 per annum. Wave and river discharge conditions during the monitoring period were smaller than average, and more infilling is expected during stormy years.

Relocating the channel and port entrance to a site in deeper water, further from the mouth of the Turanganui River, with relatively strong seabed in-situ shear strength is identified as a means of reducing dredging costs. The material dredged from the shipping channel is suitable for use in land-based reclamation, particularly if the soil structure is improved by addition of a coarser material such as of the underlying mudstone unit. The bearing capacity of the reclamation can be improved by mixing the mud/sand with concrete to create mudcrete.

Acknowledgements

At the risk of being clichéd and sounding like an Oscar speech the biggest thanks has to go out to my family; Mum, Dad, Kym and Glenn (thanks for looking after the car little Bro!), but especially mum and dad for their belief in me (I think they believed?!?) and financial support.....who would have guessed that schooling could be dragged out for so long!

The remaining list of other people that I need to thank is long and distinguished, well mostly, and I'm sure that I'll forget to thank many, so start with I'd like to an apology to all the people I've forgotten to thank.

A big thank-you has to go to Prof. Terry Healy who, with the aid (both financial and logistical) of Ben Tahata from Port Gisborne Ltd. initiated this study, and have been a huge support throughout. Drs Kerry Black, Joseph Mathew, Shaw Mead and Peter McComb from ASR Ltd. for their support and expertise, especially Kerry who put up tirelessly with the barrage of questions, and without who's help this study would possible still be going (mum, dad...you need to thank him too!). I would also like to thank Technology New Zealand, who recognised the potential benefit of this study to both science and the port industry in Gisborne and provided financial support during the initial 3-years through the Graduate Research in Industry Fellowship (GRIF) scheme, now known as the Technology for Industry Fellowship (TIF) scheme.

The assistance and guidance of Richard Gorman, for remaining sane during the onslaught of questions about Tseries, and Dr. Mel Green for suggesting to me that I continue studying, and do my Doctorate (you might want to explain that to mum and dad).

The endless hours of fieldwork for this study would never have been completed without the aid of Cliff Bloomfield from Wainui Dive, who helped with instrument deployment, collecting sand/mud, measuring ripples and the gathering of a few odd crayfish (for science of course!). Additionally thanks also to the tug crew from Gisborne (and hence Port Gisborne Ltd.) for their help, humour and laughs in the field, not to mention their knot tying expertise...hell I *almost* didn't loose an instrument. Further, no coastal student that has gone through the University of Waikato could have completed their fieldwork without the aid and assistance of the technicians, and Dirk Immenga is thanked for his hours boating around Poverty Bay, probably wondering what I was up to, and being tolerant of my treatment of the instruments.

Huge thanks also has to go to Sian Beatie, who proofread this entire thing, so if you find mistakes it's her fault, seriously, thanks Sian. Also thanks to Lee Knight, who together with Sian and Alana put up with me as a flatmate, and my crazy moods when I was cooped up inside, injured with a ruptured Achilles tendon...it was Prozac wasn't it? Thanks for the laughs and good times, although, Lee, sometimes I think we might have gone just a little too far, buts its amazing the cats turned out as well-adjusted as they did...yeah right! Additionally, I would like to thank Dahlia (who in her infinite wisdom married Lee?!) and Ezra Knight for providing me with laughs near the end, and looked after my beanbag.

I am also indebted to Sarah and Rosco for the fun times in the surf, I don't know anyone keener than Sarah in the surf, (her smile, or at least voice, lights up the surf when she gets a good wave), while Rosco has changed my approach to surfing and how I view things and people....not a bad bloke for an Australian, and a person I count as a friend.

I would also like to thank the various flatmates I have had during my study that I haven't thanked already, including the Rose-Street Girls (of which apparently I was one!?); Debbie Huijbers, Alana and Karen Taylor, also my friends and flatmates from Gisborne, Nick Webb and Monty (come on...with a name like Gerard Montgomery what else was he going to be called). Nick...give the pies back, Rosco wants to make some Ozie sammies.

Thanks also to Jamie Hutt for his friendship and the shearing of good times together, may you succeed in whatever ventures you undertake, I know you have the skill and knowledge.

I would like to thank Gareth Vaughan and his family, Marion and the kids. I hope your studies are as enjoyable for me, and that you finish slightly quicker than I did, thanks for the lesions in hackie.

And lastly, a big thanks has to go out to the numerous people who have put me up on their couches (thanks Pencil, and the Raglan Embassy), there will always be a couch, or at least floor space, for you wherever I am.

Cheers, Brett

Table of Contents

List of Figures

List of Tables

Chapter 1. The Research Issues

1.1 Introduction.

Poverty Bay is a high wave-energy coastal embayment on the New Zealand's northeast coastline (Figure 1.01 and Figure 1.02), into which two river systems, the Waipaoa River in the south and the Turanganui River adjacent to the port of Gisborne in the north, discharge significant quantities of fine fluvial sediment.

Surficial sediments consist of mixtures of sand and mud (Kensington, 1990; Miller, 1981), with the muds cohesively bonding the sediment (Beamsley et al., 1997). The variability in the relative percents of sand and mud within the seabed sediment in northern Poverty Bay make it an ideal location to examine, under field conditions, the high-energy wave-induced sediment entrainment over mixed beds. Only limited previous research has been undertaken of such systems (Toorman, 2001). Further, sedimentological and hydrodynamical processes associated with the mixing of fluvial derived freshwater and more saline oceanic water can be examined by studying the plume characteristics of the Turanganui River (Figures 1.01 and 1.02).

While is has distinctive features, northern Poverty Bay provides the opportunity to examine various interactive hydrodynamical and sedimentological processes in a small, readily accessible locality that is relevant to many coastlines worldwide. Additionally, investigations into the sediment flux characteristics help to identify the mechanisms of the physical coastal environment that effect both existing and future port operations.

The port at Gisborne represents a major export conduit for large volume bulk cargoes on the North Islands East Coast (Beamsley et al., 1997). The port hinterland extends northwards, up the East Coast of the North Island, and includes the large maturing *pinus radiata* forests of the East Cape. The maturing of the forests within the port's hinterland has resulted in a dramatic increase in the port's forecasted export tonnage over the next few decades (Figure 1.03). If the port is to transport the expected increase in export tonnage the existing port needs to expand, both in the usable storage area and the number of shipping berths capable of handling large (~200 m) ships. Failure to expand may result in exporters being forced to use other export corridors, resulting in a potential financial loss to both the port operating company and the local community due to the trickle-down effect.

Since its conception in the late 1880's Gisborne's port has experienced various operational and engineering issues (largely due to internal seiching), and has required continual maintenance dredging of the navigation channel and Swinging Basin in order to maintain an operational water depth (Whyte, 1984). Expansion of the port provides an ideal opportunity to address these issues, and potentially provide the port with a significant cost saving by minimising the operational and engineering issues, currently faced by the port operational company. A proposed port design should not only seek to minimise internal seiching, but also address the ongoing cost involved with maintenance dredging. However, in order to ensure that the decision-making process leads to optimal function, it is vital that the complexities of the physical processes in northern Poverty bay are understood.

While investigations into seiching within both the existing and proposed port designs have been undertaken several times in the past (i.e. Black et al., 2002; Black et al., 1997), the complexities associated with predicting sediment entrainment and

transport of mixed sand/mud sediment (i.e. the horizontal sediment flux) has not been comprehensively addressed. Additionally, while Miller, (1981) suggests that the downward sediment flux associated with sediment discharged into northern Poverty Bay by the Turanganui River may be an important source of sediment to the area, no previous research into the complex sediment dynamics of the river plume in the port environs has previously been undertaken. It is the downward and horizontal sediment fluxes that determine the channel infilling rate and the hence the maintenance dredging requirements.

1.1.1 Problems facing horizontal sediment flux over mixed sand/mud seabeds

For mixed sand/mud sediment, when large amounts of sand-sized particles are present as in the surficial sediment of northern Poverty Bay, the interactive behaviour between particles of different sizes needs to be understood in order to predict the sediment entrainment rate. However, Mitchener and Torfs, (1996) noted that the erosion rate of a mixed sand/mud seabed can be reduced by a factor of 5 if more than 3% mud is added to sand, and reduced by a factor of 10 if more than 20% sand was added to a mud bed. Therefore, understanding the characteristics of the cohesive bonding is essential.

The importance of cohesive bonding of the surficial sediment in northern Poverty Bay was identified by Black et al., (1997), who used a single 'cohesion factor' in the sediment transport modelling of northern Poverty Bay to account for the retardation of the entrainment rate. While the method employed by Black et al., (1997) proved adequate for the requirements of that specific study, the wider application of a single unique factor to describe the seabed cohesive properties could be improved given more comprehensive knowledge of the relationship between the surficial sediment characteristics and the retardation of the entrainment rate due to cohesive bonding. This is also relevant to mixed beds worldwide where similar simplifying assumptions have been made.

The classification of cohesive bonding is a significant obstacle to predictions of near-bed reference concentrations over mixed sand/mud seabeds. Toorman (2001) notes that there have been some studies on sedimentation, consolidation and erosional characteristics of mixed sand/mud seabeds, but the complexity of the problem is high because the properties of the aggregates depend on numerous factors, including the type of sediment, type and concentration of ions in the water and the fluid flow conditions to name a few. Recent work has focused more on quantifying the effect of cohesive bonding of the sediment using factors such as the ratio of the sand/mud mixture (e.g. Chesher and Ockenden, 1997), while work by Kamphuis and Hall (1983) found that critical shear stress for erosion increased with the plasticity index of the sediment and the shear strength of the sediment.

1.1.2 Problems facing downward sediment flux prediction in northern Poverty Bay

Sediment fluxes in Poverty Bay are further complicated by the input of both suspended and bedload sediment from the Turanganui and Waipaoa River systems.

Limited information is available on the quantity of sediment discharged into northern Poverty Bay by the Turanganui River. What estimates are available are based on either beach accretion rates or 5% of the annual Waipaoa River sediment load (Gisborne District Council, 1994 respectively; Smith, 1988 and). However, the estimated volume of sediment discharged into northern Poverty Bay by the Turanganui River is recognised to be relatively large (Gisborne District Council, 1994; Smith, 1988), with the turbid river plume often highly visible (Figure 1.04). While previous research has indicated that the Turanganui River may be an important source of sediment to the area (Miller, 1981), no previous work has attempted to quantify the impact of the suspended sediment in the plume on sediment fluxes within northern Poverty Bay, or estimated the impact of the river on channel infilling rates.

Understanding the horizontal distribution of the sediment within the Turanganui River plume, and hence the spatial variability in the downward sediment flux, requires knowledge of mixing process near the mouth of the river, and includes aspects such as density-driven currents, wind forcing of the surface water and colloidal flocculation of the relatively fine sediment suspended in the turbid river plume. Further, in order to extrapolate findings, it is necessary to be able quantify the volume of sediment discharged from the river.

1.2 Research Objectives

This study focuses on processes and mechanisms influencing both the horizontal and downward sediment fluxes, and the complexities associated with predicting sediment transport over the mixed sand/mud surficial sediment. Understanding the variability in sediment fluxes will aid the port operating company in making well-informed decisions on proposed port designs, and budgeting. This has been recognised by the management at Port Gisborne Ltd., who were implemental in initiating this study. Many ports worldwide are confronting the same problems.

As such, this study aims to examine aspects of the suspended sediment profile, and develop a method of quantifying the effect that cohesive bonding of the surficial sediment has on retarding the sediment entrainment rates and hence the horizontal sediment flux. Further, the discharge of the Turanganui River is examined, including mixing of the freshwater from the river and the saline oceanic water, the spatial variability in the turbid river plume, and the associated downward sediment flux.

The aims of the study are:

1. to map the spatial variability in the surficial sediment characteristics in northern Poverty Bay, New Zealand (Figure 1.01), including the heavy metal content, the textural characteristics and the organic content of the surficial sediment.

2. to investigate the geomechanical properties of the surficial sediments (including in-situ shear strength) and underlying country rock within the shipping approach channel to evaluate their potential for use in land reclamation, and for use in sediment entrainment investigations.

3. to expand on the understanding of the vertical variability in the near-bed wave induced suspended sediment concentration (*SSC*) by examining concentration profiles using direct measurements of the *SSC*, and examining the relationship between the eddy viscosity (ε_f) and sediment diffusivity (ε_s) for varying grain sizes within the *SSC* profile.

4. to investigate sediment entrainment rates over the cohesively bound mixed sand/mud seabeds found in Poverty Bay, and develop a relationship between the entrainment rate to the geomechanical properties of the surficial sediment.

5. to investigate the spatial variability and mixing characteristics of the Turanganui River plume, and to quantify the volume of sediment discharged into northern Poverty Bay by the river. This will aid in an understanding of the distributional characteristics of the sediment suspended in the turbid river plume, and hence the downward sediment flux.

6. to develop and calibrate a numerical model that uses the formulae and results derived during the study to predicting channel infilling rates.

1.3 Attaining the Objectives

Chapter 2 describes the state of knowledge of the physical processes operating in the study site, including wave/current characteristics, sediment transport and distribution patterns.

Chapter 3 describes the spatial variability in the seabed textural characteristics, as well as the heavy metal and organic content of the surficial sediment. The research utilises geo-referenced side-scan sonar imaging and ground truthing, while factor analysis techniques are used to correlate seabed sediment characteristic.

Chapter 4 examines the geomechanical properties of the surficial sediment, and the rock unit underlying the seabed sediment. The spatial variability in the in-situ shear strength is examined and correlated with sediment characteristics from Chapter 3. Further, Atterberg Limits of the surficial sediment are examined in order to determine aspects of the seabed behaviour under different pore-water content, including at what point the sediment begins to behave as a liquid (i.e. fluid mud). Additionally, geomechanical aspects of both the surficial sediment and the underlying rock unit are examined in order to determine their suitability for use in land-based reclamations.

Chapter 5 examines suspended sediment concentration (*SSC)* profiles over mixed sand/mud beds in a high-energy environment over a 1-minute period, including examining the gradient diffusion of different grain sized sediment within the near-bed suspended sediment profile. The chapter investigates the relationship between eddy viscosity (ε_f) and sediment diffusivity (ε_s), and aims to determine the near-bed wave orbital statistic that best predicts the vertical diffusion of sediment within the *SSC* profile.

Chapter 6 examines near-bed reference concentrations (C_0) over mixed sand/mud beds in a high-energy environment over a 1-minute period. The chapter investigates

the relationship between geomechanical characteristics, textural parameters and near-bed reference concentrations, developing theories and formulae that will be used to predict channel infilling rates. The chapter aims to correlate the retardation of the entrainment rate due to cohesive bonding of the surficial sediment with the geomechanical parameter – the in-situ shear strength. Further, the chapter aims to determine the near-bed wave orbital statistic that best predicts C_0.

Chapter 7 applies the findings from Chapters 5 and 6 over a longer time period in order to determine the suitability of using the developed formulae for predicting horizontal sediment fluxes. Further, the chapter develops methods of determining the effective fall velocity distribution of the sediment in suspension using the relationship between the measured mixing lengths (l_s) of the individual dispersed grain sizes and sediment diffusivity (ε_s). The effective fall velocity distribution is used to predict time-averaged near-bed reference concentration obtained from sediment traps.

Chapter 8 examines the mixing zone of fresh and salt water at the mouth of the Turanganui River (Figures 1.04 and 1.05). The spatial variability of the river plume is investigated and the distribution characteristic of the turbid water in the river plume examined. Further, the approximate volume of sediment discharged into Poverty Bay by the Turanganui River is predicted based on extrapolation of the measured *SSC* in the surface water of the river plume.

In *Chapter 9* a two-cell numerical model of the shipping channel is developed that incorporates the results and formulae developed in Chapters 2 to 8. The model considers both horizontal and vertical sediment fluxes, and accounts for the retardation of the entrainment rate due to cohesive bonding of the surficial sediment. The numerical model is used to validate the developed formulae by comparing predicted channel infilling rates with the infilling estimated from hydrographic surveys and maintenance dredging records.

Chapter 10 summarises the findings of the study, and examines the implications for both the exiting port and future port designs, including suggestions of how the development of future port designs can provide a significant cost-saving to the port in terms of minimising maintenance dredging requirements. Further, the chapter provides a guiding strategy for future research into the hydrological and sedimentological processes in northern Poverty Bay,

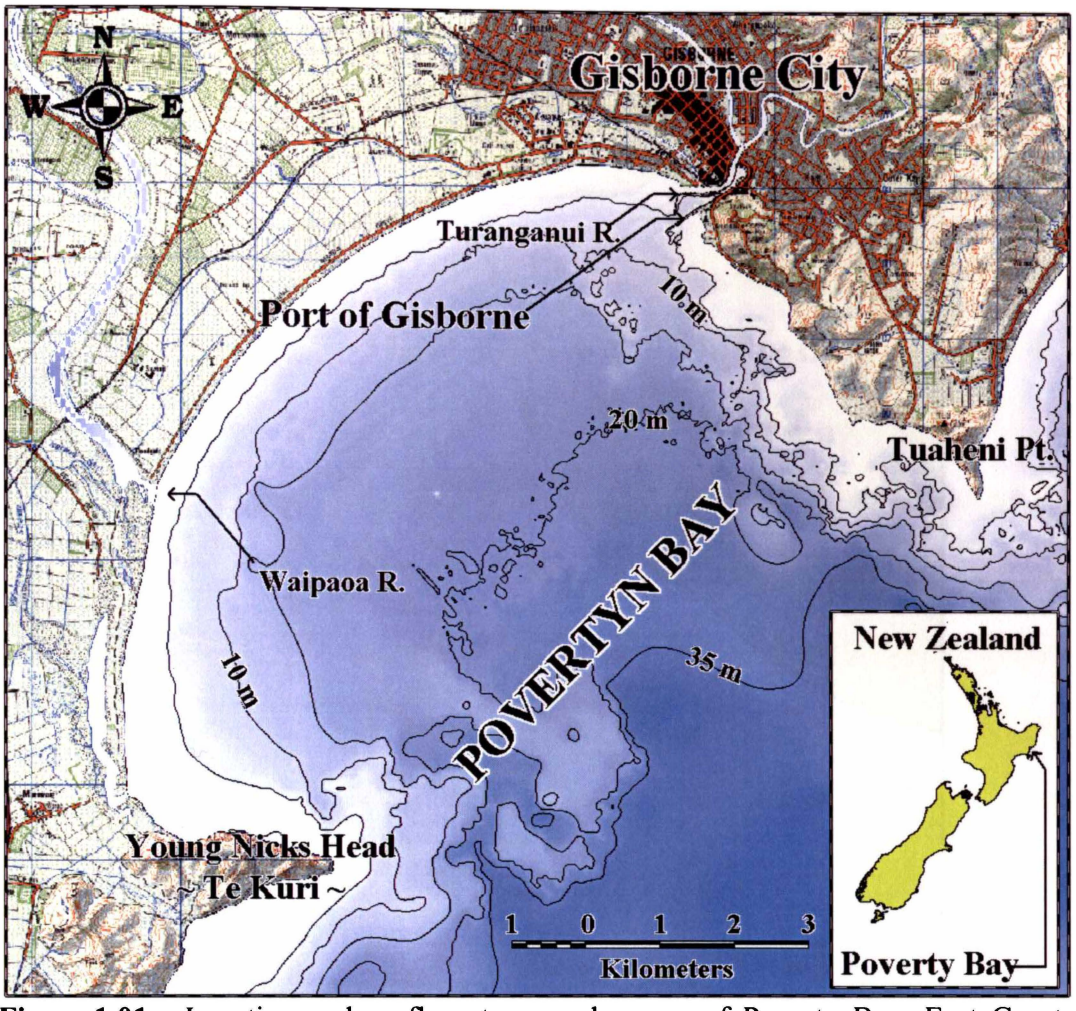

Figure 1.01 Location and seafloor topography map of Poverty Bay, East Coast New Zealand. Also shown are the locations of the Gisborne's port in the northern confines of the bay, and the Waipaoa and Turanganui Rivers. Poverty Bay is bounded between two rocky headlands, Tuaheni Point and Young Nicks Head (Te Kuri).

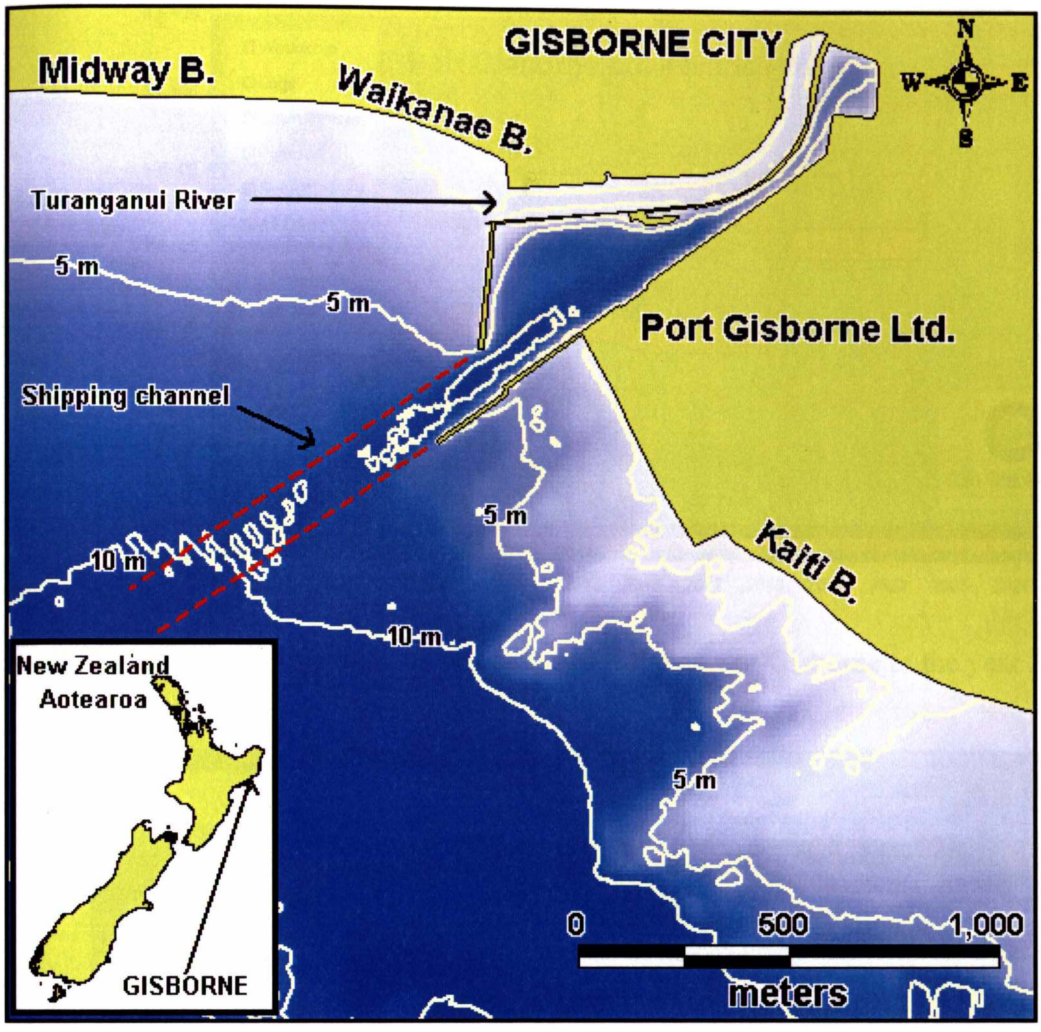

Figure 1.02 Location and bathymetry map of northern Poverty Bay; East Coast New Zealand, showing location of the port adjacent to the Turanganui River, the ports shipping approach channel, and the beaches around the city of Gisborne.

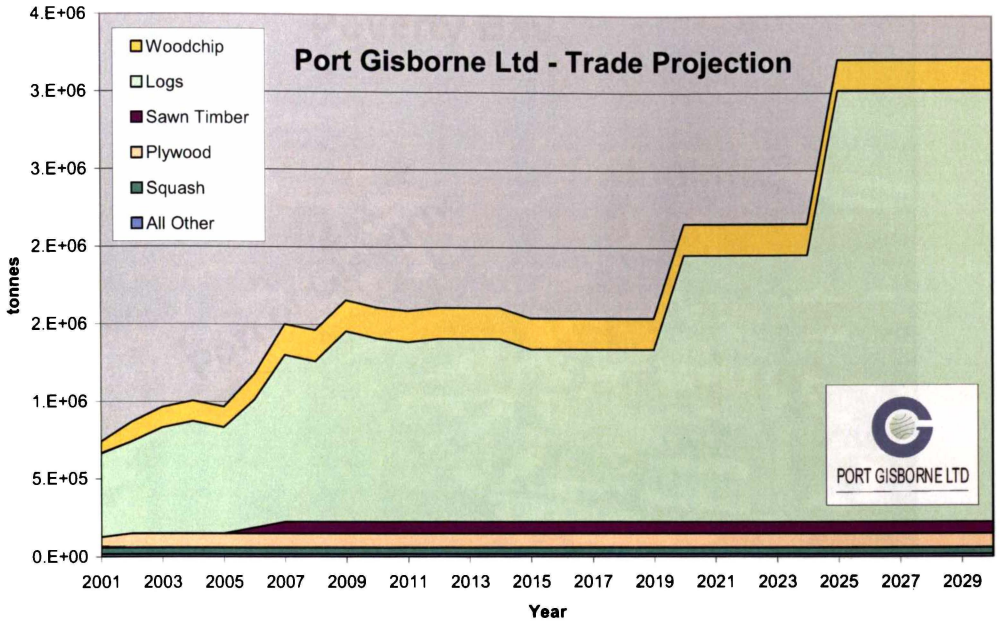

Figure 1.03 Log tonnage projections for the port of Gisborne to the year 2030

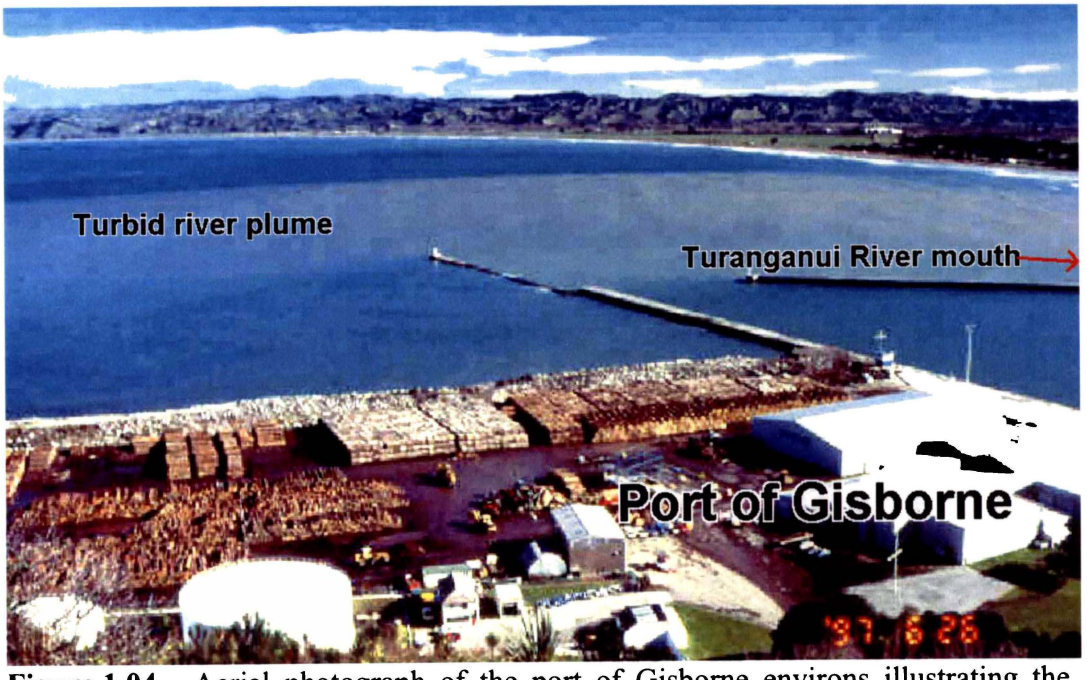

Figure 1.04 Aerial photograph of the port of Gisborne environs illustrating the extent of the turbid water in the Turanganui River plume. The downward flux associated with the discharging of turbid water from the Turanganui River in northern Poverty Bay has not previously been examined in detail (Source Prof. Terry Healy, Waikato University).

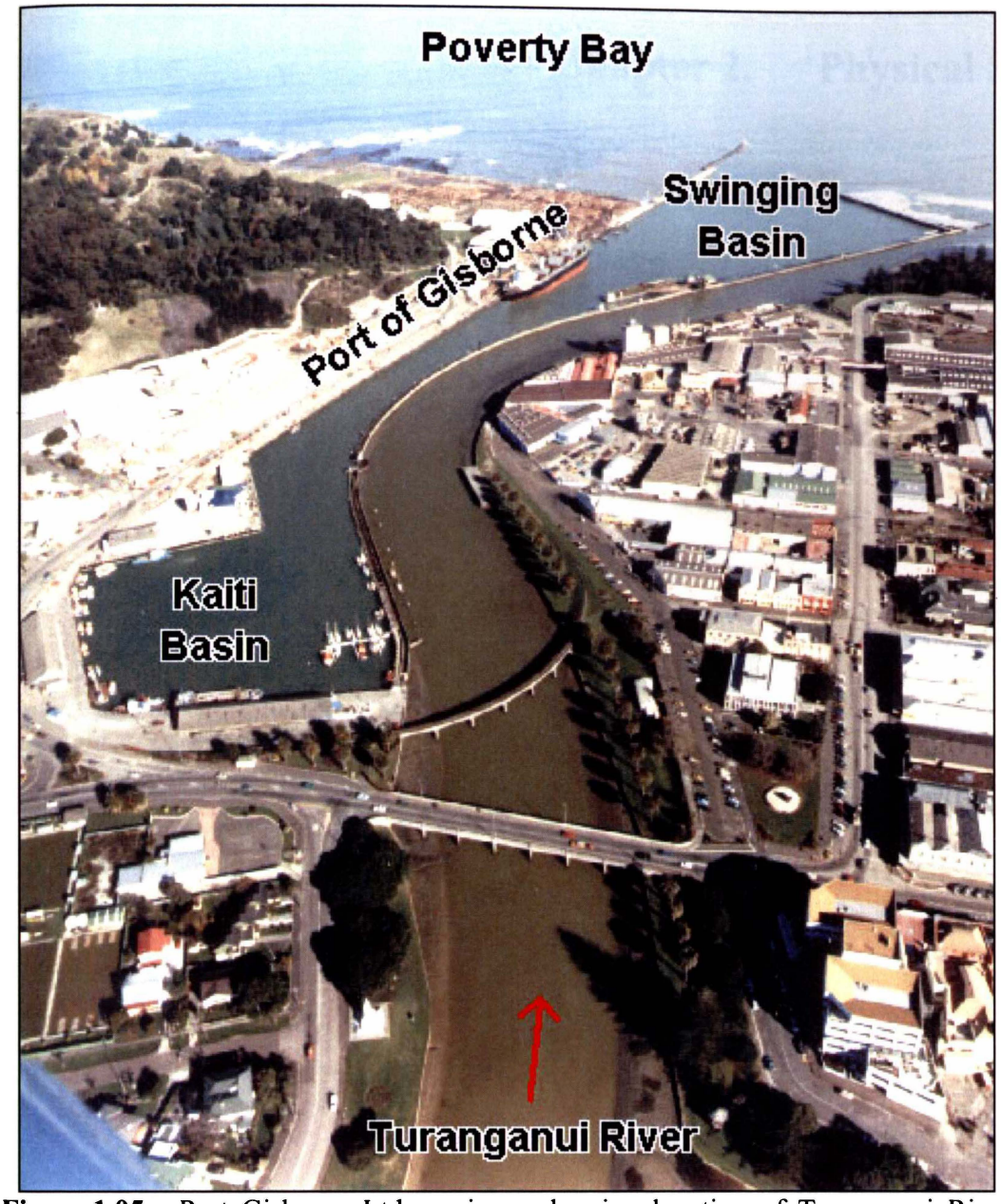

Figure 1.05 Port Gisborne Ltd. environs showing location of Turanganui River adjacent to the port. The water in the river is shown to be significantly more turbid than the water within the either Kaiti Basin, the Swinging Basin or within Poverty Bay (Source Bevan Turnpenny, Turnpenny Associates).

Chapter 2. Physical Setting

2.1 Introduction

The chapter focuses on how the mechanisms and processes effect the morphological and hydrological environment on both a bay-wide scale and within northern Poverty Bay, focusing on the cause and effect of sedimentation problems facing port operations in northern Poverty Bay, particularly the processes that influence sediment transport.

The geomorphology of greater Poverty Bay area is examined. The supply of sediment to the bay from both coastal erosion and fluvial sources and the state of knowledge of the surficial sediment distribution patterns are reviewed. Further, the existing knowledge on the wave and current (tidal, wind, oceanic, density and temperature driven) characteristics are summarized, and climatic processes (temperature ranges, precipitation and wind) are investigated.

2.2 Continental Shelf, Shoreface Origin and Geomorphology

To gain a full understanding of the physical environment in Poverty Bay, the geological setting and geomorphology of the East Coast of New Zealand's North Island needs to be considered, including the physical orientation of the Bay and the geological consequences of the bays location.

The East Coast of New Zealand's North Island is situated on the leading edge of an active plate margin located between the Pacific Plate to the east and Indian-Australian Plate to the west (Figure 2.01); with the Hikurangi Trench lying at the apex of the subduction zone (Moore, 1988; Riddolls, 1987; Suggate et al., 1978a; Suggate et al., 1978b). The coastline exhibits typical aspects of a collision coast as classified by Inman and Nordstrom (1971).

Poverty Bay, on the East Coast of the North Island, forms an approximately 13.4 km semi-circular embayment, bounded to the north by Tuaheni Point and to the south by Young Nick's Head (Figure 2.02). The bay is linked to the inner continental shelf through a 10 km wide entrance (Figure 2.02). The shelf extends approximately 20 km offshore from the entrance, with water depth increasing to in excess of 2000 m within the Hikurangi Trench (Wards, 1976). The bathymetry of the bay is relatively simple with depth contours within the bay largely shore parallel, however greater topographic complexity is evident about the two headlands fringing the bay (Figure 2.02). Surficial sediment gradates from fine sand near the exposed beaches to mud and fine sand with depth (Kensington, 1990; Miller, 1981; Navy, 1989).

Poverty Bay lies on the East Coast Allochthon (Figure 2.03) that forms the north-eastern block of New Zealand's eastern structural belt (Moore, 1988). The East Coast Allochthon is comprised of Cretaceous argillite, Tertiary sandstone and mudstone, and Quaternary alluvium and coastal sands that form the flood plains of Poverty Bay (Figure 2.04). There are also scattered areas of diapiric structures within the Tertiary sediment that are interpreted as a late Kaikoura Orogeny development (Suggate et al., 1978a; Suggate et al., 1978b). The Kaikoura Orogeny is responsible for much of the tilting, folding, and faulting found in the sediments

within the East Coast Allochthon (Kingma, 1974; Riddolls, 1987; Suggate et al., 1978a; Suggate et al., 1978b). The Kaikoura Orogeny began in the Miocene and continues into the presence, manifesting itself in high regional uplift rates (Pillans, 1986) and the common occurrence of earthquakes, generally with shallow foci (Hamilton et al., 1966). On average there are approximately 13 earthquakes of magnitude 4.0 or greater on the Richter scale occurring annually within a 100 km radius of Gisborne (Hamilton et al., 1966).

2.3 Sediment Supply to Poverty Bay

2.3.1 Fluvial Sediment Inputs into Poverty Bay

Two main river systems discharge into Poverty Bay, the Waipaoa River in southern Poverty Bay and the Turanganui River in northern Poverty Bay, adjacent to the port of Gisborne (Figure 2.02). Together the two rivers deliver sediment to Poverty Bay carried in suspension and as bedload. The volume of sediment discharged both as suspended and bedload is influenced by,

1. The lithologies that make up the catchments of the Waipaoa and Turanganui rivers (Claridge, 1960; Griffiths and Glasby, 1985; Smith, 1988),

2. The vegetation within the catchments (Claridge, 1960; Smith, 1988),

3. Seismic activity on the East Cape (Reyners, 1989), and

4. The occurrence of high intensity rain fall events, including the frequent occurrence of tropical cyclones impinging on the area (Hessell, 1980).

High sediment loads from the Waipaoa and Turanganui River systems are due, in part, to the rivers drain faulted and highly erodible Tertiary sandstone and mudstone and crushed Cretaceous argillite hill-country catchments (Figure 2.04). Respectively, the Waipaoa and Turanganui River systems drain catchments of approximately 2203 km^2 and 220 km^2 (Griffiths and Glasby, 1985; Smith, 1988).

Using survey data and historical aerial photographs Smith (1988) found that deforestation, associated with European settlement of the Waipaoa and Turanganui catchments, has resulted in the volume of sediment supplied to Poverty Bay beaches increasing by approximately 34% for both the Waipaoa and Turanganui rivers (Table 2.01).

Also, the East Coast of New Zealand, and hence Poverty Bay, experiences high rates of regional uplift, with Pillans (1986) estimating Recent regional uplift rates as high as 1-3 $mm.y^{-1}$. The high regional uplift rates permit rapid incision of streams and rivers into the highly erodible catchment rocks, thereby over-steeping the slopes and making them more susceptible to erosion (Pillans, 1986).

Elevated sediment loads (both bedload and suspended) occur in winter months as a result of the higher average rainfall during winter (Foster and Carter, 1997). The occurrence of tropical and extra-tropical depressions on the East Cape during summer and autumn months also results in high regional rainfall (Hessell, 1980) and

hence relatively large quantities of sediment are expected to be discharged from the river systems during these events.

2.3.1.1 Suspended Sediment River Discharges

An estimated 12.1 x 10^6 tonnes of suspended sediment is discharged into Poverty Bay from the Waipaoa River on an annual basis (Griffiths and Glasby, 1985), whereas the Turanganui River is estimated to contribute approximately 5% of the Waipaoa River, i.e. ~0.69x10^6 tonnes.yr^{-1} of sediment into Poverty Bay (Gisborne District Council, 1994). This corresponds to a catchment specific annual suspended yield of 5856 tonnes.km^{-2} and 3136 tonnes.km^{-2} per year for the Waipaoa and Turanganui Rivers respectively, where the catchment specific annual yield is calculated as:

$$\text{Catchment specific suspended yield} = \frac{\text{Combined suspended sediment load}}{\text{Catchment area}} \qquad (2.01)$$

Therefore, based on data collected by Griffiths and Glasby (1985) the catchment specific annual suspended yields for the Waipaoa and Turanganui rivers are the 8th and 10th largest in New Zealand respectively.

2.3.1.1 Bedload Sediment River Discharges

As well as discharging sediment into Poverty Bay in suspension, both the Turanganui and the Waipaoa rivers discharge sediment carried as bedload into the bay. Griffiths and Glasby (1985) define bedload as that material too coarse to be sampled by a suspension sediment sampler, i.e. the gravel class range of the Wentworth Scale (Appendix I) as defined by Folk (1968). The amount of sediment being discharged as bedload is highly dependent on the flow-rate of the river and therefore the proceeding rainfall in the river catchment. As such, bedload volumes show a seasonal variability, with a combined summer average for both the Waipaoa and Turanganui rivers of 0.2 x 10^6 tonnes.yr^{-1} and a combined winter average of 1.25 x 10^6 tonnes.yr^{-1} (Foster and Carter, 1997).

2.3.2 Sediment Inputs from Coastal Erosion.

Gibb (1978) identified areas of localized cliff erosion occurring at Tuaheni Point and Sponge Bay (Figure 2.02). Additionally, Miller (1981) demonstrated that the steep cliffs at Young Nick's Head were also a source of some material, as evidenced by the increase in rock fragments in sediments close to Young Nick's Head and the trends of heavy minerals in beach sediments. Smith (1988), based on aerial photographs and surveys, estimates approximately 2000 m^3 of sediment annually is deposited onto Poverty Bay beaches from both the cliffs east of Kaiti Beach and the cliffs of Young Nick's Head (i.e. 4000 m^3 total, Table 2.01).

2.3.3 Sediment Supply to Poverty Bay Beaches

Smith (1988) noted that the net sediment budget for beaches in Poverty Bay is positive and estimates that the Waipaoa and the Turanganui River supply ~47,000 $m^3.yr^{-1}$ and 4000 $m^3.yr^{-1}$ of sandy sediment respectively onto the Poverty Bay beaches (Table 2.01). The high volume of sediment being deposited onto the beaches in Poverty Bay has resulted in beach progradation Smith (1988). Using survey and aerial photographs Smith (1988) calculated beach progradation rates of between 0.5 $m.yr^{-1}$ and 5.6 $m.yr^{-1}$ (Table 2.02), with an average of 1.6 $m.yr^{-1}$. Highest progradation rates are found near the mouth of the Waipaoa River (Table 2.02, Figure 2.05) and decrease with distance. Smith (1988) also noted relatively higher progradation rates on the beaches to the south of the Waipaoa River (Table 2.02 and Figure 2.05), suggesting a southerly directed net sediment transport. Pullar and Penhale (1970) suggest that the relatively high volume of sediment discharged into Poverty Bay from the Turanganui and Waipaoa Rivers is causing a gradual infilling of the bay. The Poverty Bay lowlands are believed to have originated from this gradual infilling and are characterized by Quaternary rocks and unconsolidated gravelly, sandy or silty pumiceous sediment (Kingma, 1964; Kingma, 1965).

2.4 Surficial Sediment Distribution

The deposition of sediment into Poverty Bay (from cliff erosion and river discharging) and the sediment entrainment and transport processes operating in the bay control the distribution and extent of the textural types.

Miller (1981) identified five surficial sediment textural types in Poverty Bay;

i. *Well sorted* sands near the beaches,

ii. *Moderately well sorted* silty-sands covering most of the bay,

iii. similar to (ii), with more clay evident in the southern corner of Poverty Bay,

iv. a patch of finer sediment near Young Nick's Head, relative to that occurring in (ii) and (iii), and

v. poorly sorted material in and adjacent to the dredge spoil mound.

Surficial sediments in Poverty Bay are comprised of predominantly *Sand* and *Mud* (*Silt* and *Clay*) size classes. Relatively coarse sands are found on the beaches and near the mouth of the Waipaoa River, with silty fine sand and mud extending offshore (Beamsley et al., 1998; Kensington, 1990; Miller, 1981; Sander, 1993). Foster and Carter (1997) noted that the transition zone between predominantly *Sand* and *Mud* surficial sediments showed some temporal variability, which they attributed to seasonal climatic changes. The offshore fining of the surficial sediment reflects the increase in the strength of the dominant sediment entrainment process (wave-orbital currents) with decreased depth, which winnows out the finer sediment closer to shore (Miller, 1981).

As well as the offshore fining of the surficial sediment relatively finer surficial sediments are found in the southern part of the bay in the vicinity of Young Nick's Head (Miller, 1981). The finer surficial sediment in the southern part of Poverty Bay is most likely due to the combination of high fine sediment input from the Waipaoa River and the sheltering effect that Young Nick's Head has on waves approaching from the southerly direction (Black et al., 1997). Additionally, Foster and Carter (1997) noted the presence of a lobe of sediment originating from the Waipaoa River that extends out through Poverty Bay and over the continental shelf. As with the Waipaoa River, Beamsley et al., (1998) note the presence of a lobe of relatively fine surficial sediment about the mouth of the Turanganui River (Figure 2.06). Beamsley et al., (1998) also note an increase in the mean grain size of beach sediment with distance from the mouth of the Turanganui River, presumably a function of the availability of sediment for deposition and the entrainment and transport processes dominating in the environs near the mouth of the river.

Sediments in the Swinging Basin at Gisborne's port (Figure 2.06) are characterized as *Silt* and are finer than other surficial sediment found in northern Poverty Bay (Beamsley et al., 1998), reflecting the amount of sediment available for deposition and the sediment transport processes operating in the Swinging Basin (Beamsley et al., 1997).

The bulk mineral composition of the surficial sediment in Poverty Bay is similar owing to the common source (Miller, 1981). Indeed, Claridge (1960) notes that all the sedimentary rocks in the Turanganui and Waipaoa River catchments have similar mineralogical contents. However, some longshore variation in opaque and heavy mineral compositions of the beach sediments has been observed (Miller, 1981). Opaque minerals, such as hypersthene and augite, have been found to diminish with distance away from the Waipaoa River, whilst the heavy mineral composition on Kaiti Beach is distinct from the rest of the beaches in Poverty Bay (Miller, 1981). It is likely that the heavy mineral composition on Kaiti Beach is derived, in part, from the localised erosion of the wave-cut platform and the local cliffs (Miller, 1981). The variation in heavy mineral composition between Kaiti Beach and the other beaches in Poverty Bay is due to the existing port breakwater acting to prevent sediment from the Kaiti Beach littoral system entering the littoral zone off Waikanae Beach (Healy et al., 1980). Bay-wide, surficial sediment typically contains less than 1.0 % carbon. The organic carbon is derived from the degeneration of plant matter deposited onto the Poverty Bay beaches, whilst inorganic carbon comprises mainly Bivalve shells (Miller, 1981).

2.5 Climatic Processes

New Zealand has a maritime climate consisting of easterly moving anticyclones and low-pressure troughs, with associated frontal systems. Typically, low-pressure and frontal systems bring strong north to north-westerly winds; while high-pressure systems produce more settled conditions with winds usually from the south to southwest (Quayle, 1984). Pickrill and Mitchell,(1979) note a 5-11 day quasi-cyclic rhythmic pattern in the passage of successive troughs of low pressure crossing New Zealand. Additionally the northern part of New Zealand periodically experiences tropical cyclones and extra-tropical depression (Pullar, 1962).

Climatic conditions in Poverty Bay have been recorded at the Gisborne aerodrome since 1937, and are summarized by Hessell (1980). Typically the region experiences a large number of sunshine hours per year, with mild temperatures and low wind speeds.

In prevailing north-westerly winds, Poverty Bay experiences orographic rain shadowing, resulting from the perpendicular orientation of the Raukumara Range to the passage of frontal and low-pressure systems tracking across New Zealand, resulting in warm and dry conditions in Poverty Bay. Conversely, in easterly situations, uplift caused by the Raukumara Ranges often results in high rainfall intensities at all altitudes (Hessell, 1980).

2.5.1 Temperature and Humidity

Gisborne's mean annual air temperature ranges from 9° C in the winter to a summer average of 20° C. The Gisborne region experiences an average of 65 days per year where the air temperature exceeds 24° C, and six where the air temperature exceeds 30° C (Hessell, 1980). In his summary of atmospheric records from between 1937 and 1980, Hessell,(1980) noted air temperatures as high as 38° C during summer months and as low as –3.4° C during winter months. Low temperatures in winter are often caused by katabatic drainage of cold air from the surrounding hills (Hessell, 1980). Ground frosts have been recorded in all months except January and February, however the frequency has not been great (Pullar, 1962). Relative humidity ranges from 62% in December to 82% in July (Pullar, 1962).

2.5.2 Precipitation

Rainfall event intensities on New Zealand's East Coast exhibit both spatial and temporal variability. Highest mean monthly rainfalls occur in the winter months (Hessell, 1980), however high rainfall events associated with the impinging of tropical and extra-tropical depressions on the region occur periodically in the summer and spring months (Pullar, 1962). Northerly and south-easterly winds are the principle rain-producing winds on the East Cape and the spatial variability in rainfall distribution reflects the control topography has on these winds. Coastal mean rainfall along the East Coast varies between approximately 2000 mm (at Waipiro Bay) and 1000 mm near Manutuke (Figure 2.07). As shown in Figure 2.07, mean annual rainfall on the alluvial flood plains of Poverty Bay is approximately 1000 mm/yr, whereas mean annual rainfall in parts of the Raukumara Range is estimated to exceed 4000 mm/yr, however in the more southern parts of the divide and in the Waipaoa River catchment the mean annual rainfall is not expected to exceed 2800 mm/yr (Hessell, 1980).

2.5.3 Wind

Wind causes dynamic forcing of the water, and in Poverty Bay has the ability to direct the Turanganui and Waipaoa River plumes (Black et al., 1997) and create sea and swell waves that can entrain surficial sediment.

Mean annual wind speed at Gisborne is approximately 3-m.s^{-1}, while on average gusts greater than 63 km.h^{-1} are recorded 48 days in the year, and gusts in excess of 96 km.h^{-1} occur only once or twice per year (Hessell, 1980). During spring, summer and autumn months the development of localized Hadley convection cells result in afternoon sea breezes, with winds of up to 26 km.h^{-1} being recorded, particularly during anticyclone conditions (Hessell, 1980; Smith, 1988).

The predominant wind direction is northwest (Figure 2.08). Due to the formation of sea breezes there are markedly fewer north-westerly winds below 20 km/h in the afternoon hours (1200-1700 NZST) than in the morning. Conversely, during the afternoon hours winds directed from southeast reach a maximum, suggesting that the sea breeze is of considerable strength. Winds from the southwest and northeast occur relatively infrequently (Figure 2.08).

2.5.4 PDO and ENSO effect on the Poverty Bay Climate

Given New Zealand's location in the southwest Pacific Ocean there exists the potential for weather systems in New Zealand to be influenced by El Niño Southern Oscillations (*ENSO*) and Pacific Decadal Oscillations (*PDO*).

Nicholls (1992) notes that *ENSO* is a significant source of seasonal and year-to-year climate variability in New Zealand. The strength of the *ENSO* is quantified using the Southern Oscillation Index (*SOI*), which is a measure of the pressure difference between Tahiti and Darwin. Anomalously low values of this index correspond to El Niño conditions, while the opposite conditions, with an anomalously high *SOI* value, are called La Niña. In El Niño conditions, New Zealand tends to experience stronger and more frequent winds from the west in summer, resulting in droughts in east-coast areas such as Poverty Bay. In winter, the winds tend to be more from the south, bringing colder conditions to both the land and the surrounding ocean. This typically results in more annual rainfall in Poverty Bay over the winter months during El Niño conditions, and hence the potential for increased sediment discharge rates into the bay from both the Waipaoa and Turanganui River systems. The La Niña events that occur at the opposite extreme of the Southern Oscillation Index cycle have relatively weaker impacts on New Zealand's climate, with New Zealand tending to experience more north-easterly winds, bringing relatively moist, rainy conditions to the northeast parts of the North Island (i.e. Poverty Bay). The last La Niña event was in 1996. East coast droughts may be common during El Niños, but they can also happen in non El Niño years (for example, the severe 1988-89 drought). Serious east coast droughts do not occur in every El Niño and the districts where droughts occur can vary from one El Niño to another (Mullan, 1996).

Salinger and Mullan, (1998) have identified a long lasting "shift" in New Zealand's climate that occurred around 1977, which they believe is due mainly to a Pacific-wide natural fluctuation that is being termed the Pacific Decadal Oscillation, or *PDO*, as identified by Mantua et al., (1997). The *PDO* appears to exhibits phase reversals about once every 20-30 years. The influence of the *PDO* is well known in the northern Pacific, and has recently been noted in Australian rainfall data (Power et al., 1998). The north and east of the New Zealand's North Island has become 10 percent drier and 5 percent sunnier with more droughts in the last 20 years, which Salinger and Mullan (1998) attribute to the Pacific Decadal Oscillation (*PDO*). The changes have resulted from the strengthening of the anti-cyclonic belt that brings fair

weather to northern New Zealand, and squeezing the stronger westerly wind belt over southern and central New Zealand (Salinger and Mullan, 1998). With a reverse in the *PDO,* the east coast of New Zealand can expect wetter and cooler conditions relative to the current phase of the *PDO.*

2.6 Wave Climate

2.6.1 Previous Studies and Measured Wave Data

Several investigations into the deep-water wave statistics off New Zealand's East Cape and within Poverty Bay have been undertaken.

Harris et al., (1983) using a Datawell Wave Rider accelerometer, measured deep-water wave characteristics off Hicks Bay (Figure 2.09) over a 10-month period between March to December 1979. The deployment site was located in approximately 35 m water depth and was open to waves arriving directly from 310° to 90° T, and with refraction from 270° to 180° T (Figure 2.09). Harris et al., (1983) noted that the site was well situated for recording waves generated by tropical and subtropical wind systems. The maximum significant wave height (Max H_s) recorded during the Hicks Bay deployment was 5.2 m, with a mean significant wave height of 1.55 m. The mean wave period of the data was 9.4 s, with a maximum peak wave period of T = 15 s (Table 2.03).

Miller (1981) used wave data collected from a Wave Rider Buoy deployed in Poverty Bay by the Ministry of Works and Development (*M.W.D.*). The record spanned approximately 7 months between 17th December 1979 and 18th July 1980. The mean wave height and period recorded during the *M.W.D.* Wave Rider Buoy deployment was 1.04 m and 8.72 s respectively (Table 2.03).

Additionally, Black et al. (1997) noted that deep-water wave statistics were measured by The Ministry of Works Department (*M.W.D.*) from a Wave Rider Buoy deployed off Tatapouri Point, 10 km north of Poverty Bay (Figure 2.10). The Wave Rider Buoy record, spanning 28 months between 11th May 1982 and 27th September 1994, provides a comprehensive long-term record of deep-water wave characteristics in the vicinity of Poverty Bay. Wave statistics from the Tatapouri deployment exhibit some similarity to both the Hick's Bay and the *M.W.D.* deployment data. Maximum and mean significant wave heights were 5.2 m and 1.2 m respectively. The maximum wave period was T = 20.2 s and the mean wave period over the deployment period was T = 8.1 s.

Deep-water wave statistics were also measured within Poverty Bay in 1996 using an *InterOcean S4DW* wave/current meter. The Centre of Excellence in Coastal Oceanography and Marine Geology collected the wave/current data during the 1996-97 Assessment of Environmental Effects (*AEE*) investigation as part of Port Gisborne Ltds' resource consent application process. The wave/current meter was deployed on a taut mooring in 20 m water depth, 10 m below the water surface in central Poverty Bay (CM1, Figure 2.09). The maximum wave height was H_{max} = 3.97 m and the root-mean-squared wave height over the deployment period was H_{rms} = 1.57 m. Maximum and mean wave periods over the deployment period were T_p = 16.52 s and T = 10.71 s respectively.

2.6.2 *Inferred Poverty Bay Wave Climate*

As the port at Gisborne is exposed directly to wave approach angles between 200° and 150°T, the Tatapouri Point Wave Rider Buoy data are more likely to be typical of Poverty Bay wave characteristics than are the Hicks Bay data. Additionally, the 28-month Tatapouri wave record is more comprehensive than the shorter 10 month Hick Bay record. However, there is a good comparison between the significant wave height and peak period of the Hicks Bay and *AEE* wave data record (Table 2.03), although this may be due to a seasonality in the wave record as both datasets were recorded over winter months, the *AEE* data set being between July and August, and the Hicks Bay data including autumn through to spring. Indeed, Black et al., (1997) note that the incidence of larger mean wave heights measured during the *AEE* field data collection period is an expected response to the winter wave climate. Maximum significant wave heights were similar for the two deep-water wave records as were the largest waves recorded (7.8 m at Hicks Bay and 8.3 m at Tatapouri Point). Black et al., (1997) concluded that given the proximity of the Tatapouri Point deployment site to Poverty Bay and the sheltering of the Hicks Bay recorder from the southerly swells (which directly affect Port Gisborne, Figure 2.09) inference between the long term deep-water wave climate and the wave record collected during the *AEE*, is best made using the Tatapouri Point data.

Maximum significant wave heights and peak periods for the entire data set were greater for the 28-month Tatapouri Point deployment than for the *AEE* deployment (Table 2.03). The maximum wave height recorded during the *AEE* two-month period was approximately H_{max} = 4 m (Table 2.03), which was equalled or exceeded 21 times over the 28 month Wave Rider Buoy deployment (Black et al., 1997). The maximum deep-water wave height recorded during the Tatapouri Point deployment was H_{max} = 8.3 m (Table 2.03). The mean spectral period for the Tatapouri dataset is T = 8.1 seconds, and T = 10.7 seconds for the *AEE* dataset (Table 2.03). Maximum spectral periods for the Tatapouri and *AEE* deployments are Tp = 20.2 and Tp = 16.5 seconds respectively (Table 2.03). Differences in measured spectral periods between the two deployments are most likely due to the time frame of the records and the fact that the wave/current meter in the *AEE* deployment was on a taut mooring approximately 10 m below the surface, resulting in the attenuation of some of the higher frequency wave data.

2.6.3 *20-year Hindcast Wave Characteristics*

20-year hindcast directional wave data at the entrance to Poverty Bay (Figure 2.10) was obtained from NIWA. The data was generated using a 3rd generation WAM (*Wave Action Model*) numerical model, which accommodates the processes of wind generation, white-capping and bottom friction, and includes a direct estimate of non-linear energy transfer through four-wave interactions.

Figure 2.11 illustrates the wave height probability of occurrence based on the hindcast data. The wave height occurrence data displays a typical Chi-square distribution; with an average and medium significant wave height (H_{sig}) at the entrance to Poverty Bay of approximately 1.3 m and 1.15 m respectively, while the maximum predicted wave during the 20-year period is 7.8 m (Figure 2.11). Further,

based on the hindcast wave data the predominant wave direction is towards the NW, i.e. coming from the SE quarter (Figure 2.12). Joint probability statistical analysis illustrates that larger wave events are more likely to originate from the southerly quarter (Figure 2.13), while the predominant peak wave period ranges between 8-11 s (Figure 2.14). The largest wave predicted in the 20-year hindcast data is 7.8 m.

Extremal probability distribution analysis of the wave height data in accordance with the method outlined by the U.S. Army Corps of Engineers (United States Army Corps of Engineers, 2001) was conducted to determine the wave magnitude of different return period storm events. Extremal probability distribution analysis extends available information bases to a longer time period by generating additional realizations of the process and ensuring that the realizations are statistically consistent with known information (United States Army Corps of Engineers, 2001). Different probability distribution functions were investigated (Fisher-Tippett Type 1 and 2, Weibull distribution with k = 1, 1.4 and 2) in order to identify the distribution function that best represents the data. The magnitude of the waves with return periods of 2, 5, 10, 25 50 and 100 year are given in Table 2.04, along with the standard deviation, 95% confidence intervals and the probability of occurrence. Based on the extremal probability distribution analysis wave heights of 8.29 and 8.91 m are expected for storms with return periods of 50 and 100 years respectively (Table 2.04).

2.7 Oceanic Currents over the Continental Shelf

The East Cape and the Wairarapa Counter Currents (also known as the Canterbury Current or as an extension of the Southland Current) are the dominant oceanic currents off the East Coast of New Zealand's North Island (Chiswell, 1999b; Heath, 1975).

The East Cape Current is a geostrophic current comprising a surface tongue of subtropical water that runs southwards along the east coast of the North Island, seaward of about the 1000 m isobath (Chiswell and Roemmich, 1998; Heath, 1975). The current extends southwards to approximately the latitude of Cape Palliser (~ 42°S) at which point the current bifurcates and part of the current turns back on itself and heads northeast-wards (Figure 2.15). The remainder of the East Cape Current flows into and along the subtropical convergence, providing the northern source of subtropical water to the Subtropical Convergence Zone (Figure 2.15).

As illustrated in Figure 2.15, the Wairarapa Counter Current brings subtropical water, though of a lower temperature and salinity, from the south along the east coast of the South Island into the Subtropical Convergence Zone over the Chatham Rise (Chiswell and Roemmich, 1998; Heath, 1975). Part of the Wairarapa Counter Current extends northwards along the east coast of the North Island. The extent to which the Wairarapa Counter Current extends up the east coast is open to some debate. Ridgway (1960), in his study of circulation in Hawke Bay, noted a residual northerly-directed current in surface water that did not appear to be related to the winds over the bay. In contrast, Chiswell and Roemmich (1998) note a southerly-directed residual current off the east coast, north of Poverty Bay. Based on temperature and salinity profiles and seafloor topography Chiswell (1999a) believes that much of the Wairarapa Counter Current re-circulates into the East Cape Current near Mahia Peninsula. However, some current meter data off Waipiro Bay showed

oscillating shelf currents with a small mean flow to the northeast. On the continental shelf directly offshore from Poverty Bay Stephens (1999) found that over a 38-day current meter deployment residual currents were directed northwards, though with an average speed of only 0.014 $m.s^{-1}$, as opposed to approximately 0.20 $m.s^{-1}$ south of Mahia (Chiswell, 1999a). Further, Stephens (1999) was of the opinion that on a daily basis the wind would be far more influential in ocean circulation patterns off Poverty Bay, and that the shelf currents offshore of the bay appear variable with no one direction dominating.

2.8 Poverty Bay Circulation

Black et al., (1997) notes that current dynamics in Poverty Bay are spatially complex and temporally variable. This complexity is due to the processes forcing the current patterns within the bay and include,

1. Inner continental shelf currents'
2. River discharging,
3. Wind up-welling / down-welling,
4. Vertical mixing due to salinity and temperature gradients, and
5. Tidal currents.

2.8.1 Oceanic driven Currents in Poverty Bay

Circulation gyres within the water column in Poverty Bay have been observed by numerous authors, including Williams, (1966), Miller, (1981), Kensington, (1990), Black et al., (1997), and Stephens et al., (1999). The direction of gyre rotation is inherently linked with shelf currents. Numerical modelling, by Black et al., (1997) illustrates that with a northerly flowing shelf current an anti-clockwise gyre is established within Poverty Bay (Figure 2.16), whereas with a southerly flowing shelf current a clockwise rotating gyre is seen (Figure 2.17). Due to the orientation and the seafloor bathymetry of Poverty Bay the dominant gyre appears to flow in an anti-clockwise direction (Stephens et al., 1999). Tuaheni Point in the north of the bay acts to deflect southwest flowing shelf currents offshore away from the bay, while currents flowing northeast are deflected into Poverty Bay by Tuaheni Point to enter along the deeper northeast side of the bay (Stephens et al., 1999). The northeasterly flowing current is likely reinforced by the Coriolis influence, which in the southern hemisphere deflects currents to the left, and therefore has the potential to reinforce the potential for gyre creation in Poverty Bay.

2.8.2 Wind Currents in Poverty Bay

Up-welling in Poverty Bay has been observed in conjunction with offshore winds in excess of 5 $m.s^{-1}$ in both acoustic Doppler current profiles and three-dimensional numerical modelling (Stephens et al., 1999). Offshore (NW) winds occur approximately 45% of the time, and exceed 5 $m.s^{-1}$ for 15% of the time (Figure 2.08), and therefore up-welling is expected to occur frequently (Stephens et al., 2000; Stephens et al., 1999). Stephens et al (2000; 1999) note that the wind-driven surface shear layer and associated up and down-welling exists independently of water stratification associated with river discharge in the bay. Figure 2.18 and 2.19

illustrates the conceptual model of the wind induced circulation patterns in Poverty Bay under offshore and onshore wind conditions respectively.

Using regression analyses, Black et al., (1997) found that there is a poor correlation between current measurements within Poverty Bay and wind strength and direction, and suggests that the wind, although responsible for surface plume movement and coastal up-welling / down-welling, does not dominate over other processes in Poverty Bay.

2.8.3 Tidal Range and Currents

The Tidal range in Poverty Bay is 1.22 m at neap tide, and 1.37 m at spring tide (Gisborne Harbour Board, 1984); therefore the tidal range in Poverty Bay is classified as micro-tidal (Healy and Tahata, 1993).

The dominant *M2* tide propagates northwards up the continental shelf on New Zealand's East Coast and refracts into Poverty Bay with no appreciable phase lag (due to the relatively small aperture of the bay ~ 10 km). Therefore, tidal currents are minor (Black et al., 1997). Tidal analysis of measured currents showed the maximum semi-diurnal currents to be less than $0.05 m.s^{-1}$(Black et al., 1997).

2.8.4 Salinity/Temperature Currents Associated with River Discharging.

Using numerical modelling, Black et al., (1997) found that the river plumes dominate surface circulation (Figure 2.20). However, the plume movement was highly variable. When discharge volumes were low the river plumes were barely discernible (Figure 2.21), whereas at higher discharge volumes the plume from the Waipaoa River filled much of the bay (Figure 2.22). Black et al., (1997) notes that there is a tendency for lower salinity waters to flow out of Poverty Bay along a transect linking the Waipaoa River and Tuaheni Point, with higher salinities along the northern side of Poverty Bay between the two main river flows.

Salinity dominates the vertical density structure. By comparison temperature gradients are slight. Consequently, temperature influences in Poverty Bay appear to be small relative to other processes. However, thermoclines do act to reduce mixing and isolate the surface layer from the remainder of the water column (Black et al., 1997).

2.9 Summary

The East Coast of New Zealand, and hence Poverty Bay, is situated on the leading edge of an active tectonic boundary, formed by the collision between the Indian-Australian Plate to the west and the Pacific Plate to the east (Figure 2.01, Moore, 1988; Riddolls, 1987; Suggate et al., 1978a; Suggate et al., 1978b). The high regional uplift rates of the country rock and common occurrence of earthquakes are a manifestation of this geological setting (Hamilton et al., 1966; Pillans, 1986). Tertiary mud- and sandstones, with outcroppings of Cretaceous Argillite, dominate

the rock units within the Poverty Bay catchment. Coastal sands and river flood planes are comprised of Quaternary alluvium (Figure 2.04, Riddolls, 1987).

The seismic activity and the lithologies that comprise the Poverty Bay hinterland, together with high intensity rainfall events and vegetation cover are the main factors influencing the supply of sediment to Poverty Bay (Claridge, 1960; Griffiths and Glasby, 1985; Hessell, 1980; Reyners, 1989; Smith, 1988). The principle means by which sediment is supplied to Poverty Bay is through suspended and bedload sediment river discharge. The two main rivers that discharge into the bay are the Waipaoa River in the south and the Turanganui River adjacent to Port Gisborne in northern Poverty Bay (Figure 2.02). Together, the two rivers deposit in excess of 13×10^6 tonnes per year into Poverty Bay by both bedload and suspended sediment transport (Council, 1994; Griffiths and Glasby, 1985). A comparatively small volume of sediment (4000 m^3) is supplied to Poverty Bay from coastal and cliff erosion (Miller, 1981; Smith, 1988). Smith, (1988) notes that the supply of sediment into Poverty Bay via both river discharging and coastal erosion (including cliff erosion) results in a positive net sediment budget for the beaches in the bay, and hence long-term beach progradation, particularly in the areas adjacent to the mouth of the Waipaoa River (Figure 2.05).

The Waipaoa and Turanganui River systems also influence the surficial sediment distribution, along with sediment entrainment (typically wave-orbital currents) and transport processes (residual currents). Surficial sediments are comprised of predominantly Sand and Mud size classes, with coarser sediments found on the beaches and near the mouth of the Waipaoa River (Beamsley et al., 1998; Kensington, 1990; Miller, 1981; Sander, 1993). Surficial sediments become finer with increased water depth, reflecting the relative decrease in wave-orbital currents (the dominant sediment entrainment process) with increased depth (Miller, 1981). An area of relatively finer sediment is located in the lee of Young Nick's Head, in southern Poverty Bay (Figure 2.02), which is attributed to the sheltering affect on the southerly wave climate afforded by Young Nick's Head, and the high fine sediment input from the Waipaoa River (Black et al., 1997; Miller, 1981). Lobes of relatively finer sediment have also been observed radiating out from both the Waipaoa and Turanganui River mouths (Beamsley et al., 1998; Foster and Carter, 1997). Surficial sediment in the ports' Swinging Basin are finer than other sediment found in northern Poverty Bay, owing to the volume of sediment available for deposition and entrainment processes operating within the Swinging Basin (Beamsley et al., 1998).

New Zealand has a maritime climate consisting of easterly moving anticyclones and low-pressure troughs, with associated frontal systems (Quayle, 1984). Low pressure and frontal systems tend to bring north to north-westerly wind ahead of the front, which, due to the perpendicular orientation of the Raukumara Range to the passage of the low-pressure and frontal systems (Figure 2.03), results in orographic rain shadowing on the East Coast of New Zealand. Conversely, in winds from the easterly quarter orographic uplift of air masses often results in high rainfall intensities at all altitudes (Hessell, 1980).

Intensities of rainfall events exhibit both spatial and temporal variability. Highest monthly averages typically occur in the winter months, however high intensity rainfall events associated with tropical and extra-tropical depressions occur periodically in the summer and autumn months. The topography of the East Coast also influences rainfall intensities, with an estimated yearly average of 1000 mm/yr

and 4000 mm/yr recorded for the alluvial flood planes of Poverty Bay and in parts of the Raukumara Range respectively (Hessell, 1980).

The mean annual wind speeds at Gisborne are approximately 3-m.s^{-1}, while winds in excess of 26.7 m.s^{-1} are recorded, on average, twice a year. During spring, summer and autumn months convection cells result in afternoon sea breezes, particularly during anticyclone conditions. The predominant wind direction is northwest (Figure 2.08), with winds from the southwest and northeast occurring relatively infrequently (Hessell, 1980; Smith, 1988).

Longer period changes in New Zealand's climatic conditions have been attributed to El Niño Southern Oscillations (*ENSO*) and Pacific Decadal Oscillations (*PDO*). During El Niño conditions New Zealand tends to experience stronger and more frequent droughts in east coast areas such as Poverty Bay (Mullan, 1996). In winter, winds tend to be orientated more from the south, resulting in higher rainfall intensities during the winter months, and hence a bi-polar effect in seasonal rainfall averages, with drought conditions over the summer months and relatively high monthly rainfalls averages in winter (Mullan, 1996). La Niña events tend to have a weaker impact on New Zealand's climate, with north-easterly wind conditions predominating over New Zealand, bringing moist, rainy conditions to eastern New Zealand (Mullan, 1996). Additionally, long-term climatic trends in New Zealand show that the North Island has become 10% drier and 5% sunnier in the last 20 years, which Salinger and Mullan (1998) attribute to the current phase of the *PDO*, which brings fair weather to northern New Zealand and squeezes stronger westerly winds over southern and central New Zealand. A reversal in the *PDO* would result in wetter conditions for much of New Zealand (Salinger and Mullan, 1998).

Several investigations into the deepwater wave climate off New Zealand's East Coast have been conducted (Black et al., 1997; Harris et al., 1983; Miller, 1981). Maximum wave heights in excess of $H_{max} = 7$ m have been recorded off both Tatapouri Point and Hicks Bay (Figure 2.09), whilst mean significant deep-water wave height is fairly consistent for all data sets, at approximately 1.55 m (Figure 2.09, Table 2.03). Mean spectral periods range between $T = 10.7$ to $T = 8.1$ seconds, whilst maximum spectral periods range between $T_p = 15$ to $T_p = 20.2$ seconds. The measured wave height distribution is similar to the 20-year hindcast wave data, which suggests an average H_{sig} for the entrance to Poverty Bay of 1.3 m and a maximum H_{sig} during the 20-year hindcast period of 7.8 m (Figure 2.11). Extremal probability analysis suggests storm events with return periods of 50 and 100 years will result in significant wave heights of 8.29 and 8.91 m respectively.

Circulation patterns within Poverty Bay are influenced by several processes including, oceanic circulation over the continental shelf, wind, tides, and salinity/temperature gradients associated with river discharging (Black et al., 1997). The East Cape and the Wairarapa Counter Current dominate oceanic currents over the continental shelf off the East Coast of New Zealand. The East Cape Current forms a tongue of subtropical water that runs southwards beyond about the 1000 m isobath (Figure 2.15). The Wairarapa Counter Current extends northwards along the East Coast of the North Island (Chiswell, 1999b; Heath, 1975). The extent to which the Wairarapa Counter Current moves northwards has not been established. Stephens (1999) measured a weak residual northward flowing current offshore from Poverty Bay, flowing at a rate of 1.4 cm.s^{-1}. With numerical modelling Black et al., (1997) illustrated that with a northerly flowing shelf current an anti-

clockwise gyre is established within Poverty Bay. Conversely, with a southerly flowing shelf current a clockwise gyre is established within Poverty Bay. Due to the orientation and seafloor topography of Poverty Bay the dominant gyre appears to rotate anti-clockwise (Black et al., 1997). In addition to circulation gyres, wind forced up-welling and down-welling has been observed in both acoustic Doppler current profiles and three-dimensional numerical model runs (Stephens et al., 1999). Currents associated with tidal movements are considered to be minor (Black et al., 1997) due to there being no appreciable phase lag as the tidal wave propagates northwards up the continental shelf on New Zealand's East Coast across the relatively small aperture of the bay (~ 10 km). In contrast river discharging is the dominant process influencing surface circulation patterns within Poverty Bay. However, plume movement shows some dependence on river discharge rates. Vertically, salinity dominates the density structure, whilst thermoclines act to reduce mixing and isolate the surface layer from the remainder of the water column (Black et al., 1997).

Table 2.01 Sources and estimated volumes of sediment supplied to the Poverty Bay beaches, pre- and post-European settlement (m^3 per year).

Source	Present	Pre-European	% Change
Cliffs east of Kaiti	2000	2000	0
Turanganui River catchment	4000	3000	33
Waipaoa River catchment	47000	35000	34
Cliffs of Young Nick's Head	2000	2000	0
Total	55000	42000	31

(After Smith, 1988)

Table 2.02 Beach progradation and cliff retreat around Poverty Bay 1886-1975. Values in $m.yr^{-1}$; minus values refer to erosion. For locations refer to Figure 2.05.

Site	1886-1975	Site	1886-1975
L'	0	1	1.5
X	-0.4	2	1.3
V	-0.1	3	1.1
S	-0.2	4	0.9
O	-0.3	5	0.7
L	0	6	0.7
I	0	7	0.6
H	0.8	8	0.5
G	0.9	9	0.5
F	1.7	10	0
E	2.7	11	-0.7
D	2.8	12	-0.7
C	3.3		
B	3.7		
A	5.6		

(After Smith, 1988)

Table 2.03 Comparison between deep-water wave spectral statistics obtained from Hicks Bay (March to December 1979), offshore from Tatapouri Point (11th May 1982 and 27th Sept. 1984) and within Poverty Bay during the 1996-7 *AEE* (2nd July and 29th August 1996). Wave gauge locations are shown in Figure 2.09.

Wave Spectral Statistics				
	Hicks Bay	1997 AEE	Tatapouri wave data	Miller, 1981
Max wave recorded (m)	7.8	n/a	8.3	n/a
Max H_s (m)	5.2	3.97	5.74	n/a
Mean H_s (m)	1.55	1.57	1.22	1.04
Mean T (s)	9.4	10.71	8.09	8.72
Max T_p (s)	15	16.52	20.24	n/a

H_s = significant wave height,
T_p = peak wave period.

Table 2.04 Extremal probability distribution analysis of the 20-year hindcast wave height data, giving the magnitude of 2, 5, 10, 25, 50 and 100-year return period storm events. Extremal probability distribution analysis was preformed in accordance with the method outlined by the U.S. Army Corps of Engineers. A Fisher-Tippett Type 1 probability distribution function was found to best represent the data.

Return period (yr)	Hsig (m)	Standard deviation (Hsig)	Confidence Interval (-95%)	Confidence Interval (+95%)	Probability of wave occurrence (Pe)
2	5.41	0.39	4.65	6.17	99.9
5	6.24	0.50	5.26	7.21	89.3
10	6.86	0.58	5.71	8.00	65.1
25	7.67	0.69	6.32	9.03	33.5
50	8.29	0.78	6.77	9.81	18.3
100	8.91	0.86	7.22	10.59	9.6

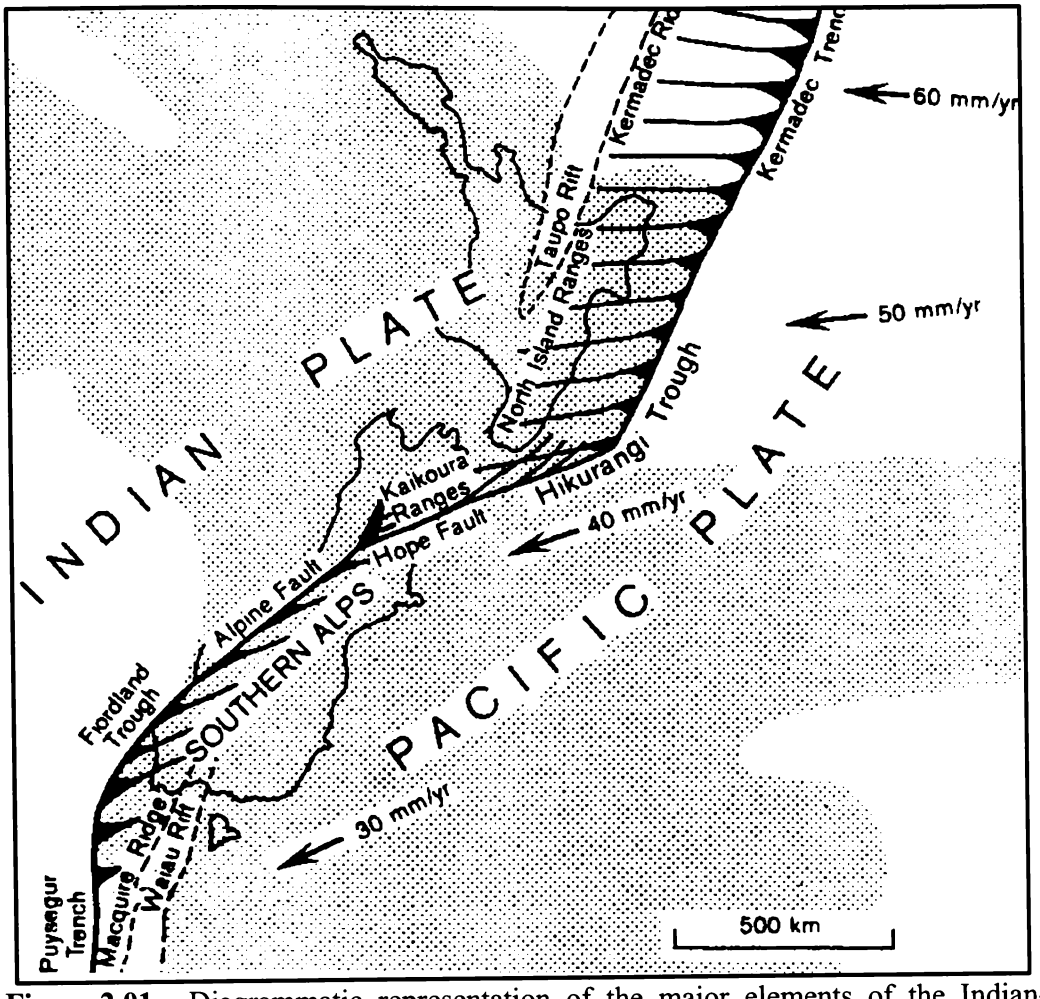

Figure 2.01 Diagrammatic representation of the major elements of the Indian-Australian and Pacific plate that strikes through New Zealand. The stippled area represents probable continental crust. Lines represent the motion of the under-thrusting plate (After Lewis, 1985).

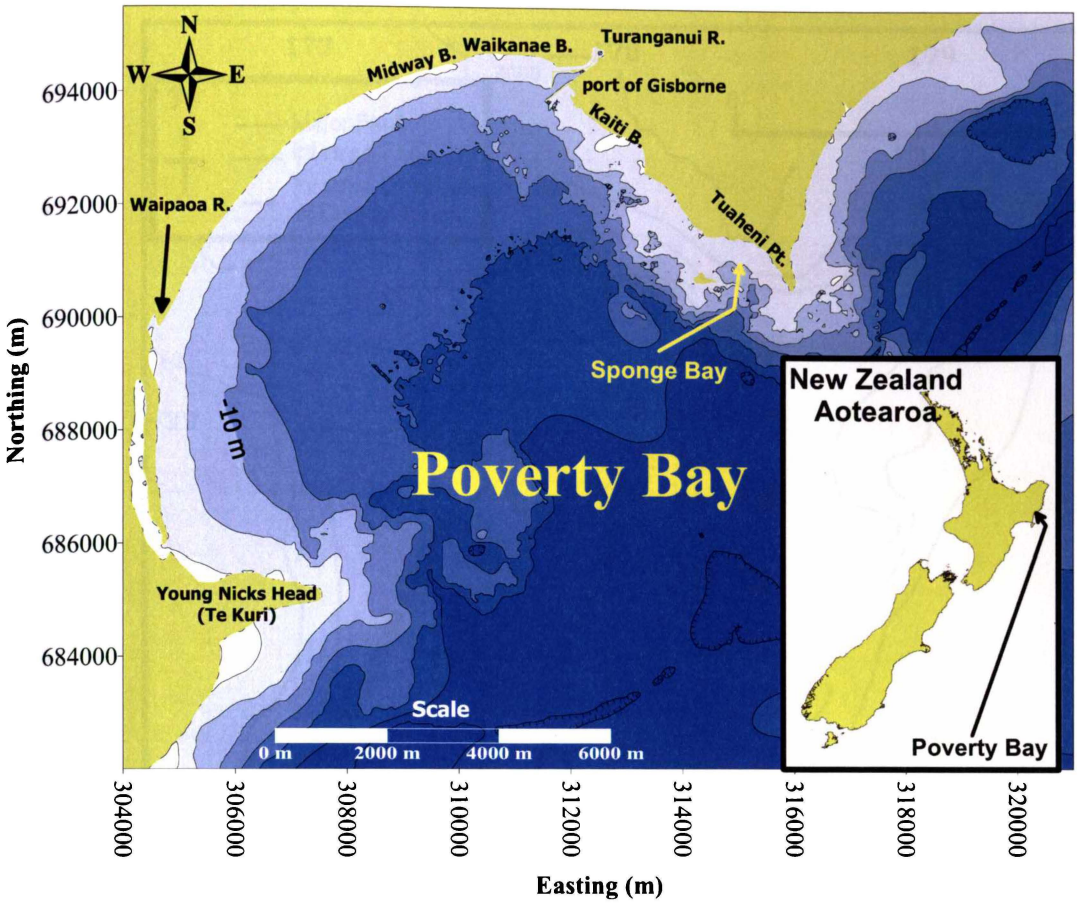

Figure 2.02 Isobathic contour chart of Poverty Bay and inner Continental Shelf illustrating how depth contours within Poverty Bay run approximately shore parallel, however exhibit more complexity about the two headlands bounding the bay.

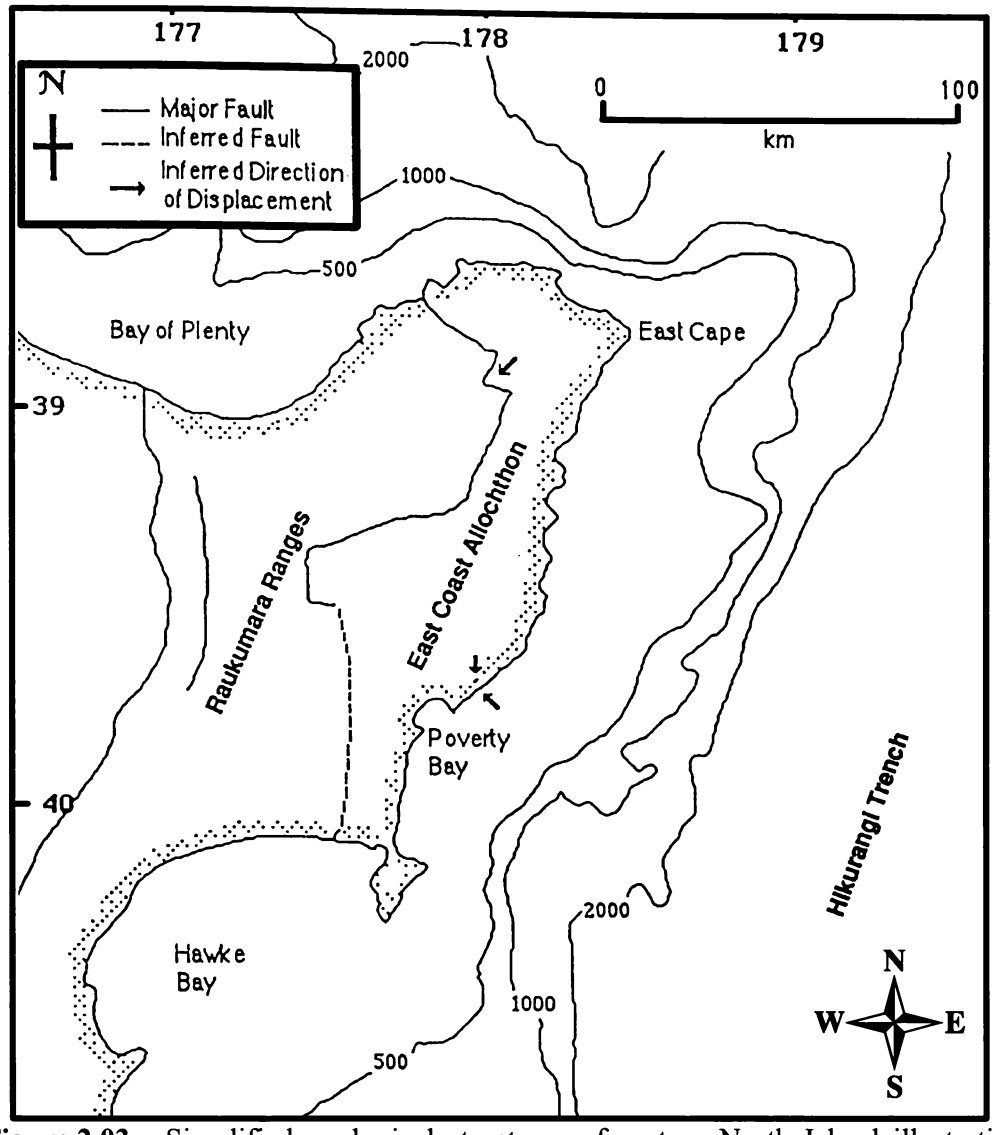

Figure 2.03 Simplified geological structures of eastern North Island illustrating the extent of the East Coast Allochthon and the approximate location of the Hikurangi Trench off the East Coast of New Zealand's North Island (After Moore, 1988).

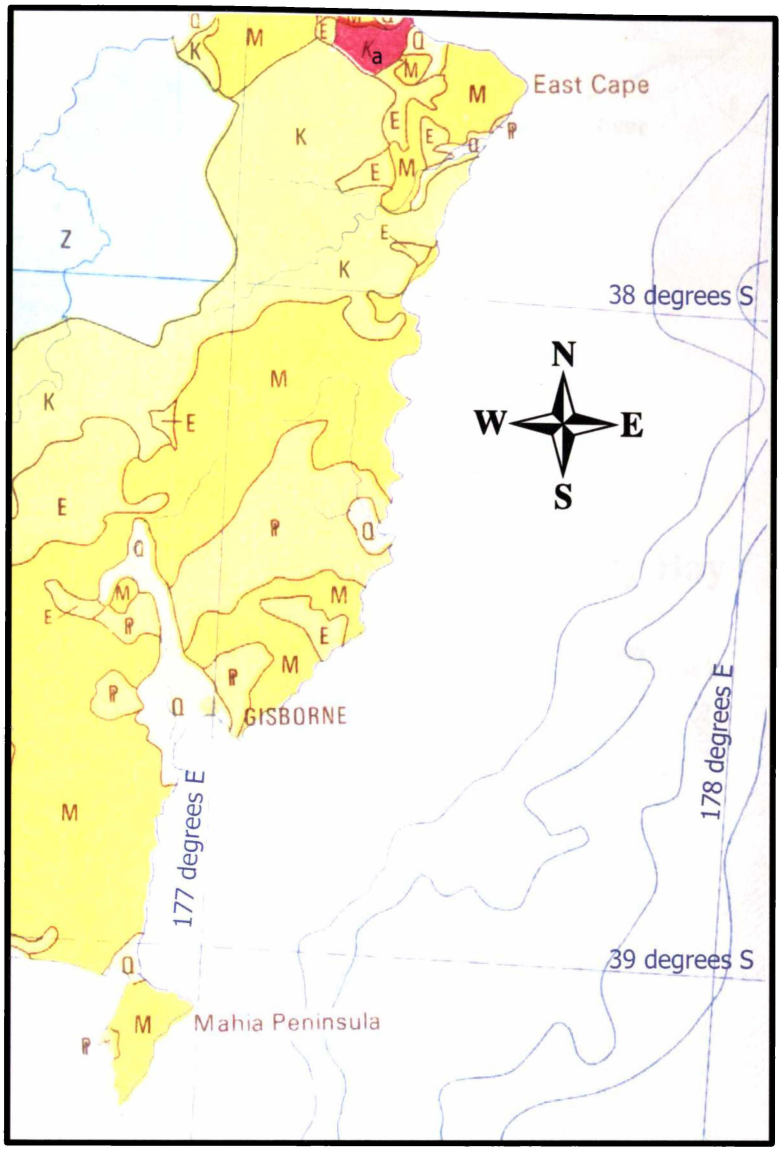

Q	Late Quarternary Alluvium, terrace gravel.
P	Pliocene Marine sandstone, mudstone, conglomerate.
M	Miocene Calcareous and non-calcareous sandstone, mudstone and minor limestone.
E	Eocene sandstone, mudstone and bentonitic mudstone.
K	Cretaceous marine sandstone and mudstone.
Ka	Cretaceous andersite

Figure 2.04 Map showing the distribution of rock facies on the East Cape, North Island, New Zealand, including their geological age of deposition (After Riddolls, 1987).

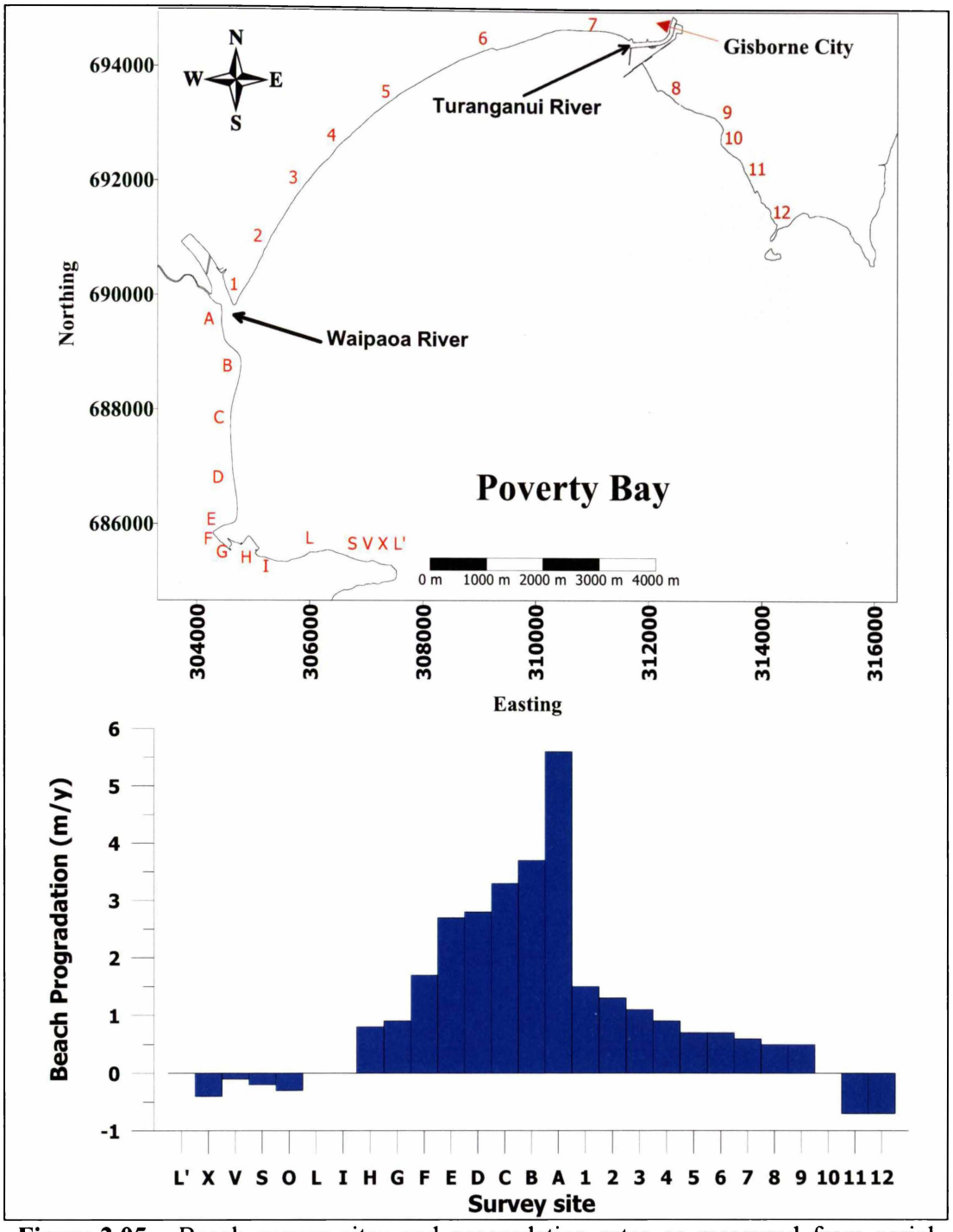

Figure 2.05 Beach survey sites and progradation rates as measured from aerial photographs and beach surveys from 1886-1975. Negative values denote net beach/cliff erosion. Data was assimilated from the work of Smith (1988).

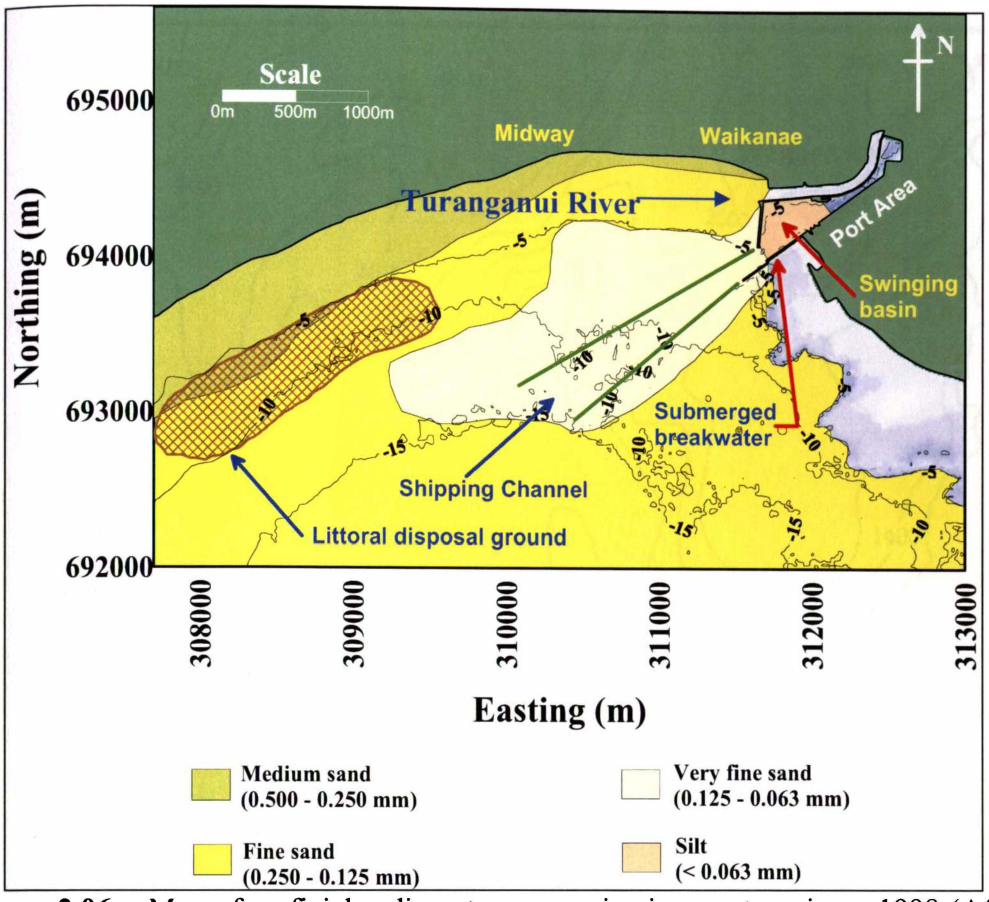

Figure 2.06 Map of surficial sediment mean grain size, port environs 1998 (After Beamsley et al., 1998)

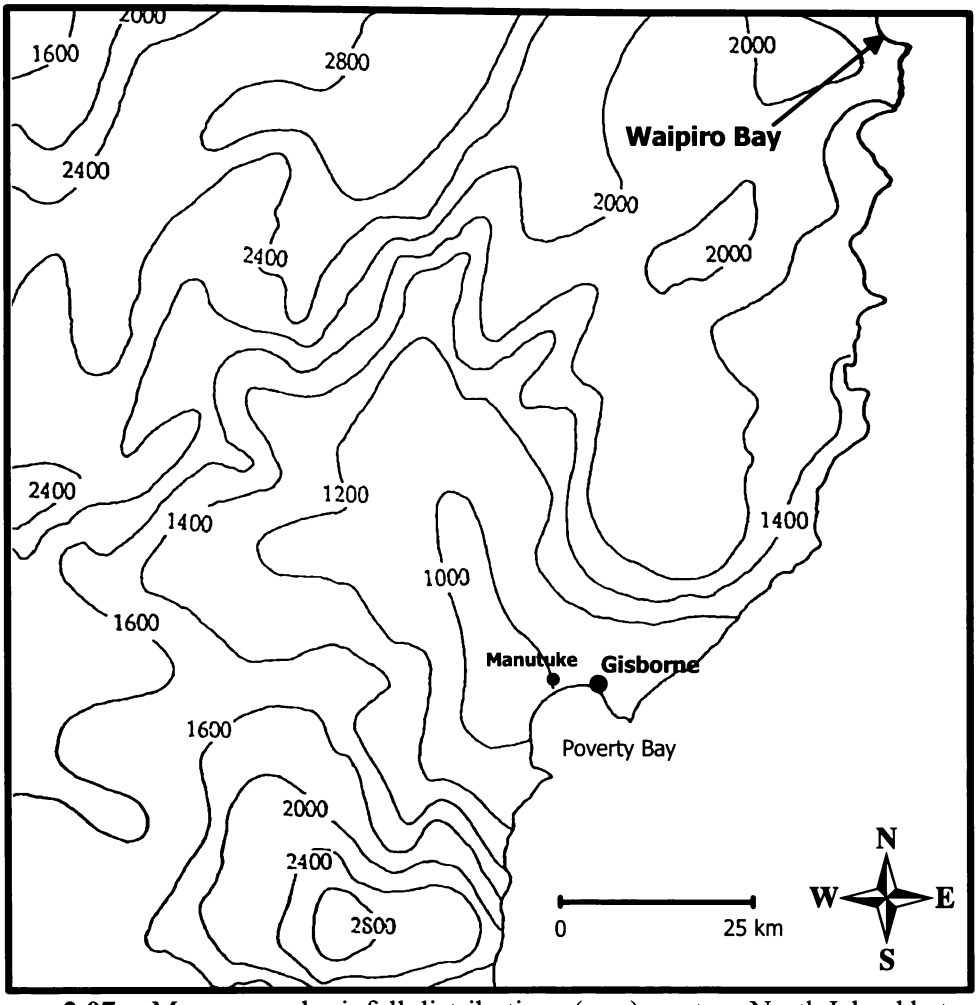

Figure 2.07 Mean annual rainfall distributions (mm), eastern North Island between 1941 and 1970 (After Hessell, 1980).

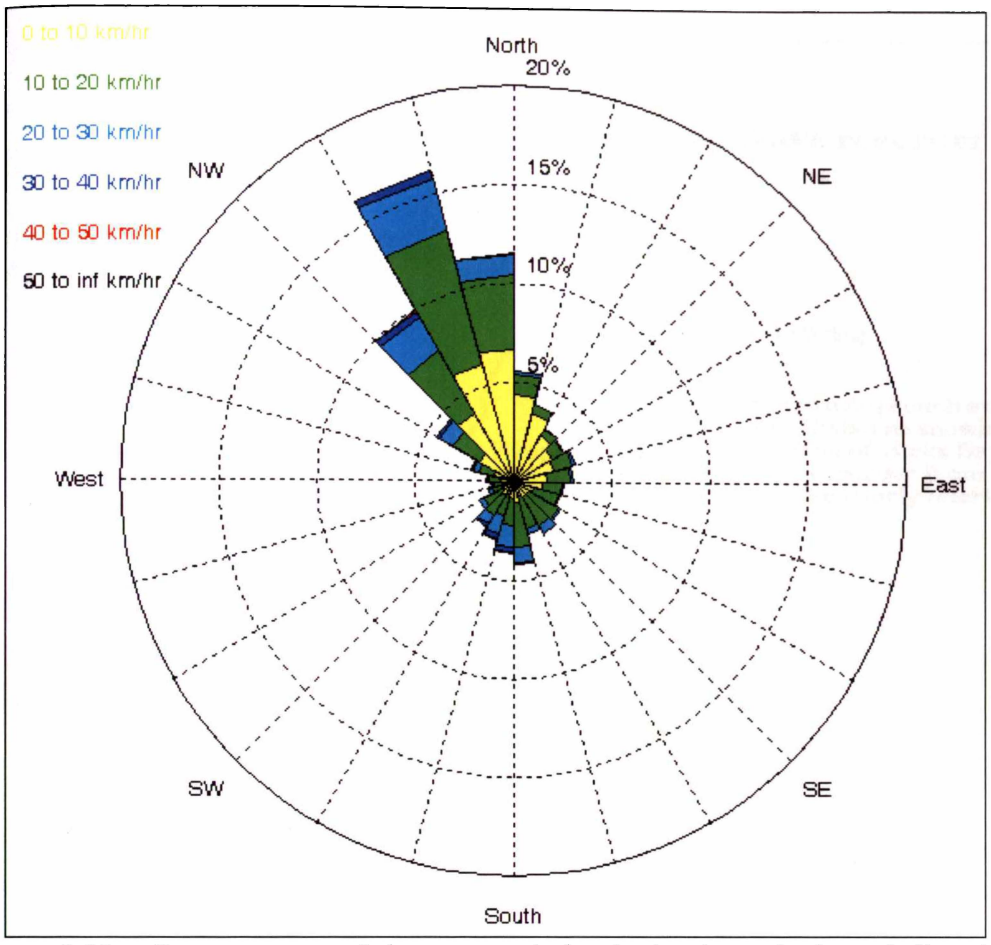

Figure 2.08 Compass rose of the mean wind velocity (magnitude and direction) for the period 1st October 1998 to 1st October 2002. Data supplied by Gisborne District Council and Hydro-Technologies Ltd.

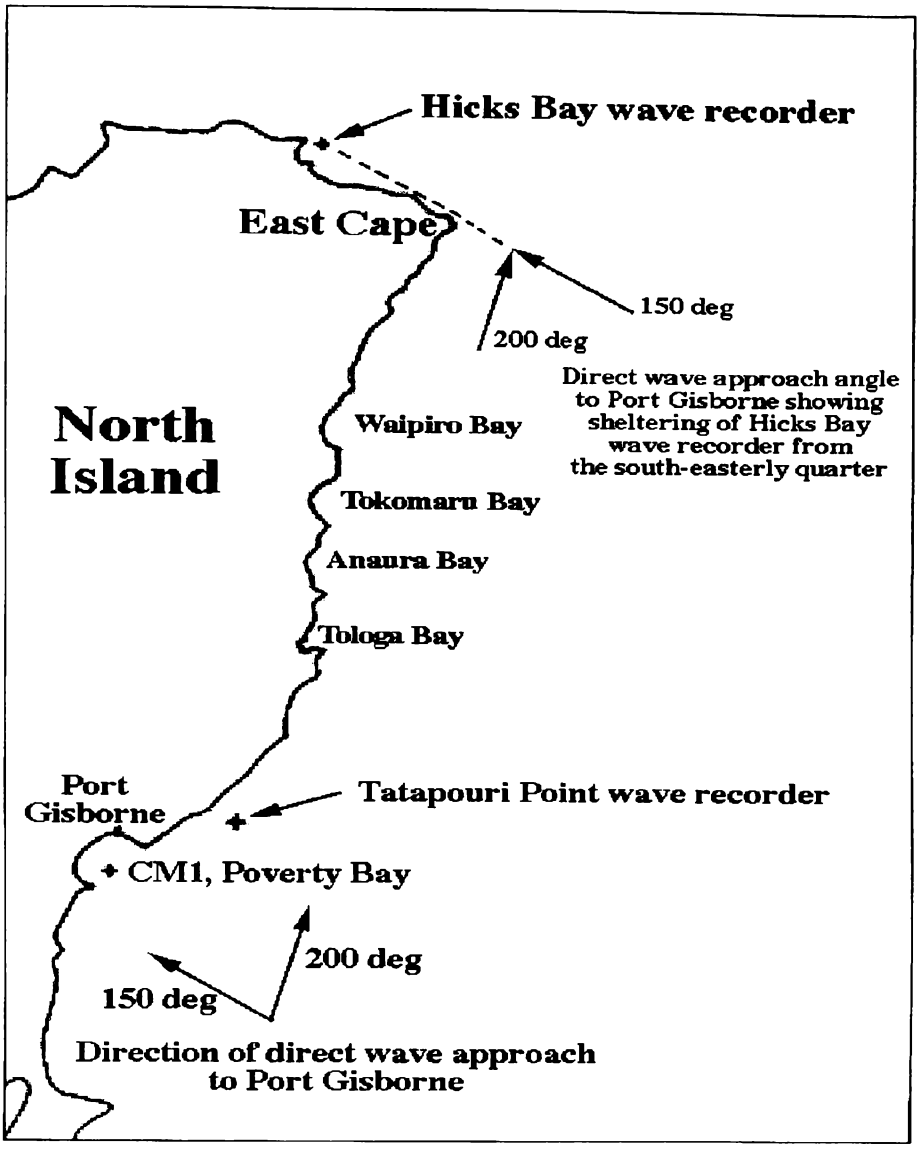

Figure 2.09 Location of wave gauges off eastern North Island, including Hicks Bay, Tatapouri and Poverty Bay wave gauge deployments. Note the sheltering effect of East Cape on waves reaching the Hicks Bay site from the southerly quarter. The position of the Tatapouri Point deployment site is approximate only. Site *CM1* is the wave gauge site used in the Port Gisborne *AEE* field programme during 1996 (After Black et al., 1997).

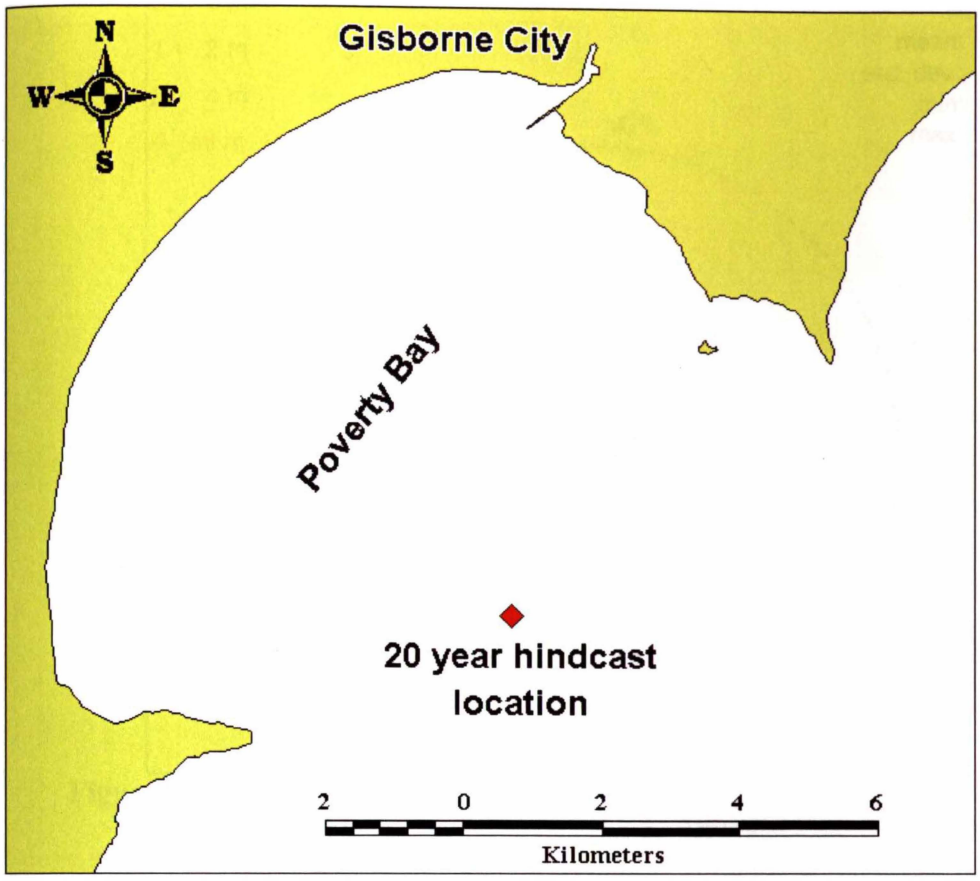

Figure 2.10 20-year hindcast wave data location at the entrance to Poverty Bay, New Zealand.

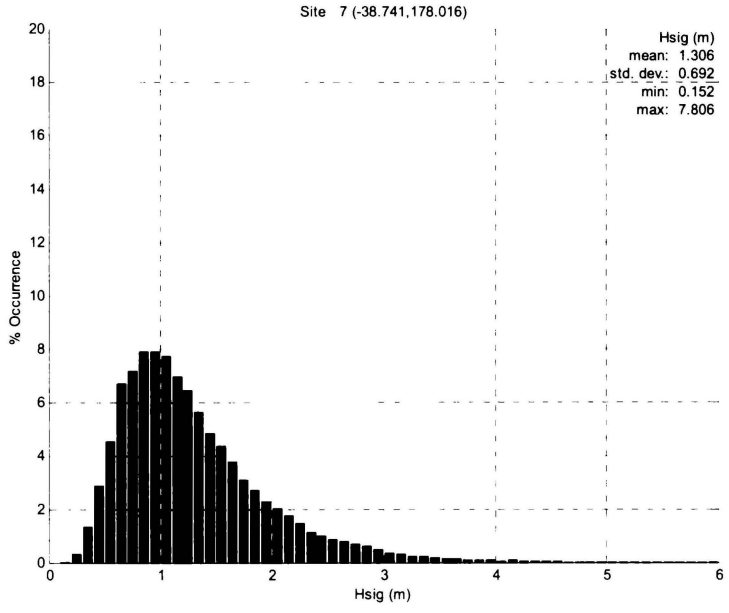

Figure 2.11 20-year hindcast mean significant (H_{sig}) wave height (m) at the entrance to Poverty Bay, New Zealand. Based on the 20-year hindcast record the mean significant wave height at the entrance to Poverty Bay is 1.3 m, the predicted maximum significant wave height during the 20 year period is 7.8 m

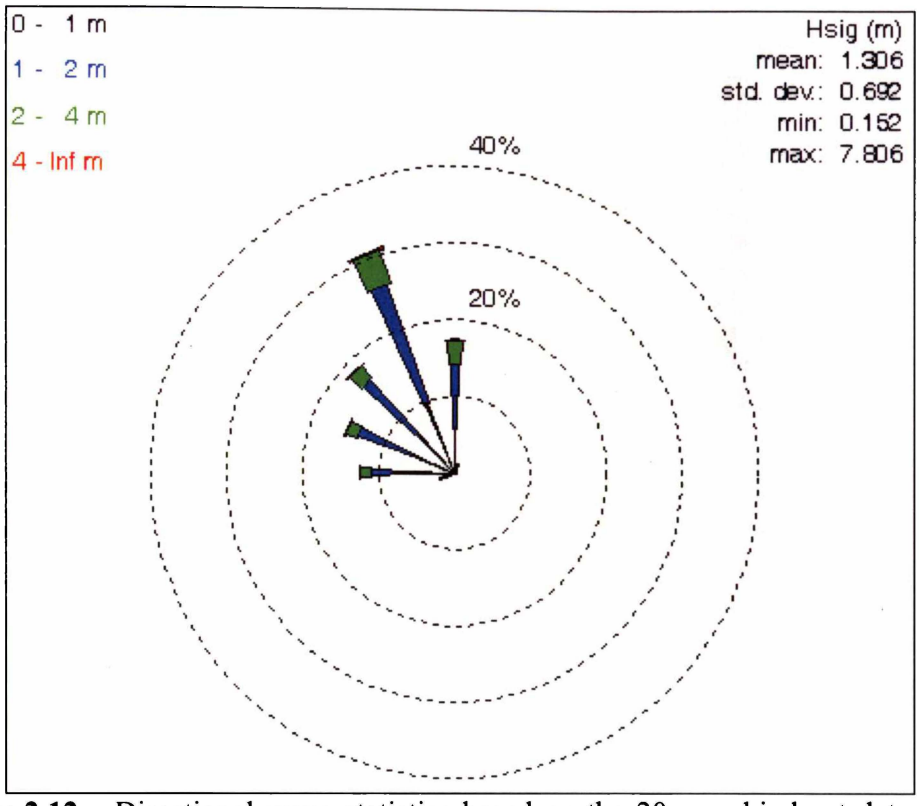

Figure 2.12 Directional wave statistics based on the 20-year hindcast data at the entrance to Poverty Bay, New Zealand. Based on the 20-year hindcast data the dominant wave direction is from the SE direction, i.e. heading to NW, into Poverty Bay

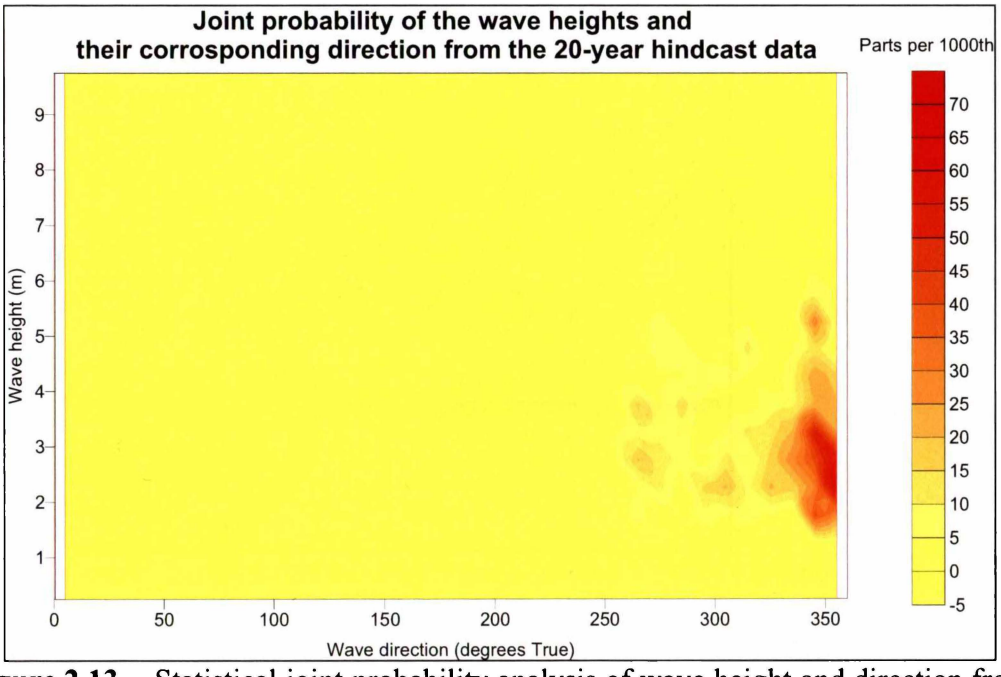

Figure 2.13 Statistical joint probability analysis of wave height and direction from the 20-year hindcast wave data from the entrance to Poverty Bay, New Zealand

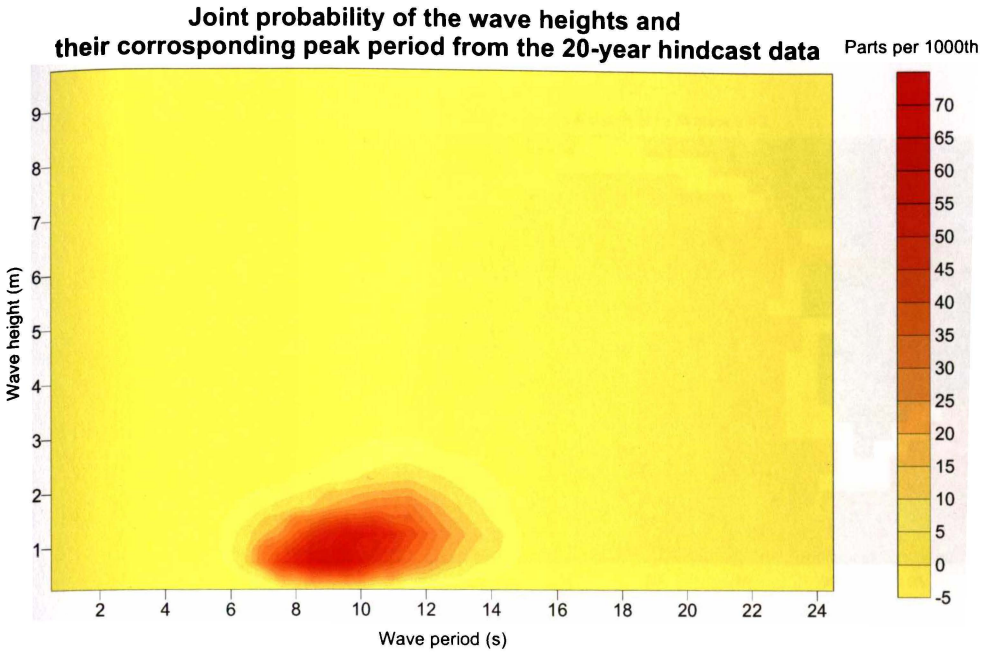

Figure 2.14 Statistical joint probability analysis of wave height and peak period from the 20-year hindcast wave data from the entrance to Poverty Bay, New Zealand

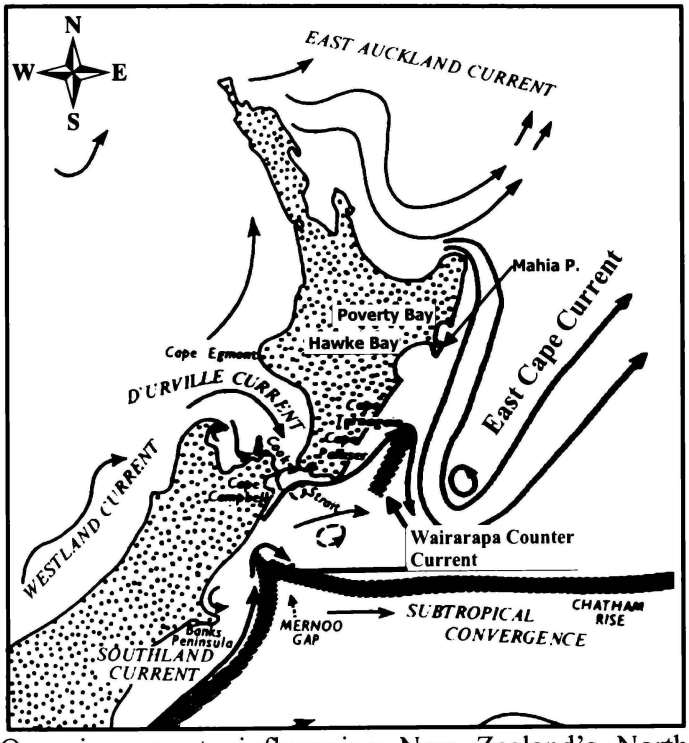

Figure 2.15 Oceanic currents influencing New Zealand's North Island (After Heath, 1975).

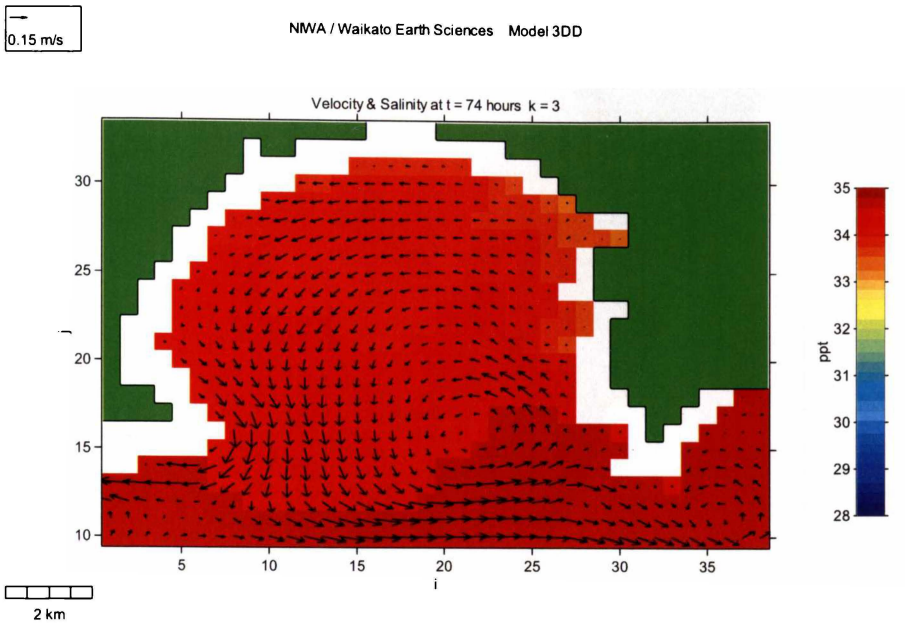

Figure 2.16 Numerical hydrodynamic model output showing a north flowing inner shelf current resulting in an anti-clockwise gyre within Poverty Bay at 3 m below water surface. Arrow bearing depicts current direction, whilst tail length indicates relative strength of the current (After Black et al., 1997).

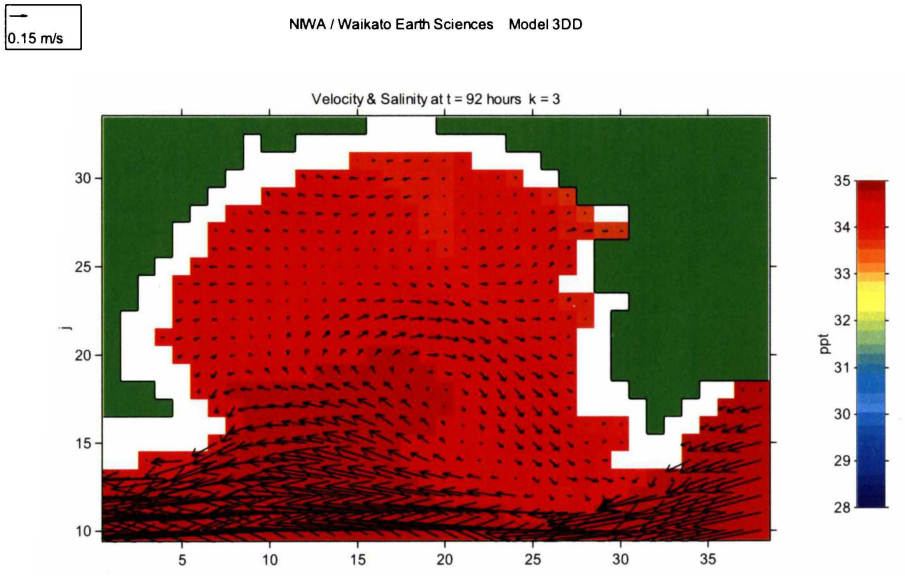

Figure 2.17 Numerical model output showing a south flowing inner shelf current resulting in a clockwise gyre within Poverty Bay at 3 m below water surface. Arrow bearing depicts current direction, whilst tail length indicates relative strength of the current (After Black et al., 1997).

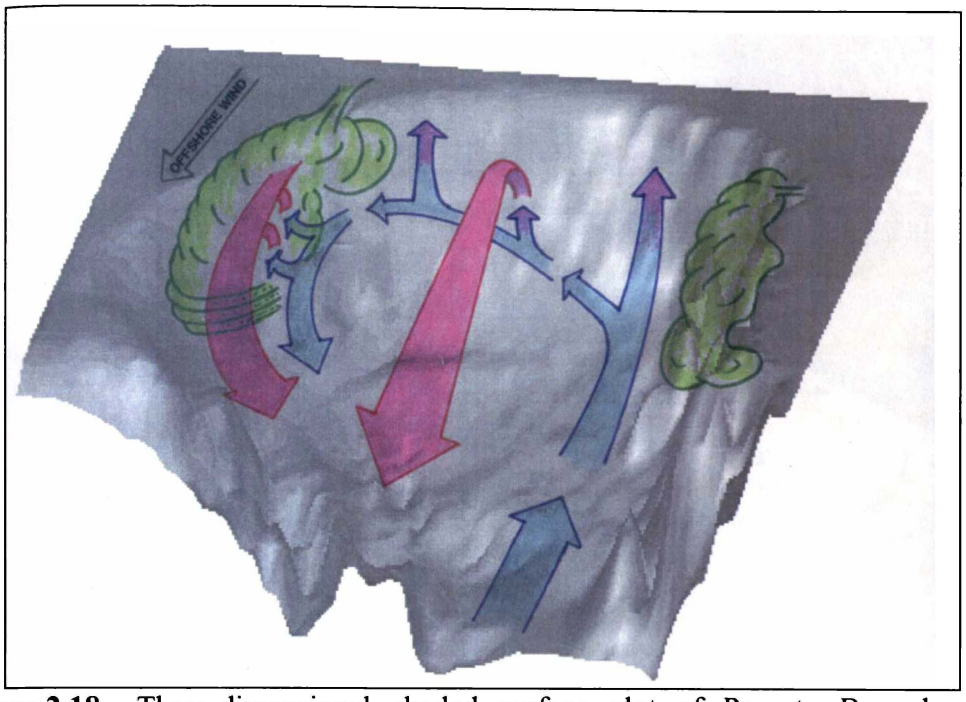

Figure 2.18 Three-dimensional shaded surface plot of Poverty Bay showing typical circulation under offshore winds. Surface water migration is marked in red and bottom water migration in blue. River plumes are depicted in green (After Stephens et al., 2000).

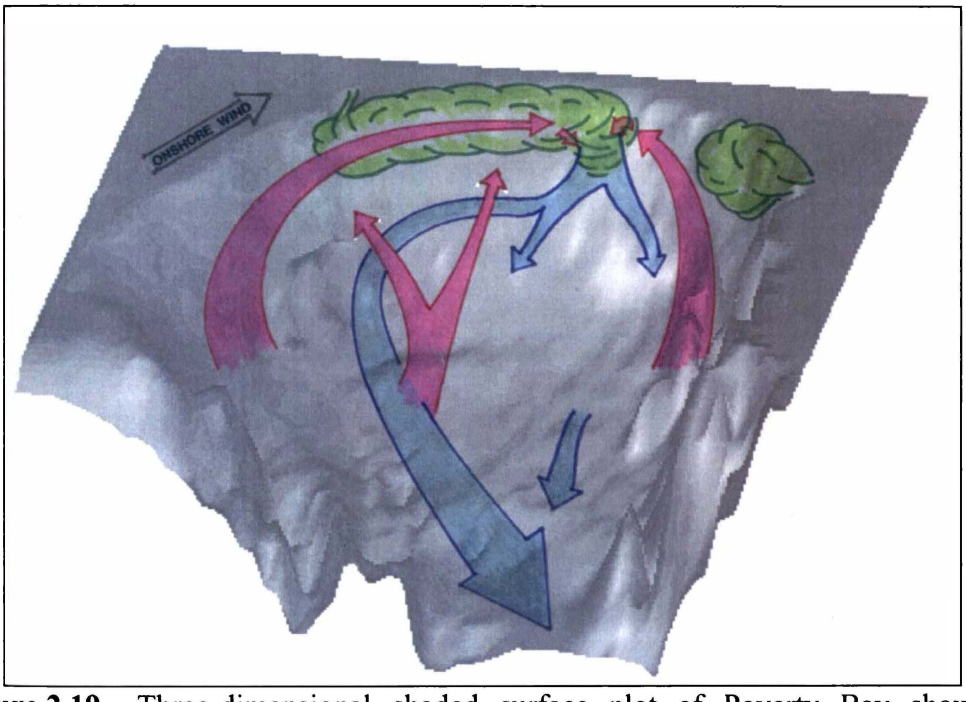

Figure 2.19 Three-dimensional shaded surface plot of Poverty Bay showing typical circulation under offshore winds. Surface water migration is marked in red and bottom water migration in blue. River plumes are depicted in green (After Stephens et al., 2000).

Figure 2.20 Aerial photograph showing the Turanganui River plume dominating the surface water circulation in northern Poverty Bay. Gisborne City is located in the background (Photo supplied by Bevan Turnpenny, Turnpenny Associates).

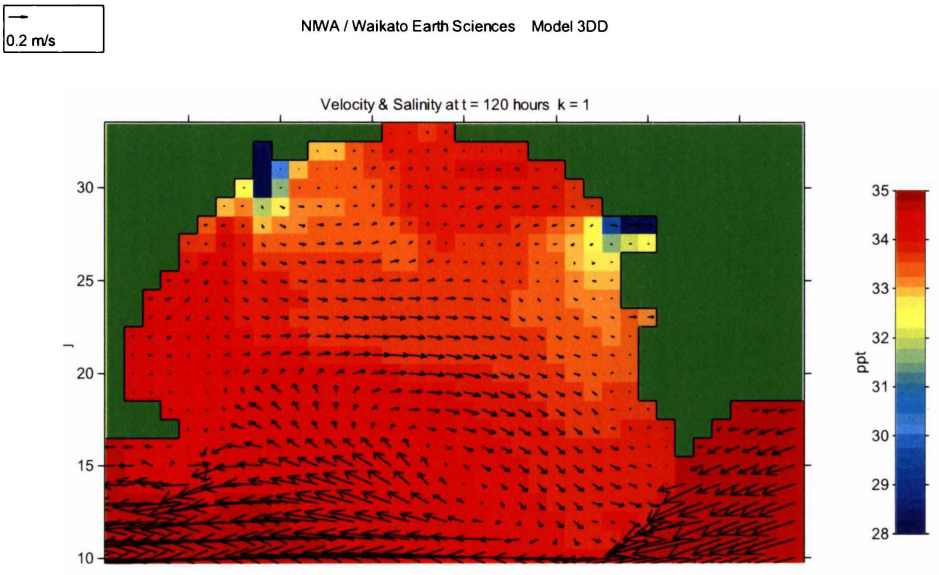

Figure 2.21 Numerical hydro-dynamical model output illustrating the effect inner continental shelf currents have on surface water current patterns in Poverty Bay during low river discharge volumes, note establishment of a clockwise rotating gyre associated with southerly flowing inner shelf current. Current vectors are scaled relative to their magnitude (After Black et al., 1997).

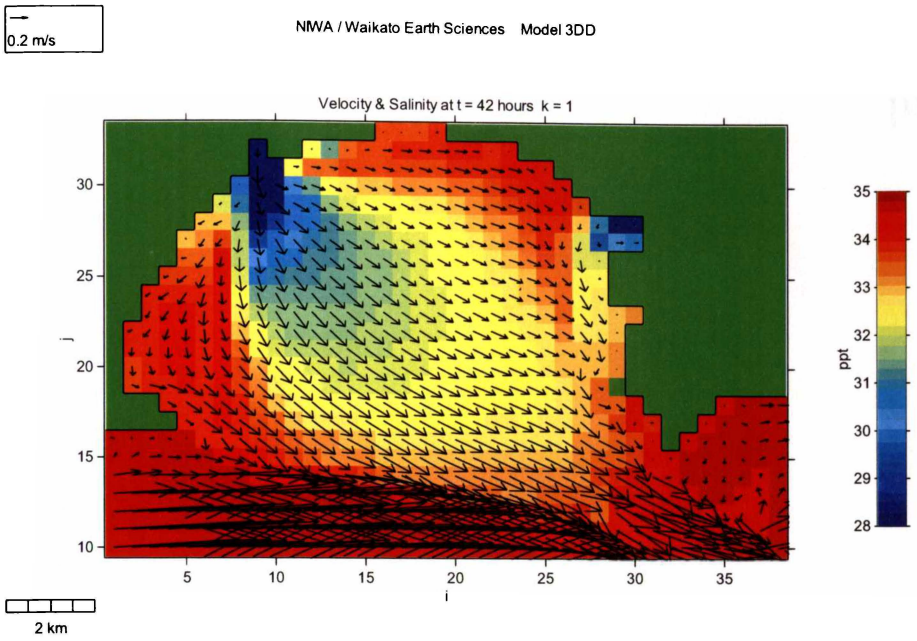

Figure 2.22 Numerical hydro-dynamical model output illustrating the effect high river discharge volumes has on circulation patterns in Poverty Bay. Discharge from the Waipaoa River dominates surface currents and even in the presence of a strong inner shelf current no circulation gyre is formed within the bay. Current vectors are scaled relative to their magnitude (After Black et al., 1997).

Chapter 3. Seafloor mapping and morphological properties

"*The sea never changes and its works, for all the talk of man, are wrapped in mystery*" - Joseph Conrad

This Chapter is an expansion on aspects of the peer-reviewed paper,

Beamsley, B. J., Healy, T. R., and Black, K., (2001). *Textural parameters and in-situ shear strength of bed sediments within an oceanic embayment.* The 15th Australasian Coastal and Ocean Engineering Conference & The 8th Australasian Port and Harbour Conference, Gold Coast, Australia, 383-388.

3.1 Introduction

A field data collection program consisting of side-scan sonar imaging and surficial sediment sampling was undertaken so that the variability in the seabed characteristics within the study area (Figure 3.01.) could be spatially mapped.

Close to 100 % side-scan sonar coverage of the field area (Figure 3.01) in conjunction with ground truthing (via *SCUBA* diver observations) provided a means to identify the spatial extent and variability of different seabed type/facies. Draping sediment characteristic and interpolated side-scan sonar maps over Digital Terrain Models (*DTM*) of the seafloor helped to identify the extent of different facies and illustrated the topographical characteristics the different facies possess.

Understanding the distributional characteristics of the surficial sediment aids in comprehending sediment transport pathways within northern Poverty Bay.

3.2 Bathymetric Mapping

3.2.1 Data Compilation

High-resolution hydrographic surveys using a real-time correction Differential Global Positioning System (D.G.P.S., Trimble 4000RL II Reference Locator base station and Trimble NT 200 Chart Plotter) and a Furuno SCV-572 sounder were used to record positions and water depths within the field area. Depth data was corrected for tidal fluctuation using the software package *HYDRO* version 6.06. The depth record was supplemented by hydrographic data provided by Port Gisborne Ltd (inclusive of the shipping channel, Swinging Basin and the dredge disposal ground areas), digitised Royal New Zealand Navy "fairsheets" and previous hydrographic surveys conducted as part of the 1997 Port Gisborne Assessment of Environmental Effects (*AEE*). The datasets provide comprehensive coverage of the study site and greater Poverty Bay area.

3.2.2 Field Area Bathymetry

The software package *SURFER* (Version 7.00.26) was used to create bathymetric grid files from which contoured bathymetry maps and digital terrain models (*DTM*) are created. The bathymetric *DTM* of northern Poverty Bay depicts conspicuous outcroppings of rocky reef (Figure 3.02). The shore platform of Kaiti Beach to the east of the port of Gisborne, as well as the rocky reef area formed by the Tokomaru, Hawea and Temoana reefs are clearly differentiated from the smooth undifferentiated topography that forms the majority of the shoreface offshore from Waikanae and Midway Beaches (Figure 3.02). Additionally, a dredge spoil mound is evident in both the digital terrain model (Figure 3.02) and the contoured bathymetry of the study site (Figure 3.03). The mound is particularly well illustrated by transect C-C' (Figure 3.04).

3.3 Side-Scan Sonar Mapping

3.3.1 Side-scan Sonar Collection

Two side-scan sonar surveys were conducted in the study site; a close to 100 % side-scan sonar coverage in March 1999, and a side-scan sonar survey of the existing dredge disposal ground following capital dredging in April 2000. The March 1999 side-scan sonar survey was used to investigate the seabed variability and to identify the boundaries between the undifferentiated silty sand facies type and the rocky/reef facies within the study area, while the boundary of the dredge material was determined from the April 2000 survey.

The March 1999 survey was conducted from The University of Waikato survey vessel (Te Rangahau), while the port pilot boat (Takitimu) was used for the April 2000 survey. Both surveys used a Kline 590 side-scan sonar, Kline 595 digital graphics recorder and D. G. P. S position fixing. Vessel track guidance was interpreted using the *HYDRO* software package (version 6.06). Depending upon water depth, the side-scan sonar fish was towed behind the vessel at a specific 'setback' distance, with position fixing adjusted accordingly. The March 1999 side-scan sonar record was ground-truthed by *SCUBA* diver observations.

3.3.2 Side-scan Sonar Processing

The digital side-scan sonar files were bottom tracked (the process of removing the water column in the side-scan sonar image) and mosaiced using the software package *ISIS* (Triton Elics International, version 6.0). The *ISIS* software exports the mosaiced side-scan sonar in a format readable by *DELPHMAP* (Triton Elics International, version 2.9.0.0), which is a purpose-build hydro-dynamic Global Information System (*GIS*) application specifically used to spatially map information collected using Triton Elics International software and hardware. From *DELPHMAP* the mosaiced side-scan sonar was exported as geo-coded TIF (Tagged image files) and read into a more general *GIS* environment, i.e. *MAPINFO* (version 6). In *MAPINFO* the boundaries of different surficial sediment types were digitised around and spatially mapped.

3.3.3 Side-scan Sonar Interpretation

Ground truthing of the March 1999 side-scan sonar record provided a means of identifying the various return signatures and to interpolate the extent of their coverage within the study site. Also, ground truthing provided the confidence to interpolate dredge spoil in the April 2000 side-scan sonar survey.

From the March 1999 side-scan survey and ground truthing five distinct seabed types or facies were recognized in the field area.

The facies types are,

i. Undifferentiated silty sand,

ii. Rocky-reef areas (including Tokomaru, Hawea Temoana reefs),

iii. Reef-gravel boulders,

iv. Shore platform rock, and

v. A distinct signature identified as dredge spoil.

Figure 3.05 depicts the March 1999 raw side-scan sonar survey return signature for the entire field area. Figure 3.06 shows the April 2000 raw side-scan sonar return signal, while Figure 3.07 and 3.08 illustrate the extent of the dredged material in the disposal ground following the surveys in March 1999 and April 2000 respectively. Figure 3.09 is a composite map of the interpolated side-scan sonar digital record of the study site from both surveys.

From Figure 3.09 it can be seen that the majority of the shoreface is comprised of undifferentiated silty sand, characterized by a featureless side-scan sonar return signature (Figure 3.10) in which *SCUBA* divers have observed various small bedforms. Bedforms identified include vortex ripples of various dimension (up to 13 cm wavelengths and approximately 2 cm amplitude) and undulating sea floor consisting of irregular depressions 1-2 cm deep and some 15 cm in diameter (personal observations 1996-1999).

The side-scan record identifies three distinct "hard" return signals that, through ground truthing, are identified as areas of rocky reef or boulder banks (facies type ii, iii and iv). In the sonagraph record the Tokomaru, Hawea and Temoana rocky reefs (facies ii) have greater spatial coverage (Figure 3.09) and the *DTM* (Figure 3.11) shows these reefs to exhibit more vertical relief than either facies types (iii) or (iv). Further, the side-scan sonar return signal depicts cracks and fissures in the rocky reef area (i.e. Tokomaru Temoana and Hawea area, Figure 3.12), which are not evident in the reef-gravel boulders facies (type iii, Figure 3.13). The shore platform facies (type iv) extends offshore from Kaiti Beach and, in part, is inter-tidal in nature (Figure 3.14). Due to its shallow depth, the extent of the shore platform facies (facies type iv) has been extrapolated from the side-scan record and Kaiti beach observations. Further, recent dredged material (facies type v) in the March 1999 and the April 2000 surveys can be differentiated from the surrounding undisturbed surficial sediments (Figure 3.7 and Figure 3.8 respectively). The dredge material in the April 2000 survey has greater coverage than the March 1999 survey. The spatial extent of the dredge material identified in the April 2000 survey is attributed to capital dredging and the consequential deposition of elevated volumes of dredged material at the existing dredge disposal site prior to the April 2000 survey.

3.4 Sediment Characteristic Mapping

3.4.1 Methodology

3.4.1.1 Sediment Sampling Programme

A sediment-sampling programme was undertaken that provided a good coverage of the study area and helped identify features observed in the side-scan sonar record. The sampling programme involved several approximate shore-normal transects (Figure 3.15) with sample site positions determined using a differential global

positioning system. *SCUBA* divers collected sediment samples from the top 2-5 cm of the seabed sediments. The sediment textural dataset was supplemented by samples collected and analysed during the 1996 Port Gisborne Ltd. *AEE* study (Beamsley et al., 1997) and from a Westham dredging report (Beamsley, 1999).

3.4.1.2 Sediment Sample Treatment Pre Textural Analysis

The most effective method of determining the 'effective' grain size (which includes colloidal flocculated particles) in mixed sand and mud sediments is measuring the grain size distribution in-situ (Berlamont et al., 1993). Because of turbulence associated with sampling and likely changes in the samples temperature and chemical properties post sampling it is unlikely that grain textural determination methods other that in-situ will give accurate indication of the 'effective' grain size (Berlamont et al., 1993). Because of equipment limitations, in-situ determination of the grain size characteristics was unobtainable. As such, grain textural characteristics were determined post sampling in a laboratory. In order to make inferences between sample sites Berlamont et al., (1993) note that it is important, particularly with mixed sand and mud sediment where flocculation may be relevant, that samples are treated identically. Further, Berlamont et al., (1993) note that for laboratory analysis of mixed mud/sand sediment, samples should be dispersed (deflocculated) and organic material should be removed following a standardised procedure, such as outlined in NZS 4402 (Standards Association of New Zealand, 1986) and described below.

A sub-sample of approximately 40-50 g of surficial sediment was washed with fresh distilled water and left until all material was observed to have settled out of solution, at which point the excess water was initially decanted and then evaporated off.

In order to remove organic material the sub-sample was immersed in 10 ml of 10 % solution Hydrogen Peroxide (H_2O_2) for a period of at least 24 hours, after which the excess fluid was evaporated off by gently heating the mixture. A 10 % solution of Calgon (sodium hexametaphosphate) was used to disperse any flocculated particles. Calgon treatment involved saturation of the sample with 10 ml of Calgon for a period at least 24 hours, after which time the samples were placed in an automatic shaker and shaken for a further 12 hours. Excess liquid is then evaporated off by gently heating the solution (Standards Association of New Zealand, 1986). To further disperse the flocculated particles each sample was subjected to 4 minutes of ultra-sonic treatment. The 4-minute time period was decided on by comparing sample distributions for a sample having undergone 2, 4, 6, 8 and 10-minute ultrasonic treatment. After 4 minutes of ultra-sonic treatment the samples distribution did not appear to change significantly (Figure 3.16, Table 3.01).

3.4.1.4 Sediment Textural Analysis

Because surficial sediment in Poverty Bay is a mixture of sand (> 62.5 μm) and mud (< 62. 5 μm) limitations are imposed on the available analysis techniques. In order to get a good representation of the sediment textural distribution, sample analysis was performed using a Malvern laser particle size analyser; model *MSS17* (Figure 3.17), which has the ability to concurrently measure both the sand and the mud sizes. The Malvern laser particle size analyser uses the principle of laser light scattering to

yield information on particle size and distribution characteristics (Malvern Instruments Ltd.). Sediment grain size distribution, mean, median and modes were calculated using the Malvern software.

Textural statistics (Appendix II) were calculated using the Folk (1968) graphical method, while descriptive terms are used to describe the textural characteristics of the surficial sediment (Appendix I). The terms used follow the Folk (1968) classification scheme.

From a sedimentological perspective, the amount of clay in the sample is defined as the percentage of the sample less than 4 μm (Allaby and Allaby, 1999; Folk, 1968; Komar, 1998), whilst pedology assumes a cut-off point at 2 μm (Allaby and Allaby, 1999). As such, clay percentages used to determine grading classifications use the 4 μm limit, whilst physical properties of the sediments (Atterberg limits, activities, in-situ moisture contents, etc. discussed in later chapters) are discussed relative to the percent of the sample less than 2 μm.

3.4.1.5 Organic Content Determination

The percent of organic matter for each sample was measured using the "loss-on-ignition" method following the method outlined by the Standards Association of New Zealand (1986).

All moisture was removed from the samples by oven drying at 105°C for 24 hours. The sample was then placed in a container of known mass (M_1). The mass of the sample and container was measured (M_2) and the sample then placed in the kiln at a temperature of 450°C.

After sufficient time for the organic matter to be ignited, the sample and container were again weighed (M_3) and the percent organic matter in the sample calculated as:

$$\text{Organic matter percent} = \frac{M_2 - M_3}{M_3 - M_1} \times 100 \qquad (3.01)$$

3.4.1.6 Creation of Sediment Characteristic Maps

Sediment characteristic maps were created using the software package *SURFER* (Version 7.00.26), which takes spatially distributed data and interpolates a regularly spaced grid. Areas above the mean high water mark, and those comprised of rocky-reef habitat, as identified from the side-scan sonar survey and ground truthing, were blanked out and not included in the interpolation algorithms.

3.4.1.7 Multivariate Analysis of Sediment Characteristic

Linear regression and factor analytic techniques were used to analysis the inter-correlations between the surficial sediment characteristic (mean grain size, relative percentages of sand/silt/clay) and the physical and environmental controls on the

sediment characteristics (i.e. distance from sediment supply, water depth and degree of agitation associated with dredging operations). The number of factors to investigate with Factor Analysis was determined using the Kaiser criterion, which states that only factors with eignevalues greater than 1 should be considered (i.e. Table 3.02). As such subsequent Factor Analysis was performed using 2 factors. To obtain a clear pattern in the factor loadings the factors have been rotated using the variance maximizing (Varimax) technique, which maximizes the variance of the 'new' factor and minimizes the variance of the 'new' variable (Cooley and Lohnes, 1966; Fruchter, 1954; King, 1969).

3.4.2 Results

3.4.2.1 Multivariate Analysis of Sediment Characteristic

Correlation coefficients (R) for the inter-correlation between seabed sediment characteristics and physical and environmental controls (Table 3.03) are determined by linear regression. Each heading of the column of the Table 3.03 represents the dependant variable, while the independent variables are represented by the row headings. Normalized variance maximized rotated factor loadings are given in Table 3.04.

Unsurprisingly, relatively high R values are evident between sand, silt and clay percentages (Table 3.03), as these size classes divide the grain size distributions. Further, Factor 1 loadings suggest that with normalized varimax factor rotation the volume percent sand, silt and clay within the surficial sediment can be described by a single new variable (Table 3.04). With sand as the independent variable, both silt and clay percentage R values are negative, where intrinsically as the sand content decreases the silt and clay content increases (Table 3.03). The negative correlation between Factor 1 loadings and volume percent sand (-0.90), and the positive correlation with the volume percent silt (0.91) and clay (0.77, Table 3.04) emphasise this correlation. Not unsurprisingly the mean grain size has relatively high R values when correlated with sand, silt and clay percentages (Table 3.03). Additionally, whether the surficial sediment distribution exhibits a single or bi-modal peak is also well correlated with the percentages of sand (R = -0.54) and clay (R = 0.72), and to a lesser extent the silt (R = 0.45). This suggests that as the sand percent decreases in the seabed sediment and the mud content increases there is a greater likelihood that the sediment distribution will be bi-modal. Further, the organic content has some correlation with the percent of sand (R = -34), silt (R = 27) and clay (R = 47) of the surficial sediment. Similar relationships are displayed by the Factor 1 loadings (Table 3.04).

The influence that depth water (the independent variable) has on the sediment textural characteristics is illustrated by high R values when mean grain size, sand, silt and clay percentages and the distribution shape (i.e. if the distribution is bi-modal or not) are treated as the dependant variables. The negative R values correlating the water depth to the percent sand (-0.64) and the mean grain size (-0.65) indicate that as the water depth increases the percent sand in the surficial sediment and hence the mean grain size, decreases (Table 3.03). Further, Factor 1 loadings (Table 3.04) suggest an inter-correlation between water depth and the surficial sediment textural characteristics; e.g. mean grain size, sand, silt, and clay volume percentages.

Sample site distance from a sediment source (i.e. the Turanganui River and the dredge disposal ground, assuming the sediment partially moves out of the disposal ground), mean grain size, and percent sand are positively correlated (0.46 and 0.38 respectively, Table 3.03), while conversely the silt and clay percentages are negatively correlated with distance from sediment source (-0.41 and –0.24 respectively, Table 3.03). This suggests that the closer a site is to a sediment source the greater the percentage of silt and clay and the finer the mean grain size of the surficial sediment.

3.4.2.2 Mean Grain Size Distribution Map

The Malvern laser particle size analyser has been used to measure the mean grain size of the surficial sediment using the moment method, as defined in Appendix I. The software used to run the Malvern laser particle size analyser calculates grain size in *SI* units (microns). Using the raw data, a mean phi size has been calculated for each sample site, where phi units are calculated as:

$$phi = -\log_2 d \tag{3.02}$$

where d is the grain size measured in millimetres.

Mean grain size is a useful textural parameter for determining the magnitude of force that must be applied to a grain by either wind or water in order to move it (Dyer, 1986; Folk, 1968). Descriptive terms used in Appendix II to describe the statistical measure of the mean grain size are based on the Udden-Wentworth grain size classification (Appendix I).

At the low-tide swash zone the mean grain size of the surficial sediment is relatively coarse (Figure 3.18, Appendix II – Beach samples); however mean grain size increases with distance from the Turanganui River mouth, both offshore and along the beach (Figure 3.18). This is illustrated by the negative correlation coefficient(R^2) between the water depth and the mean grain size (Table 3.03) and by the factor 1 loading for the water depth (0.81) and the mean grain size (-0.87, Table 3.04).

The finest seabed sediments ($d \approx 25$ μm) are found within the swinging basin, with the grain size increasing with distance beyond the entrance of the basin to approximately 220 μm (Figures 3.18 and 3.19).

The mean grain size of the surficial sediment within the existing dredge spoil ground is relatively fine (40 μm) compared to seabed sediment found in similar water depths within the study site (Figure 3.18), suggesting a degree of mixing between sediments that would be expected to naturally occur at the site and that of the disposed dredge material.

3.4.2.3 Modal Grain Size Distribution Map

The modal grain size refers to the most frequently occurring grain size within a distribution and can provide clues as to the origin of sediments. For example, if the

sediment is comprised predominantly of coarse angular particles (coarse mode) it would suggest that grains have not been weathered much and that their source is reasonably close to the sampling site, e.g. nearby coastal cliffs. The mode of a sample is therefore important because samples that exhibit bi or poly-modal distributions (where there are 2 or more modal peaks) can be indicative of a multi-sourced environment, or alternatively represent a lag, where only a certain size of particle has been entrained and transported (Friedman and Sanders, 1978).

Because many of the samples display bi-modal distributions (Appendix II), only the dominant mode has been spatially mapped within the study site.

The spatial variability in the first mode of the surficial sediment grain size exhibits a similar distribution to that of the mean grain size (Figure 3.20). The coarsest modal grain sizes are found on the low-tide swash zone on Midway and Waikanae beaches and the surficial sediment mode increases with distance from the mouth of the Turanganui River and with increased water depth (Figure 3.21). The finest modal seabed sediment in the study area is found in the Swinging Basin (Figure 3.20). The surficial sediment modal peak increases with distance from the Swinging Basin and becomes relatively coarse in the lee of the semi-submerged breakwater (Figure 3.20). Further, the modal peak of the surficial sediment within the existing dredge spoil ground is relatively fine compared with other sites of similar water depths (Figure 3.22). The contoured modal distribution exhibits an approximate radial pattern extending away from the existing dredge spoil ground (Figures 3.20).

3.4.2.4 Sorting Distribution Map

Sorting is a representation of the standard deviation of grain texture within a distribution and gives an indication of the uniformity in grain transport and deposition (Leeder, 1982). "*Poorly*" sorted samples have a large standard deviation, or a wide range of sediment sizes. Poorly sorted samples represent environments where weak sediment transport processes, incapable of entraining even fine grains, leave a wide range of sediment sizes. "Well" sorted samples denote areas with more active sediment transport processes, selectively removing or winnowing out certain sediment sizes to leave a particular size class behind (Dyer, 1986; Folk, 1968; Komar, 1998). Appendix I lists the descriptive terms used to define the sorting and their corresponding standard deviation in terms of phi units.

Folk, (1968) recognised four main factors that the degree of sorting appeared dependant on,

i. Size range of material supplied to the environment,

ii. Types of depositional processes active,

iii. Current characteristics (strength, continuity and turbulence), and

iv. Time (sediment supply rate vs. time available to sort sediment).

The majority of sediment in northern Poverty Bay is classified as poorly to very poorly sorted (Figure 3.23) and the degree of sorting of the surficial sediment is shown to increase with decreased water depth (Figure 3.23).

3.4.2.5 Skewness Distribution Map

Skewness is a measure of symmetry of the sediment distribution. In a normal distribution bell-shaped frequency curve the mean and median grain size coincides (Figure 3.24). Any tendency for a distribution to lean to one side leads to differences between the median and mean values. Deviations from the normal distribution are used to characterize the skewness of the distribution curve. A grain size distribution is described as being finely skewed when there is a surplus of fine material in the distribution (i.e. Figure 3.24), and conversely a distribution is described as being coarsely skewed when there is a surplus of coarse material in the distribution curve (i.e. Figure 3.24 Dyer, 1986; Folk, 1968; Komar, 1998; Tucker, 1988). The skewness of the distribution curves is determined using the graphical method as outlined by Folk, (1968) and described in Appendix I.

In northern Poverty Bay coarse-skewed surficial sediment only occurs in the Swinging Basin (Figure 3.25). The majority of surficial sediment in northern Poverty Bay is classified as being strongly fine-skewed (Figure 3.25), i.e. the sediment has a surplus of fine grains. However, sediments in the existing dredge spoil ground are clearly influenced by disposal of dredged material at the site and are classified as having near-symmetrical skewness (Figure 3.25). The contoured seabed sediment skewness values exhibits an approximate radial pattern extending away from the centre of the existing dredge spoil ground (Figure 3.25).

3.4.2.6 Textural Percentage Distribution Map

Because grain size distributions can be divided into percent sand, silt and clay the spatial distribution maps of the three units are similar. This is reflected by high R^2 and factor 1 loading values (Table 3.03 and 3.04). In order to avoid repetition all three distribution maps are concurrently discussed in this section.

Within the field area, Waikanae and Midway beaches have the largest percentages of sand (> 90%), and hence lowest percentages of both silt and clay (< 10% and < 5% respectively). With distance offshore from Waikanae and Midway beaches sand percentages decrease as silt and clay percentages increase (Figures 3.26, 3.27 and 3.28). The Swinging Basin has the highest percentages of silt and clay (up to 55% and 28% respectively), and consequentially the surficial sediment in the swinging basin has a relatively low sand percentage (as low as 10 %, Figure 3.26). Outside the entrance to the swinging basin the relative percent of sand in the surficial sediment increases and the relative percent of clay and silt diminish (Figures 3.26, 3.27, 3.28 and 3.29).

Surficial sediment at the existing dredge spoil ground have relatively elevated percentages of both silt and clay when compared to sites of similar depth (Figures 3.27 and 3.28), suggesting that the dumping of dredge-spoil at the disposal site modifies the surficial sediment textural characteristics.

3.4.2.7 Organic Content Distribution Map

Organic content in the surficial sediment in northern Poverty Bay ranges from approximately 1 % to slightly over 3 % by weight (Figure 3.30). Surficial sediment in the swinging basin has the highest organic content within the study area (3%, Figure 3.30, which is in agreement with the findings of (Sander, 1993). It is likely that the relatively high concentration of organic material in the Swinging Basin is sourced from both the discharging of the Turanganui River adjacent to the swinging basin (Figure 3.1) and as a direct result of port operations (i.e. from wood and wood-chip export operations).

As with the findings of Miller, (1981) and Sander, (1993), relatively high organic content is also found in the surficial sediment within the existing dredge spoil ground (Figure 3.30). The elevated organic content within the existing dredge spoil ground is probably due to the disposal of dredge material at the site, which is sourced from the swinging basin and the shipping channel.

Surficial sediment in the low-tide swash zone along both Waikanae and Midway beaches have organic contents greater than 2 % (Figure 3.30). The high organic percent of beach sediment is probably the result of the degradation of organic material (logs etc.) that is deposited on the beaches in relatively large quantities as flotsam (Figure 3.31). Organic content is shown to decrease with distance offshore from the beaches (Figures 3.30 and 3.32) and with distance from the mouth of the Turanganui River (Figure 3.33).

3.5 Heavy Metal Analysis - Channel and Swinging Basin

3.5.1 Sample collection and Heavy Metal Analysis Procedure

In order to ensure that the sediment being dredged in the capital and maintenance dredging programs does not contain levels of trace heavy metals in excess of the imposed Resource Consent Limits three surficial sediment samples considered to be representative of the dredged material were collected by a *SCUBA* diver; one from within the swinging basin and two within the shipping channel (Figure 3.34). The surficial sediment samples were packed wet into air and watertight plastic containers and shipped to R.J. Hill Laboratories, which is an accredited International Accreditation New Zealand (previously known as TELARC) laboratory. Trace heavy metal concentrations were determined in accordance with the terms of accreditation and using Inductively Coupled Plasma-Ass Spectrometry operated in accordance with the U.S. E.P.A. 200.2 methods and standards. Trace heavy metals tested for include,

i. Cadmium,
ii. Chromium,
iii. Copper,
iv. Mercury,
v. Lead, and
vi. Zinc

3.5.2 Heavy Metal Results

Concentrations of heavy metals within the shipping channel and swinging basin are below the imposed Resource Consent Limits (Table 3.05). The surficial sediment within the Swinging Basin has slightly higher concentrations of all tested trace heavy metals, probably due to the Swinging Basin being more inert in terms of sediment entrainment and transport processes and due to the relatively high percent fines (silt and clay) in the surficial sediment, which are conducive to retaining trace heavy metals (Gambrell et al., 1984).

3.6 Discussion

While side-scan sonar surveys have been used to delineate between different seabed facies within northern Poverty Bay (e.g. Healy et al., 1997; Kensington, 1990; Nelson and Healy, 1982), Black et al., (1997) using the Healy et al., (1997) facies delineation (i.e. rock-reef or soft sediment delineation) is the only study to integrate numerical sediment transport models with seabed characteristics in northern Poverty Bay. Black et al., (1997) used Miller, (1981) and Kensington, (1990) seabed textural data and limited data collected as part of the 1997 *AEE* to produce sediment textural maps for the entire bay using gird nodes spaced at 200-m.

For this study, close to 100% side-scan coverage of northern Poverty Bay in conjunction with D.G.P.S. and Geographical Information System (G.I.S.) software (*MapInfo Professional, Version 6.0*) enabled identification and accurate spatial mapping of five distinct facies types. The accurate spatial mapping of the different facies from this study expand on the previous work conducted by Miller, (1981), Kensington, (1990) and Healy et al., (1997), and provides the potential for more realistic model simulations.

Within northern Poverty Bay Miller, (1981), Kensington, (1990) and Beamsley et al., (1998) have examined the spatial distribution of seabed texture. All three studies have noted similar trends in the surficial sediment textural characteristics, with mean grain size showing a general trend to decreasing with distance offshore (Figures 3.35, 3.36 and 3.37 for Beamsley et al., 1998; Kensington, 1990; Miller, 1981 respectively). Sediment textural data from this study displays a similar trend (Figure 3.18), with factor 1 loadings of 0.81 for water depth and –0.87 for mean grain size (Table 3.04), while multivariate regression results in an R^2 of –0.65 between water depth and mean grain size (Table 3.03). Neither Miller, (1981) nor Kensington, (1990) note the surficial sediment within the existing dredge disposal site to be relatively finer, however curiously Kensington, (1990) did find the disposal site to have relatively elevated percentages of both mud and clay (Figure 3.38 and 3.39 respectively). Similar trends in the percentages silt and clay spatial variations are shown by sediment samples collected as part of this study (Figure 3.27 and 3.28 respectively) and this is reflected by the 1st modal distribution map displaying a dominant mode in the silt sized fraction within the existing dredge disposal ground (Figure 3.20).

While rock-reef area is identified in the textural distribution maps of Kensington, (1990), a disparity exists between the spatial extent of the rock-reef area as identified by side-scan sonar records collected in January 1989 (Figure 3.40) and

the seabed textural distribution maps created from seabed samples collected in February 1986 (e.g. Figure 3.36, 3.38, and 3.39).

Beach and offshore seabed sediment mean grain sizes are similar in the studies by Miller, (1981), Kensington, (1990) and for data collected as part of this study (Figures 3.37, 3.36 and 3.18 respectively), indicating little temporal change. The surficial sediment grades from fine sand (2-3 phi, 250-125 μm) to very fine sand (3-4 phi, 125-62.5 μm) between the 5 and 10-m depth contour. While the surficial sediment continues to fine with increased water depth, the offshore seabed sediment remains classified as very fine sand, except for an area of coarse silt within the existing dredge spoil ground (Figure 3.18).

The degree of sorting of the surficial sediment varies between the studies of Miller, (1981), Kensington, (1990) and for this study. Miller, (1981) found the majority of the surficial sediment within northern Poverty Bay to be classified as moderately to moderately well-sorted (Figure 3.41). In contrast, data from this study and the study by Kensington, (1990) classified the majority of the surficial sediment within Poverty Bay as poorly sorted (Figures 3.23 and 3.32 respectively). Further, the degree of sorting is shown to decreases with water depth (Figure 3.23).

Miller, (1981), Kensington, (1990) and data from this study classify the majority of the surficial sediment within northern Poverty Bay as being fine to strongly-fine skewed (Figures 3.43, 3.44 and 3.25 respectively). However, the degree of sorting increases near the beaches (Figure 3.25). The fine-skewed nature of the surficial sediment is characteristic of sediment deposited via rivers (Friedman and Sanders, 1978). Both Miller, (1981) and Kensington, (1990) note an area in the vicinity of the existing dredge spoil ground where the surficial sediment is classified as coarse-skewed (Figures 3.43 and 3.44 respectively). Likewise, data from this study indicates the surficial sediment within the existing dredge disposal ground is coarsely skewed (Figure 3.25). The skewness of the surficial sediment within the existing dredge spoil ground most likely represents the mixing of the naturally occurring sediment (given the water depth) and the sediment disposed at the site from dredging operations.

Three factors appear to control the sediment textural characteristics within northern Poverty Bay; water depth, dredging operations and river discharging. Water depth appears to have the strongest influence on the sediment textural characteristics (shown by an R^2 of –0.65 when correlated with the mean grain size), with some modification of the surficial sediment grain size distribution resulting from the disposal of dredged material at the existing dredge disposal site and the discharging of sediment as both bedload and suspended load from the Turanganui River adjacent to the port (represented by the distance of a particular site from a sediment source, R of 0.46, when correlated with the mean grain size, Table 3.03). The correlation between water depth and the grain textural characteristic of the surficial sediment is displayed by the textural distribution maps (e.g. Figures 3.18, 3.20, 3.26, 3.27 and 3.28) the Factor 1 loadings (Table 3.04) and the R values (Table 3.03). Textural maps illustrate a general fining of the surficial sediment with water depth, which is in agreement with the negative correlation in the Factor 1 loadings for water depth and mean grain size (Table 3.04).

As water depth decreases wave orbital currents become stronger and hence their ability to entrain and transport the relatively coarser sediment increases. This results

in winnowing out of relatively finer and finer sediment as the water depth decreases, and hence the fining of the surficial sediment with increased water depth. It is this relationship that has the dominant control on the surficial sediment grain size distribution and textural characteristics within northern Poverty Bay. Further, the relationship between water depth and the relative strength of the near-bed wave orbital currents results in the surficial sediment becoming increasingly sorted as the water depth decreases.

In contrast, the surficial sediment within the existing dredge disposal ground is influenced by the disposal of dredge material. The surficial sediment is relatively finer, having greater percentages of silt and clay and less sand in the distribution than surficial sediment in similar depths within the study site (Figure 3.26, 3.27 and 3.28). The surficial sediment within the existing disposal ground is classified as 'near-symmetrical' (Figure3.25), presumably due to the mixing of naturally occurring seabed sediment and sediment dredged from the swinging basing and shipping channel disposed of at the site during capital and maintenance dredging. Further, the discharging of the Turanganui River influences the surficial sediment textural characteristics in the vicinity of the river mouth, with seabed sediment about the mouth being relatively finer than sediment at similar depths offshore Waikanae and Midway beaches (Figure 3.18). The surficial sediment in the vicinity of the river mouth is classified as being near-symmetrical (Figure 3.25), suggesting that there is a balance between sediment transport and depositional processes, whereby the quantity of fine sediment deposited at the site via river discharging offsets the naturally fine-skewed nature of the surficial sediment in the majority of northern Poverty Bay.

The weight percent organic matter in the surficial sediment in northern Poverty Bay varies between less than 1% to approximately 3%. The largest weight percent organic material is found within the Swinging Basin (Figure 3.30). Further, the surficial sediment within the existing dredge disposal ground display relatively elevated organic content, as do the sediments along Midway and Waikanae Beach (Figure 3.30). It is likely that the elevated organic content in the Swinging Basin results from a combination of organic material derived from the Turanganui River, and as a result of port operations, particularly wood and wood-chip export operations. The quantity of organic material deposited in Poverty Bay from the Turanganui River is highlighted by the amount of degraded vegetation that can be found near the mouth of the Turanganui River (Figure 3.31). The quantity of degraded vegetation matter found on the beach is also responsible for the relatively elevated weight percent organic matter in the beach sediments (Figure 3.30). Because the dredged material is sourced from the Swinging Basin and shipping channel it is not surprising that the surficial sediment within the existing dredge disposal ground also displays relatively high weight percentage of organic matter (up to 3%, Figure 3.30).

3.7 Summary

Comprehensive bathymetric mapping using digitised R. N. Z. N 'fairsheets' and hydrographic surveys have been used to create bathymetry files and digital terrain models (*DTM*) of northern Poverty Bay. The *DTM* of the study site highlights the contrast between the concave-up shoreface offshore Waikanae and Midway Beaches and the shore platform offshore Kaiti Beach (Figure 3.02). The bathymetric *DTM* also highlights the relative relief of the Tokomaru, Hawea and Temoana rocks above

the undifferentiated silty sand (Figure 3.11), as well as depicting the dredge spoil mound within the existing dredge disposal ground (Figure 3.11).

Analysis of close to 100% side-scan sonar coverage in the field area has identified 5 different types or facies and is used to map the spatial extent. The facies identified including;

i. Undifferentiated silty sand,
ii. Rocky-reef areas (including Tokomaru, Hawea Temoana reefs),
iii. Reef-gravel boulders,
iv. Shore platform rock, and
v. A distinct signature identified as dredge spoil.

The spatial distribution of the 5 facies was draped over the *DTM*, highlighting the different topographical characteristics of the facies (Figure 3.11).

A surficial sediment-sampling program was used to map the spatial variability in the surficial sediment within northern Poverty Bay. Sample treatment and analysis was identical for both the sand and mud portion of the surficial sediment sample. Mean and modal textural characteristics of the surficial sediment exhibit similar spatial patterns (Figures 3.18 and 3.20 respectively). Coarsest sediments are found in the low tide swash zone of Waikanae and Midway beaches (Figure 3.18), as illustrated by the relatively large percent sand in the beach sediments (Figure 3.26). The relatively fine surficial sediment and hence high volume percent silt and clay content found in the Swinging Basin and at the existing dredge disposal ground (Figure 3.18) is attributed to the processes acting to entrain and transport the sediment and the rate of sediment supply. Shipping channel sediments are shown to become coarser with distance from the Swinging Basin (Figure 3.18 and 3.19). Water depth and hence the relative strength of the wave orbital currents is the dominant controlling process influencing the textural characteristics of the surficial sediment. As water depth decreases the relative strength of the wave-orbital velocities increases and hence its potential to entrain coarser and coarser sediment also increases. This correlation between the relative strength of the orbital velocities and the water depth results in the negative *R* value relating water depth and mean grain size (-0.65) and the inverse relation in the factor 1 loadings for water depth and mean grain size of 0.81 and – 0.87 respectively (Table 3.03 and 3.04 respectively). Factor loadings and *R* indicate that as the water depth increases the grain size of the surficial sediment will decrease.

The degree of sorting of the surficial sediment in northern Poverty Bay is classified as ranging between poorly sorted to very-poorly sorted (Figure 3.23). The degree of sorting displayed by the surficial sediment grain size distribution is attributed to the size range of sediment available for deposition from the Turanganui River (Figure 3.01) and the Waipaoa River in southern Poverty Bay. Together the two river systems deposit 13×10^6 tonnes per year annually as bed and suspended load (Council, 1994; Griffiths and Glasby, 1985). Because the relative strength of the dominant sediment entrainment and transport process (i.e. wave-orbital currents) increases as water depth decreases the degree of sorting displayed by the surficial sediment increases near the shore (Figure 3.23), reflecting the winnowing out of fines.

Surficial sediment in northern Poverty Bay is predominately strongly fine-skewed. Notable exceptions are the sediment in the Swinging Basin and sediment at the existing dredge spoil ground (Figure 3.25). Swinging basin sediment is classified as

being coarsely skewed, which is a reflection of the relatively inert sediment transport and entrainment processes operating within the basin and the size of sediment available for deposition. The surficial sediment in the existing dredge disposal ground exhibit near-symmetrical skewnesses (Figure 3.25), reflecting the mixing of the sediment that would naturally occur at the site given the water depth and the sediment disposed of at the site via dredging.

Organic content in the surficial sediment ranges for 1-3%, with the largest organic content concentrations being found within the swinging basin and along Waikanae and Midway beaches (Figure 3.30). The high concentration of organic content found in the surficial sediment in the swinging basin is attributed to wood and wood-chip exporting operations at the port and the discharging for organic material from the Turanganui River adjacent to the port (Figure 3.01). The high organic content of the sediment on Waikanae and Midway beaches is attributed to organic debris discharged from the Turanganui River, which often accumulated on Waikanae and Midway beaches, illustrated by Figure 3.31.

Table 3.01 Surficial sediment textural characteristics after 2, 4, 6, 8 and 10 minutes of ultrasonic treatment to disperse flocculated particles. Initial sample treatment consisted of Hydrogen Peroxide (H_2O_2) treatment for the removal of organic material and Calgon for the partial dispersion of flocculated particles.

Ultrasonic treatment time (minutes)	Mean	Sorting	Skewness
2	5.08	2.42	0.49
4	5.42	2.38	0.48
6	5.42	2.34	0.5
8	5.42	2.34	0.5
10	5.83	2.59	0.48

Table 3.02 Eigenvalues of 4 factors determined from multivariate Factor Analysis of the surficial sediment in-situ shears strength, textural characteristics and physical/environmental controls. Factor Analysis is used to determine structure within a dataset. The Eigenvalues are used to determine the number of factors that should be considered in multivariate Factor Analysis. Based on the Eigenvalues (i.e. Eigenvalues > 1), the data can be described using two Factors (as highlighted).

Factor	Eigenvalues	% Total variance	Cumulative Eignevalues	Cumulative %
1	**6.42**	58.34	6.42	58.34
2	**1.58**	14.33	7.99	72.67
3	0.93	8.44	8.92	81.10
4	0.75	6.86	9.68	87.96

Table 3.03 Correlation coefficient (R) matrix from the linear regression between the surficial sediment shear strength, textural characteristics and physical/environmental setting. The Turanganui River and the existing dredge spoil ground are termed "sediment sources", assuming that the disposal ground is partially dispersal and sediment entering northern Poverty Bay is radial dispersed from the mouth of the river.

	Distance to sediment source	Water depth (m)	Site in channel 1-y 0-n	Mean grain size (μm)	Bi-modal 1-y 0-n	Clay %	Silt %	Sand %	Organic content %	Clay to Sand ratio	Mud to Sand ratio
Distance to sediment source	1										
Water depth (m)	-0.06	1									
Site in channel 1-y 0-n	-0.18	-0.16	1								
Mean grain size (μm)	0.46	-0.65	-0.19	1							
Bi-modal 1-y 0-n	-0.18	0.41	-0.09	-0.35	1						
Clay %	-0.24	0.63	-0.12	-0.65	0.72	1					
Silt %	-0.41	0.62	0.13	-0.87	0.45	0.82	1				
Sand %	0.38	-0.64	-0.07	0.85	-0.54	-0.90	-0.99	1			
Organic content %	-0.02	0.24	-0.18	-0.12	0.51	0.47	0.27	-0.34	1		
Clay to Sand ratio	-0.23	0.54	-0.09	-0.61	0.72	0.97	0.80	-0.88	0.45	1	
Mud to Sand ratio	-0.29	0.53	-0.01	-0.70	0.58	0.90	0.90	-0.94	0.35	0.96	1

Table 3.04 Normalized variance maximized (Varimax) rotated factor loadings determined from multivariate Factor Analysis of the surficial sediment shear strength, textural characteristics and physical/environmental setting. Factor loadings greater then 0.5 are highlighted.

Variable	Factor 1	Factor 2
Distance from sediment source	-0.20	-0.03
Water depth	**0.81**	0.06
Site in channel 1-y 2-n	0.03	-0.12
Mean grain size	**-0.87**	0.00
Bi-modal grain size distribution; 1-y 2-n	0.35	**0.78**
Clay %	**0.77**	**0.57**
Silt %	**0.91**	0.23
Sand %	**-0.90**	-0.33
Organic content %	0.07	**0.84**
Clay to Sand ratio	**0.74**	**0.60**
Mud to Sand ratio	**0.82**	0.44
Explained variance	5.04	2.36
Proportion of total variance	0.46	0.21

Table 3.05 Heavy metal concentrations of the surficial sediment within the port of Gisborne swinging basin and the shipping channel ($mg.kg^{-1}$, dry weight). Also shown are the imposed Resource Consent limits imposed on port operations at Gisborne.

	Swinging Basin (Sample - TB)	Shipping Channel 1 (Sample - SC1)	Shipping Channel 2 (Sample - SC2)	Consent Limits
Total Cadmium (Cd) mg/kg dry wt.	0.09	0.04	0.04	1.00
Total Chromium (Cr) mg/kg dry wt.	14.6	9.9	9	100.0
Total Copper (Cu) mg/kg dry wt.	16.3	6.8	7.7	81.0
Total Mercury (Hg) mg/kg dry wt.	0.07	0.03	0.03	0.21
Total Lead (Pb) mg/kg dry wt.	12.2	6.4	6.9	66.0
Total Zinc (Zn) mg/kg dry wt.	63.3	43.2	41.5	160.0

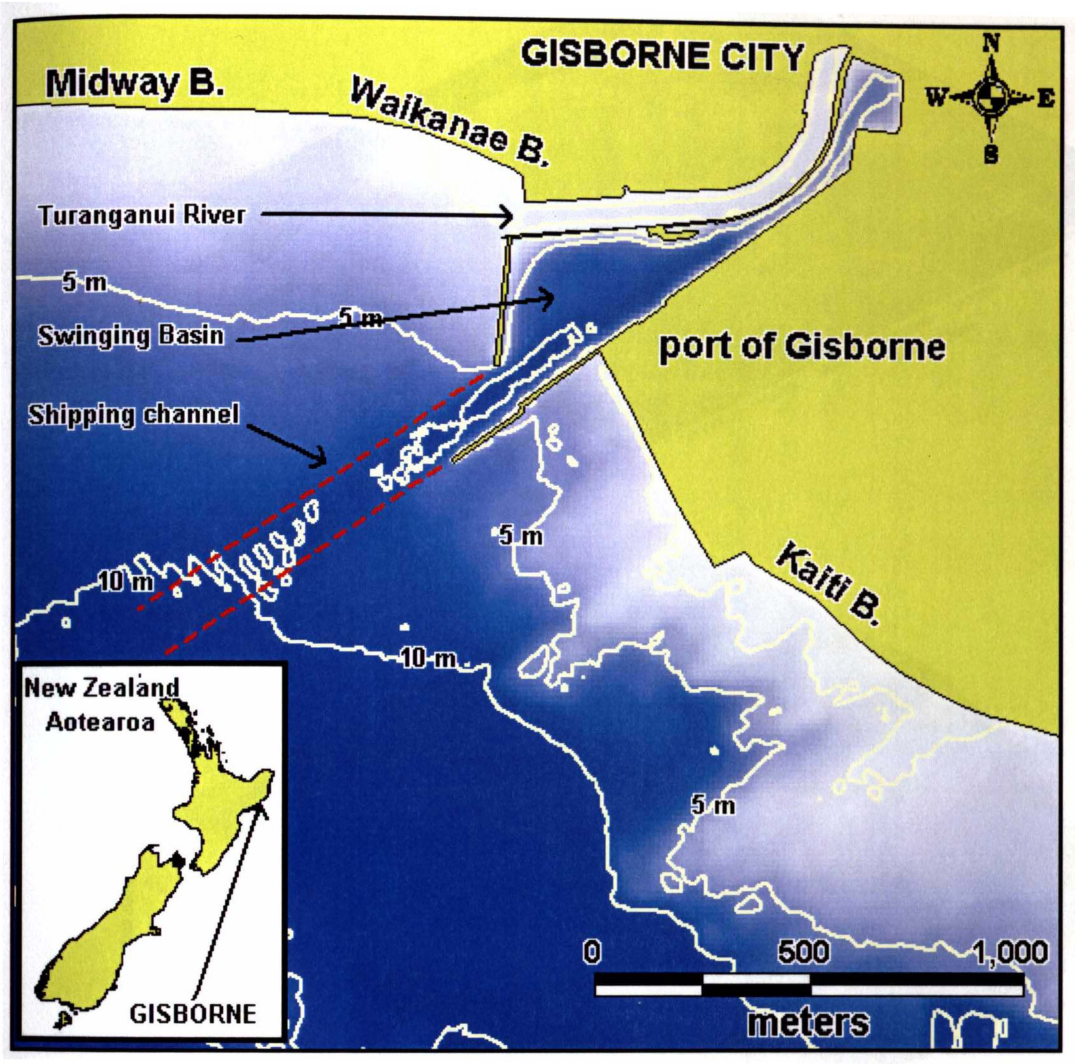

Figure 3.01 Study site location map illustrating the extent of the study area within the confines of northern Poverty Bay, as well as the location of the port of Gisborne, the Turanganui River, the shipping channel, the Swinging Basin and the surrounding beaches.

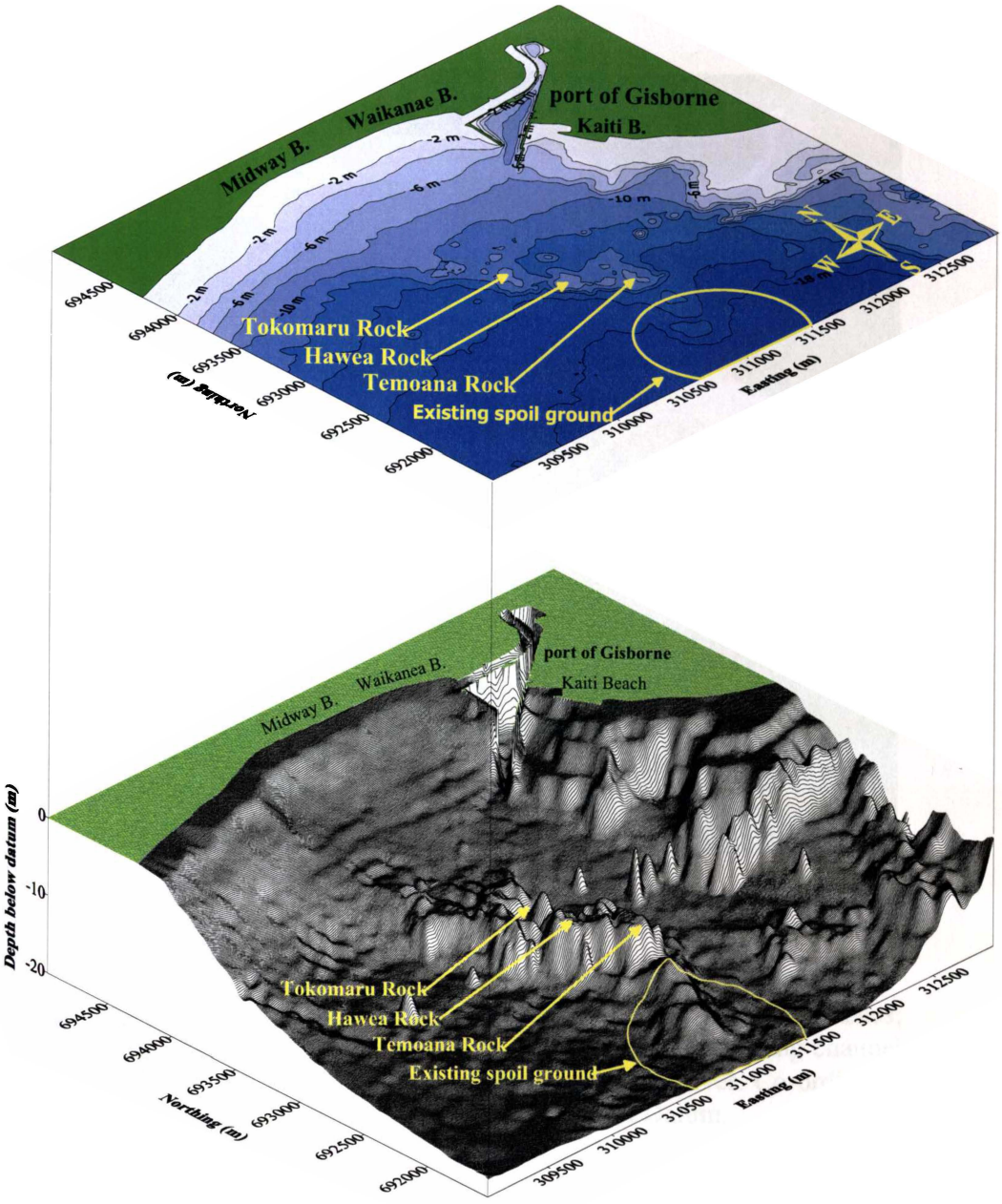

Figure 3.02 Digital Terrain Model (*DTM*) of the study sites' bathymetry. Tokomaru, Hawea and Temoana Rocks are shown in the foreground as having greater vertical relief in comparison to the relatively smooth undifferentiated seafloor topography. Also evident is the rock shore platform offshore from Kaiti Beach. Co-ordinates are in the Poverty Bay Circuit; Depths are relative to Chart Datum.

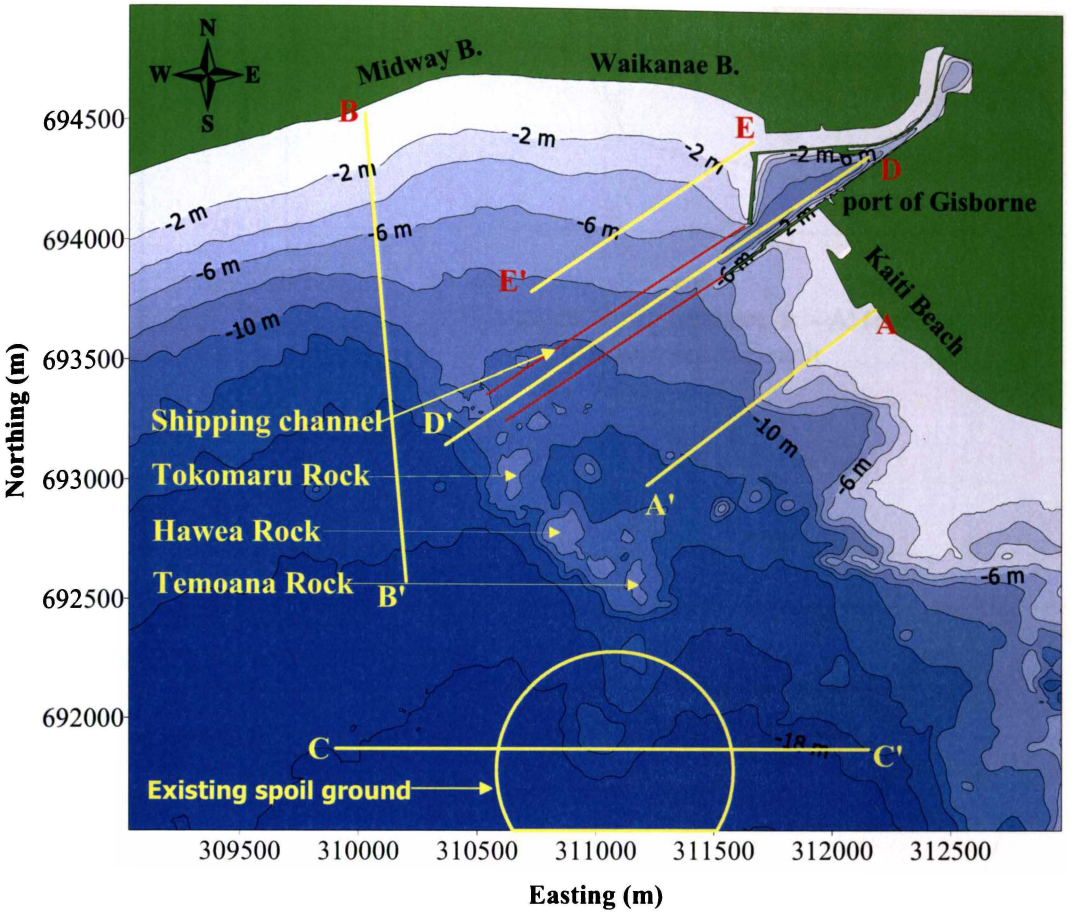

Figure 3.03 Contoured Bathymetry showing transect locations. Transect; A-A' offshore from Kaiti Beach; B-B' offshore from Waikanae and Midway beaches; C-C' through the existing dredge spoil ground; D-D' along the shipping channel and E-E' radiating out from the entrance of the Turanganui River. Co-ordinates are in the Poverty Bay Circuit; Depths are relative to Chart Datum.

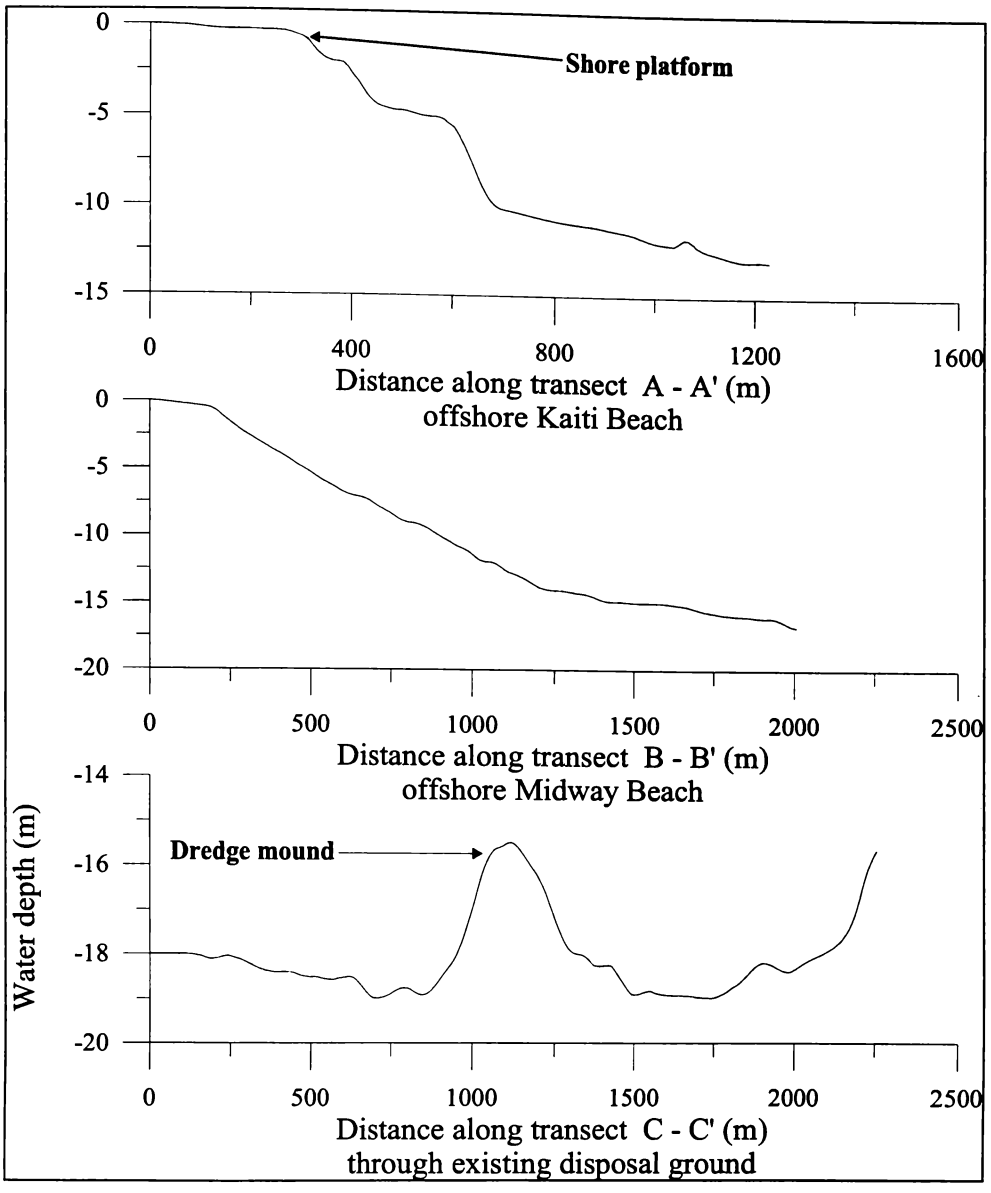

Figure 3.04 Transects of water depth below Chart Datum offshore Kaiti Beach (A-A'), Midway Beach (B-B') and through the existing disposal ground (C-C') based on interpolated bathymetry. The shore platform rocky reef is evident in the depth profile off Kaiti Beach, particularly when compared to the mild slope offshore from Midway Beach. The depth transect through the existing disposal ground illustrates the mound of dredge material.

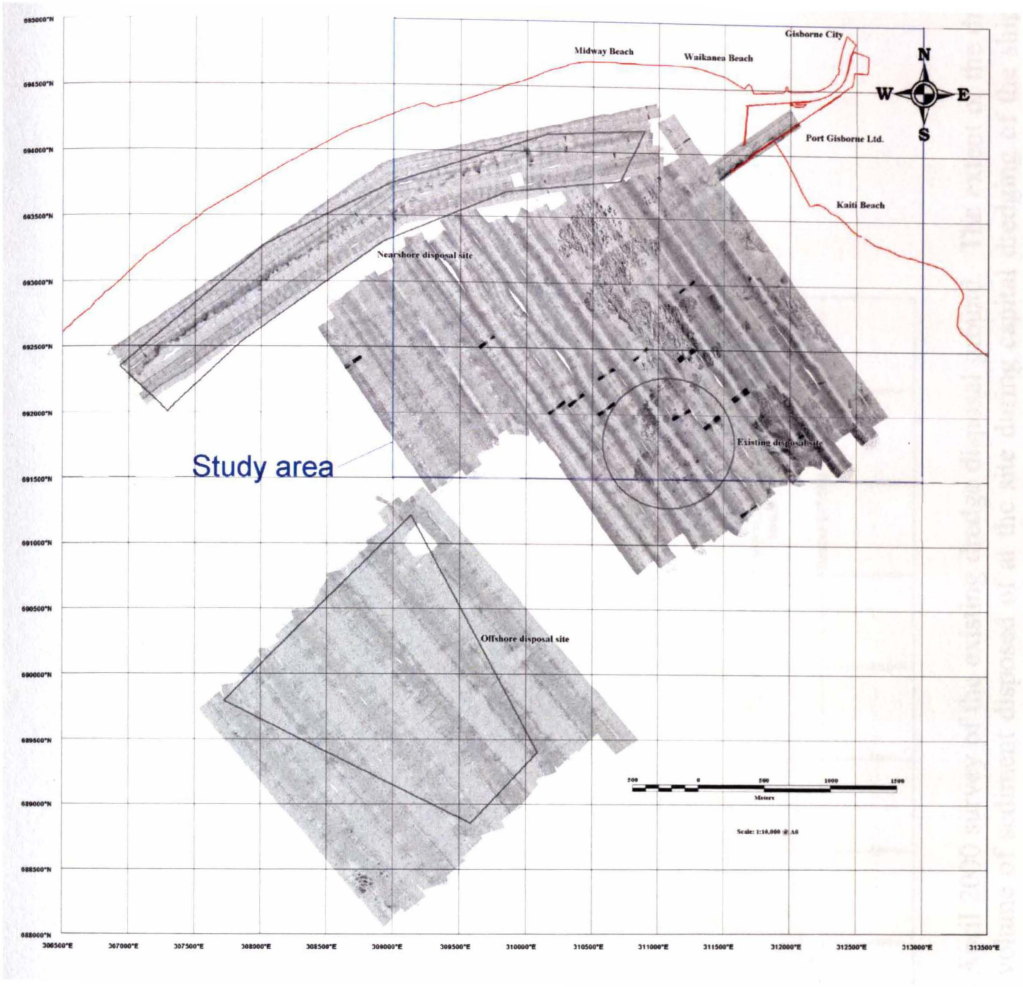

Figure 3.05 Raw side-scan sonar return signal, illustrating the almost 100 % coverage within the study area. Also shown are the existing disposal ground (circular disposal ground), the outer mud disposal ground and the near shore littoral spoil ground. Co-ordinates are in the Poverty Bay Circuit.

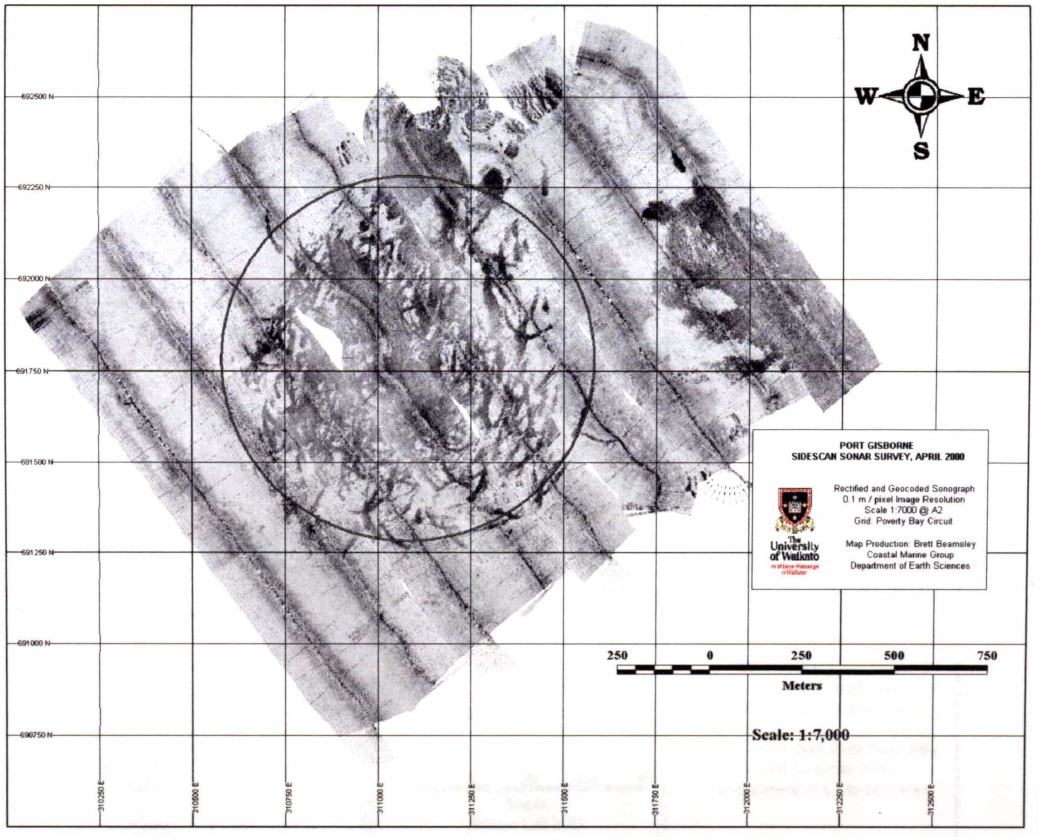

Figure 3.06 Raw side-scan sonar return signal of the April 2000 survey of the existing dredge disposal ground. The extent of the dredge material within the disposal ground reflects the volume of sediment disposed of at the site during capital dredging of the shipping channel and Swinging Basin. Co-ordinates are in the Poverty Bay Circuit.

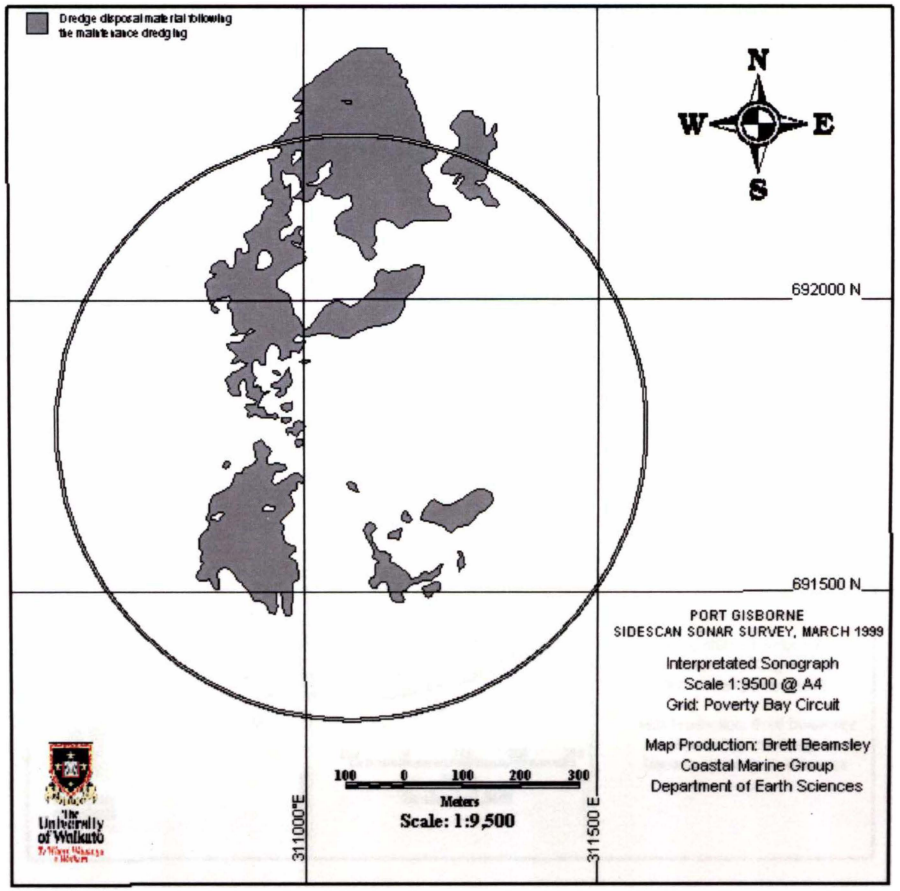

Figure 3.07 Interpreted side-scan sonar return signal showing the spatial distribution of the dredge material within the existing disposal ground following the March 1999 survey. Co-ordinates are in the Poverty Bay Circuit.

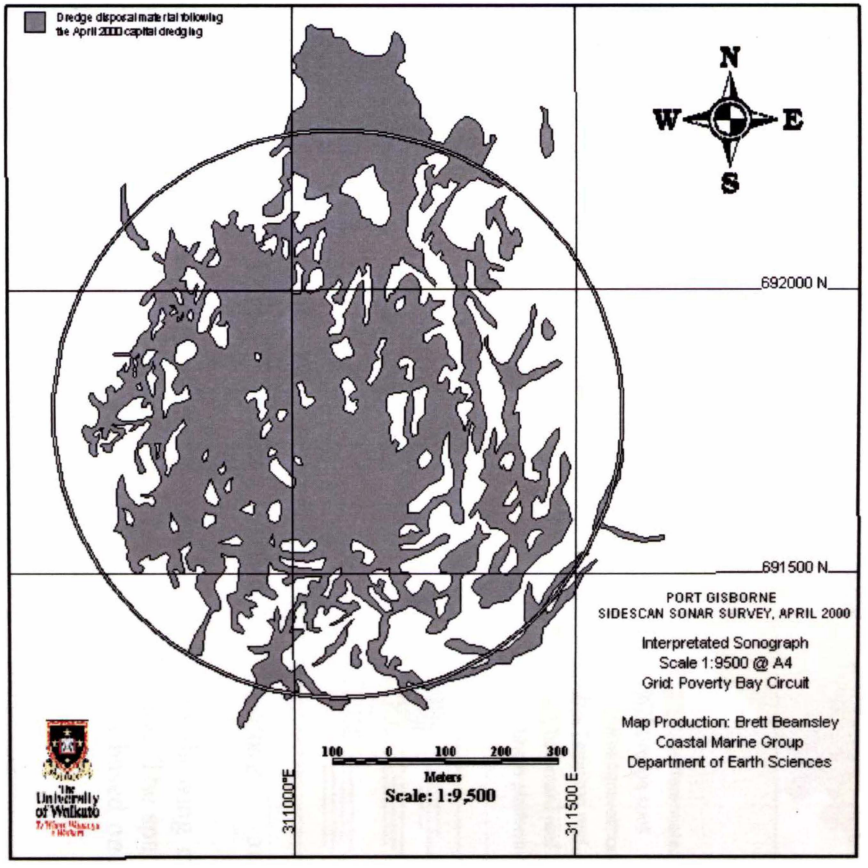

Figure 3.08 Interpreted side-scan sonar return signal showing the spatial distribution of the dredge material within the existing disposal ground following the April 2000 survey. Compared with the March 1999, the coverage extent of the dredge material within the disposal ground is greater due to the large volume of sediment disposed of at the site following capital dredging of the Swinging Basin and shipping channel. Co-ordinates are in the Poverty Bay Circuit.

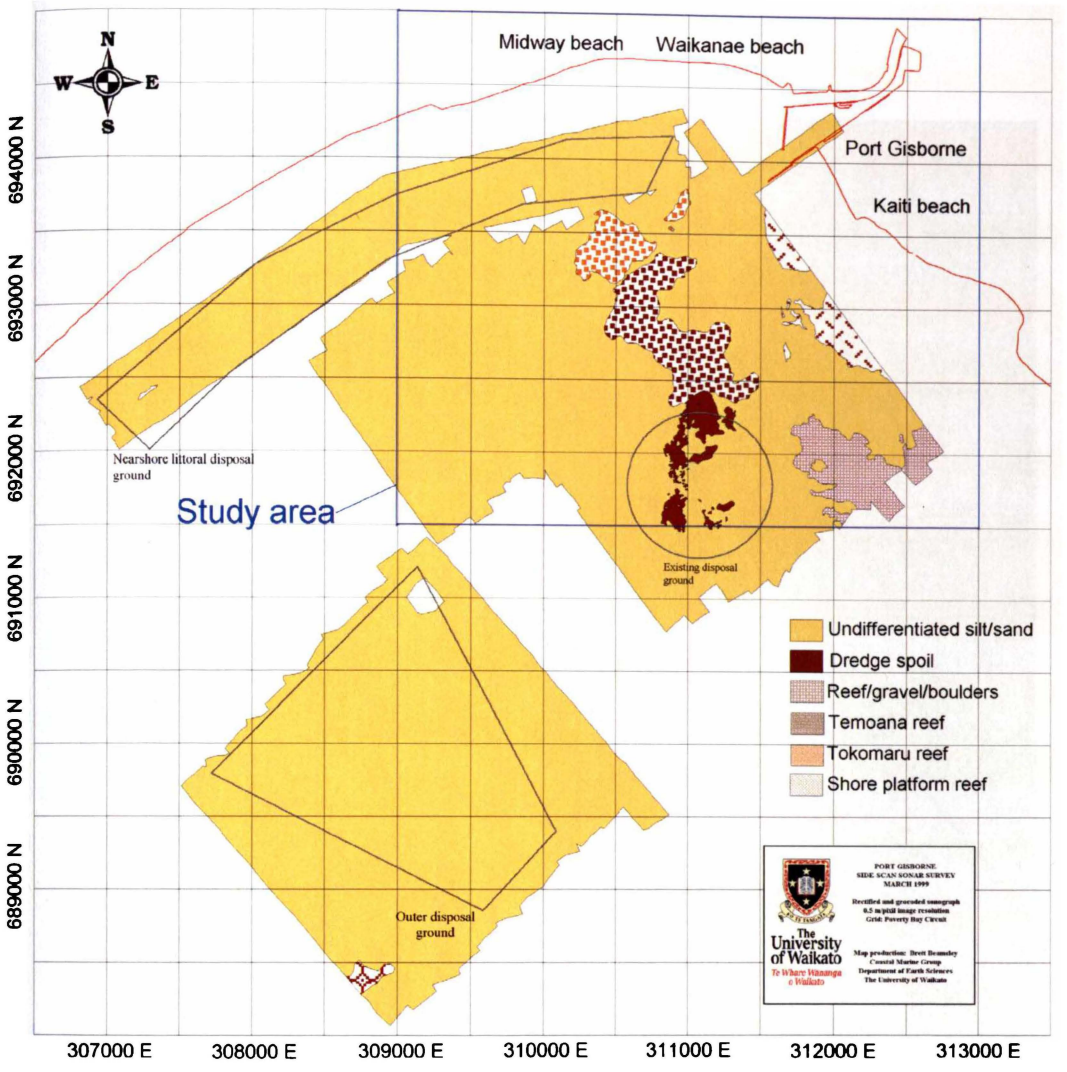

Figure 3.09 Composite interpreted side-scan sonar return signal showing the spatial distribution of the various facies within northern Poverty Bay. The spatial extent of the dredge material within the existing disposal ground is based on the April 2000 survey. Co-ordinates are in the Poverty Bay Circuit.

Figure 3.10 Close-up of the undifferentiated silty sand facies as identified from side-scan sonar record. The image shows lack of any large bedforms or rocky reef outcroppings.

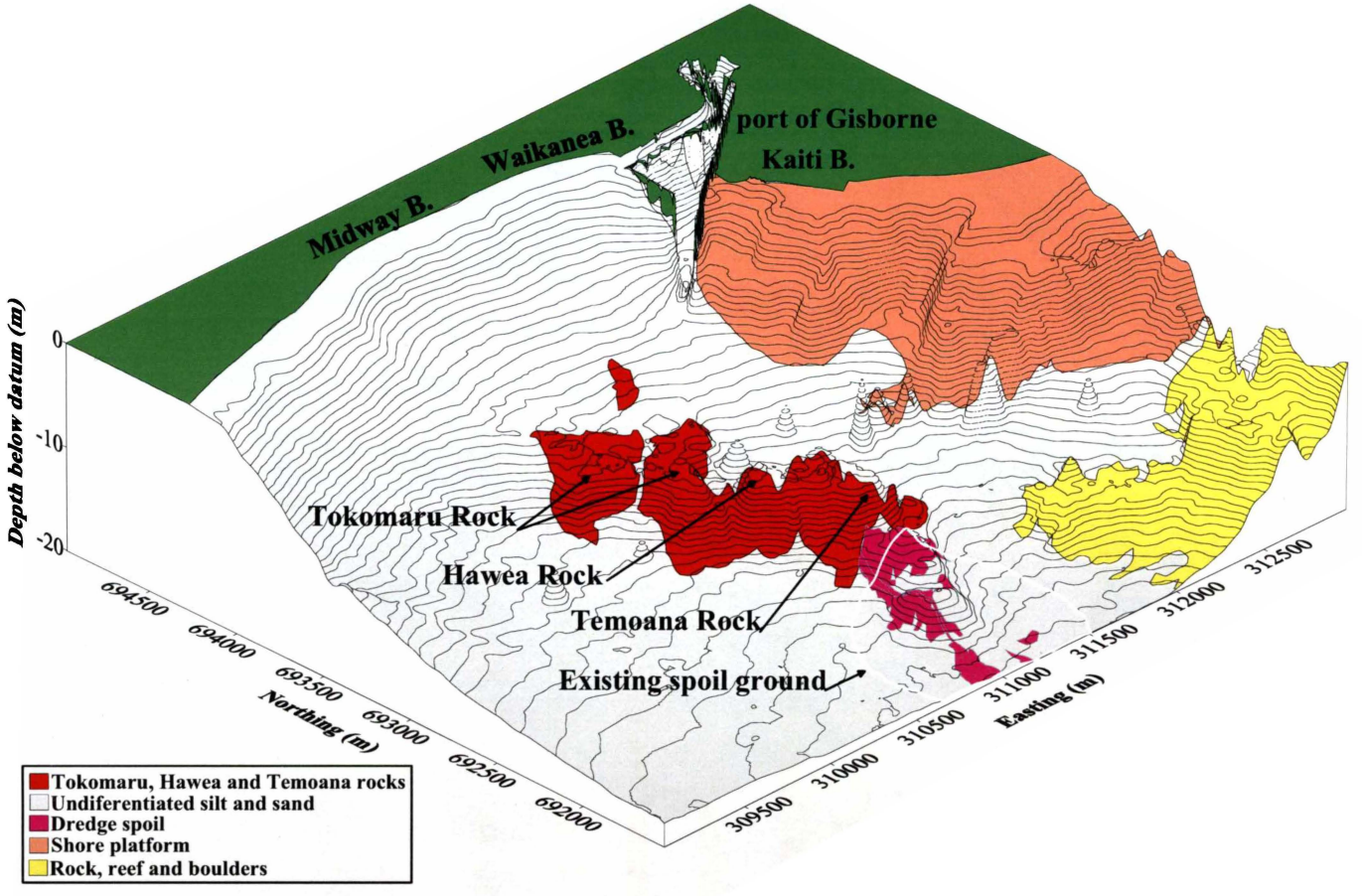

Figure 3.11 Digital terrain model of the bathymetry in the study site showing the spatial distribution of the various facies as identified from the side-scan sonar record. Tokomaru, Temoana and Hawea Rocks are shown to have relatively large vertical relief above the undifferentiated silt and sand. Relatively smaller vertical relief is exhibited by the rocky reef habitat. The dredge mound is also evident. Co-ordinates are in the Poverty Bay Circuit.

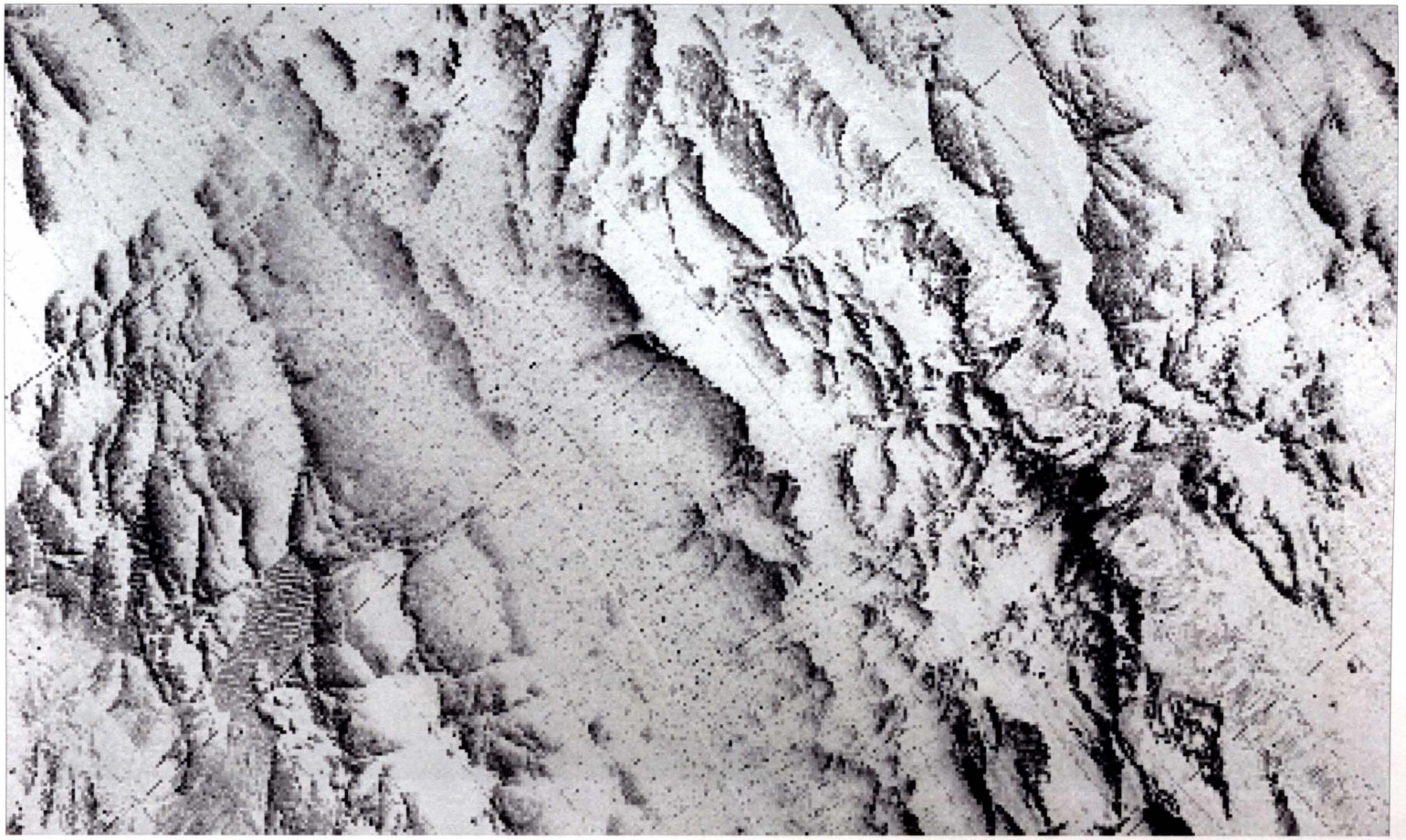

Figure 3.12 Close-up of the side-scan sonar record of Tokomaru Rock showing typical structures, including cracks and jointing within the rocks. Similar structures are found in the side-scan sonar return signal for the Hawea and Temoana rocks as well.

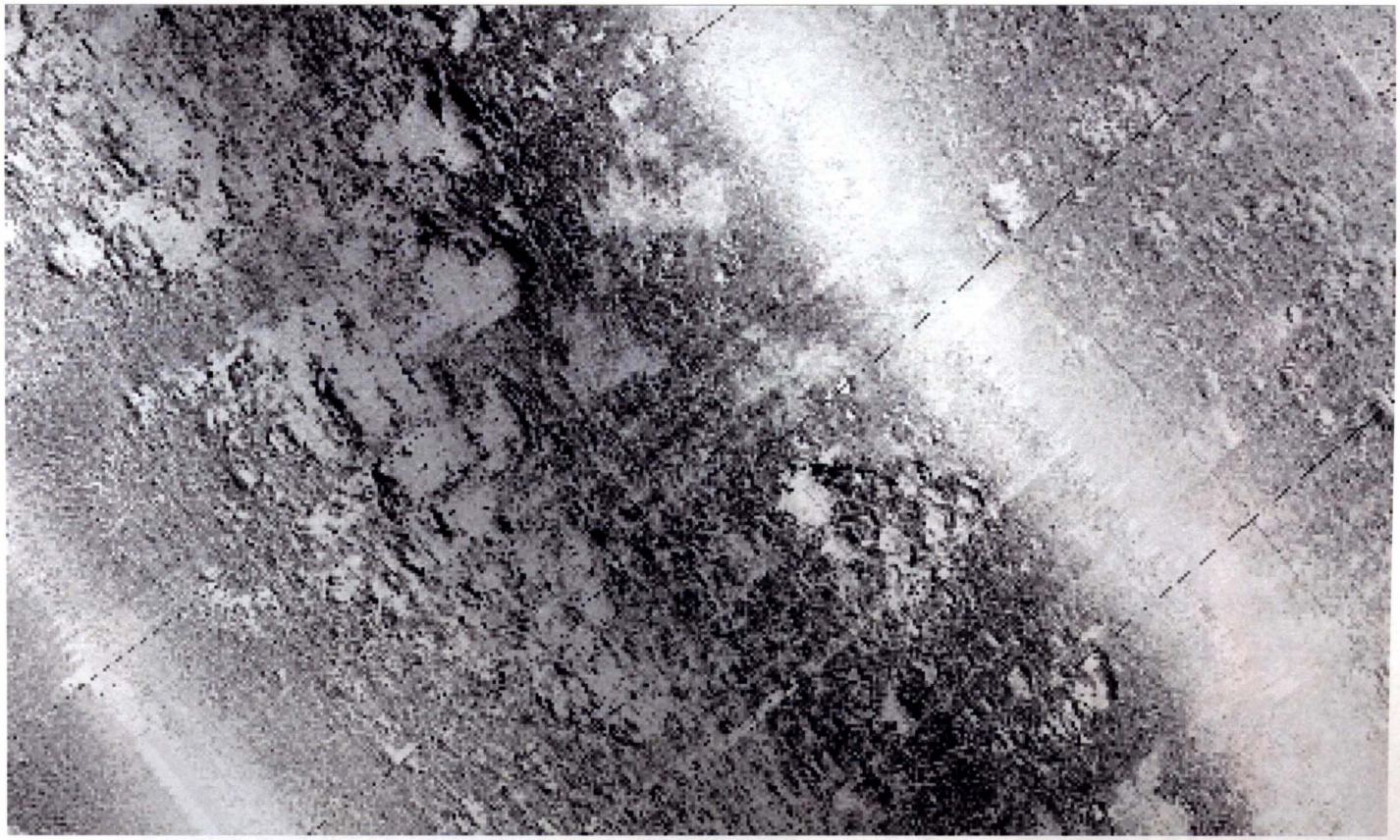

Figure 3.13 Close-up of the raw side-scan sonar record of the rocky reef facies. The image shows a lack of cracks and joints within the rocky reef facies, particularly in comparison with the Tokomaru, Hawea and Temoana rocks (Figure 3.12).

Figure 3.14 Image illustrating the extent of the inter-tidal shore platform offshore from Kaiti Beach (in the foreground). To the right is part of the port of Gisborne log storage area. In the background is Young Nick Head.

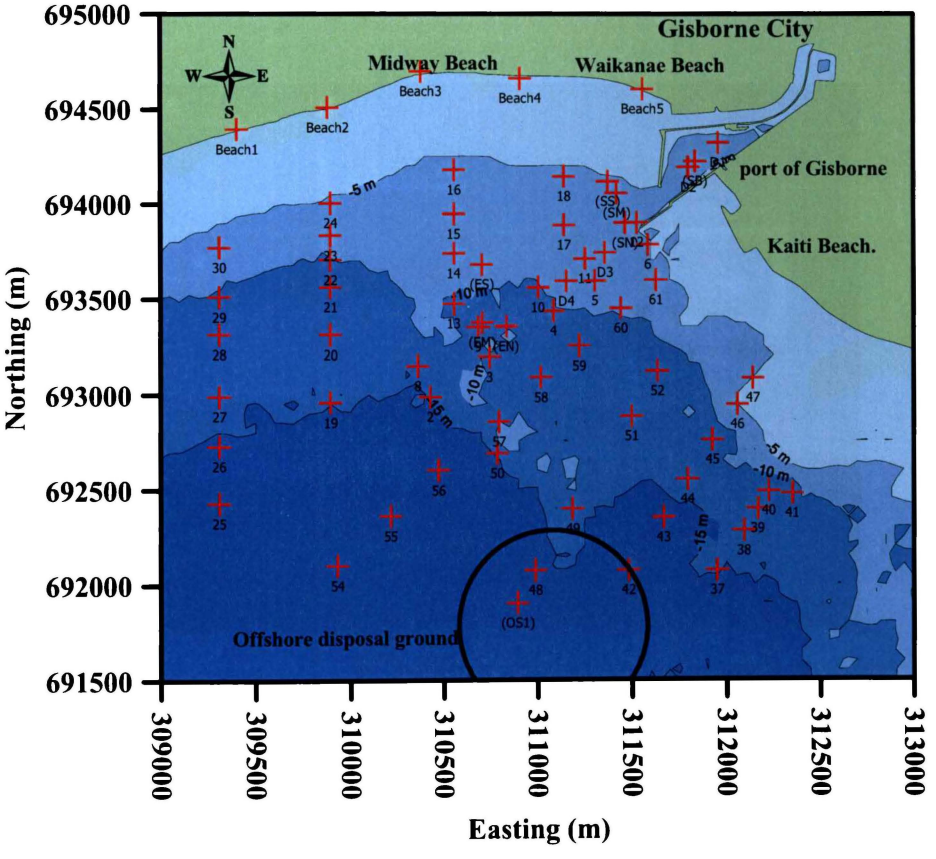

Figure 3.15 Locations of surficial sediment sample sites within the study site. Co-ordinates are in Poverty Bay Circuit.

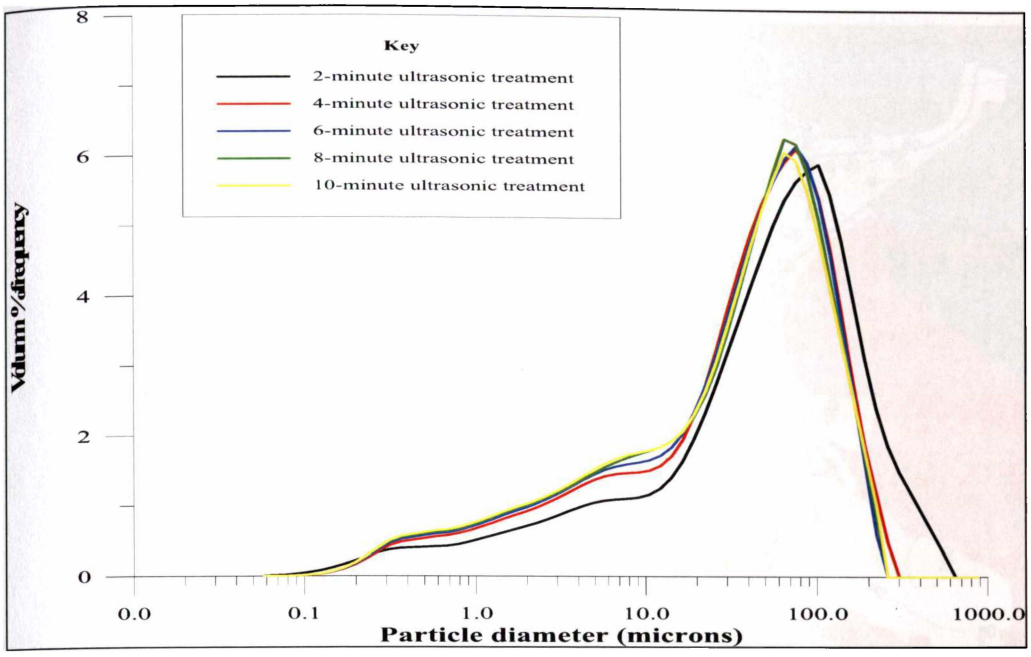

Figure 3.16 Grain size distribution for sample collected in 12 m water depth after 2, 4, 6, 8 and 10 minutes of ultrasonic treatment to disperse flocks remaining after treatment with hydrogen peroxide (to remove organic material) and Calgon (de-flock solution). The figure illustrates that after 4 minutes of ultrasonic treatment there is only limited change in the grain size distribution.

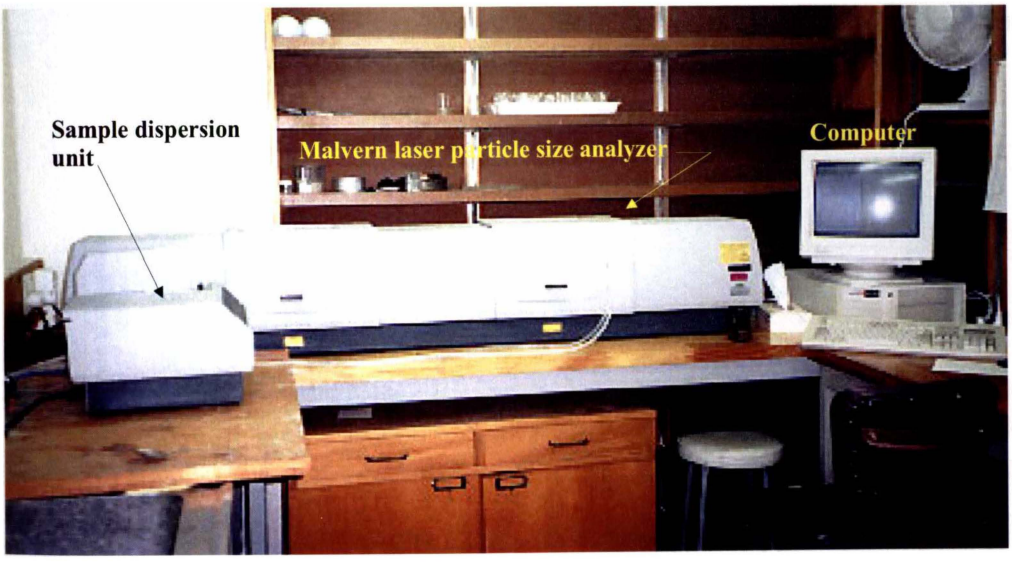

Figure 3.17 Malvern laser particle size analyser, showing the sample dispersion unit in which the sample were treated with ultrasonic noise in order to disperse the flocculated particles remaining after treatment with a de-flock solution (Calgon).

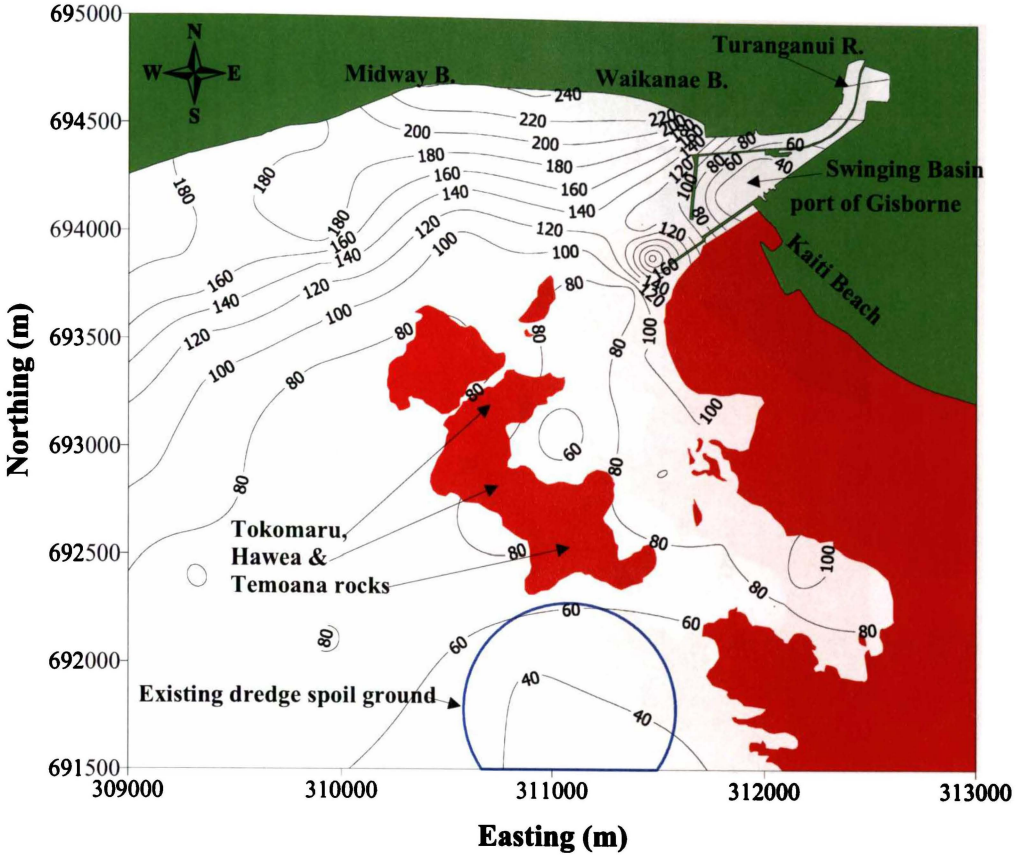

Figure 3.18 Spatial distribution of the mean grain size measured in microns (μm). Mean grain size is shown to decrease with distance offshore from Midway and Waikanae beaches. Co-ordinates are in the Poverty Bay Circuit.

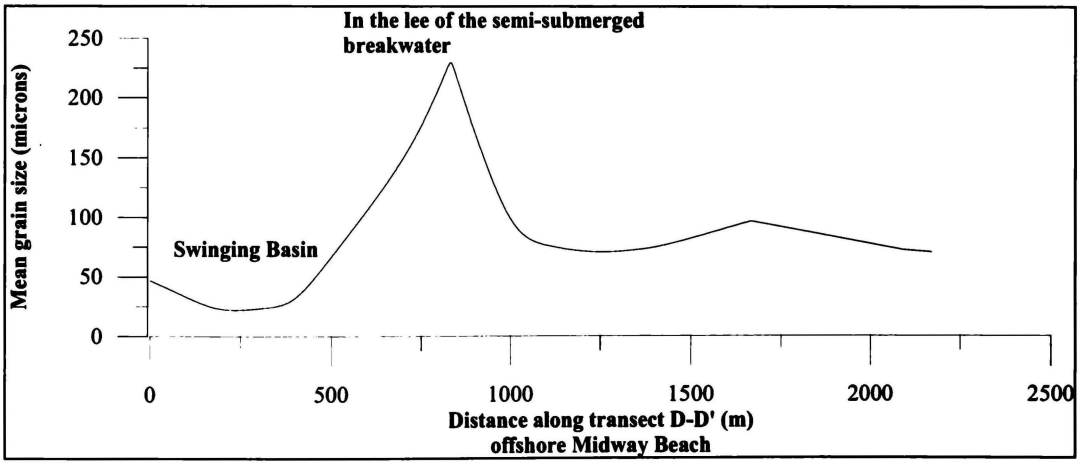

Figure 3.19 Grain size transect illustrating the variation in the surficial sediment mean grain size (μm) along the shipping channel. Largest mean grain size is shown to occur in the lee of the semi-submerged breakwater, whilst finest mean grain size is found within the Swinging Basin.

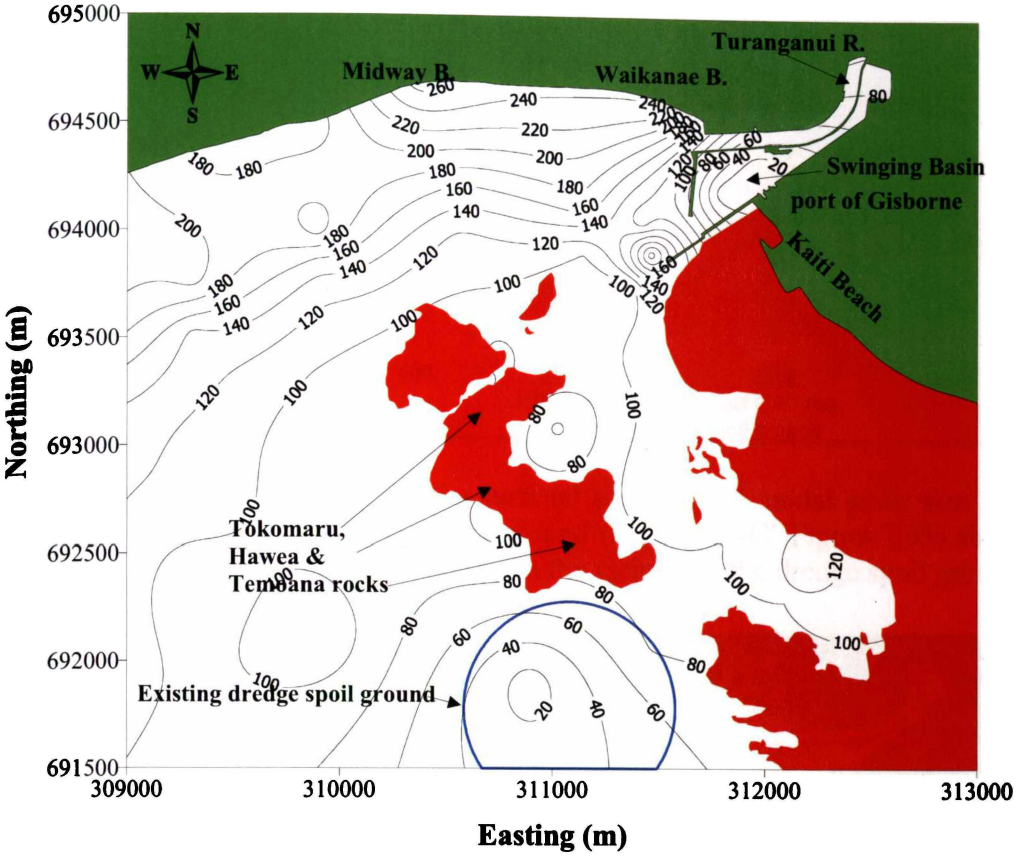

Figure 3.20 Spatial variation in the surficial sediments 1st modal grain size within the study area. Modal grain size is shown to decrease with distance offshore from Midway and Waikanae beaches. Additionally the modal grain size is shown to be finer in the vicinity of the existing dredge spoil ground, and increasing with distance from the approximate centre of the spoil ground. Co-ordinates are in the Poverty Bay Circuit.

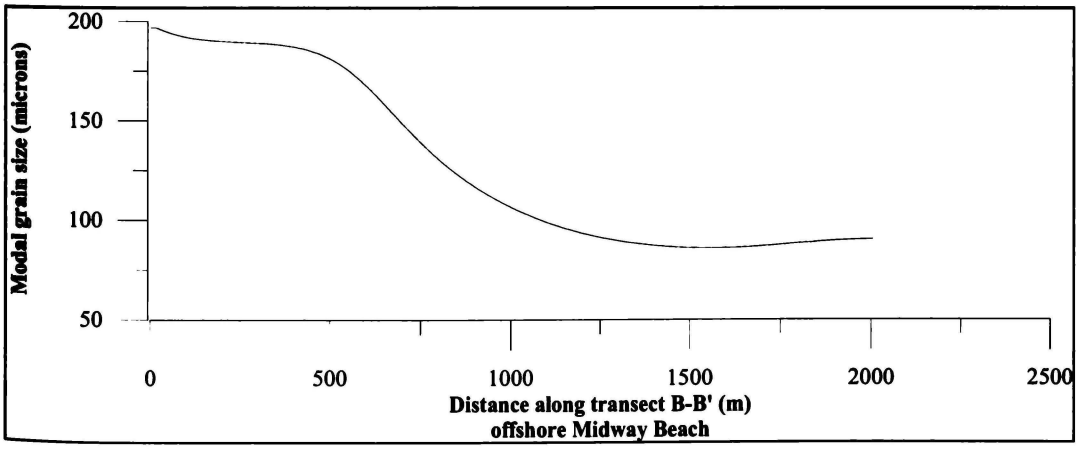

Figure 3.21 Transect of the surficial sediment modal grain size (μm) offshore from Midway Beach (transect B-B' Figure 3.03) showing the modal grain size decreases with distance from the beach.

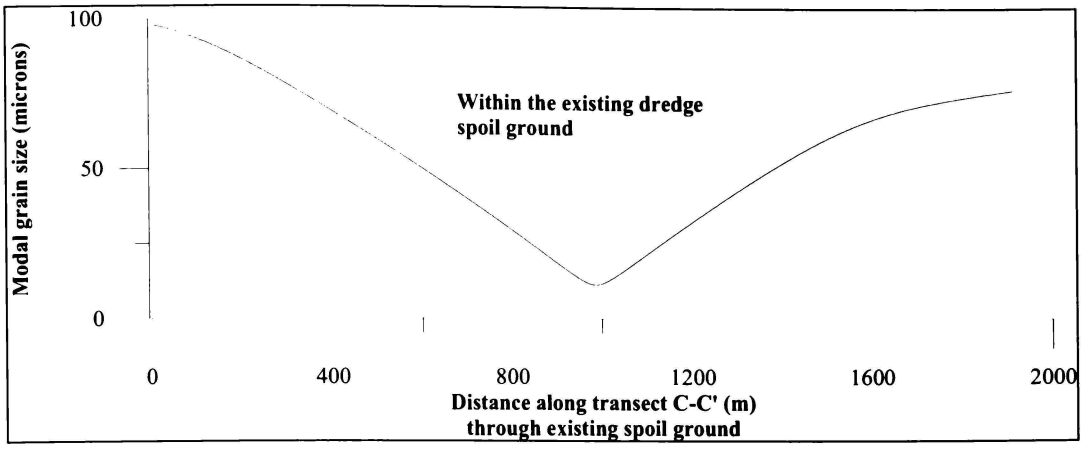

Figure 3.22 Transect of the surficial sediment 1st modal grain size (μm) through the existing dredge spoil ground (transect C-C' Figure 3.03) showing the 1st modal grain size decreases in the vicinity of the dredge spoil ground.

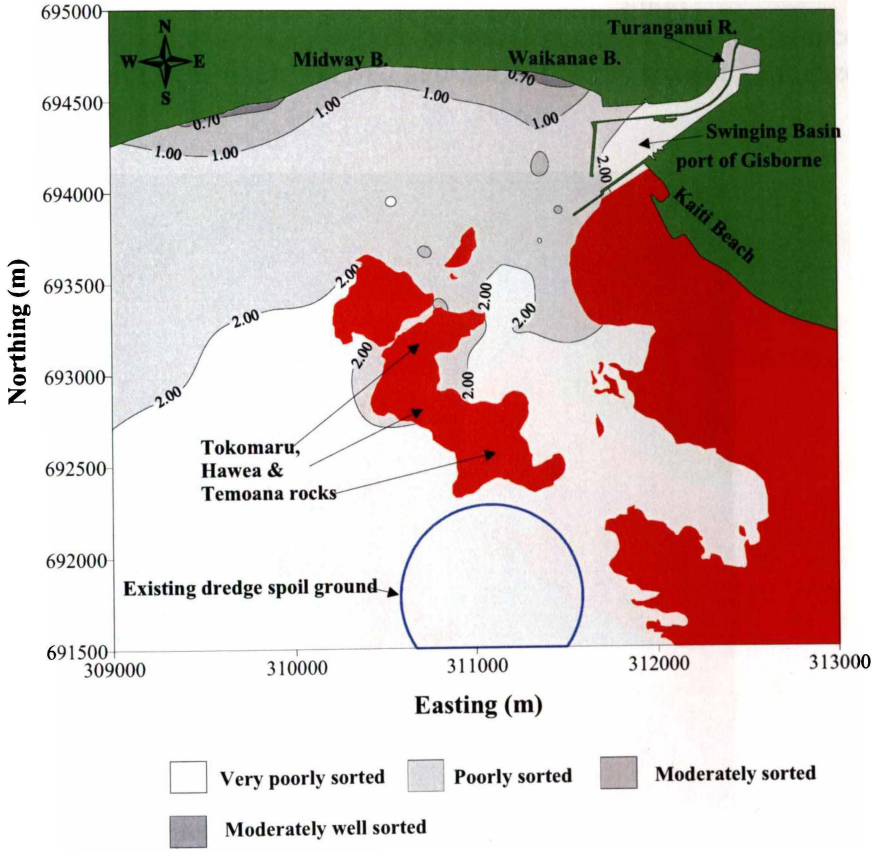

Figure 3.23 Map illustrating the spatial variability in the surficial sediment sorting characteristics within the study area. Surficial sediment becomes more poorly sorted with distance offshore from Midway and Waikanae beaches as a result of the decrease in wave-orbital currents with increased water depth. Co-ordinates are in the Poverty Bay Circuit.

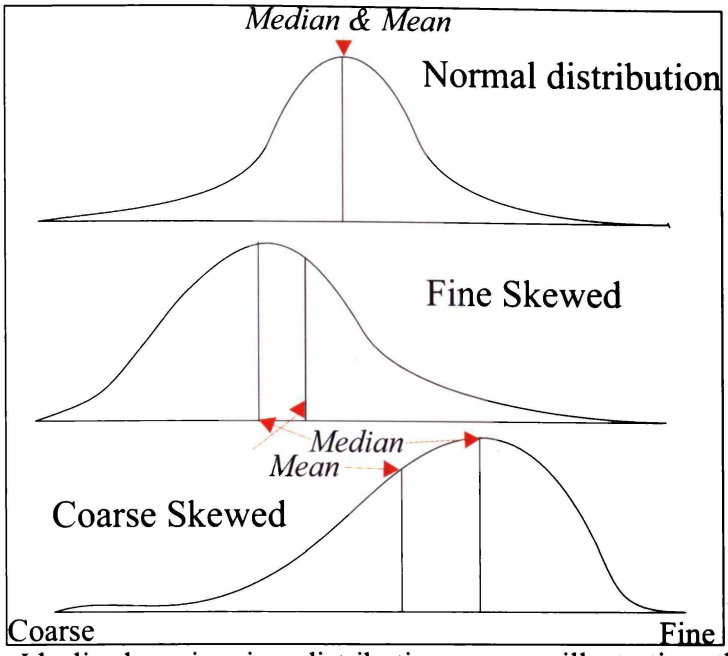

Figure 3.24 Idealised grain size distribution curves illustrating the difference between coarsely skewed, finely skewed and normal "bell" shaped grain size distribution curves.

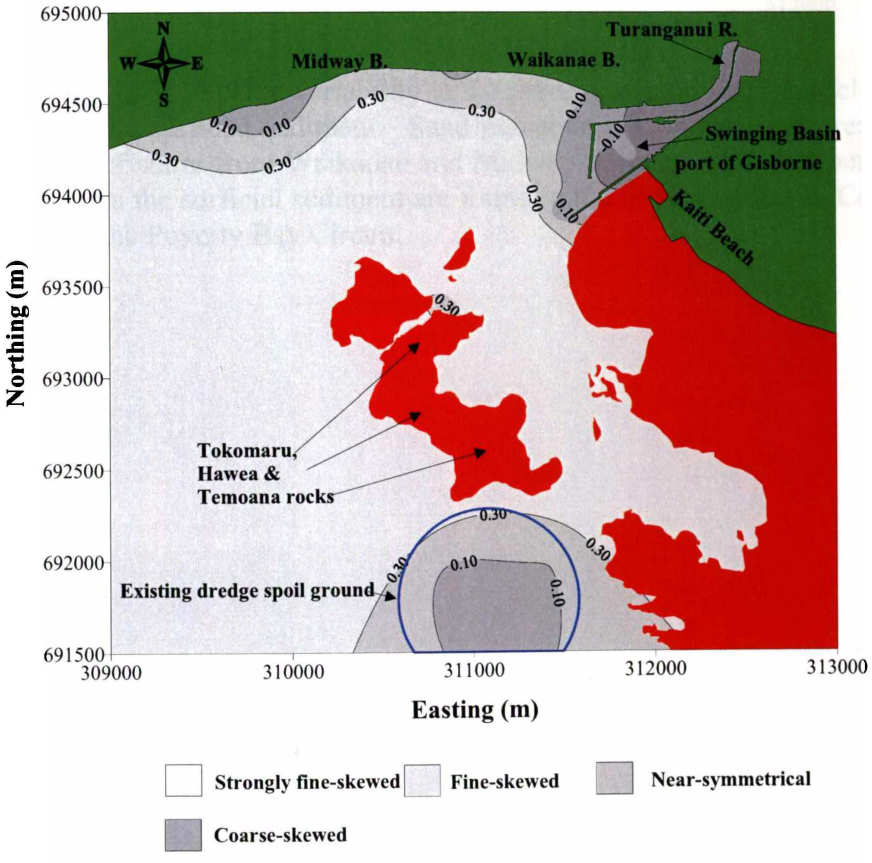

Figure 3.25 Map illustrating the spatial variability in the Skewness of the surficial sediment grain size distribution within the study area. Sediment within the existing dredge spoil ground display near-symmetrical skewnesses due to mixing of the naturally occurring sediments given the water depth and dredged material from the swinging basin and the shipping channel. Co-ordinates are in the Poverty Bay Circuit.

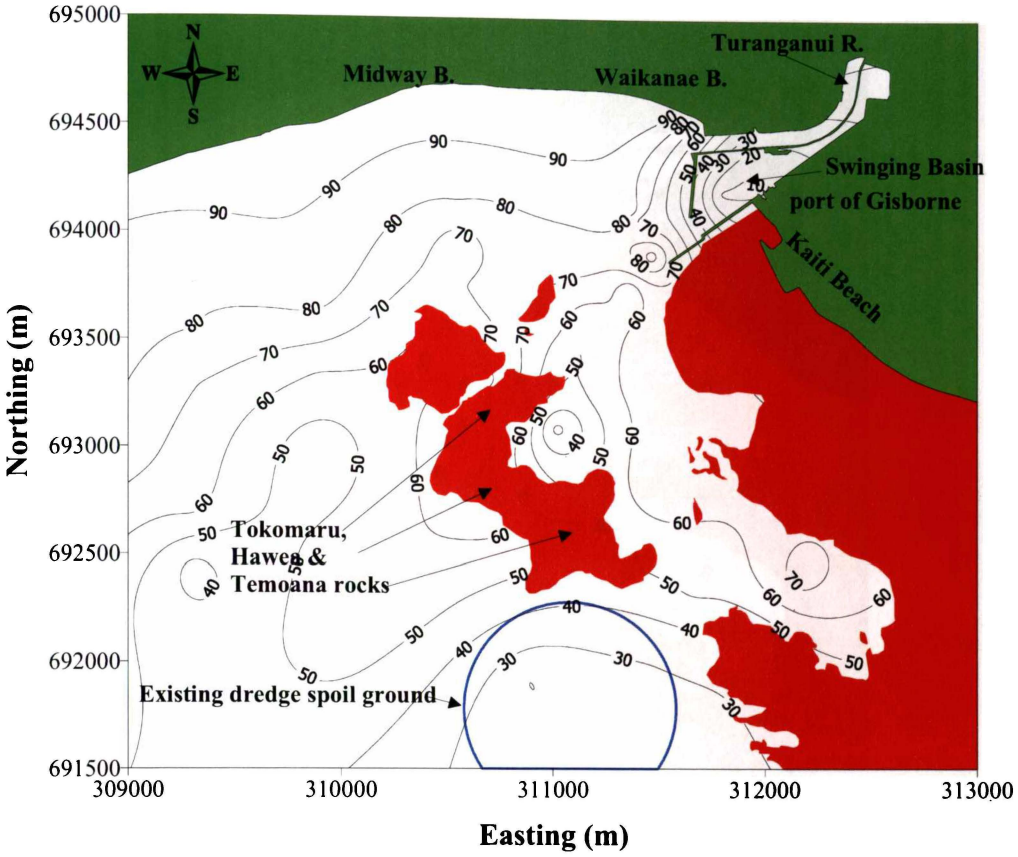

Figure 3.26 Spatial variability in the percent of sand sized particles (> 62.5 μm) in the surficial sediment. Sand percentage is shown to decrease with distance offshore from Waikanae and Midway beaches. Smallest percentages of sand in the surficial sediment are found in the Swinging Basin. Co-ordinates are in the Poverty Bay Circuit.

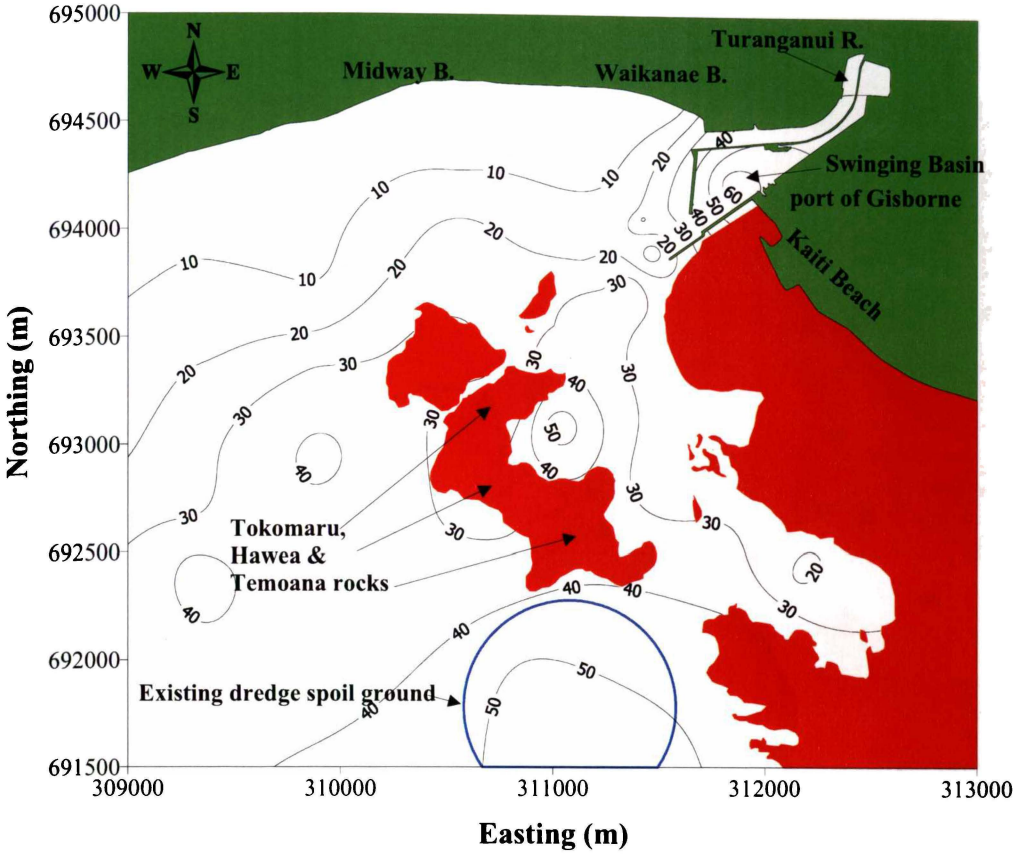

Figure 3.27 Spatial variability in the percent of silt sized particles (between 4 and 62.5 μm) in the surficial sediment. Silt percentage is shown to increase with distance offshore from Waikanae and Midway beaches. Largest percentages of silt in the surficial sediment are found in the Swinging Basin. Elevated percentages of silt are also found in the vicinity of the existing dredge spoil ground. Co-ordinates are in the Poverty Bay Circuit.

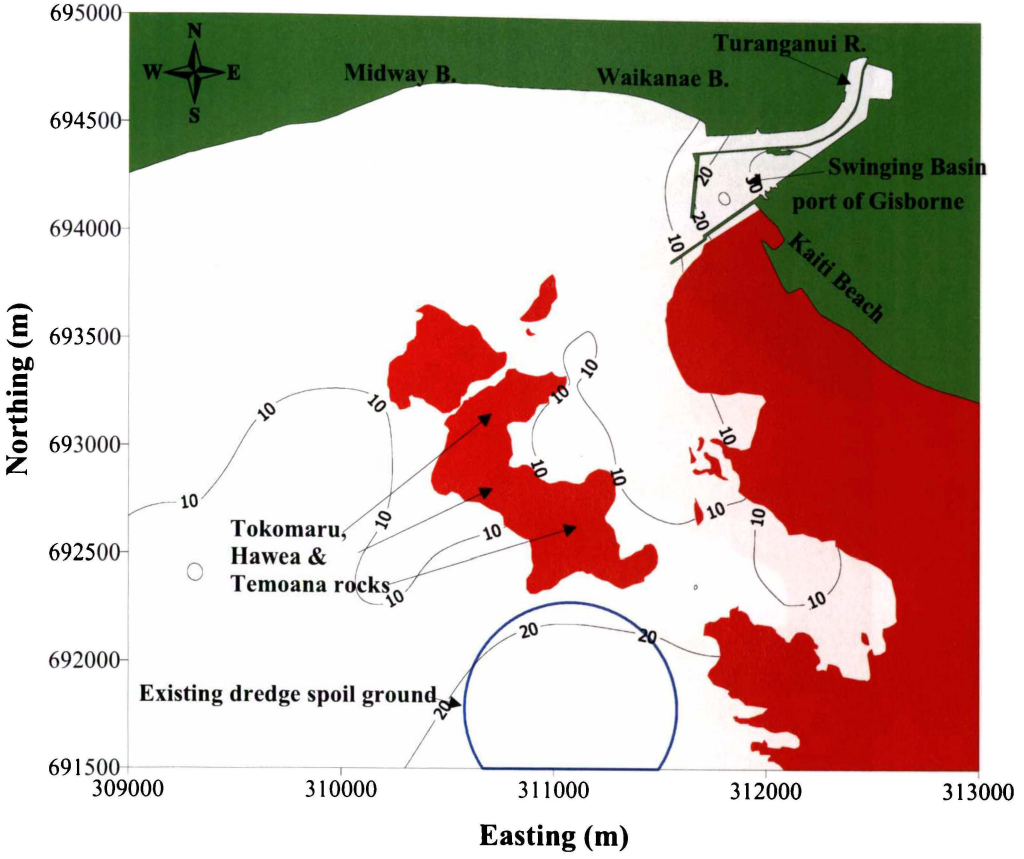

Figure 3.28 Spatial variability in the percent of clay sized particles (< 4 μm) in the surficial sediment. Clay percentage is shown to increase with distance offshore from Waikanae and Midway beaches. Largest percentages of clay in the surficial sediment are found in the Swinging Basin. Elevated percentages of clay are also found in the vicinity of the existing dredge spoil ground. Co-ordinates are in the Poverty Bay Circuit.

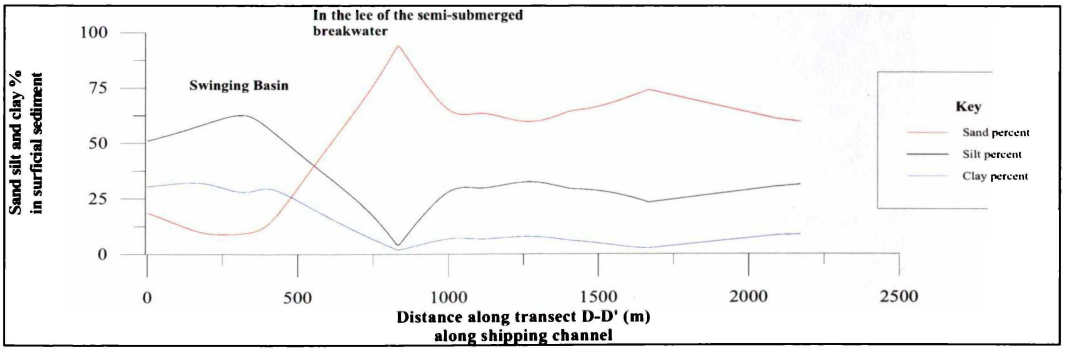

Figure 3.29 Transects of the variation in volume percent sand, silt and clay percentages within the surficial sediment with distance along shipping channel (transect D-D' Figure 4.02). Sand percentage is shown to increase and silt and clay percentages decrease, in the lee of the semi-submerged breakwater. High silt and clay percentages are found in the Swinging Basin.

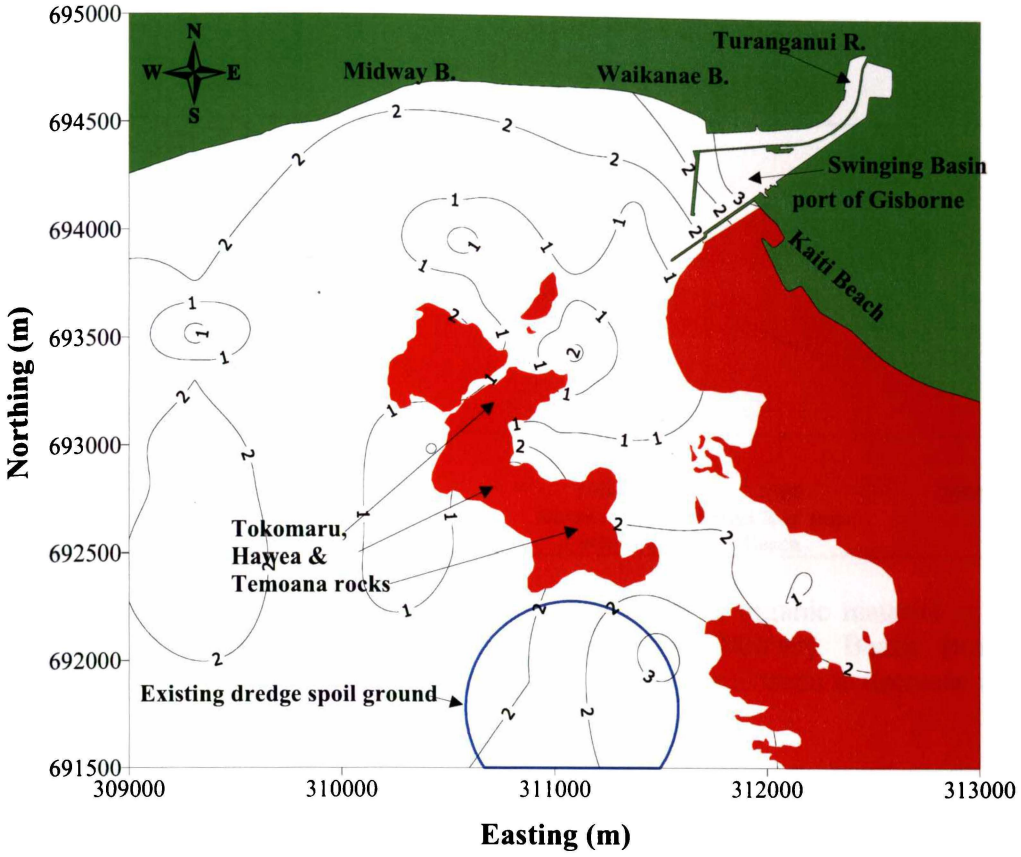

Figure 3.30 Spatial distribution in the percentage of organic content in the surficial sediment. Relatively high organic percentages are found on Waikanae and Midway beaches (due to flotsam), around the mouth of the Turanganui River, within the Swinging Basin and in the vicinity of the existing dredge spoil ground. Co-ordinates are in the Poverty Bay Circuit.

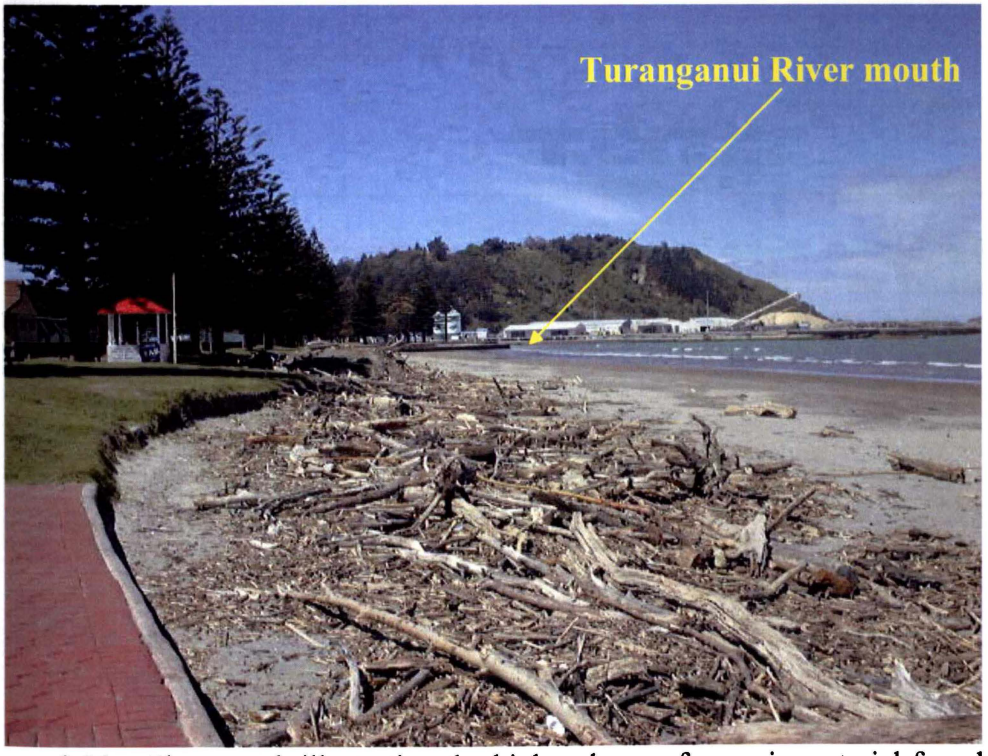

Figure 3.31 Photograph illustrating the high volume of organic material found on the beaches about the mouth of the Turanganui River.

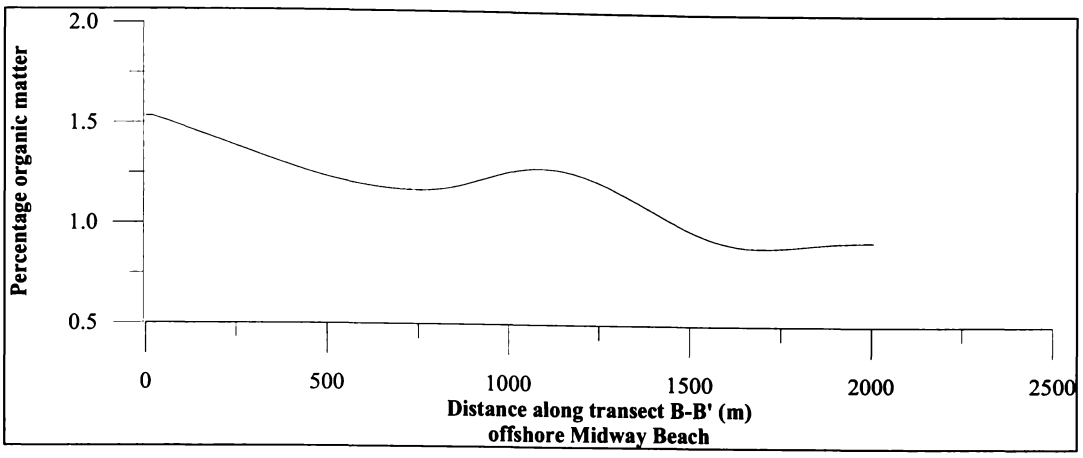

Figure 3.32 Transect showing the percentage of organic material in the surficial sediment with distance offshore from Midway Beach (transect B-B', Figure 3.03). Organic content shows a general trend to decrease with distance offshore.

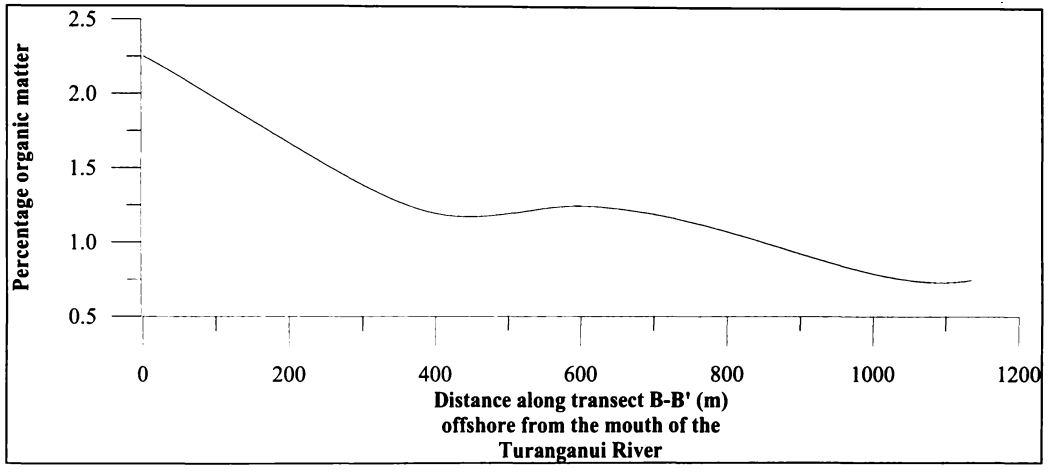

Figure 3.33 Transect showing the percentage of organic material in the surficial sediment with distance offshore from the mouth of the Turanganui River (Transect E-E', Figure 3.03). Organic content shows a general trend to decrease with distance offshore from the river mouth.

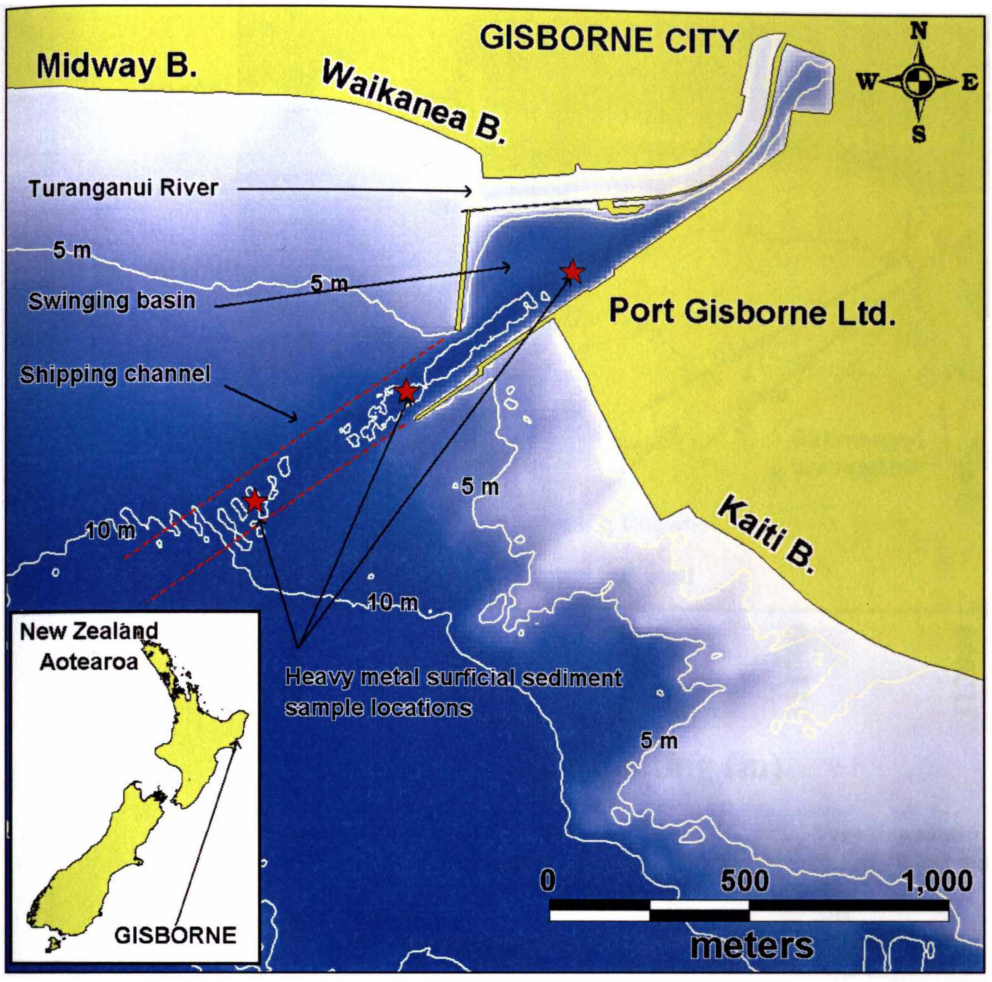

Figure 3.34 Heavy metal surficial sediment sample locations within the port Gisborne Swinging Basin and shipping channel. Samples were analysed for: Cadmium; Chromium Copper; Mercury; Lead and Zinc at Hill Laboratories, which is accredited by International Accreditation New Zealand.

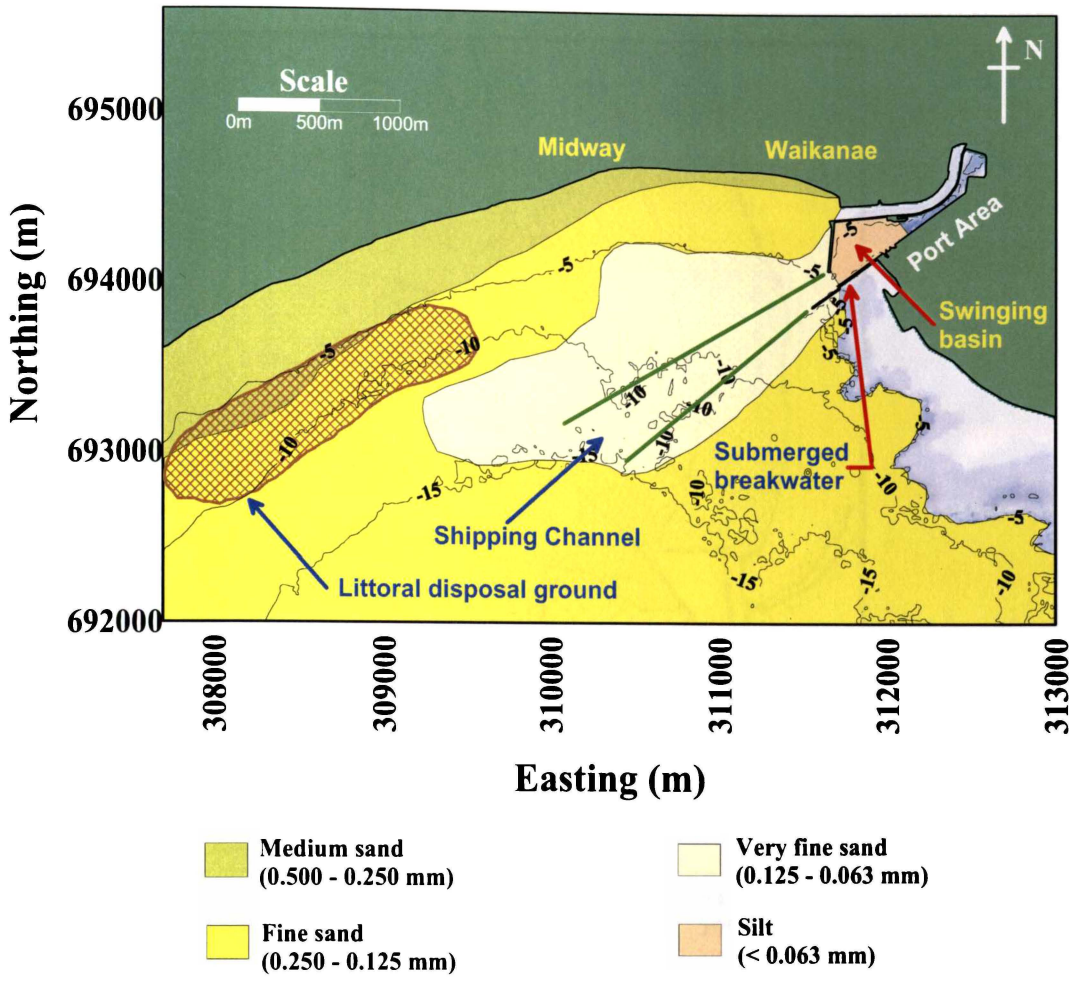

Figure 3.35 Map of surficial sediment mean grain size as given by Beamsley et al., (1998). Note the lack of rocky reef facies within northern Poverty Bay, which should be treated as devoid of surficial sediment in numerical sediment transport modelling.

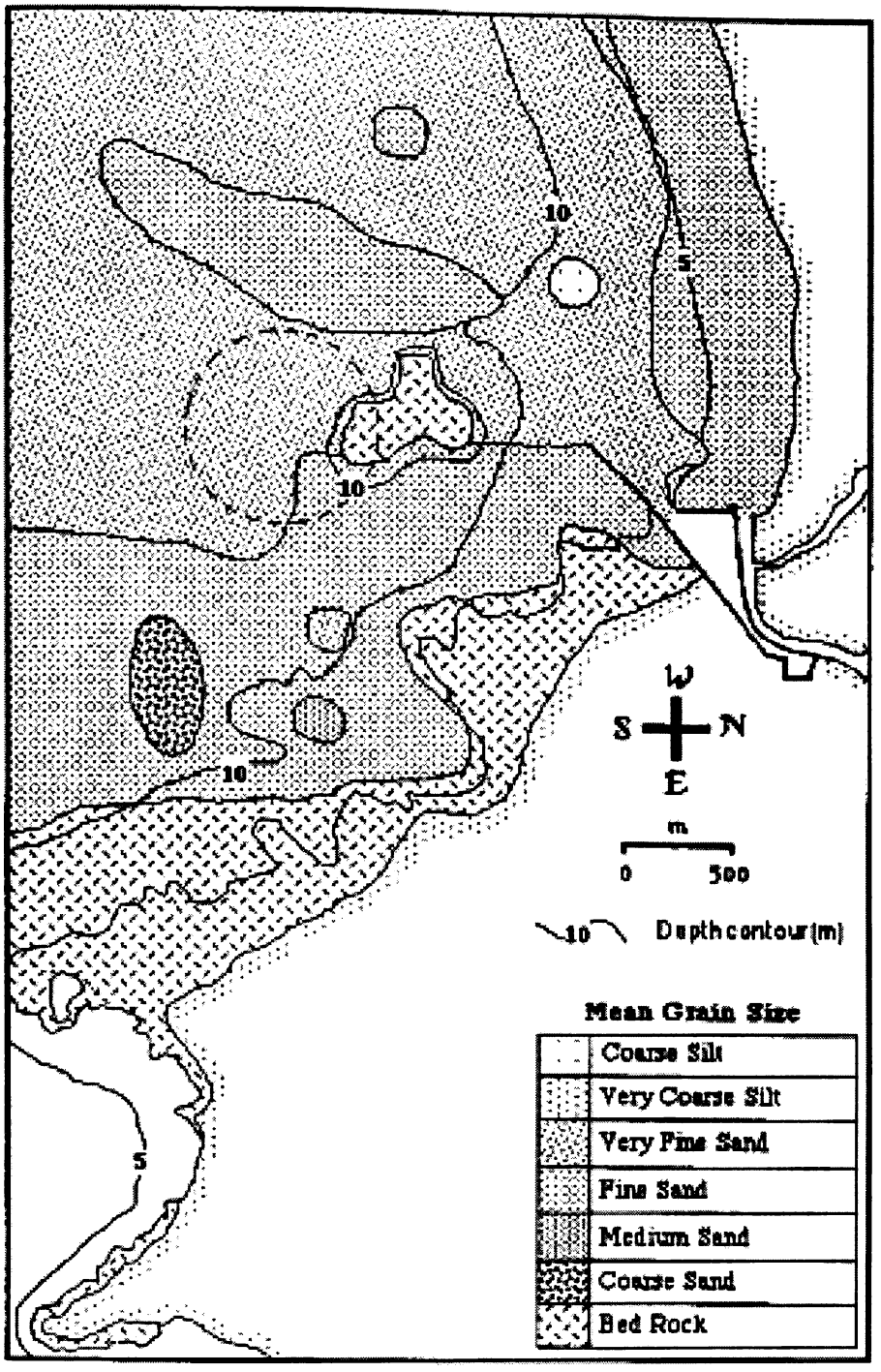

Figure 3.36 Map of surficial sediment mean grain size as given by Kensington, (1990). Grain sizes descriptive terms based on the Folk, (1968) classification scheme.

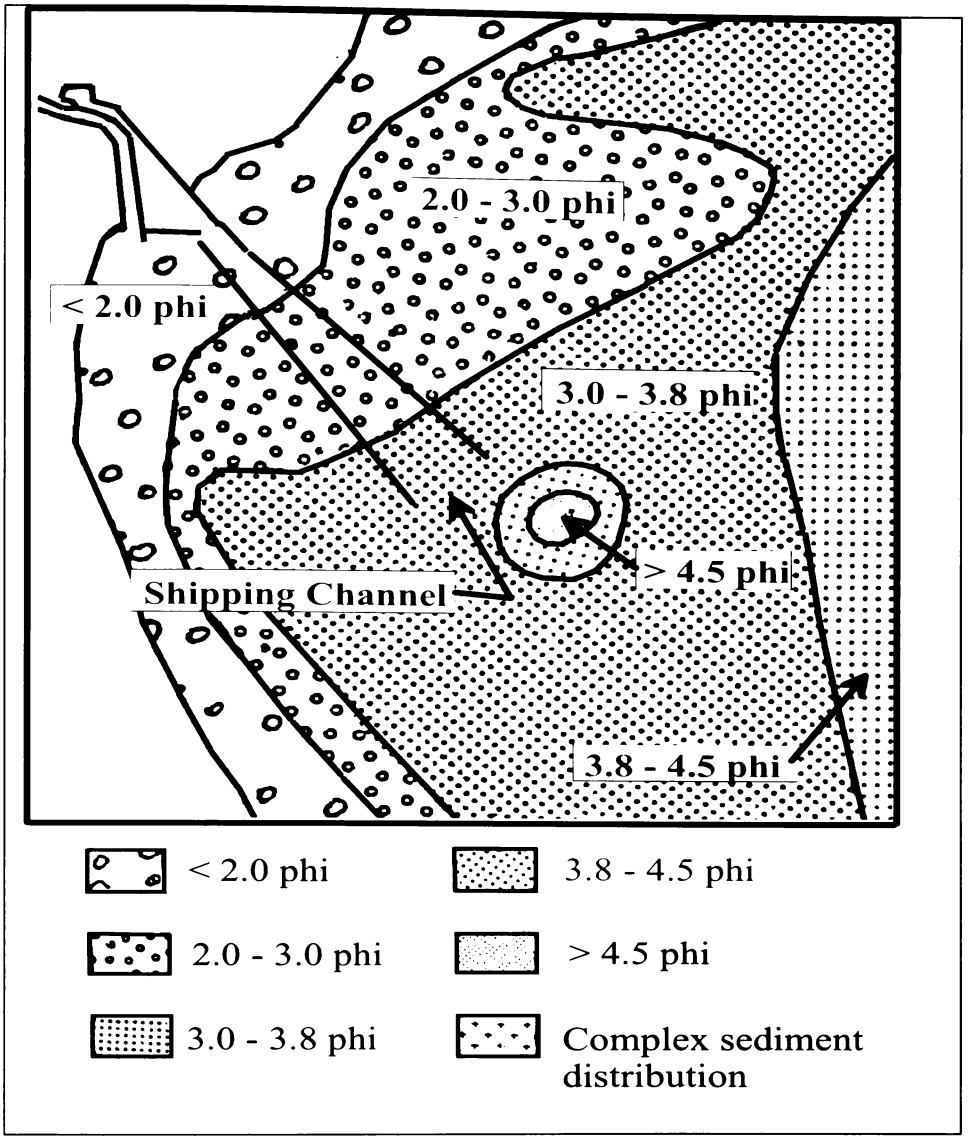

Figure 3.37 Map of surficial sediment mean grain size (phi) as given by Miller, (1981). Note the lack of rocky reef facies within northern Poverty Bay, which should be treated as devoid of surficial sediment in numerical sediment transport modelling.

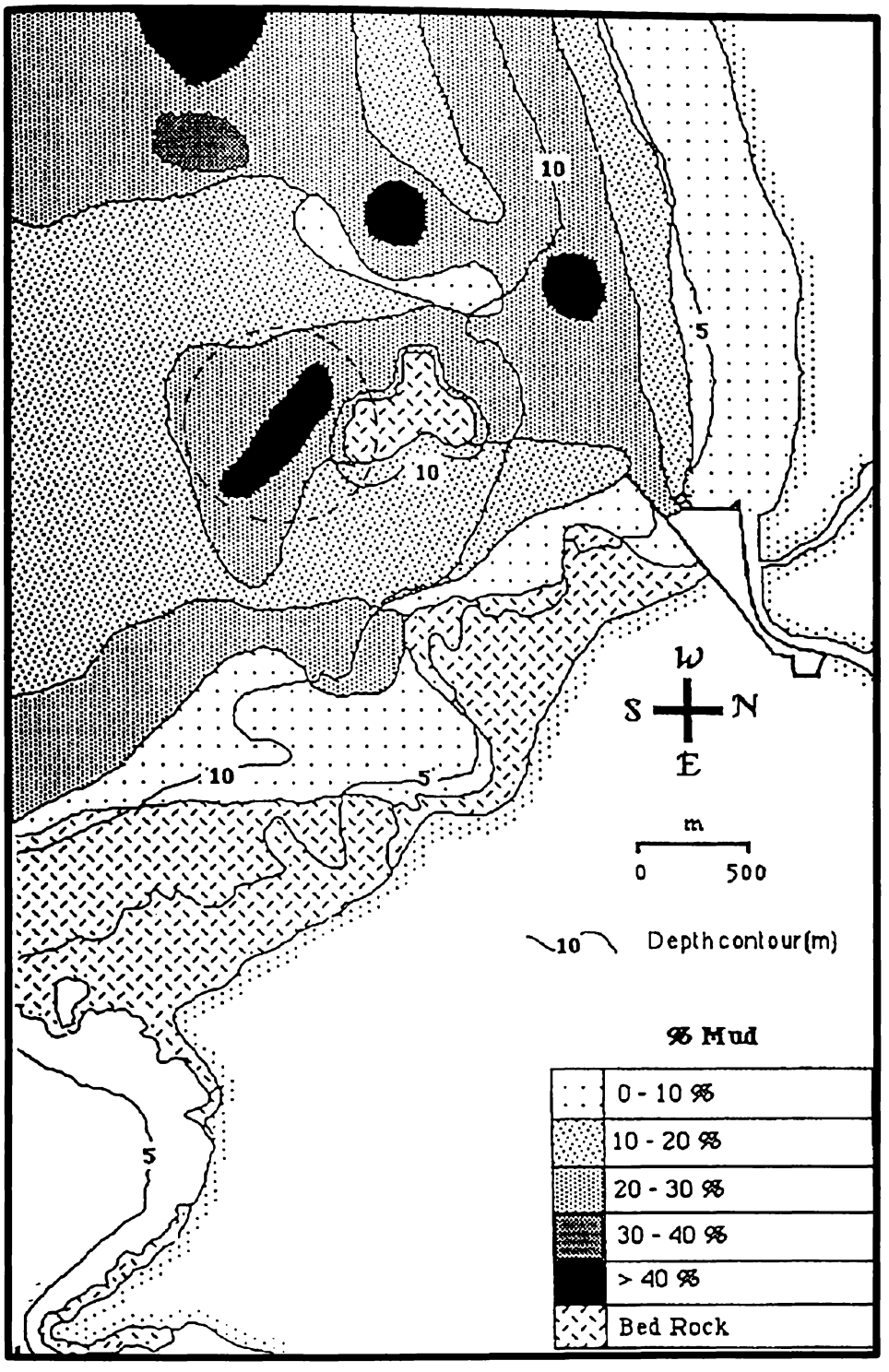

Figure 3.38 Volume percent mud in surficial sediment from Kensington, (1990). The majority of sediment samples were collected in 1986 and some in 1989. Highest mud content in the surficial sediment is found within the existing disposal ground (>40%), however the mean grain size distribution map produced by Kensington (Figure 3.36) does not identify the sediment within the disposal ground to be relatively fine.

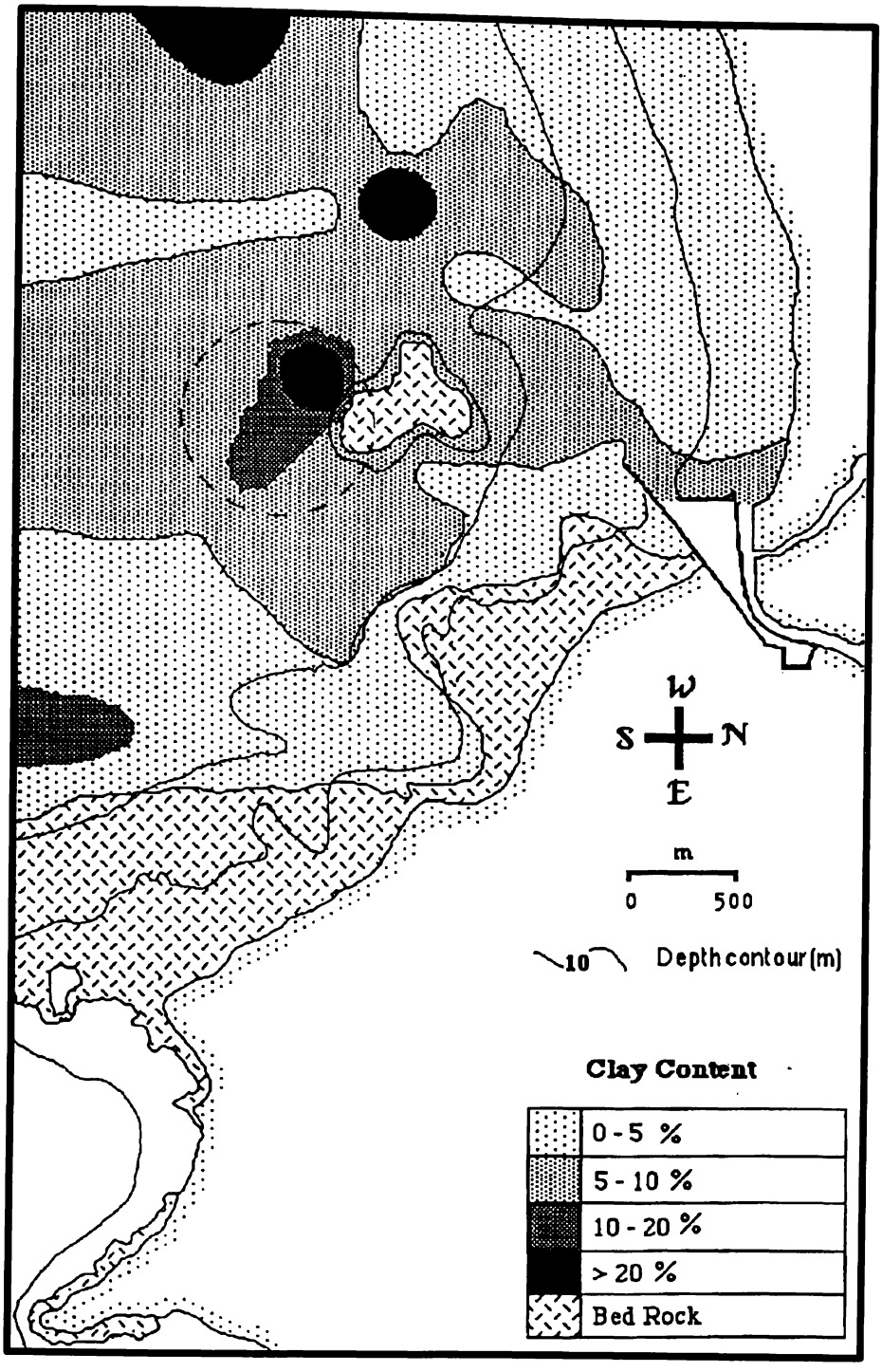

Figure 3.39 Volume percent clay in surficial sediment from Kensington, (1990). The majority of sediment samples were collected in 1986, and some in 1989. The volume percent clay within the existing disposal ground exceeds 20%; however the mean grain size distribution map produced by Kensington (Figure 3.36) does not identify the sediment within the disposal ground to be relatively fine.

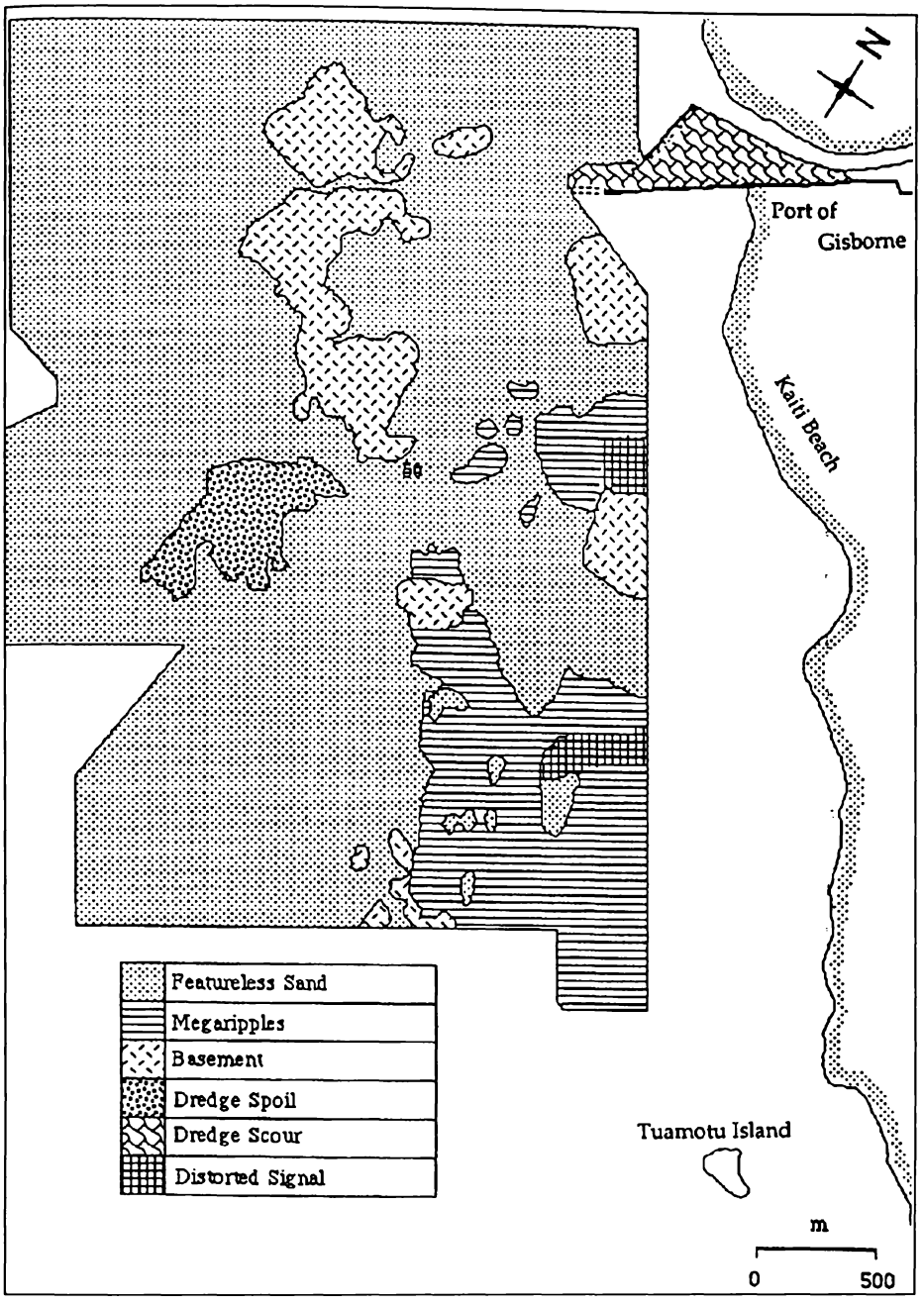

Figure 3.40 Map illustrating the extent of the side-scan sonar coverage within northern Poverty Bay conducted by Kensington, (1990) in January 1989. The spatial extent of the rock reef basement facies is similar to that identified in this study, however a disparity exists between the extent identified in Kensington's side-scan survey and that identified in the seabed textural maps e.g. Figure 3.36.

Figure 3.41 Map illustrating the spatial distribution of the surficial sediment sorting characteristics as measured by Miller, (1981). Miller determined that the majority of sediment within Poverty Bay (including northern Poverty Bay) was classified as being moderately well sorted, which is in contrast to the data collected as part of this study (Figure 3.23)

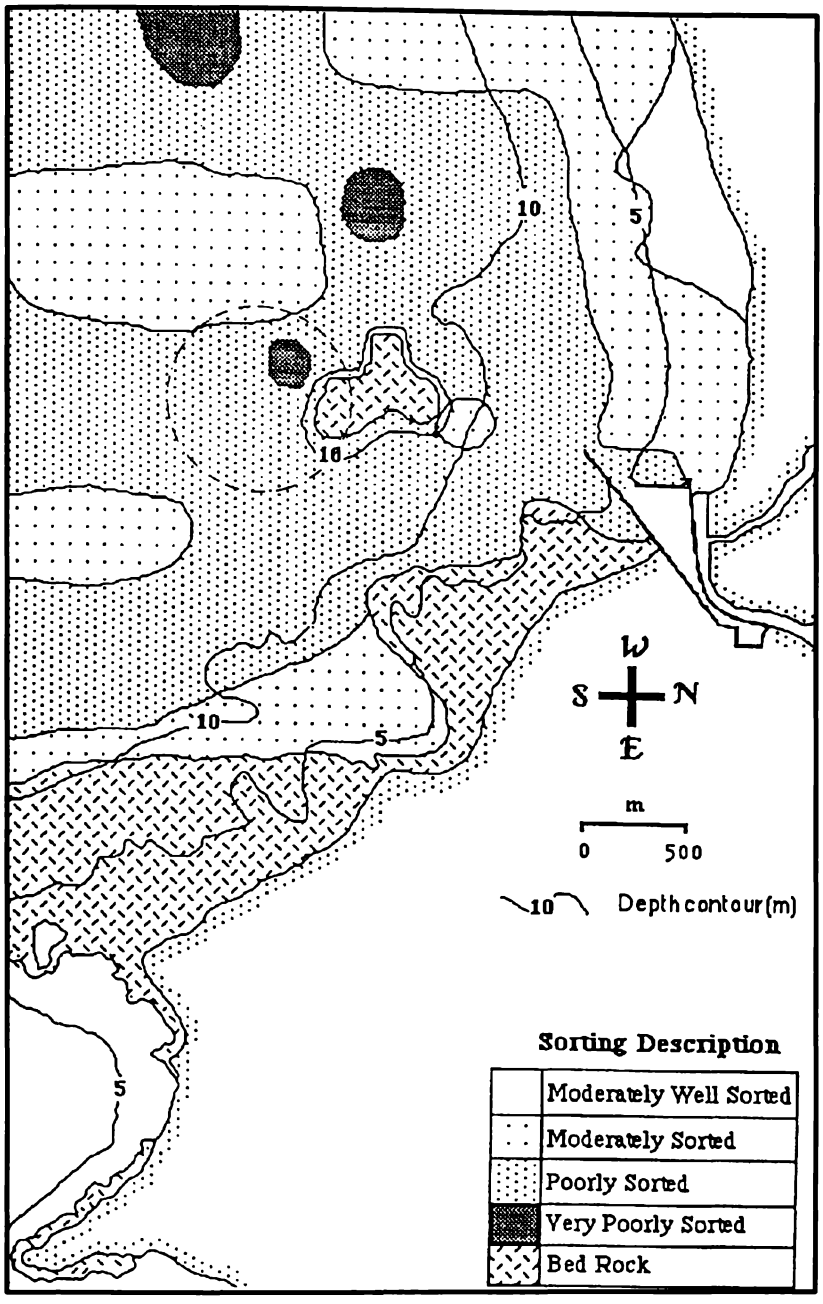

Figure 3.42 Map illustrating the spatial distribution of the surficial sediment sorting characteristics as measured by Kensington, (1990) from sediment samples collected in 1986 and supplemented by samples collected in 1989. As with the data collected for this study (Figure 3.23) the majority of the surficial sediment within northern Poverty Bay is classified as being poorly sorted.

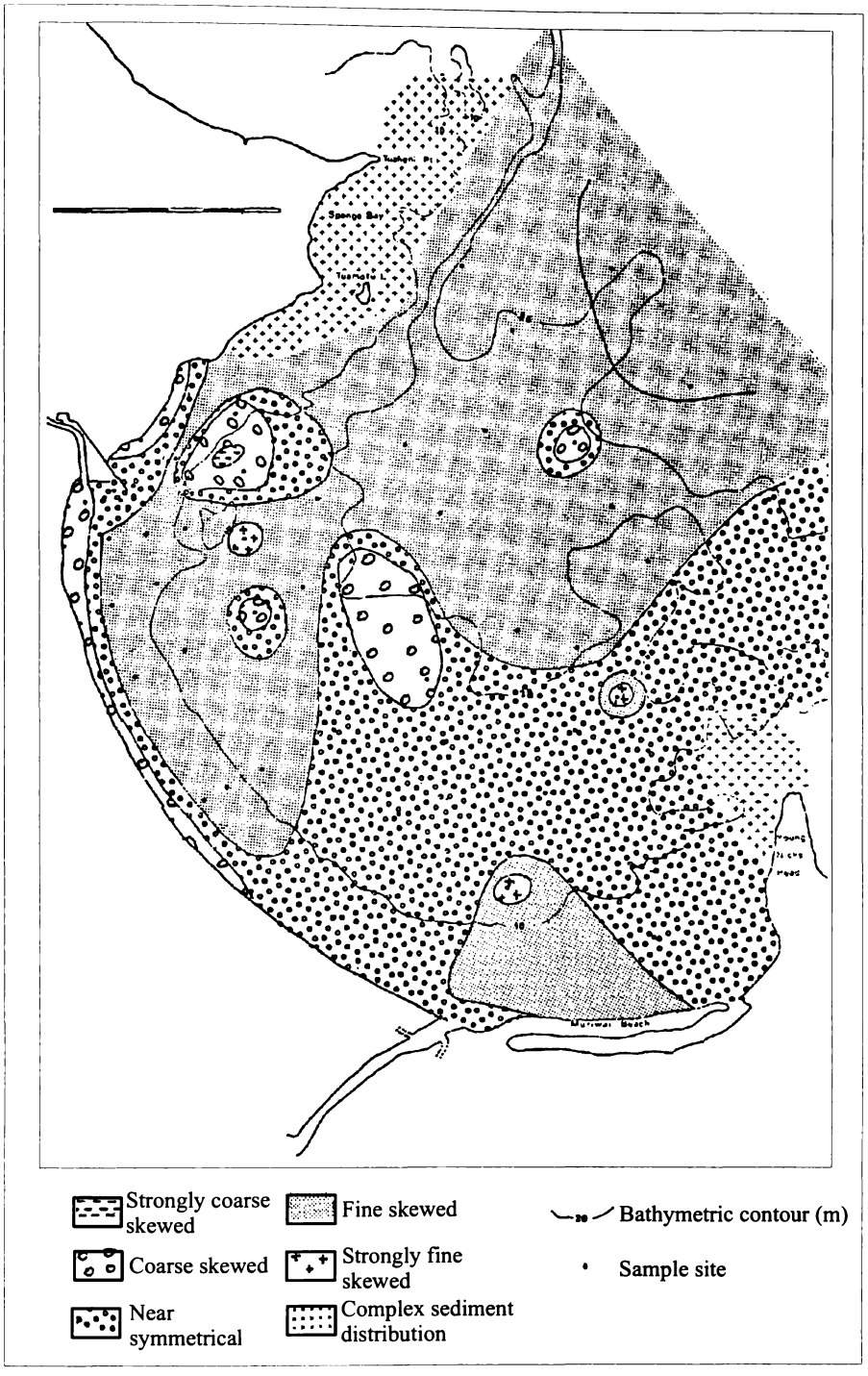

Figure 3.43 Map illustrating the spatial distribution of the surficial sediment skewness characteristics as measured by Miller, (1981).

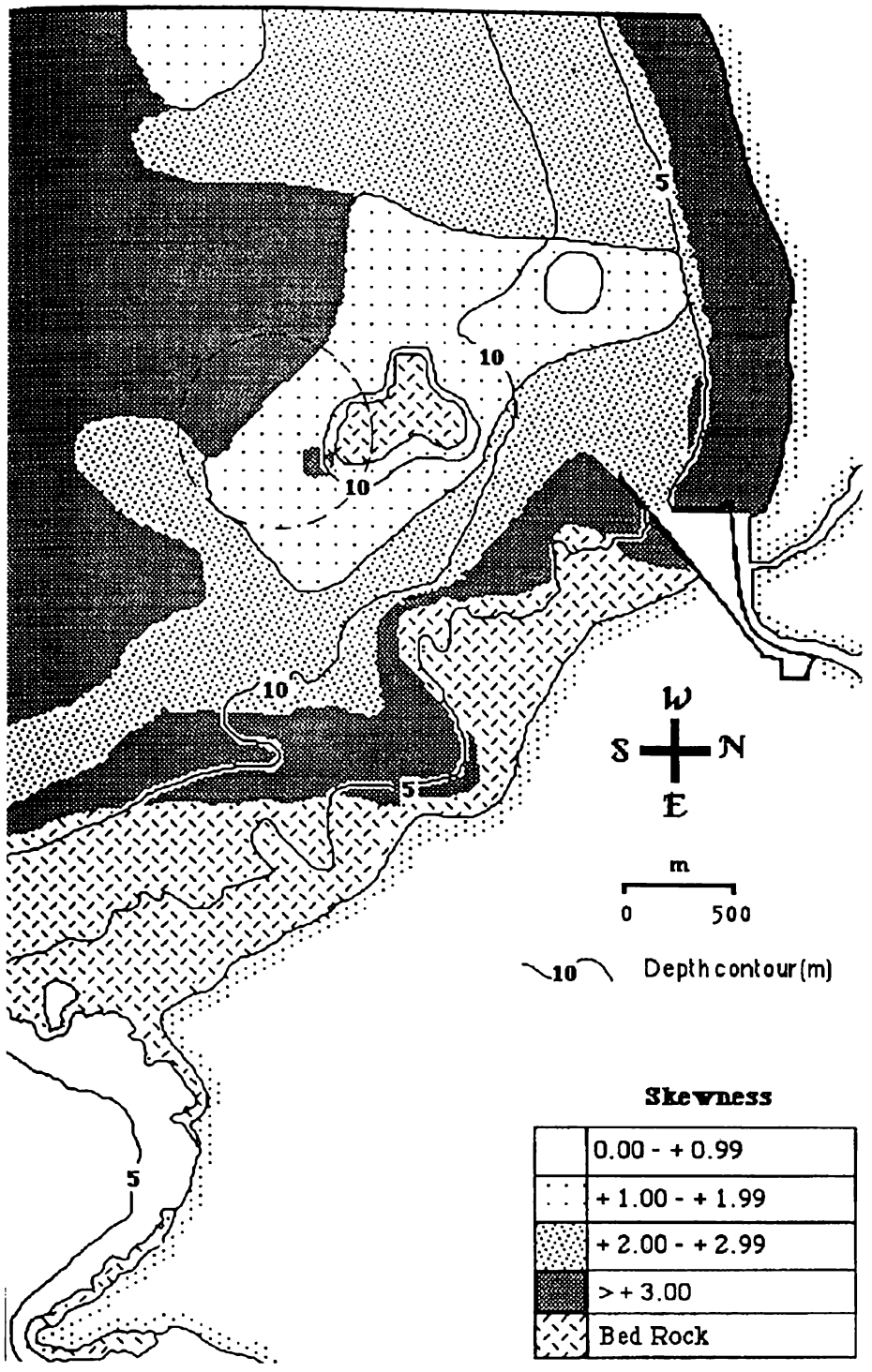

Figure 3.44 Map illustrating the spatial distribution of the surficial sediment skewness characteristics as measured by Kensington, (1990) from sediment samples collected in 1986 and supplemented by samples collected in 1989.

Chapter 4 Sediment geomechanical properties

"*The land is dearer for the sea,*
The ocean, for the shore" - Lucy Larcom

4.1 Introduction

The surficial sediment in northern Poverty Bay consists predominantly mixed sand and mud sediment (Chapter 3). Additionally, *SCUBA* divers have observed the surficial sediment to be cohesively bound (personal observations, 1996-2000). Geomechanical properties of cohesively bound surficial sediment, such as shear strength, have been identified as important characteristics that affect not only the critical shear stress of erosion, but also the erosion rate (Kamphuis and Hall, 1983). Typically the relatively simplistic approach of defining the erosional properties of cohesively bound sediment using the ratio of sand to mud is used (Amos et al., 1995; Collins, 1989; Kamphuis and Hall, 1983; Kuti and Yen, 1976; Mitchener and Torfs, 1996; Murray, 1977). However, Berlamont et al., (1993) illustrated the complexity in describing cohesive sediment by characterising cohesive sediment using 28 parameters. Rather than having to determine the complex array of parameters that define the cohesive properties of surficial sediment, from a physical process perspective, it is more desirable to define the surficial sediment geomechanical properties and relate these to the entrainment processes. Work by Kamphuis and Hall (1983) found that critical shear stress for erosion increased with the plasticity index (derived from Atterberg Limits) of the sediment and the shear strength of the sediment.

Knowing the spatial variability of the in-situ shear strength within northern Poverty Bay, and correlating with the entrainment rate (as examined in later chapters) can provide an understanding of the variability in the relative entrainment rate within northern Poverty Bay. Further, to comprehensively understand the role of the mixed sand/mud sediment on the geomechanical properties of the seabed sediment other geomechanical parameters of the sediment are determined (e.g. Plastic Limit, Liquid Limits, in-situ moisture content, bulk density etc). Additionally, Chapter 3 illustrates that while the majority of the study site consists of mixed sand/mud surficial sediment; there are also large areas of rocky-reef habitat. To further the understanding of the geomechanical properties Point Load and Slake Durability Index tests have been carried out on the local 'papa mudstone' that forms the rocky-reef habitat within the study site.

The primary goal of this chapter is to establish a means of classifying the geomechanical characteristics of the surficial sediment based on some relatively easily definable sediment characteristic or combination of characteristics (i.e. median grain size, mud content). Further, understanding the geomechanical properties of the sediment will provide information on the suitability of the material as fill in land reclamations, and the compaction and consolidation processes likely to affect sediment disposed of at the dredge spoil grounds.

4.2 Methodology

4.2.1 In-Situ Shear Strength Measuring Programme

In conjunction with the sampling programme outlined in Chapter 3, up to 12 in-situ shear strength measurements were taken at each of the sampling sites (Figure 4.01) using a Geonor hand-held shear vane (Figure 4.02). Multiple shear strength measurements provided an indication of the reproducibility of the measurement, and

statistical measures of the sample population (i.e. average, mean and confidence intervals). In-situ shear strength measurements were taken at each of the seabed textural sample sites (Chapter 3), allowing the statistical correlation between the in-situ shear strength and the seabed sediment characteristics (i.e. % sand, silt and clay, organic content, d_{50}, etc) to be examined.

4.2.2 Core sample collection

In order to obtain suitable samples for laboratory geomechanical analysis (i.e. bulk density, moisture content, Atterberg Limits) it was necessary to obtain samples in as near to in-situ conditions as possible. In order to achieve this short cores collected from within and adjacent to the shipping channel and at the existing offshore dredge spoil ground (Figure 4.03 and Table 4.01) using 1.5 m long, 100 mm diameter PVC pipes (Figure 4.04) and following the procedure outlined by Warren, (1992). Sites were chosen to provide information on the geomechanical properties of the sediments around the shipping channel, which is prone to infilling (Black et al., 1997) and at the existing dredge disposal site, which is classified as being semi-dispersal and experiences artificially high sediment depositional rates due to dredge disposal (Healy and Tahata, 1993). The PVC pipes were driven into the sediment by *SCUBA* divers working in teams of two, using an iron weight guided by a fixture attached to one end of the pipe (Figure 4.04). Once the pipes were far enough into the sediment a bung was fitted to the exposed end of the pipe, the core extracted by the divers and the bottom end capped before being recovered. At the surface, caps were sealed in place with tape to ensure an airtight seal and to preserve the sediments in-situ conditions.

Care was taken while sampling to avoid compaction of the sediment during coring in order to ensure that samples remained as undisturbed as possible for the determination of such in situ properties as field bulk densities and moisture contents.

Cores were labelled as to sampling locality and date of acquisition. One short (~300 mm) and three long (~1 m) cores were taken at each location, as well as small sample bags of surficial sediment used to determine the seabed sediment characteristics.

4.2.3 In-Situ Moisture Content (w)

The moisture content of a sample is assumed to be the quantity of water contained in the pore space of the sediment which is removed by oven drying at 105-110°C over a period of 12-24 hours (Head, 1984; Vickers, 1978). This procedure removes all the water in non-cohesive samples. However, clay minerals in cohesive soils have the ability to retain water even after oven drying. This characteristic is dependant on the shape, size and mineral composition of the clay particles (Head, 1984).

Head (1984) notes that for the purpose of routine soil/sediment testing the moisture content relates only to water that is removed by oven-drying at temperatures of 105-110°C. Thus the moisture content of a sample is given by,

$$\text{Moisture content} = \frac{\text{Loss in mass}}{\text{Oven - dry mass}} \times 100 \tag{4.01}$$

Moisture contents of the samples were calculated following the method outlined in Vickers (1978). Initially, a sample of approximately 30 g was taken from the top 10 cm of the cored sample and placed in a container with a lid of known mass (M_1). The mass of the sample, container and lid was measured (M_2) and the sample then placed in the oven at a temperature of 105-110°C for a period of between 12-24 hours. After oven drying the sample, container and lid are again weighed (M_3) and the moisture content of the sample calculated as:

$$\text{Moisture content} = \frac{\text{Mass of Water}}{\text{Mass of solid matter}} \times 100 \tag{4.02}$$

$$\text{Moisture content} = \frac{M_2 - M_3}{M_3 - M_1} \times 100 \tag{4.03}$$

For each site three in-situ moisture contents were calculated (Table 4.02), with a summary given in Table 4.03.

4.2.4 Bulk Density

Bulk density is defined as the mass of bulk soil, including solid particles, water and air, contained in a unit volume (Head, 1984). The bulk density of the samples was determined following the method outlined by Head (1984).

A container of known internal volume (V_1) is weighed both with (M_2) and without (M_1) the presence of the sample. From these measurements the bulk density of the sample can be calculated as:

$$\rho = \frac{M_2 - M_1}{V_1} \tag{4.04}$$

4.2.5 Creation of Spatial Variably In-situ Shear Strength Maps

The in-situ shear strength spatial variability map was created using the software package *SURFER* (Version 6.04.27), which takes spatially distributed data and interpolates a regularly spaced grid. Areas above the mean high water mark and those comprised of rocky-reef habitat, as identified from the side-scan sonar survey and ground truthing, were excluded from the interpolation algorithm.

4.2.6 Multivariate Analysis of Sediment Characteristic

Linear regression and factor analytic techniques were used to analyse the inter-correlations between the surficial sediment textural characteristic, the physical and environmental controls on the sediment characteristics (i.e. distance from sediment supply, water depth and degree of agitation associated with dredging operations) and the in-situ shear strength. The number of factors to investigate with Factor Analysis

was determined using the Kaiser criterion, which states that only factors with eignevalues greater than 1 should be considered (Table 4.04). As such, subsequent Factor Analysis was performed using 3 factors. To obtain a clear pattern in the factor loadings the factors have been rotated using the variance maximizing (Varimax) technique, which maximizes the variance of the 'new' factor and minimizes the variance of the 'new' variable (Cooley and Lohnes, 1966; Fruchter, 1954; King, 1969)

4.2.6 Methods of Determining Atterberg Limits

Atterberg first proposed the idea of standard indices of soil behaviour in 1911. These are now widely known as Atterberg limits, the two most important of which are the liquid and plastic limits (Carrier and Beckman, 1984). The objective of the Atterberg limits test is to obtain basic index information about the soil used to estimate strength and settlement characteristics. It is the primary form of classification for cohesive soils. Fine-grained soil is tested to determine the liquid and plastic limits, which are moisture contents that define boundaries between material consistency states. These standardized tests produce comparable numbers used for soil identification, classification and correlations to strength. Atterberg limits enable tentative conclusions to be drawn about the strength, compressibility and the plasticity of a sample (Vickers, 1978).

The cone-penetration method, as outlined by Vickers (1978) was used to determine the plasticity indices, liquidity indices, activities, plastic and liquid limits for each of the cored samples. A cone penetrometer (Figure 4.05) rather than the Casagrande Apparatus was employed because of its ease of use, the re-produciblity of the results, and because the procedure is less dependant upon the judgement of the operator (Head, 1984; Vickers, 1978).

4.2.6.1 Definitions

The plastic limit (*PL*) defines the moisture content at which the behaviour changes from a semi-plastic to a plastic material. The plastic limit is a measure of the sample's cohesive strength and is controlled by the type and amount of clay minerals found within the sediment (Grim, 1962). The liquid limit (*LL*) defines the moisture content above which the sample behaves like a liquid. From these a range of moisture contents over which the sample behaves like a plastic solid (the plasticity index, *PI*) can be found. In reality the change in state is gradual and the points of transition are not clearly defined, with the limits being arbitrarily assigned. The range over which the sample behaves like a plastic also indicates the sensitivity of the sample to the moisture content (Baver et al., 1972; Head, 1984; Vickers, 1978).

$$PI = LL - PL \tag{4.05}$$

By plotting A-line or Plasticity charts (Figure 4.06) the sediments are able to be classified in terms of their plasticity, ranging from low to extremely high in accordance with British practice as outlined by Head (1984). The British A-line classification scheme is used because it provides a more detailed description of the sample's plasticity than the New Zealand scheme. The New Zealand method for determining a sample's plasticity using an A-line chart only distinguishes between

high and low plasticities. Under the New Zealand scheme samples that have liquid limits in excess of 50% are classified as having high plasticity, whilst those with liquid limits less than 50% are classified as having low plasticity.

The liquidity index (*LI*) relates the plastic and liquid limits to the natural moisture content of the soil and is a useful measure of the sample's field consistency and the degree of compaction. The lower the liquidity index the greater the compaction (Sorensen, 1984). The liquidity index is given as:

$$LI = \frac{w - PL}{PI} \tag{4.06}$$

Activity (*A*) is the ratio of the plasticity index to the percentage of particles in the clay size range, which for geological engineering purposes is taken as the percent of a sample less than 2 μm,

$$A = \frac{PI}{\%\ clay\ sized\ fraction} \tag{4.07}$$

Vickers (1978) notes that the activity of a sample is a measure of the plasticity of the clay-sized particles. The colloidal activity, or simply activity, of the sites can be classified in accordance with Head's (1984) classification scheme where:

Inactive clays	$A < 0.75$
Normal clays	$0.75 < A < 1.25$
Active clays	$1.25 < A < 2$
Highly active clays (e.g. bentonite)	$A > 2$

Head (1984) notes that the calculation of Atterberg limits, indices and the activity can be used to indicate the types of clays that are present in a sample (Table 4.05). Activity is calculated using clay percentage (eqn. 4.07) and as such provides more detailed information on the sample's clay mineral assemblage than do Atterberg limits and indices, which are evaluated using the entire sediment distribution.

4.2.6.2 Procedure

The drop cone penetration method as outlined by Vickers (1978) was used in accordance with NZS 4402 (1986) to measure the plastic and liquid limits of the samples. For the purposes of this work however, several departures from the methods outlined in Vickers (1978) and NZS 4402 (1986) were made. Penetration values of 2.8 mm and 20 mm were adopted for the plastic and liquid limit respectively following the recommendations of Allbrook (1980). Also, because the samples exist in a saturated state, to get useful results it was necessary to dry the samples below their natural water content. The standing period of 24 hours to allow water to equilibrate, as outlined in NZS 4402 (1986), was exceeded due to the time required to dry the samples to a moisture content suitable to begin testing. Additionally, seawater instead of distilled water was used where necessary to increase the moisture content in the sample during testing.

A thick homogeneous paste was mixed for 10 minutes and placed into a cylindrical metal cup (55 mm diameter by 40 mm deep, Figure 4.05), taking care not to entrap any air in the cup. The surface of the paste was then scribed horizontal and the tip of the cone lowered so that it just touched the surface of the paste, at which point the dial reading was taken. The cone was then released to penetrate the surface of the sample for 5 seconds, at which point a second dial reading was taken. The difference between the initial and final dial readings was recorded as the cone penetration (h). A sub-sample of the paste was then removed and used to determine the moisture content, following the procedure for measuring moisture content previously outlined. More of the paste was then added to the cup and the test repeated a second and third time so that averages for the moisture content and cone penetration could be calculated. This procedure was repeated for various moisture contents until the cone penetration exceeded 20-25 mm. Regression analysis was used to determine the liquid and plastic limits (Figure 4.06), from which plasticity and liquidity indices and activities were calculated. The plasticity of the samples was classified using a plasticity chart, or an A-line graph (Figure 4.07).

4.2.7 Geotechnical Analysis of Underlying Rock

4.2.6.1 Sample Collection

Samples of the rock underlying the sediment in the shipping channel were collected from the cutter suction dredge "Pukunui" (Figure 4.08) during maintenance dredging operations. The samples were sealed in plastic bags and refrigerated so that the in situ properties of the rock were maintained as closely as possible for later evaluation. The rock samples were bluish-grey in colour and were easily broken into appropriate sizes for the determination of geotechnical parameters.

4.2.6.2 Point Load Test

The point load test apparatus (*Model EL77-010*) is comprised of a loading frame, ram and platens that are compressed manually using a hydraulic pump (Figure 4.09). The applied load is measured via an electronically controlled hydraulic pressure gauge connected to the ram. Point load tests were completed following the suggested methods of Brook (1985) and in accordance with the guidelines set out in by Brown, (1985). Because of the dimensions of the samples, point-load tests were performed using the irregular lump method as outlined in Brown, (1985). Rock sub-sample lumps of size 50 ± 35 mm and shaped as shown in Figure 4.10, were prepared by trimming larger pieces with a knife. Sub-sample dimensions were noted and the sample placed between the platens, which were closed to make contact with the smallest dimension of the lump at a point away from the edges and corners of the sample. The load was steadily increased such that failure occurred within 10-60 seconds and the failure load "P" was recorded. In cases where the fracture point passed through only one loading point the tests were rejected.

Uncorrected point load strengths (I_s) were calculated as:

$$I_s = P / D_e^2 \qquad (4.08)$$

where the failure load (P) has been corrected for the area of the platen by multiplication by a factor of 1.4425×10-3 m^2 (the area of the platen) and D_e is the "equivalent core diameter" which for the irregular lump test is given as:

$$D_d^2 = WD / \pi \tag{4.09}$$

where W is the average width and D is the depth of the irregular lump (Figure 4.10). Size corrected point load failures ($I_{s(50)}$) were calculated using the dimensionless size correction factor, F, where:

$$F = \left(D_e / 0.050 \right)^{0.45} \tag{4.10}$$

and where:

$$I_{s(50)} = F \times I_s \tag{4.11}$$

The corrected load point load failure ($I_{s(50)}$) was then converted to a uniaxial compressive strength measurement (σ_c):

$$\sigma_c = I_{s(50)} \times 22 \tag{4.12}$$

The constant of 22 in eqn. 4.12 is that proposed by Brook (1985) to convert between $I_{s(50)}$ and σ_c. The mean values of $I_{s(50)}$ and σ_c were calculated by deleting the two highest and lowest values from the valid tests and calculating the average of the remaining values. This enabled the classification of the rock unit in terms of the ISRM classification scheme (Brown, 1985) as outlined in Appendix I.

4.2.6.3 Slake-Durability Index Tests

The slake-durability test is designed to assess the resistance offered by the sample to weakening and disintegration when subjected to two standard cycles of drying and wetting. The apparatus consists of a test drum comprising of a 2 mm mesh of length 100 mm and diameter 140 mm, with a solid fixed base (Figure 4.11). The test yields a slake-durability index (I_d), representing the percentage of an original rock sample retained after a specific number of slaking and drying cycles. Low slake-durability indices indicate that a specimen breaks down readily and this behaviour is often associated with the presence of active clay minerals, such as montmorillonite or mixed-layer clay species (Bell and Pettinga, 1984). Beavis (1985) noted that difficulty often arises in the interpretation of slake-durability indices because their evaluation involves both the slaking (through wetting and drying) and the mechanical abrasion of the sample during the rotation of the drum.

Following the standards set out in Brown, (1985), a representative sample of ten rock lumps, each weighing approximately 40-60 g to give a total mass of 450-550 g, were placed in a clean drum and dried to a constant mass at a temperature of 105°C. The mass of the drum and sample was measured (A), then after cooling the drum was placed in a trough of water (Figure 4.11) and rotated 200 times during a period of 10 minutes. The drum was removed, dried to a constant mass and weighed again after

cooling (*B*). The test was repeated three times to get second and third cycle slake-durability indices (Table 4.06), after which the drum was cleaned, dried and weighed (*D*). The slake-durability indices are calculated as:

$$I_{d1} = \frac{B - D}{A - D} \times 100 \tag{4.13}$$

Gambles (1971) classification scheme (Appendix I) as cited by Brown, (1985) was then used to classify the slake-durability properties of the underlying rock. For soft rocks the second cycle slake-durability index is used for classification, although a third cycle may be used to evaluate rocks of higher durability, or to infer behavioural characteristics.

4.3 Results

4.3.1 In-Situ Shear Strength Distribution

The shear strength of the surficial sediment shows a trend to increase with water depth (Figure 4.12) as shown by factor 3 loading for shear strength (0.88) and water depth (0.69, Table 4.07). However, the surficial sediment within the existing dredge disposal ground has relatively low shear strength, as does the sediment near the mouth of the Turanganui River (Figure 4.12). The pattern of shear strength is attributed to the degree of consolidation and compaction that the surficial sediment is able to undergo between consecutive depositional events, be it dredge spoil disposal or via deposition of material from the Turanganui River plume.

4.3.2 Multivariate Analysis of In-situ Shear Strength and Sediment Characteristic

The inter-correlation between the surficial sediment characteristics is examined more fully in Chapter 3. This section deals principally with the correlation of the surficial sediment textural characteristics with the in-situ shear strength.

Correlation coefficients (R^2) for the inter-correlation between seabed sediment characteristics and physical and environmental controls (Table 4.08) are determined by linear regression. Each heading of the column of the Table 4.08 represents the dependant variable, while the independent variables are represented by the row headings. Normalized variance maximized rotated factor loadings are given in Table 4.07.

With shear strength as the independent factor, the largest correlation between any other dependant factor is water depth (R = 0.42), followed by mean grain size with a correlation coefficient, R, of -0.36. All other correlations have coefficients of determinations values less that 0.3 (Table 4.08). The negative R value for when the mean grain size is the dependant variable suggests that as mean grain size decreases the in-situ shear strength of the surficial sediment should increases. Further, factor 3

loadings (Table 4.07) also suggest that shear strength, mean grain size and water depths are related and, that by normalized varimax rotation, can be described by a single factor (factor loadings of 0.88, -0.59 and 0.69 respectively). No other dependant variable provides a correlation greater than 0.3 (Table 4.08) or factor loadings larger than 0.5 (Table 4.07)

4.3.3 Estimation of Surficial Sediment Shear Strength

Multivariate linear regression and non-linear estimation techniques were used to investigate the relationship between textural parameters and physical properties of the surficial sediment (treated as independent variables) to the surficial sediments shear strength (treated as the dependent variable). A comparison of the two techniques is performed in order to determine the most suitable prediction formula for estimating surficial sediment shear strength.

Independent variables used in the multivariate analysis for the determination of the surficial sediment shear strength were,

i. Minimum distance from sediment source (i.e. Turanganui River mouth or centre of dredge spoil ground),
ii. Water depth below datum (CD),
iii. Percent organic content, and
iv. Ratio of percent mud to sand

The number of independent variables was reduced to eliminate the aspect of chance in the multiple linear regression analysis and piecewise non-linear estimations. Justification for the chosen independent variables is as follows. The location parameters provide some insight into the degree of compaction and consolidation that the surficial sediment has undergone, i.e. the degree of agitation the surficial sediment receives via wave-orbital currents (predominantly depth dependant) and the time the surficial sediment has had to consolidate between depositional events (i.e. assuming that the closer to a sediment source the shorter the time between consecutive depositional events). The non-dimensional ratio of mud to sand was chosen to provide some indication as to the degree of cohesion within the sand matrix that the silt and clay impart on the structure of the surficial sediment, as too was the percent of organic material that has been reported to influence the cohesive nature of surficial sediment (Berlamont et al., 1993). Because a high correlation has been shown between the sample sites water depth and the grain size parameters (d_{50}, sand, silt and clay %, Chapter 3), the sample sites water depth rather than a measure of the surficial sediment grain size has been used as an independent variable

4.3.3.1 Multiple Linear Regression

Multiple linear regression is used to determine a relationship between one or more independent variable and a dependant variable (e.g. shear strength) by applying a least squares estimation, which aims to minimizing the sum of squared deviations of the observed values for the dependent variable from those predicted assuming a linear relationship (StatSoft, 1995).

Using a least squares estimation of the surficial sediment shear strength and performing multiple linear regression on the comparison of the predicted to the observed shear strength produced a low adjusted R^2 value of 0.15 (Table 4.09), which is illustrated by the scatter in the plot of predicted and observed shear strengths (Figure 4.13). Table 4.09 lists the standardised regression coefficients determined using multiple linear regression analysis (*BETA* coefficient = regression or slope coefficient). Water depth is shown to be statistically the most important predictor of the in-situ shear strength, with a standardised regression coefficient of 0.52 (Table 4.09). The low adjusted R^2 value suggests that multiple linear regression analysis may not be the optimal method for predicting the shear strength of the surficial sediment.

Based on the multiple linear regression analysis the fitted equation is defined as,

$$\chi' = 1.23 - 0.09X_1 + 0.52X_2 - 0.18X_3 - 0.13X_4 \qquad (4.14)$$

Where χ' is the in-situ shear strength, X_1 is the distance from sediment source (i.e. the Turanganui River mouth/dredge disposal ground), X_2 is the water depth (h), X_3 is the organic content and X_4 is the ratio of mud to sand.

4.3.3.2 Piecewise Non-linear Estimation with Breakpoint

Unlike multiple linear regression analysis, non-linear estimation does not assume that the relationship between the independent variable or variables and the dependant variable is linear in nature (StatSoft, 1995). Piecewise non-linear estimation with breakpoint regression is used to determine if there is some non-linear relationship between the surficial sediments shear strength and the textural and physical/environmental properties of the surficial sediment. The fitted equation is of the form,

$$y = (b01 + b11 \times X1 + ... + bm1 \times Xm) \times (Y \leq bn) + (b02 + b12 \times X1 + ... + bm2 \times Xm) \times (Y) bn) \qquad (4.15)$$

Thus, two separate linear regression equations are estimated, one for the y values that are less than or equal to the breakpoint ($b0$) and one for the y values that are greater than the breakpoint.

Non-linear estimation with breakpoint regression of the seabed shear strength (dependant variable) and the distance from sediment source, the water depth, the percent organic content, and the ratio of percent clay to sand (treated as independent variables) results in an adjusted R^2 value of 0.82 (Table 4.10), which is illustrated by the scatter in the plot of predicted against observed surficial sediment shear strength (Figure 4.14). Predicted and observed shear strength values are given in Table 4.11.

The coefficients determined with the non-linear estimation technique are listed in Table 4.10. The relationship shown by the non-linear estimation can be used to spatially map the surficial sediments shear strength in northern Poverty Bay using the independent variables (i.e. distance from source, water depth, the organic content and the ratio of mud to sand).

The relative change in the magnitude of the coefficients on either side of the breakpoint division provides information on which of the coefficients plays a

significant role in defining the surficial sediments shear strength. The fitted regression line suggests that for sediment with in-situ shear strengths less than ~1.7 kPa (i.e. the breakpoint in the fitted line) the ratio of mud to sand and organic content contribute the most to the in-situ shear strength of the surficial sediment (coefficients of 0.6 and 0.65 respectively). At in-situ shear strengths in excess of ~1.7 kPa the organic content appears to be relatively more important (i.e. coefficient of 0.11), while the emphasis on the mud to sand content in the fitted equation is less (i.e. coefficient of 0.365). The coefficients associated with the *water depth* and *distance from source* do not vary much either side of the breakpoint of the fitted line. The results illustrate the importance of the organic content in determining the in-situ shear strength, particularly for surficial sediment with relatively large in-situ shear strength.

4.3.4 Atterberg Limits Results

The Atterberg limits are a measure of the effect of water on the consistency of cohesive soil. Water has a tremendous effect on the state of cohesive soils. With the addition of sufficient water the clay can become completely liquid. Between the solid and liquid states, a cohesive soil can exist in a plastic state, in which the soil can undergo plastic deformation (Craig, 1994).

4.3.4.1 Plastic Limits (*PL*)

Plasticity is an important characteristic in the case of fine-grained soils; the term plasticity describes the ability of a soil to undergo unrecoverable deformation at constant volume. Plasticity is due to the presence of clay minerals or organic material. The plastic state of a fine-grained soil at a particular water content is known as its consistency. The consistency depends on the interaction between the clay minerals. Expulsion of water from the soil pores results in a decrease in cation layer thickness, and an increase in the net attractive forces between particles, and hence the strength of the soil. For a soil to exist in a plastic state the magnitudes of the net interactive forces must be such that the particles are free to slide relative the each other, with cohesion between them being maintained (Craig, 1994).

Plastic limits range from 27% (in and adjacent the shipping channel) to approximately 46% in the Swinging Basin (Table 4.12). Variation between sites is attributed to the clay type and the percentage of clay present in each sample.

4.3.4.2 Liquid Limits (*LL*)

Samples in and adjacent the shipping channel and at the proposed offshore spoil ground have relatively low liquid limits compared with those of the Swinging Basin and the Spoil Ground (Table 4.12) and those quoted by Roberts (1993) for the Ports of Auckland and Onehunga of 112% and 93% respectively. These lower values reflect the minor amount of clay found in the samples. The Swinging Basin and the existing Spoil Ground have significantly higher liquid limits (81% and 44% respectively, Table 4.12). These higher values are attributed to the greater quantity of the clay-sized fraction found in the samples.

4.3.4.3 Plasticity Index (PI)

The plasticity index is a measure of the soils ability to absorb water before it weakens and reaches the liquid limit, at which point remoulded material is said to behave like a liquid (Craig, 1994).

Sites in and adjacent the shipping channel typically have low plasticity indices ranging between 4% and 6% (Table 4.12). The low plasticity index values for these sites reflect the relatively limited quantity of clay-sized sediment in the samples. Also, the low plasticity indices indicate that the samples are sensitive to moisture content. These plasticity indices are similar to those reported by Ryan (1989) for Purakau Channel, Manukau Harbour sediments.

The Swinging Basin and the existing Spoil Ground have larger plasticity indices, 35% and 16% respectively (Table 4.12). The higher plasticity index values for these sites again reflect the relative abundance of clays in the samples.

A-line or plasticity charts (Figure 4.15) classify the sediments of the Swinging Basin as silty and having a very high plasticity, whilst the sediments within and adjacent to the shipping channel are classified as medium plasticity silty sediments. The existing Spoil Ground is also classified as having medium plasticity, but shows a definite increase in the plasticity over the shipping channel sediments, representative of the mixing of the dredge spoil sediments and the natural sediments at the site. The plasticity value of the sediment within Spoil Ground suggests that the disposal site can be described as partly dispersal consistent with the findings of Healy and Tahata, (1993).

4.3.4.4 Liquidity Index (*LI*)

The liquidity index relates the plastic and liquid limits to the natural moisture content of the sediment. All samples have liquidity indices greater than one ($LI > 1$) indicating that the samples have in-situ moisture content greater than the liquid limit (Table 4.12).

Additionally, the values of the liquidity indices suggest that these sediments have only undergone limited compaction (Carrier and Beckman, 1984). Lower liquidity indices indicate expulsion of water from the sediments through compaction. However, the densification of marine sediments is low and overall diagenesis consists of predominantly chemical transformation (Amaryan, 1993), that is, the densification of the sediments is primarily due to the bonding of particles into aggregates by chemical transformation.

4.3.4.5 Activity

The Atterberg limits are related to the amount of water absorbed by a cohesionless soil on the clay surface. But also, the amount of water absorbed by a cohesionless soil is proportional to the clay content in the soil mass. The Activity parameter provides a more direct (or normalised) measure of the water absorbing capacity of the clay minerals within the soil mass (Craig, 1994).

Activities of the sediments (Table 4.12) suggest that all sites, except for the existing Spoil Ground, can be classified as highly active. The existing Spoil Ground is classified as having normal activity.

4.3.4.6 Clay Type

The dominant clay types in the marine sediment in Poverty Bay has been extensively examined by Miller, (1981). Miller, (1981) noted limited variation in the clay minerals assemblage, suggesting uniformity of source of the clay minerals or comprehensive mixing of the clay-size fraction in the bay. Miller, (1981) determined that the surficial sediment in Poverty Bay consisted of varying quantities of Montmorillonite, Illite and Kaolinite clay minerals.

Montmorillonites have a structure in which one-sixth of the aluminium ions have been replaced by magnesium (Selby, 1993). The crystal lattice of Montmorillonite consists of weak oxygen to oxygen linkages, with the interlayer occupied by hydrated cations, organic ions and water molecules that are exchangeable with the soil solution, and result in an expandable crystal lattice (Tompson and Troeh, 1973).

Illites are similar to Montmorillinites, however the crystals tend to aggregate and, as a result, the aggregate structure tends to attract less water. In comparison to Montmorillonite, Illite has a much more limited hydration capacity. The swelling-shrinking characteristics and internal coefficient of friction of Illite, whilst less than Kaolinite, are more favourable than those of Montmorillonite from a aeromechanics perspective (Beavis, 1985).

Kaolinite is a two layered clay mineral comprising of gibbsite and silica sheets, or an isomorphous variation upon this usually with the inclusion of an aluminium ion in place of a silicon ion in the silica sheet. The two sheets are bonded together by strong hydrogen bonds. This gives a rigid structure that resists separation by cation or water molecules in the interlayer space. Therefore, the crystal lattice is non-expanding and samples dominated by this mineral species have no tendency to swell or shrink upon varying moisture contents (Tompson and Troeh, 1973).

As previously noted the Atterberg limits, indices and activity of a sample can be used to indicate the dominant clay mineral or clay mineral assemblage, and can be compared with the known clay mineralogy of the marine sediment based on the findings of Miller, (1981). The clay mineral assemblage inferred from the Head (1984) scheme includes varying quantities of Smectite (particularly montmorillonite), Illite and Kaolinite (Table 4.12), consistent with the findings of Miller, (1981).

The Liquid and Plastic limits and Plasticity indices indicate a dominance of Kaolinite at all sites (Table 4.12), whilst the high activities at most sites (aside from the existing Spoil Ground) suggest significant quantities of clays such as montmorillonite and Illite. The low activity of sediments at the existing Spoil Ground suggests the preferential removal of the more active Smectite clays from the sediments. Although the mechanism for this is unclear it is likely to be associated with the agitation of the sediment during dredging operations. Results are consistent with the findings of Miller, (1981).

The clay mineral assemblage is consistent with the dominant clay mineral assemblage of sediments from Sponge Bay, Young Nicks Head and the two river systems discharging into Poverty Bay (Miller, 1981).

4.3.5 Geotechnical Investigation of the Underlying Rock

4.3.5.1 Point Load

Classification of the corrected point load failure and uniaxial compressive strength measurements (Table 4.13) using the scheme of Brown, (1985) suggest that the rock underlying the sediment of the shipping channel and Swinging Basin can be classified as *very weak rock* (1.0-5.0 $MN.m^{-2}$). That is, the rock is able to be crumbled with firm blows from the point of geological hammer and can be peeled by a pocket-knife. The uniaxial compressive strength of the underlying rock unit determined in this study are similar to those reported for the rock unit by Tonkin & Taylor Ltd. (1994) of 2.3-2.8 MN/m^{-2}.

4.3.5.2 Slack-Durability Index Test

Results are presented as averages with 95% confidence intervals (Table 4.14). The second cycle slake-durability indices for the underlying rock suggest a medium to low slake-durability classification (Table 4.14, Appendix I).

4.4 Discussion

The spatial distribution of the seabed shear strength was mapped in order to elucidate relationships between sediment properties and the cohesiveness of the surficial sediment. Quantitative determination of the in-situ shear strength of the surficial sediment within Poverty Bay has previously not been undertaken, although the cohesive nature of the sediment has been formerly noted (Kensington, 1990). Further, dredge operators have noted that dredged sediment is often 'cloggy', retaining a certain degree of structure (even after the agitation associated with dredging) and sticking to the side-walls of the dredge hopper (pers. comms. Dredge operators, 1998).

Previous investigations into the sediment transport characteristics have treated the surficial sediment as non-cohesive (Kensington, 1990). However, the importance of cohesive bonding on sediment entrainment and transport processes of mixed sand and mud sediment has been noted by numerous authors (Amos et al., 1995; Kamphuis and Hall, 1983; Kuti and Yen, 1976; Murray, 1977) and treating cohesive surficial sediment as non-cohesive can lead to erroneously large estimations of sediment transport rates (Black et al., 1997), as both the erosion rate and the erosional shear strength of the sediment is effected by the cohesiveness of the sediment (Amos et al., 1995; Kamphuis and Hall, 1983; Kuti and Yen, 1976; Murray, 1977).

Typically, cohesive sediment is classified using numerous parameters or parameter sets (Berlamont et al., 1993), however work by Kamphuis and Hall (1983) found that

critical shear stress for erosion of cohesively bound mixed sand/mud sediment increased with the plasticity index of the sediment and the in-situ shear strength, providing a relative simple means of accounting for the cohesive bonding of the sediment. Mapping the surficial sediment shear strength and understanding the relative difficulty in entraining cohesively bound sediment (examined in later chapters) it will be possible to apply non-cohesive sediment entrainment formulae to confidently predict sediment fluxes and estimate channel infilling rates. Relating the cohesiveness to the shear strength has the advantage over the plasticity of the surficial sediment in that it can be measured relatively easily in-situ using a hand-held shear vane (Figure 4.02).

Multivariate analysis indicates a relatively poor correlation between the shear strength (as dependent variable) and individual sediment textural or physical environmental parameters (independent variables), suggesting that no single aspect of the surficial sediment textural or environment parameters can be used to statistically describe the in-situ shear strength (Table 4.08). However, multivariate analysis does provide an indication of the relative importance of the different parameters in defining the in-situ shear strength.

Linear regression and factor analysis indicated that water depth and mean grain size (presumably more a function of the entire grain size distribution) influence the shear strength of the surficial sediment (R^2 values of 0.42 and -0.36 respectively), with water depth being statistically the most important predictor of the in-situ shear strength (Table 4.09. Normalized varimax rotated factor 3 loadings result in values of 0.88, -0.59 and 0.69 for shear strength, mean grain size and water depth respectively. The dominant entrainment process in Poverty Bay is near-bed wave orbital velocities, which are depth dependant; i.e. the greater the water depth the less the relative magnitude of the near-bed wave orbital velocity (Figure 4.16). This dependency explains the strong inverse correlation between the water depth and the grain size of the surficial sediment, as the stronger the magnitude of the near-bed orbital velocities the larger the relative grain size of the surficial sediment able to be entrained and winnowed out of the seabed.

Given these findings, it would appear that the relative shear strength of the surficial sediment increases due to the content of mud in the sediment matrix increasing, which in turn is attributed to the dominant entrainment processes (wave-orbital velocity) decreasing with increased water depth. In relatively shallow water, fines are winnowed out and the cohesive bonding within the sediment matrix decreases. Further, the degree of compaction and consolidation of the surficial sediment is in part related to the relative strength of the dominant entrainment process. Under weak entrainment forces surficial sediment has time to compact and consolidate, expelling surplus pore water. However, this process is time dependant, varying with the depositional history of the seabed, i.e. if recent sedimentation has occurred then the degree of compaction and consolidation will be less (Mitchener and Torfs, 1996).

Given the findings of Berlamont et al., (1993), who used several parameters or parameter sets to define the cohesive bonding of marine sediments, it is not surprising that there is no strong statistical correlation between the in-situ shear strength and any single sediment textural or environmental parameter investigated as part of this study. Rather, it is the interaction of several parameters or textural characteristics that define the cohesive strength and hence the critical shear stress for erosion of the mixed sand/mud surficial sediment, which Kamphuis and Hall (1983)

note is definable by the in-situ shear strength. Multiple linear regression and non-linear estimation techniques were employed to investigate the cumulative effect of several of the independent variables in the estimation of the in-situ shear strength.

Correlating a reduced number of independent variables (Section 4.3.3) to the shear strength using multiple linear regression does not suggest any significant statistical relationship between the in-situ shear strength and the independent variables investigated in this study (adjusted $R^2 = 0.15$). This is not surprising, as the cohesive bonding of the surficial sediment (defined by the in-situ shear strength) has been shown to be dependent on various parameters or parameter sets (Berlamont et al., 1993). Additionally, the relationship of the sediment textural characteristics to the critical shear stress of erosion appears to be non-linear in nature, increasing by a factor of 2 with the addition of 50% sand to mud, increasing by a factor of 10 with 30% mud added to sand (Mitchener and Torfs, 1996), and to be at an optimum somewhere in between (Alvarez-Hernandez, 1990).

Piecewise non-linear estimation with breakpoint analysis produced reasonable estimates of the in-situ shear strength of the surficial sediment using the independent variables. Non-linear estimation with breakpoint analysis assumes that the relationship between dependent and independent variable is generally non-linear, but that the slope is different in different regions of the dependant variable (StatSoft, 1995). The fitted regression equation defines a breakpoint at $\chi = 1.68$ kPa and has an adjusted R^2 value of 0.83. Of the independent variables used to estimate the in-situ shear strength, the sample site water depth is identified as the most statistically significant. The water depth quantitatively parameterises the near-bed wave orbital velocity, which influences both the seabed sediment grain size distribution and the agitation experiences, and hence the compaction and consolidation of the surficial sediment. Both textural characteristics (specifically the ratio of sand to mud in mixed sediment) and the degree of compaction and consolidation have been noted as important parameters in defining the cohesive bonding of the surficial sediment (Alvarez-Hernandez, 1990; Amos et al., 1995; Berlamont et al., 1993; Collins, 1989; Kamphuis and Hall, 1983; Murray, 1977). As such, it is not surprising that water depth is shown to be the most statistically significant independent variable used to estimate the in-situ shear strength in this study.

While in-situ shear strength measurement of the surficial sediment is used to evaluate the relative strength of the cohesive bonding and hence critical shear stress of erosion, other geomechanical parameters of the surficial sediment (i.e. Atterberg Limits, bulk densities, in-situ moisture content) are used to evaluate the suitability of the seabed sediment for use as fill in land-based reclamations. As Resource Consent conditions sanction the removal of sediment from within the shipping channel and the Swinging Basin, only the geomechanical characteristics of sediment within these areas only have been investigated.

Swinging Basin sediments have very high plasticities, low permeability, and are more compressible, suggesting they will consolidate over a longer period of time under load than sediments of a lower plasticity (Head, 1984). The high activity of the clay fraction in the Swinging Basin sediments (Table 4.12) suggests that they contain a significant component of soft active clays, resulting in high natural moisture contents (Head, 1984). High in-situ moisture contents and the presence of active clays suggest that material would undergo high degrees of consolidation if used in land reclamations. Low bulk densities suggest Swinging Basin sediments

would undergo significant consolidation in an upland disposal site. The relative percentage of silt and clay in the sediment within the Swinging Basin (55% and 28% respectively, Chapter 3) compared to shipping channel sediment (<20% and <10% respectively, Chapter 3) suggest the Swinging Basin sediments will have a lower permeability and a correspondingly greater ability to retain water than sediments from the shipping channel.

The clay mineral assemblage in the sediments of the Swinging Basin includes Montmorillonite, Illite and Kaolinite (Table 4.12). The weak bonds of Montmorillonites allow for the inclusion of water into the crystal lattice, hydrating the mineral and resulting in the expansion of the structure. When this occurs the Montmorillonite sheets become enclosed in films of water, resulting in high plasticities and low coefficients of internal friction. The structure can lose water as readily as it can take it up; with water loss Montmorillonite soils are subject to severe shrinkage and cracking (Beavis, 1985). Whilst less than Montmorillonite, Illite has a greater capacity to bond water particles to itself than Kaolinite (Lambe and Whitman, 1979). The greater capacity to bond water to the Illite clay particles results in the soils ability to increase the amount of moisture in the sample, reducing the internal friction angle and hence the samples bearing capacity. Kaolinite forms stable soils since its tight, non-expandable structure resists the introduction of water into the lattice. Kaolinite soils typically have low plasticities and high coefficients of internal friction (Beavis, 1985). The high clay content and the inferred mineral assemblage imply that if Swinging Basin sediments were to be used as landfill, then the consolidation period could be expected to be greater than that of a coarser material. A reclamation consisting of 100% Swinging Basin sediments would have a bearing capacity of approximately 75 kN/m^2 (Table 4.15). Given that soil in log handling areas can be subjected to a maximum load of about 112 $kN.m^{-2}$ (Beamsley et al., 1997), the soft sediments from the Swinging Basin would be unsuitable for reclamation fill.

Chapter 3 showed the surficial sediment in the shipping channel to be significantly coarser than the sediments of the Swinging Basin, primarily in response to a higher wave and current energy environment. Although silts and fine sands dominate the shipping channel sediments, and only have limited quantities of clay sized material (Chapter 3, Figure 3.26, Figure 3.27 and Figure 3.28), the activities suggest that those clays are classified as active to highly active. The Atterberg limits reflect the clay amount rather than the type or behaviour. The plastic limits of the surficial sediment in and adjacent to the shipping channel range between ~ 26% to 32% and the liquid limits between ~ 32% to 37% (Table 4.12). The A-line or plasticity chart of the sediments in and adjacent to the shipping channel (Figure 4.15) classifies these sediments as silts with medium to low plasticity, implying that the sediments have relatively greater permeability than the Swinging Basin sediments. The relatively higher permeability of the sediment in and adjacent to the shipping channel imply that, in comparison to the swinging Basin sediment, a land based reclamation using shipping channel sediment will not be as susceptible to compression, nor consolidate as much over a long period of time under load (Head, 1984).

The in situ moisture contents of the sediment within and adjacent to the shipping channel (35% - 45%) are significantly lower than that of the Swinging Basin sediments (110%) reflecting the coarser nature of the sediments (Table 4.03). In general, the finer the sediments, the higher the porosity and total moisture content but the lower the flux of water through the sediment (measured as permeability). From a

geotechnical point of view, the inclusion of water in the pore space between particles weakens the soil structure and reduces its bearing capacity, especially if the water is under pressure and can lead to failure if the sediments are subjected to a sufficient load (Head, 1984; Head, 1988). A reclamation consisting of 100% unconsolidated shipping channel sediments would have a bearing capacity of approximately 100 $kN.m^{-2}$ (Table 4.15). Given that soil in log handling areas can be subjected to a maximum load of approximately 112 $kN.m^{-2}$ (Beamsley et al., 1997), then sediment from the shipping channel alone would be unsuitable for reclamation fill. Mixing with coarser material would improve the geomechanical behaviour of the sediment by increasing the materials permeability and allowing more ready drainage, as would consolidation. One potential source of coarser material within the study area is the Tertiary 'Papa' mudstone that forms the underlying strata and exposed rocky reef area within northern Poverty Bay. Further, mixing concrete with the sediment dredged during maintenance and capital dredging to create mudcrete will increase the structural strength of any reclamation. Additionally, including the Tertiary mudstone in any potential reclamation will improve the soil structure, and hence the structural strength of the reclaimed land. Mudcrete solidifies quickly; forming strong and stable reclamations, and has been used successfully by Ports of Auckland (Vazey, 2002). A major advantage of mudcrete reclamation is that the reclamation requires little settlement time, and can be used almost immediately for container handling and heavy equipment (Vazey, 2002).

The Tertiary mudstone would form the underlying base-rock unit for any reclamation within the study area and as such it is important to determine the geomechanical characteristics of the rock Unit (Brown, 1985). Uniaxial compressive strength tests on the Tertiary mudstone that underlies the sediment of the port and shipping channel suggest that the rock has only a limited uniaxial compressive strength under the classification scheme of Brown, (1985), suggesting that the rock will fail under only small loads and is classified as very weak rock (1.0-1.5 $MN.m^{-2}$). The low uniaxial strength of the rock indicates a low ultimate bearing capacity, while slake-durability tests classify the mudstone as having a medium to low slake-durability index ($I_{d2} \approx$ 60). The geomechanical properties of the underlying rock unit are such that they are unsuitable for use in breakwater construction because they have a low uniaxial strength and disintegrate relatively easily under repeated cycles of wetting and drying,

4.5 Summary

Previous research has noted that the erosional critical shear strength for cohesively bound mixed sand/mud sediment increased with the shear strength of the sediment (Kamphuis and Hall, 1983), providing a means to quantitatively parameterise the cohesive bonding. In-situ surficial shear strength measurements within northern Poverty Bay show the shear strength of the seabed sediment to be spatially variable, suggesting that a spatially variable parameterisation of the cohesive bonding of the surficial sediment is more suitable to use when predicting re-entrained sediment fluxes than a single "cohesion factor" (defined as the ratio of predicted to observed near-bed reference concentrations) as used in earlier studies (Black et al., 1997).

No simple relationship between the in-situ shear strength and any of the sediment textural and environmental parameters used in this study is shown to exist. However, statistical analysis indicates that water depth and the median grain size of the

surficial sediment are statistically the best predictors of the in-situ shear strength, with R^2 values of 0.42 and -0.36 respectively. This correlation is assumed to reflect the dominance of the near-bed wave orbital velocity on the surficial sediment characteristics. The near-bed orbital velocities not only influence the grain size composition of the seabed by winnowing and entrainment processes, but also affect the degree of compaction and consolidation that the surficial sediment can undergo.

While no simple relationship is shown to exist between individual sediment textural and environmental parameters, non-linear estimation techniques with breakpoint analysis using the cumulative effect of several of the sediment textural and environmental parameters is shown to satisfactorily predict the in-situ shear strength of the surficial sediment (adjusted $R^2 = 0.83$). The need to use several parameters to estimate the in-situ shear strength illustrates the complexity in defining the in-situ shear strength and hence the cohesive bonding of mixed mud and sand sediment.

In determining the suitability of the sediment within northern Poverty Bay for use in a land based reclamation only sediment to be dredged as part of maintenance and capital dredging programmes has been considered, i.e. Swinging Basin and shipping channel sediment and the Tertiary mudstone that underlies the unconsolidated sediment and forms the exposed rocky reef habitat.

Swinging Basin sediment also are unsuitable for use as fill in a land based reclamation because of the ultimate bearing capacity of the soil following consolidation and drainage will not be sufficient to support a modern port log storage area. Additionally, the bearing capacity of a soil consisting of sediment from the shipping channel would not be adequate for a log storage area, however, with the inclusion of coarser material to improve drainage and soil structure, and the addition of concrete to form mudcrete, the ultimate bearing capacity of the soil should be sufficient for a log or container storage area. One potential source of coarser material is the Tertiary mudstone. Though relatively weak and not suitable for use in construction of breakwaters, the mudstone could be used as fill in a land based reclamation consisting of shipping channel sediment; increasing the drainage, soil structure and ultimate bearing capacity of the reclamation to a point suitable for log storage.

Table 4.01 Core sample collection positions. Site locations given in Figure 4.03

Site	Northing (m)	Easting (m)
Shipping channel, seaward end, northern side (EN)	693352.57	310835.87
Shipping channel, seaward end, middle (EM)	693373.10	310706.82
Shipping channel, seaward end, southern side (ES)	693678.39	310704.33
Shipping channel, port end, northern side (SN)	694115.96	311374.99
Shipping channel, port end, middle (SM)	694054.84	311421.32
Shipping channel, port end, southern side (SS)	693897.50	311466.05
Swinging Basin (SB)	694222.60	311836.37
Existing Spoil Ground (OS1)	691901.92	310893.35
Site CM1, proposed offshore spoil ground (CM1)	689611.92	308872.6

Table 4.02 In-situ field moisture contents. Site abbreviations are explained in Table 4.01, site locations given in Figure 4.03

Site	Tin No.	Mass of tin (g)	Tin & wet soil (g)	Tin & dry soil (g)	Mass of water (g)	Mass of solid (g)	Moisture content (%)	Moisture factor	Average moisture content (%)	Average moisture factor
SB	A1	37	80.8	58.3	22.5	21.3	105.63	2.06		
	A2	38.4	88.7	62.2	26.5	23.8	111.34	2.11		
	A3	38.4	86.8	61	25.8	22.6	114.16	2.14	110.38	2.1
CM1	I1	29.7	72.2	60.9	11.3	31.2	36.22	1.36		
	I2	29.5	62.1	52.5	9.6	23	41.74	1.42		
	I3	29.9	64.6	55.3	9.3	25.4	36.61	1.37	38.19	1.38
OS1	B1	37	82.6	67.4	15.2	30.4	50	1.5		
	B2	38.8	88.3	70.9	17.4	32.1	54.21	1.54		
	B3	37.7	93.6	71.6	22	33.9	64.9	1.65	56.37	1.56
ES	C1	27.5	68.6	55.4	13.2	27.9	47.31	1.47		
	C2	38.7	80.2	67.8	12.4	29.1	42.61	1.43		
	C3	38.8	81.5	68.2	13.3	29.4	45.24	1.45	45.05	1.45
EM	D1	38.6	72.2	59.7	12.5	21.1	38.68	1.59		
	D2	29.5	75.5	63.4	12.1	33.9	35.69	1.36		
	D3	29.7	67.8	57.1	10.7	27.4	39.05	1.39	37.81	1.45
EN	E1	29.5	74.2	62.9	11.3	33.4	33.83	1.34		
	E2	29.9	64.1	54.5	9.6	24.6	39.02	1.39		
	E3	29.8	65.6	57.3	8.3	27.5	30.18	1.3	34.35	1.34
SS	F1	29.9	71	59.1	11.9	29.2	40.75	1.41		
	F2	29.6	67.1	56.9	10.2	27.3	37.36	1.37		
	F3	29.9	61	51.8	9.2	21.9	42.01	1.42	40.04	1.4
SM	G1	30	71.2	59.9	11.3	29.9	37.79	1.38		
	G2	29.5	74.5	62.4	12.1	32.9	36.78	1.37		
	G3	29.7	67.5	57.1	10.4	27.4	37.96	1.38	37.51	1.38
SN	H1	29.7	70.2	59.1	11.1	29.4	37.76	1.38		
	H2	29.8	73.5	61.9	11.6	32.1	36.14	1.36		
	H3	29.8	67.5	57.4	10.1	27.6	36.59	1.37	36.83	1.37

Table 4.03 Moisture content, bulk density, organic percent and clay volume of sediment cores determined from representative samples from within the top 10 cm of the cored samples. Site abbreviations are explained in Table 4.01, site locations given in Figure 4.03.

Site	Average moisture content (%)	Bulk density ($kg.m^{-3}$)	Organic matter by weight (%)	Clay volume – 2 μm (%)
EN	34.35	1864.59	0.761	1.86
EM	37.81	1826.64	1.021	2.07
ES	45.05	1880.32	0.781	1.88
SN	36.83	1879.12	0.964	1.18
SM	37.51	1842.61	0.988	2.73
SS	40.04	1892.6	0.909	1.48
SB	110.38	1381.22	2.773	13.45
OS1	56.37	1644.73	1.512	16.41
CM1	38.19	1855.81	1.074	1.82

Table 4.04 Eigenvalues of 6 factors determined from multivariate Factor Analysis of the surficial sediment in-situ shear strength, textural characteristics and physical/environmental setting. Factor Analysis is used to determine structure within a dataset. The Eigenvalues are used to determine the number of factors that should be considered in multivariate Factor Analysis.

Factor	Eigenvalues	% Total Variance	Cumulative Eigenvalues	Cumulative %
1	**6.45**	53.74	6.45	53.74
2	**1.71**	14.26	8.16	68.00
3	**1.28**	10.70	9.44	78.70
4	0.76	6.37	10.21	85.07
5	0.68	5.64	10.89	90.71
6	0.46	3.83	11.34	94.54

Table 4.05 Typical ranges of index properties of some common clay minerals

Clay mineral	Liquid limit range	Plasticity index range	Activity (approx)
Kaolinite	40-60	Oct-25	0.4
Illite	80-120	50-70	0.9
Sodium montmorillonite	700	650	7
Other montmorillinites	300-650	200-550	1.5
Granular soils	20 or less	0	0

(After Head, 1984; Head, 1988)

Table 4.06 Slake-durability indices of the rock that comprises the reef and strata underlying the muddy-sand surficial sediment within northern Poverty Bay

		Sample 1	Sample 2	Sample 3	Sample 4	Average	95% confidence interval
Initial mass of sample before oven dried (10 samples ~45-65g each) (kg)		0.50	0.54	0.53	0.49		
Mass of drum & sample after 2-6 hr at 105 degrees C (kg)	A	1.65	1.69	1.66	1.62		
Mass of drum & retained sample after 1st test (kg)	B	1.50	1.57	1.53	1.51		
Mass of drum & retained sample after 2nd test (kg)	C 1	1.45	1.47	1.44	1.44		
Mass of drum & retained sample after 3rd test (kg)	C 2	1.41	1.42	1.40	1.41		
Mass of drum (kg)	D	1.14	1.15	1.13	1.14		
Slake-durability index I_{d1} (%)		71.34	76.76	75.87	76.27	75.06	2.46
Slake-durability index I_{d2} (%)		60.45	59.28	58.45	62.35	60.13	1.65
Slake-durability index I_{d3} (%)		52.94	49.90	52.37	54.87	52.52	2.01

Table 4.07 Normalized variance maximized (Varimax) rotated factor loadings determined from multivariate Factor Analysis of the surficial sediment shear strength, textural characteristics and physical/environmental setting. Factor loadings greater than 0.5 are highlighted.

Varimax normalized factor loadings	Factor 1	Factor 2	Factor 3
Shear strength	-0.16	0.03	0.68
Distance to sediment source	-0.21	0.66	-0.09
Water depth	0.52	0.12	0.69
Site in channel 1-y 2-n	-0.15	-0.77	-0.13
Mean grain size (microns)	-0.54	0.48	-0.59
Bi-modal 1-y 0-n	0.81	0.06	-0.08
Clay %	0.95	-0.09	0.19
Silt %	0.73	-0.41	0.49
Sand %	-0.82	0.34	-0.43
Organic content %	0.65	0.3	-0.18
Clay to Sand ratio	0.95	-0.11	0.14
Mud to Sand ratio	0.86	-0.24	0.29
Explained Variance	5.48	1.74	2.22
Proportion of Total Variance	0.46	0.15	0.19

Table 4.08 Correlation Matrix of the correlation coefficient (R) from the linear regression between the surficial sediment shear strength, textural characteristics and physical/environmental setting. The Turanganui River and the existing dredge spoil ground are termed "sediment sources", as representative of high sediment depositional environments.

Correlation Matrix. R2 values	Shear strength	Distance to sediment source	Water depth (m)	Site in channel 1-y 0-n	Mean grain size (μm)	Bi-modal 1-y 0-n	Clay %	Silt %	Sand %	Organic content %	Clay to Sand ratio	Mud to Sand ratio
Shear strength	1											
Distance to sediment source	-0.09	1										
Water depth	0.42	-0.06	1									
Site in channel 1-y 0-n	-0.05	-0.18	-0.16	1								
Mean grain size (μm)	-0.36	0.46	-0.65	-0.19	1							
Bi-modal 1-y 2-n	-0.08	-0.18	0.41	-0.09	-0.35	1						
Clay %	-0.03	-0.24	0.63	-0.12	-0.65	0.72	1					
Silt %	0.29	-0.41	0.62	0.13	-0.87	0.45	0.82	1				
Sand %	-0.21	0.38	-0.64	-0.07	0.85	-0.54	-0.9	-0.99	1			
Organic content %	-0.1	-0.02	0.24	-0.18	-0.12	0.51	0.47	0.27	-0.34	1		
Clay to Sand ratio	-0.03	-0.23	0.54	-0.09	-0.61	0.72	0.97	0.8	-0.88	0.45	1	
Mud to Sand ratio	0.12	-0.29	0.53	-0.01	-0.7	0.58	0.9	0.9	-0.94	0.35	0.96	1

Table 4.09 Coefficients determined by multiple linear regression for the prediction of the surficial sediment shear strength based on sediment textural and physical/environmental characteristics. Water depth (*highlighted*) is shown to be statistically the most important predictor of the in-situ shear strength.

Multiple linear regression	BETA	Standard error of BETA	B	Standard error of B
Intercept			**1.23**	**0.32**
Distance from sediment source (X_1)	-0.09	0.15	-0.00	0.00
Water depth below Chart Datum (X_2)	**0.52**	**0.17**	**0.07**	**0.02**
Organic content (%) (X_3)	-0.18	0.15	-0.17	0.15
Ratio of mud to sand (X_4)	-0.13	0.18	-0.11	0.16
R= 0.48				
R^2= 0.23				
Adjusted R^2= 0.15				

Table 4.10 Coefficients determined by multivariate non-linear estimation with break point for the prediction of the surficial sediment shear strength based on sediment textural and physical/environmental characteristics. The resultant R^2 value is relatively high (adjusted $R^2 = 0.83$)

Piecewise non-linear estimation with breakpoint	Estimate
Const.*B0*	0.7977
Distance to sediment source	0.0001
Water depth	0.0385
Organic content %	-0.065
Mud to Sand ratio	-0.06
Const.B0	1.9013
Distance to sediment source	-0.0002
Water depth	0.0248
Organic content %	0.1101
Mud to Sand ratio	0.0365
Regression line breakpoint	1.6763
R	0.91
R^2	0.83
Adjusted R^2	**0.83**

Table 4.11 Measured and predicted surficial sediment shear strength values and residuals. Predicted values have been determined using a non-linear estimation with break-point statistical technique with coefficients summarised in Table 4.10

Site	Measured in-situ shear strength (kPa)	Predicted in-situ shear strength (kPa)	Residual	Site	Measured in-situ shear strength (kPa)	Predicted in-situ shear strength (kPa)	Residual
Site 2	2.196	2.08	0.12	Site 29	1.724	1.73	0.00
Site 3	2.074	1.94	0.13	Site 30	1.188	1.23	-0.04
Site 4	1.969	2.15	-0.18	Site 31	1.348	1.56	-0.22
Site 9	1.665	1.25	0.41	Site 32	1.512	1.51	0.00
Site 10	1.388	1.21	0.18	Site 33	1.613	1.45	0.17
Site 11	1.719	2.04	-0.32	Site 34	1.409	1.40	0.01
Site 13	1.280	1.18	0.10	Site 35	1.067	1.38	-0.31
Site 14	1.229	1.18	0.05	Site 36	1.188	1.26	-0.08
Site 15	0.945	1.16	-0.22	Site 37	1.427	1.17	0.25
Site 16	0.806	1.05	-0.25	Site 38	1.976	2.16	-0.19
Site 17	1.148	1.06	0.09	Site 39	1.190	1.35	-0.16
Site 18	0.793	0.97	-0.18	Site 42	0.831	1.23	-0.40
Site 19	1.260	1.39	-0.13	Site 43	2.295	2.35	-0.06
Site 20	1.850	2.04	-0.19	Site 44	2.210	2.26	-0.05
Site 21	2.030	1.96	0.07	Site 50	1.634	1.40	0.23
Site 22	2.066	1.91	0.16	Site 51	1.746	2.09	-0.35
Site 23	1.890	1.89	0.00	Site 54	2.307	2.27	0.04
Site 24	1.467	1.13	0.33	Site 55	2.358	2.25	0.10
Site 25	1.665	1.52	0.15	Site 57	2.597	2.27	0.33
Site 26	2.057	2.09	-0.03	Site 58	2.259	2.18	0.08
Site 27	1.949	2.03	-0.08	Site 59	2.354	2.04	0.32
Site 28	1.845	1.93	-0.08	Site 60	2.243	2.05	0.20

Table 4.12 Atterberg limits and consistency indices determined using a drop cone penetrometer. Abbreviations are explained in Table 4.01, site locations given in Figure 4.01. The clay mineralogy of the marine sediment in Poverty Bay has been comprehensively examined by Miller, (1981) and is consistent to the clay mineralogy based on the soils Activity.

Site	Plastic limit (%)	Liquid limit (%)	Plasticity index (%)	Liquidity index	Activity	Clay % (2μm)	Dominant clay(s) (based on limits, indices and Activities)
EN	29.6	33.7	4.1	1.16	2.2	1.86	Montmorillonite/illite/kaolinite
EM	31.84	36.55	4.72	1.27	2.28	2.07	Montmorillonite/illite/kaolinite
ES	29.64	33.72	4.08	2.55	2.17	1.88	Montmorillonite/illite/kaolinite
SN	25.65	31.85	6.2	1.8	5.25	1.18	Montmorillonite/illite/kaolinite
SM	25.83	32.01	6.18	1.89	2.26	2.73	Montmorillonite/illite/kaolinite
SS	29.14	33.93	4.79	2.27	3.24	1.48	Montmorillonite/illite/kaolinite
SB	46.11	81.25	35.14	1.83	2.61	13.45	Montmorillonite/illite/kaolinite
OS1	28.53	44.22	15.69	1.77	0.96	16.41	Montmorillonite/illite/kaolinite
CM1	29.11	33.9	4.8	1.89	2.64	1.82	Montmorillonite/illite/kaolinite

Table 4.13 Point load indenter strength measurements. Averages are calculated by deleting the two highest and lowest value from the valid tests following the procedure outlined by Brown, (1985)

Width 1 (m)	Width 2 (m)	Average width (m)	Depth (m)	Failure load, P (M.Pa)	Failure load (N)	De^2 (m2)	De (m)	Uncorrected point load strength ($N.m^{-2}$)	Size correction factor	Corrected point load strength ($N.m^{-2}$)	Corrected point load strength ($MN.m^{-2}$)	Uniaxial compressive strength ($MN.m^{-2}$)
0.057	0.060	0.058	0.048	0.350	504.910	0.004	0.060	141145	1.08	152995	0.15	3.37
0.040	0.048	0.044	0.038	0.330	476.058	0.002	0.046	227898	0.96	218870	0.22	4.82
0.042	0.061	0.051	0.063	0.260	375.076	0.004	0.064	90452	1.12	101360	~~0.10~~	~~2.23~~
0.030	0.051	0.040	0.036	0.200	288.520	0.002	0.043	154753	0.94	144868	0.14	3.19
0.033	0.041	0.037	0.038	0.310	447.206	0.002	0.042	251619	0.93	233026	0.23	5.13
0.058	0.043	0.050	0.045	0.270	389.502	0.003	0.054	134419	1.03	138959	0.14	3.06
0.029	0.035	0.032	0.025	0.110	158.686	0.001	0.032	156960	0.82	128033	0.13	2.82
0.037	0.063	0.050	0.033	0.410	591.466	0.002	0.046	279423	0.96	269154	~~0.27~~	~~5.92~~
0.049	0.050	0.050	0.035	0.370	533.762	0.002	0.047	245231	0.97	237704	~~0.24~~	~~5.23~~
0.042	0.040	0.041	0.040	0.180	259.668	0.002	0.046	124515	0.96	119538	~~0.12~~	~~2.63~~
									Average		0.17	3.73
									Standard deviation		0.04	0.98

Table 4.14 Slack durability indices of the papa mudstone underlying the shipping channel and Swinging Basin sediments.

		Sample 1	Sample 2	Sample 3	Sample 4	Average	95% confidence interval
Initial mass of sample before oven dried (10 samples ~45-65g each) (kg)		0.5017	0.5405	0.5259	0.4868		
Mass of drum & sample after 2-6 hr at 105 degrees C (kg)	**A**	1.6463	1.6924	1.655	1.6248		
Mass of drum & retained sample after 1st test (kg)	**B**	1.5025	1.5668	1.5281	1.5093		
Mass of drum & retained sample after 2nd test (kg)	**C1**	1.4479	1.4723	1.4365	1.4415		
Mass of drum & retained sample after 3rd test (kg)	**C2**	1.4102	1.4216	1.4045	1.4051		
Mass of drum (kg)	**D**	1.1446	1.1519	1.1291	1.138		
Slake-durability index I_{d1} (%)		71.337	76.762	75.87	76.274	75.061	2.46
Slake-durability index I_{d2} (%)		60.454	59.278	58.452	62.346	60.133	1.65
Slake-durability index I_{d3} (%)		52.94	49.898	52.367	54.869	52.519	2.01

Table 4.15 Sediment type and approximate bearing capacity

Soil type	Bearing value (kN/m^2)	Remarks
Dense gravel or dense sand and gravel	>600	
Medium dense gravel or medium dense sand and gravel	200-600	
Loose gravel or loose sand and gravel	<200	
Compact sand	>300	
Medium dense sand	100-300	
Loose sand	<100	
Very stiff boulders clay and hard clays	300-600	Susceptible to long-term
Stiff clays	150-300	Consolidation settlement
Firm clays	75-150	
Soft clays and silts	<75	
Very soft clays and silts	-	

(After British Standard, 1986)

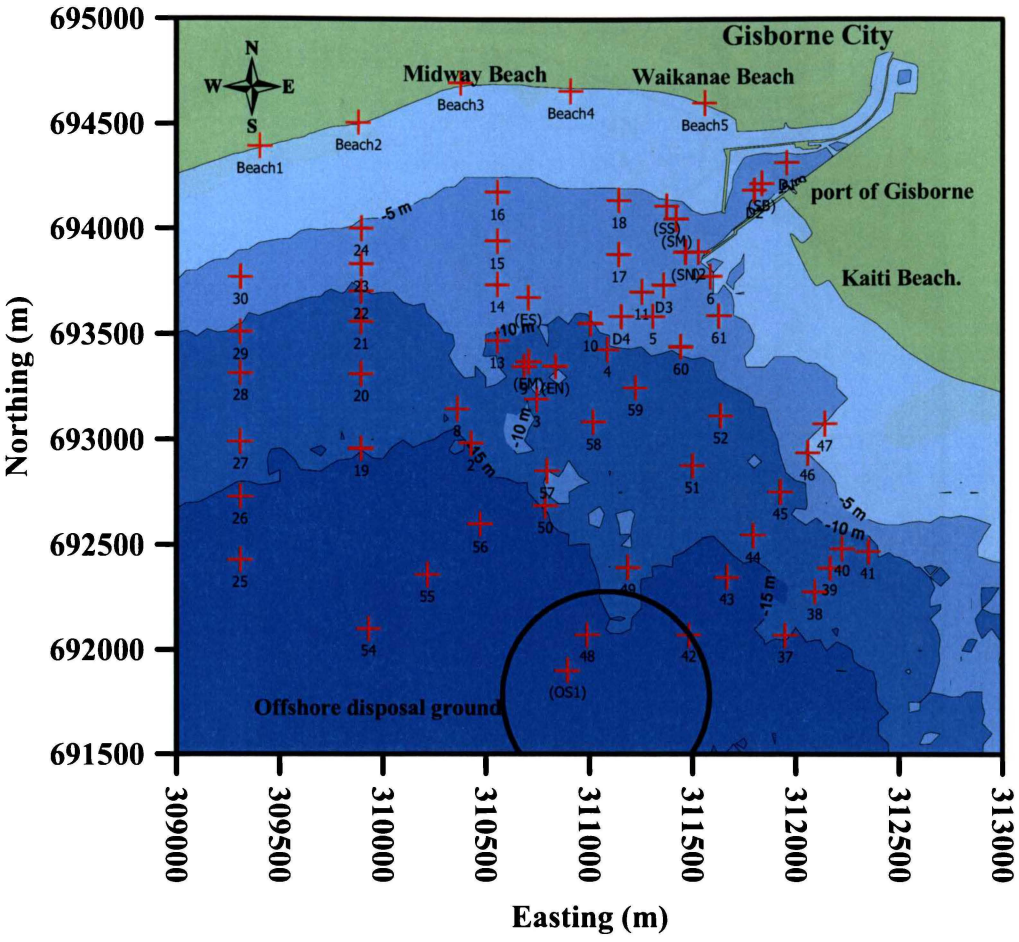

Figure 4.01 Locations of surficial sediment sample sites within the study site. Co-ordinates are in Poverty Bay Circuit.

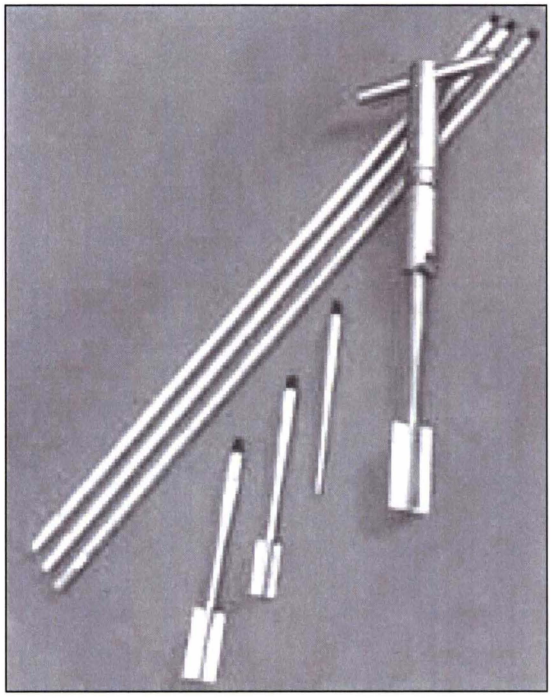

Figure 4.02 Geonor hand-held shear vane used to determine the in-situ shear strength of the surficial sediment.

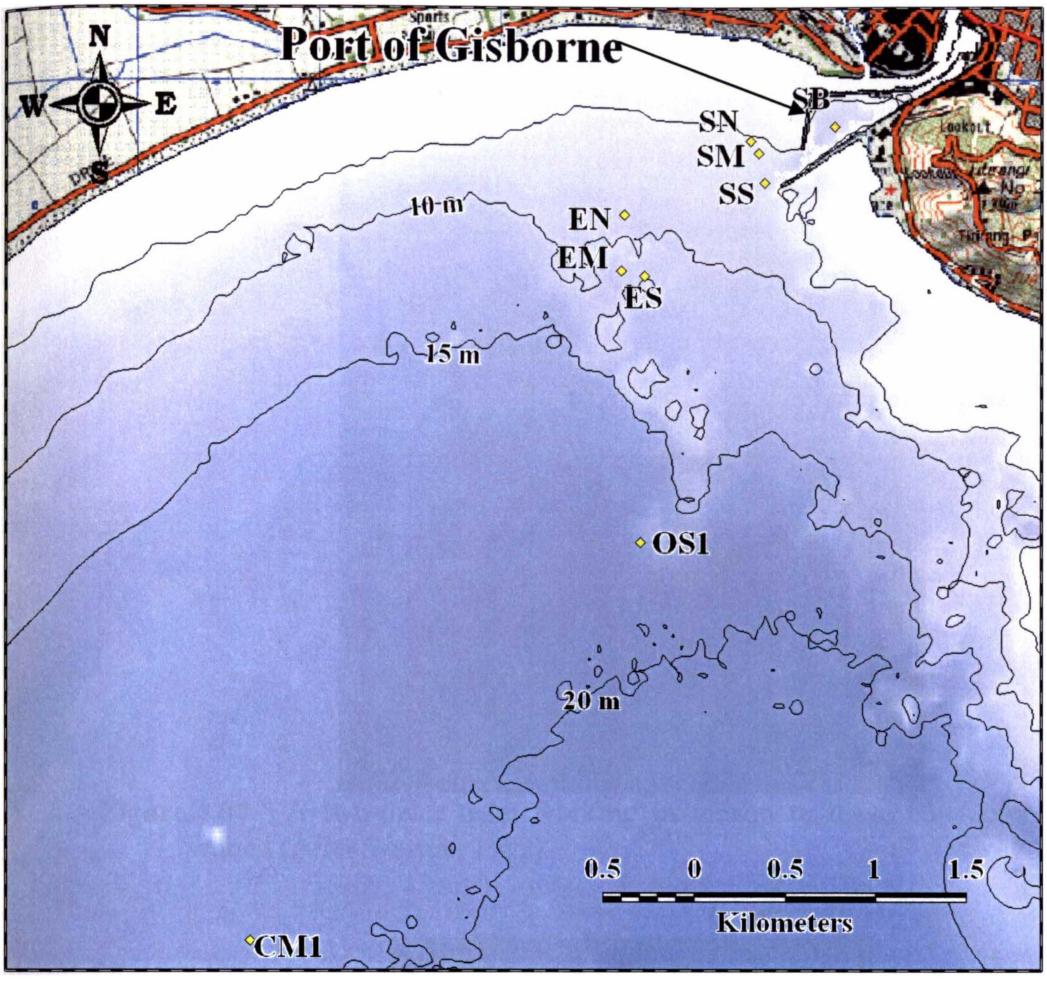

Figure 4.03 Core collection sites within Poverty Bay. Sample location abbreviations are explained in Table 4.01. Cores were collected to ensure that sediment in as close to in-situ condition was available for laboratory geomechanical tests.

Figure 4.04 A two-diver team working in unison to drive PVC pipes into the seabed (After Warren, 1992)

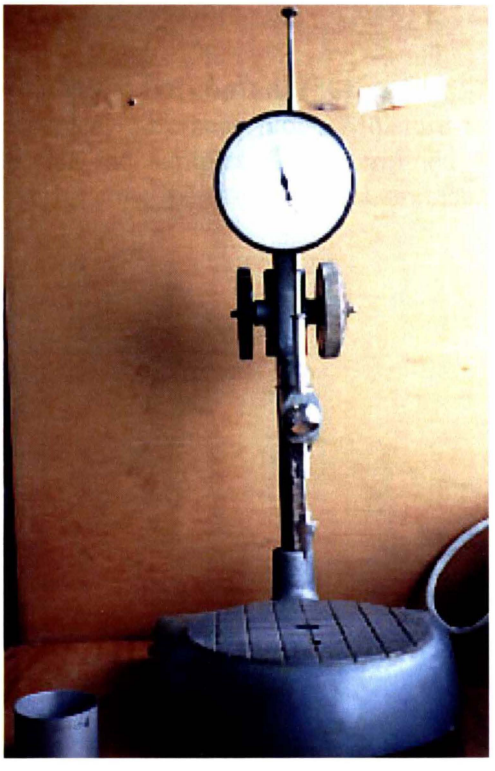

Figure 4.05 The drop-cone penetrometer and sample cup used in Atterberg limits. Also shown is the cylindrical cup in which the sample is placed.

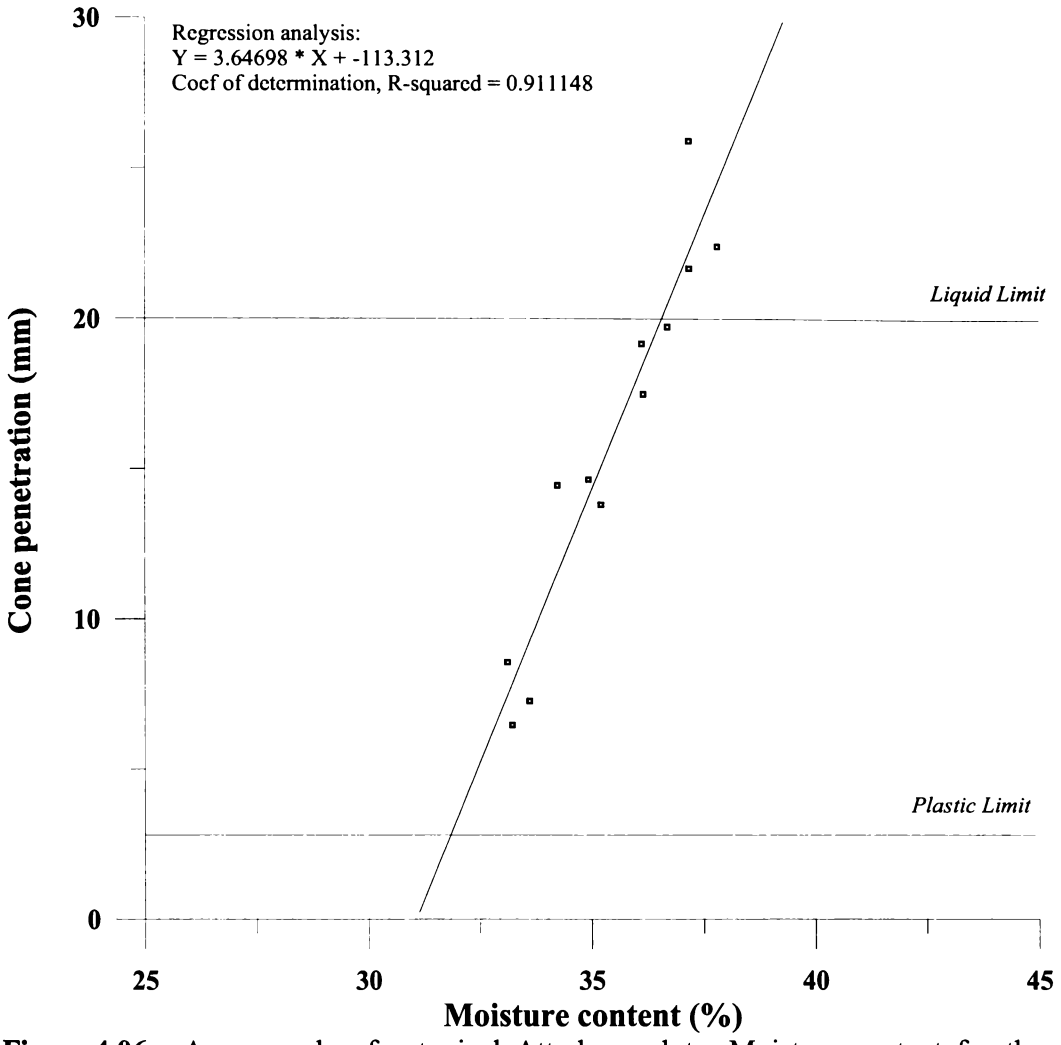

Figure 4.06 An example of a typical Atterberg plot. Moisture content for the Plastic and Liquid limits for the samples are determined through linear regression and correspond to cone penetration measurements of 2.8 and 20 mm respectively.

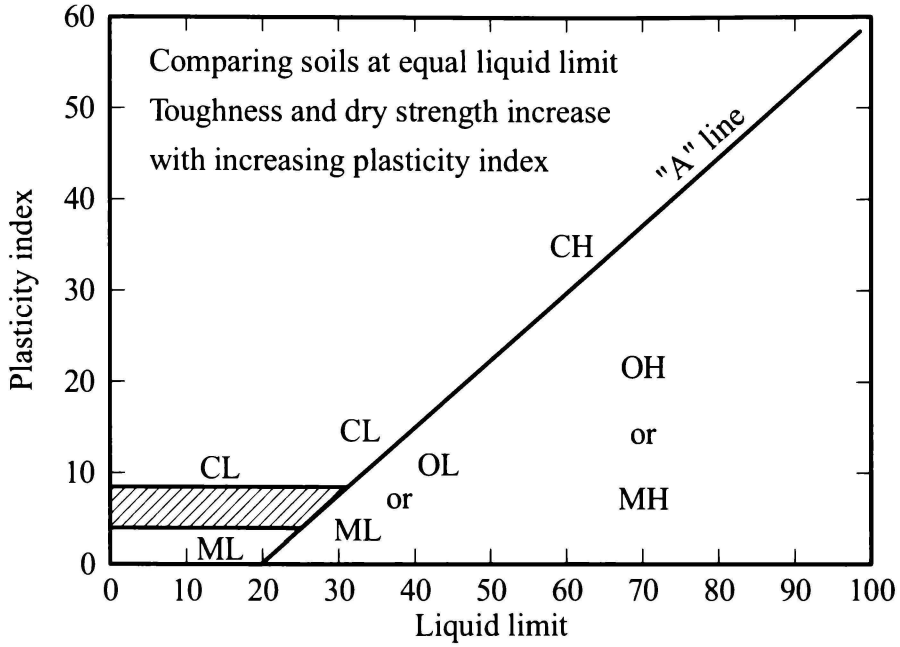

Figure 4.07 Idealised plasticity classification chart, definitions are, *CL* = Low plasticity clay, *MH* = High plasticity silt, *ML* = Low plasticity silt, *OH* = High plasticity organic soil (Rare), *Pt* = Peat (After Craig, 1994).

Figure 4.08 Cutter-suction dredge 'Pukunui' operated by Port Gisborne Ltd. for maintenance dredging of the shipping channel at the port of Gisborne.

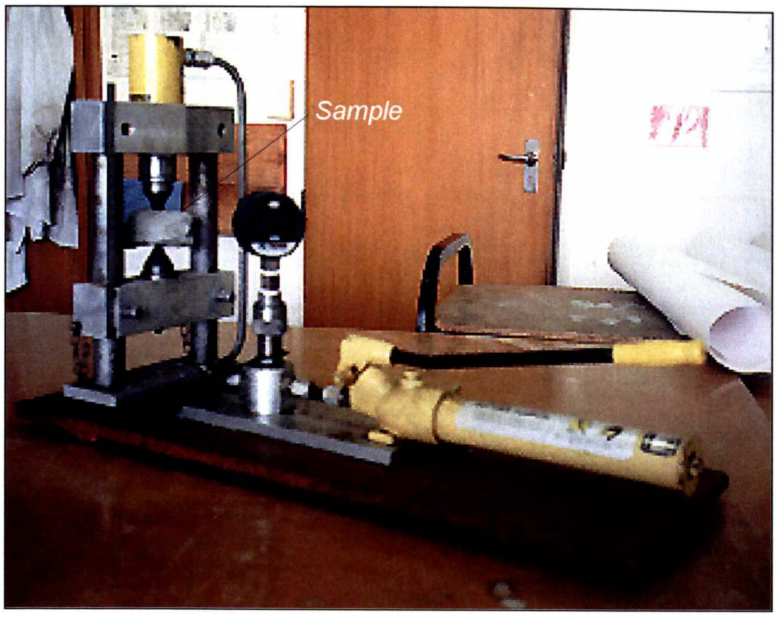

Figure 4.09 Point load tester with a sample ready for analysis (*Model EL77-010*). Pressure is applied via the two conical heads at the top and bottom of the sample until the sample fails.

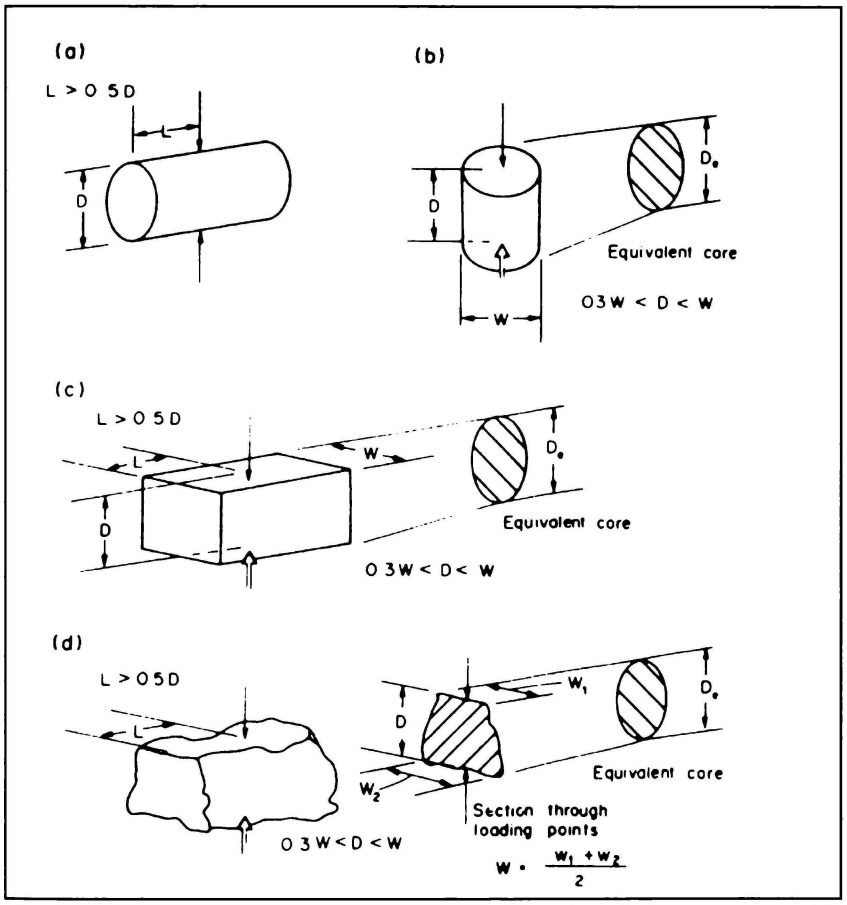

Figure 4.10 Specimen shape requirements for (a) the diametral test, (b) the axial test, (c) the block test and (d) the irregular lump test (after Brown, 1985).

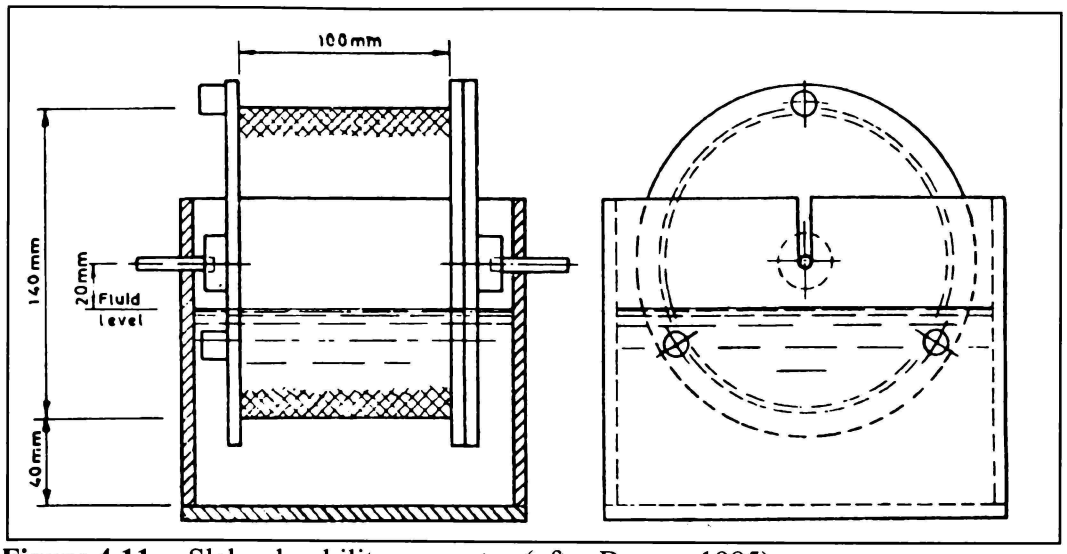

Figure 4.11 Slake-durability apparatus (after Brown, 1985).

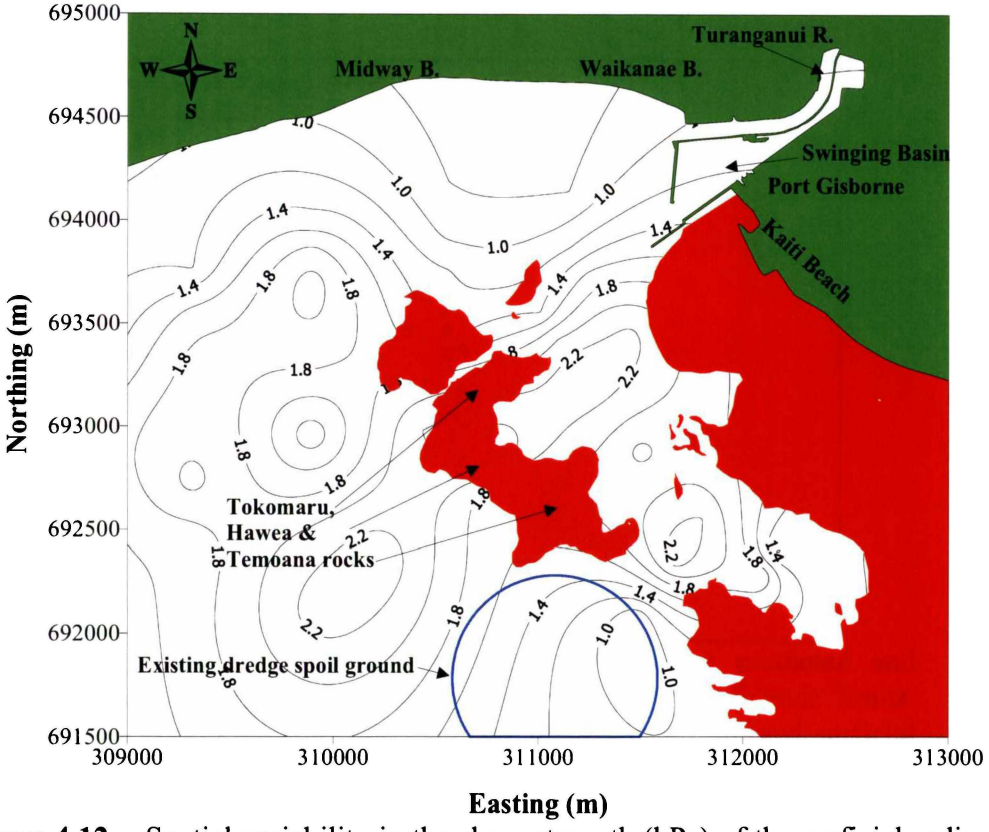

Figure 4.12 Spatial variability in the shear strength (kPa) of the surficial sediment as measured by a hand held shear vane (Figure 4.02). The shear strength of the surficial sediment shows a general trend to increase with distance offshore from Waikanae and Midway beaches. The shear strength of the surficial sediment in the vicinity of the existing spoil is relatively smaller.

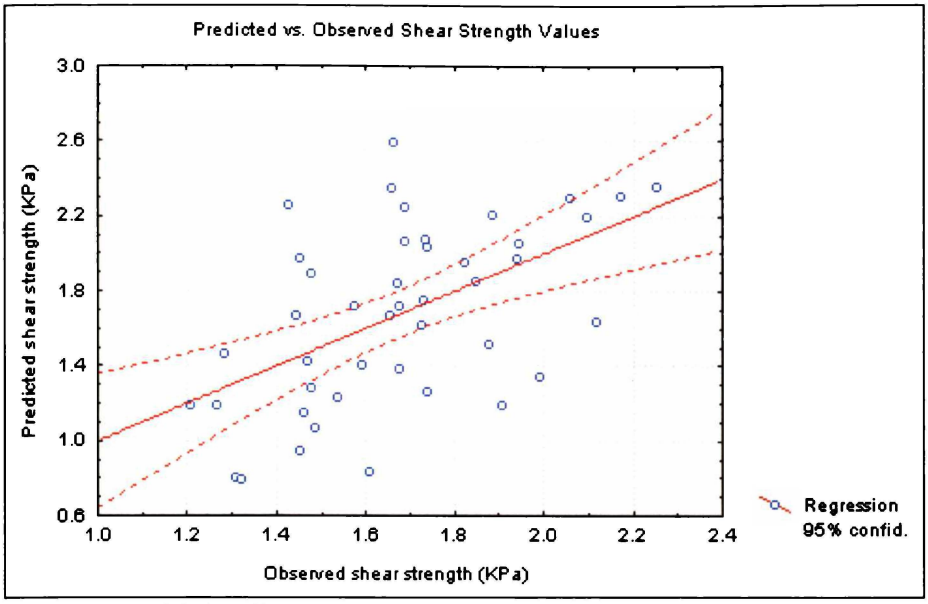

Figure 4.13 Multiple linear regression of predicted and observed surficial sediment shear strengths with 95 % confidence limits.

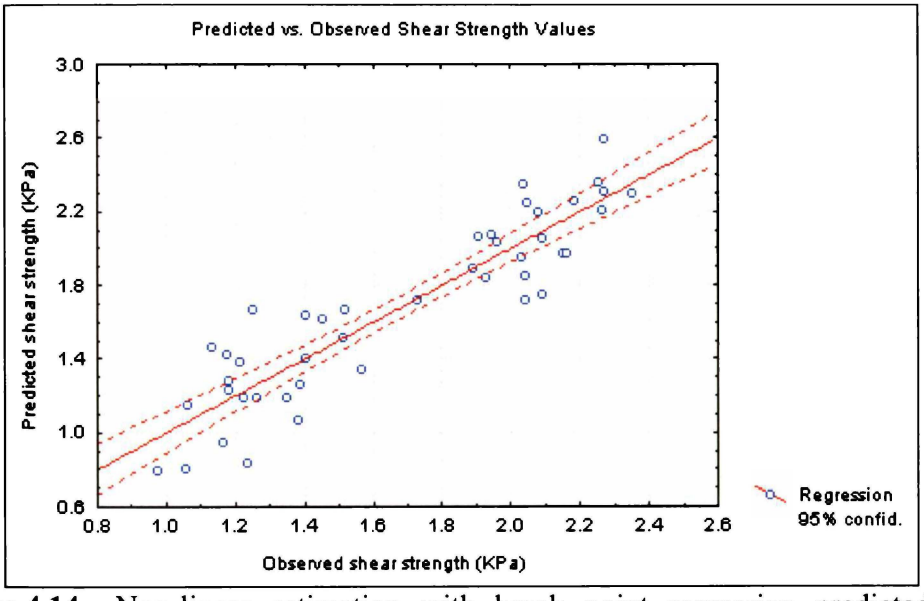

Figure 4.14 Non-linear estimation with break point regression predicted and observed surficial sediment shear strengths with 95 % confidence limits. Graph shows a good correlation between the predicted to observed surficial sediment in-situ shear strength.

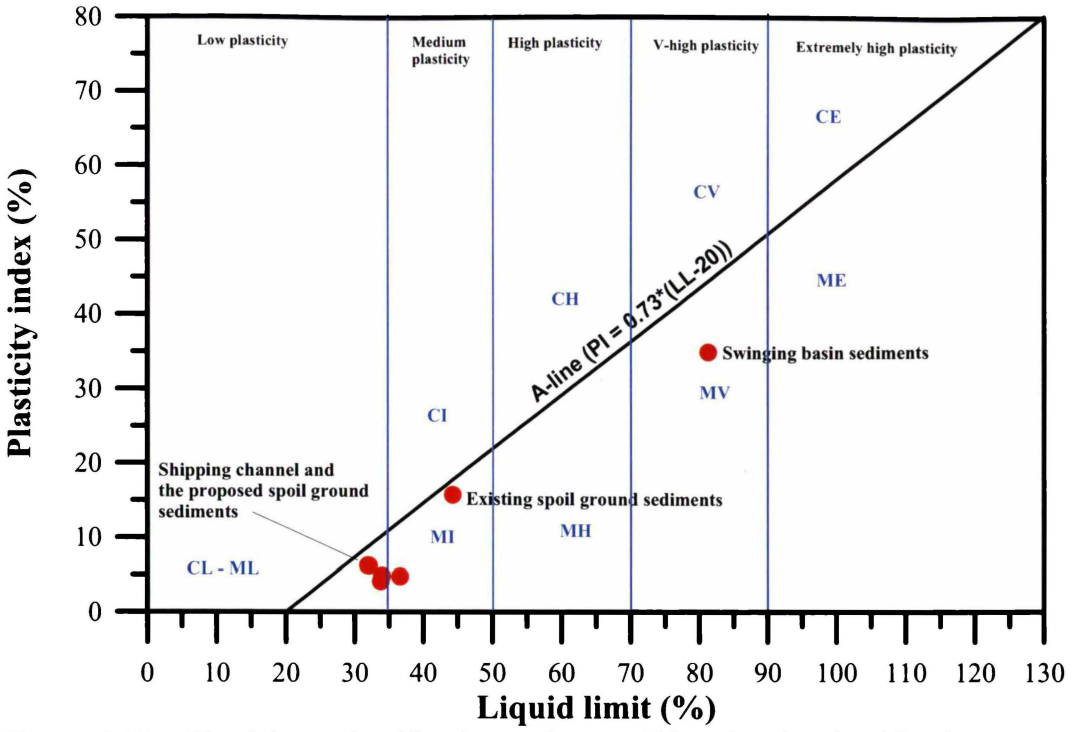

Figure 4.15 Plasticity classification chart. Abbreviated classifications are described in Figure 4.7. The New Zealand method for determining the plasticity of a sample only distinguishes between high and low plasticity, with Liquid limits > 50% having high plasticity and Liquid limits < 50% having low plasticity. (Classification of samples using British practice as outlined by Head, 1984)

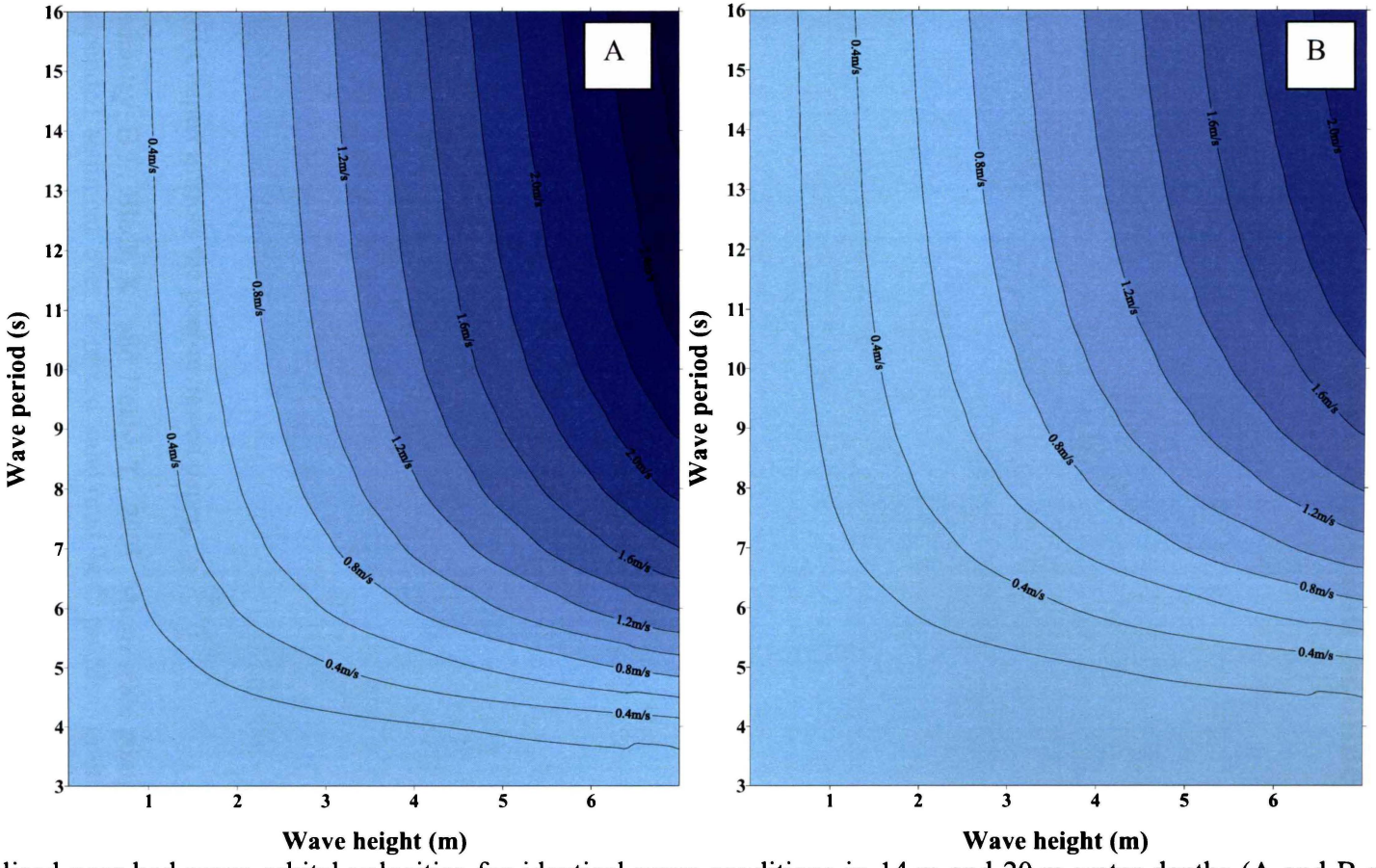

Figure 4.16 Idealised near-bed wave orbital velocities for identical wave conditions in 14 m and 20 m water depths (A and B respectively). The magnitude of the near-bed wave orbital velocities at 14 m water depth are relatively larger than at 20 m, illustrating the influence of water depth on the magnitude of the near-bed orbital velocity.

Chapter 5. Micro-scale Pumped Measurements of Suspended Sediment Over a Mixed Sand/Mud Bed: Profiles, Grain Sizes and Sediment Diffusivity

"*The ocean is a fluid world*" - Charles Caleb Colton

This Chapter mirrors the peer-reviewed paper,

Beamsley, B.J., Black, K., and Healy, T., 2001. Micro-scale pumped measurements of suspended sediment over a mixed sand/mud bed: profiles, grain sized and sediment diffusivity. Journal of Coastal Research Special Issue 34, (ICS 2000 New Zealand) pp. 342-356

5.1 Abstract

Micro-pumps were used to record suspended sediment concentration very near the seabed under irregular, unbroken waves at 4 sites with mixed sand/mud seabeds in Poverty Bay, New Zealand. The 4 sites filled the criteria of have successively higher mud content in depths of 4, 6, 8 and 10 m. Samples were taken over a 1-minute period using an array of 5 inline impeller pumps at elevations of 0.02, 0.04, 0.08, 0.16 and 0.32 m. *RMS* orbital velocities ranged from 0.21 to 0.54 m.s-1 while residual currents were 0.00 to 0.05 $m.s^{-1}$.

Surficial sediments have a single modal peak in the sand size fraction, with fines tailing off, but the suspended sediment concentrations display a bi-modal grain size distribution with fine sand and mud modal peaks. Both peaks become finer and the distributions become more poorly sorted with elevation above the bed, and the 1st modal peak changes from fine sand size to mud at an elevation dependent on the strength of the near-bed orbital motion. The chapter considers the grain size, concentration profile and eddy diffusivities / mixing lengths as a function of elevation.

All suspended sediment concentration profiles display a distinct concave-up profile shape in log-linear space, both for the full grain size distribution and when each size class in the grain size population is considered individually. Piecewise analysis of vertically consecutive suspended sediment concentrations show that the mixing length profile has a gradient close to the value of the von Karman constant ($\kappa = 0.4$).

The ratio of the sediment diffusivity derived from the concentration profile to eddy viscosity derived from the wave-induced friction velocity ($\beta=\varepsilon_s/\varepsilon_f$) is found to be less than 1.0, in keeping with prior studies. However, a new function is presented for β where,

$$ln(\beta) = -0.95 - \frac{0.4\psi}{ln(\psi)}$$

and $\psi = w_f/U^*$, while wf is the sediment fall velocity and U^* is the friction velocity. The least scatter occurred when U^* was derived from U_{max}, the maximum orbital velocity in the 1-minute measurement period.

5.2 Introduction

Measurement of suspended sediment concentration (*SSC*) profiles under unbroken waves has attracted considerable attention. *SSC* measurements are typically made either by inferring concentration based on the backscattering of acoustic or optical signals (e.g. Aagaard and Greenwood, 1999; Black and Vincent, 2001), or by direct sampling with traps or pumps (e.g. Black and Rosenberg, 1994; Kos'yan, 1985). Trap and pumped samples provide an opportunity to examine vertical variability of suspended sediment grain size. However, the intrusive nature of sediment traps and pump nozzles make high-resolution near-bed investigation of *SSC* difficult, particularly if sediment traps are

used, due to aspect ratio and time-averaging considerations. Sediment trapping is only applicable to time-averaged concentration determination, where deployment time scales are relatively large (i.e. 10's of minutes to several hours). Further, considerably more logistical effort is associated with collecting and processing both trapped and pumped suspended sediment samples than OBS or ABS *SSC* measurement techniques. Additionally, the operation of suspended sediment pumps may be affected by turbulent eddies which deflect the grain paths, potentially effecting the value of the measured *SSC*. Regardless, one of the benefits that pumped water/sediment samples have over backscatter instruments is the elimination of grain size dependency (Black and Rosenberg, 1994). Additionally, the high-resolution pumped sampling of near-bed *SSC* can be used to consider grain size textural variation with elevation and wave conditions at the intermediate time scales.

Previous research has illustrated that the mean and/or median grain size of sandy sediments on beaches varies vertically (Black and Rosenberg, 1992; Kos'yan, 1985) but the variability of the entire grain size distribution within the water column in field conditions over mixed sand/mud beds is less well understood. Laboratory studies have shown concentration profile gradients to be inversely related to grain size (Nielsen, 1983; Nielsen, 1992; Van Rijn, 1993) and the findings of Black and Rosenberg, (1992) suggest that the inverse relationship also occurs under irregular unbroken waves over natural seabeds. Nielsen, (1983) considered the vertical variation of grain size and concluded that changes in the concavity of the profile were representative of a shift in dominance from diffusive to convective suspension processes. Because of the very broad range of grain sizes in the mixed sand/mud beds in Poverty Bay (approximately $4 - 400$ μm), opportunities arise for further exploration of such dependencies as a function of grain size under natural wave conditions.

Predictive *SSC* profile equations generally make assumptions about the distribution of either the mixing length (l_s) or sediment diffusivity (ε_s) with elevation. For example, the time-averaged Nielsen model assumes a vertically uniform l_s near the bed, while perhaps the simplest non-uniform model assumes that l_s varies as a linear function of elevation near the bed (Fredsoe and Deigaard, 1992). Similarly, ε_s profiles based on eddy viscosity (ε_f) have been described as being vertically uniform or parabolic near the bed, sometimes grading into vertically uniform at some distance above the bed (Van Rijn, 1993). However, with the variation in grain size with elevation, the determination of both l_s and ε_s can be difficult to achieve from concentration alone (Black and Vincent, 2001).

In addition, some incongruity exists in the deterministic relationship between ε_f and ε_s ($\varepsilon_s/\varepsilon_f = \beta$). Carstens, (1952) concluded that β was less than 1 due to the sediment particles not being able to react fully to turbulent fluctuations, while conversely Singamsetti, (1966) determined β to be larger than 1 due to the greater strength of the centrifugal force on the suspended sediment as a result of the relatively larger sediment density. Further, Van Rijn, (1984b), based on ε_s profiles in the upper half of a unidirectional flow as measured by Coleman, (1970), determined β-factors to be a function of the ratio of sediment fall velocity (w_f) and the near-bed friction velocity (U^*), and to be greater than 1. Comparatively, Green and Black, (1999) determined β values for field conditions under waves (bi-directional currents) that are generally less than one,

and note that the choice of the statistical measure of the wave orbital speed used to characterise the friction velocity will influence the determination of β.

Further, under bi-directional currents (i.e. wave orbital currents) and assuming ε_f near the bed is not vertically uniform; the applicability of the van Rijn relationship has not been sufficiently examined. Indeed, it is possible that, for low concentrations (where hindered particle settling is not relevant) and under bi-directional orbital velocities near the seabed, these processes may alter the function used for β.

In this chapter, high-resolution, pumped water/sediment samples, from up to 5 different elevations above a mixed mud/sand bed are used to examine grain size variability, *SSC* characteristics, ε_s and l_s, the magnitude and definition of β, and the orbital motion statistics used to define U^*.

5.3 Methodology

5.3.1 Sampling programme

A sampling programme adjacent to the port of Gisborne, New Zealand (Figure 5.01) was undertaken to provide information on sediment fluxes and suspended sediment concentration profiles under unbroken irregular waves. Samples were collected using an array of 5 downward facing, inline impeller pumps (Figure 5.02) at elevations of 0.02, 0.04, 0.08, 0.16 and 0.32 m above the seabed in water depths of 4, 6, 8 and 10 m (Figure 5.01). The estimated pumped sampling volume is within 0.005 m of the nozzle aperture. While the downward orientation of the pump nozzles adds to the uncertainty in the relative location of the sampling volume above the seabed, the orientation stopped sand accumulating in the pipes between sampling. Additionally, between sampling the sediment within the inlet tubes would settle out of the pipes, limiting the potential errors in the estimation of the *SSC*. Sampling was conducted on the 1st (6 and 8 m), 7th (10 m) and 8th (4 m) of July, 1999. In order to maintain a flow-rate of ~ 2 m.s^{-1} samples were pumped to the boat in 4 m depths, and, at the other sites, to a free-floating underwater platform manned by a diver at 4 m above the seabed, to reduce the increased friction experienced in longer hoses.

Simultaneously, continuous wave and current data were recorded using an *InterOcean S4ADW* vector-averaging wave/current meter, sampling at 2 Hz at 1.15 m above the seabed, with measurements taken to the seabed using linear wave theory. To eliminate contamination of the data by turbulence associated with instrument frames, the current meter was situated approximately 2 m from the pump array, on a bearing perpendicular to the wave-approach direction. At each site, divers measured bedform and bed undulation dimensions, and surficial sediment sample was collected from the top 2-4 cm of the seabed.

5.3.2 Sample preparation and treatment prior to grain size and wf determination

Pumped water-sediment samples were divided by mechanically mixing each sample into a homogeneous solution and sub-sampling with a pipette. Dividing each sample allowed for the evaluation of both *SSC* and grain size textural parameters.

Because sediment flocculation may be relevant, a standardised treatment procedure was used. Berlamont et al. (1993) note that, for the treatment of mixed sediment, organic material should be removed and sediment de-flocculated, so that all grain textural measurements are based on the individual sediment grains, rather than the flocs. In accordance with New Zealand Standard 4402, hydrogen peroxide was used to remove the organic material while de-flocculation was achieved using ultra-sonic and sodium hexametaphosphate treatment (Standards Association of New Zealand, 1986).

5.3.3 Grain size and fall velocity determination

The grain size distribution of the surficial and suspended sediment was determined using a Malvern laser light diffraction particle size analyser (Model MSS17), which has the ability to simultaneously measure both the sand and the mud sizes (Malvern Instruments Ltd.). Grain size textural characteristics were calculated using the Malvern software, which also allowed the volume percent of individual grain size bins to be determined. The laser method is recommended particularly for sample inter-comparisons and to study the changes in grain size distributions over broad grain size ranges (Berlamont et al., 1993).

Equivalent fall velocities (w_f) were calculated using the equation described by Gibbs et al., (1971), and assuming equivalent quartz density, where,

$$W_f = \frac{-3\delta + \sqrt{9\delta^2 + g\rho_f(\rho_s - \rho_f)(0.015476 + 0.1841r)}}{\rho_f(0.011607 + 0.14881r)} \times \frac{1}{100} \qquad (5.01)$$

and δ = dynamic viscosity of fluid in poise, taken as 1.14×10^{-2},
g = acceleration of gravity in $cm.s^{-2}$,
r = sphere radius in cm,
ρ_f = density of fluid in $g.cm^{-3}$, taken as $0.1025 g.cm^{-3}$, (i.e. $1025\ kg.m^{-3}$) and
ρ_w=density of sphere in $g.cm^{-3}$, taken as $0.2065\ g.cm^{-3}$ (i.e. $2065\ kg.m^{-3}$).

Equivalent fall velocities were chosen, rather than direct measurement, to provide a consistent methodology. That is, the observations are not dependent on flocculation factors or multiple analysis methodologies. Fall velocities are used to calculate the mixing lengths (l_s) and in empirical suspended sediment concentration profiles (as described below).

5.3.4 *Defining friction velocity and wave friction factor*

The shape of the suspended sediment concentration profile is, in part, dependent on near-bed orbital velocities, and *SSC* profiles are often calculated using the friction velocity U^*, defined as,

$$U^* = \left(0.5 f_w U^2\right)^{1/2} \tag{5.02}$$

where U is a measure of the near-bed horizontal orbital velocity, and f_w is the wave friction factor, which Swart (1974) defines as,

$$f_w = \exp\left[5.213\left(k_b / a_s\right)^{0.194} - 5.977\right] \tag{5.03}$$

k_b is the bed roughness which, for a fixed planar bed, is given as,

$$k_b = 2.5 d_{50} \tag{5.04}$$

and d_{50} is the median grain size, while a_s is the near-bed semi-excursion distance defined as,

$$a_s = U / \omega \tag{5.05}$$

where ω is the wave radian frequency, calculated using the significant zero down-crossing wave period.

For an irregular wave pattern, the representative near-bed horizontal orbital velocity used to characterise the friction velocity and the near-bed semi-excursion distance is not well defined. For this paper, four different values of the near-bed horizontal orbital velocity are examined, which are,

i. The significant near-bed horizontal orbital velocity (i.e. average of the top 1/3 wave orbital velocities), $U_{1/3}$,
ii. The single maximum measure of the near-bed horizontal orbital velocity from the time-series, U_{max},
iii. The root-mean-square near-bed horizontal orbital velocity, U_{rms}, and
iv. The third moment of the near-bed horizontal orbital velocity, U_3

U_3 is defined as,

$$U_3 = 1.4\left[\left(\sum_{j=i}^{N}\left|U_j\right|^3\right)/N\right]^{1/3} \tag{5.07}$$

where U_j is the jth on/offshore near-bed orbital velocity (Black and Rosenberg, 1991).

5.3.5 *Concentration profiles*

Descriptions of time-averaged *SSC* profiles under waves are usually based on assumptions about either the ε_s or l_s profile. l_s is defined as a measure of the distance that a fluid is transported across a flow before it is mixed with the surrounding water (Fredsoe and Deigaard, 1992), while ε_s is a measure of the turbulent mixing of the sediment within a body of fluid (Nielsen, 1992). This paper examines three cases, which are,

(1) Vertically-uniform l_s (Nielsen, 1992),
(2) Near-bed linear approximation of the parabolic l_s profile, and
(3) A curve-linear ε_s profile (Green et al., 1999).

5.3.5.1 *Uniform mixing length assumption (Nielsen model)*

The convection-diffusion equation describes a balance between turbulent diffusion and gravity, resulting in a logarithmic decrease in concentration with elevation (Glenn and Grant, 1987). For a time-averaged vertical distribution of suspended sediment, this equation has been used to predict the vertical variation in *SSC* (Black, 1994; Deigaard et al., 1986; Fredsoe et al., 1986; Mocke and Smith, 1992). The time-dependent convection-diffusion equation is given as,

$$\frac{\partial C}{\partial t} - w_f \frac{\partial C}{\partial z} = \frac{\partial}{\partial z}\left[\varepsilon_s \frac{\partial C}{\partial z}\right] \tag{5.08}$$

where both convective and diffusive processes are acting (Van Rijn, 1993) and,
t = time,
z = elevation above the seabed, and
C = volume concentration of sediment.

Nielsen (1992) defines the time-averaged form of eqn. 5.08 which assumes a constant ε_s as,

$$C_z = C_a \exp^{(-z/l_s)} \tag{5.09}$$

where C_z is the *SSC* at elevation z and C_a is the near-bed reference concentration (not treated in this paper).

Eqn. 5.09 assumes mixing and turbulence to be vertically-uniform and related to w_f by,

$$\varepsilon_s = l_s w_f \tag{5.10}$$

Relating concentration and elevation in log-linear space and performing linear regression provides a measure of l_s as,

$$l_s = -1/\alpha \tag{5.11}$$

where α is the gradient of the regression line.

5.3.5.2 *Near-bed linear approximation of the mixing length profile*

By assuming that l_s is uniform between vertically consecutive concentration measurements then, from eqn. 5.09, the mid point mixing length (l_{smid}) can be defined as,

$$l_{smid} = \frac{(-(z_2 - z_1))}{\log_2\left(C_1/C_2\right)} \tag{5.12}$$

where C_1 and C_2 are the *SSC* at elevation z_1 and z_2 respectively, and $z_2 > z_1$.

The change in mixing length with elevation can then be considered. We compare the results to a near–bed linear approximation of the parabolic profile (Fredsoe and Deigaard, 1992), defined as,

$$l_s = \kappa z \tag{5.13}$$

where κ is von Karman's constant ($\kappa = 0.4$). Three cases are examined using,

(1) Median grain size,
(2) Individual grain size fractions, and
(3) Sand, silt and clay size classes.

5.3.5.3 *Vertical variation in sediment diffusivity*

While the Nielsen model is based on uniform l_s and the linear-approximation of the parabolic profile assumes linearly increasing l_s with elevation, Green et al. (1999) describe a curve-linear concentration profile equation based on vertically varying ε_s. The predicted concentration profile is concave-up in log-linear space close to the bed, grading (at an elevation z_m) smoothly into a straight line. The concentration field is assumed to result from a balance between settling flux and pure gradient diffusion, and an apparent sediment diffusivity that varies with elevation, i.e.,

$$C_z w_f = \varepsilon_s \, \partial C_z / \partial z \tag{5.14}$$

where ε_s is determined using a linear approximation of the parabolic ε_f profile, such that in the domain $z < z_m$,

$$\varepsilon_s = \beta \kappa U^* z \tag{5.15}$$

while at elevations greater than z_m, ε_s is vertically uniform, and defined as,

$$\varepsilon_s = \beta \kappa U^* z_m \tag{5.16}$$

where for low concentrations (c < 10 kg.m^{-3}) β is defined as $\beta = \varepsilon_s / \varepsilon_f$ (Van Rijn, 1993). Solving eqn. 5.15 for ε_s in the domain $z < z_m$ and the boundary condition $C_z = C_a$ (C_a taken to be at 0.01 m for this paper in accordance with Green and Black, 1999), eqn. 5.14 yields,

$$C_z / C_a = \left(\frac{z}{z_a} \right)^{\frac{-w_f}{\beta \kappa U_*}} \tag{5.17}$$

solving eqn. 5.16 for ε_s and the boundary condition $C_z = C_a$ in the domain $z > z_m$, and using eqn. 5.14 yields,

$$C_z / C_a = \exp\left(\frac{-w_f}{\beta \kappa U_*} \left(\frac{z - z_m}{z_m} + \ln \frac{z_m}{z_a} \right) \right) \tag{5.18}$$

Fitting of the curve-linear profile to the measured profile (normalised by the measurements at 0.02 m) involves the iterative estimation of β and z_m for a minimised squared error between observed to predicted concentrations. The value of z_m is varied in order to determine the point where the profile changes from being best described by a vertically varying to a vertically uniform ε_s. The β-factor is used to fit the predicted profile to the measured concentration profile and controls the gradient of the normalised concentration curve (Figure 5.03).

Curve fitting was performed using the 4 different statistical values of the near-bed orbital velocity previously described to determine the most suitable statistical measure to be used in describing U^* (eqn. 5.02). Only the sand-sized fraction (> 62.5 μm) is considered for the determination of β.

5.3.5.4 Examination of the β-factor

The β-factor is considered to describe the ratio of the diffusion of a fluid 'particle' to that of a discrete sediment particle, and is defined as,

$$\beta = \varepsilon_s / \varepsilon_f \phi \tag{5.19}$$

where the ϕ-factor is an expression of the influence of the sediment particles on the turbulent structure of the fluid which, in low regimes (low concentrations, C^{α} < 10 kg.m^{-3}), can be taken as 1 (Van Rijn, 1993), reducing eqn. 5.19 to,

$$\beta = \varepsilon_s / \varepsilon_f \tag{5.20}$$

Based on work done by Coleman (1970), Van Rijn (1984b; 1993) defines β for steady flow conditions as,

$$\beta = 1 + 2\psi \tag{5.21}$$

where ψ is the ratio of w_f to U^* (i.e. $\psi = w_f/U^*$).

Van Rijn (1984b) determined this relationship (eqn. 5.21) from measurements of ε_s in the upper part of a unidirectional flow, and by fitting to the ε_f profile,

$$\varepsilon_f = 0.25\kappa U_* h \tag{5.22}$$

where h is water depth.

5.4 Results

5.4.1 Seabed description

The seabed at Sites A, D and E (Figure 5.01) consisted of small moribund ripples with wavelengths ranging from a maximum of 13 cm (Site D) to 9 cm (Sites A and E), and a vertical relief of up to 1 cm (Sites A, D and E). The seabed at Site B consisted of small hummocky undulations with a horizontal extent of approximately 5-10 cm, and a vertical relief of approximately 0.5-1 cm. There were no persistent ripple patterns evident at Site B. Mean grain size of the surficial sediment shows a trend to decrease with increased water depth (Table 5.01), corresponding to the mud volume percent increasing with increased water depth.

5.4.2 Wave characteristics

Average significant wave heights and periods for each of the sampling periods (i.e. relating to sites A, B, D and E) are given in Table 5.02. The significant wave heights and periods during sampling at sites A, B and D are approximately representative of average conditions for Poverty Bay based on the data of Miller (1981) and that collected as part of the 1997 AEE (i.e. Table 2.03). In contrast, during sampling at site E the average wave height (0.7 m) was slightly less than the average wave condition predicted by Miller (1981), i.e. 1.0 m (Table 2.03). However, the average wave period measured during sampling at site E (12.9 s) is slightly longer than the average period from either the 1997 AEE data or that of Miller (1981). A time-series of significant

5.4.3 Measured SSC profile (entire grain size distribution).

Figure 5.04A, B, C and D show the measured *SSC* profiles at the sample sites A, B, D and E respectively. Assuming a constant l_s and fitting eqn. 5.09 yields median l_s values of 0.12, 0.08, 0.15 and 0.12 m for sites A, B, D and E respectively, while the average R^2 for each site is 0.87, 0.79, 0.86, and 0.73 respectively (Table 5.03). The mixing lengths are similar to those reported by Black and Rosenberg (1991) under unbroken waves for medium-sized sand.

Although regression analysis provides a good 'fit' to the measured data (assuming a constant l_s), all profiles display distinct concave-up profile shapes when plotted in log-linear space (Figure 5.04, discussed below). This suggests that the ε_s and the l_s are not vertically uniform or, alternatively, that there is some systematic variation in the grain size distribution in suspension responsible for the concave-up profile, and so both aspects are examined in the following sections.

5.4.4 Grain size distribution variation with elevation above the seabed.

The surficial sediments at all sites have a dominant modal peak located in the sand size fraction, with the distribution classified according to the Folk (1968) scheme as being finely-skewed (Table 5.01), which manifests as an excess of fines (Figure 5.05).

The suspended grain size distributions exhibit a systematic change with elevation above the seabed (Figure 5.05). A bi-modal grain size distribution is evident, one mode in the fine to very-fine sand-size fraction (62.5 – 125 μm) and another in the mud size fraction (< 62.5 μm). With increased elevation above the bed, the dominant mode shifts from the fine-sand size fraction to the mud size fraction (Figure 5.06), the peaks of both the fine sand and the mud modal curves become slightly finer with elevation (Figures 5.05) and the grain size distributions tend to become more poorly sorted (Figure 5.07). Further, the magnitude of near-bed orbital velocity appears to influence the level at which the dominant mode changes from fine sand to mud size. At relatively large orbital velocities, the sand appears to be entrained to a higher elevation (Figure 5.08 and Figure 5.09C). Conversely, at relatively low horizontal orbital velocities, the modal peak of the suspended sand is less well defined, and shows a distinct tailing off at the coarse end of the grain size distribution (Figure 5.09B). It is possible that, at relatively low orbital velocities, the coarser sediment cannot be effectively entrained or, there is not enough energy available to diffuse the sediment any distance above the seabed, as is suggested by Figure 5.08.

5.4.5 Measured SSC profile (grain size classes and bins).

Given the systematic variation in the grain size distribution with elevation above the seabed, it is possible that the observed concave-up concentration profiles are a function of the changing shape of the full grain size distribution with elevation above the seabed. Figure 5.10A, B and C shows a typical *SSC* profile shape for the measured sand, silt and clay size fractions and Figure 5.10D for individual grain size bins.

Regression analysis, assuming a uniform mixing length, results in relatively high coefficients of determination for the individual grain size classes (Table 5.04). However, all profiles within the grain size classes and narrower grain size bins still display distinct concave-up profile shapes (Figure 5.10 and Figure 5.11). Thus, this shape cannot be explained by vertically changing grain sizes alone.

5.4.6 *Vertical variation in mixing length*

The concave-up profile shapes (Figure 5.11) suggest a vertical variation in ε_s and l_s. The vertical variation in l_s was investigated by determining the mid-point mixing length between vertically consecutive *SSC* measurements (eqn. 5.12). The same three different cases (full grain size, grain classes and grain bins) were examined. The mean and the median gradients from all the samples for the three cases are shown in Table 5.05, as are the correlation coefficients (R^2) for each of the cases. The average correlation coefficient for all cases is $R^2 = 0.67$, suggesting that the vertical increase in l_s is linear, with a gradient (γ),

$$l_s = \gamma z \tag{5.23}$$

Table 5.05 shows that measured gradient ranges from $0.2<\gamma<0.8$ with mean and median of 0.47 and 0.36 respectively. An example of how the mixing lengths between consecutive concentration measurements vary with elevation is shown in Figure 5.12.; the intervals on Figure 5.12 show the correlation to be statistically significant at the 90% confidence interval. The latter values bound the theoretical value of κ=0.4 and confirm that l_s evidently increases linearly with elevation with a gradient in accordance with eqn. 5.13. Based on piecewise analysis between *SSC* at 0.02 and 0.04 m elevations, near the bed l_s appears to approach a value of 0.06 m (Table 5.05).

Notably, the measured gradient is independently derived from sediment concentration profiles, while κ=0.4 arises from the theoretical eddy viscosity distribution for a logarithmic velocity profile.

5.4.7 *Vertical variation in sediment diffusivity*

The curve-linear *SSC* profile shape equations (eqn. 5.17 and 5.18) satisfactorily fit the measured normalised sand *SSC* profiles (Figure 5.13, Table 5.06). For the majority of cases, the value of z_m equals the highest measured sample elevation in the profile (i.e. 0.32 m), suggesting that within the measured range the sediment diffusivity is increasing with elevation. The choice of the statistical measure of the orbital velocity used to describe the friction velocity does not appear to be significant, as shown by the squared error (Table 5.06).

5.4.8 *The effect of β on the SSC profile*

This section compares the determined β-factors (from curve-fitting) with the relationship proposed by Van Rijn (1984b), and defines a new relationship for β. The β-factor is defined as the ratio of ε_s to the ε_f (eqn. 5.20), and therefore increasing β has the effect of increasing the gradient of the *SSC* profile (Figure 5.03).

Comparisons of the determined β-factors to those predicted by the Van Rijn (1984b) relationship (eqn. 5.20) show a poor correlation regardless of the near-bed horizontal orbital velocity statistical measure used to characterise U^* (Figure 5.14). The value of

the fall velocity (w_f) used in the analysis was determined from the d_{50} of the individual pumped samples (using eqn 5.01).

Using regression analysis, new equations relating β to ψ were obtained for the different statistical measures of the near-bed horizontal orbital velocity over the 1-minute measurement periods (Figure 5.15 A, B, C and D; Table 5.06). The fitted curve equations are listed in Table 5.06, with the respective coefficients of determination (R^2). The least amount of scatter (R^2 = 0.85) is achieved by using the maximum near-bed horizontal orbital velocity U_{max} (Table 5.06). As such, a formula for predicting β for *SSC* profile predictions over intermediate time periods based on U_{max} is proposed, which is,

$$ln(\beta) = -0.95 - \frac{0.4\psi}{ln(\psi)} \tag{5.24}$$

The curve shape of eqn. 5.24 displays an initial gradual increase in β followed by a rapid increase at $w_f/U^* \approx 0.7$, while the approximate upper limit is $w_f/U^* \approx 0.8$-1 (Figure 5.15 D).

5.5 Discussion

Measurements at micro-scale (within 0.32 m of the sea bed) were made under highly controlled conditions in-situ. The bed sediments consisted of a wide range of grain sizes from 1 to 550 μm, making it feasible to gain insight into the water column behaviour of *SSC* from muds to sands under identical wave conditions. In all size classes, the behaviour was systematic with a reduction in concentration with elevation (more accentuated for the large grain sizes) and a tendency for a concave-up concentration profile.

Both sand and mud modal peaks become progressively finer with elevation (Figure 5.05), and the distribution becomes more poorly sorted (Figure 5.07). Further, the dominant modal peak tends to switch with elevation above the bed from being in the sand size class to mud size class (Figure 5.06). When the sediment population is broken into individual bins, the concentration profile gradients are inversely related to grain size (Figure 5.11) in accordance with the fines becoming relatively more dominant with elevation, as observed in Figure 5.05.

Near-bed orbital velocities, which scale ε_s (eqn. 15.5 and 5.16), were shown to influence the elevation to which the suspended sediment is mixed upwards (Figure 5.08 and 5.09). The decrease in grain size appears to be continuous with elevation from near the seabed. This has ramifications for backscatter *SSC* measurements, when calibrated using surficial sediment only, suggesting that for mixed sand/mud seabeds at least, care must be taken when using backscatter instruments for measuring *SSC* otherwise erroneous concentration measurements could result from the vertical variation in grain textural parameters.

Log-linear regression of *SSC* with elevation produces R^2 values ranging from 0.58 to 0.97. However, while a linear fit to the data is achieved, the assumption that l_s is

vertically uniform is a simplification of the observed concentration profile, as all measured profiles display distinct concave-up shapes (Figure 5.04).

It is possible that the observed profile shape for the entire grain size distribution is caused by grain size variation or the result of vertical variation in the physical processes acting to mix the sediment. However, the concave-up shape occurs for individual sand grain size classes (sand, silt and clay) and bins (Figure 5.10). The concave-up *SSC* profile shape suggests that l_s and ε_s vary vertically in this environment above the seabed otherwise, from eqn. 5.10, if l_s or ε_s were uniform with elevation, the profiles would not be concave in the grain size bins (eqn. 5.10). Near the bed (i.e. based on piecewise measurement of l_s between 0.04 and 0.02 m) l_s is approximately 0.06 m (Table 5.05). The measured vertical variability in the l_s profile is well represented by a linear approximation of the parabolic l_s profile near the bed, given as,

$$l_s = \kappa z \tag{5.13}$$

Analysis of ε_s suggests that within the measured range ($z = 0.32$ m) ε_s similarly varies with elevation.

We can imply from this result that gradient diffusion explains the observations, in accordance with Van Rijn (1993) and Nielson (1992). Nielson (1992) notes that if the measured l_s are small compared with the overall height of the sediment concentration profile (as in our measurements) then pure gradient diffusion can be used to describe the upward sediment flux (i.e. Table 5.03).

The applicability of the diffusivity model of Green et al. (1999), which uses a two-layer ε_f model, has been confirmed, where ε_f increases linearly with elevation near the bed.

In relation to the β-factor, Table 5.06 highlights the influence of the statistic used to represent near-bed orbital velocity when calculating U^*. The highest adjusted correlation coefficient (R^2=0.85) is achieved when U_{max} is used to characterise U^*. The magnitude of β is highly dependent on the chosen orbital velocity, and increases when the magnitudes of the orbital motion statistic are smaller, e.g. when U_{rms} is used instead of U_{max}.

The U_{max} equation is more practical, as it does not involve rising ψ to an unrealistic power (i.e. ~ 9 and 7 for $U_{1/3}$ and U_3 respectively). When U^* is characterised using U_{max} the fitted curve displays a distinct increase in gradient at approximately the point where $\psi (=w_f/U^*) \approx 0.7$, and an approximate upper limit of between 0.8 and 1. The value 0.8 is a commonly adopted threshold for particles to be moved in suspension (Fredsoe and Deigaard, 1992).

The β-factor, or ratio of ε_s to ε_f has been shown by various authors to vary about unity (Carstens, 1952; Green and Black, 1999; Singamsetti, 1966; Van Rijn, 1984b; Van Rijn, 1993). The variability is attributed to the inertial properties of the sediments in suspension (for $\beta < 1$), or centrifugal forces acting on the sediment relatively more than the fluid (due to density considerations) forcing the sediment to the outside of the eddies and resulting in greater mixing ($\beta > 1$). However, comparisons of β-factors determined using different statistical measures of the near-bed horizontal orbital velocity to

characterise U^* suggest that the variability about unity may be strongly influenced by the definition of U^*.

It may be that the ratio of ε_s to ε_f is of order 1, given the right statistical choice of the near-bed horizontal orbital velocity when characterising U^*. However for predicting concentration profiles over a relatively short period (e.g. 1 minute) where, for wave periods of 8 and 16 seconds, only 4 to 8 waves are physically acting to entrain and mix sediment, U^* characterised using U_{max} results in the best fit of theory to measured data. The applicability of using U_{max} over a short period (~ 1 min) highlights the non-linear dependence that entrainment of sediment has on the higher wave orbital velocities. Over relatively longer sampling periods it is likely that a different, more robust, orbital statistic will be more suited to defining the friction velocity. Although β is defined as the ratio of ε_s to ε_f, it is essentially used as a correction factor for predictive *SSC* profile equations, particularly in relation to the choice of orbital velocity statistic.

5.6 Conclusion

Suspended sediment concentrations were examined using an array of 5 inline water pumps that collected water-sediment samples under unbroken waves. This allowed for the determination of suspended sediment grain size distribution characteristics and concentration profiles. Concurrently, wave characteristics were measured at a frequency of 2 Hz at a site adjacent to the pumped water-sediment sampling site. *SSC* profiles and suspended grain size distributions were examined at 4 sites in water depths of 4, 6, 8 and 10 m in Poverty Bay, New Zealand (Figure 5.01).

The grain size distributions of the surficial sediment are asymmetrical, exhibiting a modal peak in the fine sand size with the distribution shape showing a gradual decrease towards the fine and a rapid decrease towards the coarse end of the grain size distribution, while conversely the suspended sediment distribution is distinctly bi-modal (Figure 5.05). Suspended sediment grain size distributions systematically vary with elevation above the bed. Figures 5.08 and 5.09 illustrate the dependence of grain size on near-bed horizontal orbital velocity (measured as U_3); where, under comparatively large orbital velocities, relatively coarser material can be suspended higher in the *SSC* profile.

For all cases *SSC* profiles exhibit concave-up profile shapes when plotted in log–linear space. Additionally, the gradient of the *SSC* profiles are inversely related to the sediment grain size/fall velocity. The concave-up profile shape shown by both the entire sample and within grain size bins suggests that l_s and ε_s vary with elevation.

Near the bed within the measured range of 0.32 m above the seabed, the l_s profile can be defined by a linear approximation of the parabolic l_s profile (rather than a vertically uniform l_s), where $l_s = \kappa z$. Close to the bed the measured l_s is approximately 0.06 m. Further, ε_s is found to vary with elevation in the same way.

A new equation to predict the β-factor is presented,

$$ln(\beta) = -0.95 - \frac{0.4\psi}{ln(\psi)}$$

The β-factor is dependent on the statistical measure of the near-bed horizontal orbital velocity used to define U^*. Through curve fitting, U_{max} is shown to be the best predictor ($R^2 = 0.85$; Table 5.06) over a record duration of 1 minute. Although β is defined as the ratio of ε_s to ε_f, it is essentially used as a correction factor for predictive *SSC* profile equations.

Table 5.01 Physical characteristic of the sample sites, including water depth, bedform dimensions and surficial sediment characteristics.

	Water depth (m)	Type of bedform	Bedform dimensions	Mean grain size, μm	1st modal grain size, μm	Median grain size, μm	Skewness
A	8	Rounded ripples	$\eta \sim 1$ cm $\lambda \sim 9$ cm	107	128	141	0.7
B	6	Hummocky undulations	0.5-1 cm high 5-10 cm diameter	152	175	177	0.7
D	10	Rounded ripple	$\eta \sim 1$ cm $\lambda \sim 13$ cm	95	114	131	0.6
E	4.2	Rounded ripple	$\eta \sim 1$ cm $\lambda \sim 9$ cm	188	200	207	0.5

Table 5.02 Average significant wave height (m) and mean wave period (s) as measured during sampling at sites A, B, D and E.

	Significant wave height (m)	Mean wave period (s)
Site A	1.5	10.0
Site B	1.3	9.0
Site D	1.3	9.7
Site E	0.7	12.9

Table 5.03 Mixing lengths and R^2's determined by assuming a vertically constant mixing length and sediment diffusivity and applying the Nielsen *SSC* profile model (eqn. 5.09) calculated using the entire grain size distribution.

Site	Mixing length (m)	R^2	Site	Mixing length (m)	R^2	Site	Mixing length (m)	R^2	Site	Mixing length (m)	R^2
A1	0.12	0.82	B1	0.09	0.88	D1	0.15	0.69	E1	0.12	0.71
A2	0.10	0.90	B2	0.08	0.80	D2	0.57	0.86	E2	0.06	0.58
A3	0.13	0.97	B3	0.07	0.86	D3	0.10	0.97	E3	0.11	0.77
A4	0.08	0.79	B4	0.10	0.74	D4	0.19	0.85	E4	0.10	0.87
A5	0.24	0.85	B5	0.08	0.67	D5	0.11	0.91	E5	0.13	0.73
Median	0.12	0.87	**Median**	0.08	0.79	**Median**	0.15	0.86	E6	0.19	0.66
									E7	0.23	0.80
									Median	0.12	0.73

Table 5.04 Mixing lengths and R^2's determined by assuming a vertically constant mixing length and sediment diffusivity and applying the Nielsen *SSC* profile model (eqn. 5.09) calculated using Sand, Silt and Clay sized fractions from the suspended sediment grain size distributions.

Sample	Sand l_s	R^2	Silt l_s	R^2	Clay l_s	R^2
	>62.5 μm		62.5 to 4 μm		< 4 μm	
A2	0.12	0.93	0.12	0.93	0.13	0.90
B1	0.13	0.89	0.12	0.88	0.15	0.78
D1	0.12	0.88	0.20	0.89	0.15	0.24
E1	0.15	0.77	0.15	0.96	0.04	0.06

Table 5.05 Average and median gradients from piecewise analysis of l_s illustrating that the gradients approximate the von Karman's constant (0.4), which indicates that near the bed the mixing length profile shape can be represented by a linear approximation of the parabolic (Rouse) profile shape. Further, average mid-point mixing length measurements between 0.02 and 0.04 m suggest near the bed mixing length values approach approximately 0.06 m.

	Average l_s between 0.02 and 0.04 m	Average slope	Median slope	Average R^2
Whole sample	0.08	0.34	0.25	0.65
Sand fraction > 62.5 μm	0.04	0.6	0.49	0.68
Silt fraction 62.5 to 4μm	0.11	0.28	0.16	0.68
Clay fraction < 4μm	0.07	0.31	0.17	0.60
222 to 190 μm bin	0.04	0.58	0.68	0.70
120 to 103 μm bin	0.04	0.75	0.43	0.71
88 to76 μm bin	0.05	0.41	0.33	0.69
Average	**0.06**	**0.47**	**0.36**	**0.67**

Table 5.06 Fitted curve equations relating β to ψ ($=w_f/U^*$), where U^* is characterised by different statistical measures of the near-bed horizontal orbital velocity. As shown by the adjusted coefficients of determination, when U^* is characterised by U_{max} there is less scatter in the data. Also listed are the squared errors of observed to predicted *SSC* for U^*.

Near-bed orbital velocity statistical measure used to characterise U^*	Fitted equation that produced the least amount of scatter (R^2)	Adjusted correlation coefficients, R^2	Average squared error of observed to predicted *SSC*
U_3	$\beta = 0.64 + 2.48\psi^{6.68}$	0.73	0.86
$U_{1/3}$	$\beta = 1.12 + 0.19\psi^{9.09}$	0.51	0.85
U_{rms}	$\beta = 0.83 + 0.90\psi^{3}$	0.53	0.85
U_{max}	$ln(\beta) = -0.95 - \frac{0.4\psi}{ln(\psi)}$	0.85	0.86

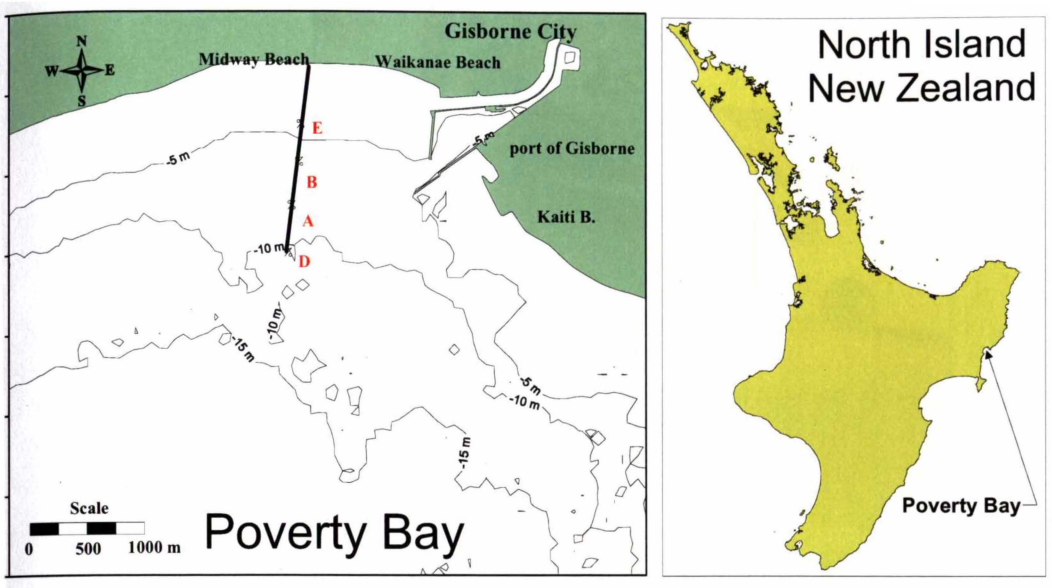

Figure 5.01 Experimental site in the northern corner of Poverty Bay, New Zealand, showing the location of the sample sites offshore from Midway Beach and their relative depths. Actual depths were determined at time of sampling.

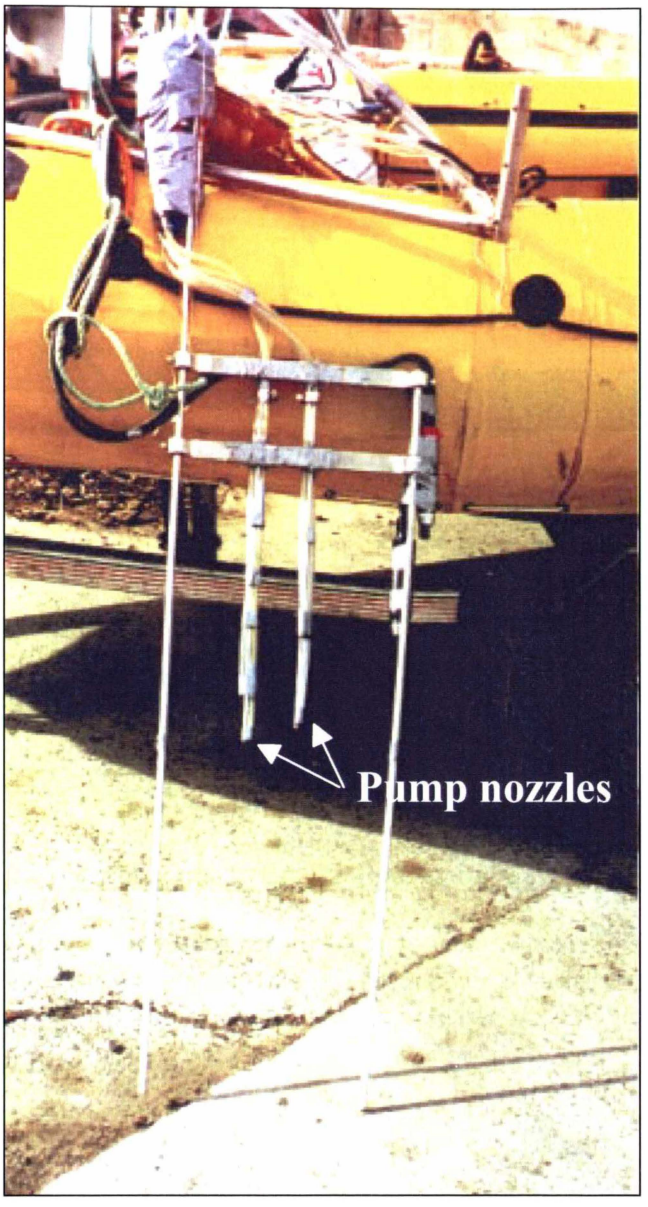

Figure 5.02 Pump array used to take samples of the suspended sediment concentration under un-broken waves. Nozzle apertures were positioned at elevations of 0.02, 0.04, 0.08, 0.16 and 0.32 m above the seabed, and samples were pumped to a sample platform (not shown here) approximately 4 m above the bed.

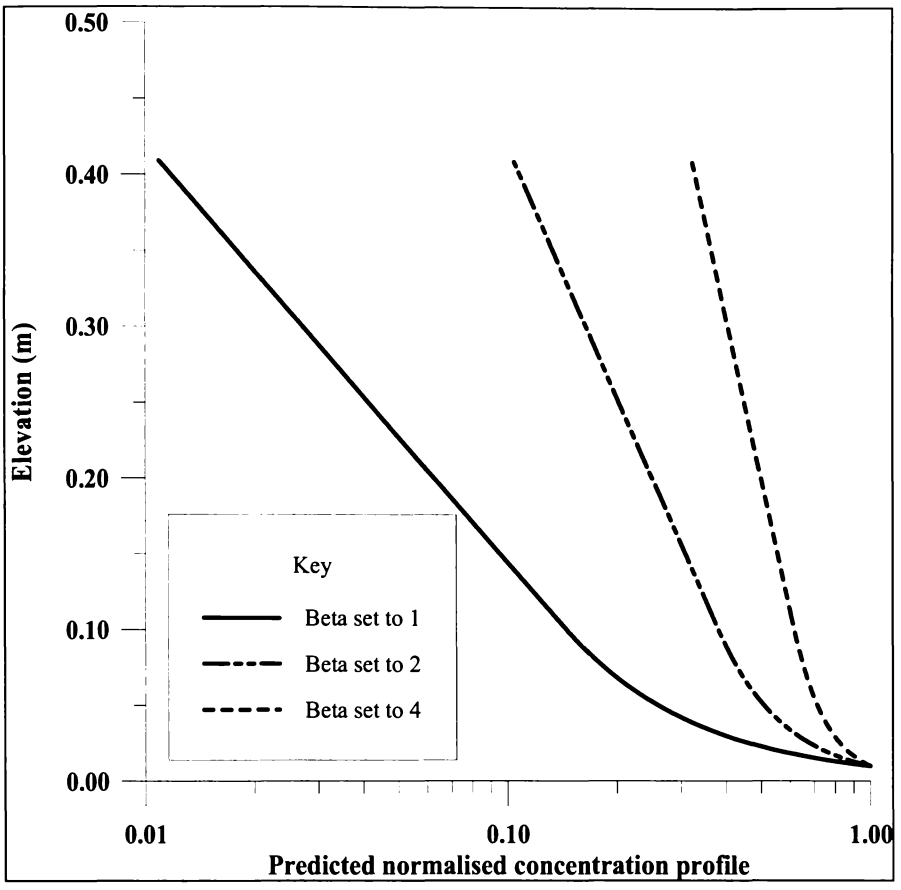

Figure 5.03 Suspended sediment profile shapes calculated using eqn. 5.17 and 5.18, z_m set to 0.1 m and the other parameters fixed. The β-factor is varied to illustrate the effect that β has on the profile shape. As β increases the gradient of the profile increases.

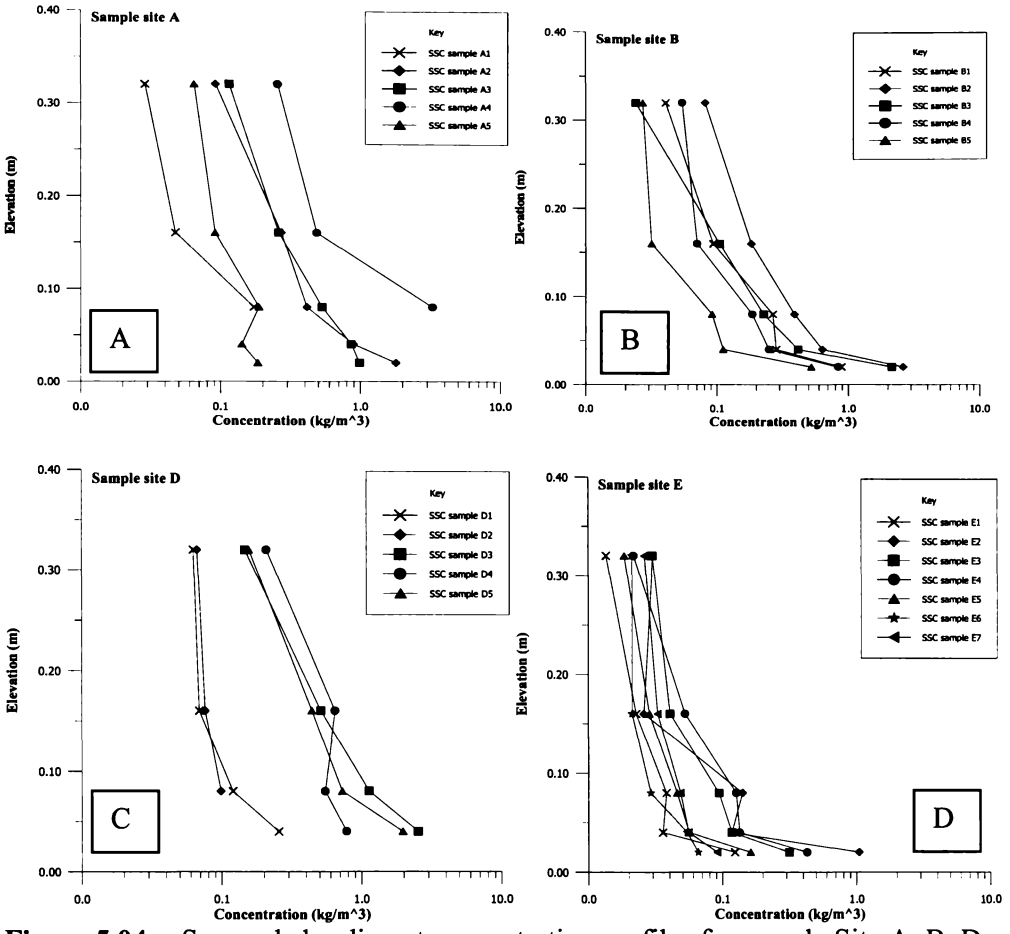

Figure 5.04 Suspended sediment concentration profiles for sample Site A, B, D and E under unbroken waves. Profiles typically display a distinct concave-up shape when plotted in $\log_{10}(C_z) - z$ space.

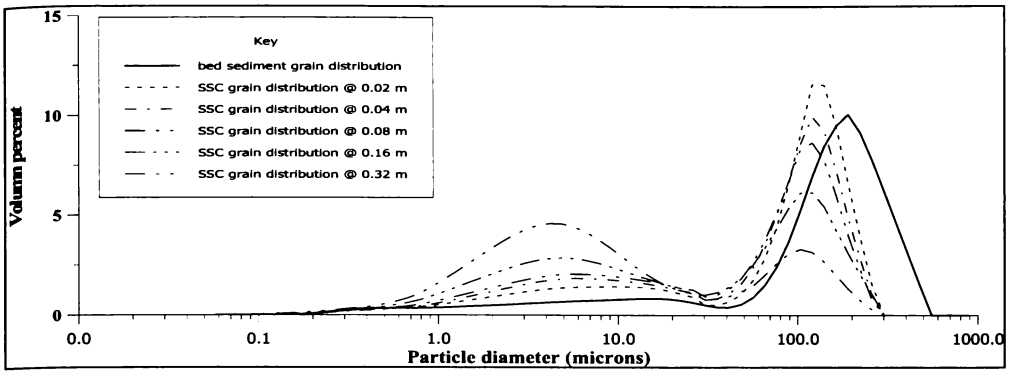

Figure 5.05 Typical surficial and suspended sediment grain size distribution curves, as measured by a Malvern particle size analyser, illustrating a highly systematic change in grain size distribution with elevation above the seabed. Suspended sediment distributions are shown to display a distinct bi-modal characteristic and to be significantly different from the surficial sediment distribution. The relative volume percentages of the two modal peaks are shown to change with elevation, and the 1st modal peaks changes from being located in the sand size fraction (>62.5 μm) to being located in the mud size fraction (< 62.5 μm) with elevation. Additionally the modal peaks are shown to become progressively finer with elevation.

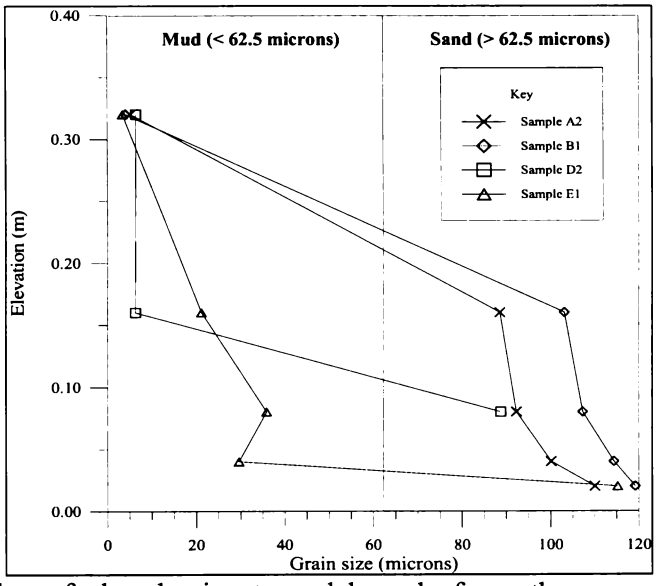

Figure 5.06 Plot of the dominant modal peak from the suspended grain size distribution against elevation, illustrating that the 1st modal peak switches from being located in the sand size fraction (> 62.5 μm) to being located in the mud size fraction (< 62.5 μm) with elevation above the bed.

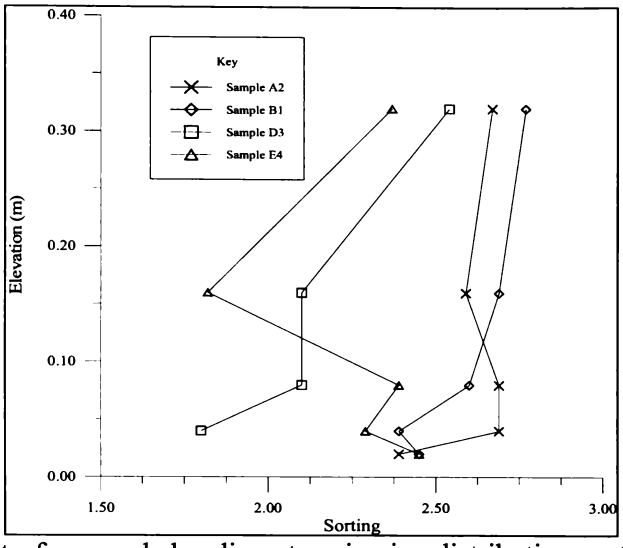

Figure 5.07 Plot of suspended sediment grain size distribution sorting characteristic, illustrating a trend for sediment to become more poorly sorted with elevation above the bed

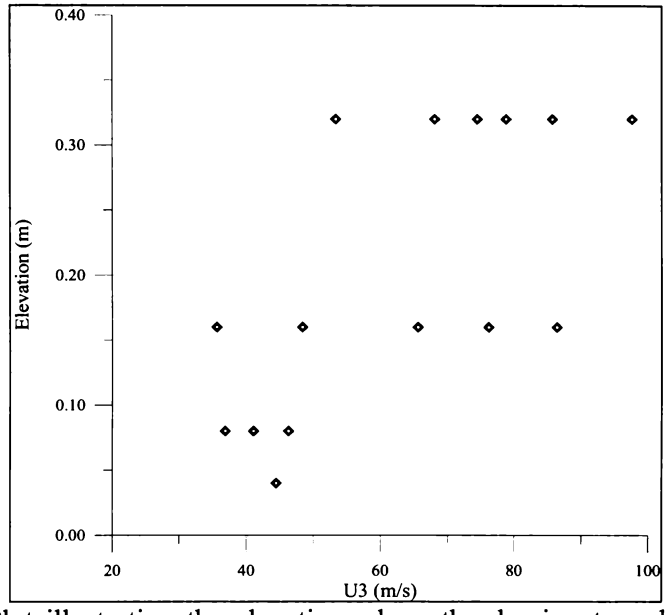

Figure 5.08 Plot illustrating the elevation where the dominant modal peak changes from fine sand to mud size against the near-bed turbulence level (U_3). The figure shows that under comparatively larger near-bed turbulence levels relatively coarser sediment is entrained higher in the concentration profile.

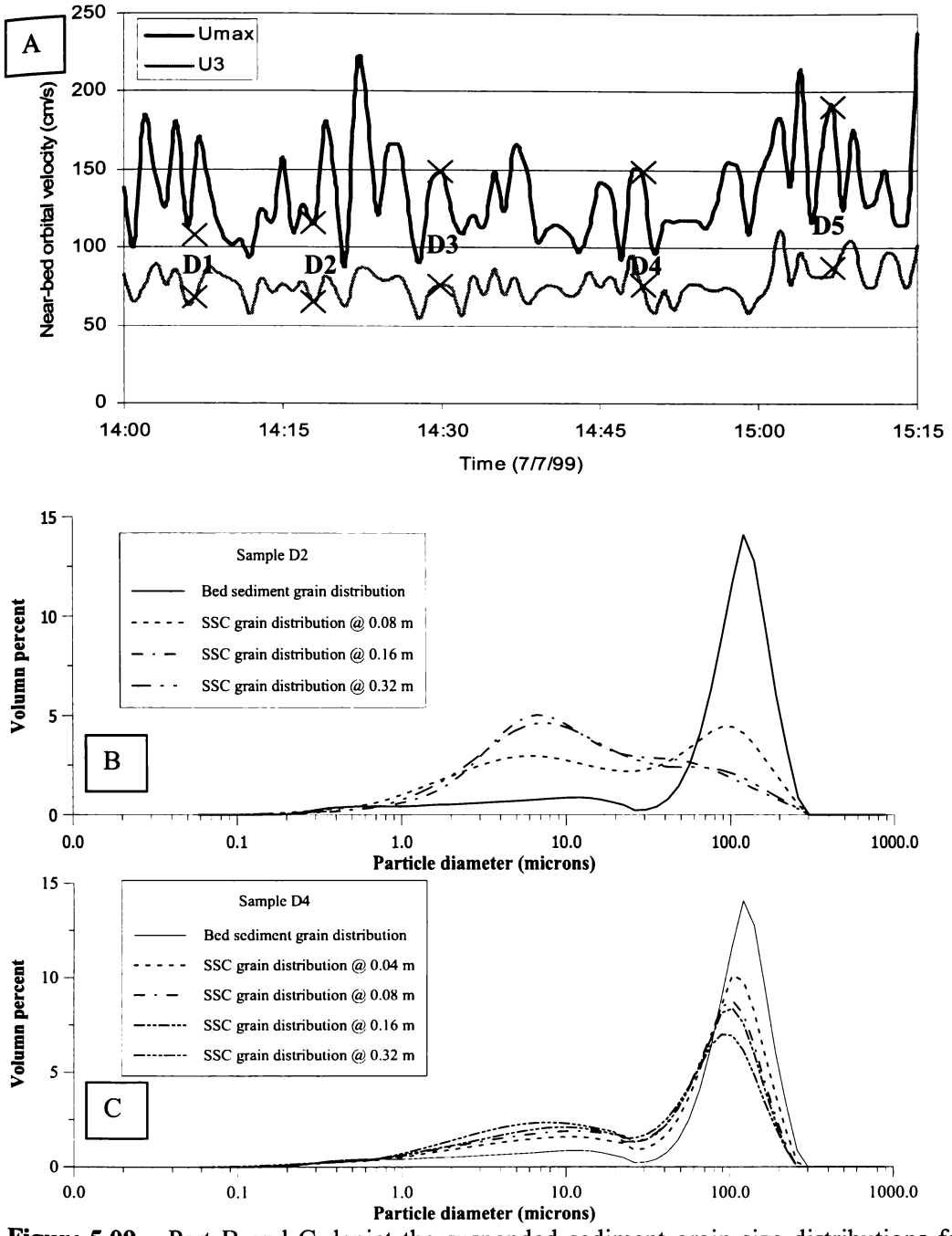

Figure 5.09 Part B and C depict the suspended sediment grain size distributions for two separate *SSC* profile samples (sample D2 and D4 respectively), while part A shows the near-bed horizontal orbital velocity (U_{max} and U_3)over the sampling period. The suspended sediment grain size distribution is shown to be dependent on the near-bed orbital velocities, at low velocities there is evidence of preferential entrainment of the finer part of the surficial sediment grain size distribution and a tailing off of relatively coarser sediment, while at higher orbital velocities the entire surficial sediment grain size distribution is represented in the suspended sediment grain size distribution.

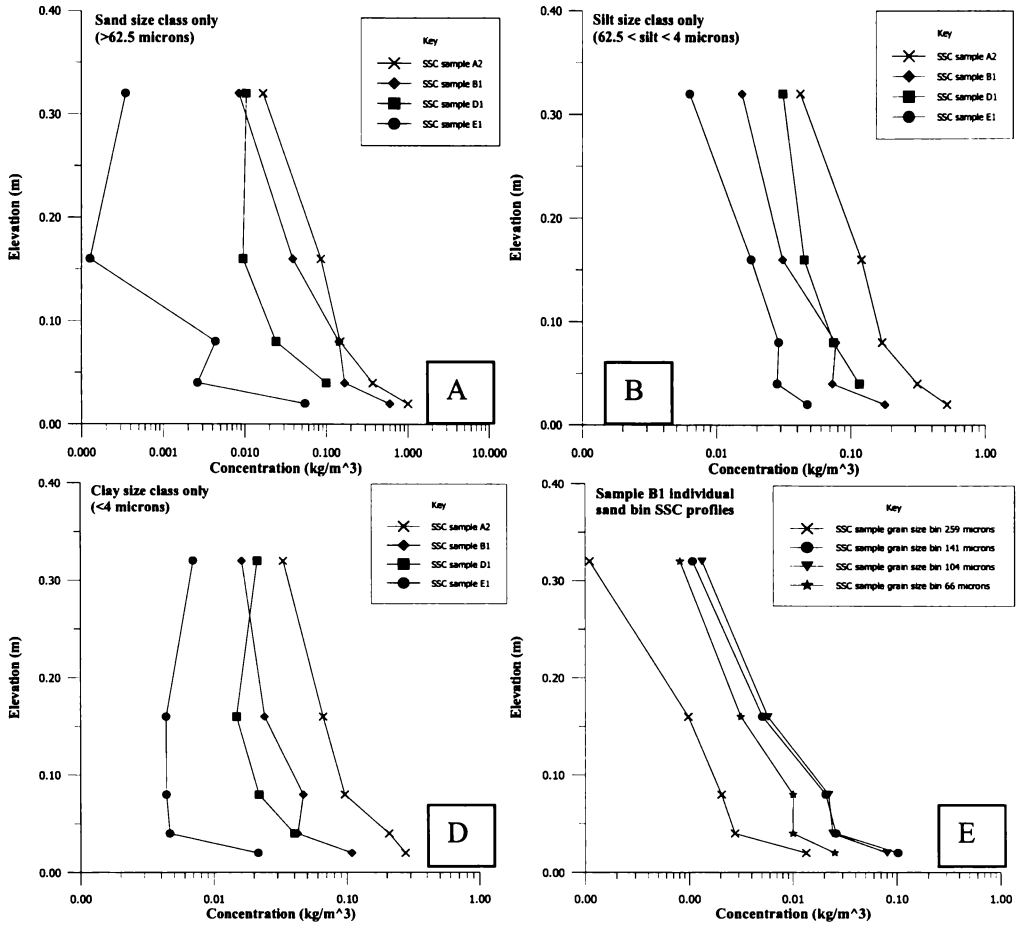

Figure 5.10 Sand, silt and clay size fraction suspended sediment concentration profiles for sample site A, B, D and E under un-broken waves (Part A, B, and C respectively). Also shown are concentration profiles for individual sand size bins. All profiles display a distinct concave-up shape when plotted in $\log_{10}(C_z) - z$ space.

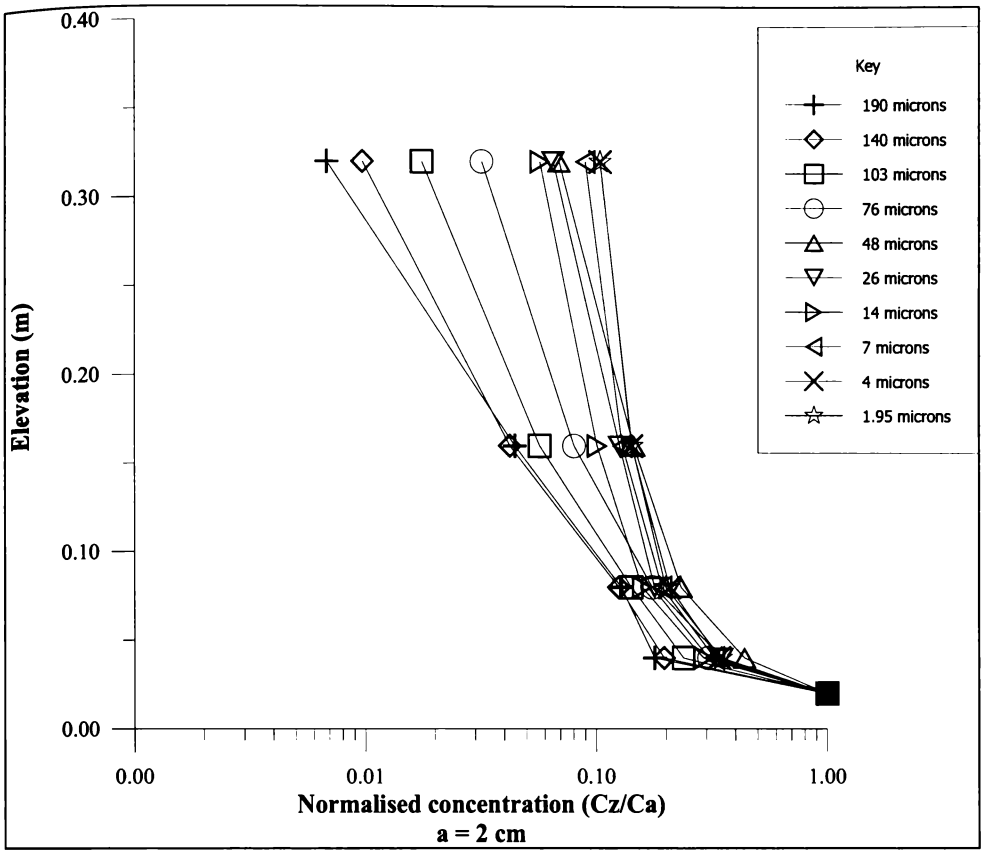

Figure 5.11 Normalised *SSC* profile shapes for individual grain size bins (sample B2). All profiles display a distinct concave-up profile shape when plotted in $\log_{10}(C_z)$ – $_z$ space. Additionally the gradient of the concave-up profile is shown to vary with grain size, showing a trend to become steeper as the particle grain size/fall velocity decreases.

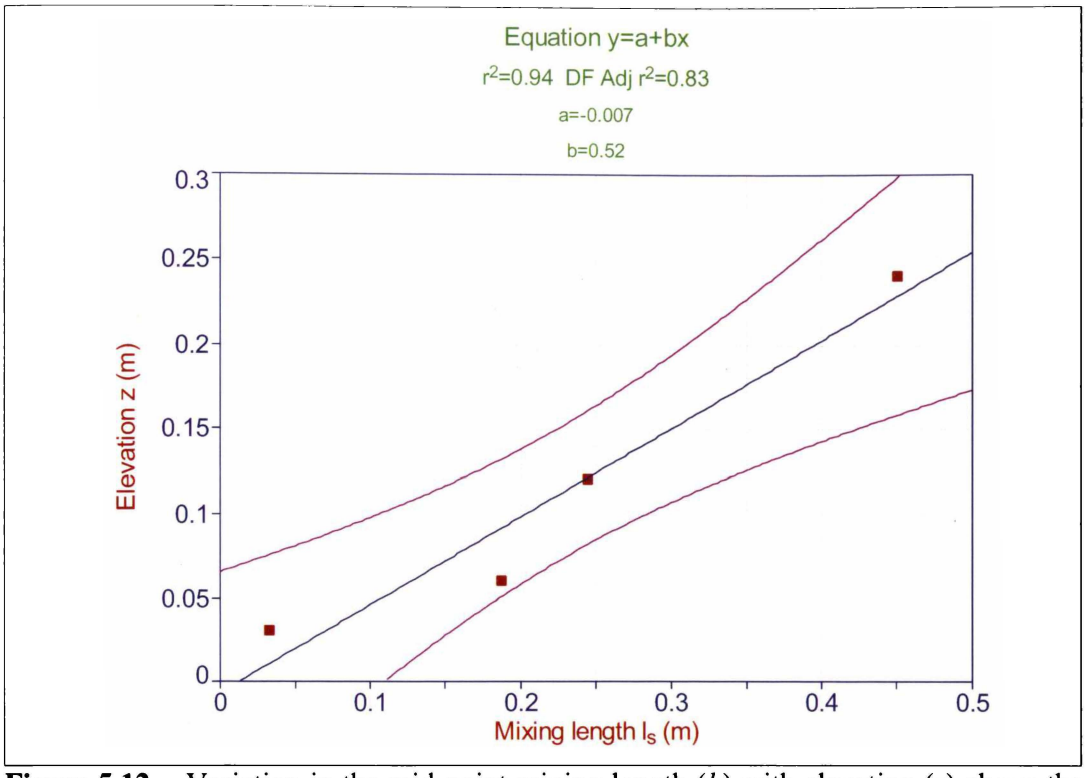

Figure 5.12 Variation in the mid-point mixing length (l_s) with elevation (z) above the seabed for the measured *SSC* profile B2. The relationship has an adjusted R^2 of 0.82. Also shown are the 90% confidence intervals. The mid-point mixing length is shown to increase with elevation above the seabed with a gradient of 0.52, similar to the theoretical value of κ=0.4 for a logarithmic velocity profile.

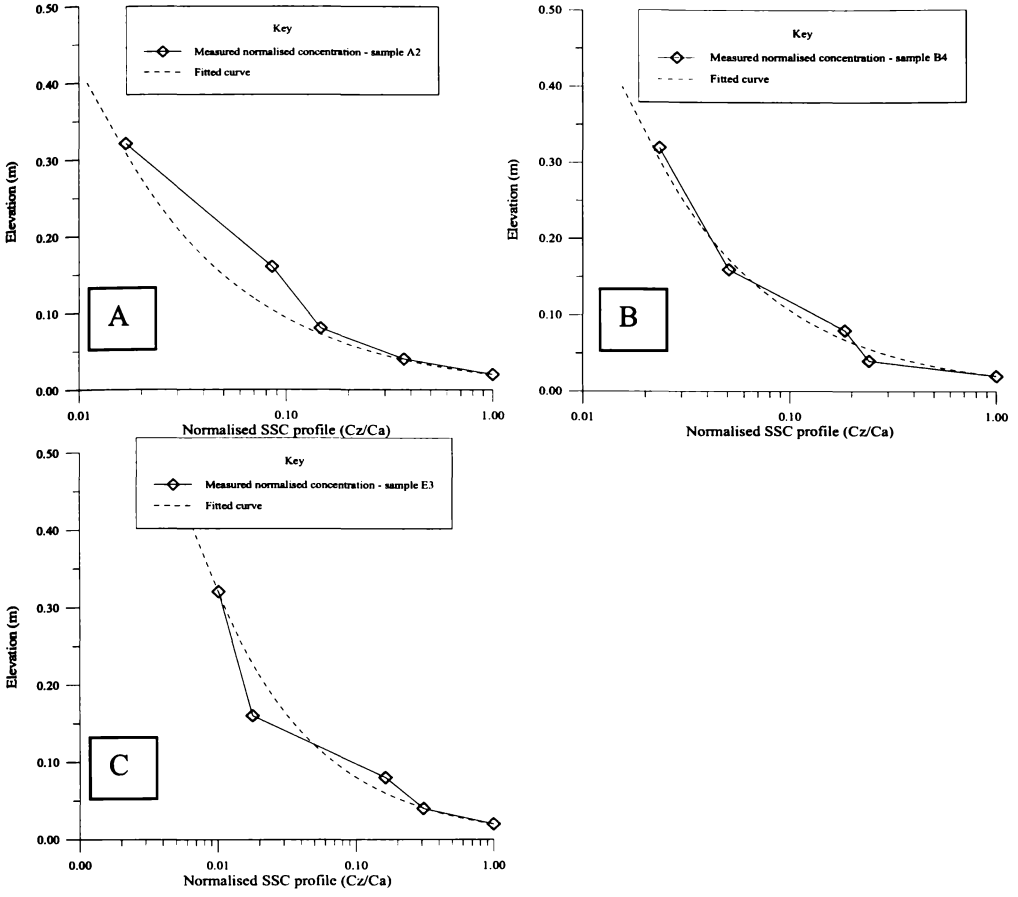

Figure 5.13 Curve-linear concentration profiles fitted to the measured data for samples A2, B4 and E3 (part A, B and C respectively) calculated from eqn. 5.16 and 5.17 and using U_{max} to characterise U^*. Within the measured profile range the curve fitting indicates that the sediment diffusivity is increasing and is not vertically uniform (i.e. $z_m > 0.32$ m).

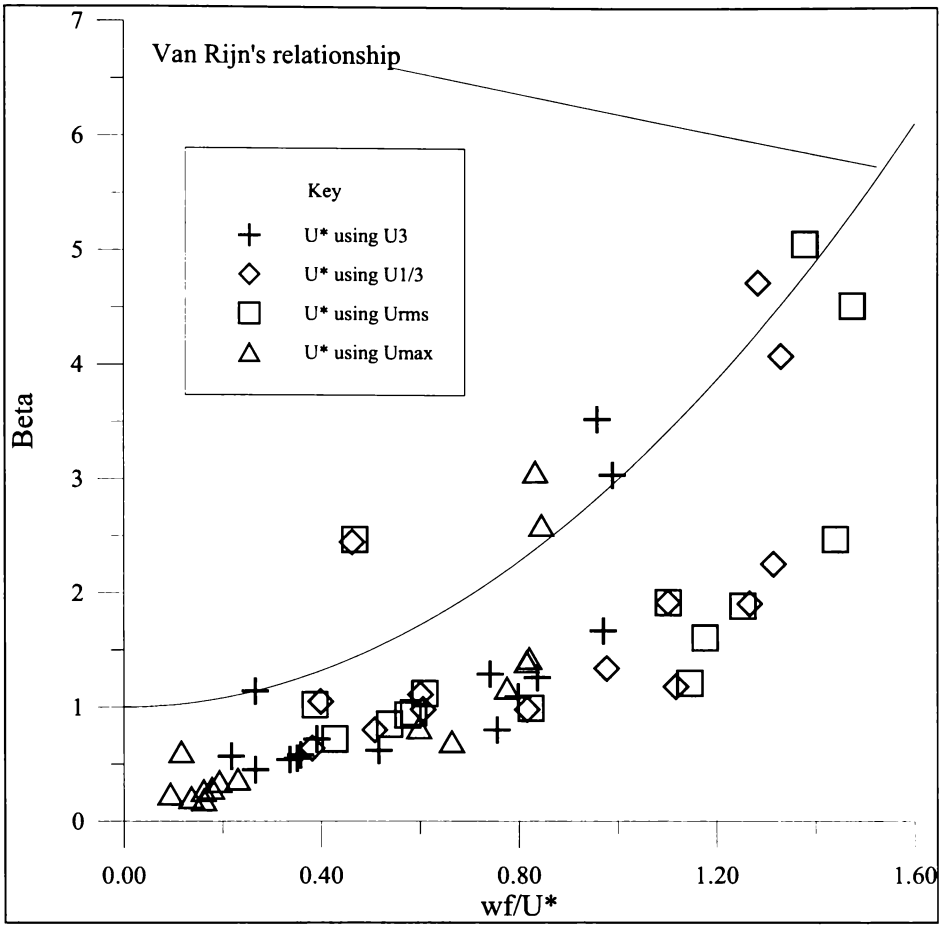

Figure 5.14 Plot of β against w_f/U^* showing the effect the choice of the statistical measure of the near-bed horizontal orbital velocity used to characterise U^* has on the determination of β. Comparing the determined values of β to the relationship proposed by Van Rijn (1993) illustrates a poor correlation regardless of the statistical measure of the horizontal orbital velocity used to characterise U^*, and suggests a different relationship.

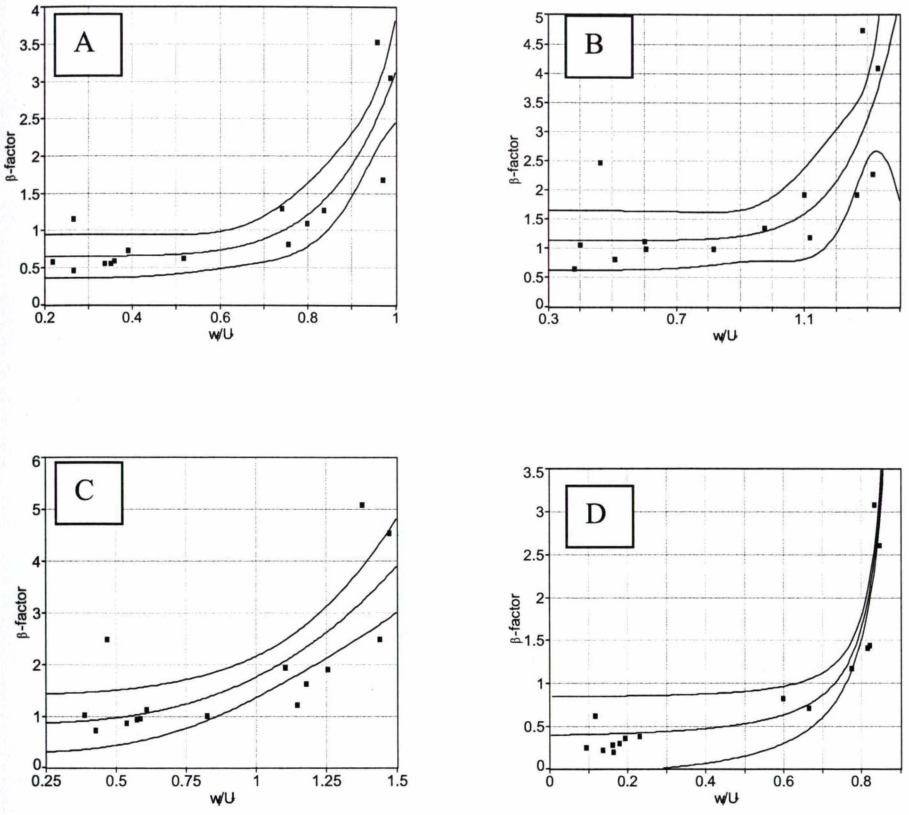

Figure 5.15 Plots of the determined β-factor (from fitting eqn. 5.16 and 5.17 to the measured normalised *SSC* profile) against w_f/U^*, where U^* is characterised using U_3, $U_{1/3}$, U_{rms} and U_{max} for parts A, B, C and D respectively, and with fitted curves based on maximised correlation coefficient (R^2). Also shown are 90% confidence intervals. The smallest amount of scatter about the fitted curves is achieved when U_{max} is used to characterise U^*, with an adjusted R^2 of 0.85, compared to adjusted R^2's of 0.73, 0.51, and 0.53 when U^* is characterised using U_3, $U_{1/3}$, and U_{rms} respectively.

Chapter 6. Sediment entrainment over a cohesively bound mixed sand/mud seabed under unbroken waves

"*I watched two little waves Marching to the shore, One died with a yawn the second with a roar*" - William Saphier.

6.1 Abstract

A method is presented for determining the near-bed reference concentration over cohesive mixed sand/mud seabeds. Including consideration of measured bedform dimensions, a relationship is established between the surficial sediment physical characteristics (in situ shear strength as a measure of cohesiveness and grain size) and wave-induced entrainment.

Sediment entrainment was measured using micro-scale high-resolution pumps within 0.2 m of the seabed, at 4 open coast sites ranging in water depth from 4 to 10 m. No correlation was found to exist between the ratios of estimated to predicted near bed reference concentration (ζ) and either the median grain size or the volume percent ratio of sand to mud of the surficial sediment. In contrast, a good correlation was found to exist between ζ and the normalised in-situ shear strength (χ) of the sediment (Adjusted $R^2 = 0.99$), with the relationship of the form,

$$\ln(\zeta) = -0.51 - 1.30\chi^3$$

C_0 was predicted with flow enhancement due to rippled bedforms accounted for and U^* characterised by the third-moment of the horizontal orbital velocity (U_3).

6.2 Introduction

The determination of near-bed reference concentration (C_0) in field conditions, while attracting considerable attention in the literature (Aagaard et al., 2002; Aagaard and Greenwood, 1999; Black, 1994; Glenn and Grant, 1987; Green et al., 2000; Green and Black, 1999), is problematic to resolve. Calculation of C_0 generally require several assumptions about the grain size of either or both the suspended and surficial sediment, as well as knowledge of the entrainment processes, the *SSC* profile shape, the velocity parameter used to characterise the near-bed friction velocity, and the influence of bedforms and bedload sediment transport on the entrainment of sediment, to name but a few. Further, methods of measuring the *SSC* and near-bed reference concentration using either intrusive (i.e. sediment traps, pumped water samples) or non-intrusive (i.e. optical or acoustic back-scatter instruments) methods suffer from limitations.

Measuring *SSC* and C_0

The problems associated with measuring C_0 are compounded when dealing with sediment mixtures of sand ($> 62.5\ \mu$m) and mud ($< 62.5\ \mu$m). Non-intrusive measurements of *SSC* and C_0 in mixed sediment environments using optical or acoustic back-scatter instruments (*OBS* and *ABS* instruments) should be treated cautiously due to their high dependency on the grain size of the sediment used to calibrate the instrument (Black and Rosenberg, 1994; Hatcher et al., 2000). Variations in optical and acoustic back-scatter inferred *SSC* can occur if the wrong sediment grain size is used to calibrate the instrument and using the surficial sediment to calibrate a back-scatter instrument adds to the assumptions being made, as the suspended sediment grain size has been shown to vary vertically in both laboratory and field experiments and to be distinct from the surficial sediment (Beamsley et al., 2001b; Black and Rosenberg, 1992; Kos'yan, 1985; Van Rijn, 1993).

Intrusive methods of determining *SSC* and C_0 usually consist of either pumped samples of water and sediment or sediment trapping, both of which provide an indication of the time-averaged sediment concentration rather than an instantaneous measure of the near-bed reference concentration. However, turbulence associated with the intrusive nature of pumped or sediment trapping methods can make the determination of the actual *SSC* difficult, and care should be taken to limit the associated turbulence. Further, considerably more logistical effort is associated with collecting and processing both trapped and pumped suspended sediment samples than OBS or ABS *SSC*. Sediment trapping and pumped samples have an advantage in that the vertical variation in sediment grain size can be closely examined (Beamsley et al., 2001b; Black and Rosenberg, 1992; Kos'yan, 1985; Van Rijn, 1993), and the measurement technique does not quantify the suspended sediment based on the surficial sediment characteristics, but rather measures the suspended sediment concentration directly.

Predicting C_0

The classification of cohesive bonding is a significant obstacle to predictions of near-bed reference concentrations over mixed sand/mud seabeds. Toorman (2001) notes that there have been some studies on sedimentation, consolidation and erosional characteristics of mixed sand/mud seabeds, but the complexity of the problem is high because the properties of the aggregates depend on numerous factors, including the type

of sediment, type and concentration of ions in the water and the fluid flow conditions to name a few. Furthermore, cohesion is influenced by colloidal organic matter, microbes and polysaccharides (Augustinus, 2002; Kjerfve et al., 2002). Berlamont et al., (1993) characterised cohesively bound sediment using 28 parameters, including physico-chemical properties of the overflowing fluid, physico-chemical properties of the mud, characteristics of the bed structure and water-bed exchange processes.

For mixed sand/mud sediment, when large amounts of sand-sized particles are present, the interactive behaviour between particles of different sizes is not fully understood. Chesher and Ockenden (1997) developed a 2-dimensional numerical model in which the influence of the sand/mud mixture ratio on erosion characteristics is included. However, the normal practice is to treat the entrainment of coarse material separately from the mud fraction (Mehta et al., 1989). Indeed, this was the approach adopted by Black et al., (1997) in their sediment transport numerical modelling of the port of Gisborne environs in northern Poverty Bay. Black et al., (1997) determined the near-bed reference concentration for the relatively coarse portion of the grain size distribution alone (defined as > 45 μm in that study) and applied a single "cohesion factor" (discussed in Section 4.4) to account for the cohesive bonding of the sand portion of the surficial sediment for which a correction factor was applied based on the quantity of mud in the surficial sediment. While this method proved adequate for the requirements of that specific study, the wider application of a single unique factor to describe the cohesive properties of the surficial sediment could be improved given more comprehensive knowledge of the relationship between the surficial sediment characteristics and the critical shear stress for erosion.

The critical shear stress for erosion of cohesive sediment has been estimated to increase when mud is added to sand (Amos et al., 1995; Collins, 1989; Kamphuis and Hall, 1983; Kuti and Yen, 1976; Mitchener and Torfs, 1996; Murray, 1977). Addition of 50% sand to a mud matrix can increase the critical shear stress by a factor of two; conversely the addition of 30% mud can increase the erosional resistance of sand by a factor of 10 or more. If enough mud is added to sand then the sediment behaves as a mud and should be accounted for when modelling erosion from a mixed bed (Mitchener and Torfs, 1996). Mitchener and Torfs (1996) note that the transition from sandy to muddy-type erosion occurs between 3-15% mud by weight.

Mitchener and Torfs (1996) also note that the addition of mud to sand not only delays the onset of erosion, but also reduces its rate once begun. Similarly the erosion rate of mud decreases with increased sand content. The erosion rate of a mixed sand/mud bed can reduce by a factor of 5 if more than 3% mud is added to sand. It also reduced by a factor of 10 if more than 20% sand was added to a mud bed (Mitchener and Torfs, 1996). The reduction in erosion rate should also be included when applying sediment transport formulae to mixed sediment.

Rather than having to determine the complex array of parameters that define the cohesive properties of surficial sediment, it is desirable to define a relatively simple empirical relationship between the near-bed reference concentration and some geomechanical characteristic of the surficial sediment such as shear strength. Work by Kamphuis and Hall (1983) found that critical shear stress for erosion increased with the plasticity index of the sediment and the shear strength of the sediment, thus supplying a

possible means of establishing an empirical relationship between the surficial sediment characteristics and the near-bed reference concentration.

This paper considers the entrainment of sediment above a cohesively bound mixed sand/mud seabed in Poverty Bay, New Zealand (Figure 6.01); investigating the suitability of the non-cohesive entrainment formulae for predicting C_0 by comparing the predicted C_0 with C_0 estimated from suspended sediment concentration (*SSC*) profiles collected using an array of inline pumps (Figure 6.02), and using a simple empirical measure (i.e. shear strength) of the surficial sediment to account for the sediment cohesion.

6.3 Methods

6.3.1 Data collection

The suspended near-bed sediment concentrations under unbroken wave conditions were investigated at four sites in northern Poverty Bay, adjacent to the port of Gisborne, New Zealand (Figure 6.01). The experiment sites had water depths (h) ranging from 4.2 m to 10 m (at time of data collection). Samples were collected using an array of five downward facing inline impeller pumps (Figure 6.02) positioned at elevations of 0.02, 0.04, 0.08, 0.16 and 0.32 m above the seabed. The estimated pumped sampling volume is within 0.005 m of the nozzle aperture. While the downward orientation of the pump nozzles adds to the uncertainty in the relative location of the sampling volume above the seabed, the orientation stopped sand accumulating in the pipes between sampling. A minimum of five concentration profile measurements were measured at each site. Samples with flow velocities less than 1.2 $m.s^{-1}$ (~5-10% of the samples) in the inlet tube were not used in determining the near bed reference concentrations (C_0) in order to ensure that a relatively accurate representation of the suspended sediment grain size and concentration was being collected (Bosman et al., 1987).

Continuous directional wave and current data were simultaneously recorded using a seabed mounted *InterOcean S4ADW* wave/current meter, sampling at 2 *Hz*. Wave statistics were determined by breaking the continuous directional wave data into 1-minute bursts. Given the period range, four to eight wave crests can be expected to have passed over the instrument array during the 1-minute sample duration. The *S4ADW* and mooring frame were placed at a distance of approximately 2 m (at 90° to the incident wave crests) from the pump array in order to eliminate contamination of the data by sediment entrained due to hydrological turbulence from the instrument frames. Wave orbital measurements were extrapolated a short distance of 1.15 m to the bed using linear wave theory. A representative surficial sediment sample was collected from each of the experiment sites from the top 2-4 cm of the seabed. Each seabed sample consisted of several individual samples taken within a radius of approximately 3 m of the experiment sites, thereby ensuring that a representative sample of the surficial sediment was obtained. Additionally, SCUBA diver observations were used to confirm that the surficial sediment sample collected was representative of the surficial sediment at each of the experiment sites.

6.3.2 *Surficial sediment*

Surficial sediment grain size distribution characteristics were determined using a Malvern laser light diffraction particle size analyser (model *MSS17*), which estimates the entire grain size distribution including the fine silt and clay components (< 62.5 μm). Initially each sample was dispersed (using sodium hexametaphosphate and ultra-sonic treatment) to break-up flocculated particles and organic material was removed using a 10% hydrogen peroxide solution in accordance with the New Zealand Standard 4402 (Standards Association of New Zealand, 1986).

A hand-held shear vane (Figure 6.03), operated by a *SCUBA* diver, was used to determine the in-situ shear strength, with 12 or more readings at each site. This number of measurements provided the means to gauge statistical characteristics of the measured population of the in-situ shear strength including mean, median, population standard deviation and confidence intervals. Care was taken to ensure that the seabed remained as undisturbed as possible during determination of the shear strength.

To help distinguish correlations between grain size and in-situ shear strength (from the shear vane), shear strength and sediment characteristics (including water depth) at approximately 60 seabed sites around northern Poverty Bay and 5 beach face swash zone sites from within Poverty Bay and beyond were measured. The swash zone samples were used to help determine the difference between cohesively and non-cohesively bound sediment (i.e. sediment consisting of predominantly sand as opposed to consisting of sufficient mud to cohesively bind the sediment).

6.3.3 *Friction velocity, bed roughness and predicting reference concentrations*

Initiation of surficial sediment motion is, in part, dependent on near-bed orbital velocities and near-bed reference concentrations are often determined using the near-bed friction velocity U^* (Black and Rosenberg, 1994), given by,

$$U^* = \left(0.5 f_w U^2\right)^{1/2} \tag{6.01}$$

where U is a measure of the near-bed horizontal orbital velocity. For unbroken waves, Black and Rosenberg (1991) found the third moment of velocity (U_3) in a time-series best represented the variance of U. U_3 is given by,

$$U_3 = 1.4\left[\left(\sum_{j=i}^{N}\left|U_j\right|^3\right)/N\right]^{1/3} \tag{6.02}$$

where U_j is the jth principal near-bed orbital velocity measurement in a time-series of N values (Black and Rosenberg, 1991).

Additionally, the findings of Beamsley et al. (2001a) highlight the importance of the maximum near-bed horizontal orbital velocity (U_{max}) on the *SSC* profile over an intermediate time scale of 1 minute. As such U_{max} is also used in defining the friction velocity, U^*, where U_{max} is the single largest near-bed horizontal orbital velocity in the measured time-series.

In eqn. 6.01, f_w is the wave friction factor, defined by Swart (1974) as,

$$f_w = \exp\left[5.213\left(k_b/a_s\right)^{0.194} - 5.977\right] \qquad (k_b/a_s) < 0.63 \qquad (6.03)$$

$$f_w = 0.3 \qquad (k_b/a_s) > 0.63 \qquad (6.04)$$

where a_s is the near-bed semi-excursion distance written as,

$$a_s = U/\omega \qquad (6.05)$$

where ω is the wave radian frequency determined using the significant zero down-crossing wave period. For a fixed planar bed Swart (1974) used a bed roughness, k_b, defined as,

$$k_b = 2.5d_{50} \qquad (6.06)$$

where d_{50} is the median grain size.

Nielson (1983; 1992) proposed a variation of eqn. 6.06 to include roughness associated with bedload sediment transport and rippled bedforms,

$$k_b = B_m(\psi' - \psi_c)^{0.5} d_{50} + 8\frac{\eta}{\lambda}\eta + 2.5d_{50} \qquad (6.07)$$

Where η and λ are the measurements of the ripple height and wavelength respectively, B_m is the bedload sediment transport multiplier, ψ_c is the critical shields entrainment parameter (derived from the Shields curve) and ψ' is the wave-induced skin friction factor, defined as,

$$\psi' = \frac{f_w U^{*2}}{2sgd_{50}} \qquad (6.08)$$

where g is the gravitational acceleration (9.81 m.s^{-1}) and $s = (\rho_s - \rho)/\rho$ (ρ_s and ρ are the sediment and water densities respectively).

The Nielson (1983; 1992) apparent bed roughness expressions vary only in the value of the B_m. Nielsen's (1983) form of the equation uses a bedload transport multiplier of 190, while Nielson's (1992) form of the equation uses a value of 170.

Du Toit and Sleath (1981) proposed an alternative means for accounting for the bedform enhanced near-bed stress, with a correction factor applied to the wave-induced skin friction factor, ψ', where,

$$\psi'' = \frac{\psi'}{(1-\pi\eta/\lambda)^2} \tag{6.09}$$

For irregular waves over flat and rippled beds, Nielsen (1986) found C_0 was related to the wave-induced skin-friction by;

$$C_o = 0.005\rho_s\psi'^3 \tag{6.10}$$

This semi-empirical equation was found to be robust for turbulent flow conditions (McComb, 2001).

This paper examines the suitability of different combinations of the near-bed horizontal orbital statistic and the method of including bedform enhanced sediment entrainment in determining C_0. Four methods of accounting for the effect of roughness associated with bedload sediment transport and the presence of bedforms on sediment entrainment are investigated (Table 6.01). Additionally, for each method C_0 has been determined using a friction velocity categorized by both U_3 and U_{max}, resulting in a total of 8 combinations investigated.

6.3.4 Estimating time-averaged C_0

6.3.4.1 Time-averaged C_0 predictive theory

Near the bed, suspended sediment concentration profiles are well represented by the convection-diffusion equation that describes a balance between turbulent diffusion and gravity (Black and Rosenberg, 1994; Black and Vincent, 2001; Green et al., 2000; Green and Black, 1999; Green et al., 1999; Nielsen, 1983; Nielsen, 1984; Nielsen, 1986; Nielsen, 1992). For both the convective and diffusive sediment entrainment process, and indeed the combination of the two, the near-bed concentration profile is usually described using the conservation equation for the volume of sediment, which may be written as,

$$\frac{\partial C}{\partial t} = -div(u_s C) \tag{6.11}$$

Which expresses that a divergence of the sediment flux field (q=Cu_s) must result in a change in the local sediment concentration, where C is the sediment concentration and u_s is the horizontal velocity of the sediment particles.

Assuming a simple case where there is a horizontal uniform sediment concentration and velocity field, then the conservation equation can the be simplified to

$$\frac{\partial C}{\partial t} = -\frac{d}{dz}\left(Cw_0\right) = -\frac{dq_z}{dz} \tag{6.12}$$

Where w_0 is the vertical sediment velocity and q_z is the total sediment flux (transport rate per unit area) in the z direction, which is considered to consist of a downward component $-w_fC$ due to gravity and a upward flux which can be of a convective (subscript C) or diffusive (subscript D) nature, or a combination of both. The total vertical sediment flux can be written as,

$$q_z = -w_f C + q_D + q_C \tag{6.13}$$

Or alternatively,

$$\frac{\partial C}{\partial t} = w_f \frac{dC}{dz} - \frac{dq_D}{dz} - \frac{dq_C}{dz} \tag{6.14}$$

Nielson (1992) notes that natural *SSC* profiles usually result from a combination of both diffusive and convective processes. However, if only pure gradient diffusion is considered (consistent with the mixing length being small relative to the *SSC* profile), then the above equation can be reduced to

$$\frac{\partial C}{\partial t} = \omega_f \frac{dC}{dz} + \frac{dq_D}{dz} \tag{6.15}$$

And hence, with the diffusive sediment flux (q_D) given as $q_D = -\varepsilon_s \frac{\partial C}{\partial z}$ (where ε_s is the sediment diffusivity) eqn. 6.15 can be written as,

$$\frac{\partial C}{\partial t} = w_f \frac{dC}{dz} + \frac{d}{dz}\left(\varepsilon_s \frac{\partial C}{\partial z}\right) \tag{6.16}$$

For the steady concentration component (C) eqn 6.16 becomes

$$w_f \frac{dC}{dz} + \frac{d}{dz}\left(\varepsilon_s \frac{\partial C}{\partial z}\right) = 0 \tag{6.17}$$

Integrating this equation once yields

$$w_f C + \varepsilon_s \frac{d\overline{c}}{dz} = 0 \tag{6.18}$$

Or alternatively

$$\frac{d}{dz}\ln(C_z) = -\frac{w_f}{\varepsilon_s} \tag{6.19}$$

where C_z is the suspended sediment concentration at elevation z. A general solution to equation 6.19 is given as,

$$C_z = C_0 \exp^{-w_f \int_0^z \frac{dz}{\varepsilon_s}} \tag{6.20}$$

Which, as the mixing length (l_s) is given as $l_s = \varepsilon_s / w_f$ (Nielson, 1992), can be written as

$$C_z = C_a \exp^{(-z/l_s)} \tag{6.21}$$

where C_a is the estimated concentration at elevation 'a' (which when a $\rightarrow$ 0 is the reference concentration), Fredsoe and Deigaard (1992) define the mixing length (l_s) as the distance a fluid (water/sediment mix) is transported by turbulent fluctuations across the flow before it is mixed with the surrounding water, and thereby adjusts its longitudinal flow velocity to that occurring at the new level.

Black and Rosenberg (1991) and Fredsoe and Deigaard (1992) note that if ε_s is taken to be parabolic between the bed and the surface (e.g. Fredsoe et al. 1985), the vertical distribution of C becomes,

$$C_z / C_a = \left(\frac{d-z}{z_a} \times \frac{a}{d-a} \right)^{\frac{-w_f}{\beta \kappa U_*}} \tag{6.22}$$

Where $\frac{w_f}{\beta \kappa U_*}$ is the Rouse Number (R), d is the mean depth, and C_a is the reference concentration at level a.

The parabolic sediment diffusivity relationship is derived from the parabolic velocity profile, which near the bed goes to 0. From a practical perspective, if the sediment diffusivity goes to zero then no entrainment from the seabed will occur (i.e. C_0 = 0). Obviously sand is entrained within the concentration profile, and near the bed the mixing length is often taken to be a constant (e.g. Black and Vincent, 2001).

In terms of results from this study, Chapter 5 has shown that the concentration profile was found to be concave-up in log-linear space (i.e. Figure 5.04), suggesting that the sediment diffusivity varied with elevation above the seabed. However, within the

bottom ~0.08 m the measured concentration profiles were essentially linear in log-linear space (i.e. Figure 5.04) and the mixing length was found to be small compared to the overall scale of the concentration profile (i.e. ~0.1 to 0.07 m). The approximately linear nature of the measured profiles near the bed agrees with the findings of Nielson (1992), who notes that within approximately the first 4 ripple heights ($0<z/\eta<4$, i.e. approximately 0.04 to 0.08 cm for data from this study) suspended sediment profile shapes are practically linear. Assuming that within approximately 0.08 m of the seabed the concentration profile is essentially linear then, near the bed a pure diffusion approach to defining the concentration profile, and hence the near-bed reference concentration, can be used.

6.3.4.2 Estimating C_0 from the *SSC* profile

Mixing lengths are found by performing linear regression on the *SSC* profiles (i.e. C_z) in log-linear space. As mixing lengths have been shown to vary with elevation above the bed (Beamsley et al., 2001a; McComb, 2001), only the 3 *SSC* data points closest to the seabed (i.e. 0.02, 0.04 and 0.08 m elevation above the bed) were used to determine the near-bed value of l_s and hence the C_0 of each profile.

An inverse relationship has been shown to exist between the gradient of the suspended sediment concentration profile (*SSC*) and the suspended sediment grain size in both laboratory trials (Nielsen, 1983; Nielsen, 1992; Van Rijn, 1993) and under field conditions (Beamsley et al., 2001a; Black and Rosenberg, 1992). Accordingly, C_0 estimates are determined using the entire grain size distribution broken into a series of bins, rather than some arbitrary statistical characteristic of the surficial sediment grain size (e.g. d_{50} – the median grain size). In the present study this was achieved by deriving the *SSC* profile for discrete grain size intervals and extrapolating each to the seabed using eqn. 6.12. This allows l_s to be determined for each of the discrete grain size bins and, where only one measurement of the *SSC* was available, median mixing length values from the corresponding grain size bin were used to extrapolate the single data point to the seabed. This provided near-bed reference concentration measurements for the discrete grain size intervals. The total C_0 was determined by summing the values for the individual grain size bin values C_0.

6.4 Results

6.4.1 Wave and current observations

Figure 6.04 shows the near-bed wave orbital velocities and zero-down crossing period data for the four experiment sites. Notably, U_{max} exhibits a more peaked distribution than U_3, illustrating that U_3 is a more stable measure of the near-bed horizontal orbital velocity. Zero down-crossing periods range from approximately 6 to 20 s (Figure 6.04). All wave and current data has been filtered within the range 0.04 to 0.2 Hz.

6.4.2 Seabed characteristics

Statistically, the surficial sediment at the entrainment experiment sites is classified as fine to very fine sand (d_{50} = 250 – 62.5 μm, Table 6.02), though the percent of mud in each of the samples is relative large (18-25% by volume). The classification of the surficial sediment as fine to very fine sand suggests that non-cohesive entrainment formulae is suitable for predicting near-bed reference concentrations, however the amount of mud in the sediment distribution indicates that the surficial sediment can be classified as mixed sand/mud. Bedforms at Sites A, D and E consisted of vortex ripples with measured wavelengths ranging from 9 to 13 cm and heights of approximately 1 cm. The seabed at Site B did not exhibit any persistent ripple aspect and is classified as undulating. Table 6.02 summarises bedform geometry and sediment characteristics.

Surficial sediment grain size decreases with increasing water depth (Figure 6.05, Table 6.02). This observed decrease in d_{50} with increasing water depth is consistent with the larger sample set of surficial sediment at sites within Poverty Bay (Figure 6.05). Only limited variation between the mean, median and modal grain size distribution statistics is apparent at each of the sites (Figure 6.06) and significantly all grain size distribution curves consisted of a single modal peak.

No simple correlation is evident between the in-situ shear strength of the surficial sediment and either d_{50}, the ratio of sand to mud (*s/m*) by volume in the grain size distribution or the sample water depth (Figures 6.07, 6.08 and 6.09 respectively). However a good correlation between the sandy swash zone samples (< 9% mud, Table 6.02) from several silicate beaches around the North Island of New Zealand and the in-situ shear strength is shown to exist (R^2 = 0.90, Figure 6.07). Assuming a typical open coast beach/nearshore has a grain size of 250 μm; regression analysis suggests the sediment will have an in-situ shear strength of approximately 1.98 kPa.

The in-situ shear strength is a measure of the actual strength due to both the cohesive bonding and the inter-granular packing of the sediment. The fact that no correlation is shown to exist between the in-situ shear strength and either d_{50} or the ratio of sand to mud (*s/m*) suggests that other factors or parameters of the seabed are affecting the structural strength of the sediment.

In sampling the surficial sediment the *SCUBA* divers described the texture of the sediment at all four sites (Sites A, B, D and E) as being cohesively bound and tacky, the degree of which varied between sites, with the sediment at Site E described as being only slightly cohesively bound, almost to the point of non-cohesive sand.

6.4.3 Comparisons of predicted and estimated near-bed reference concentration

This section compares the predicted C_0 calculated using the different combination of equations listed in Table 6.01 with the estimated C_0 determined by extrapolating *SSC*

data to the seabed. Table 6.03 lists the estimated near-bed reference concentrations (C_0') and *SSC* measurements at 0.02, 0.04, and 0.08 m elevation above the seabed.

From Figure 6.10 it can be seen that the predicted near-bed reference concentration is dependant on the orbital statistic used to defining the friction velocity (U^*). C_0 predictions (C_0') based on a U^* characterised by the maximum near-bed orbital velocity are significantly larger than the estimated C_0 (C_0^*) from the pumped samples, regardless of the method used (Table 6.01), while a U^* characterised using U_3 provides more realistic predictions of the estimated near-bed reference concentration.

Average and median values of C_0'/C_0^* along with standard deviations and 95% confidence intervals (C.I.) for each of the experiment sites as well as the relative entrainment rate factor (the reciprocal of C_0'/C_0^*) are given in Table 6.04. The statistical measures of the ratio of predicted to observed C_0's (average, median and C.I. values) are based on 5 or more estimated C_0 determined from the measured *SSC* profiles.

Regardless of the method used to predict C_0 (Table 6.01), the entrainment rate factor for each of the sites is less then 1 indicating that the predicted C_0 values are consistently larger that the estimated C_0 from the pumped water/sediment samples. Further the value of the entrainment rate factor is shown to vary between sites. The inability of the theoretical formulae to accurately predict the near-bed reference concentration for all sites suggests either a failure in the theory being used or that some characteristic of the surficial sediment is acting to retard the entrainment rate (i.e. $C_0' > C_0^*$). Entrainment rate factors less that 1 are consistent with the surficial sediment being cohesively bound, as cohesive bonding acts to inhibits both the onset of erosion and the erosion rate once erosion has begun (Amos et al., 1995; Collins, 1989; Kamphuis and Hall, 1983; Kuti and Yen, 1976; Mitchener and Torfs, 1996; Murray, 1977). In the next sections comparisons between the surficial sediment characteristics and the entrainment rate factors are examined.

6.4.4 Entrainment rate factors and surficial sediment characteristics

Entrainment rate factors are defined as the ratio of estimated to predicted C_0, and as such values less than 1 indicate excess in the predicted C_0 above that estimated from the pumped water/sediment samples. From Table 6.04 the entrainment rate factor is shown to vary between sites, and as such this section examines the variability in the entrainment rate factor as a function of the surficial sediment characteristics.

6.4.4.1 Entrainment rate factor and d_{50}

Figure 6.11 illustrates that there is no apparent correlation between the relative entrainment rate factors and the median grain size of the surficial sediment regardless of the method used to account for the effect of bedload sediment transport and the presence of bedforms on sediment entrainment (Table 6.01), or the orbital statistic used to characterise the friction velocity (U^*). Regression analysis results in adjusted R^2 values of the fitted curves typically less than 0.005. The fact that no correlation is shown

between d_{50} of the surficial sediment and the entrainment rate factor indicates that the inability of the predictive formulae to adequately determine C_0 is not a function of some grain size dependency in the formulae being used.

6.4.4.2 Entrainment rate factor and the ratio of sand to mud (*s/m*)

In keeping with the findings of Chesher and Ockenden (1997), Mitchener and Torfs, (1996); Amos et al. (1995); Collins, (1989); Kamphuis and Hall, (1983); Murray, (1977) and Kuti and Yen, (1976), the dimensionless ratio of sand to mud (*s/m*) by volume is correlated to entrainment rate factor in this section.

Comparisons between the entrainment rate factor and the ratio of sand to mud (*s/m*) in the surficial sediment (Figure 6.12) indicate that regardless of the orbital statistic used to characterise the friction velocity (U^*) or the method of accounting for the effect bedload sediment transport and bedforms have on sediment entrainment (Table 6.01) no correlation is evident. Regression analysis results in adjusted R^2 values of the fitted curves typically less than 0.005. While other researchers have used the ratio of sand to mud to account for the effect cohesive bonding has on reducing the entrainment and erosion rate of mixed sand/mud sediment (e.g. Chesher and Ockenden, 1997), data from this experiment does not indicate any relationship between the entrainment rate factor and the ratio of sand to mud.

The ratio of volume percent sand to mud is perhaps a simplistic method of accounting for the effect cohesive bonding has on sediment entrainment and transport rates over mixed sand/mud seabeds. As such, in the next section the entrainment rate factor is compared to the normalised in-situ shear strength of the surficial sediment.

6.4.4.3 Entrainment rate factor and the normalised in-situ shear strength (χ)

Kamphuis and Hall (1983) found that critical shear stress for erosion increased with the in-situ shear strength of the surficial sediment, further Toorman, (2001) notes that it has been assumed that the erosion rate can be represented by an empirical relationship between shear strength, determined with a vane test or other appropriate devices. As such, this section examines the relationship between the relative entrainment rate factor and the normalised in-situ shear strength as measured using a hand-held shear vane (Figure 6.03). The in-situ shear strength has been normalised using the equivalent shear strength of typical non-cohesive beach sediment (i.e. d_{50} = 250 μm) using the relationship determined in section 6.4.2.

Figure 6.13 illustrates the correlation between the entrainment rate factor and the surficial sediment in-situ shear strength. When U_3 is used to characterise U^*, regression analysis indicates that there is a good correlation between the entrainment rate factor and

the normalised in-situ shear strength regardless of the method used to account for the effect bedload sediment transport and bedforms have on sediment entrainment, with R^2values in excess of 0.76, and adjusted R^2 values (accounting for the degrees of freedom in the data) as large as 0.99 (Table 6.05). In contrast, defining U^* using U_{max} results in a poor correlation, with adjusted R^2values typically less than 0.005.

While defining U^* using the relatively stable U_3 results in comparatively large R^2 values regardless of the method used (Table 6.01), accounting for the enhanced flow over the crests of the vortex ripples using the correction factor proposed by Du Toit and Sleath, (1981), i.e. Method 2, results in the largest adjusted R^2 statistics. As such a fitted equation based on the Du Toit and Sleath, (1981) method of accounting for the enhanced flow over vortex ripples is presented,

$$\ln(\zeta) = -0.51 - 1.30\chi^3 \qquad (6.23)$$

Assuming the validity of the predictive formulae in estimation of the near-bed reference concentration and assuming that the difference between the predicted and observed is a function of the cohesive characteristics of the surficial sediment, then this relatively simplistic relationship can be used to account for the retardation effect cohesive bonding has on sediment entrainment in cohesively bound mixed sand/mud environments.

6.5 Discussion

The swash zones sediment samples typically consisted of sand with only a limited amount of mud (< 9% by volume), whereas the surficial sediment within the shallow shoreface beyond the surf zone in Poverty Bay, including the experiment sites, consists of relatively larger percentages of mud (Table 6.02). The correlation between the in-situ shear strength and d_{50} of the swash zone samples is attributed to purely non-cohesive packing of the sediment grains and the data are shown to plot distinct from the seabed sediment data within Poverty Bay, including the entrainment experiment sites (Figure 6.07). *SCUBA* diver observations and the volume of mud in the surficial sediment of the experiment sites suggest that the sediment at all the entrainment sites was cohesively bound. Mud content of the seabed at the entrainment sites were in excess of 17% by volume (Table 6.02), which is greater than the 3-15% at which Mitchener and Torfs (1996) found sediment began to behave as a cohesively bound structure. This data implies that the transition from non-cohesive packing to cohesive bonding occurs between 9 to 18% mud by volume (corresponding to Waikanae Beach and sample Site E respectively).

The lack of correlation between the in-situ shear strength and the sediment grain size characteristics of the cohesively bound mixed sand/mud seabed sediment suggests that the magnitude of the cohesive bonding cannot be represented using sediment grain size characteristics alone. This finding is consistent with numerous authors who have noted that the classification of a cohesively bound seabed is dependant on various factors, not solely the grain size characteristics (Augustinus, 2002; Berlamont et al., 1993; Kjerfve et al., 2002).

Average values of the relative entrainment rate (ζ) at each site have been calculated based on the estimated C_0 (C_0') from 5 or more measured *SSC* profiles and C_0 predicted (C_0^*) by accounting for the effect of roughness associated with bedload sediment transport and the presence of bedforms on the entrainment of sediment as given in Table 6.01. From Table 6.04 the relative entrainment rate factor (i.e. the ratio of estimated to predicted C_0) is shown to be less than 1 for all cases, and to vary between experiment sites. Entrainment rate (ζ) values less than 1 are consistent with the surficial sediment being cohesively bound, as cohesive bonding acts to reduce the effective erosion rate and increases the critical shear strength at which erosion begins (Amos et al., 1995; Collins, 1989; Kamphuis and Hall, 1983; Kuti and Yen, 1976; Mitchener and Torfs, 1996; Murray, 1977). As such, the variation ζ as a function of the surficial sediment characteristics has been investigated.

Over the 1-minute sampling period no correlations were apparent in relating either the median grain size (d_{50}) of the surficial sediment or the ratio of sand to mud to ζ regardless of the orbital statistic used to characterise the friction velocity, or the method of accounting for enhanced sediment entrainment above the observed vortex ripples. The lack of correlation between the entrainment rate factor and d_{50} suggests that the variation in ζ is not a function of grain size alone, and is not due to the failing of the C_0 predictive formulae for relatively fine grained sediment. Assuming that the variation in ζ is due to cohesive bonding of the surficial sediment, then accounting for the effect of cohesion on the retardation of sediment entrainment using a single statistical measure of the sediment distribution (i.e. d_{50}) or a ratio of sand to mud is a relatively simplistic approach, as factors such as compaction, consolidation, organic and in-organic cohesive bonding, characteristics of the bed structure and water-bed exchange processes are not accounted for. The number of parameters or parameter sets needed to define cohesive sediment is such that some direct measure of the sediment shear strength may be more appropriate. Indeed, Toorman (2001) notes that traditionally it has been assumed that the erosion strength can be represented by an empirical relationship with the seabed in-situ shear strength. This was shown by Kamphuis and Hall (Kamphuis and Hall, 1983), who found the critical shear stress for erosion increased with the shear strength of the seabed.

This paper has correlated the relative entrainment rate factor ($\zeta = C_0^*/C_0$') of cohesively bound sediment to the normalised in-situ shear strength (χ) of the seabed (as measured by a hand held shear vane). Because the distinction between cohesive bonding and non-cohesive packing is ill defined for mixed sand and mud sediment, being able to define a relationship between the relative entrainment rate (ζ) and the in-situ shear strength is particularly important, as in-situ shear strength measurements take into account both the cohesive bonding and the inter-granular packing of the sediment

Results indicate a log-linear relationship between ζ and the normalised in-situ shear strength (χ) of the sediment (Figure 6.13 A). Further, the correlation is based on defining U^* using U_3, which shows less variability and is more stable than U_{max}, as illustrated in Figure 6.04. While Beamsley et al. (2001a) showed U_{max} to be important in determining aspects of the *SSC* profile over an intermediate time period (i.e. 1 minute), defining a friction velocity using the relatively stable U_3 statistic of an extended (i.e. 9 min) orbital velocity distribution is more realistic that using the single largest orbital

event in the time-series. The suitability of using U_3 in defining U^* for sediment entrainment purposes is consistent with the findings of Black and Rosenberg (1991), and assuming U_3 represents the approximate upper 10^{th} percentile in an orbital velocity time-series (as determined by Black and Rosenberg, 1991), is also consistent with the findings of Kos'yan (1985), who suggested that the 85-90^{th} percentile velocity was most suitable for predicting sediment entrainment and transport rates over natural beaches.

Largest adjusted correlation coefficients (*Adjusted* $R^2 = 0.99$, Table 6.05) were obtained when the effect vortex ripples have on enhancing flow characteristics near their crests was accounted for using the velocity correction to the skin friction shields parameter suggested by Du Toit and Sleath, (1981), i.e. *Method 2*, Table 6.01. From Table 6.05 it can be seen that when C_0 is predicted using a friction velocity characterised using U_3 and *Method 2* is used to account for the enhancement of sediment entrainment due to a rippled seabed, the entrainment of cohesively bound sediment can be retarded by a factor of more that 10 (i.e. $\zeta < 0.1$), which is consistent with the findings of Mitchener and Torfs (1996).

Using the in-situ shear strength of the seabed to account for the effect cohesive bonding has on retarding the entrainment rate does not resort to classifying the complexities of cohesively bound sediment using either simplistic ratios of the seabed textural characteristics (i.e. ratio of sand to mud percent), or a single measure of the grain size distribution. The robustness of using the in-situ shear strength to characterise the reduction in entrainment due to cohesive bonding is illustrated by the similarities in the seabed shear strengths and ζ value between Sites E and D. If a simplistic ratio of sand to mud, or a single statistical measure of the grain size distribution were used to characterise the effect cohesive bonding has on retarding sediment entrainment, then Sites E and D would be expected to have completely different ζ values and be at opposite extremes of the dataset, which is not shown to be the case (Table 6.04). Additionally, including the effect vortex ripples have on enhancing sediment entrainment is desirable, as vortices associated with the hydraulic flow over the bedforms have the potential to move considerable amounts of sediment away from the bed and increase the amount of sediment in suspension (Fredsoe and Deigaard, 1992).

6.6 Conclusion

Sediment entrainment under non-broken waves has been investigated at 4 sites ranging in water depth from 4 to 10 m using micro-scale high-resolution pumped *SSC* measurements, from which near-bed reference concentrations have been estimated. The surficial sediment is described as a mixed sand/mud seabed, with mud contents > 17%. The estimated C_0 are compared with non-cohesive predictive formulae for determining C_0 inclusive of bedform measurements, surficial sediment characteristics and measured near-bed wave orbital velocities. The experiment site was located within northern Poverty Bay, adjacent to the port of Gisborne on the east coast of New Zealand's North Island.

SCUBA diver observations and percentage mud by volume (>17 % mud) in the surficial sediment suggest that the seabed sediment at the experiment sites is cohesively bound. The strength of cohesive sediment varied between sites, with the sediment at Site E described as being only slightly cohesively bound, almost to the point of unconsolidated sand. No correlation was found between the in-situ shear strength of the cohesively bound seabed sediment and the seabed d_{50}, suggesting the shear strength of the sediment is not solely a function of grain size. In contrast, a good correlation (R^2=0.90) was found between the in-situ shear strength and the d_{50} grain size of relatively mud free (<9% mud) swash zone sediment from various beaches. The shear strength of the sandy swash zone samples is attributed to inter-granular packing.

Comparisons between the estimated and predicted C_0 are not in agreement, with the ratio of estimated to predicted C_0 (i.e. the entrainment rate factor, ζ) found to be consistently less than 1, and to vary between sites. The variation in ζ as a function of the surficial sediment characteristics has been investigated, and no correlation has been found between ζ and either the median grain size (d_{50}) or the ratio of sand to mud of the surficial sediment, regardless of the orbital statistic used to characterise the friction velocity (U^*) or the method of accounting for enhanced entrainment above vortex ripple bedforms. The lack of any correlation between ζ and either the d50 or the ratio of sand to mud in the surficial sediment highlights the complexities associated with defining the entrainment parameters of cohesively bound sediment. The number of parameters or parameter sets needed to define cohesive sediment is such that a direct measure of the in-situ shear strength of the sediment is more appropriate, and as such a relationship between ζ and the normalised in-situ shear strength (χ) has been sort. The in-situ shear strength accounts for factors such as the physico-chemical properties of the mud; characteristics of the bed structure, bed history, compaction, consolidation and water - bed exchange processes.

A relationship between ζ and the normalised in-situ shear strength (*Adjusted* R^2 = 0.99) for cohesively bound sediment has been defined as,

$$\ln(\zeta) = -0.51 - 1.30\chi^3$$

This relationship is based on predicted C_0 where the friction velocity (U^*) is characterised using the third-moment of the horizontal orbital velocity (U_3) and using a modified effective Shields parameter which takes into account the effect flow enhancement near the crests of the ripple bedforms has on enhancing entrainment rates.

Table 6.01 List of the variation of equations used to account for the effect of bedforms and bedload sediment transport on the determination of C_0. Method 1 assumes a planar bed with apparent roughness solely due to grain size roughness. Method 2 accounts for the effect of ripples on the suspension of sediment by modifying the wave induced skin friction factor. Methods 3 and 4 include the apparent roughness due to both the presence of ripples and due to the momentum transfer from the moving sediment over the rippled bedforms. Methods 3 and 4 vary only in the value of the bedload sediment transport multiplier (i.e. B_m = 190 or 170). Each of the methods has been assessed using a friction velocity defined using both U_{max} and U_3

METHOD	DISCRIPTION	EQUATION
Method 1	Fixed planer bed apparent roughness - k_b	$k_b = 2.5d_{50}$
Method 2	Fixed planer bed apparent roughness (k_b), bedforms accounted for by modifying ψ' (Du Toit and Sleath, 1981)	$k_b = 2.5d_{50}$ and $\psi'' = \frac{\psi'}{(1-\pi\eta/\lambda)^2}$
Method 3	Bedform and bedload transport inclusive apparent roughness - k_b (Nielsen, 1983)	$k_b = 190\times(\psi'-\psi_c)^{0.5} d_{50} + 8\frac{\eta}{\lambda}\eta + 2.5d_{50}$
Method 4	Bedform and bedload transport inclusive apparent roughness - k_b (Nielsen, 1992)	$k_b = 170\times(\psi'-\psi_c)^{0.5} d_{50} + 8\frac{\eta}{\lambda}\eta + 2.5d_{50}$

Table 6.02 Surficial sediment parameters and bedform measurements at the four suspended sediment experiment sites in Poverty Bay and at 5 beaches around the northeast coastline of New Zealand.

Site Id	Site A	Site B	Site D	Site E	Mount Maunganui Main Beach	Mount Maunganui Clyde St. Beach	Ohope Beach	Gisborne Midway Beach	Gisborne Waikanae Beach
Depth (m)	8	6	10	4	swash zone	swash zone	swash zone	swash zone	swash zone
Shear strength (kPa)	2.58	2.21	2.04	2.03	0.94	1.3	2.51	1.71	2.54
Mean (μm)	107	152	95	188	430	384	187	225	181
d_{50} (μm)	110	145	99	169	416	374	184	227	180
Mode (μm)	128	175	114	200	455	389	181	244	182
Clay % by volume	9	8	8	7	0	0	1	3	3
Silt % by volume	14	13	17	11	1	1	2	6	5
Mud % by volume	23	21	25	18	2	1	3	9	8
Sand % by volume	78	79	75	82	99	99	97	91	92
sand/mud (s/m)	3.4	3.8	3	4.6	65.7	110.1	34.7	10.6	11.2
Type of bedform	Rounded ripples	Hummocky undulations	Rounded ripples	Rounded ripples	n/a	n/a	n/a	n/a	n/a
Bedform dimension (cm)	$\eta = 1$ $\lambda = 9$	0.5-1 cm high 5-10 cm length	$\eta = 1$ $\lambda = 13$	$\eta = 1$ $\lambda = 9$	n/a	n/a	n/a	n/a	n/a

Table 6.03 Estimated near bed reference concentrations (C_0) and *SSC* at 0.02, 0.04 and 0.08 m elevation above the bed. Samples with flow rates less than 1.2 ms^{-1} in the inlet tubes have been excluded from the table and are donated with an n/a.

	Estimated C_0 based on measured *SSC* data			
Sample	C_0	C_z 0.02 m	C_z 0.04 m	C_z 0.08 m
A1	0.37	n/a	n/a	0.17
A2	2.7	1.79	0.89	0.41
A3	1.47	0.98	0.86	0.53
A4	8.21	n/a	n/a	3.28
A5	0.19	0.18	0.14	0.19
B1	0.93	0.89	0.28	0.27
B2	3.31	2.61	0.64	0.39
B3	3.11	2.14	0.42	0.23
B4	0.97	0.84	0.25	0.19
B5	0.58	0.52	0.11	0.09
D1	0.73	n/a	0.25	0.12
D2	0.21	n/a	n/a	0.1
D3	6.26	n/a	2.54	1.13
D4	1.16	n/a	0.78	0.55
D5	6.07	n/a	1.97	0.73
E1	0.9	0.12	0.04	0.04
E2	1.39	1.04	0.12	0.14
E3	0.38	0.31	0.12	0.09
E4	0.41	0.43	0.13	0.13
E5	0.18	0.16	0.06	0.05
E6	0.1	0.07	0.05	0.03
E7	0.1	0.09	0.06	0.05

Table 6.04 Ratios of estimated to predicted C_0 (C_0'/C_0^*), with predicted C_0 values determined using the methods outlined in Table 6.01. The statistical measures are based on 5 or more estimates of C_0 determined from the measured *SSC* profiles. Corresponding water depths are 4, 6, 8 and 10 m for Sites E, B, A and D respectively. Relative entrainment rate factors (ζ) are determined by taking the reciprocal of the average value (i.e. 1/average).

		Predicted using U_3				***Predicted using U_{max}***			
		Method 1	**Method 2**	**Method 3**	**Method 4**	**Method 1**	**Method 2**	**Method 3**	**Method 4**
Site A	*Average*	2.2	33.4	373.0	332.8	1636	8602	292484	249511
	Median	1.0	14.4	95.8	86.4	127	665	11092	9673
	Standard deviation	3.2	47.7	660.2	586.6	3302	17360	626194	533572
	95% Confidence interval	3.1	46.8	646.9	574.9	3236	17013	613657	522890
	Relative entrainment rate (ζ)	**0.446**	**0.030**	**0.003**	**0.003**	**0.0006**	**0.000116**	**0.000003**	**0.000004**
Site B	*Average*	1.9	9.9	180.9	157.7	41	214	5184	4451
	Median	1.2	6.2	132.1	114.4	42	220	5408	4715
	Standard deviation	2.0	10.5	175.1	153.0	30	158	3970	3359
	95% Confidence interval	1.9	10.3	171.6	150.0	30	155	3891	3292
	Relative entrainment rate (ζ)	**0.529**	**0.101**	**0.006**	**0.006**	**0.02459**	**0.00468**	**0.00019**	**0.00022**
Site D	*Average*	1.4	7.2	138.7	120.6	210	1104	50467	42526
	Median	0.9	4.6	126.2	108.2	196	1033	19652	17009
	Standard deviation	1.5	7.6	110.5	95.5	156	819	56326	47130
	95% Confidence interval	1.4	7.5	108.3	93.6	153	802	55199	46187
	Relative entrainment rate (ζ)	**0.734**	**0.140**	**0.007**	**0.008**	**0.00476**	**0.00091**	**0.00002**	**0.00002**
Site E	*Average*	1.5	6.8	88.1	78.4	14	70	1017	896
	Median	1.5	7.5	87.0	77.7	4	23	298	265
	Standard deviation	0.2	2.1	19.3	16.9	24	127	1743	1533
	95% Confidence interval	0.2	2.0	18.9	16.5	23	124	1708	1502
	Relative entrainment rate (ζ)	**0.678**	**0.148**	**0.011**	**0.013**	**0.07357**	**0.01431**	**0.00098**	**0.00112**

Table 6.05 Fitted equations and corresponding coefficients of determination (R^2) for the comparison between the normalised in-situ shear strength (χ - as measured using a hand-held shear vane - Figure 6.03) and the entrainment rate factor (i.e. the ratio of observed to predicted C_0) with the effect of bedforms and bedload sediment transport on the magnitude of sediment entrained accounted for using the methods outlined in Table 6.01. U^* is defined using the 3rd moment of the near-bed horizontal orbital velocity (U_3). When U^* is defined using U_{max} the adjusted R^2 values of the fitted curves are approximately 0, i.e. no correlation. The in-situ shear strength has been normalised using the shear strength of typical sandy sediment ($d_{50} \sim 250\mu m$).

Method	Fitted equation	R^2	adjusted R^2
Equation form	$\ln(y) = a + b \times X^3$		
Method 1	$\ln(\zeta) = 0.09 - 0.43 \times \chi^3$	0.84	0.51
Method 2	$\ln(\zeta) = -0.51 - 1.30 \times \chi^3$	1.00	0.99
Method 3	$\ln(\zeta) = -3.18 - 1.34 \times \chi^3$	0.76	0.29
Method 4	$\ln(\zeta) = -3.06 - 1.33 \times \chi^3$	0.76	0.36

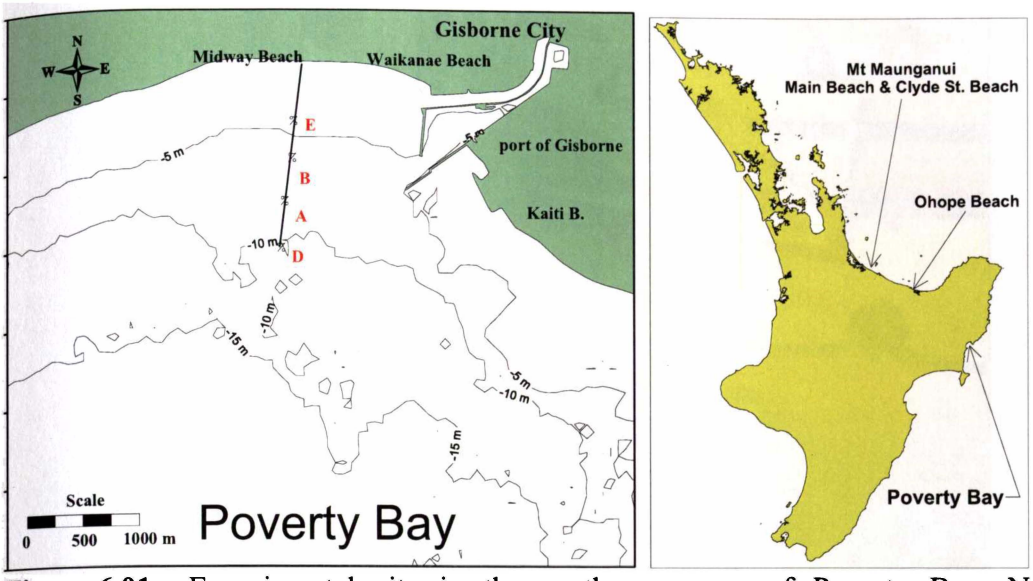

Figure 6.01 Experimental site in the northern corner of Poverty Bay, New Zealand, showing the location of the sample sites offshore from Midway Beach. Also shown are the locations of beaches from which in-situ shear strength measurements of swash zone sediment were taken.

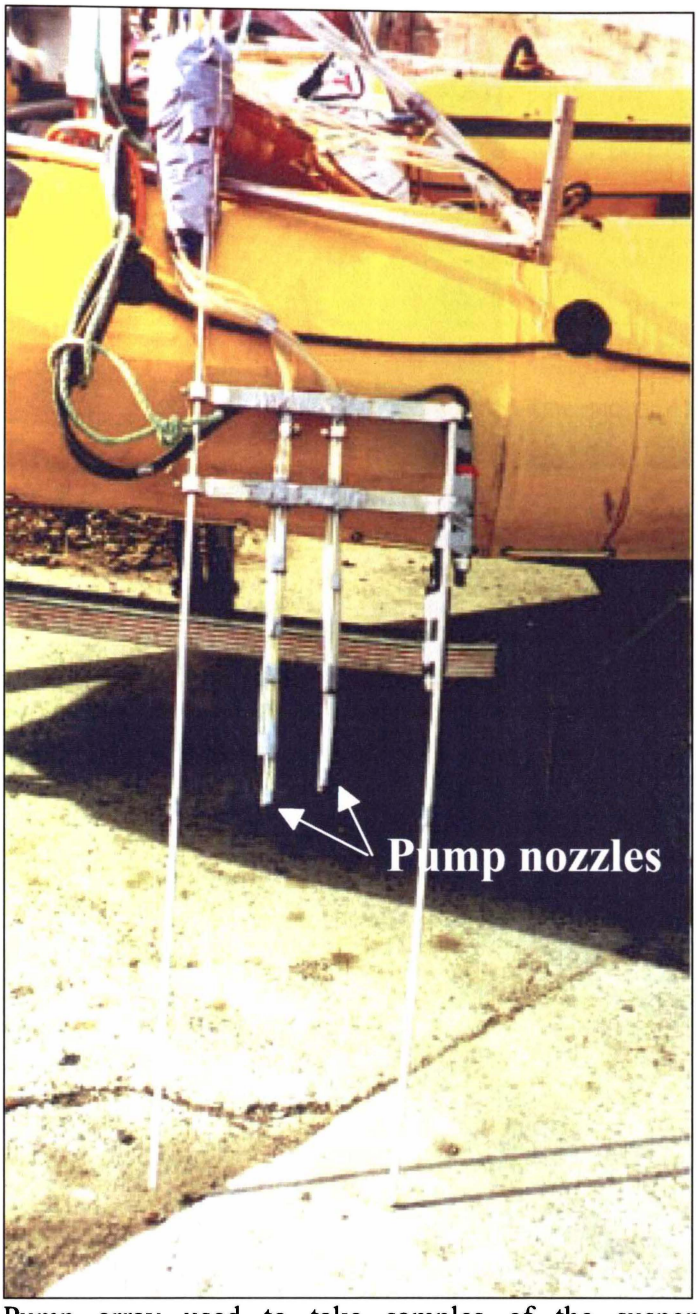

Figure 6.02 Pump array used to take samples of the suspended sediment concentration under un-broken waves. Nozzle apertures were positioned at elevations of 0.02, 0.04, 0.08, 0.16 and 0.32 m above the seabed and samples were pumped to a sample platform (not shown here) approximately 4 m above the bed. Suspended sediment samples from only the lower three pump nozzles were used in the estimation of C0.

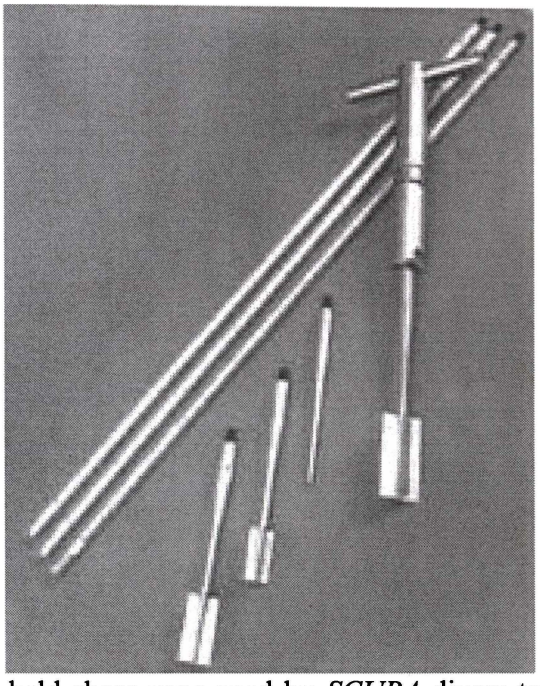

Figure 6.03 Hand held shear vane used by *SCUBA* divers to measure the in-situ shear strength of the seabed and swash zone sediment.

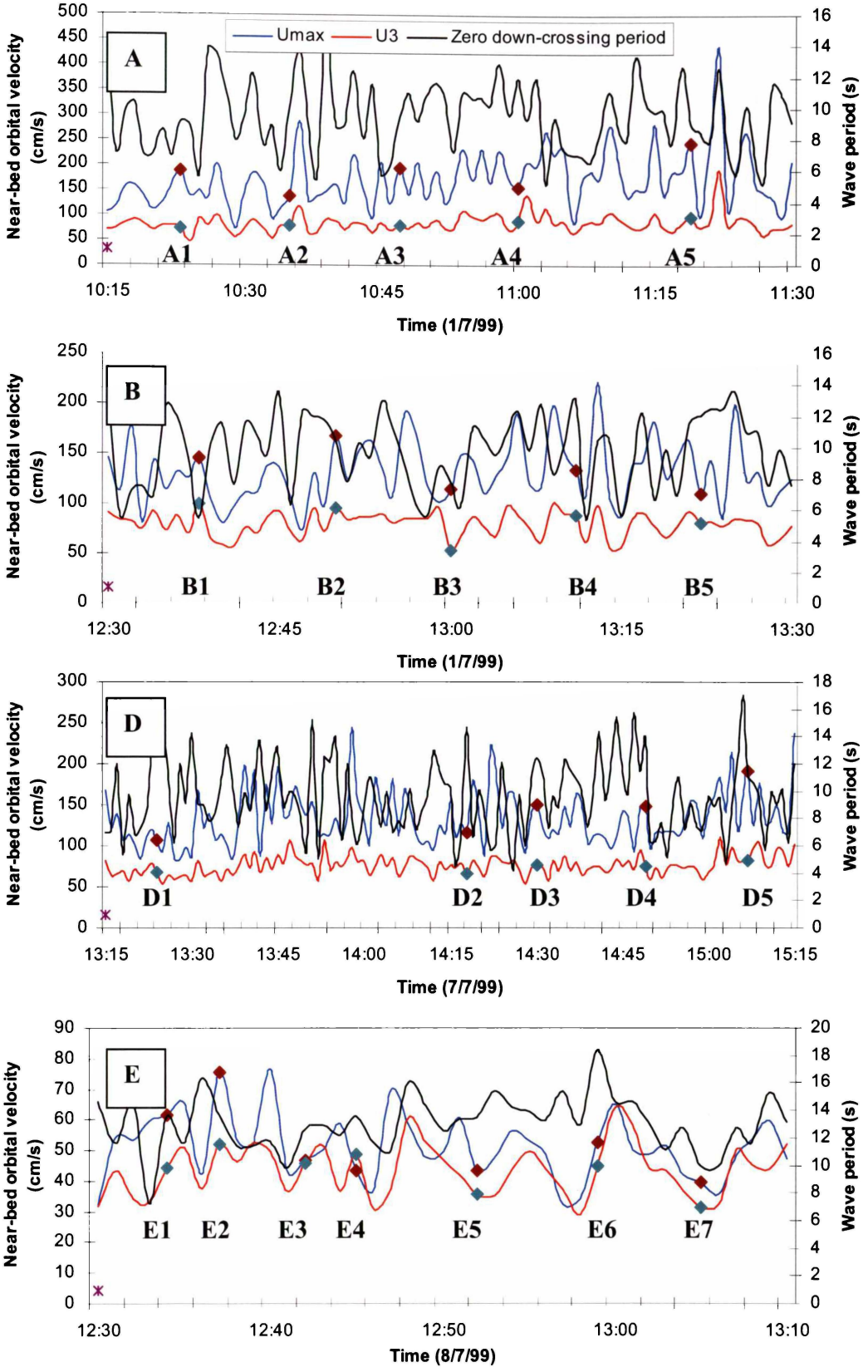

Figure 6.04 Measured wave orbital velocities and zero down-crossing wave periods at the four sample sites during the sampling period. Wave statistics were measured using an *InterOcean S4ADW* vector-averaging wave/current meter sampling at 2 *Hz*. Also shown are the sampling times.

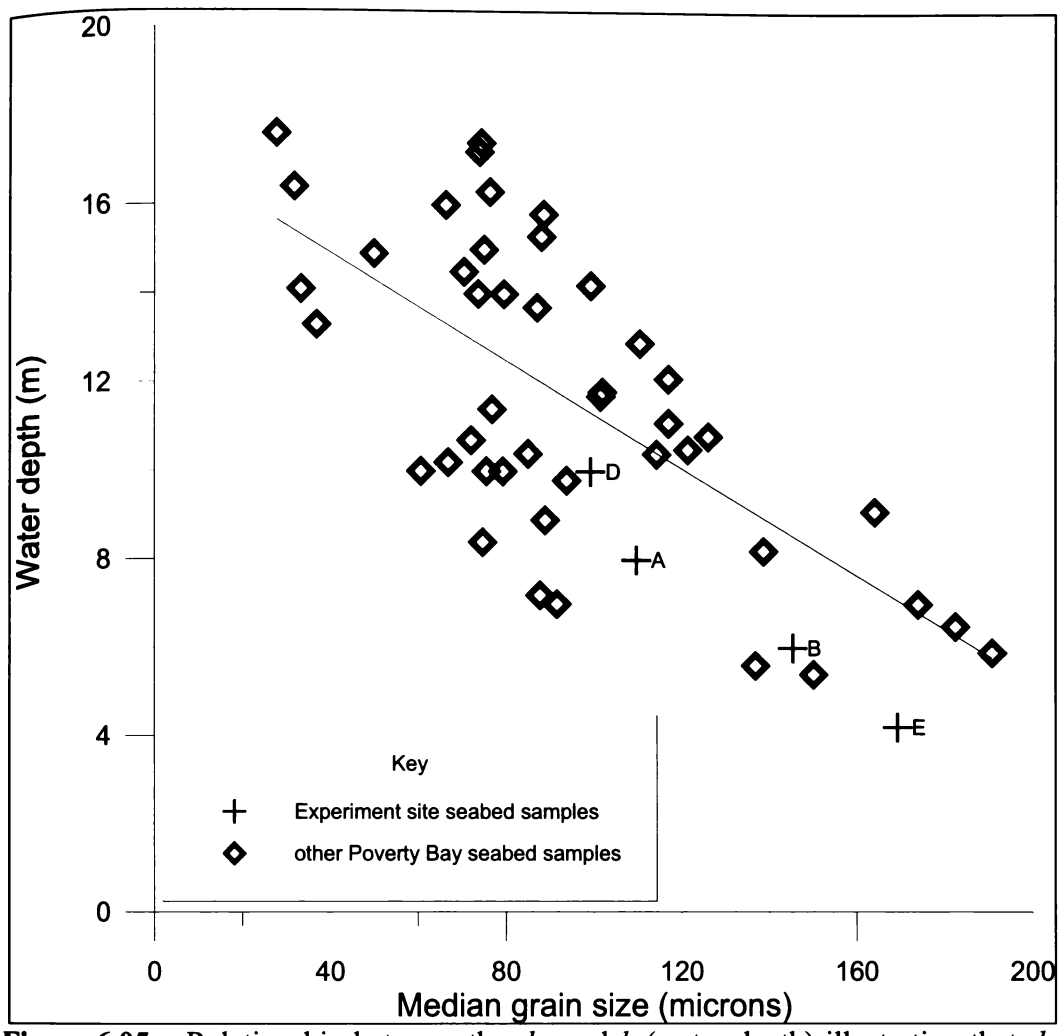

Figure 6.05 Relationship between the d_{50} and h (water depth) illustrating that d_{50} decreases with increased water depth, including the sediment entrainment experimental sites (labelled A, B, D and E). Water depths were measured at the time of sampling.

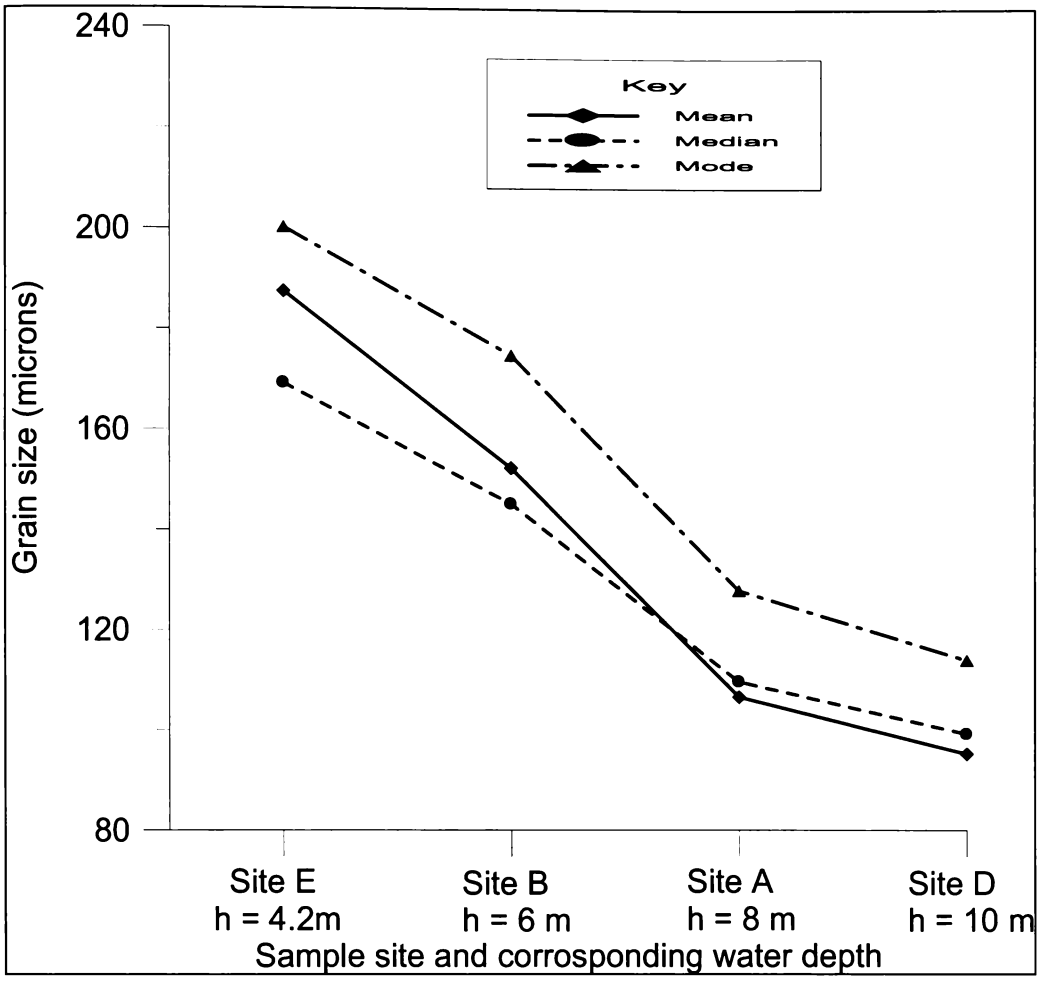

Figure 6.06 Mean, median and modal grain sizes for each of the sample sites. Median and mean grain sizes are similar for each of the sites, particularly at Sites A and D (corresponding to 8 and 10 m water depths respectively). Water depths (*h*) were measured at the time of sampling.

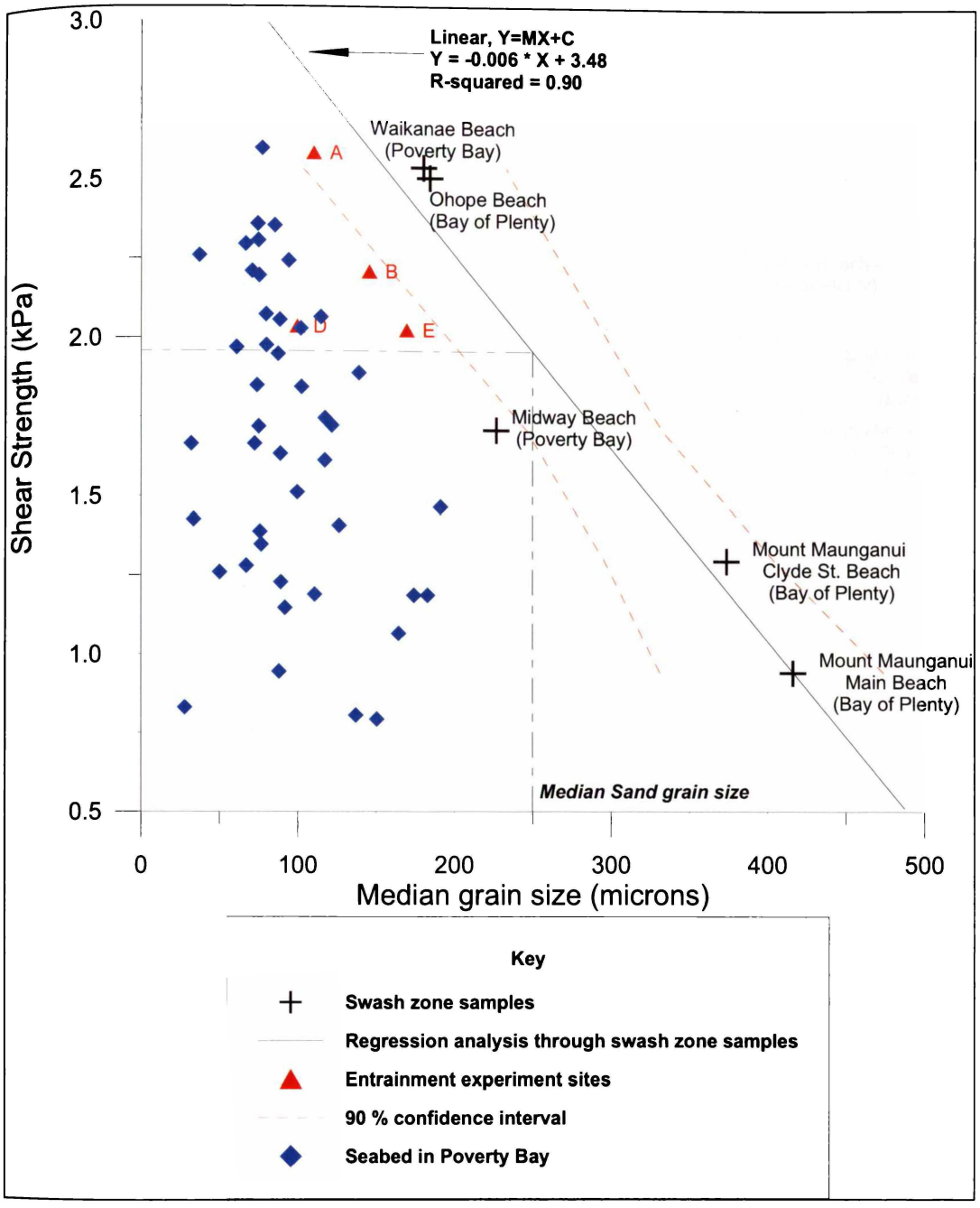

Figure 6.07 d_{50} and in-situ shear strength (kPa) correlation illustrating no obvious relationship exits between the surficial sediment within northern Poverty Bay and the in-situ shear strength. However, for sediment consisting of predominantly sand a correlation is shown between shear strength and d_{50}. Assuming a beach grain size of *Median Sand* (250 μm); a typical shear strength value for non-cohesive sandy sediment is 1.98 kPa.

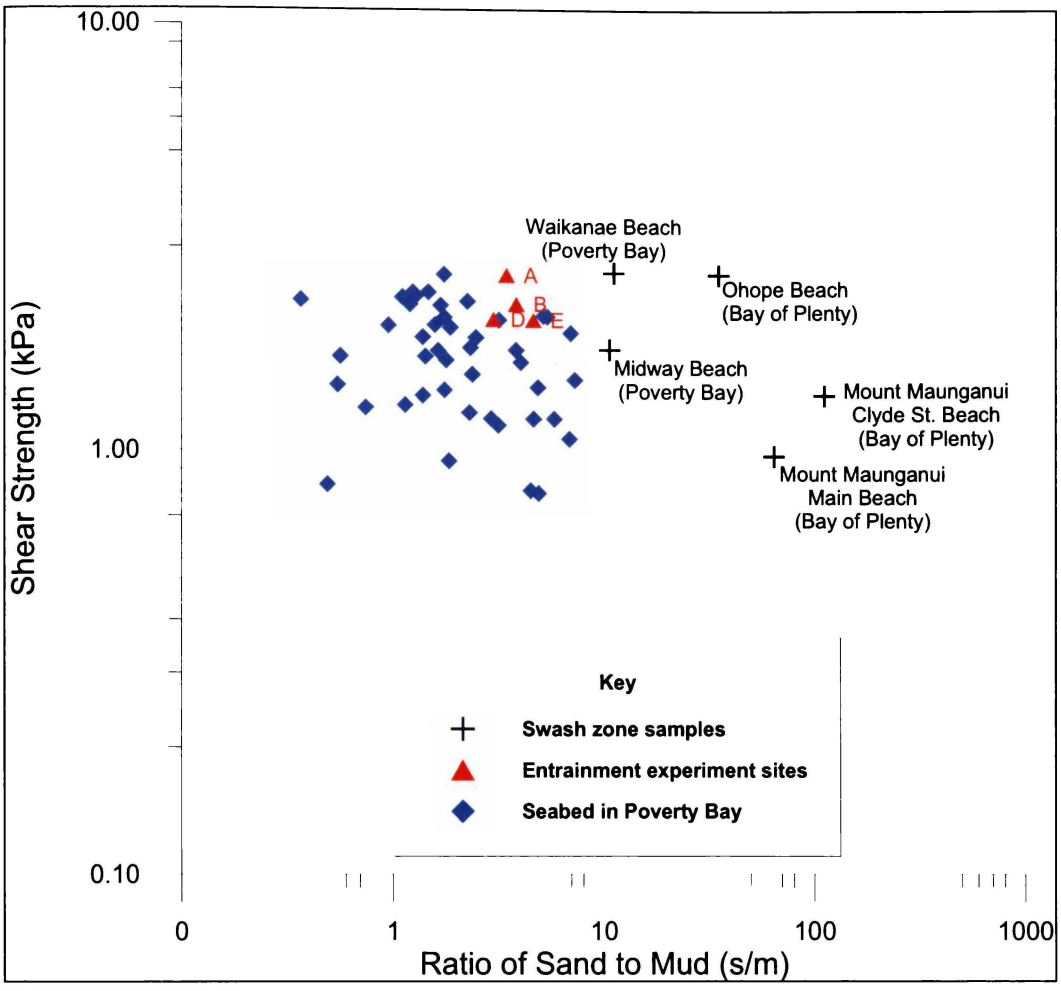

Figure 6.08 Comparisons between in-situ shear strength and the ratio of sand to mud (*s/m*). The seabed sediment from within Poverty Bay plots as a distinct cluster from the sandy swash zone samples. No obvious relationship is shown to exist between the in-situ shear strength and the ratio of sand to mud (*s/m*).

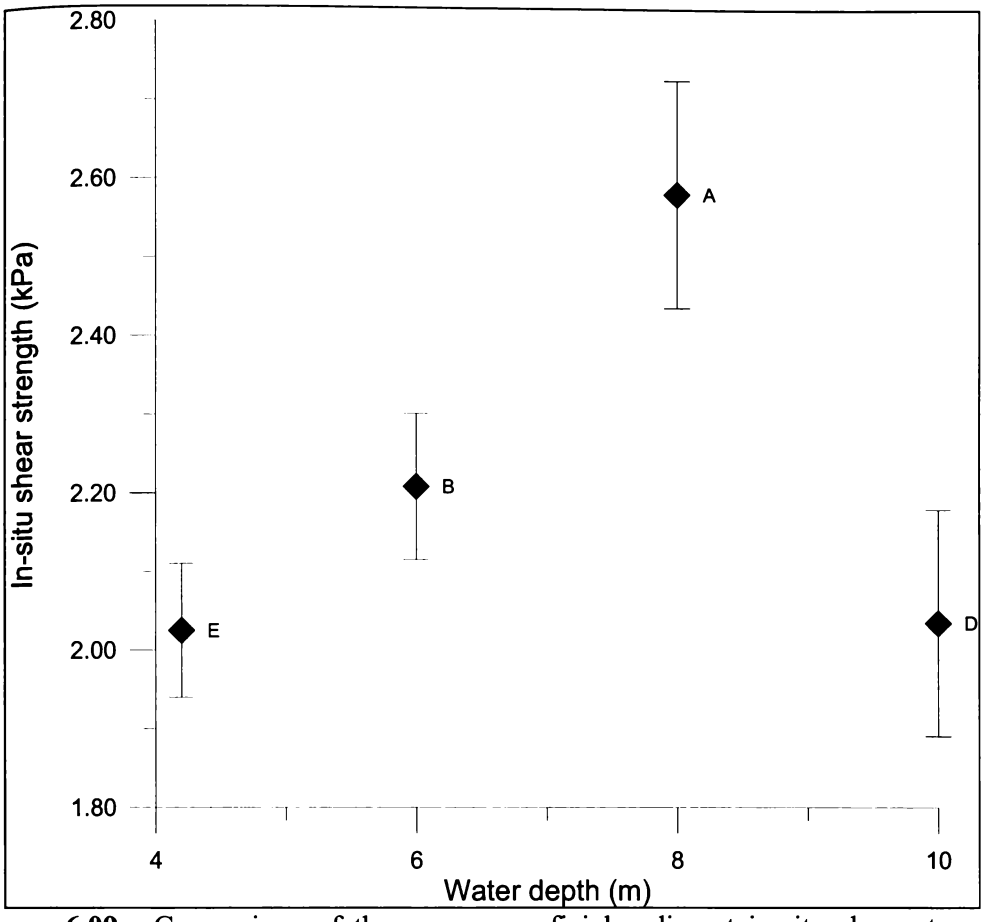

Figure 6.09 Comparison of the average surficial sediment in-situ shear strength (based on a minimum of 12 readings) and the sample site water depth (h). No obvious relationship exists between the water depth (h) and the in-situ shear strength. Also shown are 95% confidence intervals in shear strength about each of the shear strength measurements (derived from the sample population).

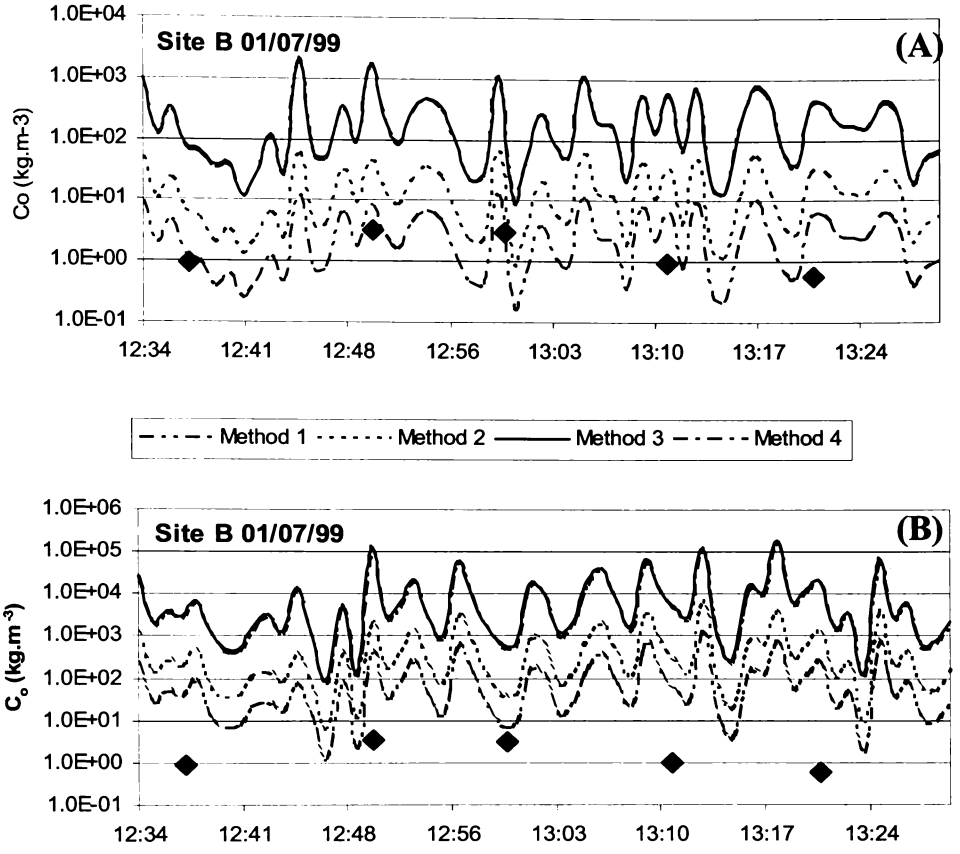

Figure 6.10 Time-series of predicted C_0 at Site B determined using a friction velocity (U^*) defined using the third moment of the horizontal near-bed orbital velocity (U_3) and the maximum near-bed orbital velocity (U_{max}) from the measured time-series (A and B respectively). Also shown are the estimated C_0 values from the pumped water/sediment samples. Classifying U^* using U_{max} results in predicted C_0 values significantly larger then those estimated, while using a U^* determined by the U_3 statistic appears to result in a better agreement between predicted and observed.

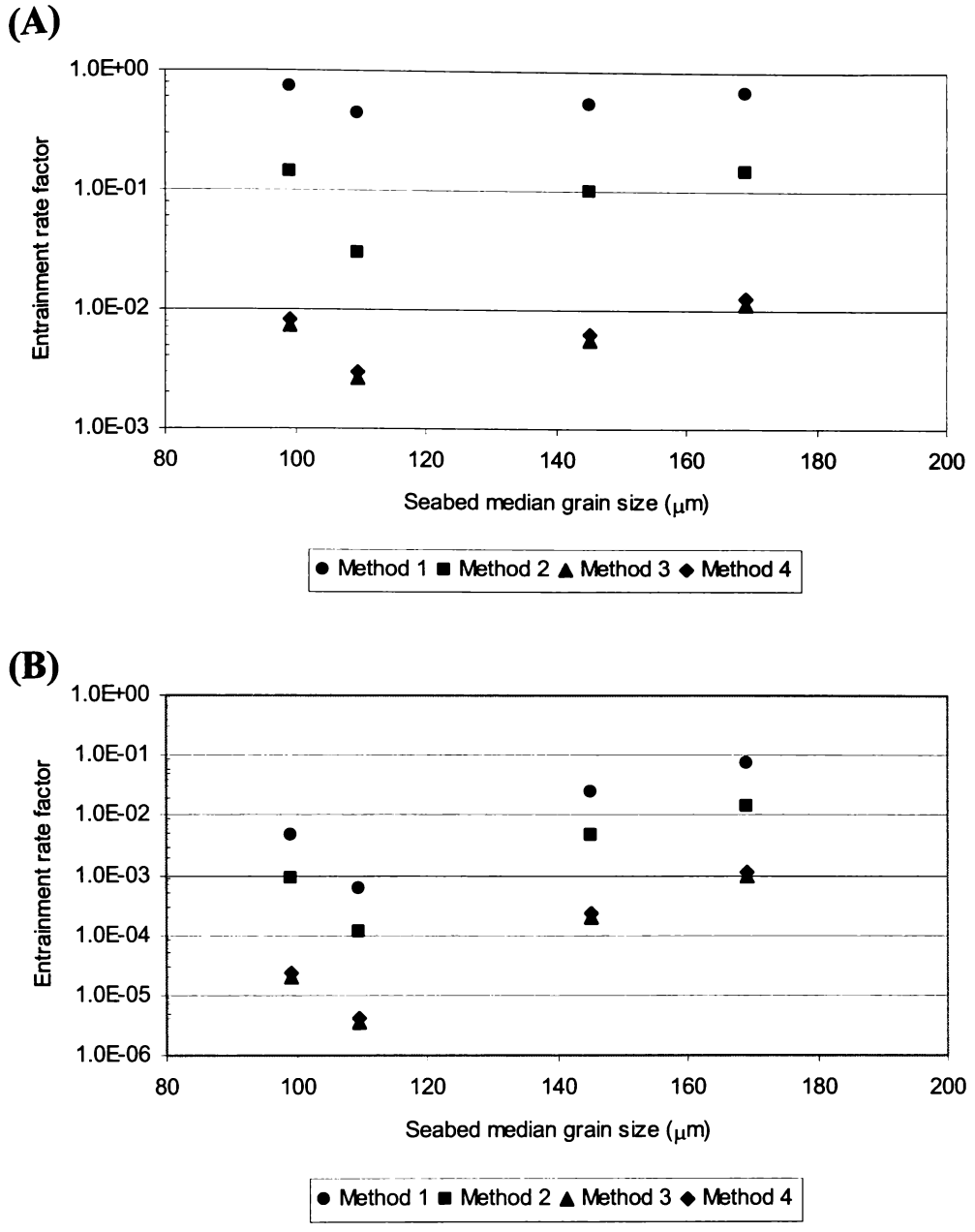

Figure 6.11 No correlation is shown to exist between the median grain size of the surficial sediment and the entrainment rate regardless of the orbital statistic used to characterise U^* (U_3 and U_{max} respectively for A and B) or the method of accounting for the effects of bedload sediment transport and the presence of bedforms on sediment entrainment (Table 6.1).

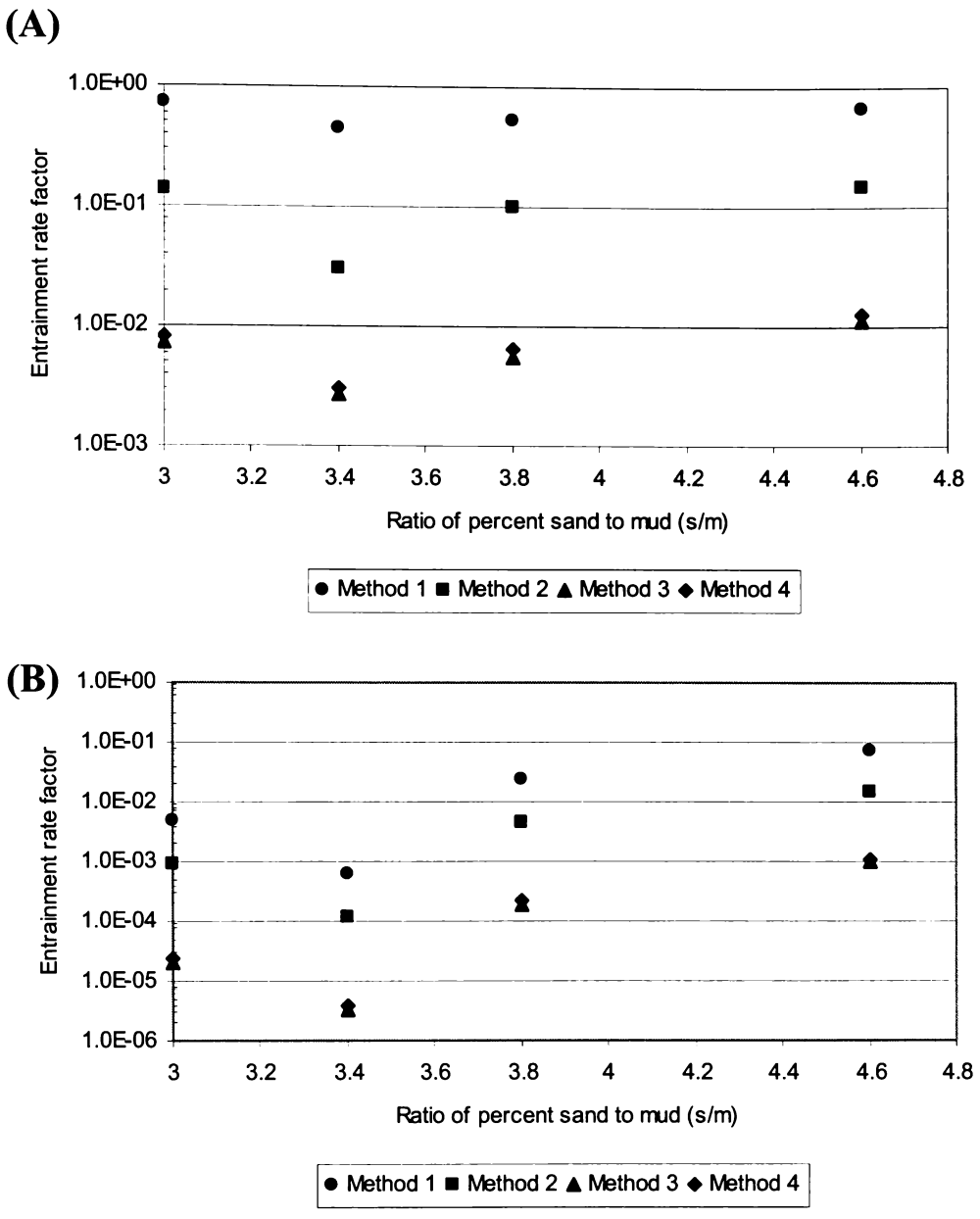

Figure 6.12 No correlation is shown to exist between the ratio of volume percent sand to mud in the surficial sediment and the entrainment rate regardless of the orbital statistic used to characterise U^* (U_3 and U_{max} respectively for A and B) or the method of accounting for the effects of bedload sediment transport and the presence of bedforms on sediment entrainment (Table 6.1).

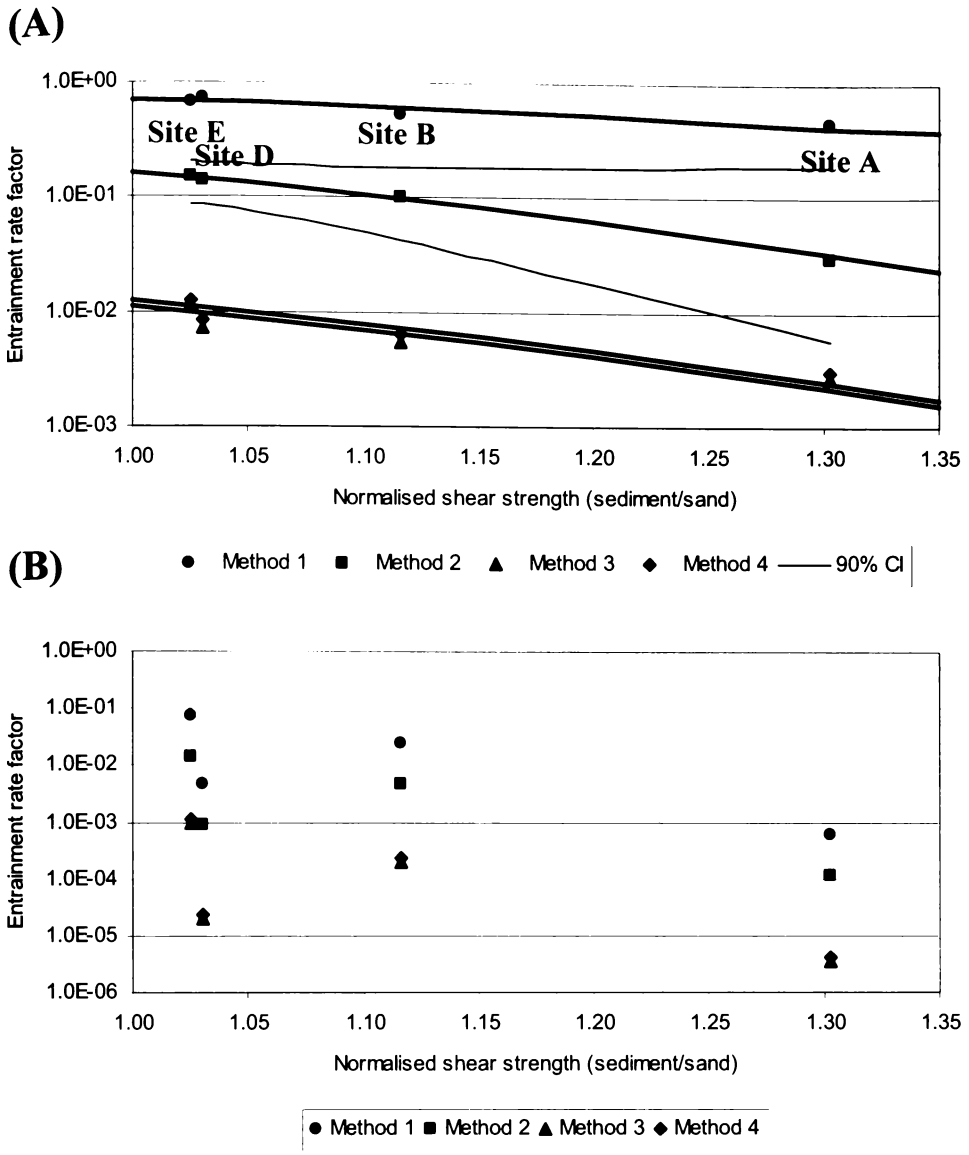

Figure 6.13 Characterising the friction velocity (U^*) using the relatively stable third moment of the horizontal orbital velocity (U_3) results in a good correlation ($R^2 > 0.76$, Table 6.05) between the entrainment rate factor and the normalised in-situ shear strength of the surficial sediment (**A**). In contrast, when U_{max} is used to characterise the friction velocity no correlation is observed between the entrainment rate factor and the normalised shear strength (**B**).

Chapter 7. Downward settling flux profile evolution using reconstituted fall velocity distribution

"*What language is thine, O sea?*
The language of eternal question" - Tagore

7.1 Introduction

This chapter applies the findings from Chapter 5 and 6 over a broader temporal scale in order to determine their suitability in predicting sediment fluxes. An understanding of the sediment fluxes is central in estimating infilling rates of the port of Gisborne shipping channel. Estimated near-bed reference concentrations from an autonomous water sampler are compared with theory predicted C_0 values inclusive of in-situ shear strength following the findings of Chapter 6. Additionally, the dependency of sediment traps on the fall velocity statistic used to convert downward sediment fluxes to time-averaged *SSC* in a mixed sand/mud environment is investigated, and a method for estimating the effective fall velocity distribution from pumped water samples is proposed.

7.2 Background

While Chapters 5 and 6 describe the suspension and entrainment characteristics of mixed sand/mud sediment at a time-scale of 1-minute, to provide confidence in predicting sediment entrainment and transport characteristics over a longer time-period the extrapolation of the findings to a broader temporal scale needs to be addressed. The labour and logistical intensity associated with a pump sample array such as used in Chapters 5 and 6 make the system impractical for use over a broader temporal scale. However, actual measurements of suspended sediment concentration (*SSC*) can be achieved using autonomous water samplers, set to sample at specific times. While autonomous water samplers usually provide only a series of single measurements of the *SSC*, results from Chapters 5 and 6 provide the confidence to extrapolate the single *SSC* measurement to the seabed in order to estimate the near-bed reference concentration (C_0). Pumped water/sediment samples have an advantage over other methods in predicting or estimating the near-bed reference concentration in that they provide a direct measurement of the *SSC* and do not suffer from theoretical considerations or grain size/fall velocity dependencies.

Sediment traps offer an alternative method of estimating the near-bed reference concentration by providing representative time-integrated measurements of the settling of suspended material (Boyce et al., 1990; White, 1990). Kraus (1987) notes that sediment traps have several advantageous features including being relatively inexpensive, low maintenance, easy to operate and provide actual measurement of the sediment that is being transported by waves and currents. Further, Kraus (1987) notes that sediment traps can provide masses, grain size distributions and vertical distributions of the downward sediment flux ($kg.m^{-2}.s^{-1}$) which, given the fall velocity (w_f) of the entrained sediment can be converted to a time-averaged suspended sediment concentration. The fall velocity statistic used to convert the downward sediment flux to a time-averaged *SSC* is derived post retrieval of the sediment trap from the captured sediment; either as an equivalent fall velocity based on a known relationship to the grain size, or as the measured fall velocity (Flint, 1998). One of the disadvantages associated with sediment traps is that the results are crucially dependant on the fall velocity statistic or distribution used to convert the downward sediment flux to the time-averaged C_0. Armanini and Ruol (1988) note that in many cases the median diameter alone is not able to represent correctly the concentration distribution, and suggest in order to overcome these limitations it is convenient to divide the distribution curve into a discrete number of classes. The

total near-bed reference concentration can be determined as the sum of the C_0 values from the individual classes. While the equivalent fall velocity of the median grain size (d_{50}) may be applicable when investigating suspended sand sized particles, the d_{50} of a dispersed mixed sand/mud grain size distribution in which flocculation is important may have no correlation to the actual d_{50} of the flocculated entrained sediment distribution. Because of the numerous parameters affecting flocculation of fine sediment (i.e. salinity, temperature, turbulence, organic content etc) the determination of the in-situ w_f distribution under laboratory conditions is difficult (Berlamont et al., 1993). Additionally, in environs where significant quantities of relatively fine sediment are being entrained and particle flocculation is expected, the dispersed w_f distribution is not likely to be a true representation of the effective w_f distribution (Berlamont et al., 1993; Mehta et al., 1989; Mitchener and Torfs, 1996). Further, Berlamont et al., (1993) notes that it is the effective w_f of the flocculated particles that is the salient parameter for sediment particles in suspension, governing the transport processes. As such, in order to determine sediment fluxes from sediment trap data within a mixed sand/mud environment, such as that of northern Poverty Bay, the process of flocculation and its effect on the downward settling flux needs to be addressed.

7.3 Method

7.3.1 Field data collection

For a 89 day period between 10/03/99 and 07/06/99 a data collection program consisting of wave and current measurement, autonomously collected pumped water/sediment samples, surficial sediment characteristic measurements, and sediment trap deployments was conducted at a site adjacent to the port of Gisborne shipping channel (Figure 7.01).

Wave and current characteristics were measured using an *InterOcean* S4ADW current meter recording 9-minute bursts of wave and current characteristics at a frequency of 2 Hz every two hours.

Daily pumped water/sediment samples were collected autonomously using a Hydrocamel™ water sampler (Figure 7.02); while the downward sediment flux was measured using sediment traps (Figure 7.03). While the pumped samples and pumping mechanism are housed within the bulk of the Hydrocamel™ the actual intake nozzle was located approximately 4 m distant from the Hydrocamel, thereby limiting the potential impact turbulence associated with the flow of water past the Hydrocamel™ might have of the value of the *SSC*. The Hydrocamel™ intake nozzle was located adjacent to the wave and current meter, facing perpendicular to the dominant direction of the near-bed wave orbital velocities. The Hydrocamel™ water sampler provides for 20 samples to be collected. As such it was necessary to retrieve and re-deploy the instrument several times during the survey period (i.e. 10/03/99 and 07/06/99). For each deployment care was taken to ensure that the nozzle was orientated correctly (i.e. perpendicular to the dominant direction of the near-bed wave orbital velocities), and the elevation of the nozzle was noted, and never more than 0.15 m above the seabed. The sediment traps were constructed from 90 mm diameter by 400 mm long PVC pipes, with an aperture at the top to allow settling of

sediment into the cavity of the trap. Two or more sediment traps were deployed simultaneously at different elevations to provide downward flux sediment profile characteristics (the elevations of which varied between deployments). Both instruments were serviced at approximately 3-week intervals, during which time representative surficial sediment samples were collected from the top 2-5 cm of the seabed, and bedform dimensions were measured. Grain size analysis for three sub-samples from each of the surficial sediment samples was preformed to ensure that an accurate estimate of the surficial sediment grain size was obtained. In addition, the in-situ shear strength of the surficial sediment was measured using a Geonor hand-held shear vane (Figure 7.04).

7.3.2 Dispersed Grain size and fall velocity determination

In order to allow comparisons between experiments, the sediment collected within the pumped samples and sediment traps, as well as the seabed sediment, was treated identically throughout all experiments within this study.

Pumped water-sediment samples were divided by mechanically mixing each sample into a homogeneous solution and sub-sampled with a pipette, allowing for the evaluation of both *SSC* profile characteristics and grain size textural parameters. The sub-sample of the pumped water samples and the representative sub-sample of both the sediment collected within the sediment trap and the surficial sediment were dispersed and organic matter removed following the procedure outlined in Chapter 4 and 5.

A Malvern laser light diffraction particle size analyser (Model MSS17) was used to determine the entire dispersed sand and mud grain size distribution of the surficial and suspended sediment, while grain size textural characteristics were calculated using the Malvern software, which also allowed the volume percent of individual grain size bins to be determined.

Equivalent fall velocities (w_f) of the dispersed grain size distribution were calculated using the equation described by Gibbs et al., (1971) as given in Chapter 5 (eqn 5.01).

7.3.3 Predicted near-bed reference concentration.

A near-bed reference concentration time series was predicted following the methodology outlined in Chapter 6, section 6.3.3. The method assumes the entrained sediment is non-cohesive. In keeping with the findings of Chapter 6, a correction factor has been applied to the Shields parameter (ψ') to account for the effect enhanced flow near the crest of vortex ripples has on sediment entrainment (eqn 6.09). The measured ripple height (η) and wavelength (λ) as defined in Table 7.01 were used to determine the modified effective Shields parameter (ψ'').

The predicted near-bed reference concentration assuming non-cohesive sediment transport and entrainment is compared with the estimated C_0 from pumped samples. Additionally, knowing the in-situ shear strength of the surficial sediment, eqn 6.23 is used to predict C_0 accounting for the effect of cohesion on the entrainment, and results compared with the estimated C_0 from pumped samples. Because the in-situ shear strength varied during the experiment period (Table 7.01), the average shear

strength for the entire period (2.18 kPa) is used in equation 6.14 when determining the near-bed reference concentration.

7.3.4 Sediment diffusivity, fall velocity and mixing lengths characteristics

Because the pumped water samples from the Hydrocamel do not provide information on the *SSC* profile, profile characteristics have been inferred from the entrainment and profile experiment Site D (Chapter 5 and 6). Site D is comparable in terms of both surficial sediment characteristics and water depth to that of the Hydrocamel deployment site.

Beamsley et al. (2001a) note that normalised *SSC* profiles for the individual grain size bins have a distinct concave-up shape, and vary as a function of grain size. Assuming purely diffusive, then implicitly the sediment diffusivity would need to vary as a function of fall velocity in order to explain the variation in *SSC* profile shape. Assuming pure gradient diffusion and a steady concentration component C_z, then integration of equation 5.08 (Chapter 5) yields,

$$w_f C_z + \varepsilon_s \frac{dC_z}{dz} = 0 \tag{7.04}$$

Equation 7.04 can also be written as,

$$\frac{d}{dz}\ln(C_z) = -\frac{w_f}{\varepsilon_s} \tag{7.05}$$

Solving eqn 7.05 for fall velocity (w_f) gives

$$w_f = -\frac{d}{dz}\ln(C_z) \times \varepsilon_s \tag{7.06}$$

Given that the mixing length (l_s) is defined as the negative reciprocal of the change in the natural log of concentration with elevation, such that,

$$l_s = -\frac{1}{d/dz \ln(C_z)} = -1/\alpha \tag{7.07}$$

Equation 7.06 can be written as,

$$w_f = \varepsilon_s / l_s \tag{7.08}$$

The mixing length for individual grain size fractions is measured from the pumped suspended sediment concentration profile, while the sediment diffusivity (ε_s) can be estimated as a function of fall velocity (eqn 7.08).

As the friction velocity (U^*) and the eddy viscosity (ε_f) are measures of the fluid turbulence and are constant for all grain sizes in suspension within a specific *SSC* profile, then, given the asymptotic relationship between β (= $\varepsilon_s/\varepsilon_f$) and the ratio of the fall velocity to the friction velocity (w_f/U^*) illustrated by eqn 5.24 (Chapter 5), a similar asymptotic relationship can be assumed to exist between ε_s and the effective w_f, such that,

$$\varepsilon_s = fn\left(w_f\right) \tag{7.09}$$

where, in the case of flocculation, w_f is the effective fall velocity.

The form of the equation relating ε_s to w_f will depend on the relationship between U^* and ε_f and need not be of a similar form to that of eqn 5.24, however an asymptotical increase in sediment diffusivity is expected with increased fall velocity.

Given eqn 7.09, it can be expected that the individual grain size fractions that constitute a flocculated particle will have identical sediment diffusivities, and hence concentration profiles shapes. As such, the approximate grain size/fall velocity at which particle flocculation begins should be manifested in the clustering of sediment concentration profiles. Assuming a constant ε_s for the clustered *SSC* profiles, then an approximation of the flocculated fall velocity distribution can be reconstituted using eqn 7.08.

While it is unlikely that the sediment collected by the sediment traps had identical flocculated fall velocity characteristics to the sediment in suspension at Site D (Chapter 5 and 6), this Chapter will illustrate that the use of the reconstituted fall velocity distribution provides a robust method of predicting the time-averaged suspended sediment concentration from the downward flux as measured by sediment traps.

7.3.5 Time-averaged near-bed reference concentration

7.3.5.1 Estimated C_0 from pumped water/sediment samples

Pumped water/sediment samples from the Hydrocamel™ were used to estimate near-bed reference concentrations using the time-averaged convection-diffusion equation as defined by Nielson (1986), Chapter 5 eqn 5.09 (given that near the bed the concentration profile is essentially linear in log-linear space; Section 6.3.4.1). As the Hydrocamel provides only a *SSC* measurement at a single level (C_z), *SSC* have been extrapolated to the seabed using eqn. 5.9 and assuming a mixing length of 0.15. The value of $l_s = 0.15$ is consistent with the findings from Chapter 5, i.e. median mixing length value; Site D (section 5.4.3). Near-bed reference concentrations are determined by summation of the C_0 of the individual grain size fractions within the distribution.

7.3.5.2Estimated C_0 from sediment trap downward sediment flux measurements

The deployment duration in seconds (T_d) and the mass of sediment trapped within each of the sediment traps (M) allows the downward sediment flux (f_d) to be determined, where

$$f_d = {}^{M}\!/_{A}\!/_{T_d} \tag{7.10}$$

in which A is the area of the aperture through which the sediment settles.

The time-averaged suspended sediment concentration (C_z) is determined as a function of the sediment fall velocity (w_f), such that,

$$C_z = {}^{f_d}\!/_{w_f} \tag{7.11}$$

Equation 7.11 illustrates that the determination of the time-averaged suspended sediment concentration from sediment trap data is critically dependant on the fall velocity.

Typically, in the absence of a measured fall velocity distribution, an equivalent fall velocity is inferred from the grain size characteristics using some empirical relationship such as that proposed by Gibbs et al. (1971), i.e. eqn 5.1.

Three methods are investigated in order to establish the most suitable means of accounting for the dependency of the sediment traps on fall velocity in the evaluation of the near-bed reference concentration,

i. Determined from the summation of C_0 values for individual equivalent fall velocity fractions within the entire dispersed grain size distribution,
ii. C_0 determined using the equivalent fall velocity of the dispersed median grain size (d_{50}) of the sediment captured within the sediment trap, and
iii. Determined from the summation of C_0 values for individual effective fall velocity fractions within the distribution,

The equivalent fall velocities in Methods *i.* and *ii.* are derived directly from the dispersed grain size distribution of the trapped sediment using eqn 5.01, while the effective fall velocity is inferred in the following sections from pumped *SSC* measurements from Site D, which is comparable in terms of depth and sediment characteristics (Chapter 5), and assuming eqn. 7.08.

7.4 Results

7.4.1 Temporal seabed sediment and bedform characteristics

Table 7.1 lists the experimental site surficial sediment characteristics. Grain size (d_{50}, mode), in-situ shear strength and bedform dimensions are shown to vary during

the monitoring period. The variations in the statistical measures of the grain size distribution are consistent with the changes in mud and sand percentages.

The in-situ shear strength is shown to increase with decreasing grain size, and an increasing proportion of mud within the sediment distribution (Figure 7.05 and 7.06). The relationship between the sediment grain size characteristics and the in-situ shear strength is consistent with findings in Chapter 4.

The predominant bedforms observed at the experiment site were symmetrical ripples, presumably formed by near-bed wave orbital velocities. The ripple wavelength (λ) and height (η) is found to vary throughout the experiment, presumably in response to the wave-orbital velocities. A correlation is shown to exist between the median grain size (d_{50}) of the surficial sediment and the steepness of the rippled bedforms ($=\eta/\lambda$), with steepness increasing with increasing grain size (Figure 7.07). Not surprisingly a strong relationship between the volume percent mud in the grain size distribution and the ripple steepness is also found (Figure 7.08).

7.4.2 Wave statistics, residual current and near-bed orbital velocity characteristics

Significant wave heights (H_s) and peak spectral wave periods (T_p) between 10/03/99 and 15/06/99 are illustrated in Figure 7.09. H_s varied between less than 0.5 m to approximately 2.5 m, while T_p ranged between approximately 4 s to 18 s. The wave record illustrates several relatively large wave events occurred during the survey period, with the largest and longest in duration occurring in the period 30/04/99 to 05/05/99. During this time the significant wave height was consistently 1.5 m or more, peaking at $H_s = 2.5$ m. All wave and current data have been filtered within the range 0.04 to 0.2 Hz to ensure that only entrainment due near-bed wave orbital velocities is being considered.

Residual near-bed current magnitude and directions are illustrated in Figure 7.10. The residual current speed has an average of 0.17 $m.s^{-1}$ and a standard deviation of 0.02 $m.s^{-1}$, while the median current is directed towards 146°T.

Figure 7.11 shows the maximum, root-mean squared and third moment (as defined in eqn 5.07) principle near-bed orbital velocity. Not surprisingly a strong correlation is displayed between the magnitude of the near-bed orbital velocity statistic and H_s (Figure 7.11 and 7.09 respectively).

7.4.3 Sediment diffusivity and effective fall velocity

In the marine environment where water salinity is relatively large all clay particles become cohesive, and the dominance of inter-particle cohesion over gravitational forces increase with decreased particle size (Mehta et al., 1989). As such, it is probable that the mud sized portion of the grain size distribution, and particularly particles finer than coarse silt (~ 41 μm, i.e. $w_f < 0.0013$ $m.s^{-1}$) will experience some flocculation.

The variation in the sediment diffusivity as a function of the equivalent fall velocity (w_f) within the range $w_f > 0.0013$ m.s^{-1} (i.e. 41 μm) is illustrated in Figure 7.12 (determined using the methodology outlined in section7.3.4). Regression analysis of the relationship illustrates that there is a strong correlation between the equivalent w_f of the dispersed grain size distribution and the sediment diffusivity ($R^2 > 0.90$ for all profiles) as determined from eqn. 7.08, with the relationship of the form,

$$\varepsilon_s = a + b\exp^{-w_f} \tag{7.12}$$

in which the parameters a and b are measures of the turbulent diffusion of the sediment, and vary between profiles. The relationship is asymptotic in log-linear space and suggests limited variation in the sediment diffusivity for $w_f < 0.0013$ m.s^{-1}. Although, the exact size of the flocculated particles is not known, the asymptotic relationship suggests that under turbulent flow the particles with fall velocities within the range $w_f < 0.0013$ m.s^{-1} essentially behave identically within the suspended sediment concentration profile, i.e. similar sediment diffusivities.

Figure 7.13 shows concentration profiles for individual fall velocity bins within the distribution from a site in 10 m water depth with sediment characteristics similar to that of the shipping channel (i.e. Site D). The concentration profiles are shown to cluster at 0.0005 m.s^{-1} $< w_f <$ 0.0017 m.s^{-1} indicating that the sediment with $w_f <$ ~0.0017 m.s^{-1} are experiencing similar distribution characteristics within the *SSC* profile, suggestive of flocculation.

7.4.2.1Calculation of the effective fall velocity distribution

Assuming uniform ε_s for the range $w_f < 0.0013$ m.s^{-1} and knowing the mixing length of the individual dispersed grain size fractions from the distribution based on Site D, then from eqn 7.08 the effective fall velocity (w_{fc}) of the relatively fine fraction of the grain size distribution is obtained.

Figure 7.14 illustrates the grain size distribution of the dispersed equivalent w_f and the reconstituted effective fall velocity (w_{fc}) from a site in similar water depth and with similar sediment characteristics. The distribution of the reconstituted effective fall velocity is relatively coarser than the dispersed w_f distribution, with a shift in d_{50} from 35 μm to 48 μm. The effective fall velocity represents the approximate flocculated fall velocity distribution.

7.4.4 Estimated and predicted C_0 from pumped samples and theory

Figure 7.15 illustrates the predicted near-bed reference concentration time-series based on U_{max}, U_{rms} and U_3 orbital statistic. Figure 7.15 also shows the estimated near-bed reference concentrations as determined from the pumped water samples. The pumped water samples provide a direct measurement of the *SSC* that is not dependant on fall velocity. The total error (ζ) between the estimated and predicted near-bed reference concentrations for each of the instances where predicted and estimated C_0 values are available is determined as,

$$\zeta = \sum_{i=1}^{n} \frac{\left(C_{0\,i}' - C_{0\,i}^{*}\right)^2}{(C_{0\,i}^{*})^2} \qquad (7.13)$$

where C_0', and C_0^* are the predicted and estimated near-bed reference concentrations respectively. Table 7.02 lists the total error for each of the variations in orbital statistic used to characterise the friction velocity, and the effect of including and excluding the in-situ shear strength in the prediction of the near-bed reference concentration.

Smallest total errors were achieved when U^* was characterised using U_3 and the effect of cohesive bonding of the surficial sediment is accounted for following the findings of Chapter 6 (Table 7.02). Comparatively, when U^* is characterised using the root-mean-squared orbital velocity or the maximum orbital velocity within the 9-minute time-series the fit of predicted to estimated C_0 is poor. Classifying U^* using U_{rms} results in predicted C_0 values consistently less that those estimated from the pumped water samples. When U_{max} is used to determine the friction velocity (U^*) predicted C_0 values are consistently larger than the estimated values (Figure 7.15), and the total error is relatively large (Table 7.02).

7.4.5 Comparison between pumped and trapped C_0 estimates

Sediment trap deployment details are listed in Table 7.03, including deployment and retrieval times, trap elevations and median and modal peak(s) grain sizes.

Equation 7.11 illustrates that the evaluation of the time-averaged suspended sediment concentration is crucially dependant on the value of the equivalent fall velocity used. Figure 7.16 illustrates the variation between the estimated C_0 from the pumped water samples and the estimated time-averaged near-bed reference concentrations from the sediment trap data as estimated using,

i. the summation of C_0 values for individual equivalent fall velocity fractions within the dispersed grain size distribution,
ii. C_0 determined using the equivalent fall velocity of the dispersed median grain size (d_{50}) of the sediment captured within the sediment trap, and
iii. the summation of C_0 values for individual effective fall velocity fractions within the distribution as determined from equation 7.08 assuming a constant sediment diffusivity within the range $w_f > 0.0013$ m.s^{-1}.

When the time-averaged near bed reference concentration is determined using method (*i*) the total C_0 value is significantly over-estimated (i.e. several orders of magnitude) due to the w_f dependency of equation 7.11 Figure 7.16). Additionally, a poor correlation is shown between the pumped sample estimated C_0 values and the sediment trapped time-averaged C_0 when d_{50} of the trapped sediment is used to determine the time-averaged *SSC* (method ii, Figure 7.16). Using the reconstituted effective fall velocity distribution, as measured from pumped water sample *SSC* profiles (section 7.3.2), is shown to provide a satisfactory and more robust estimate of the time-averaged near-bed reference concentrations (Figure 7.16).

Assuming that the average estimated pump concentration each of the trapping periods is representative of the actual time-averaged sediment concentration, then the lowest total error between the time-averaged estimated C_0 from the pumped samples and the C_0 estimated from the sediment traps is achieved using the reconstituted effective fall velocity distribution (Table 7.04). Using either the entire dispersed fall velocity distribution or the equivalent fall velocity of the median grain size results in significantly larger total errors (Table 7.04).

Further, using the reconstituted fall velocity distribution to determine the time-averaged C_0 from the sediment trap data results in a good agreement with the predicted C_0 values when the U_3 is used to characterise the friction velocity and the effect of the in-situ shear strength is accounted for (Figure 7.17).

Comparing the time-averaged C_0 from the predicted time-series and those estimated from the sediment traps using the estimated fall velocity distribution indicate that the lowest total error (ζ) is achieved (Table 7.04). Other variations of the orbital statistic used to define U^* and the fall velocity distribution used in estimating the time-averaged C_0 from the sediment trap data result in significantly larger total errors (Table 7.04). Figure 7.17 compares the time-averaged C_0 value from the sediment trap deployments, determined using the reconstituted effective fall velocity distribution, and the C_0 time-series as predicted using U_3 to characterise U^* and accounting for the effect of in-situ shear strength on retarding sediment entrainment, and illustrates a good agreement between predictions.

7.5 Discussion

Surficial sediment characteristics including the in-situ shear strength are shown to vary during the survey period. The observed seabed characteristics at any one time are a function of the time-history of the seabed. Preferential settling of a suspended sediment distribution results in grain size and density increasing with depth into the seabed profile (Hayter, 1984; Mitchener and Torfs, 1996). The effect of preferential settling on bed structure can be enhanced due to flocculation, salt intrusion and the presence of plant material (Mitchener and Torfs, 1996). Further, Hayter (1984) notes shear strength increases with depth into the seabed profile, primarily as a function of increased compaction due to the overburden increasing the frictional resistance and the interlocking between particles (physical component), and the inter-particle forces (physico-chemical component). The variation in sediment characteristics and shear-strength with depth into the profile leads to characteristic erosional behaviour. When the fluid shear stress, τ, is less than the critical shear stress for erosion, τ_c, no erosion occurs, however when $\tau > \tau_c$ the seabed begins eroding and there is an initial high degree of suspended sediment. Initially, preferential erosion of fines into suspension and coarser, cohesive aggregates as bedload occurs, however as the seabed is eroded the in-situ shear strength and grain size of the eroding sediment increases and hence the magnitude of the suspended and bedload sediment decreases. This results in a two-phase erosional model (Figure 7.18) consisting of an initial fast phase of upper layer erosion, followed by a slower erosion of the lower layer (Kamphuis and Hall, 1983; Kuijper et al., 1989; Mehta, 1984; Mehta et al., 1989; Mitchener and Torfs, 1996). Given these erosional and depositional characteristics it is not unexpected to observe some variation in seabed sediment texture during the monitoring period in response to the presiding processes (i.e. deposition or erosional).

The ripples observed during the monitoring period are vortex ripples. Ripple steepness' range from 0.125 to 0.194 and are shown to increase with increasing volume percent sand within the surficial sediment, possibly in response to the increase in the angle of repose of the sediment. Alternatively, the steepness of the ripples and the volume percent sand in the surficial sediment may a function of the near-bed orbital velocities immediately prior to sampling (which can potentially cause winnowing out of the relatively fine fraction of the seabed grain size distribution and affect the characteristic of the ripples). The maximum measured ripple steepness value of 0.194 is close to the value of 0.2 as proposed by Nielsen (1992) based on experimental data. The in-situ shear strength of the surficial sediment is also shown to vary during the monitoring period, showing a tendency to increase with decreasing grain size, or increasing mud content (Figure 7.05 and 7.06), The correlation between grain size and in-situ shear strength is consistent with the findings of Beamsley, et al. (2001b).

Comparisons between the predicted and estimated near-bed reference concentrations from pumped water samples over the mixed sand/mud seabed where cohesion is important illustrate that the best correlation is achieved when U_3 is used to characterise the friction velocity (U^*), and in-situ shear strength is accounted for. The importance of accounting for in-situ shear strength in determining C_0 is consistent with the findings of Chapter 6, while the suitability of using a friction velocity characterised by U_3 is in keeping with the findings of both Chapter 6 and Black and Rosenberg (1992). Further, while from Chapter 6, U_3 was found to be the most robust orbital statistic in predicting C_0 over a 1-minute burst, results from this experiment indicate that U_3 is also the most suitable orbital statistic in determining U^* for the evaluation of C_0 over longer periods (i.e. 9 minutes bursts). Black and Rosenberg (1992) found that the U_3 statistic corresponds approximately to the 92nd percentile of the velocity distribution, while data from this experiment indicates that U_3 is on average slightly less than $U_{1/10}$ (i.e. the 90th percentile of the velocity distribution, Figure 7.19). The suitability of using U_3 to describe the friction velocity is in keeping with the findings of Kos'yan (1985), who suggested that the 85-90th percentile velocity was most suitable for natural beaches.

Comparisons between the time-averaged C_0 from sediment trap data and those estimated from the pumped *SSC* measurements illustrate that C_0 is crucially dependant on the value of the equivalent w_f used to convert the downward settling flux to a time-averaged suspended sediment concentration. Using the dispersed equivalent w_f distribution results in unrealistically large estimated time-averaged C_0, several orders of magnitude larger than those estimated by pumped water samples (Figure 7.16). Likewise, a poor correlation is achieved by using the equivalent w_f of the median grain size from the dispersed distribution (Figure 7.16).

Given the percent mud in the surficial and entrained sediment, it is likely that flocculation of the relatively fine particles is occurring, in which case the dispersed fall velocity distribution would not be a true representation of the effective w_f distribution. It is the effective w_f of the flocculated particles that is the salient parameter for sediment particles in suspension, governing the transport processes (Berlamont et al., 1993). Given that the individual particles that constitute an aggregated particle will experience identical sediment diffusivities (ε_s), and assuming flocculation of the relatively fine proportion of the dispersed distribution, then the reconstituted w_f distribution as illustrated in Figure 7.14 can be expected to

approximate the flocculated distribution, or at the very least represent the behaviour of the sediment in suspension.

Assuming that the time-averaged C_0 for each of the sediment trap deployment durations can be represented by the average of the estimated C_0 from the pumped samples during the same duration, then lowest total error between the sediment trap estimated C_0 and the pumped water sample estimated C_0 is achieved when the reconstituted fall velocity distribution is used to convert the downward settling flux to a suspended sediment concentration (Table 7.04). Further, using the reconstituted fall velocity distribution to determine the time-averaged C_0 also results in the best agreement with the predicted C_0 when U_3 is used to define U^* and the retardation of the sediment entrainment due to cohesive bonding is accounted for using the measured in-situ shear strength and the relationship derived in Chapter 6. The reconstituted fall velocity distribution is significantly different from the dispersed distribution and does not consist of unrealistic quantities of fine sediment (Figure 7.14).

Re-defining the fall-velocity distribution from the dispersed characteristics of the entrained sediment is shown to be a robust method of estimating the effective w_f distribution. The actual flocculated fall velocity distribution will be dependent on numerous parameters including, but not limited to, sediment mineralogy, concentration, and turbulence levels (Dyer and Manning, 1999; Fennessy and Dyer, 1996; Kranck, 1984; Mehta, 1984; Mehta et al., 1989; Milligan and Hill, 1997). The concentration and turbulence levels are in turn dependant on the magnitude of the dominant entrainment mechanism, i.e. near-bed wave orbital velocities, which varies during the recorded time-series. Therefore, the actual flocculated fall velocity distribution is likely to have varied during each of the trap deployments. Regardless, the effective w_f distribution results in a better correlation between sediment trap time-averaged C_0 and both C_0 predicted from theory or estimated from pumped water samples than either the entire dispersed fall velocity distribution or the equivalent w_f of the median grain size.

7.6 Summary

Seabed characteristics, including in-situ shear strength, grain size, and bedform dimensions have been found to be temporally variable at the experiment site adjacent to the port of Gisborne shipping channel. Preferential settling results in grain size increasing with depth into the seabed (Hayter, 1984; Mitchener and Torfs, 1996), and as such the variation of the seabed characteristics has been attributed to the evolution of the seabed in response to the presiding process, i.e. depositional and erosional. The observed variation in the surficial sediment in-situ shear strength is shown to be partly dependant on the surficial sediment texture, consistent with the findings of Chapter 4.

Comparisons with the estimated C_0 from pumped water samples indicate that, over a 9-minute burst period, a friction velocity (U^*) characterised using the orbital statistic U_3 provides the most consistent and robust predictions of the near-bed reference concentration. Further, accounting for the in-situ shear strength of the cohesively bound sediment was found to result in the lowest total error between predicted and estimated C_0. The findings are in agreement with results from Chapter 6 over the relatively shorter duration of 1-minute.

A comparison between the dispersed equivalent w_f within the range $w_f < 0.0013$ m.s^{-1} and the sediment diffusivity (ε_s) indicate an asymptotic relationship with sediment diffusivity decreasing with w_f. Below $w_f = 0.0013$ m.s^{-1} the sediment diffusivity is essentially constant within the *SSC* profile. Additionally, normalised *SSC* profiles of particles with dispersed equivalent w_f within the range $0.0005 < w_f < 0.0017$ m.s^{-1} are found to be similar. Given that particles with equivalent fall velocities below $w_f = 0.0013$ m.s^{-1} behave similarly within the concentration profile an effective w_f distribution is able to be determined using the measured mixing lengths (l_s) and assuming a constant sediment diffusivity (ε_s). The effective w_f distribution is found to be significantly different from the dispersed equivalent w_f distribution, and is assumed to approximate the flocculated w_f distribution, or at the very least describe the diffusion of the sediment within the concentration profile.

In mixed sand/mud environments the time-averaged C_0 estimated using sediment traps is found to be crucially dependant of the w_f statistic used to convert the downward sediment flux to C_0. Using the entire dispersed equivalent w_f distribution results in *SSC*, and hence C_0 estimates several orders of magnitude larger than those estimated from pump samples. Further, using the equivalent fall velocity of the median grain size (d_{50}) also resulted in a poor correlation to the C_0 estimated from the pumped samples. In contrast, using the effective w_f distribution as determined from pumped *SSC* measurements was found to result in the lowest total error between the C_0 estimated using the pumped and sediment-trapped data. Further, a good agreement between C_0 predicted from theory and estimated from trap data was achieved when the effective w_f distribution was used to estimate the time-averaged C_0 and C_0 was predicted using a friction velocity characterised by U_3 and cohesive bonding was accounted for following the findings of Chapter 6.

Table 7.01 Variation in the surficial sediment characteristics during the experiment period. The data illustrate that the volume percent of mud and sand within the surficial sediment varied during the experiment period and hence the mode and median grain size of the sediment. Ripple dimensions and in-situ shear strength are also shown to vary during the experiment period.

DATE	d_{50} (μm)	Mode (μm)	Sand %	Mud %	In-situ shear strength (kPa)	Ripple length (m)	Ripple height (m)	Ripple steepness
23/03/99	86	99	69	31	1.98	0.06	0.010	0.167
09/04/99	92	110	72	28	1.20	0.18	0.035	0.194
16/04/99	86	98	70	30	2.39	0.14	0.020	0.143
22/04/99	90	99	75	25	2.44	0.08	0.015	0.188
11/05/99	75	85	62	38	2.88	0.08	0.010	0.125

Table 7.02 Total error in the variation between predicted and estimated near-bed reference concentration. The predicted near-bed reference concentrations are determined from the time-series of near-bed orbital velocities, while the estimated C_0 are determined from pumped water samples. Different statistics of the near-bed orbital velocity are investigated to determine which provides the least error in predicted to estimated C_0. Also, the effect of in-situ shear strength on the predicted C_0 and the corresponding error is illustrated.

Orbital statistic	U_{max}		U_{rms}		U_3	
Method	In-situ shear strength not accounted for	In-situ shear strength accounted for	In-situ shear strength not accounted for	In-situ shear strength accounted for	In-situ shear strength not accounted for	In-situ shear strength accounted for
Total error	3173.11	7.84	0.91	0.97	7.92	0.88

Table 7.03 Sediment trap deployment information and modal and median grain size data of the captured sediment.

Deployment Number	Deployment date	Retrieval data	Trap elevation	Median grain size (μm)	Modal peak(s) grain size (μm)
1	10/03/99 15:45	23/03/99 16:00	0.41	14	11 and 59
	10/03/99 15:45	23/03/99 16:00	0.62	7	8
	10/03/99 15:45	23/03/99 16:00	0.92	16	18
2	23/03/99 17:45	09/04/99 11:06	0.44	27	53 and 6
	23/03/99 17:45	09/04/99 11:06	1.08	49	84, 15 and 7
3	16/04/99 17:00	22/04/99 16:30	0.42	75	97.67
	16/04/99 17:00	22/04/99 16:30	0.91	65	88 and 8
4	14/05/99 14:00	07/06/99 15:00	0.42	19	62 and 8
	14/05/99 14:00	07/06/99 15:00	0.66	19	53 and 8

Table 7.04 Total errors between the estimated time-averaged C_0 from the pumped samples and the time-averaged estimate from the sediment trap data. Lowest total errors (*highlighted*) occur when the trap estimated C_0 is determined using the re-constituted effective w_f distribution.

Method	Using entire wf distribution	Using equivalent w_f of d_{50} of the captured sediment	Using the reconstituted w_f distribution
Total error	1.04E+07	146.36	**0.05**

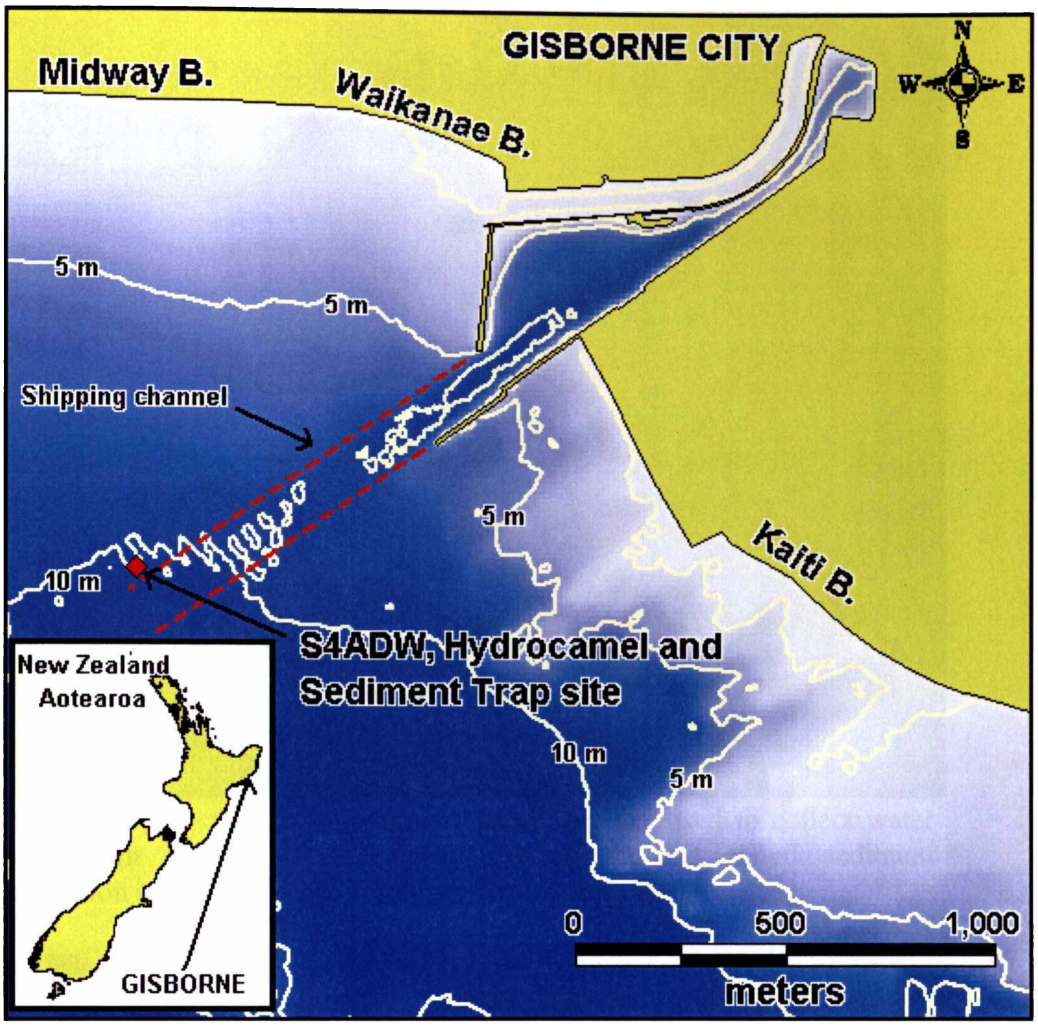

Figure 7.01 Location of S4ADW, Hydrocamel™ and sediment trap deployment site adjacent to the port of Gisborne shipping channel.

Figure 7.02 The Hydrocamel™ autonomous water sampler used to collect water and sediment samples for determination of the suspended sediment concentration and the near-bed reference concentration.

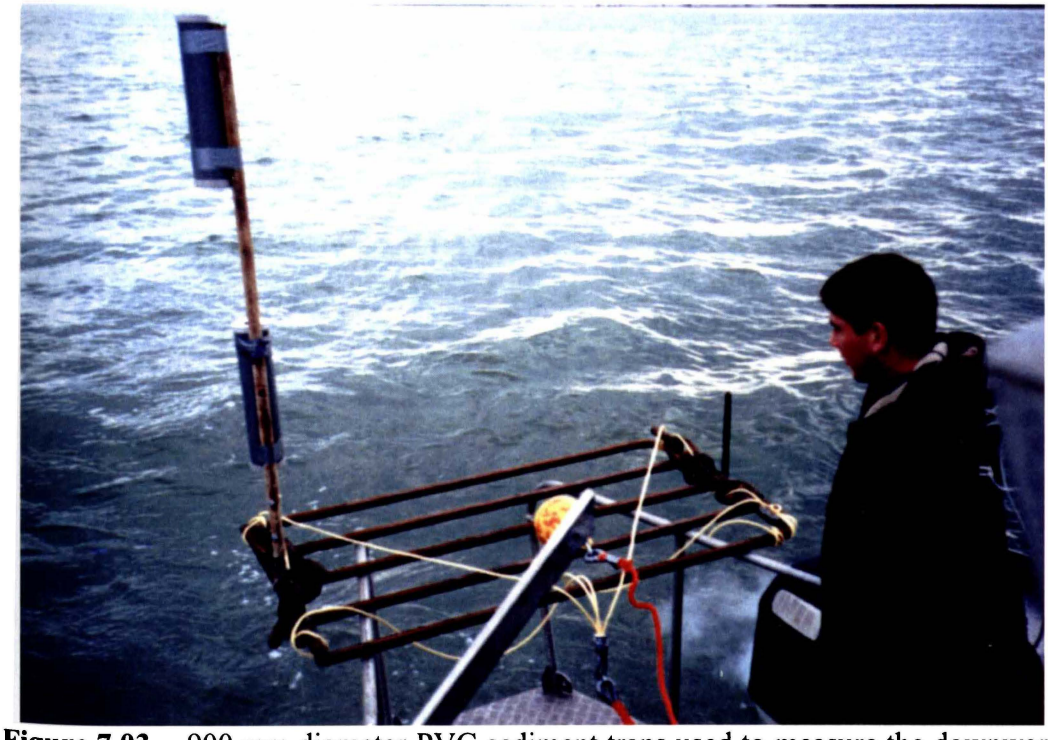

Figure 7.03 900 mm diameter PVC sediment traps used to measure the downward sediment flux adjacent to the port of Gisborne shipping channel (After Black et al., 1997).

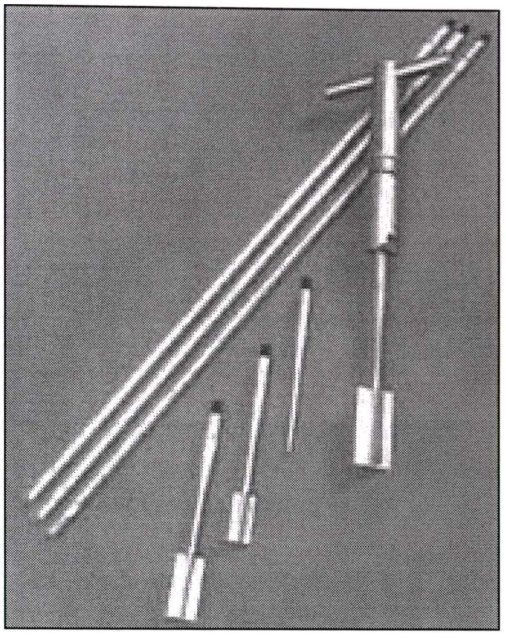

Figure 7.04 Geonor hand-held shear vane used for the determination of the shear strength of the surficial sediment.

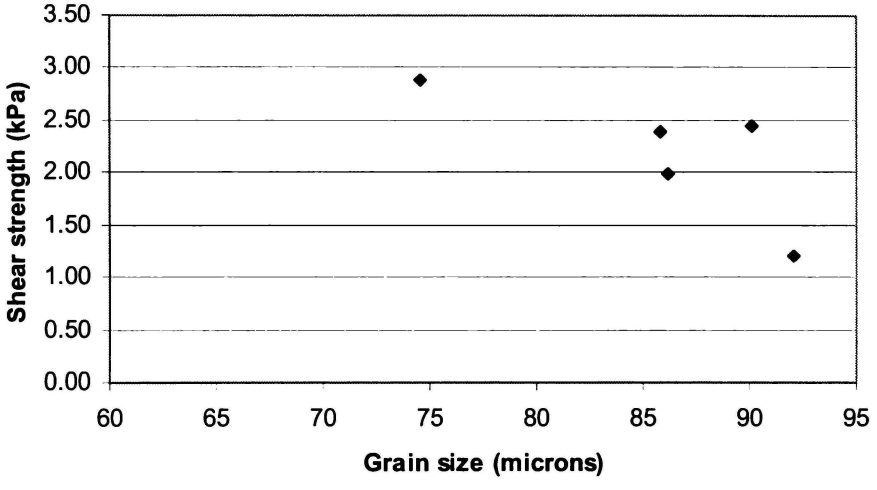

Figure 7.05 Correlation between the in-situ shear strength and d_{50} of the surficial sediment. In-situ shear strength shows a tendency to increase with decreasing d_{50}.

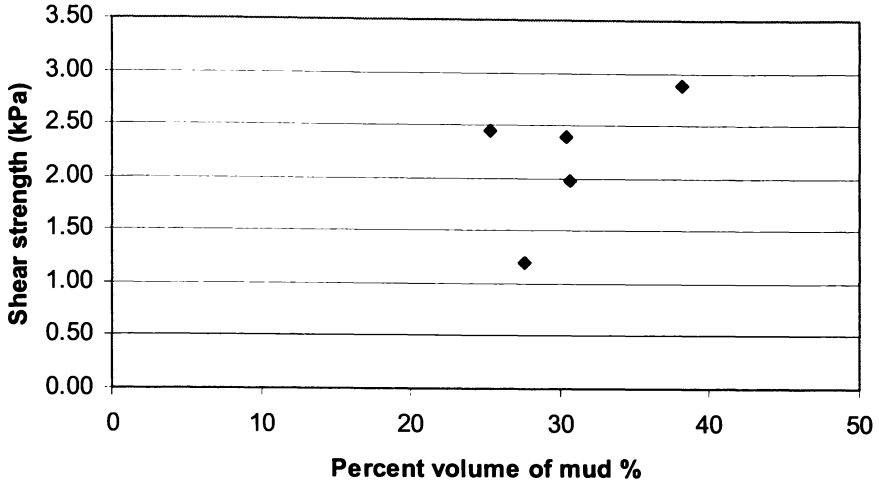

Figure 7.06 Correlation between the in-situ shear strength and the volume percent mud of the surficial sediment. In-situ shear strength shows a general trend to increase with increasing volume percent mud.

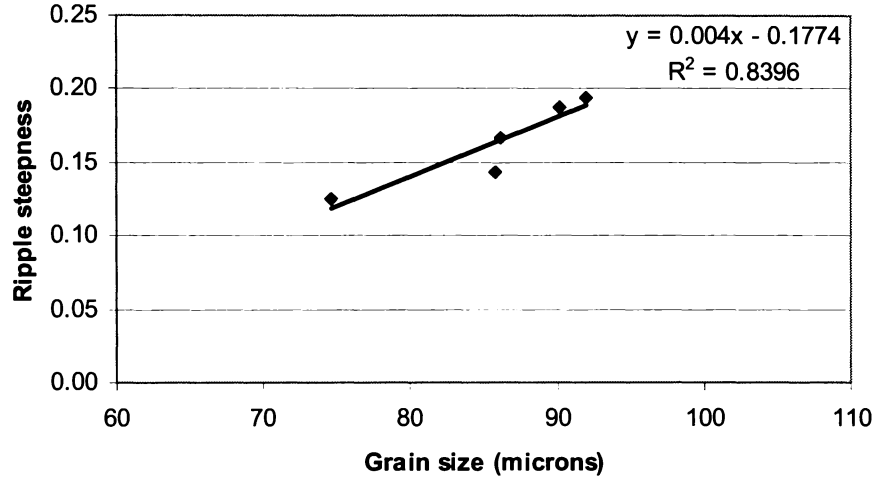

Figure 7.07 Correlation between the ripple steepness and the median grain size (d_{50}) of the surficial sediment. The ripple steepness is shown to increase with increasing d_{50}.

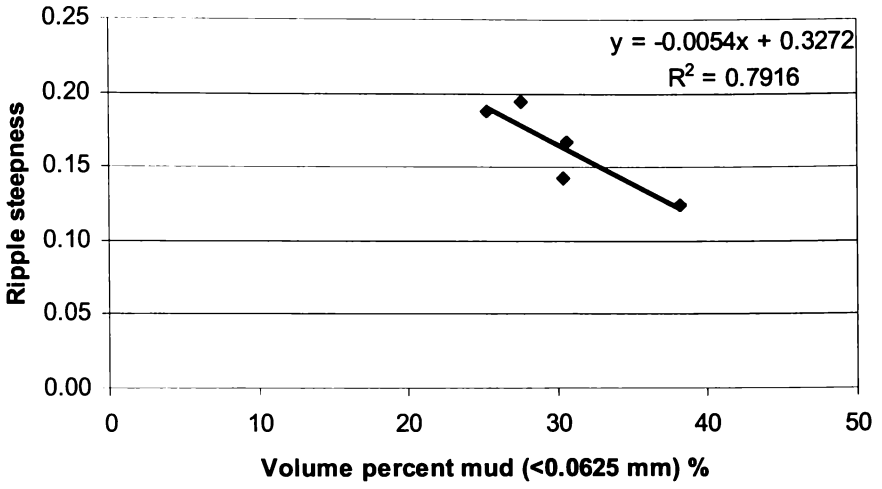

Figure 7.08 Correlation between the ripple steepness and the volume percent mud in the surficial sediment. The ripple steepness is shown to decrease with increasing mud content.

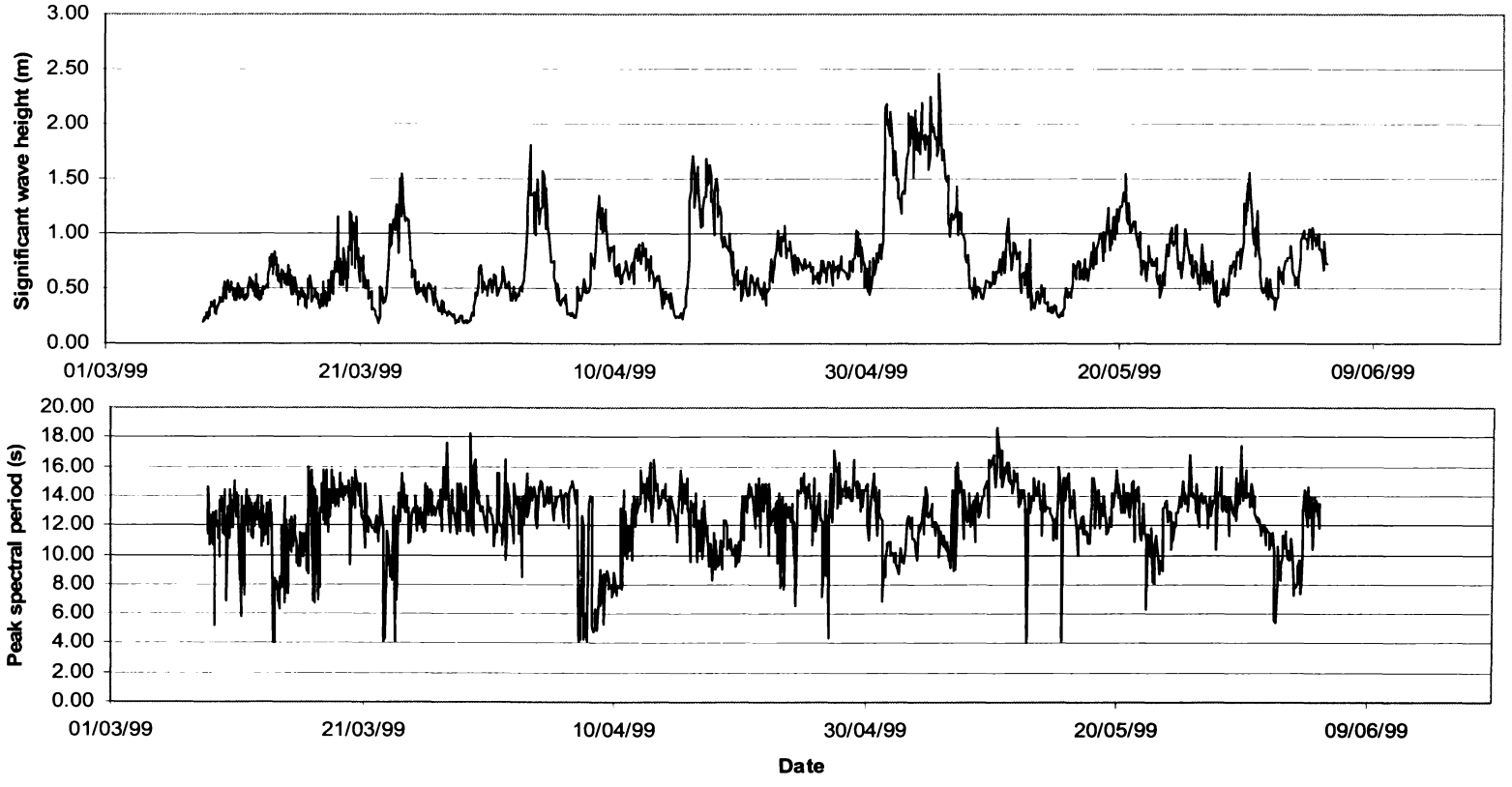

Figure 7.09 Significant wave height (H_s) and peak spectral wave period (T_p) between 10/03/99 and 15/06/99 at the experiment site adjacent to the port of Gisborne shipping channel. Significant wave heights vary from less that 0.5 m to more that 2 m, while the peak wave periods varied from approximately 4 s to more that 18 s. Wave statistics were recorded for a 9-minute burst every two hours at a frequency of 2 Hz using and *InterOcean* S4ADW wave current meter.

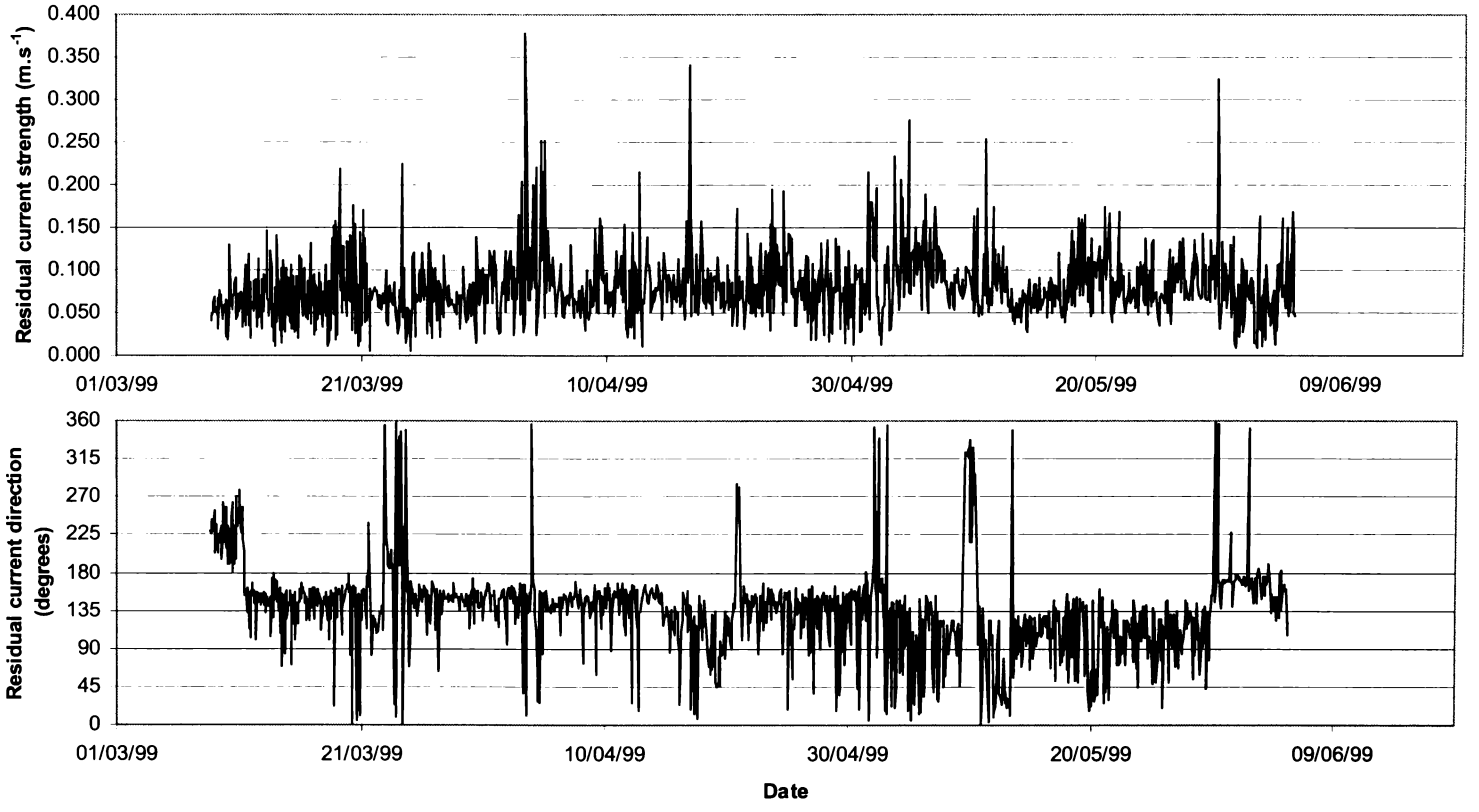

Figure 7.10 Residual current speed and direction between 10/03/99 and 15/06/99 at the experiment site adjacent to the port of Gisborne shipping channel as measured using an *InterOcean* S4ADW wave current meter. The average residual current speed is 0.17 $m.s^{-1}$, while the median current direction is 146°T

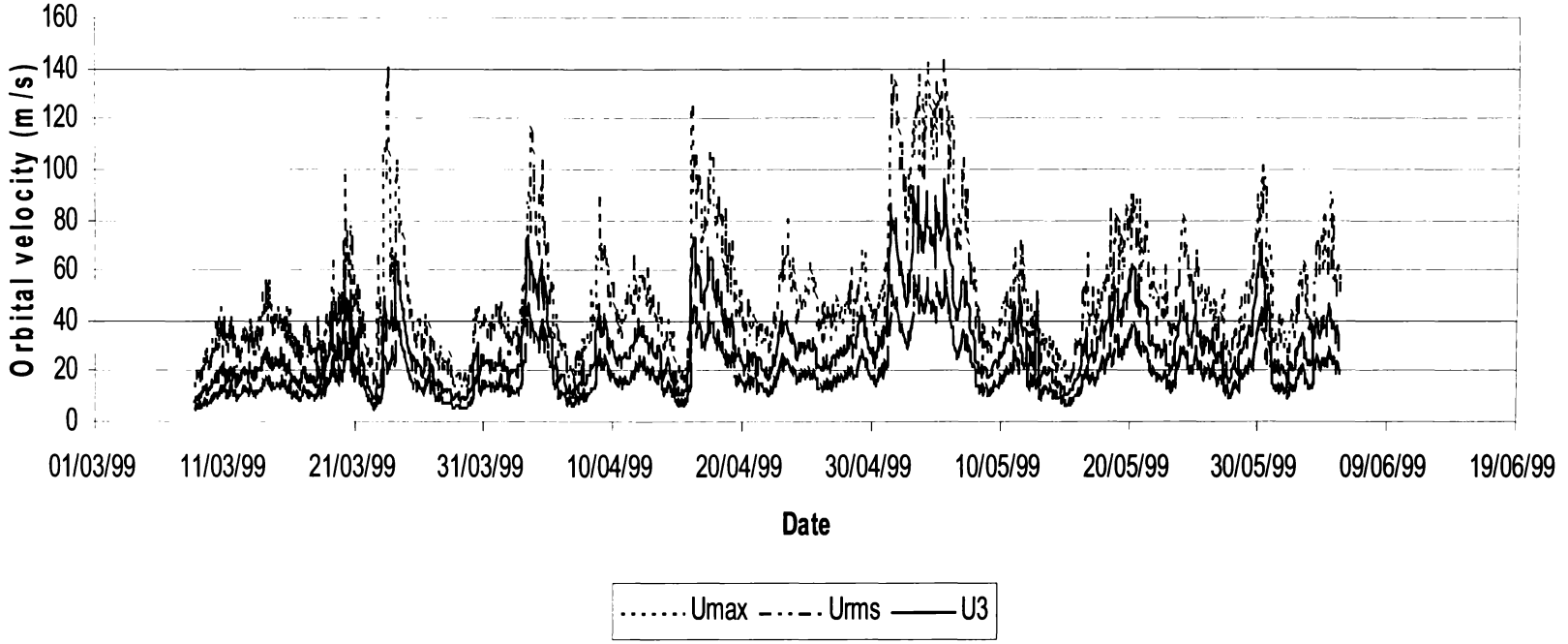

Figure 7.11 Near-bed orbital statistics U_{max} (the maximum orbital velocity experienced during the burst period), U_{rms} (the root-mean-square orbital velocity) and the third moment of the orbital velocity, U_3 as measured using an *InterOcean* S4ADW current meter. The U_3 statistic is shown to be more stable than U_{max}, while representing the larger events relatively more that the U_{rms} orbital statistic.

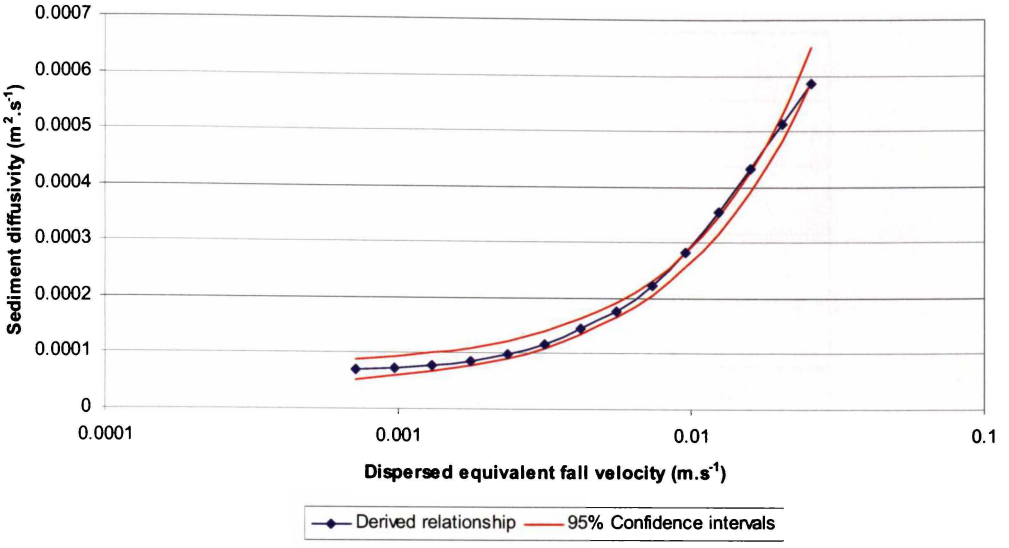

Figure 7.12 An example of the variation in sediment diffusivity (ε_s) as a function of the dispersed equivalent fall velocity within the range $w_f < 0.0007$ m.s^{-1}. The sediment diffusivity for each of the dispersed w_f values has been determined from a suspended sediment concentration profile and the measured mixing lengths using equation 7.08. Sediment diffusivity is shown to decrease asymptotical with decreasing w_f within the range $w_f < 0.0007$ m.s^{-1} (i.e. 30 μm).

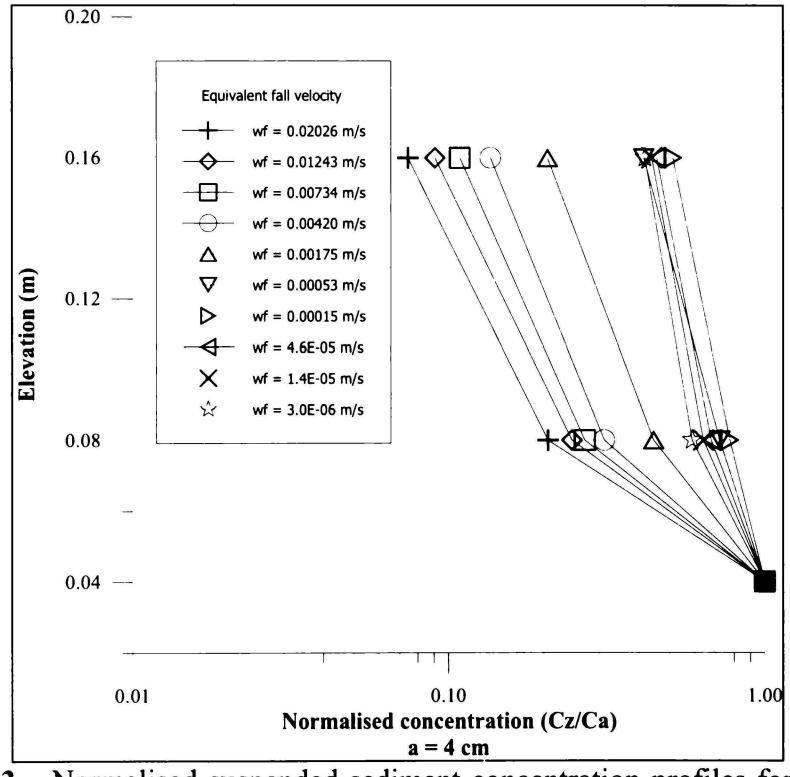

Figure 7.13 Normalised suspended sediment concentration profiles for individual dispersed fall velocity bins from within the distribution of entrained sediment. The individual profiles are clustered at 0.0005 m.s^{-1} $< w_f <$ 0.0017 m.s^{-1}, indicating that the dispersed sediment within that range are experiencing similar diffusivity within the water column, suggestive of flocculation.

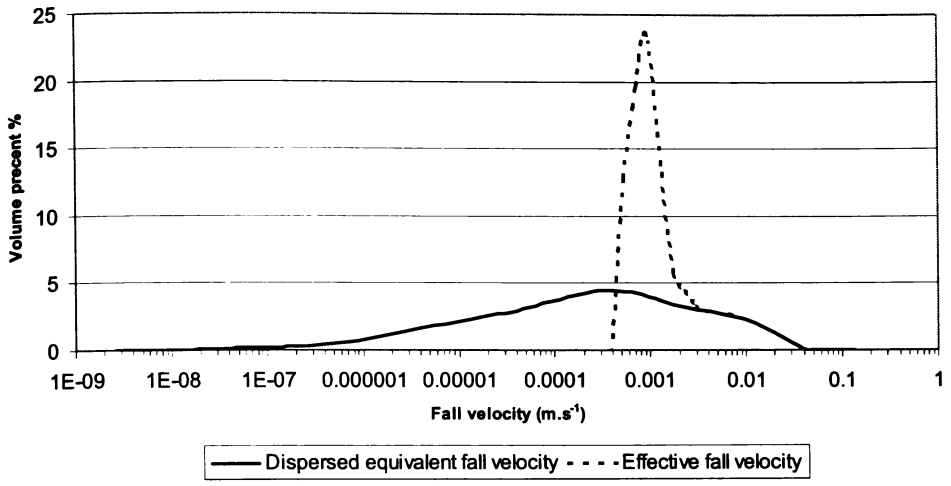

Figure 7.14 Dispersed equivalent and effective fall velocity distributions from a site in 10 m of water within northern Poverty Bay. The dispersed equivalent fall velocity distribution is derived directly from sample analysis, while the effective fall velocity has been determined assuming a constant fall velocity within the range $w_f < 0.0013$ m.s^{-1} and the measured mixing lengths from the *SSC* profile.

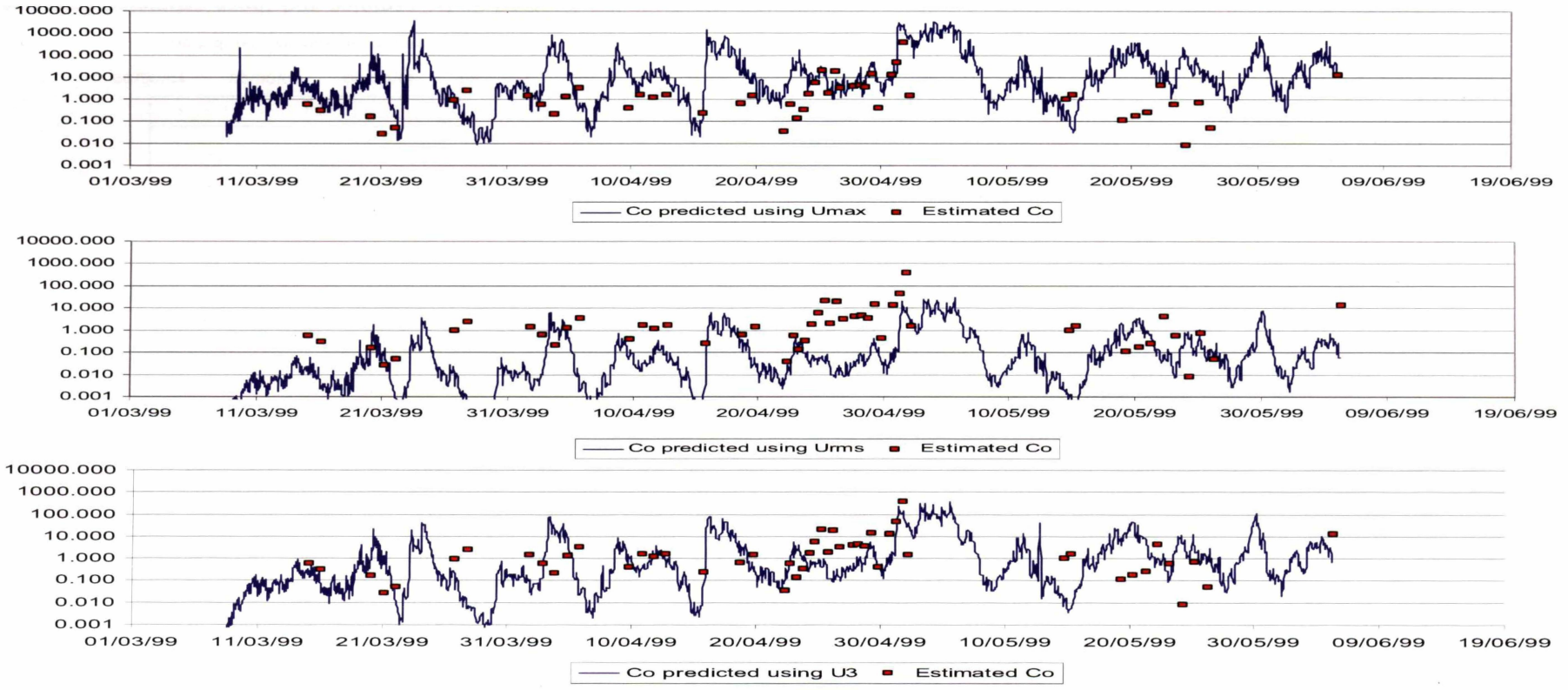

Figure 7.15 Near-bed reference concentration time-series and estimated C_0 determined from pumped water/sediment samples. The three cases illustrated represent the predicted near bed reference concentration time-series with the friction velocity (U_*) determined using the U_{max}, U_{rms} and U_3 orbital statistic respectively. Classifying the friction velocity using the U_3 statistic of the orbital velocity distribution is shown to provide the best agreement between predicted and estimated C_0. In-situ shear strength is accounted for following the findings of Chapter 6.

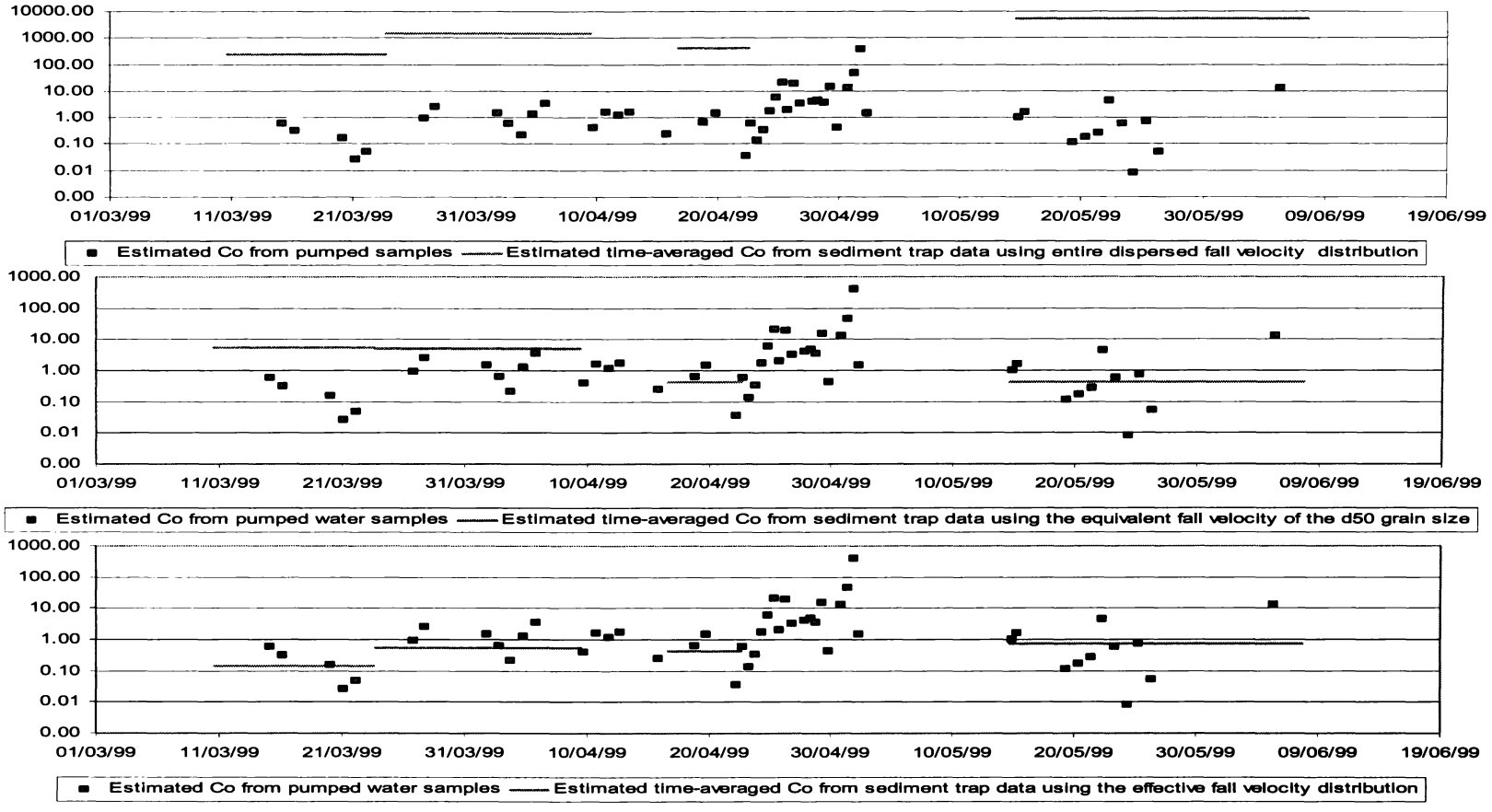

Figure 7.16 Comparison between the estimated near-bed reference concentrations from the pumped water samples and those estimated from the sediment trap data. The time-averaged C_0 values from the sediment traps have been determined using (i) the entire dispersed fall velocity distribution, (ii) the equivalent fall velocity of the d_{50} of the sediment collected within the sediment traps, and (iii) the effective fall velocity (w_{fc}) distribution inferred from pumped *SSC* measurements.

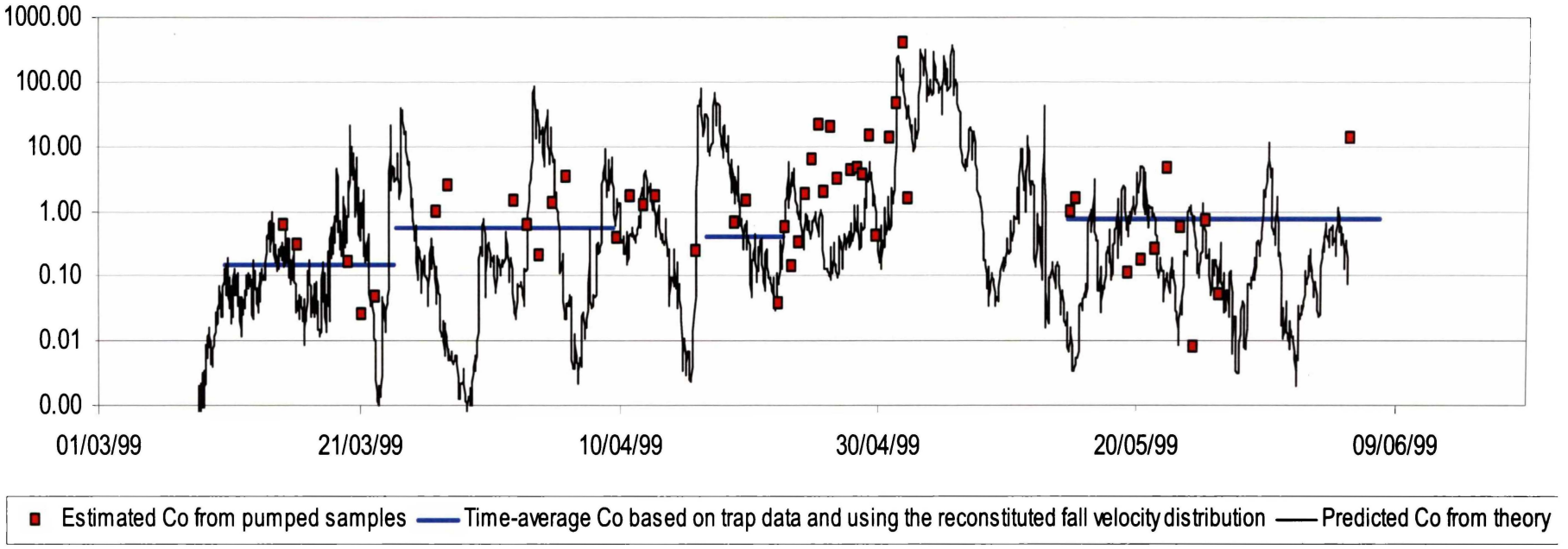

Figure 7.17 Comparison between the estimated time-averaged near-bed reference concentrations from the sediment trap data as determined using the re-constituted effective fall velocity and the C_0 predicted accounting for the effect of bedforms on sediment entrainment using the method outlined by Du Toit and Sleath, (1981), with the friction velocity characterised using U_3 and accounting for the retardation of sediment entrainment due to the in-situ shear strength of the surficial sediment.

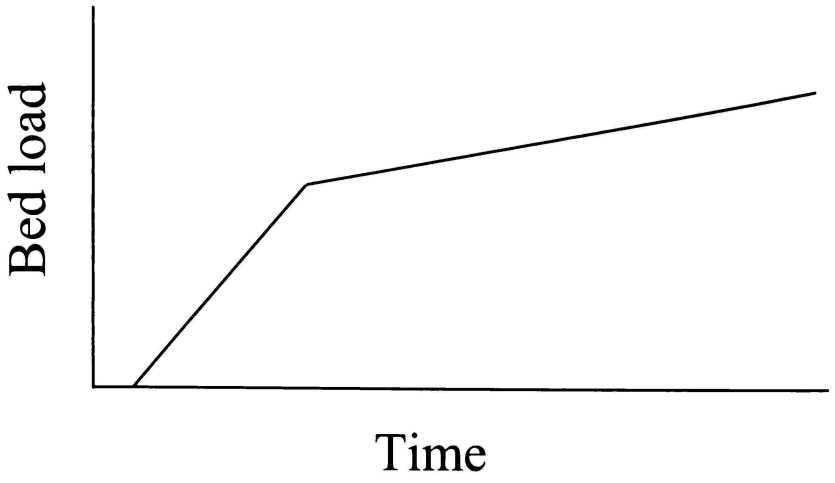

Figure 7.18 Schematic diagram illustrating how bedload varies with time under uniform shear stress consisting of an initial fast phase of upper layer erosion, followed by a slower erosion of the lower layer.

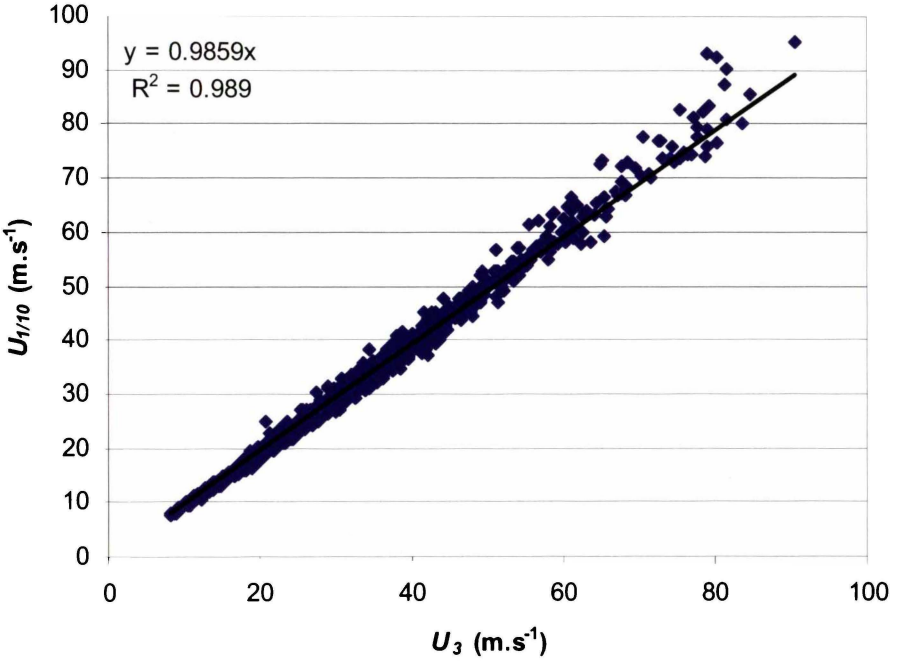

Figure 7.19 Comparison between U_3 and $U_{1/10}$ illustrating that the different statistics of the velocity distribution are similar. From regression analysis the gradient of the fitted line is less than 1 (i.e. 0.99), suggesting that for this data set the U_3 statistic is representative of a velocity percentile less than the upper $^1/_{10}$ (i.e. $U_3 < U_{1/10}$ for this dataset).

Chapter 8. Mixing near the mouth of a tidal river, Turanganui River, Poverty Bay New Zealand.

"*The ocean is a body of water occupying about two-thirds of a world made for man – who has no gills*" - Ambrose Bierce

8.1 Introduction

While numerous studies have investigated circulation patterns in Poverty Bay on the bay-wide scale (e.g. Black et al., 1997; Kensington, 1990; Miller, 1981; Stephens, 2001; Stephens et al., 2000; Stephens et al., 1999; Williams, 1959) the intricacies of the Turanganui River plume dynamics and its affect on sediment distribution and sedimentation rates in northern Poverty Bay (Figure 8.01) have not been previously examined in detail.

On a bay-wide scale, previous work by Black, et al. (1997) and Stephens (2001) has identified wind velocities and river discharge as being the principle forcing mechanism that affect the plume characteristics, and hence sediment distribution, of both the Turanganui River adjacent to the port of Gisborne and the Waipaoa River in the southern part of Poverty Bay. Additionally, Black, et al. (1997) and Stephens (2001) note baroclinic currents affect the mixing and distribution of both Waipaoa and Turanganui River plumes. While these studies are useful in understanding the complex circulation patterns within the broader Poverty Bay context, more work in understanding the distribution characteristics of the Turanganui River plume and its effect of sediment distribution in northern Poverty Bay is needed. However, while a more complete understanding of the distribution characteristics of the Turanganui River plume helps in understanding the sediment distribution, the complexities associated with the mixing of inland and coastal waters needs to be addressed in order to better comprehend sedimentation patterns of the fine suspended sediment discharged into northern Poverty Bay by the Turanganui River.

The mixing of fresh and saline water creates a complex interaction of both sediment and hydrodynamical processes including density and temperature driven currents, often associated with eddies and up-welling. Further, complicated flocculation processes of the fine-grained suspended sediment occur due to the mixing of turbid freshwater and more saline seawater, where not only does the salinities of the water affect the flocculation, but also variation in temperatures, turbulence level and concentration (Berlamont et al., 1993; Mehta et al., 1989). Higher salinities result in more ions in solution, which act to suppress inter-particle electrochemical repulsive forces, thereby allowing the attractive Van-der Waals forces to dominate and the dispersed particles to flocculate (Mehta et al., 1989). The flocculated particles have a fall velocity greater than the individual particles that comprise the flocs. While Krone (1962) found the settling velocity of flocculated cohesive sediments to increase with increased salinity up to about 10 ppt, Whitehouse, et al. (1960) noted that the increase in salinity beyond 10 ppt was important for the flocculation of dispersed montmorillonitic materials, such as found within Poverty Bay sediments (see for example Chapter 4 and Miller, 1981). Given that flocculation of fine sediment due to the mixing of saline and fresh water will occur, then understanding the dynamics of the mixing and distribution of the plume is required in order to understand the resulting spatial distribution of the fine suspended sediment.

To understand the distribution, mixing and fine suspended sediment depositional processes of the Turanganui River plume, the mixing of saline and freshwater near the entrance to the port of Gisborne adjacent to the mouth of the river was investigated using spatially and temporally distributed CTD (conductivity, temperature and depth) and turbidity profiling. The Turanganui River is only

~ 1.2 km long and has two tributary rivers, the Taraheru and the Waimata Rivers (Figure 8.02). Together, the tributary rivers drain a hill-country catchment area of approximately 220 km^2 (Figure 8.03) consisting of highly faulted erodible Tertiary sandstone and mudstone and crushed Cretaceous argillite (Griffiths and Glasby, 1985; Smith, 1988). The Turanganui River is estimated to contribute about $0.69x10^6$ tonnes/yr of suspended sediment into Poverty Bay (Gisborne District Council, 1994), which often highly discolours the surface water of the northern Poverty Bay (Figure 8.02).

8.2 Methods

8.2.1 River volume and atmospheric monitoring

Wind direction and magnitude (mean and gust velocities), rainfall (cm) and air temperature (°C) were measured hourly between 28/05/99 and 15/6/99 at a site adjacent to the mouth of the Turanganui River by the *Gisborne District Council and Hydro-Technologies Ltd*, while barometric pressure was measured daily at the Gisborne Airport (Figure 8.04). To place the data in a broader temporal context the atmospheric conditions during the survey are compared with the extended temporal data.

The Turanganui River is a tidally affected river approximately 1.2 km in length that discharges adjacent to the port of Gisborne. Because the Turanganui River is tidal no gauging stations are located on the river. As such, the discharge from the Turanganui River was estimated by summation of the discharge of the Waimata and Taraheru Rivers, the two tributary rivers. In order to get a true representation of the input of fresh water into the Turanganui River, the gauging stations on the Waimata and Taraheru Rivers are located above the point of maximum tidal penetration of seawater (Figure 8.04). Due to irregular temporal-spacing of discharge data from the Waimata and Taraheru Rivers, daily mean discharge have been interpolated using a piecewise spline interpolation method to provide regularly spaced (in time) data.

In order to place the survey period data in a broader temporal context, 20-year river discharge data for the Waimata River has been analysed using extremal probability analysis following the methods outlined in the Coastal Engineering Manual (United States Army Corps of Engineers, 2002a). The Waimata River data was chosen rather than the composite of both the Waimata and Taraheru River data as the composite data did not extend over a sufficient time span to allow 20-year extremal probability analysis. The available data has been limited to span a 20-year period from May 1978 – May 1998. The 20-year period includes the extreme storm event Cyclone Bola (08/03/88) that heavily impacted on the East Coast of New Zealand in terms of both atmospheric and oceanic conditions. Extremal probability analysis was used to determine the return period of various magnitude flood events inclusive of and beyond the period of data coverage.

8.2.2 Salinity and Temperature profiling

Between 28/05/199 and 20/06/99 a total of 21 individual surveys of the Turanganui River plume were undertaken. On each of the surveyed days the 3-dimensional spatial variability in river plume salinity and temperature was measured at up to 22

cast locations around the mouth of the Turanganui River and the port of Gisborne environs (Figure 8.05). The locations of the CTD survey site were determined by taking transit line bearings off fixed features on the land (i.e. Building edges, channel lead marks etc.), as GPS position fixing was not available. The latitude and longitude of the survey positions were determined using DGPS at the completion of the surveying period. The error due to using the transit line bearing method of determining the relative position is estimated to be approximately ±10 m. While the spatial distribution of the surveying sites is not ideal (due to the initial method used determine each sites position) the data provides useful information on the spreading of the Turanganui River plume and for estimation of channel infilling rates (examined in Chapter 9). Wave conditions prevented measurements near the river entrance. An *Ocean Sensors CTD* (Model OS200) instrument (Figure 8.06) was used to measure the vertical variability in temperature, conductivity and salinity at each of the cast sites. Cast positions were determined using a real-time correction Differential Global Positioning System (D.G.P.S., Trimble 4000RL II Reference Locator base station and Trimble NT 200 Chart Plotter). Table 8.01 lists the cast locations relative to the local circuit. The software package *SURFER* (Version 7.00.26), which takes spatially distributed data and interpolates a regularly spaced grid, was used to interpolate the salinity and temperature data into 2-dimensional charts and transects.

Because the Turanganui River is tidal, in order to get the indication of the maximum dispersion of the river plume each survey was conducted under mid ebb-tidal conditions, corresponding to the approximate peak velocity discharge of the Turanganui River.

A total of 21 surveys were conducted on separate days, spanning 28th May to 20th June, 1999, however due to instrument failure only 16 surveys provided enough data to spatial map the river plume within the port environs.

8.2.3 Wave and current measurements

Wave and residual current characteristics between 28/05/99 and 15/6/99 were measured at a site adjacent to the port of Gisborne shipping channel (Figure 8.07) using an *InterOcean S4ADW* directional wave and current meter. The current meter was deployed approximately 2 m above the seabed in 10 m water depth on a bottom-mounted frame. The instrument sampled velocities directions at a frequency of 2 Hz, for a period of 9 minutes every two hours, allowing wave characteristics and residual current velocities to be measured.

8.2.3 Turbidity monitoring

8.2.3.1 Turbidity profiling

In addition to *CTD* casts, at several of the sites representative water samples were collected at various depths within in the profile using a *Niskin Bottle* (Figure 8.08). Table 8.01 lists the cast locations and depths where water samples were collected. The relative turbidity of each of the samples was determined post-survey using a *Hach Portalab Turbidimeter* (model 16800), which measures the turbidity of the water in nephelometric turbidity units (*NTU*). The *Hach Portalab Turbidimeter* instrument and turbidity standards are illustrated in Figure 8.09.

Prior to the measurement of each samples turbidity the *Hach Portalab Turbidimeter* was zeroed electronically and the range checked at 1.0, 10 and 100 NTU scale using the supplied standards. Repetitive sample measurements insured repeatability of results.

8.2.3.2 Instrument calibration

In order to quantify the volume of sediment in suspension, a relationship between the suspended sediment concentration (*SSC*) and the measured NTU value is necessary.

A representative sample of the suspended sediment was divided into 5 sub-samples. Each of the five sub-samples was mixed with differing quantities of distilled water in order to obtain 5 solutions with distinct turbidity (both NTU and *SSC*). The NTU of each of the samples was determined using the *Hach Portalab Turbidimeter* (model 16800). The mass of sediment was determined by filtering the solution through filter paper. All moisture was first removed from the filter papers by drying the paper in an oven until a constant mass (M_1) was reached. The filter papers were kept in desiccators to prevent mass changes due to the inclusion of atmospheric moisture in the filter paper. The mixture was then passed through a filter paper and the quantity of water measured (Q_1). The filter paper and sediment were dried in an oven for a minimum of 12 hours to remove any moisture and weighed again (M_2). This enabled the sediment concentration (C_z) of the mixture to be calculated as,

$$C_z = \frac{(M_2 - M_{1)}}{Q_1} \tag{8.01}$$

where M_1 and M_2 are measured in kilograms (kg) and Q_1 is measured in cubic meters (m^3).

Table 8.02 lists the NTU and *SSC* values of the 5 samples. Regression analysis between the recorded NTU from the *Hach Portalab Turbidimeter* (model 16800) and the sediment concentrations was performed and illustrates a significant correlation between the two variables ($R^2 = 0.82$). Figure 8.10 illustrates the regression analysis.

8.2.3.3 Grain size and fall velocity of plume entrained sediment

Sample analysis was performed using a Malvern laser particle size analyser; model *MSS17,* which has the ability to concurrently measure both the sand and the mud sizes. Refer to Chapter 3 for details.

Equivalent fall velocities (w_f) were calculated using the equation described by Gibbs, et al. (1971), and assuming equivalent quartz density, as given in eqn 5.01.

8.2.4 Richardson Number for vertical mixing of waters

The mixing ability of the buoyant river plume water and the underlying, more saline seawater at a site adjacent to the shipping channel (Cast site 8) was investigated using Richardson Numbers. The Richardson Number (R_i) is commonly used to

describe the capacity of density driven currents to transfer momentum and sediment across a halocline, and is a measure of the ratio of turbulent (velocity shear stress) to stabilising influences (density gradient).

$$R_i = g\left(\frac{\partial \rho}{\partial z}\right) \Big/ \rho\left(\frac{\partial u}{\partial z}\right)^2 \qquad (8.02)$$

and g = acceleration due to gravity (9.81m.s^{-1}),
∂z = difference in water depth between the layers,
∂u = difference in velocity between the two layers (m.s^{-1}), and
$\partial \rho$ = density difference between the two water bodies

Water density was determined using a linear fit to the *UNESCO* equation of state, where,

$$D(t,S,P) = D(t_r,S_r,P_r) + Dt(t - t_r) + DS(S - S_r) + DP(P - P_r) \qquad (8.03)$$

where t_r, S_r and P_r are the potential temperature, salinity and pressure respectively, and D_t, D_S, D_P, represent derivatives of density with respect to the subscripted variables.

By resolving the balance between the baroclinic reference phase, river discharge and wind velocity vectors, the potential maximum shear velocity can be determined (e.g. Figure 8.11). The river discharge velocity component was determined assuming uniform radial spreading of the river plume with a direction of 230°T. The wind velocity component was estimated assuming an atmosphere-ocean momentum transferral rate of 1-2% in accordance with the findings of Prandle and Mathews (1990). The reference phase speed of the river plume (c_p) due to baroclinic conditions was determined using the relationship of Garvine (1987), given as,

$$c_p = (g' h_0)^{0.5} \qquad (8.04)$$

in which h_0 is the depth of the river plume and g' is the reduced gravity defined as,

$$g' = g(\rho_s - \rho_f) \Big/ \rho_f \qquad (8.05)$$

where ρ_s is the density of the relatively dense saline water and ρ_f is the density of the relatively buoyant freshwater river plume. A directional component of 230°T for the baroclinic driven currents was used.

Figure 8.12 and 8.13 illustrate the relationship between the Richardson Number and the variation of normalised eddy diffusivity (ε_s) (sediment/salt transfer between layers) and eddy viscosity (ε_f) (momentum transfer between layers) coefficients respectively using the formulae of Parrels and Karelse (1982) and Black (1990). The relationship illustrates that the larger the Richardson Number the more inhibited the transfer of eddy diffusivity and viscosity between water bodies.

8.2.5 *Horizontal decay in SSC*

Change in concentration of the sediment at a horizontal distance '*x*' from the mouth of the river is dependant on,

- The interfacial mixing across the halocline due to turbulent mixing and re-suspension of sediment, and
- The settlement of sediment out of the plume due to gravitational settling

If we consider the Richardson Number to be sufficient to inhibit re-suspended sediment from being entrained into the plume, then in a two dimensional frame of reference (Figure 8.14) the change in concentration (ΔC) is due to rate of settlement (proportional to the fall velocity, i.e. w_f), across a unit distance (d) can be defined as,

$$\Delta C = C_{z_i} - C_{z_i+d} \tag{8.06}$$

or alternatively, if we consider a unit length of 1 m (Figure 8.14)

$$\Delta C = C_t \times w_f \times \Delta t \tag{8.07}$$

The resident time (Δt) of the plume within the unit distance is a function of the river plume velocity (U) and distance (d), i.e.,

$$\Delta t = {}^{d}\!/_{U} \tag{8.08}$$

allowing eqn. 8.07 to be written as,

$$\Delta C = C_z \times w_f \times {}^{d}\!/_{U} \tag{8.09}$$

In the absence of new sediment entering the system, then the time-averaged form of this equation is exponential, and can be written,

$$C_{(t)} = C_0 e^{-t/D_x} \tag{8.10}$$

where D_x is a decay factor determining the rate of concentration reduction and is a function of the fall velocity and turbulent mixing.

From eqn 8.09, ΔC is a function of the velocity of the plume at any given point, which in turn is a function of the distance from source (x) and the discharge of the river (φ_{river}), such that,

$$U = f(x, \varphi_{river}) \tag{8.11}$$

Given the dependency of the plume velocity on distance due to spreading, then, assuming w_f is constant; an increase in the downward flux per unit length can be expected with distance.

8.3 Results

8.3.1 Atmospheric Conditions

8.3.1.1 During the Survey Period

Figure 8.15 summarises the atmospheric conditions during the plume-monitoring program (28th May to 20th June, 1999). The barometric pressure during the survey period appears to oscillate with a period of approximately 6-7 days, consistent with the passage of frontal systems across New Zealand. Maximum and minimum barometric pressure during the survey period was 1028 and 991 hPa respectively (Figure 8.15).

Four distinct rainfall events (3 mm or greater) were recorded during the survey period, with all but one correlating with decreasing or low barometric pressure (1011 to 991 hPa) and winds from the southerly quarter (Figure 8.15). The longest duration rainfall event occurred between 05/06/99 and 06/06/99 and corresponds to relatively high barometric pressures (1019 hPa) and winds rotating through north to south (Figure 8.15) consistent with the passage of a depression tracking across the top of the North Island of New Zealand held in place by high-pressure system to the south (Figure 8.16).

Atmospheric temperatures during the survey period display a strong diurnal variation consistent with solar heating. The air temperatures ranged from 3 to 22° C; with the higher temperatures occurring post mid-day, while the lower temperatures occurred at night (Figure 8.15).

Wind characteristics are consistent with the passage of frontal systems across New Zealand (as illustrated in Figure 8.16), however superimposed on the regional winds was a diurnal velocity variation consistent with the formation of localised convection cells. The localised convection cells formed by the advection of air masses result in relatively strong afternoon onshore sea breezes (south-easterly quarter) and evening and morning offshore winds presumably enhanced by down-welling of relatively cold, dense air from the surrounding hill country, i.e. katabatic winds (northwest quarter ~315°T, Figure 8.15). The wind direction and strength compass rose (Figure 8.17) illustrates that the dominant wind direction during the survey period was from the NW.

8.3.1.1 Relative to a longer time-span

Figure 8.18 illustrates the broader temporal atmospheric data, and illustrate that the conditions experienced (i.e. barometric, wind velocity, rain and temperature) during the survey period are typical of the environs. A seasonal variation in air temperature is apparent, with relatively cooler temperatures during late autumn and winter months, while air temperatures often exceed 30° C during summer months. The wind rose (Figure 8.19) illustrates that the dominant wind direction was from the N-NW, while relatively strong winds (30 $km.hr^{-1}$ or greater) tend to either come out of the NW or SW quarters. The broader wind characteristics are similar to the winds experienced during the survey period.

Joint probability analysis of the wind direction and the hourly time component illustrates an increase in the probability of afternoon onshore winds (Figure 8.20), presumably in association with the formation of localised convection cells.

8.3.2 River discharge

8.3.2.1 During the Survey Period

Because the Turanganui River is tidally affected, the approximate discharge of the river was determined using the composite of the discharge from the Waimata and Taraheru Rivers (Figure 8.21) as measured at the Goodwin and Hansen Road gauging stations respectively (Figure 8.04). The Waimata River peak discharge appears to lag the Taraheru River and the rainfall events (Figure 8.21), presumably due to the Waimata River catchment area and river network system extending further into the hinterland (Figure 8.04).

At the beginning of the survey period the discharges of the rivers are relatively quiescent (Figure 8.21). However, during the survey period two relatively minor and one relatively large flood event occurred (Figure 8.21). The two minor events occurred on the 9th – 10th June and 15th – 16th June 1999 and had discharges at the mouth of the Turanganui River of approximately 11.2 $m^3.s^{-1}$ and 6.6 $m^3.s^{-1}$ respectively. The relatively large flood event occurred on the 5th – 6th of June 1999 and had a discharge of approximately 63 $m^3.s^{-1}$; a factor of 10 larger than the minor event on the 15th – 16th June 1999, and approximately twice the mean discharge from the Waipaoa (32.3 $m^3.s^{-1}$, Stephens, 2001). The flood-event profile shape displays an initial rapid increase in the volume of water being discharged, followed by an exponential decay in the discharge. Not surprisingly the discharge of the rivers display a strong correlation to rainfall events (Figure 8.15), with the most pronounced and extensive rainfall event recorded during the survey period cumulating in the relatively large flood event on the 5th – 6th of June.

Figure 8.21 illustrates that the Taraheru River contribute only a small portion of the total discharged volume, typically in the range of 2%, presumably due to the differing size and orographic characteristics of the Taraheru River catchment (Figure 8.03 and Figure 8.04).

8.3.2.1 Relative to a longer time-span

Extremal probability analysis of the Waimata River discharge data suggests a Weibull Distribution with a shape parameter (k) of 0.75. The correlation coefficient was relatively large (R^2 = 0.94). However the Cyclone Bola event, with a discharge for the Waimata River peaking at 693 $m^3.s^{-1}$, is shown as a distinct outlier (Figure 8.22). The Turanganui River average and median discharge is 4.8 $m^3.s^{-1}$ and 1.35 $m^3.s^{-1}$ respectively, while extreme events can have discharges 1-2 orders of magnitude larger (Figure 8.22). The magnitudes of various return period flood events are given in Table 8.03. The approximate discharge of the Turanganui River has been estimated by applying a 2% correction factor to account for the contribution of the Taraheru River.

Based on the extremal probability analysis, the relatively large flood event that occurred during the survey period (discharge = 69 $m^3.s^-1$) has a probability of occurring greater than twice a year (i.e. return period < 0.5 year, Table 8.03), suggesting that the discharge, and presumably the volume of sediment introduced into the port of Gisborne environs, is likely to occur several times during the year and is not atypical of the environment.

Significantly, the discharge associated with Cyclone Bola (693 $m^3.s^{-1}$) is larger than a flood event with a return period of 100 years (Table 8.03) and was a factor of 10 larger than the relatively large flood event monitored during the survey period. Figure 8.23 illustrates the discharges of the Waimata and Taraheru Rivers for the period 01/05/78 to 01/10/02. While the available data coverage for the Taraheru River does not span this entire period, the scale of the x-axis was maintained for both rivers for ease of comparison. The data illustrate that 1999 (the year of the river plume survey) was relatively quiescent in terms of river discharge (Figure 8.23), with the majority of other years covered by the data experiencing a larger number of flood events of equal or greater magnitude than the flood event that occurred during the survey period (Figure 8.23). The river discharge associated with Cyclone Bola is approximately twice the magnitude of any other flood event within the dataset (Figure 8.23).

8.3.3 Wave and residual currents characteristics

Significant wave height (H_s) and peak spectral wave periods (T_p) between 28/05/99 and 15/06/99 at a site adjacent to the shipping channel (Figure 8.07) as measured using an *InterOcean* S4ADW are illustrated in Figure 8.24. During this period significant wave heights range between less than 0.5 m and almost 2 m, with an average of 0.81 m (slightly less than the average significant wave height from the 20-year hindcast record, i.e. 1.15 m, Section 2.6.3), The peak spectral periods range between 5 s and 19 s, with an average of 12.3 s (similar to the predominant peak wave period range, Section 2.6.3).

Figure 8.25 illustrates the residual current directions and magnitudes between 28/05/99 and 15/06/99. Residual current speeds range from 9-22 $cm.s^{-1}$. Between 28/05/99 and 05/06/99 the residual current directions (~100-170° T) are consistent with the formation of an anti-clockwise gyre within Poverty Bay as demonstrated by Williams, (1959), Miller, (1981), Kensington, (1990), Black, et al., (1997) and Stephens, (2001). However on the 6th of June the direction of the residual current changes to approximately 60° T, consistent with the formation of a bottom return flow of oceanic water beneath the river plume (Figure 8.25). The change in current direction correlates with an increase in river discharge following the flood event on the 5-6th June 1999.

8.3.4 Salinity and Temperature Plume Characteristics

Table 8.04 gives the wind direction and speed, Turanganui River discharge, *MHW* and *MLW* times and range. Wind direction and speed and the Turanganui River discharge are also depicted in Figure 8.26.

The interaction of the relatively buoyant freshwater discharged from the Turanganui River and the more dense saline seawater results in distinctive salinity, temperature and conductivity profile characteristics within the plume. Plume thickness was found to vary between approximately 1-3 m. Figure 8.27 schematically illustrates the isohaline characteristics of well-mixed, partly mixed and highly stratified salinity profiles as defined by Pritchard (1955) and Cameron and Pritchard (1963). Richardson Numbers (*Ri*) for each of the surveyed days are given in Table 8.05.

Richardson numbers (*Ri*) are shown to vary between 0.04 and 0.34 (Table 8.05), which, from Figures 8.12 and 8.13, suggests that the vertical salinity structure of the river plume varies between well mixed (i.e. relatively small ε_{s_z} and ε_{f_z}) and highly stratified (i.e. relatively large ε_{s_z} and ε_{f_z}). An example of the variation in profile characteristics observed during the monitoring period is given in Figures 8.28 and Figure 8.29. Based on the conceptual model of Pritchard (1955) and Cameron and Pritchard (1963) as illustrated in Figure 8.27 the variation in profile characteristics range between being described as well mixed to highly stratified.

Three transects through the river plume in the vicinity to the port entrance (Figure 8.30) were used to investigate the vertical mixing process. The range of salinity measured in the experiment were similar to the values obtained by Kensington, (1990), while the densities determined using the *UNESCO* equation of state (eqn 8.03) are similar to those reported by Stephens, (2001).

The type of profile structure varies primarily in response to river discharge. In low flow conditions (e.g. 0.41 $m^3.s^{-1}$ on the 02/06/99) the fresh water discharged from the Turanganui River appears to be partially mixed with saline flood tidal waters and only a weak river plume was evident in both the salinity and temperature spatial distribution maps (Figure 8.31). Transect data for the same period show the river plume to be well mixed, with low salinity, temperature and density gradients (Figure 8.32). In contrast, when the discharge was relatively high (i.e. 6.91 $m^3.s^{-1}$ on the 8th June 1999) the salinity and temperature profiles were well stratified and the river plume well defined in both the spatial maps and transect data (Figures 8.33 and Figure 8.34).

The river discharge, wind velocities and baroclinic conditions affect the horizontal spreading of the river plume on the surface. When the plume discharge velocity was comparatively small (low flow conditions) the wind forces the plume either towards the coastline (wind from the southerly quarter) or towards the shipping channel (winds from the northerly quarter, e.g. Figures 8.35). Prandle and Mathews (1990) estimated an atmosphere-ocean momentum transferral rate of 1-2%, therefore the velocity component of the surface water, and hence the plume, due to the ocean-atmosphere interaction will be dependant on velocity of the wind. During periods of light winds the velocity component of the surface water due to the ocean-atmosphere interaction is comparatively small, and the directional spreading aspects of the river plume appears to be more a function of the velocity component associated with the discharging of water at the mouth of the river, and as such a function of the direction in which the mouth of the river faces (Figure 8.36).

The Swinging Basin appears to remain relatively saline when compared with the water immediately outside the port entrance, and water temperatures tend to be slightly elevated, resulting in identifiable surface temperature and salinity gradients near the entrance to the Swinging Basin (Figures 8.32, 8.33, 8.34, 8.35 and 8.36).

8.3.5 Plume turbidity characteristics

8.3.5.1 3-dimensional turbidity observations

River discharge and wind characteristics for each of the days where turbidity measurements were made are shown in Figure 8.37. The amount of sediment in suspension varies in response to the river discharge. In low flow conditions the *SSC* within the river plume was relatively small; alternatively during flood events the volume of sediment was relatively large (Figure 8.38).

The distribution of surface *SSC* of the river plume is similar to the salinity distribution, and is affected by the river discharge, wind velocities and baroclinic conditions. In low flow conditions wind direction forces the turbid plume either towards the coastline (onshore winds) or towards the shipping channel (offshore winds). Offshore wind conditions result in more turbid water in the vicinity of the shipping channel (Figure 8.39). The influence of the wind on the salinity distribution of the plume for the same days is shown Figure 8.40. In relatively large flow conditions the wind forcing on the directional component of the river plume is not as pronounced. Aerial photographs of the Turanganui River turbid plume (Figure 8.41 and Figure 8.42) illustrate the affect wind forcing has of the plume distribution characteristics.

In low flow conditions, Richardson Numbers (*Ri*) are relatively small, indicative of little inhibition in the vertical movement of wave induced re-suspended sediment into the river plume. Plume characteristics on 01/06/99 along Transect 2 are shown in Figure 8.43. On 01/06/99 the *Ri* at Cast site 8 ranged between 0.09-0.14, which is on the boundary between well mixed to highly stratified (Fischer et al., 1979). The uniformity of the *SSC* with depth at Cast site 8 on 01/06/99 suggests limited inhibition to the vertical movement of the wave induced re-suspended sediment. In contrast, the density gradient at Cast sites 9 and 10 are relatively larger (i.e. larger *Ri*) and appear to inhibit the re-suspended sediment from moving vertically into the river plume (Figure 8.43). Figure 8.44 illustrates another example of the separation of the re-suspended sediment and the turbid waters of the river plume (14/06/99, $Ri = 0.10$-0.15 at Cast site 8). Where the density gradients are larger (Cast sites 7, 9 and 10) the vertical motion of the re-suspended sediment is more inhibited, while at Cast site 8 the re-suspended sediment is shown to mover higher within the profile and to mix with the turbid water of the river plume (Figure 8.44).

During relatively large flood events (e.g. on 06/06/99) the water column becomes highly stratified and the density gradient is large (Figure 8.45). Correspondingly *Ri* numbers are relatively large ($Ri = 0.24$-0.38 at Cast site 8), suggesting strong inhibition between the vertical movement of the wave induced re-suspended sediment into the turbid river plume. However, transect data indicates near uniform *SSC* at Cast site 7 ad 8, while Cast site 9 and 10 suggest a bottom return flow of less turbid oceanic water underneath the river plume (Figure 8.45). Significant wave heights during the period were relatively larger, $H_s > 1.5$ m (Figure 8.24), and it is probable that wave induced turbulence resulted in the mixing between the saline bottom water and the relatively freshwater river plume as observed in the turbidity transect (Figure 8.45).

Suspended sediment concentrations at 4 m subsurface are found to have a consistent spatial distribution, often larger than, and independent of the surface plume characteristics. Largest *SSC* in this layer is found near the entrance to the Swinging Basin, and shows a tendency to decrease with distance from the river mouth (Figure 8.46) and increasing water depth as expected.

8.3.5.2 Theoretical surface water river plume SSC variation with distance

The sediment concentration decrease in the surface water of the river plume with distance from the river mouth is a function of the dispersion of the river plume (velocity and distance) and settlement of the sediment out of the plume, and is analogous to a temporal variation in concentration due to settling out of fines from the surface plume of the river (section 8.2.5).

Using the relationship defined in section 8.2.5 regression analysis of the horizontal distance (x) against the natural log of the suspended sediment concentration in the surface layer ($ln(C_x)$) enabled discrete decay factors (D_x) to be calculated for each day (i.e. different river discharge), where,

$$D_x = -1/\beta \tag{8.12}$$

and β is the slope of the regression line.

Knowing the decay rate factor, (D_x) the intercept of the regression line gives the reference concentration, C_{ob} at the mouth of the river ($x = 0$) for each specific day,

$$C_x = C_{ob} e^{(-x/D_x)} \tag{8.13}$$

Figure 8.47 gives and example of the regression analysis, while Table 8.06 lists the decay rate (D_x) and regression coefficients (R^2) for different river discharges. The decay rate factor is shown to exponentially decrease with increase river discharge (φ_{river}, Figure 8.48), following the equation form,

$$D_x = 591 + 2850 \exp\left(-\varphi_{river}/2.1\right) \tag{8.14}$$

The dependency of the decay factor on river discharge suggests some factor of the river discharge speed (U_{river}) or the concentration of particles in the river plume is an important mechanism in the determination of the downward sediment flux.

8.3.5.3 Empirical surface water river plume SSC variation in response to river discharge

At a sample site of distance 'x' (m) from the river mouth the suspended sediment concentration was found to be a linear function of the river discharge (e.g. Figure 8.49), where the gradient of the line describes the rate of change in the C_x with respect to the discharge. The regression equations and coefficients of

determination (R^2) for Cast sites 10, 9, 8 7 and 6 (adjacent to the shipping channel) are listed in Table 8.07, and are of the form (eqn - Cast 8),

$$C_{x(\text{Cast } 8)} = 0.0195 \times \varphi_{\text{river}} + 0.0979 \tag{8.15}$$

The fitted equations suggest a background ambient surface *SSC* within northern Poverty Bay of 0.06-0.1 kg.m^{-3} (regression line intercepts). The gradients of the regression equations vary as a linear function of 'x', i.e. the distance of the site from the mouth of the river (Figure 8.50), governed by the equation,

$$dC_x/d\varphi_{\text{river}} = -2e-05 \times z + 0.032 \tag{8.16}$$

The relationship indicates that the closer the Cast site to the mouth of the river the more dependent the suspended sediment concentration on river discharge. Presumably, the turbidity of the plume shows more uniformity with distance from the river mouth due to mixing.

8.3.5.4 Extrapolation to C_0 – the SSC at the mouth of the river

While no direct measurement of the C_0 (the *SSC* at the mouth of the river) were made, the suspended sediment concentration at Cast site 8 (x = 720 m) as a function of the river discharge (φ_{river}) can be estimated (eqn. 8.15) and used to extrapolate C_0 using eqn. 8.14 and eqn. 8.13. Accordingly, Figure 8.51 illustrates the predicted variation in C_0 between 1979 and 2002. C_0 values during the year in which the survey was conducted are relatively small, while Cyclone Bola produced inferred *SSC* at the Turanganui River entrance twice as large as any other event on record (Figure 8.51).

Results suggest approximately 200,000 kg of fine suspended sediment enters Poverty Bay from the Turanganui River on a daily basis, corresponding to 7.6×10^7 kg of sediment on an annual basis (Table 8.08).

8.3.6 Downward sediment flux and potential sedimentation index

In order to quantify the downward sediment flux of the relatively fine sediment from the river plume with distance along the shipping channel some assumptions have been made.

i. The average surface *SSC* along the length of the shipping channel can be estimated using cast sites adjacent to the channel i.e. Cast site 10, 9, 8 7 and 6,
ii. the processes of re-suspension is ignored, and sediment concentration due to river discharging are assumed vertically uniform, and
iii. all sediment is assumed to remain at the site and not be re-worked or transported laterally, analogous to a sediment sink at each site.

These assumptions allow the *potential* height of sediment available for deposition (Δh) along the length of shipping channel to be estimated.

Regression equations for each of the Cast sites are summarised in Table 8.07, and are used to predict the surface *SSC* relative to the river discharge, while the mean, modal and median (d_{50}) grain size and equivalent fall velocity (w_f) of typical suspended sediment at the mouth of the Turanganui River are given in Table 8.09. The equivalent fall velocity (w_f) describes the time sediment takes to settle out of solution through a vertical distance of 1 m under the influence of gravity and in the absence of turbulence, while C_x describes the mass of sediment within a unit area. Therefore, the mass of sediment (kg) deposited per day (Q_{kg}) assuming no re-suspension or lateral transport, and vertically uniform C_x, per unit area (kg.m^{-2}) is defined as,

$$Q_{kg} = 86400 \times (w_f \times C_x) \tag{8.17}$$

Assuming a sediment bulk density of ρ_{sed} =1300 kg.m^{-3} (Chapter 5), then the *potential* height of sediment available for deposition (Δh).

$$\Delta h = Q_{kg} / \rho_{sed} \tag{8.18}$$

Normalising the Δh values for each of the Cast sites by the equivalent Δh value at Cast site 7 allows the variation in the normalised *potential* sedimentation indices (ΔI) along the shipping channel (Figure 8.52) to be investigated, where

$$\Delta I = \Delta h_i / \Delta h_{Cast7} \qquad (i = 6, 7, 8, 9 \text{ and } 10) \tag{8.19}$$

Largest values of ΔI are found to occur approximately 300 m from the entrance to the Swinging Basin, and tend to decrease with distance from the river mouth (Figure 8.52).

8.4 Discussion

Comparisons between the river discharge data and atmospheric conditions (wind velocities, barometric pressure and rainfall) indicate that the conditions experienced during the monitoring period 28/05/99 to 20/06/99 are typical of the environs. Wind velocities, rainfall, atmospheric temperature and barometric pressure variations during both the survey period and the extended temporal coverage are consistent with the summary of climate and weather conditions for Gisborne (Hessell, 1980).

The extent and orographic characteristics of the Waimata catchment result in the Waimata River contributing significantly more water to the Turanganui than the Taraheru catchments. The Taraheru River is estimated to contribute only approximately 2% to the overall volume discharge of the Turanganui River and is significantly less than the 30% as estimated by Walpole (1997) or the $^1/_6$ of the Waipaoa River as used by both Stephens (2001) and Gorman, et al (1997). The extent of the Waimata catchment also results in a slight lag (approximately 1 hour) in peak flood discharge between the Waimata and Taraheru Rivers. River discharges during the survey were predominantly quiescent, however a relatively large flood event with a discharge volume of 63 m^3.s^{-1} on the 6th June 1999, and two relatively minor events with discharges of 11.95 m^3.s^{-1} and 6.62 m^3.s^{-1} occurred during the survey. Extremal analysis suggests a flood event of 63 m^3.s^{-1} magnitude for the

Turanganui River has a return period of less that a ½ yr, and is similar to the discharge of the Waipaoa flood event numerically modelled by Stephens (2001).

During the monitoring period significant wave heights ranged from 0.5 m to 2 m, while peak spectral periods ranged between 5 s and 19 s, and are consistent with the broader temporal wave records for the area as reported by Black, et al. (1997) and Miller (1981). During low river flow condition ($\varphi_{river} < 1\ m^3.s^{-1}$) residual current directions in 10 m water depth are consistent with the dominant anti-cyclonic gyre in Poverty Bay as observed by Williams (1966), Bell (1985), Black, et al. (1997), Stephens, et al. (2000) and Stephens (2001). However, when the flow rate of the Turanganui River is relatively larger, bottom current directions suggest a return flow of more saline oceanic water beneath the river plume, consistent with the numerical model simulations of Black, et al. (1997).

Black, et al. (1997) Stephens, et al. (2000) and Stephens (2001) illustrate the complexity of the circulation patterns within Poverty Bay and identified wind and density driven currents, as well as gyres associated with the propagation of shelf currents across the entrance to Poverty Bay as the dominant forcing mechanism controlling the distribution of the river plumes from both the Waipaoa and Turanganui River. This present study has shown that the spreading characteristics of the Turanganui River plume in the port of Gisborne environs are dependant on the river discharge volume, the wind velocity and baroclinic conditions. During high flow rates the directional spreading is effected primarily by density driven currents and the discharge velocity vector. In more moderate flow conditions and strong winds the plume is driven primarily by the ocean-atmosphere momentum transferral. In strong winds from the S-SE quarter the river plume is forced towards the coastline, while conversely in strong wind conditions from the NW quarter the plume is forced offshore and is relatively well defined within the survey area. Based on the extended temporal wind record, the dominant wind direction is from the N-NW (Figure 8.19) suggesting that, on average, the river plume will be directed towards the shipping channel.

The river plume varies between well mixed to highly stratified, with the degree of mixing dependant upon river discharge. In low flow conditions, profile and transect data show the river plume to be well-mixed or homogeneous, consistent with tidal flow dominating and bottom friction being large enough to generate sufficient turbulence to mix the entire water column (United States Army Corps of Engineers, 1991). Richardson Numbers during low flow periods are shown to be relatively small (Table 8.05), suggesting that the shear forces between the freshwater/saltwater interface is sufficient to overcome the density gradient, resulting in the entrainment and mixing of the two water bodies. When the salinity gradient of the plume is described as 'well mixed' following the conceptual model of Pritchard (1955) and Cameron and Pritchard (1963) the Richardson Numbers range from between 0.8-0.14, which is consistent with the approximate transition from well mixed to strongly stratified (R_i = 0.08 to 0.8) as defined by Fischer, et al. (1979).

In relatively high river discharge conditions the outward flowing relatively buoyant freshwater overrides the more dense saline seawater and results in a bottom return flow of the more saline water. The density, salinity and temperature gradients within the profile are relatively large, and correspondingly so are the Richardson Numbers, suggesting the density gradient is sufficient to inhibit the vertical re-suspension of sediment by turbulent eddies.

The water within the Swinging Basin of the port of Gisborne is consistently more saline and denser than the water immediately outside the port entrance, resulting in a relatively high horizontal density gradient seaward of the Swinging Basin. The relative rapid increase in salinity increases the availability of ions in solution which in turn suppress inter-particle electrochemical repulsive forces, thereby allowing the attractive Van-der Waals forces to dominate and the dispersed particles to flocculate (Mehta et al., 1989). Increasing the size of the flocculated particle and hence the relative fall velocity (Berlamont et al., 1993; Kanayama et al., 1992; Mehta et al., 1989) has the potential to increase the relative rate of sedimentation in the vicinity of the entrance to the Swinging Basin.

Surface water suspended sediment concentrations mirror the distribution of the river plume as observed in the salinity data. However, near the seabed re-entrainment of the surficial sediment is observed, and concentrations increase shoreward and in the lee of the breakwater, consistent with relatively more agitation of the seabed by wave-orbital velocities with decreased water depth. Transect data indicates that when the river plume is well mixed and the Richardson Number is low, the *SSC* is relatively uniform throughout the water column. However when the Richardson Numbers is high, typically density gradients are also relatively large, and the upward sediment flux due to re-suspension is inhibited, resulting in separation of the upward and downward sediment fluxes. The approximate value of the Richardson Number where vertical movement of re-suspended sediment begins to be inhibited by the density gradient of the plume is $R_i = 0.10$, which is similar to the value for the transition from well mixed to strongly stratified as noted by Fischer, et al. (1979).

The horizontal variation in the concentration of water in the surface water (C_x) was found to be an exponential function of the distance from the mouth of the Turanganui River (x) and the decay rate factor (D_x), which decreases as an exponential function of the river discharge. The form of the fitted equation is identical to the time-averaged gradient diffusion equation for the near-bed *SSC* profile as defined by Nielsen, (1992), and suggests that the decrease in *SSC* of the surface water with distance can be explained in terms of gradient diffusion. The decay rate factor is analogous to the mixing length (l_s) in the Nielsen equation (eqn. 6.12) and quantifies the distance the plume (water/sediment) travels before it is mixed with the surrounding water.

The decay rate factor, D_x, has been found to decrease as a linear function of increasing river discharge. The increased mixing (i.e. decreased D_x) at higher discharge rates implies that either turbulent diffusion is larger at higher discharge rates, or the fall velocity (w_f) of the sediment in suspension, and hence the downward flux of sediment due to gravity, is greater. These findings are consistent with the findings of Hill et al. (2000) who noted that the flocculated particle size increased as a function of concentration (which was found to increase with increased river discharging).

At higher river discharges the shear velocity between the buoyant river plume and the underlying, more saline seawater is likely to be comparatively larger, suggesting relatively more turbulent mixing between layers. However, the density gradient that acts to inhibit vertical mixing (Fischer et al., 1979), was also found to increase with increased river discharge. The Richardson Number (R_i), which is a measure of the ratio of turbulent (velocity shear stress) to stabilising influences (density gradient),

was found to increase with increased river discharge (Figure 8.53), and suggests that at higher discharges rates the density gradient is sufficient to inhibit the turbulent diffusion of sediment across the halocline. As such, it is unlikely that the increased shear velocity between the buoyant river plume and the underlying seawater is the sole mechanism for the decay rate factor decreasing with increasing river discharge.

Assuming that the suspended sediment within the river plume will experience flocculation, then the effective fall velocity of the suspended sediment is dependant on the magnitude of the flocculated particle. Berlamont, et al. (1993) and Kanayama, et al. (1992) report particle settling velocity increases with concentration, reaching a maximum at a concentration of 2-10 $kg.m^{-3}$. At concentrations higher than 10 $kg.m^{-3}$ the flocs are broken and settling velocities decrease rapidly due to mutual hindrance (Berlamont et al., 1993). During the monitoring period the *SSC* within the river plume was found to increase within increased river discharge. The largest *SSC* within the river plume was measured on the 06/06/99, and did not exceed 2 $kg.m^{-3}$ (Figure 8.38). As such, the data suggests that the effective fall velocity of the suspended sediment within the river plume can be expected to have increased with increasing sediment concentration, hence providing a possible mechanism for the decrease in the decay rate factor with increased river discharge.

The *SSC* of the surface water at Cast sites adjacent to the shipping channel is strongly correlated to the discharge of the river. Normalised p*otential* sedimentation indices (ΔI) along the length of the shipping channel are shown to vary, with the largest index (and hence highest potential sedimentation rate of fine suspended sediment) located approximately 300 m from the entrance to the Swinging Basin, i.e. ~100 m seaward from the tip of the breakwater. Based on hydrographic survey data, Miller, (1981), Kensington, (1990) and Hutt, (1997) have identified the area ~100 m from the end of the breakwater as having relatively high sedimentation rates. The surficial sediment within the channel ~100 m from the tip of the breakwater consists of approximately 10-20% mud by mass (Chapter 3), and has an in-situ shear strength of 1.6 kPa (Chapter 4). The relatively high ΔI in this area may provide sufficient quantities of mud to cohesively bond the sand within the surficial sediment matrix.

Based on predictions of the suspended sediment concentration at the mouth of the Turanganui River, approximately 7.6×10^{7} kg of fine suspended sediment enters Poverty Bay from the discharging of the Turanganui River on an annual basis (Table 8.08). The predicted mass of sediment discharged by the Turanganui River based on the extrapolation of the measured *SSC* to the river mouth is slightly larger that that estimated by Smith, (1988) of 1.1×10^{7} $kg.yr^{-1}$ determined based on shoreline accretion (determined assuming equivalent quartz density, 2650 $kg.m^{-3}$). The inconsistency between the prediction net sediment mass discharged from the Turanganui River and those estimated by Smith, (1988) is not surprising, as it is unlikely that an accurate estimate of the sediment discharged from the Turanganui River can be determined from shoreline accretion alone. Based on 5% of the predicted annual suspended sediment discharged from the Waipaoa River, the Gisborne District Council (1994) estimated the volume of sediment discharged by the Turanganui River as 6.9×10^{8} $kg.yr^{-1}$. The volume of sediment discharged into Poverty Bay attributed to the Turanganui River by Gisborne District Council (1994) is an order of magnitude larger than both those predicted during this study and that of Smith, (1988). Both the estimates of Smith, (1988) and Gisborne District Council (1994) have been inferred, while this study has measured the *SSC* within the river plume and extrapolated the results using a fitted equation ($R^2 = 0.82$) of a form

similar to the time-averaged gradient diffusion equation for the near-bed *SSC* profile as defined by Nielsen, (1992).

8.5 Conclusion

An investigation into the distribution characteristics of the Turanganui River plume, adjacent to the port of Gisborne, was undertaken using spatially and temporally spaced CTD and turbidity profiling between 28-05-99 and 20-06-99. Atmospheric conditions and river discharge data was made available by the Gisborne District Council, and used in both the analysis of the river plume data and to determine that the conditions during the survey period were typical of the environment. Dominant wind directions are from the N-NW; however showed a strong diurnal characteristic, with afternoon onshore winds due to the formation of localised convection cells.

The average discharge of the Turanganui River is 4.8 $m^3.s^{-1}$, however during flood events discharges are often an order of magnitude larger, and the Cyclone Bola event was two orders of magnitude larger; with the Turanganui River having a discharge of 693 $m^3.s^{-1}$. A significant flood event with a discharge of 63 $m^3.s^{-1}$ was recorded during the survey period, which extremal analysis suggests has a return period of less than ½-year.

The surface distribution of the river plume is influenced by wind velocity, discharge, and baroclinic conditions. In high flow conditions the aspect of the river plume is dominated by the baroclinic conditions and discharge velocity of the river. Conversely, in high wind conditions the directional aspect of the plume is more a function of the wind direction, in winds from the N-NW the river plume is forced offshore towards the shipping channel, while in S-SE winds the plume is forced towards the coastline and is not as defined in the channel area.

The Turanganui River plume varies in thickness between approximately 1-3 m, while the mixing characteristics of the river plume vary between well mixed, during relatively low flow conditions, to highly stratified at discharges > 1-2 $m^3.s^{-1}$. Surface density gradients are relatively high near the entrance to the Swinging Basin, with the Swinging Basin waters having relatively larger salinities and densities. Residual bottom current directions during relatively high river discharge suggest a bottom return current, and this is illustrated in transect data that depicts an intrusion of more dense, relatively saline oceanic water beneath the river plume. At lower discharges the near-bed residual current direction is consistent with the formation of an anti-clockwise gyre in Poverty Bay as identified by Stephens, et al. (2000) and Black, et al.(1997).

Suspended sediment concentrations in the surface waters of the river plume increase with river discharge. The distribution of the *SSC* at the surface is similar to the salinity and temperature distribution and is a function of the wind velocity, discharge and baroclinic conditions. In contrast, the *SSC* at 4 m below the surface (beneath the river plume) appears to have a re-suspended sediment component, and increases with decreased water depth, consistent with the relative wave-orbital velocity increasing. At Richardson Numbers greater than approximately $Ri > 1.0$-1.5 separation of the *SSC* in the river plume and the re-suspended sediment is apparent, suggesting that the density gradient is sufficient to overcome turbulent re-suspension. In contrast, when

Ri is relatively small the *SSC* appears to be relatively uniform with depth, suggesting mixing. The Ri value at which the vertical re-suspension of sediment begins to be inhibited is similar to the transition from well mixed to strongly stratified (R_i = 0.08 to 0.8) as defined by Fischer, et al. (1979).

The concentration of sediment in the surface water (C_x) varies as an exponential function of distance (x) and a decay rate factor (D_x). In turn the decay rate factor is found to be a function of the discharge of the river, and shown to decrease with increased river discharging, suggesting that at higher discharges the concentration of sediment in the river plume decreases at a relatively faster rate, presumably due to either increased shear between the relatively freshwater of the river plume and the saline bottom water, or due to enhanced flocculation (and hence fall velocity) due to the relatively higher concentration of sediment at larger discharges.

Linear relationships are shown to exist between the river discharge and the *SSC* in the surface water at sites adjacent to the shipping channel, with highest concentrations, and hence potential sedimentation indices (ΔI) occurring approximately 300 m from the entrance to the Swinging Basin. Further, the relationships suggest a background ambient surface *SSC* within northern Poverty Bay of 0.06-0.1 $kg.m^{-3}$.

The linear relationship between the suspended sediment concentration and discharge, and the exponential relationship between the distance and concentration is used to predict C_0 values, the concentration of suspended sediment at the mouth of the river. Accordingly, ~208,000 kg, and 7.6×10^7 kg are predicted to be discharged into Poverty Bay from the Turanganui River as suspended sediment on a daily and annual basis respectively. This study provides the first estimate of the annual mass of sediment discharged into Poverty Bay from the Turanganui River based on actual measured *SSC*, rather than inferred from shoreline accretion (i.e. Smith, 1988) or the mass of sediment discharged into the bay by the Waipaoa River (i.e. Gisborne District Council, 1994).

While the spatial distribution of the CTD measurement sites are perhaps not ideal for examining the distribution pattern of the Turanganui River plume and estimating the concentration of suspended sediment at the mouth of the river, all derived relationships are shown to be statistically significant at the 95% level or better.

Table 8.01 Cast locations in Poverty Bay Circuit co-ordinates. NTU measurements casts and depths are also listed.

Cast Number	Northing (m)	Easting (m)	NTU measurement depths (m)
1	694267	311866	*n/a*
2	693552	311448	*n/a*
3	693670	311420	0, 2, 4, 6
4	693760	311424	*n/a*
5	693933	311449	0, 2, 4
6	694109	311478	0, 1, 2
7	694048	311334	0, 2, 3
8	693902	311186	0, 2, 4
9	693849	311039	0, 2, 3, 4
10	693757	310920	0, 2, 4, 6
11	693629	310827	*n/a*
12	693577	310835	*n/a*
13	693095	311156	*n/a*
14	693305	311033	*n/a*
15	693550	311114	0, 2, 4
16	693808	311189	*n/a*
17	692587	310745	*n/a*
18	692269	310971	*n/a*
19	691815	311534	*n/a*
20	691745	311816	*n/a*
21	693677	310548	*n/a*
22	693440	310214	*n/a*

Table 8.02 NTU and *SSC* values of the 6 samples used to calibrate the NTU measurements. Also shown are the regression equation and correlation coefficient R^2 of the fitted curve.

Sample	NTU Value	SSC (kg/m^3)
1	32	0.53
2	13	0.07
3	17	0.40
4	34	0.72
5	57	0.86

Table 8.03 Flood event return periods and relative discharge magnitudes for the Waimata River. Return periods have been determined using extremal probability analysis based on 20-year river discharge data spanning the period May 1978 to May 1998.

R^2 =	0.94					
	Waimata R.					Tarndale R.
Return period (yr)	Discharge ($m^3.s^{-1}$)	Standard deviation (Discharge)	Confidence interval (-95%)	Confidence interval (+95%)	Probability of exceedance (%)	Discharge 95% correction factor ($m^3.s^{-1}$)
0.5	81	60	-36	198	100.0	83
1	133	92	-47	312	100.0	136
2	190	127	-59	438	99.9	193
5	271	178	-77	619	89.3	277
10	337	219	-92	766	65.1	344
25	429	276	-112	971	33.5	438
50	503	322	-128	1134	18.3	513
100	579	369	-145	1302	9.6	590

Table 8.04 CTD survey information including survey times, atmospheric conditions (wind velocity and air temperature), Turanganui River discharge and mean high and low water (MHW, MLW) time and height. Locations at which CTD measurements were taken are illustrated in Figure 8.05.

Survey date	Survey start time	Survey finish time	Average wind direction (degrees)	Average wind speed ($km.hr^{-1}$)	Air temperature (degrees)	Average discharge ($m^3.s^{-1}$)	MHW time	MHW height	MLW time	MLW height
28/05/1999	06:50	07:50	313	20.8	17.4	0.89	4:28	1.86	10:39	0.59
29/05/1999	07:44	09:20	235	8.8	16.7	0.74	5:09	1.84	11:21	0.58
30/05/1999	08:29	10:08	297	11.2	17.5	0.73	5:47	1.81	12:00	0.57
31/05/1999	09:19	10:50	269	4.1	17.3	0.74	6:26	1.79	12:40	0.57
1/06/1999	10:02	11:46	248	18.0	15.2	0.71	7:07	1.78	13:22	0.58
2/06/1999	10:55	13:27	122	11.0	18.5	0.41	7:53	1.77	14:06	0.60
3/06/1999	11:47	14:02	256	11.2	14.7	0.73	8:41	1.76	14:52	0.62
4/06/1999	12:00	14:15	329	5.8	14.8	0.85	9:31	1.76	15:42	0.63
6/06/1999	13:16	15:52	125	8.8	14.7	63.46	11:04	1.78	17:16	0.62
8/06/1999	15:01	16:37	317	13.6	15.1	6.91	12:38	1.82	18:48	0.56
14/06/1999	07:55	09:46	14	3.1	13.7	3.86	5:34	2.03	11:52	0.29
15/06/1999	08:48	10:36	211	15.5	20.2	3.34	6:31	2.03	12:47	0.31
17/06/1999	10:48	12:29	283	10.3	17.1	3.73	8:27	2.01	14:38	0.41
18/06/1999	11:44	13:49	285	10.4	15.8	3.17	9:24	1.99	15:35	0.48
19/06/1999	13:04	14:56	239	5.3	14.5	2.79	10:19	1.97	16:32	0.54
20/06/1999	13:40	15:10	330	14.4	16.7	2.51	11:14	1.95	17:26	0.59

Table 8.05 Richardson Numbers used to describe the capacity of the density driven currents to transfer momentum and sediment across a halocline, for the period 28/05/1999 to 20/06/999 at Cast site 8. Wind, discharge and baroclinic speed and directional components of the river plume assuming a 1% and 2% momentum transferral between the wind and surface water velocities. Residual bottom current direction and magnitudes are based on *InterOcean S4ADW* current meter measurement as a site adjacent to the shipping channel.

Survey date	wind, discharge and baroclinic speed (1%) $m.s^{-1}$	wind, discharge and baroclinic speed (2%) $m.s^{-1}$	angle (degrees) 1%	angle (degrees) 2%	Residual bottom current ($m.s^{-1}$)	Direction	Richardson Number (1%wind)	Richardson Number (2%wind)
28/05/99	0.10	0.14	267	284	0.19	113	0.06	0.05
29/05/99	0.10	0.13	231	232	0.17	106	0.10	0.10
30/05/99	0.09	0.12	248	260	0.19	173	0.17	0.09
31/05/99	0.06	0.07	237	242	0.17	174	0.11	0.06
01/06/99	0.09	0.14	240	243	0.17	174	0.06	0.04
02/06/99	0.13	0.13	217	203	0.18	172	0.73	0.59
03/06/99	0.09	0.12	239	243	0.17	169	0.14	0.09
04/06/99	0.12	0.12	238	246	0.19	154	0.31	0.23
06/06/99	0.36	0.36	226	222	0.17	38	0.38	0.24
08/06/99	0.29	0.30	238	245	0.19	62	0.34	0.28
14/06/99	0.09	0.09	233	237	0.16	35	0.15	0.10
15/06/99	0.18	0.22	226	223	0.19	55	0.13	0.09
17/06/99	0.14	0.16	240	247	0.18	45	0.14	0.10
18/06/99	0.16	0.18	238	245	0.18	45	0.18	0.13
19/06/99	0.12	0.14	231	232	0.18	45	0.13	0.09
20/06/99	0.11	0.13	250	269	0.18	45	0.15	0.13

Table 8.06 Decay rate factors of *SSC* within the river plume and river discharge. Decay rate factors (D_x) are determined as the gradient of the line relating $\ln(C_x)$ to distance (x), while the R^2 statistic defines the fit of the regression line to the data. Only results in which the correlation coefficient, R^2, were greater than 0.75 were used in the analysis.

Decay rate factors (D_x)	Discharge ($m^3.s^{-1}$)	Correlation coefficient (R^2)
588	63.46	0.93
909	3.17	0.86
1429	3.34	0.92
1429	2.79	0.88
2500	0.85	0.84

Table 8.07 Regression analysis results relating river discharge (φ_{river}) and the suspended sediment concentration (SSC) at various locations along the shipping channel. The high R^2 values provide the confidence to extrapolate the equations over a broader temporal range.

Cast site	Equation	R^2	Distance from river mouth (m)
6	$C_{x(Cast\ 6)} = 0.025x\varphi_{river} + 0.06$	1.00	380
7	$C_{x(Cast\ 7)} = 0.023x\varphi_{river} + 0.10$	0.99	510
8	$C_{x(Cast\ 8)} = 0.019x\varphi_{river} + 0.10$	0.99	720
9	$C_{x(Cast\ 9)} = 0.015x\varphi_{river} + 0.10$	0.98	860
10	$C_{x(Cast\ 10)} = 0.014x\varphi_{river} + 0.10$	0.98	1010

Table 8.08 Average daily and yearly mass of sediment deposited into Poverty Bay by the Turanganui River. Sediment masses have been estimated using eqn. 8.09, 8.08 and 8.07. C_0 is the *SSC* of the surface water at the mouth of the Turanganui River.

Average daily C_0 ($kg.m^{-3}$)	0.50
Average daily discharge ($m^3.s^{-1}$)	4.82
Average kg per day	208,632
Average kg per year	76,150,635
Average kg per year from GDC	690,000,000

Table 8.09 Mean, modal and median grain (d_{50}) size characteristics and equivalent fall velocity (w_f) of typical suspended sediment within the river plume at the mouth of the Turanganui River, Poverty Bay, New Zealand.

Distribution characteristic	Size
Mean	66 μm
Mode	69 μm
Median (d_{50})	61 μm
Equivalent (w_f)	0.0028 $m.s^{-1}$

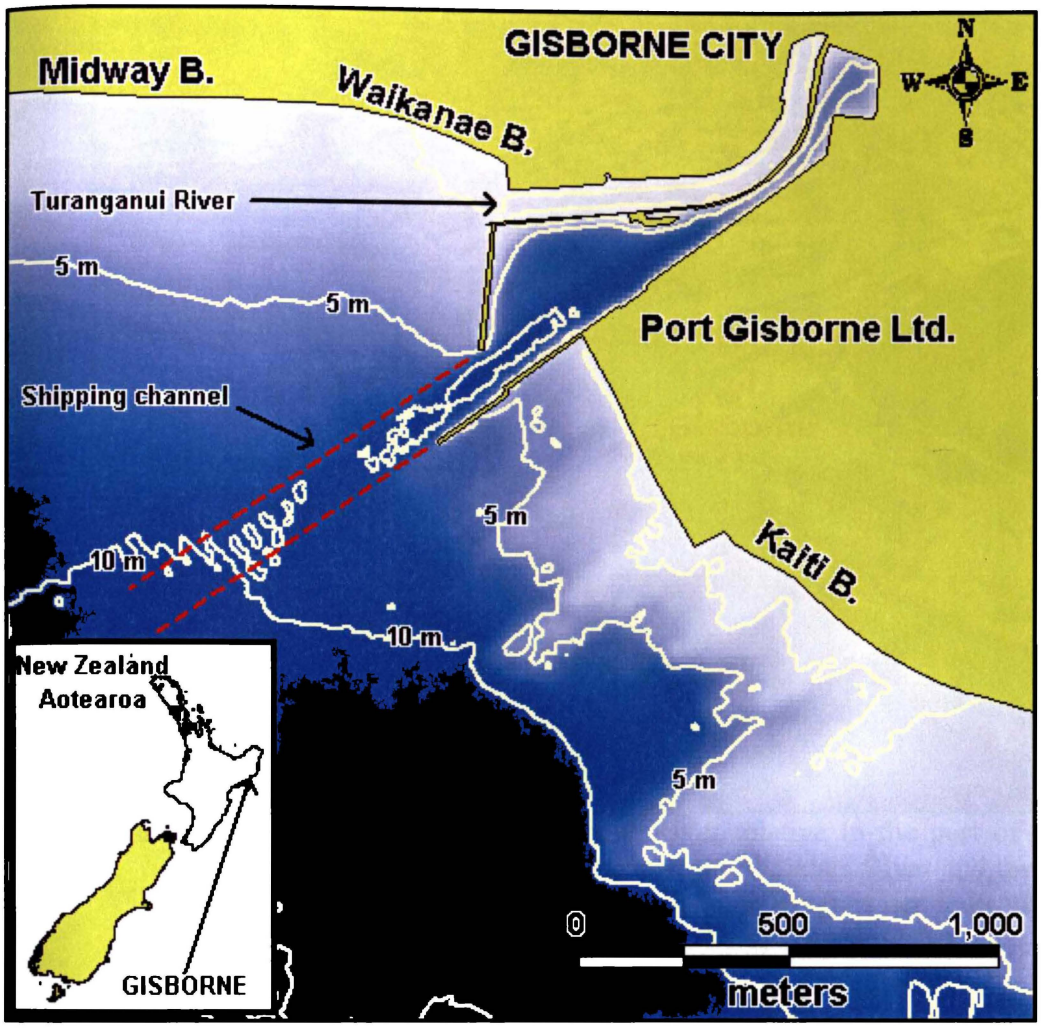

Figure 8.01 Chart illustrating the location of Poverty Bay and the port of Gisborne on the East Coast of New Zealand's North Island.

Figure 8.02 Location of the Turanganui River relative to the port of Gisborne. Also shown are the two tributary rivers; the Waimata River and the Taraheru River. The turbid water of the Turanganui River water indicates a high-suspended sediment load (Supplied by B. Turnpenny).

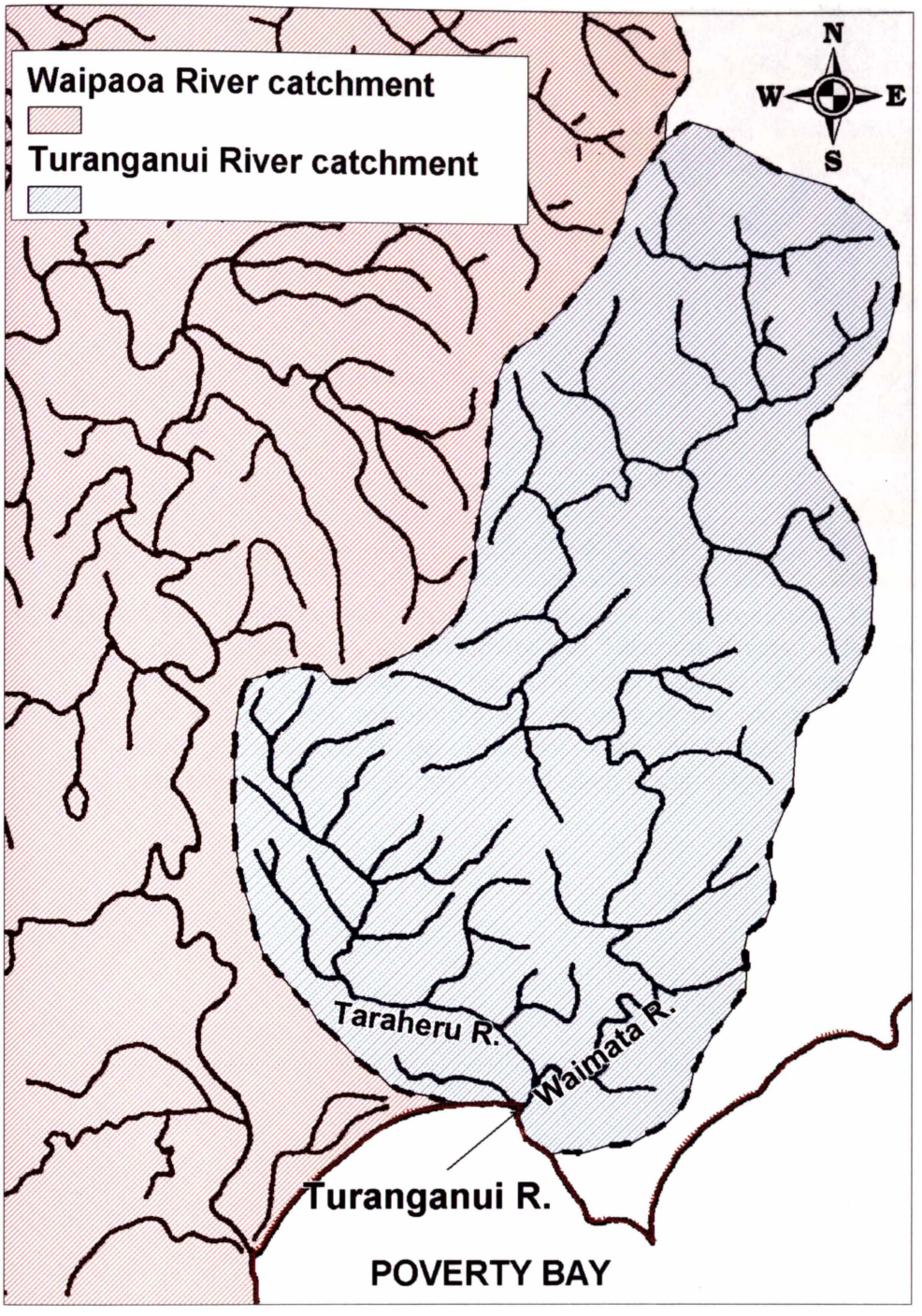

Figure 8.03 Turanganui River catchment, including the Waimata and Taraheru River catchment areas. The catchment consists of approximately 220 km^2 of highly erodible and faulted Tertiary sandstone and mudstone and crushed Cretaceous argillite (adapted from Kensington, 1990).

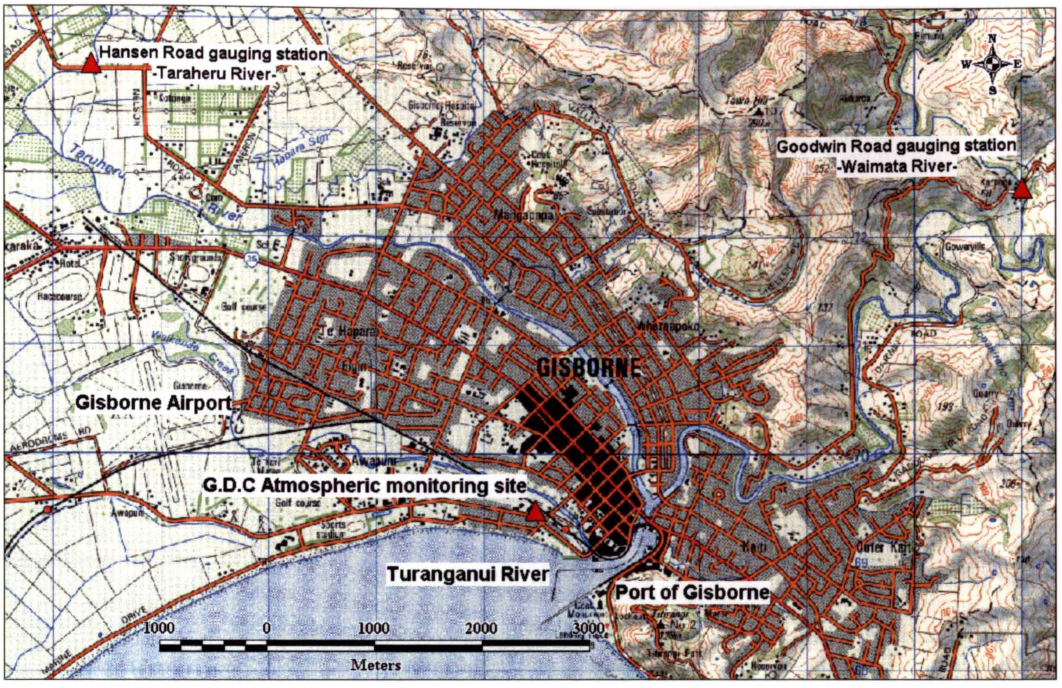

Figure 8.04 Topographical map illustrating the approximate location of the gauging stations on the /Waimata and Taraheru Rivers. Also shown is the approximate location of the Gisborne District Council and Hydro-Technologies Ltd. monitoring site adjacent to the mouth of the Turanganui River. Compared to the Taraheru River catchment, the Waimata River catchment consists of comparatively steep topography.

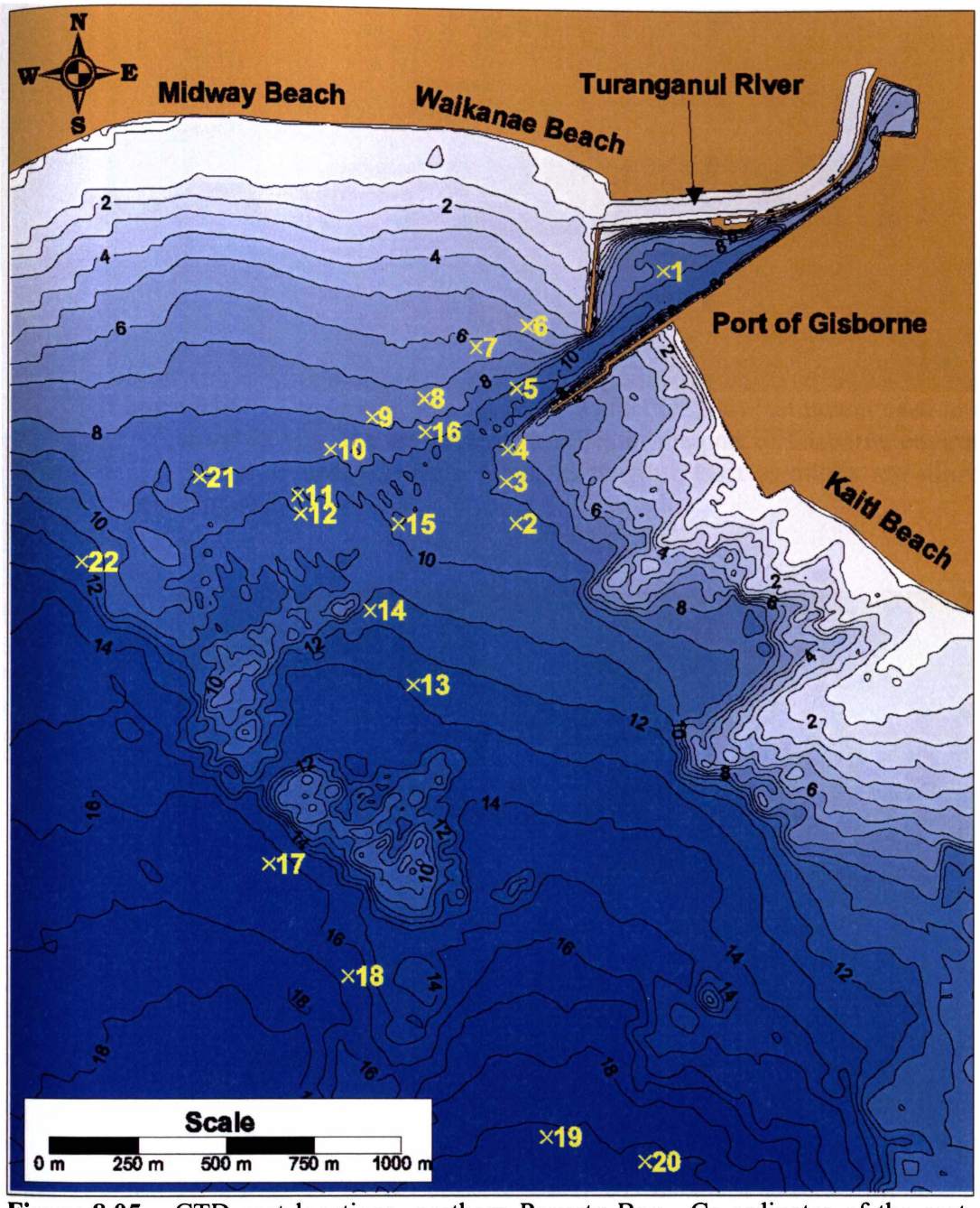

Figure 8.05 CTD cast locations, northern Poverty Bay. Cc-ordinates of the cast locations are given in Table 8.01(Poverty Bay Circuit). The monitoring period extended from 28/05/99 to 20/06/99.

Figure 8.06 The *Ocean Sensors CTD* (Model OS200) instrument used to measure conductivity and temperature profiles in the port of Gisborne environs. The sensor is approximately 1.5 m in length. Cast locations are illustrated in Figure 8.05

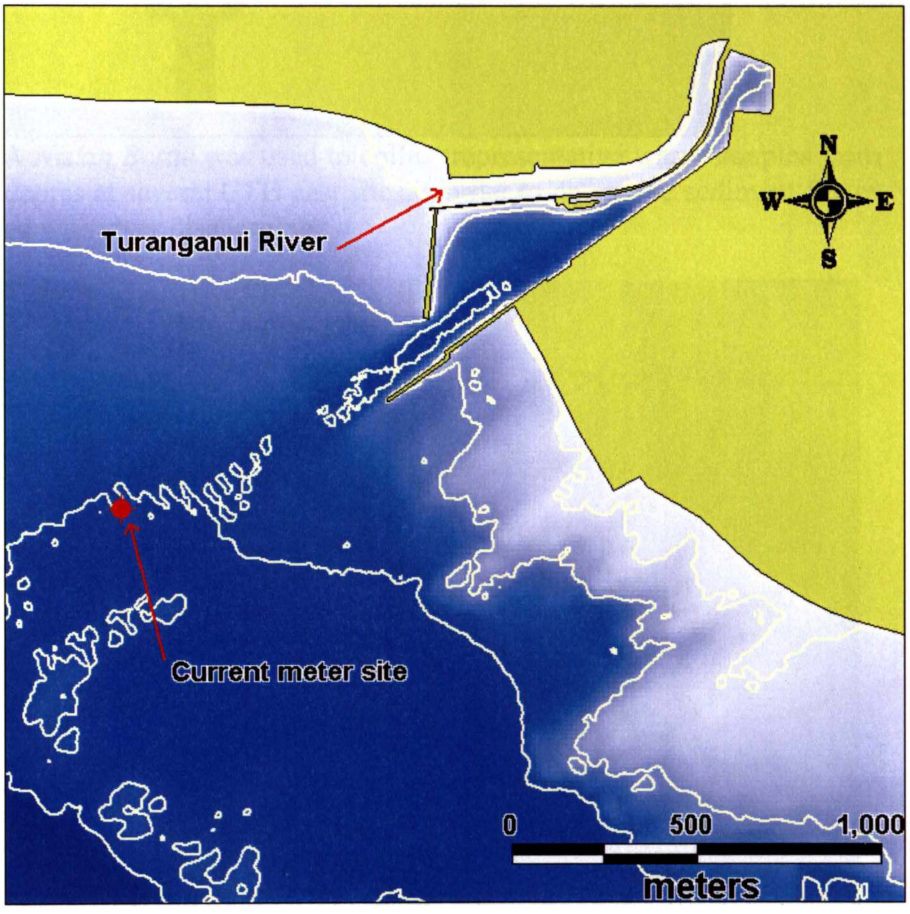

Figure 8.07 The *InterOcean S4ADW* current meter deployment site adjacent to the shipping channel in the port of Gisborne environs. The monitoring period extended from 28/05/99 to 20/06/99.

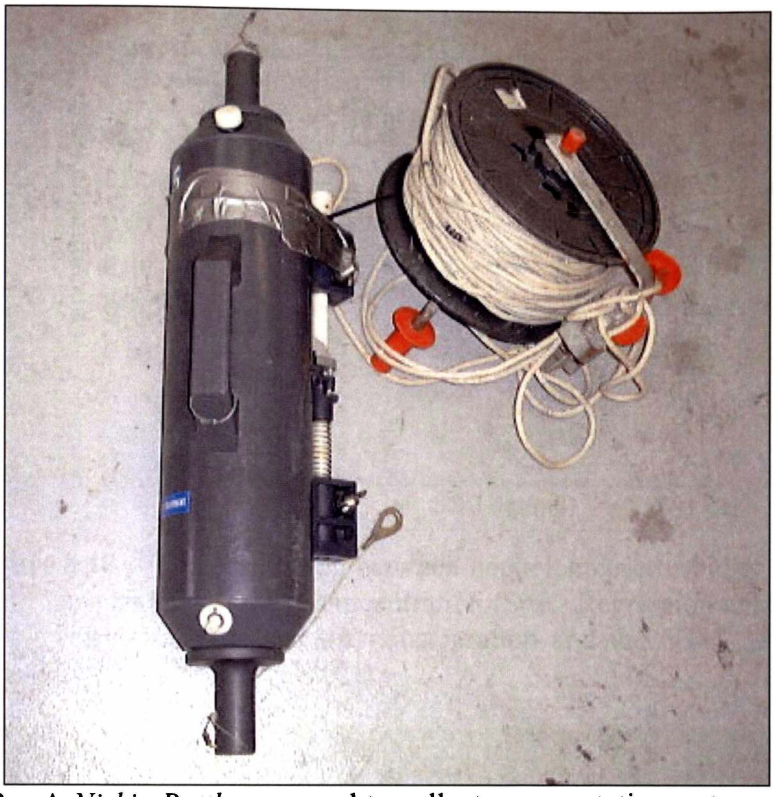

Figure 8.08 A *Niskin Bottle* was used to collect representative water samples from various depths at several CTD cast sites in order to determine sediment fluxes associated with river discharging.

Figure 8.09 The *Hach Portalab Turbidimeter* (model 16800) and turbidity standards used to determine the relative turbidity of a solution in either field or laboratory conditions. The turbidity is measured in nephelometric turbidity units (NTU).

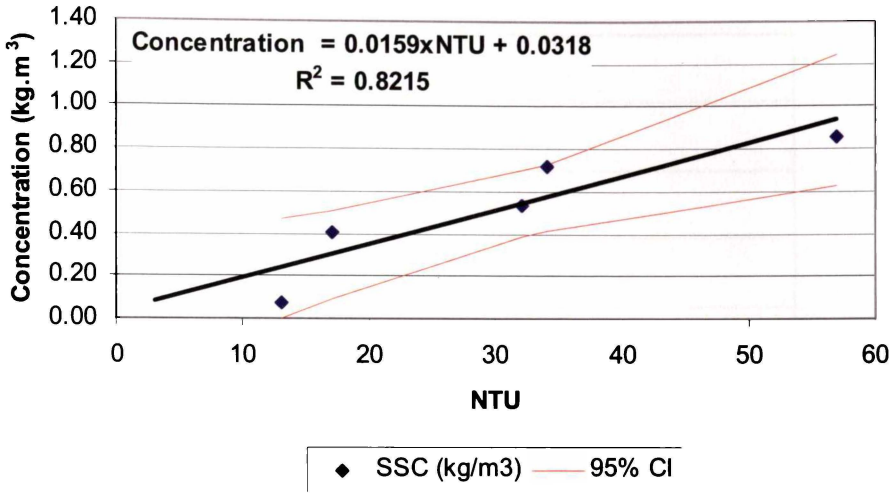

Figure 8.10 The correlation between nephelometric turbidity units (NTU) and the suspended sediment concentration (Site. Regression analysis suggests a good correlation between the concentration and the NTU. Also shown are 95% Confidence Intervals (CI).

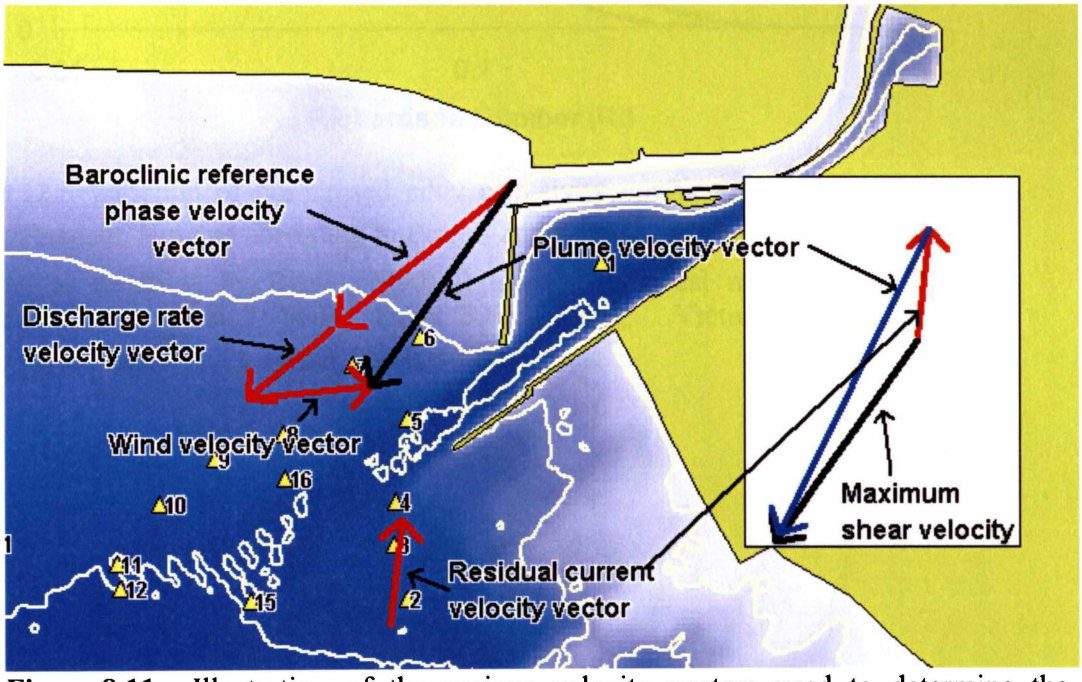

Figure 8.11 Illustration of the various velocity vectors used to determine the maximum shear velocity between the buoyant surface plume from the Turanganui Rive and the residual current velocity vector. By resolving the balance between the baroclinic reference phase, river discharge and wind velocity vectors (i.e. speed and direction), the potential maximum shear velocity can be determined.

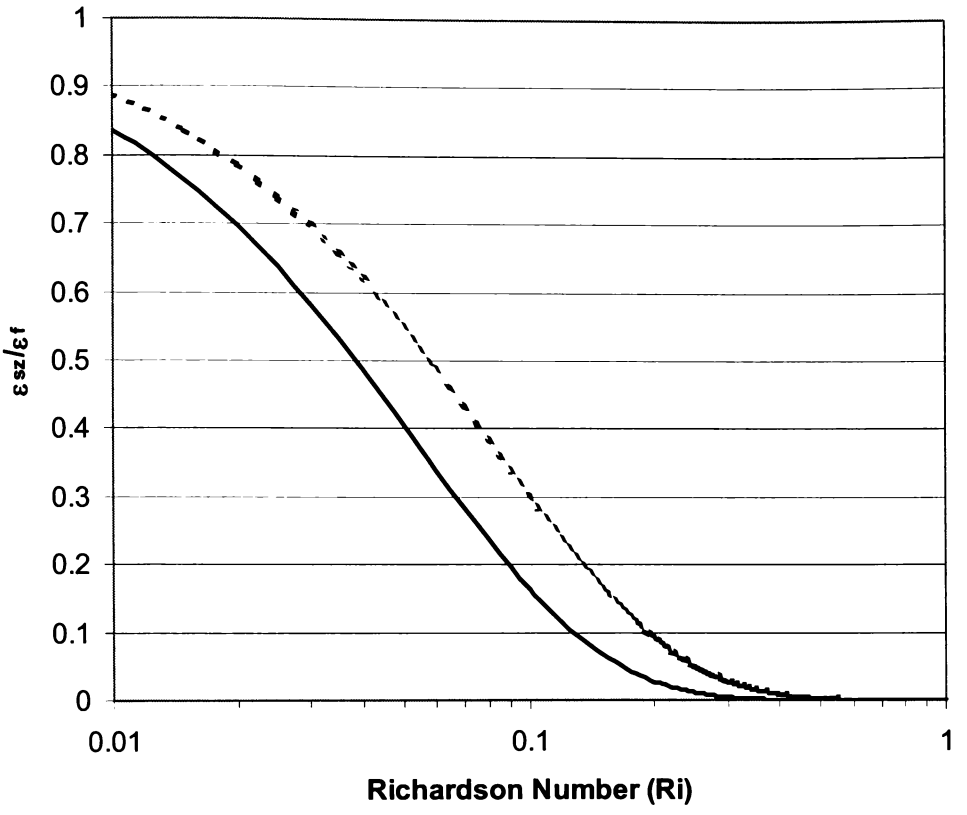

Figure 8.12 Variation of normalised eddy diffusivity coefficients with gradient Richardson Number according to Perrels and Karelse, $\varepsilon_{sz} = \varepsilon_s \left[\exp(-18R_i)\right]$, and as modified by Black (1990) following numerical modelling of the McLennan Strait and Lake Wellington, Victoria, Australia, $\varepsilon_{sz} = \varepsilon_s \left[\exp(-12R_i)\right]$ (after Black, 1990)

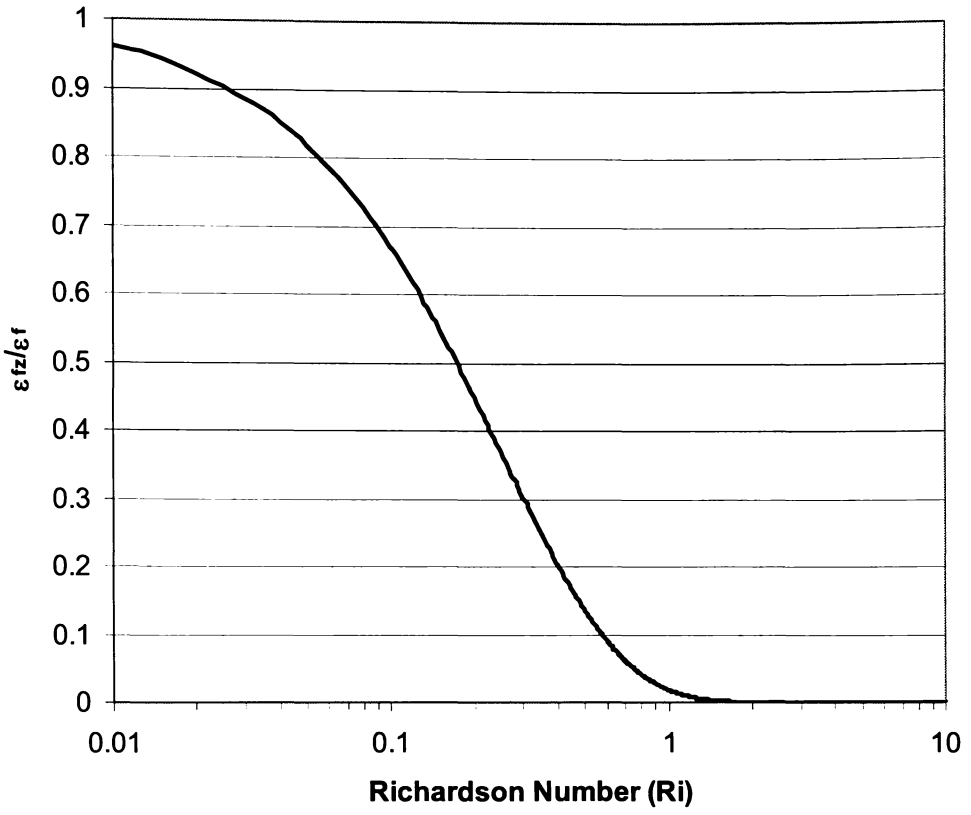

Figure 8.13 Variation of normalised eddy viscosity coefficients with gradient Richardson Number according to Perrels and Karelse $\varepsilon_{f_z} = \varepsilon_f[\exp(-4R_i)]$ (after Black, 1990)

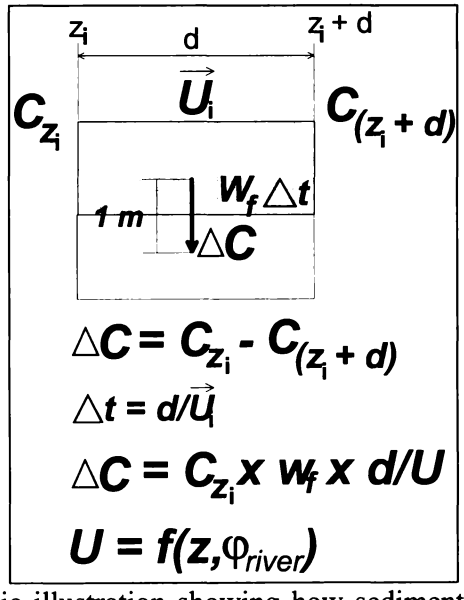

Figure 8.14 Schematic illustration showing how sediment concentration within a river plume varies with time, which is analogous to distance.

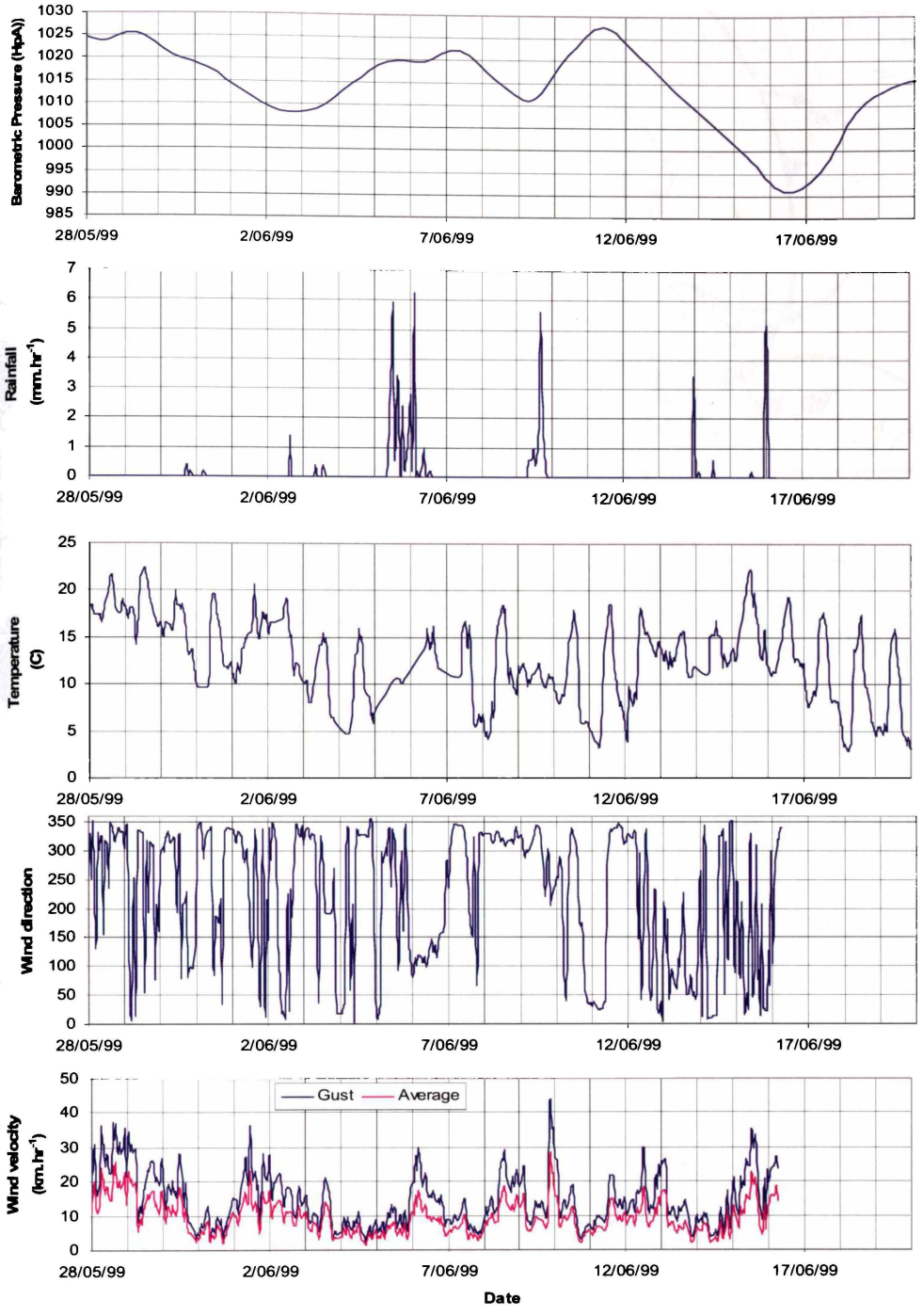

Figure 8.15 Atmospheric conditions during the plume monitoring period (28th May to 20th June, 1999). Barometric pressure was recorded daily at the Gisborne Airport. Wind direction and strength (mean and gust), rainfall and ambient air temperature were measured hourly at the Gisborne District Council and Hydro-Technologies Ltd. monitoring site adjacent to the Turanganui River mouth (Figure 8.04). Data supplied by Gisborne District Council and Hydro-Technologies Ltd.

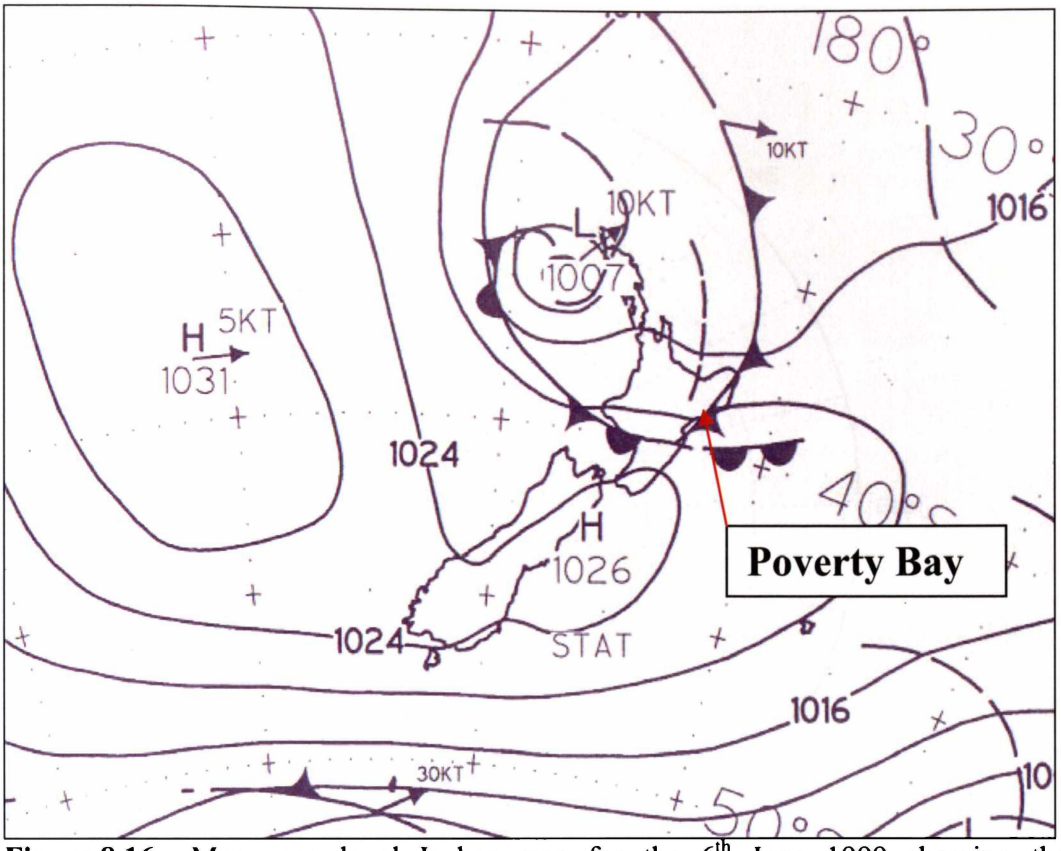

Figure 8.16 Mean sea level Isobar map for the 6th June 1999 showing the formation of a depression to the northwest of New Zealand with associated frontal systems. The passage of the low-pressure system across New Zealand resulted in winds rotating from the north through to south and resulted in the largest, most persistent rain event recorded during the survey period (Supplied by Metservice, New Zealand).

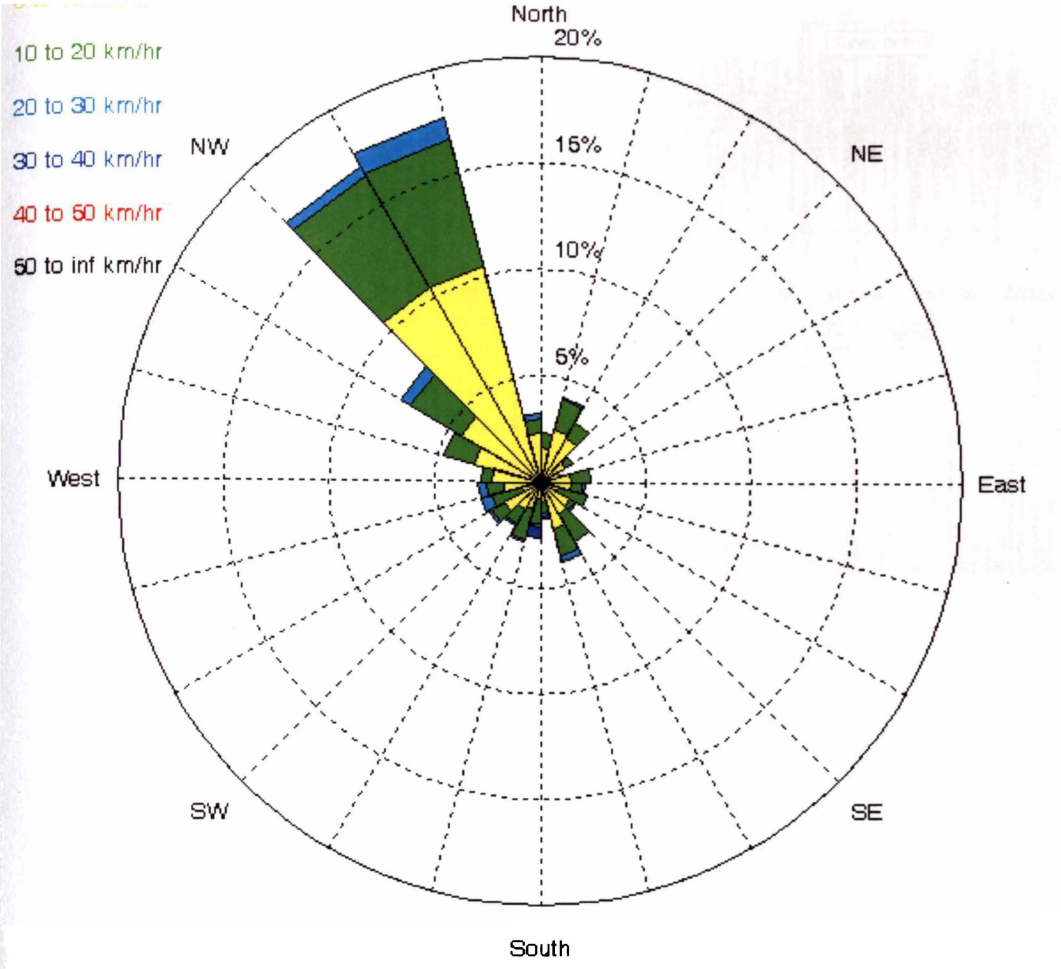

Figure 8.17 Compass rose of the mean wind velocity (magnitude and direction from) during the plume-monitoring period (28th May to 20th June, 1999). The predominant wind direction during the survey period was from the N-NW; however the strongest winds were from the south. Data supplied by Gisborne District Council and Hydro-Technologies Ltd.

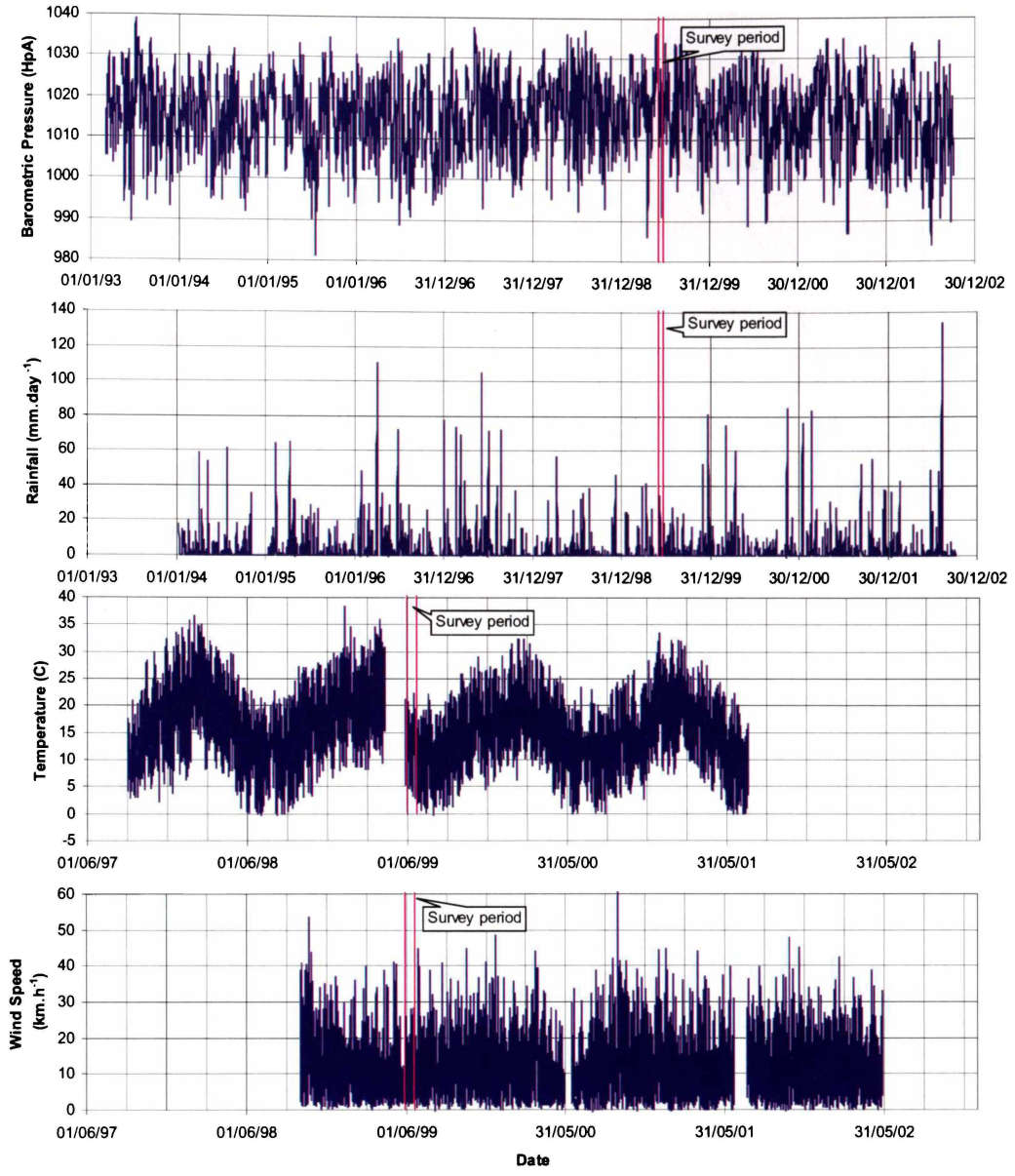

Figure 8.18 Extended temporal atmospheric data. Barometric pressure was recorded daily at the Gisborne Airport. Wind strength (mean) and ambient air temperature were measured hourly while the rainfall was measured daily at the Gisborne District Council and Hydro-Technologies Ltd. monitoring site adjacent to the Turanganui River mouth (Figure 8.04). Data supplied by Gisborne District Council and Hydro-Technologies Ltd. Note that the data spans different time periods.

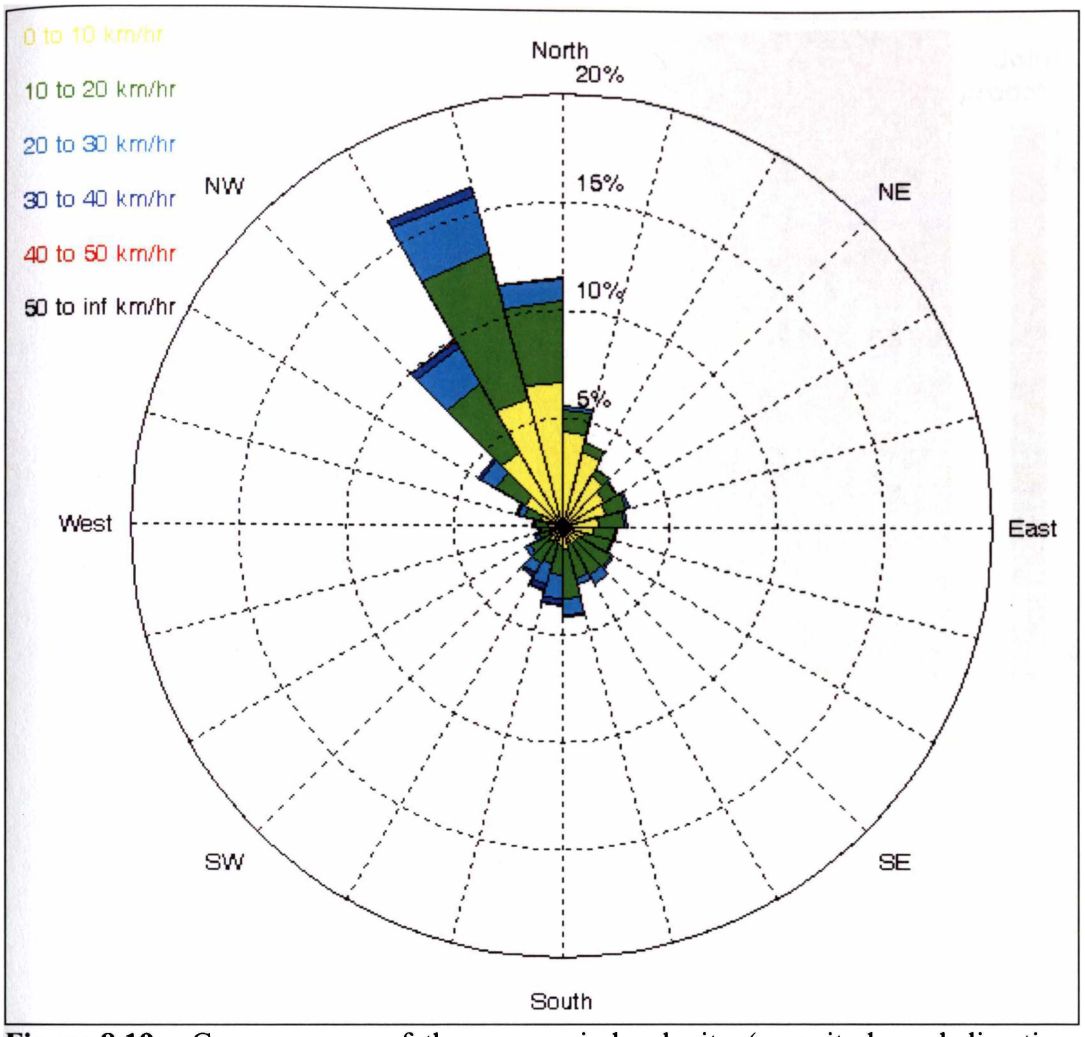

Figure 8.19 Compass rose of the mean wind velocity (magnitude and direction from) for the period 1st October 1998 to 1st October 2002. Data supplied by Gisborne District Council and Hydro-Technologies Ltd.

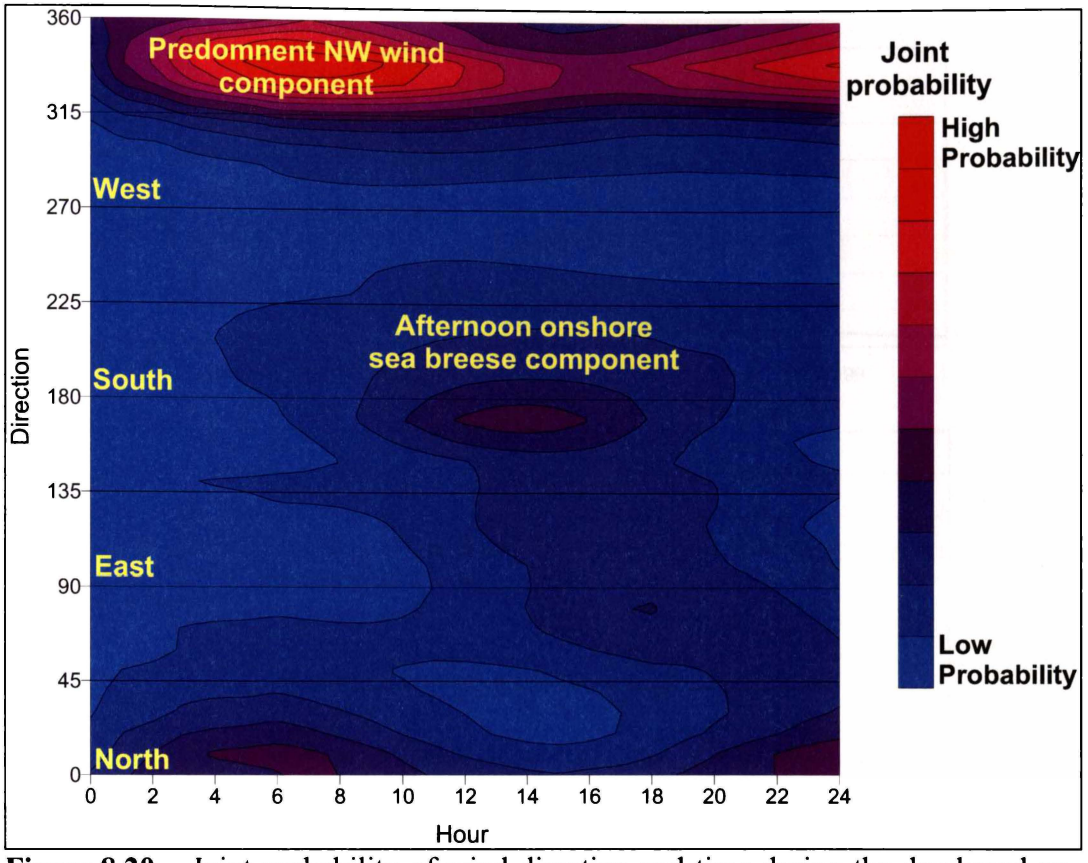

Figure 8.20 Joint probability of wind direction and time during the day based on hourly wind measurement for the period 1st October 1998 to 1st October 2002. The joint probability analysis illustrates that the dominant wind direction is from the NW direction during much of the day, however there is a distinct shift in the probability due to the formation of localised convection cells resulting in relatively strong afternoon onshore (SE quarter) breezes.

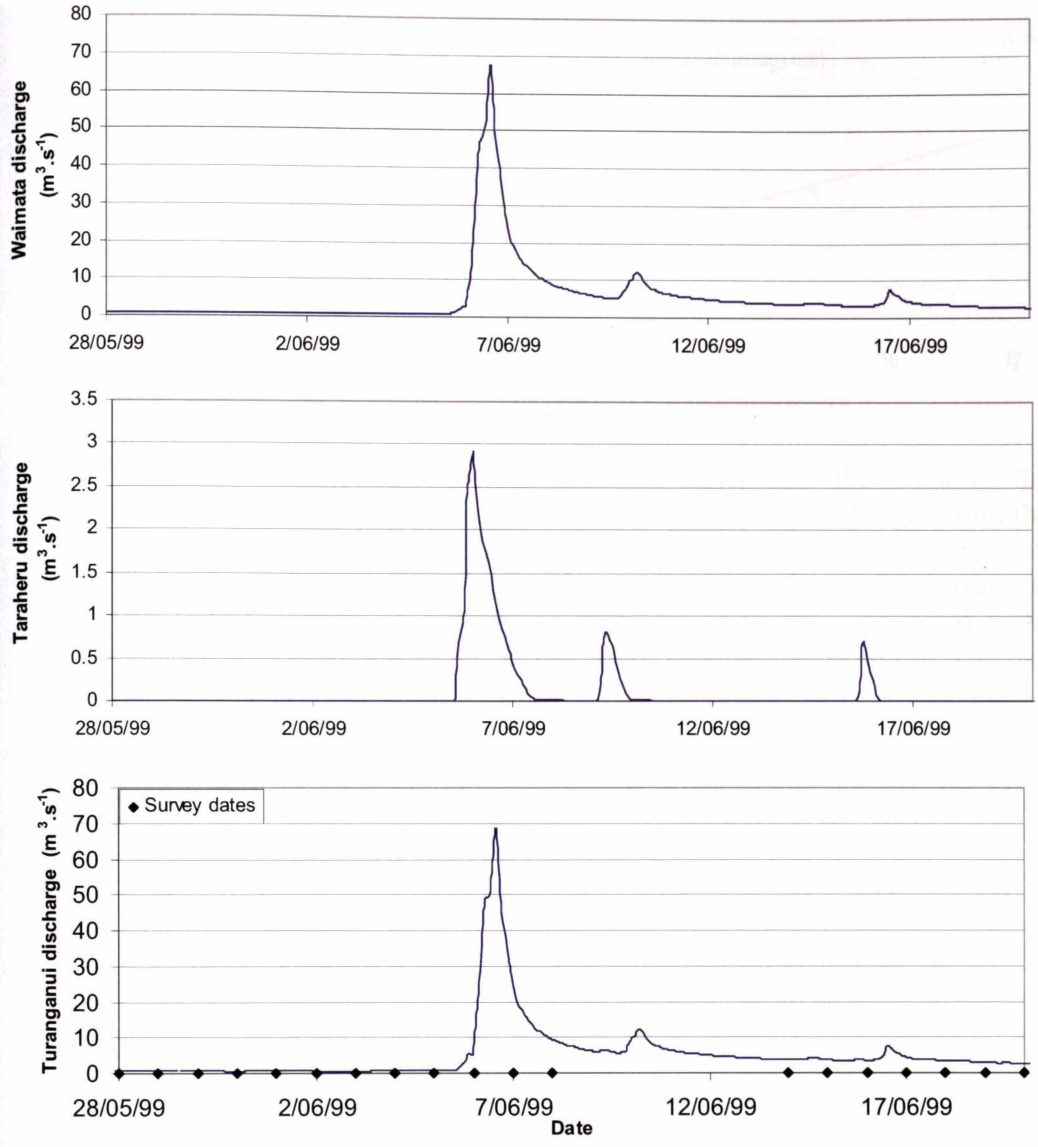

Figure 8.21 Discharge volumes from the Waimata, Taraheru and Turanganui Rivers for the period 28/05/99 to 20/06/99. The Waimata and Taraheru Rivers are the sole tributaries of the Turanganui River and have been used to determine the discharge of the Turanganui River. Data supplied by Gisborne District Council and Hydro-Technologies Ltd. Also shown are the survey dates.

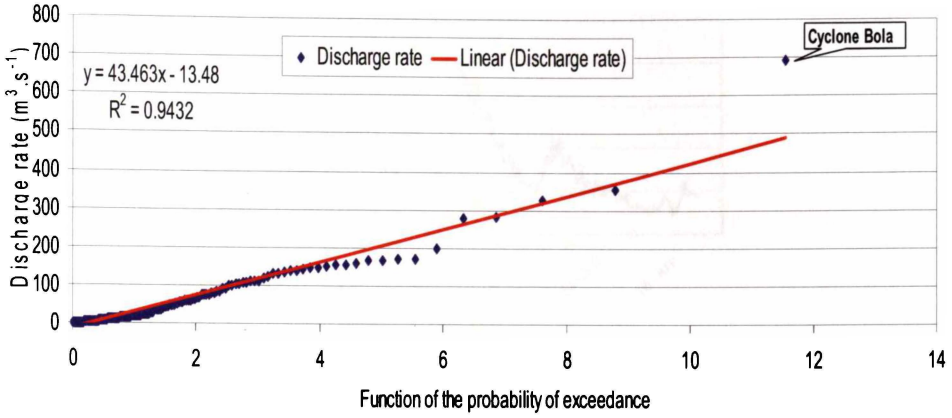

Figure 8.22 Regression analysis used to determine the suitable distribution characteristics of the largest monthly significant discharges from the 20-year Waimata River discharge data. Regression analysis suggests the suitability of a Weibull distribution with a shape parameter of k = 0.75, corresponding to a correlation coefficient (R^2) of 0.94. The discharge associated with Cyclone Bola plots as a distinct outlier. Data supplied by Gisborne District Council and Hydro-Technologies Ltd.

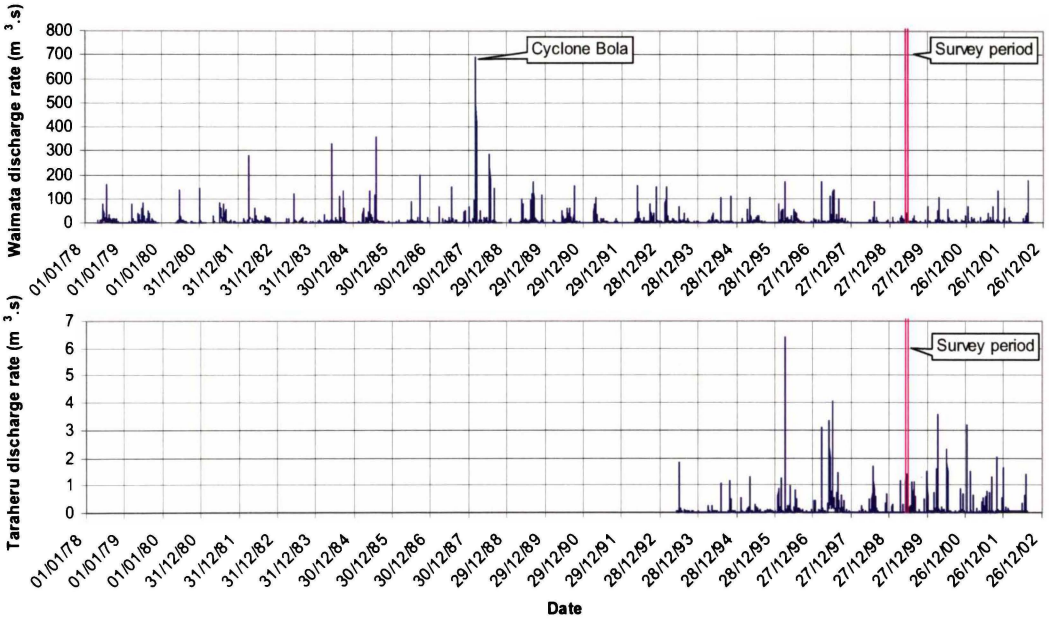

Figure 8.23 Discharge volumes from the Waimata and Taraheru Rivers for the period 01/05/78 to 01/10/02. The Waimata and Taraheru Rivers are the sole tributaries of the Turanganui River and are used to determine the discharge of the Turanganui River, with the Taraheru River contributes approximately 2% to the discharge of the Turanganui River. The year that the survey data falls into appears to be relatively quiescent. Cyclone Bola plots as a distinct outlier, and is close to twice the magnitude of any other flood event within the record. Data supplied by Gisborne District Council and Hydro-Technologies Ltd.

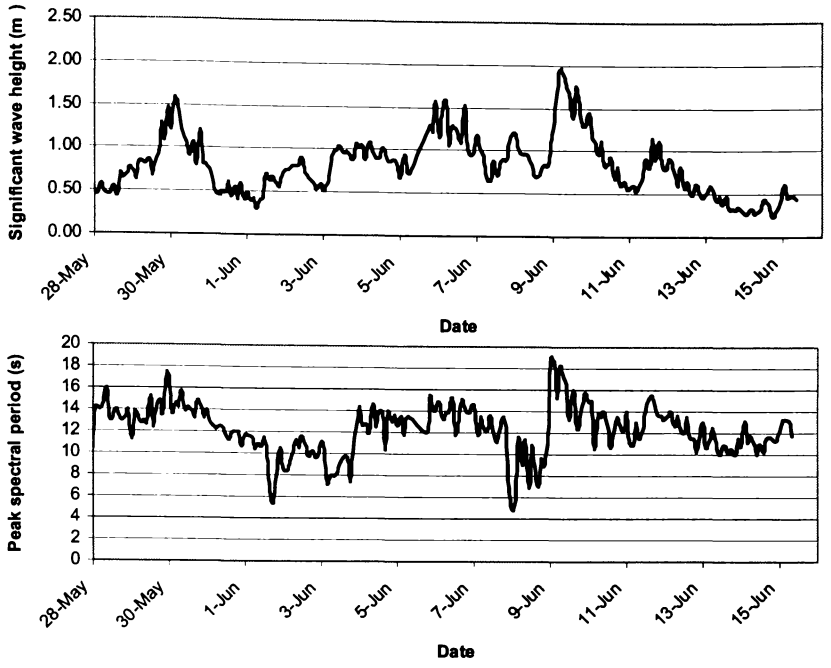

Figure 8.24 Significant wave height and peak spectral wave periods for the period 28/05/99 to 15/06/99 at the site adjacent to the port of Gisborne shipping channel measured using an *InterOcean* S4ADW. Wave heights range from less than 0.5 m to nearly 2 m, while peak spectral periods range from approximately 5 s to 19 s.

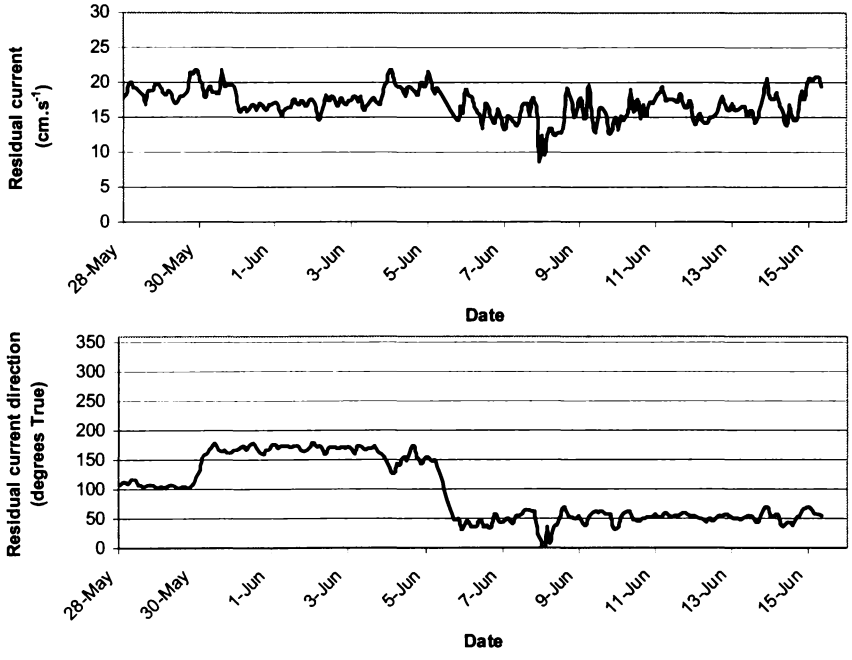

Figure 8.25 Residual current direction and magnitude for the period 28/05/99 to 15/06/99 at the site adjacent to the port of Gisborne shipping channel. A conspicuous direction change occurs on the 6th of June consistent with a bottom return flow underneath the river plume.

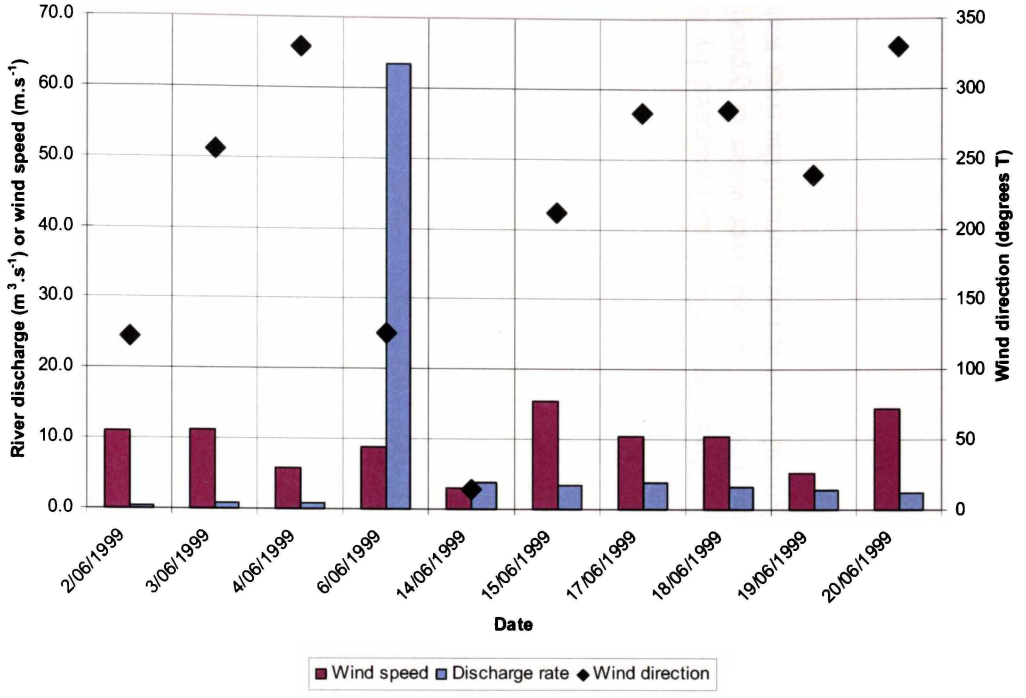

Figure 8.26 Wind direction and speed and Turanganui River discharge for each of the days surveyed. Discharges varied from quiescent (~1 $m^3.s^{-1}$) to relatively large (> 60 $m^3.s^{-1}$).

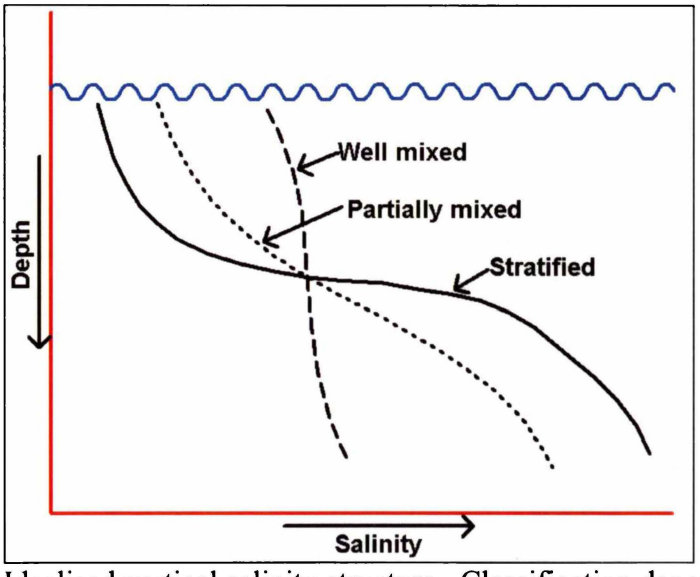

Figure 8.27 Idealised vertical salinity structure. Classification depends on salinity difference between surface and bottom values (After Pritchard, 1955 and Cameron and Pritchard, 1963)

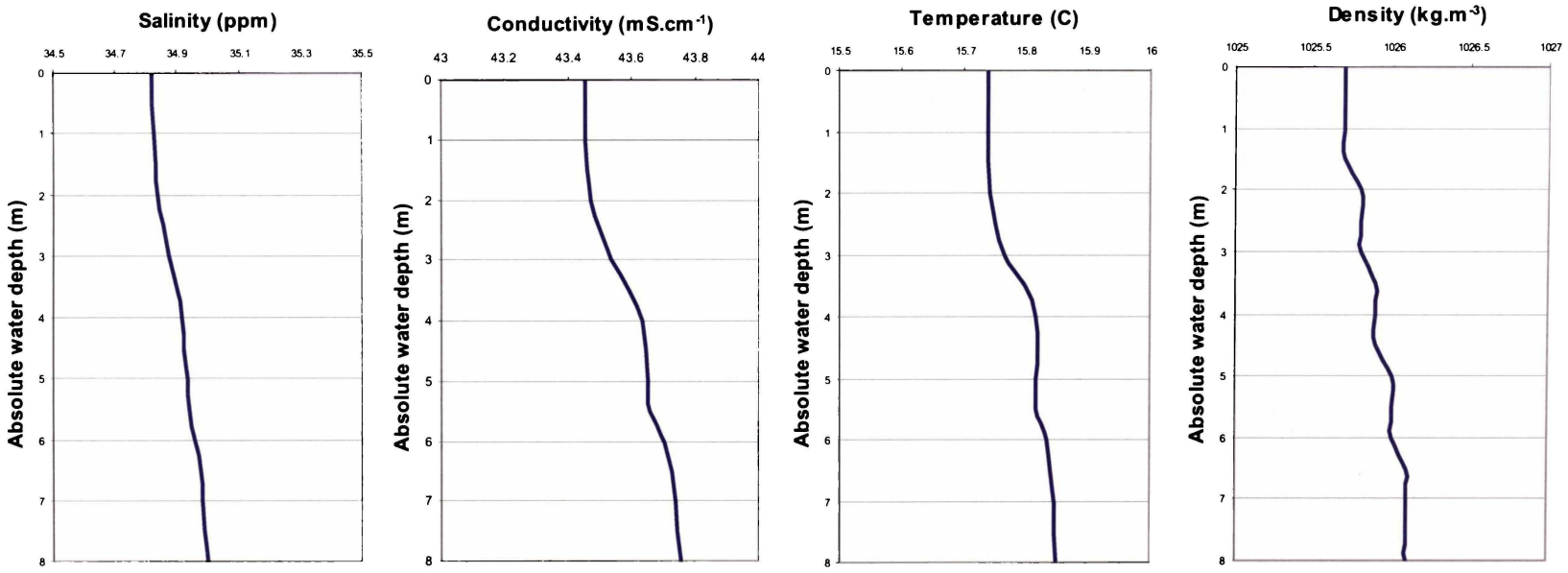

Figure 8.28 Salinity, conductivity temperature and density depth profiles of the plume of the Turanganui River from Site 9 as measured by the *Ocean Sensors CTD* (Model OS200) instrument on the 1st June 1999 showing a well-mixed structure. The discharged river water is typically less dense and not as saline as the seawater and sits on top forming the typical profiles shown here. Typically the temperature of the river water is also cooler.

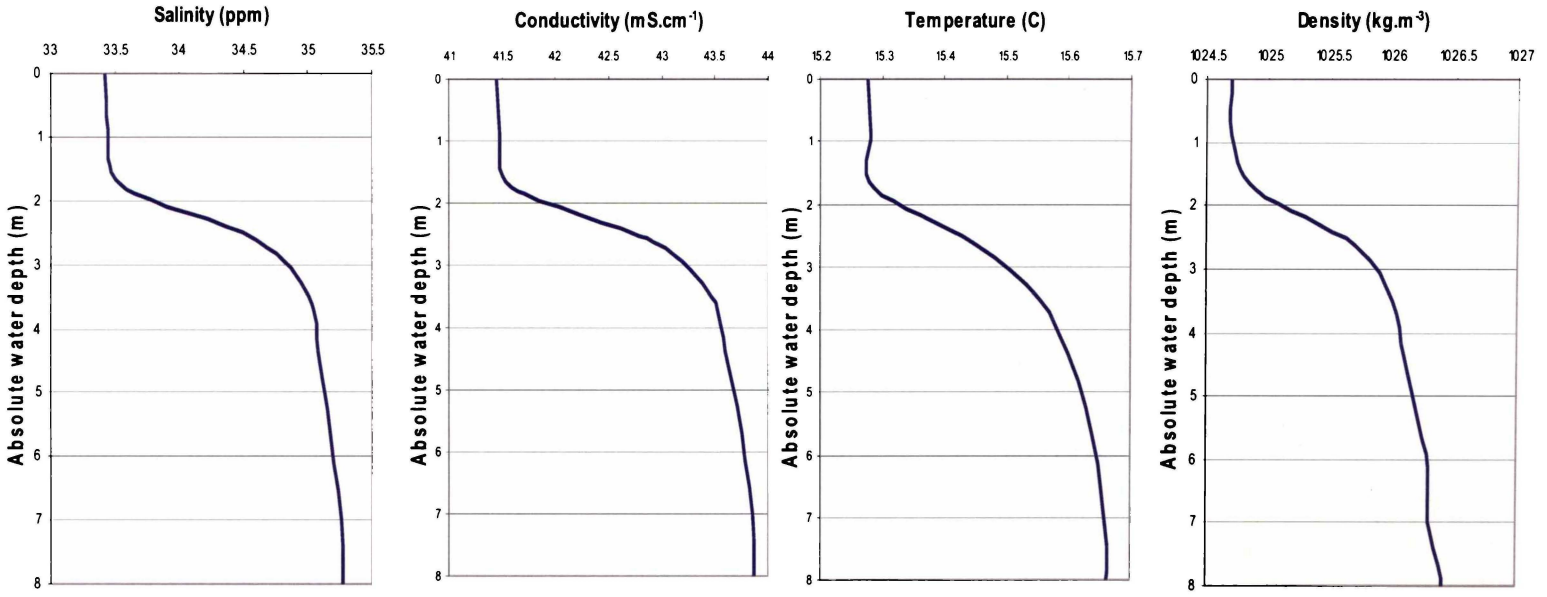

Figure 8.29 Salinity, conductivity, temperature and density depth profiles from the plume of the Turanganui River from Site 9 as measured by the *Ocean Sensors CTD* (Model OS200) instrument on the 8th June 1999 showing a highly stratified structure. The discharged river water is typically less dense and not as saline as the seawater and sits on top forming the typical profiles shown here. Typically the temperature of the river water is also cooler.

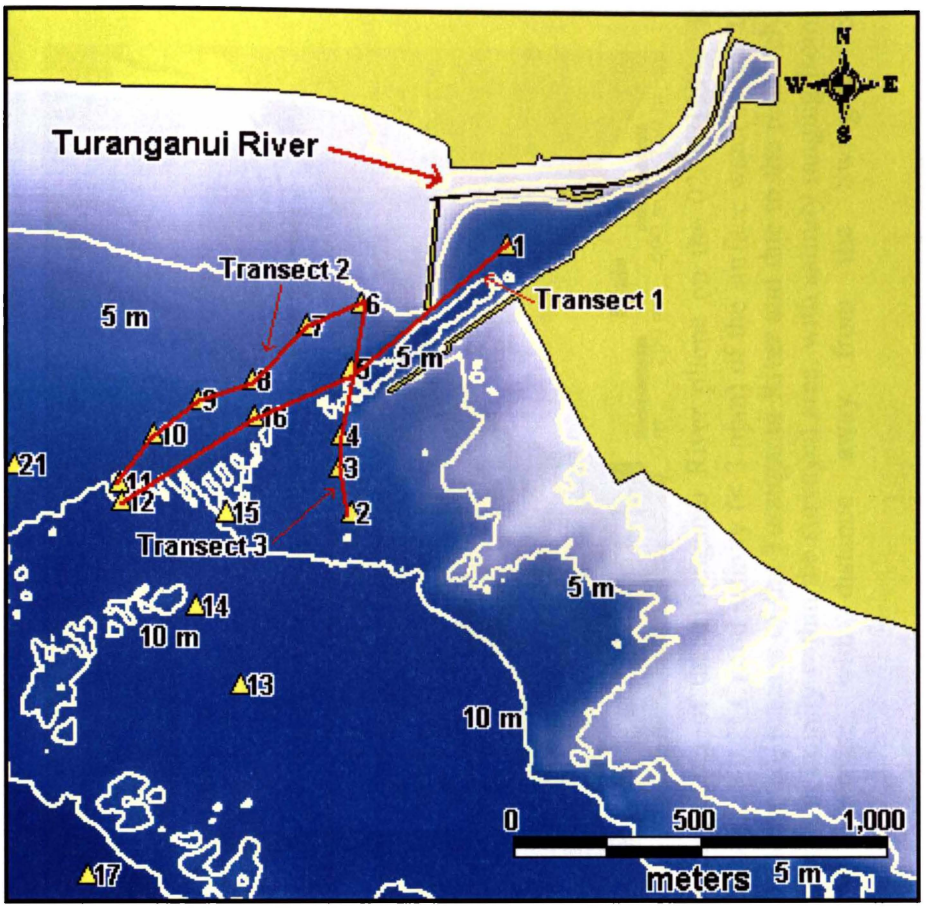

Figure 8.30 Salinity and Temperature transect locations; port of Gisborne environs.

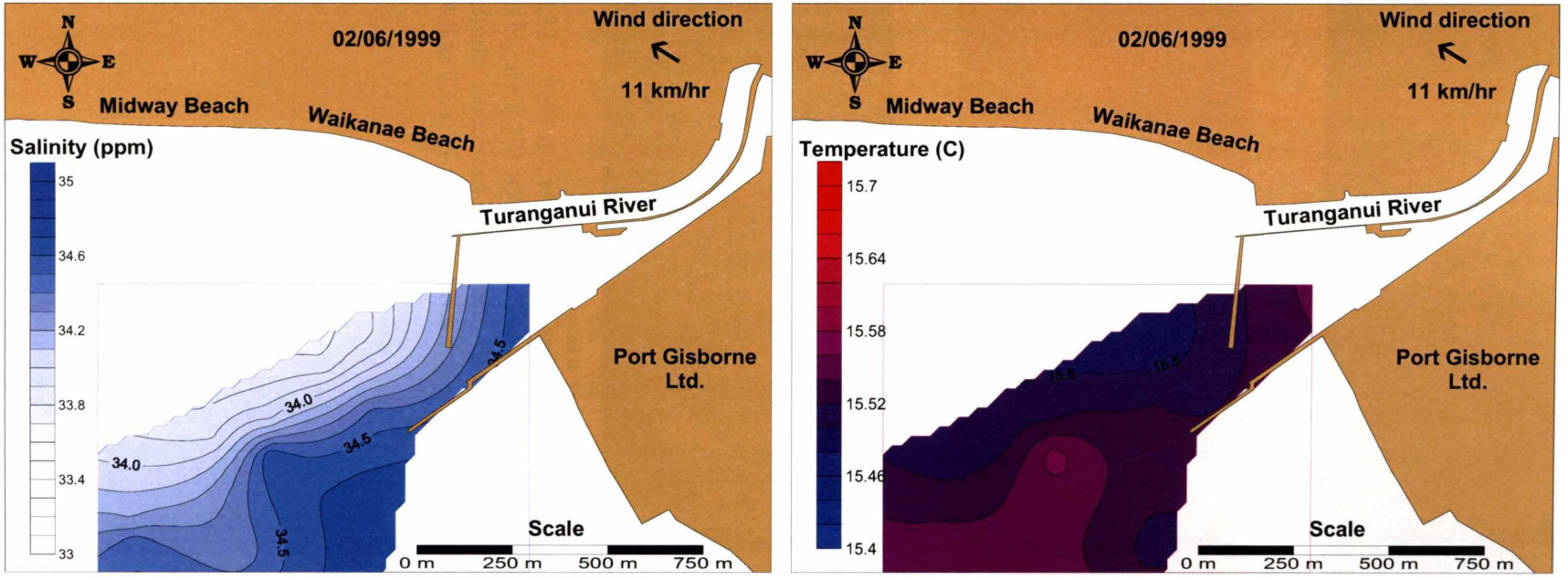

Figure 8.31 Spatial variability in salinity and temperature within the surface layer of the Turanganui River plume on the 02/06/1999. River discharge was 0.41 $m^3.s^{-1}$. The limited variation in both the temperature (i.e. ~0.2° C) and salinity (< 2 ppm) of the surface water is due to the partial mixing of the seawater and freshwater within the lower, tidally affected, reaches of the Turanganui River and due to the relatively low discharge volume of the river. The salinity isohalines show little variation in salinity within the surveyed area, with salinity ranging from 33.7 to 34.8 ppm. The salinity of the water is shown to decrease with distance away from the Swinging Basin.

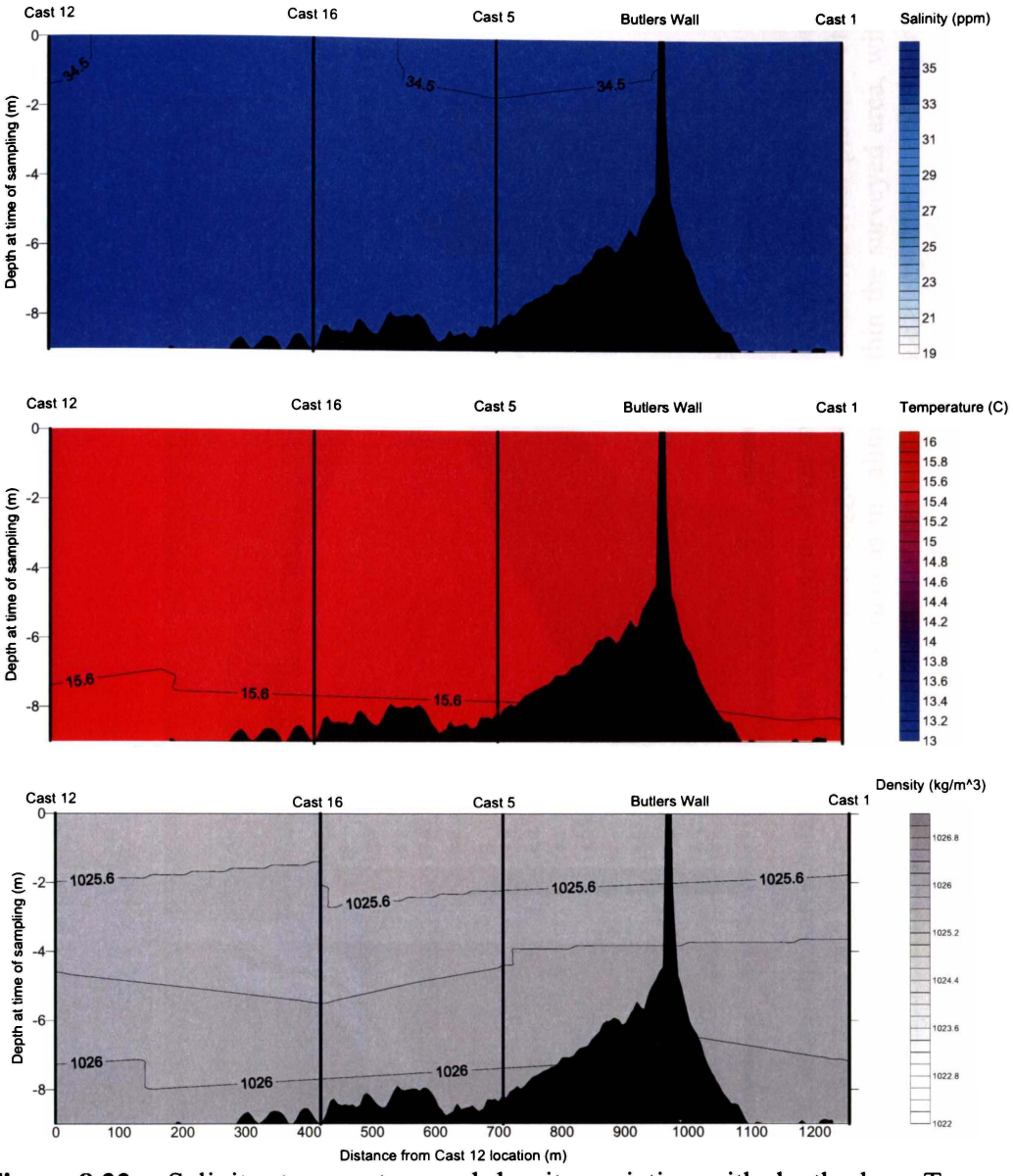

Figure 8.32 Salinity, temperature and density variation with depth along Transect 1 (Figure 8.29) within the Turanganui River plume on the 02/06/1999. The salinity isohalines show little variation in salinity with depth, ranging from 34.8 to 33.8. Similar stratification is shown in Transect 2 and 3.

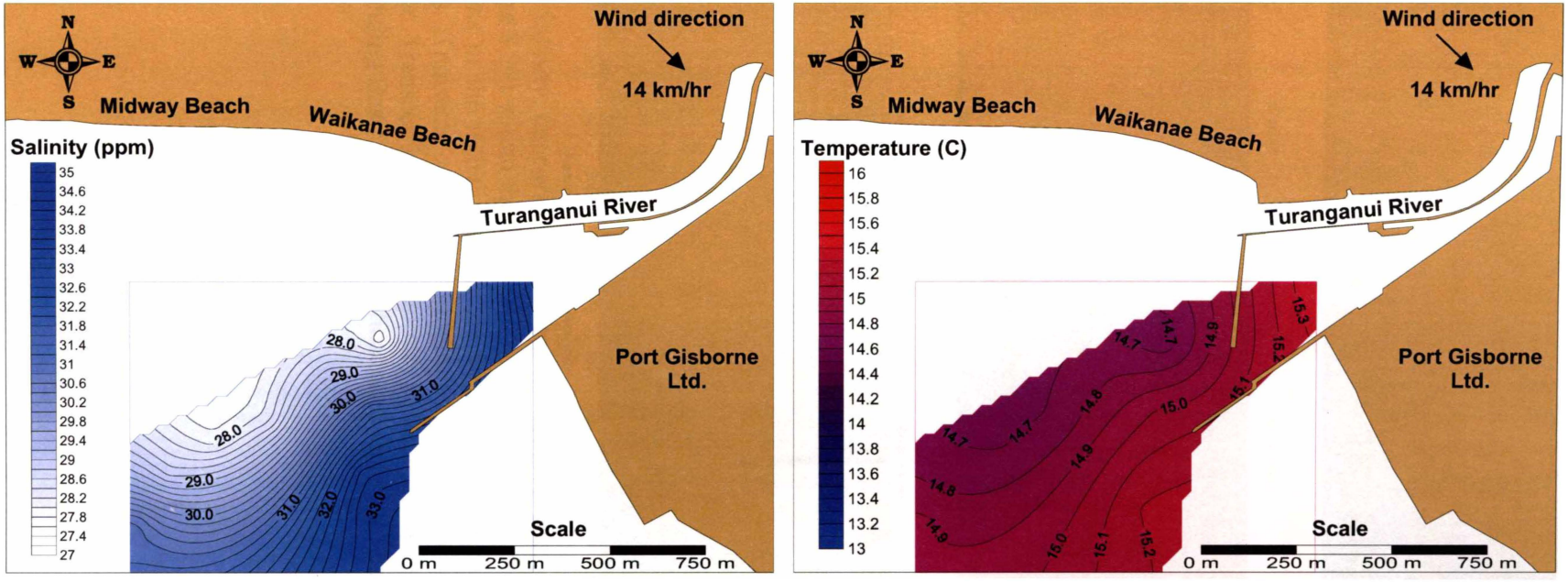

Figure 8.33 Spatial variability in salinity and temperature within the surface layer of the Turanganui River plume on the 08/06/1999. River discharge was 6.91 $m^3.s^{-1}$. The variation in both the temperature and salinity of the surface water suggests a well-stratified river plume. The salinity isohalines show the salinity of the surface water to vary between relatively large variations in salinity within the surveyed area, with salinity ranging from 27.6 to 33.2 ppm. The salinity and temperature of the water is shown to decrease with distance away from the Swinging Basin.

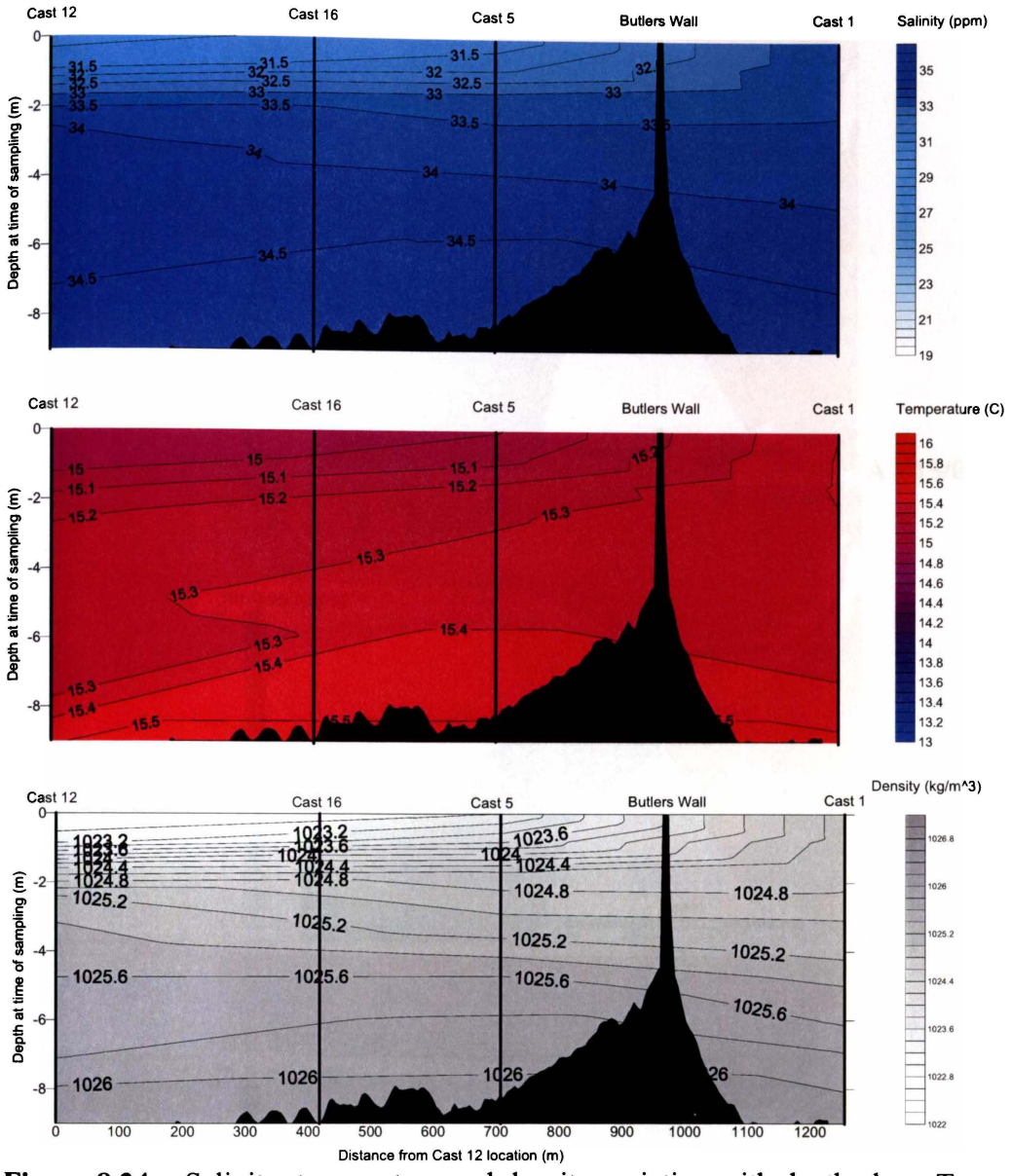

Figure 8.34 Salinity, temperature and density variation with depth along Transect 1 (Figure 8.29) within the Turanganui River plume on the 08/06/1999. Large variations in the isohalines indicate a well-stratified river plume with little mixings. Transects suggest a bottom return flow of more saline warmer seawater. Transect 1 shows the salinity to decrease with distance away from the Swinging Basin. Similar stratification is shown in Transect 2 and 3.

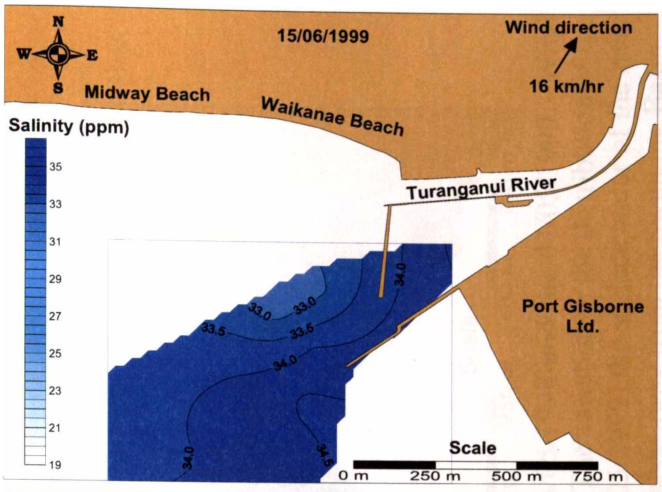

A - 15/06/1999

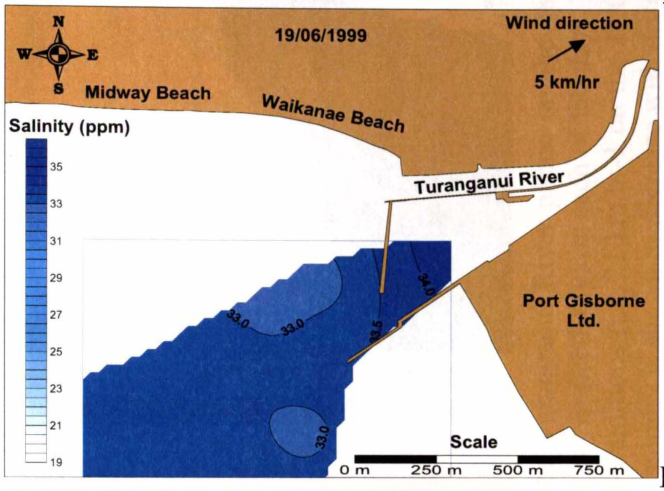

B - 19/06/1999

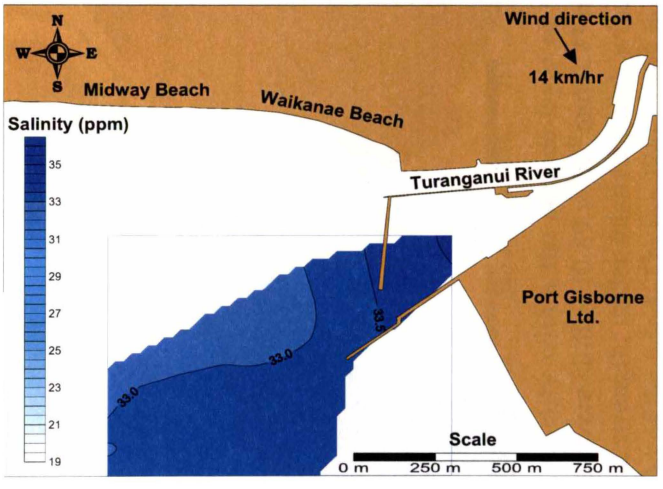

C - 20/06/1999

Figure 8.35 Illustrations of the spatial variability in salinity in the surface water of the Turanganui River plume on the 15th, 19th and 20th of June 1999 (discharges 3.34 $m^3.s^{-1}$, 2.79 $m^3.s^{-1}$ and 2.51 $m^3.s^{-1}$ respectively). Under relatively strong onshore winds the river plume is forced to hug the coastline, while under relatively strong offshore winds or only light onshore winds the river plume shows more dispersion. In C the isohaline is approximately perpendicular to the wind direction. Salinity is shown to decrease with distance away from the Swinging Basin.

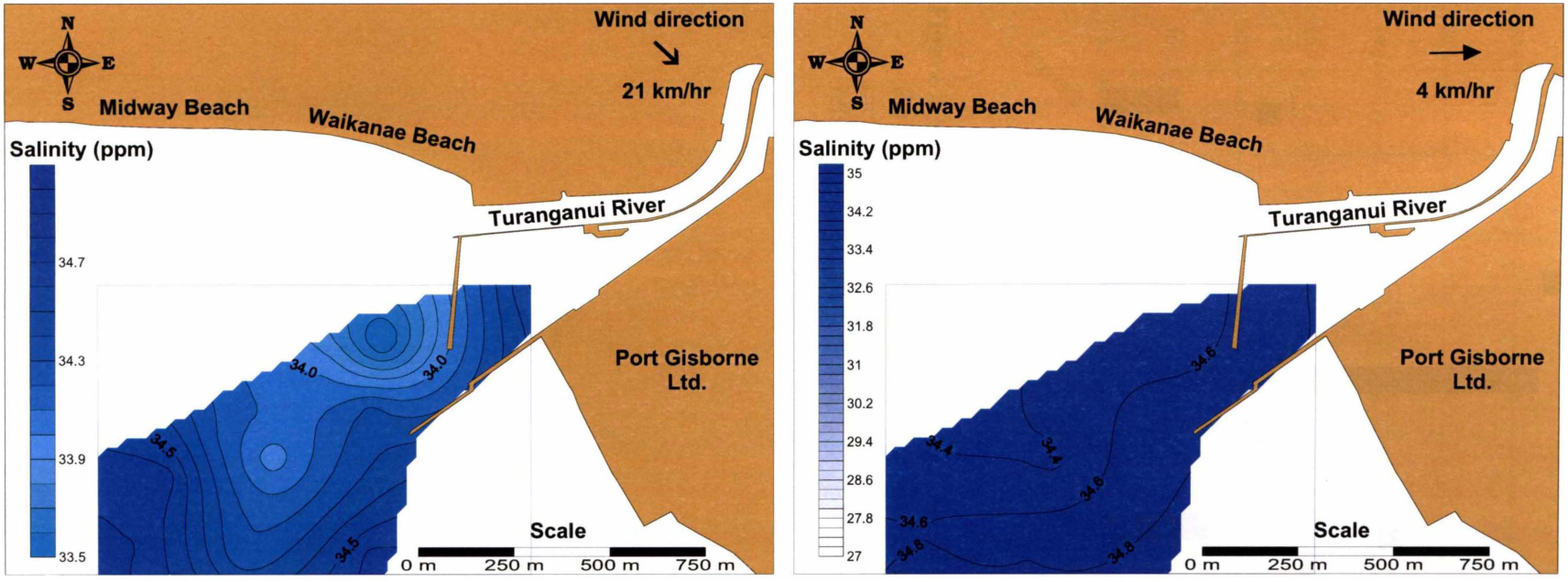

Figure 8.36 Spatial variability in salinity within the surface layer of the Turanganui River plume on the 28/05/1999 and the 31/05/1999. Wind directions and river discharges were similar (0.89 $m^3.s^{-1}$ and 0.73 $m^3.s^{-1}$ respectively) on each of the days. The variation in the distribution of the isohalines is attributed to wind strength; under relatively high wind conditions (i.e. 21 km.hr-1 on the 28/05/1999) the surface water of the river plume is driven in the direction of the wind. On the 28/05/1999 the salinity is shown to decrease with distance away from the Swinging Basin.

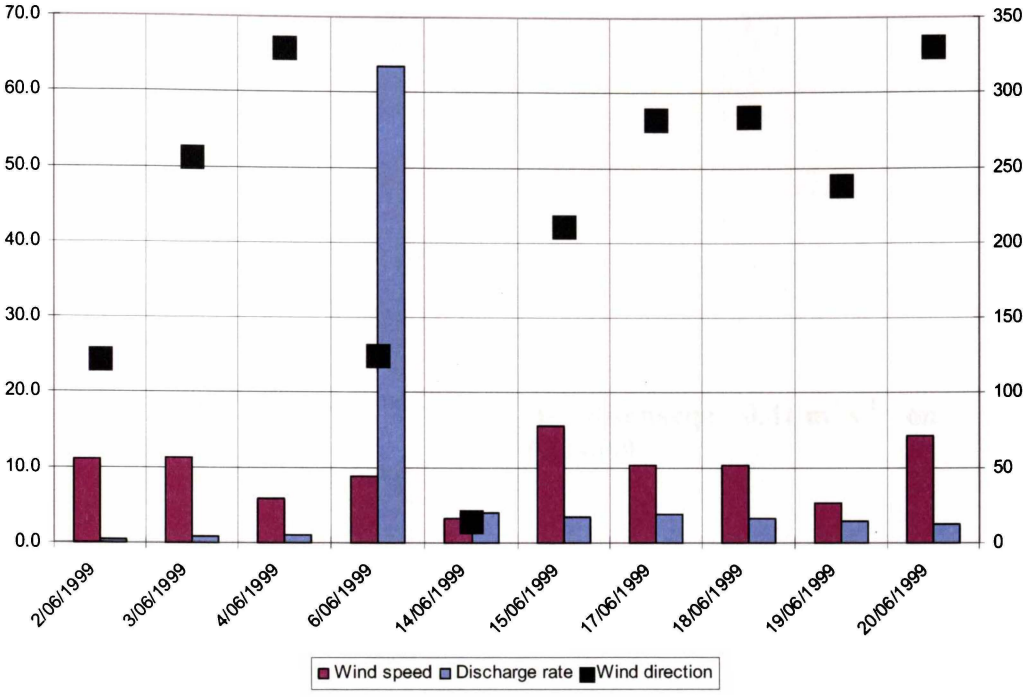

Figure 8.37 Wind direction and speed and Turanganui River discharge for each of the days surveyed where water nephelometric turbidity units (NTU) were measured. Discharges varied from relatively quiescent (~1 $m^3.s^{-1}$) to relatively large (>60 $m^3.s^{-1}$).

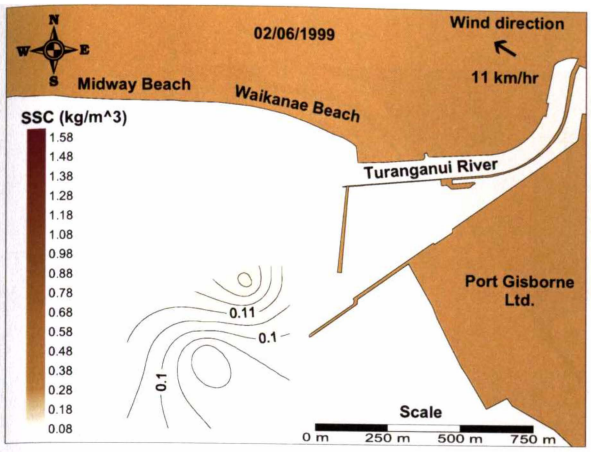

A- discharge 0.41 $m^3.s^{-1}$ on 02/06/99

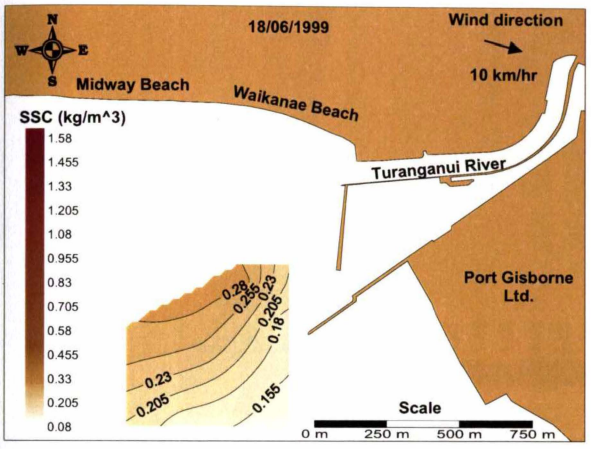

B- discharge 3.17 $m^3.s^{-1}$ on 18/06/99

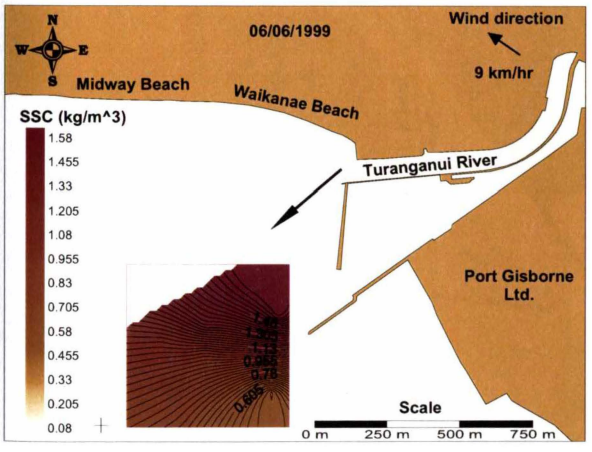

C- discharge 63.46 $m^3.s^{-1}$ on 06/06/99

Figure 8.38 Suspended sediment concentrations within the plume of the Turanganui River show a high dependency on the volume of water being discharged; the larger the quantity of water being deposited into Poverty Bay the more sediment in suspension within the plume.

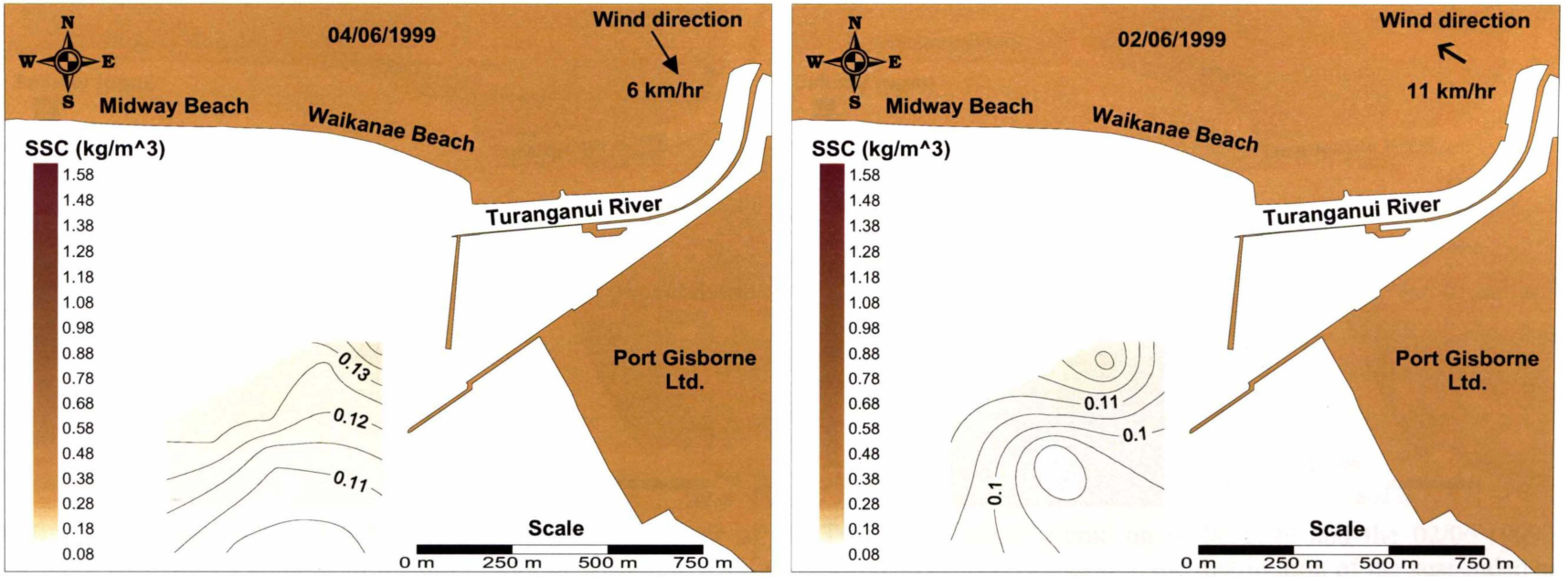

Figure 8.39 Spatial variability in turbidity (SSC) within the surface layer of the Turanganui River plume on 04/06/1999 and the 02/06/1999. River discharges were similar on each of the days (0.85 $m^3.s^{-1}$ and 0.41 $m^3.s^{-1}$ respectively). The variation in the distribution of the suspended sediment is attributed to wind direction; under offshore wind conditions relatively more surface water is forced towards the shipping channel, while under onshore wind conditions the surface water tends to be forced towards Waikanae and Midway beaches and out of the surveyed area.

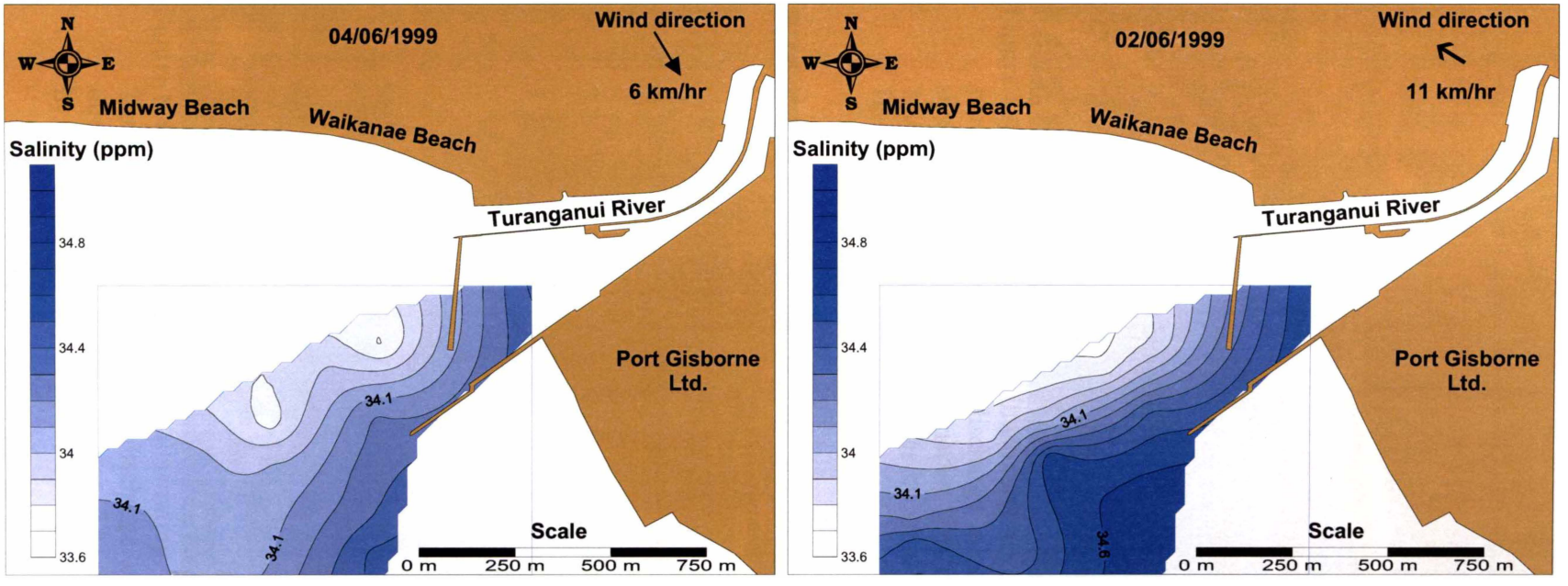

Figure 8.40 Spatial variability in salinity within the surface layer of the Turanganui River plume on 04/06/1999 and the 02/06/1999. River discharge was similar on each of the days (0.85 $m^3.s^{-1}$ and 0.41 $m^3.s^{-1}$ respectively). The variation in the distribution of the suspended sediment is attributed to wind direction; under offshore wind conditions relatively more surface water is forced towards the shipping channel, while under onshore wind conditions the surface water tends to be forced towards Waikanae and Midway beaches and out of the surveyed area.

Figure 8.41 Aerial photograph illustrating the distribution of the Turanganui River plume in relatively low discharge conditions, i.e. 0.8 $m^3.s^{-1}$, and winds directed from the southerly quarter. The turbid river plume is forced towards Midway and Waikanae Beaches by wind forcing. Photo supplied by Prof. T. Healy.

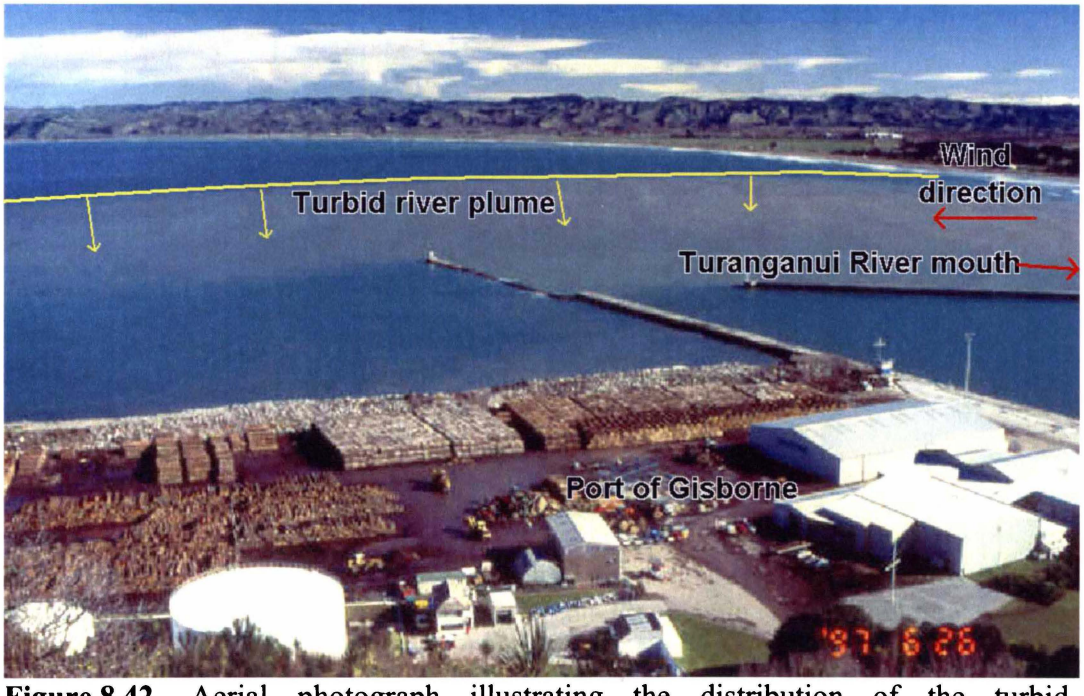

Figure 8.42 Aerial photograph illustrating the distribution of the turbid Turanganui River plume in discharge conditions of 3.5 $m^3.s^{-1}$ and winds directed from the northerly quarter. The turbid river plume is forced offshore by wind forcing. Photo supplied by Prof. T. Healy.

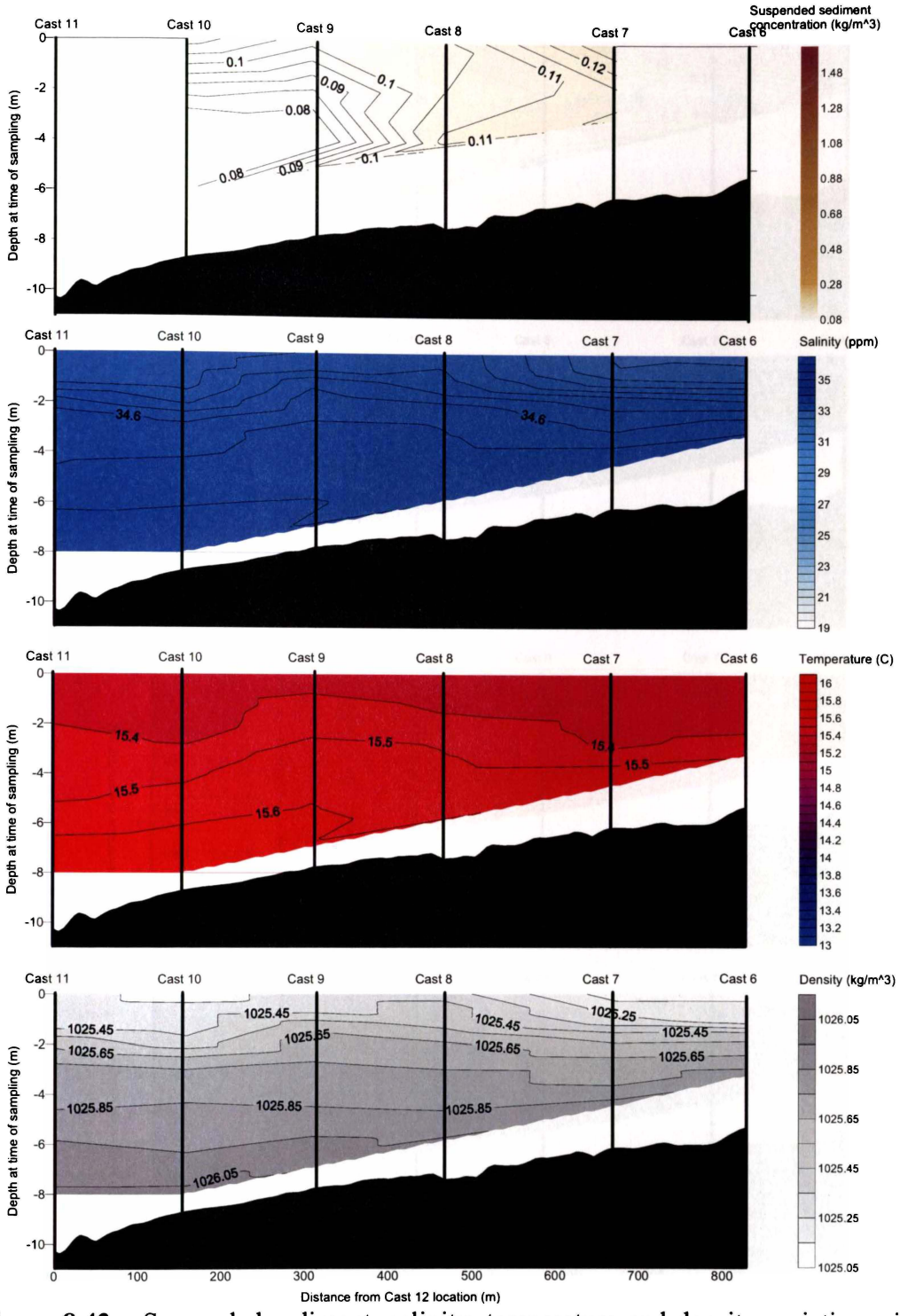

Figure 8.43 Suspended sediment, salinity, temperature and density variation with depth along Transect 2 (Figure 8.29) within the Turanganui River plume on the on 01/06/1999. At Cast site 8 the Richardson Number is 0.09-0.14, and suggests little inhibition in the downward sediment flux, as illustrated by similar SSC through the water column. In contrast, at Cast site 9 the density gradient (i.e. clustering of the density contours) appears to inhibit the downward flux of sediment.

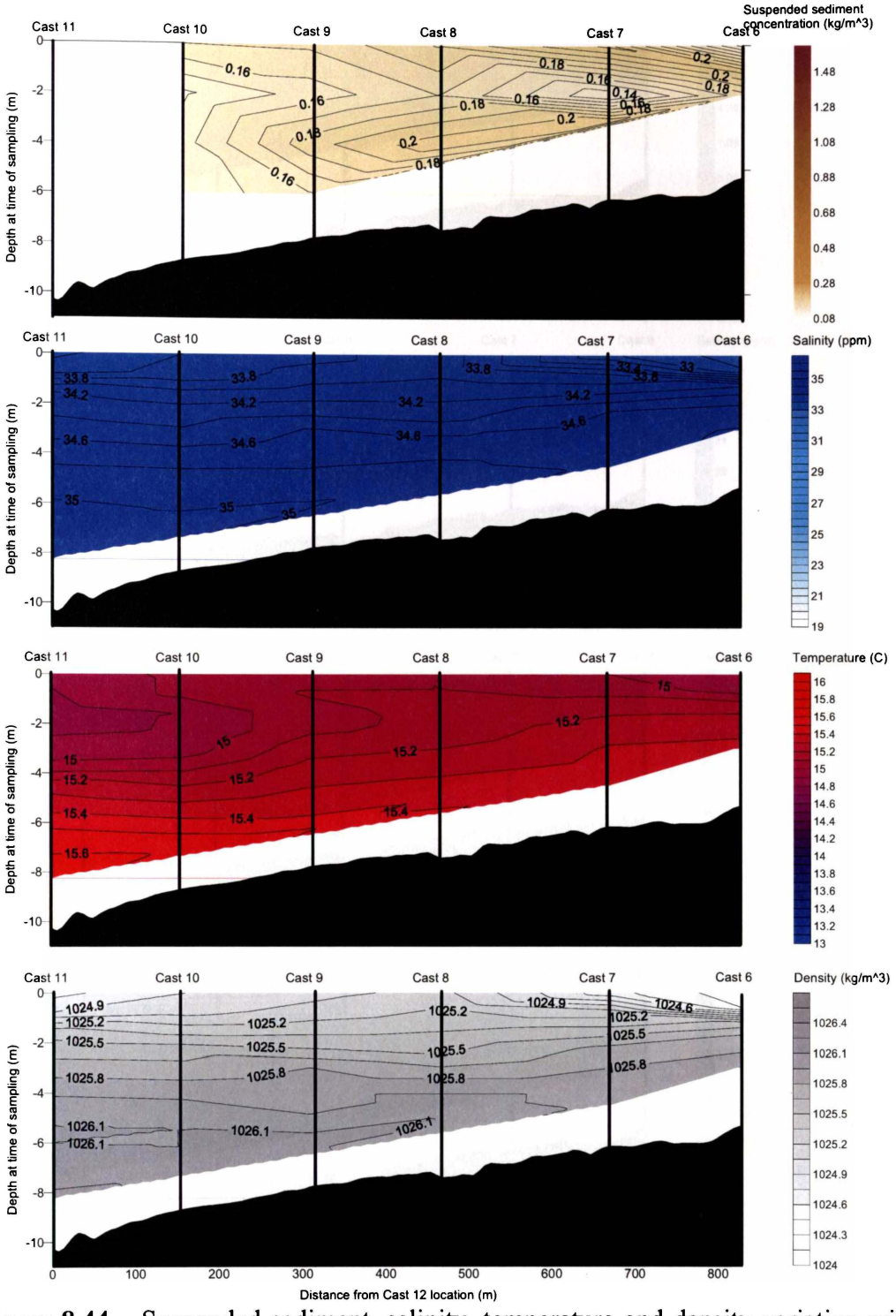

Figure 8.44 Suspended sediment, salinity, temperature and density variation with depth along Transect 2 (Figure 8.29) within the Turanganui River plume on the on 14/06/1999. Transect data suggest that the density gradient causes a separation between the relatively fresh surface water and the more saline bottom water. The density gradient inhibits both the downward and upward sediment flux associated with river discharging and re-suspension respectively.

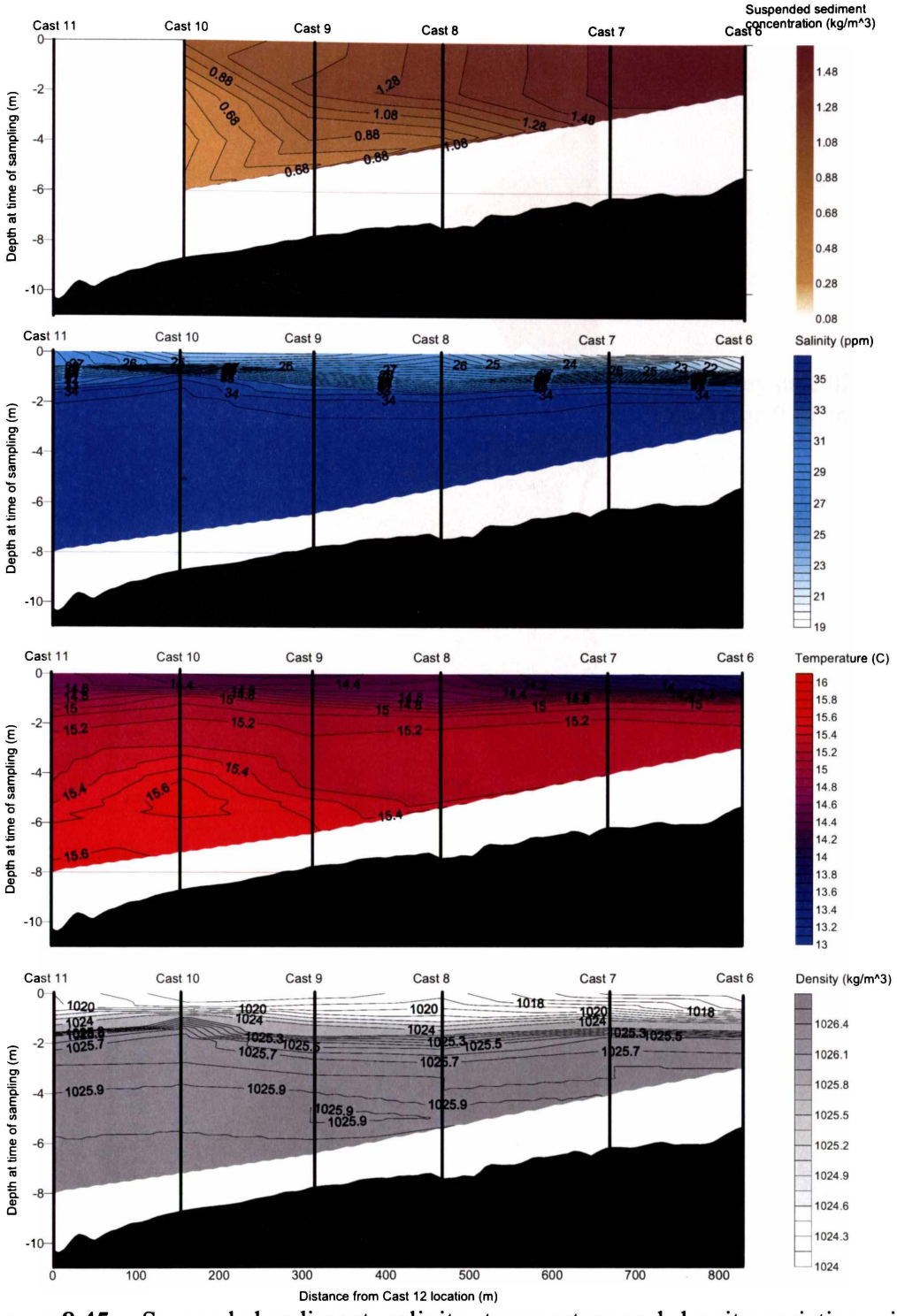

Figure 8.45 Suspended sediment, salinity, temperature and density variation with depth along Transect 2 (Figure 8.29) within the Turanganui River plume on the on 06/06/1999. Transect data suggest that the density gradient causes a separation between the relatively fresh surface water and the more saline bottom water. The density gradient inhibits both the downward and upward sediment flux associated with river discharging and re-suspension respectively.

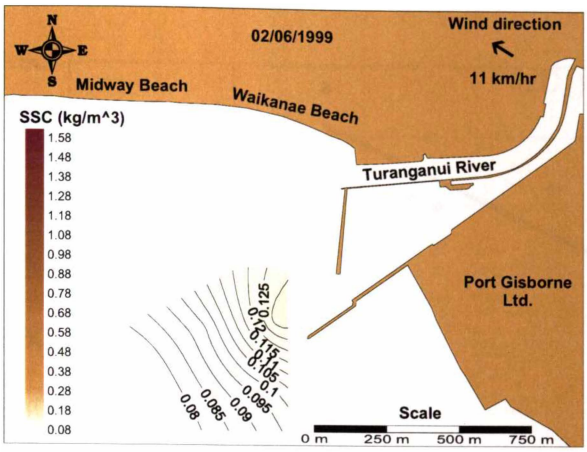

A -Survey date 02/06/99, Discharge 0.41 $m^3.s^{-1}$

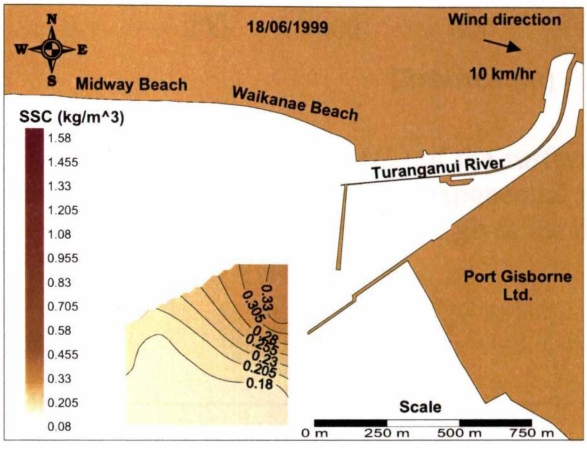

B -Survey date 18/06/99, Discharge 3.17 $m^3.s^{-1}$

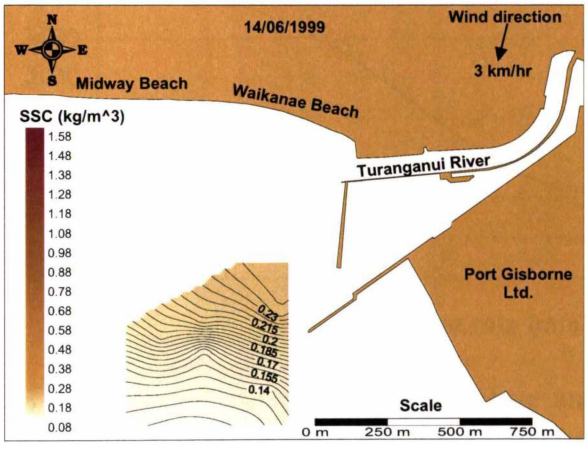

C -Survey date 14/06/99, Discharge 3.86 $m^3.s^{-1}$

Figure 8.46 Suspended sediment concentrations at 4 m below the water surface during different river discharges and wind velocities. The 4 m sub-surface distribution of the *SSC* is similar regardless of the wind velocities and river discharge, with largest concentrations near the river mouth, and in the lee of the breakwater.

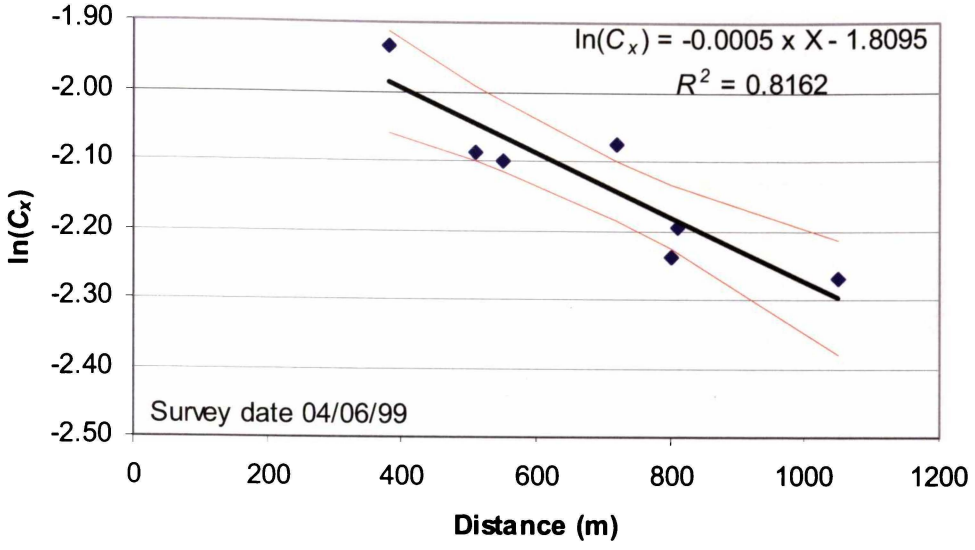

Figure 8.47 Correlation between $\ln(C_x)$ of the surface water and distance (x) from the mouth of the river showing an exponential relationship between the *SSC* and distance. The gradient of the line gives the decay factor (t_D). Also shown are 95% Confidence Intervals (CI).

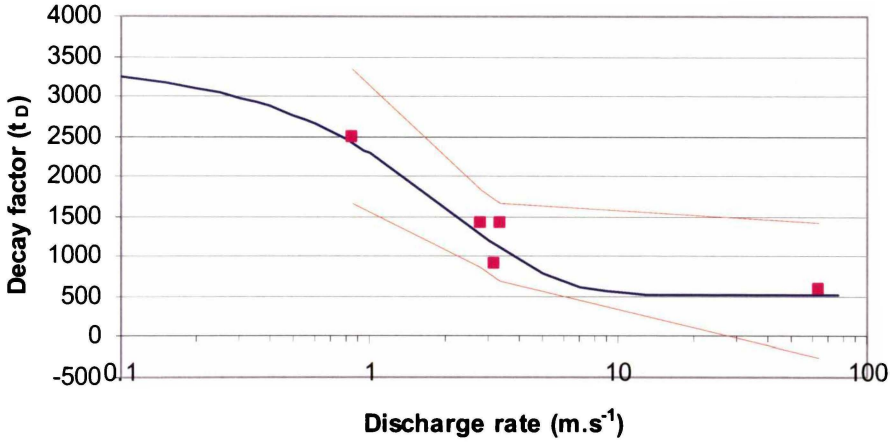

Figure 8.48 Correlation between river discharge and decay factor, showing the decay factor to decrease as a function of river discharge, also shown are the upper and lower 95% Confidence Intervals. The dependency of the decay factor on the river discharge suggests that the shear velocity at the interface between the freshwater of the plume and the saline bottom water is an important mechanism driving the downward sediment flux. Higher rates of flow create more turbulence at the interface, and promote downward sediment flux.

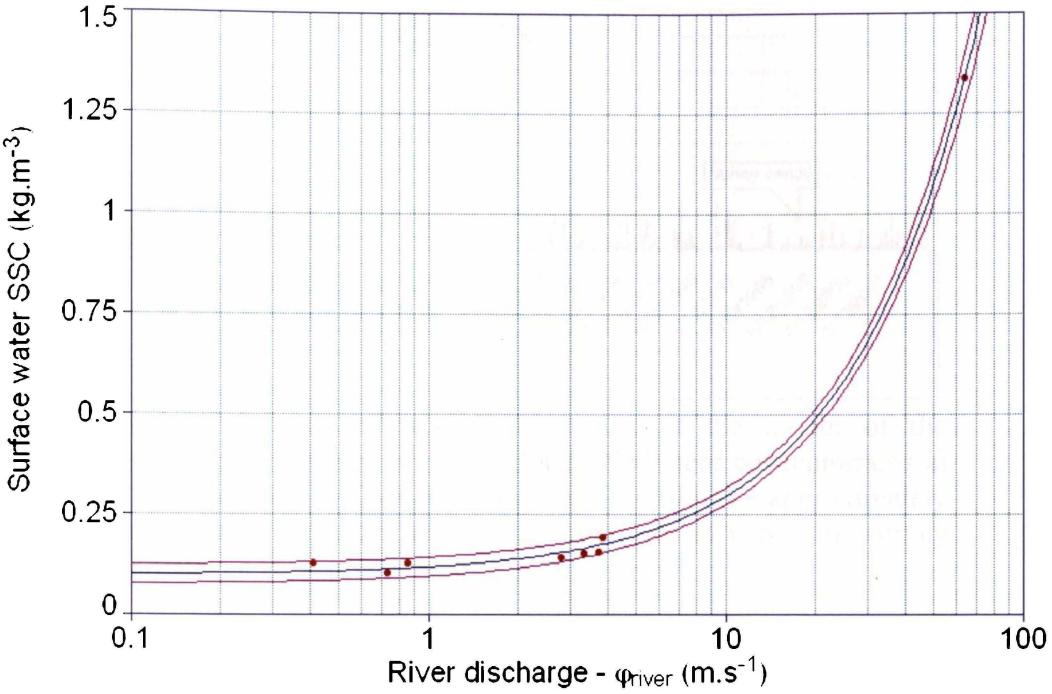

Figure 8.49 Surface water *SSC* at Cast site 8 as a function of river discharge (φ_{river}). Regression analysis shows a linear relationship between the *SSC* and the river discharge (equations given in Table 8.07), the intercept of which represents the background ambient surface *SSC* within northern Poverty Bay. The gradient of the line is specific to the site, and a function of distance. 95% Confidence Intervals are also shown.

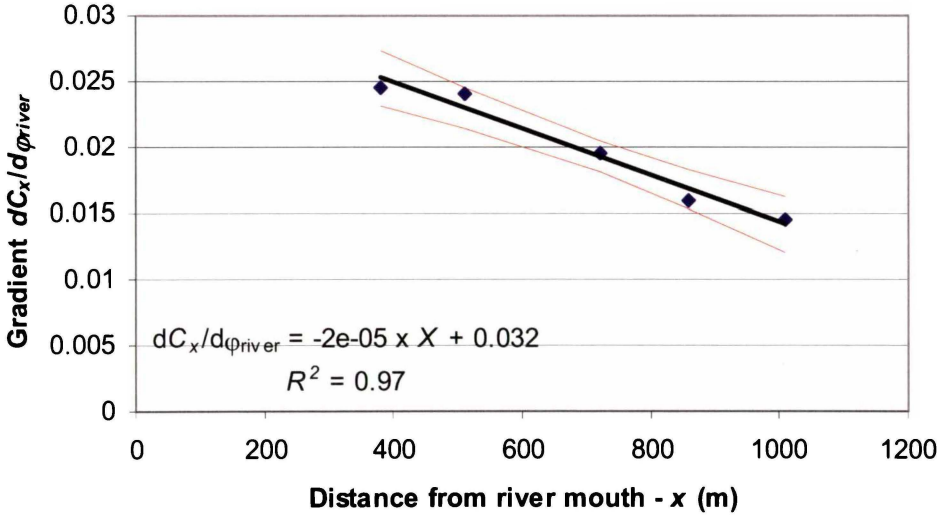

Figure 8.50 Change in *SSC* as a function of changing river discharging (φ_{river}) related to the distance of the Cast site from the mouth of the Turanganui River. The closer the Cast site to the mouth of the river the more dependent the suspended sediment concentration on river discharges.

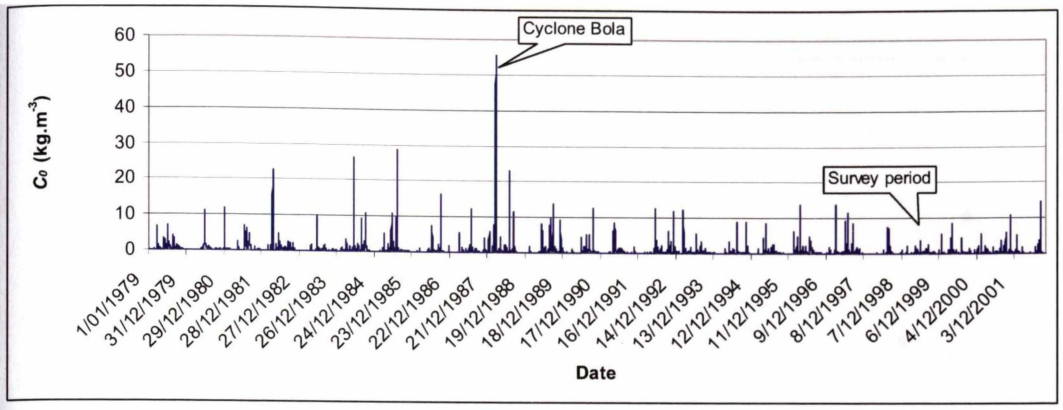

Figure 8.51 Inferred suspended sediment concentration at the mouth of the Turanganui River (C_0) between 1979 and 2002. Sediment concentrations at the mouth of the river during Cyclone Bola are inferred to be approximately twice the magnitude of any other event, while the year in which the survey period was undertaken is relatively quiescent.

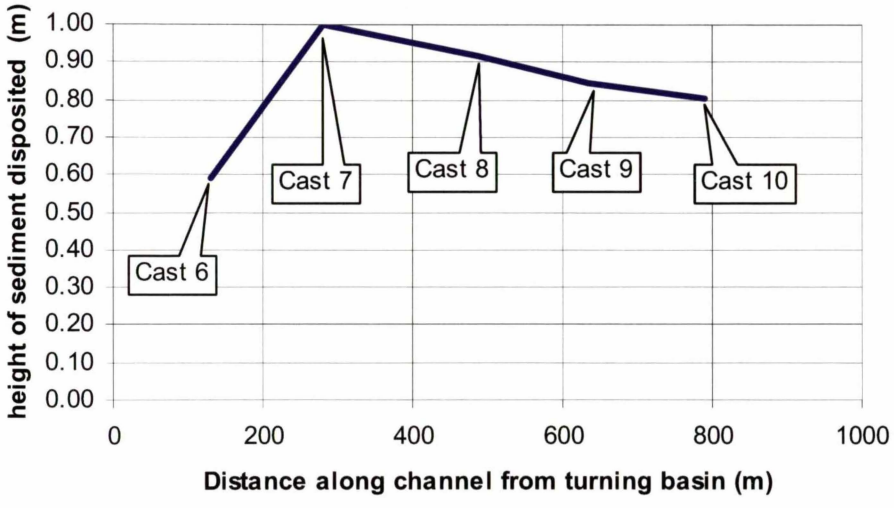

Figure 8.52 *Potential* sedimentation index (ΔI) values along the shipping channel between 28/05/99 and 20/06/99 due to river discharging silt-sized sediment. ΔI is based on river discharge and estimated C_x of the surface water at each of the Cast locations. Sediment re-suspension, lateral transport and baroclinic inhibition to the vertical sediment flux and wave driven re-suspension of sediment are ignored.

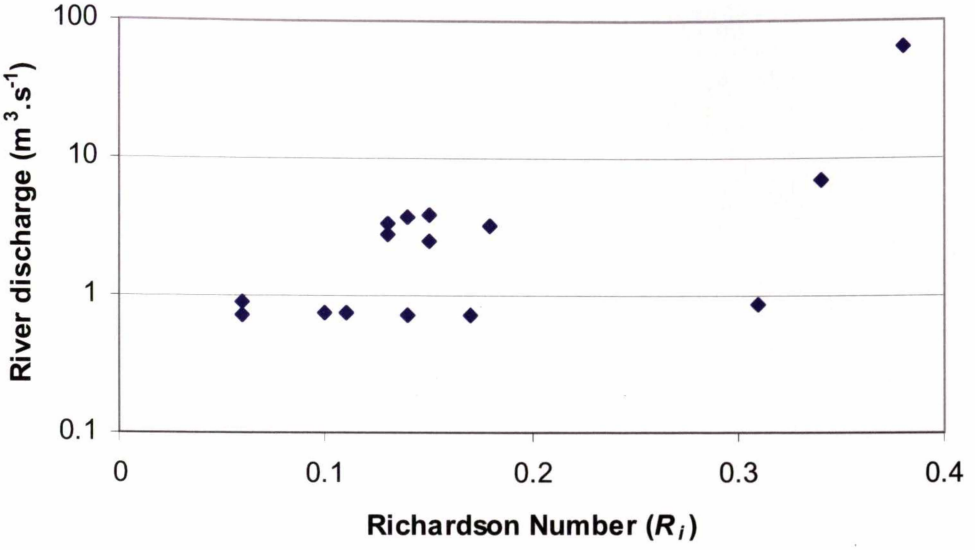

Figure 8.53 The Richardson Numbers at site 8 show a general trend to increase as a function of river discharge, suggesting that the density gradients at higher river discharges are sufficient to inhibit the momentum and sediment transferral between the buoyant river plume water and the underlying, more saline seawater.

Chapter 9. Evaluation of the developed formulae for predicting sediment flux within northern Poverty Bay.

"*An ocean is forever asking questions*
And writing them aloud along the shore" - Edward Arlington Robinson

9.1 Introduction

The measured volumetric change of the port of Gisborne navigation approach channel (Figure 9.01) provides a means of validating the formulae developed during this study. Channel infilling occurs due to both horizontal and vertical sediment fluxes as schematised in Figure 9.02. The horizontal sediment fluxes primarily results from sediment entrainment and horizontal transport due to near-bed wave orbital currents and mean near-bed currents respectively. Aspects of sediment entrainment over the mixed sand/mud sediment within northern Poverty Bay have been examined in Chapters 5, 6 and 7. The vertical sediment flux results from the downward raining of the relatively fine sediment in suspension, of which the turbid water discharged from the Turanganui River is the salient contributor. Characteristics of the river plume have been examined in Chapter 8.

A 2-cell numerical model that considers a 1-m wide strip of channel has been developed, as schematised in Figure 9.03, which greatly simplifies infilling predictions. While being a simplistic representation of the channel, the numerical model uses the developed formulae and results from Chapters 3 to 8 to predict channel infilling rates. The model considers the complex interactions of cohesively bound sediment entrainment due to near-bed wave orbital velocities, the horizontal transport of the entrained sediment by mean near-bed velocities, and the downward sediment flux from the turbid river plume.

The numerical model has been used to examine infilling characteristics along the length of the channel, with varying adjacent water depths and sediment characteristics, including cohesive bonding of the seabed. Channel infilling rates are predicted using the 2-cell numerical model, while actual infilling rates are determined from hydrographic surveys on March 10th and June 2nd and dredging records for the corresponding period.

The application of a 2-cell numerical model, which considers hydrodynamic and sedimentological characteristics, for predicting channel infilling represents an alternative to the implementation of a full 3-dimensional hydrodynamic model.

9.2 Methods

Comparisons of estimated to predicted channel infilling rates from the 2-cell numerical model are used to evaluate the ability of the formulae developed during this study to predict infilling characterises of the port of Gisborne shipping channel. Channel volumetric changes at 4 sites in which the adjacent water depth (h) is within the range 6 m $\leq h \geq$ 9 m are examined. The surficial sediment characteristics within and on the flanks of the channel at each of the sites are variable (Table 9.01), consistent with the findings of Chapters 3 and 4.

9.2.1 Estimated channel volumetric change

Measured total (gross) channel volumetric change within a specified period is determined as the sum of the net volumetric change and the volume of sediment

removed during dredging operations. The net volumetric change for the specific period is determined using hydrographic surveys, while dredging records provide a record of the quantity of sediment removed during maintenance and capital dredging.

9.2.1.1 Dredging records

Port Gisborne Ltd. has supplied maintenance dredging records for the period 10/03/99 to 02/06/99. Sediment is removed from both the Swinging Basin and the shipping channel by maintenance dredging (pers comms, Harold, 2001), a total area of approximately 226,900 m^2. The volume of sediment removed during maintenance dredging is estimated based on the number of hopper loads of the '*Pukunui*' (Figure 9.04), and has an error estimate of ± 10% (pers comms, Harold, 2001).

9.2.1.2 Hydrographic surveys instrumentation and procedure

Hunter Hydrographic Services conducted hydrographic surveys of the port of Gisborne Swinging Basin and shipping channel on March 10th and June 2nd 1999. A Trimble 4000RL II D.G.P.S. reference locator base station and receiver were used to determine the position of the G.P.S antenna on the *Takitimu*, and an offset applied to the navigation data to account for the location of the transducer head with respect to the antenna. Water depths were measured using a Soundig 30 Echo Sounder, while a TSS325 Heave Compensator was used to remove the effect of vessel pitch and roll from the sounding data. Tidal measurements were manually taken at 10-minute intervals from the Tide-Board located within Kaiti Basin. Additionally, pre and post survey bar-checks were conducted on each of the survey days, and calibrated against a standard tape. Prior to the survey on March 10th a squat-test of the Takitimu was conducted, and a value of 0.06 m was used for all survey data reduction. Survey run-lines were run perpendicular to the strike of the shipping channel at approximately 10 m intervals. Cross-lines run the length of the channel were used to check for gross-errors in the survey data (Hunter, 1999).

9.2.1.2.1 Survey accuracy estimates

Hydrographic surveying is a two-legged, open-end traverse, with associated errors due to horizontal positioning in the X-Y plane, as well as elevation and water depth errors, all of which are independent of each other (United States Army Corps of Engineers, 2002b). The overall accuracy of an observed bottom depth elevation is dependant on many random and systematic errors that are present in the process used to measure that elevation. The error in a single depth point is represented by a 3-D error ellipsoid as shown in Figure 9.05, where the dimensions of the ellipsoid are indicated by the standard errors in all three dimensions - s_x, s_y and s_z.

Horizontal positional accuracy with the navigation system used during the survey is considered to be approximately 1-2 m, however the accuracy of the system post the removal of selective availability is considered to be greater (Coates, 2000). Because the interpolation of the survey data into regular spaced grids is of the order 5 m, the

error in the accuracy of the navigation system is considered negligible in the gross estimation of the volumetric changes in the shipping channel.

The accuracy of depth measurement is determined by considering the root-mean square error of the vertical measurement component, which is the square root of both the random errors and the systematic biases such that,

$$RMS_{error} = \sqrt{\sigma^2{}_{(RandomError)} + \sigma^2{}_{Bias}} \qquad (9.01)$$

Given that only absolute volume differences between surveys are of interest the bias component can be ignored. The random error components of eqn. 9.01 are those present in the measurement system that cannot be easily minimized by calibration, and include errors due to such thing as,

i. echo sounder accuracy (± 0.10 m),
ii. tide gauge/reading accuracy (± 0.05 m),
iii. seiching measurements (negligible), and
iv. heave compensation accuracy (±0.05 m)

The seiching measurement, while important within the confines of the Swinging Basin, is not considered relevant when determining the gross estimation of the volumetric changes in the shipping channel. The combined errors give a depth sounding *RMS* error of ± 0.12 m for each survey. The composite error between the difference of two surveys is,

$$RMS_{errorDifference} = \sqrt{\sigma^2{}_{(RandomErrorSurvey1)} + \sigma^2{}_{(RandomErrorSurvey2)}} \qquad (9.02)$$

As such, the error in the difference between two hydrographic surveys of the shipping channel is ± 0.17 m, and error-bounds of the estimated channel infilling rate can be determined.

9.2.1.3 Interpolated bathymetric charts

The software package *SURFER* (version 7.00.26) was used to interpolate a regular spaced grid to the hydrographic sounding data, and to determine the volumetric changes between surveys. The interpolation method "Kriging" was used to generate the interpolated bathymetric grids. This interpolation method accurately retains the survey data (*SURFER* 7.00.26 online help).

9.2.1.4 Estimated channel gross volumetric change

Gross channel infilling rates for a specific period were determined as the sum of the volume estimated to have been removed during dredging operations and the volumetric change between consecutive hydrographic surveys.

The daily sedimentation rate of the channel was calculated by applying the equation,

$$SC_i = \frac{(V_n - V_{n-1}) + V_{DM}}{I_d} \quad (9.03)$$

where SC_i = the mean rate of infilling ($m^3.day^{-1}$);
V_n = the total volume of channel sediment for a particular survey (m^3);
V_{n-1}= the total volume of channel sediment for the previous survey (m^3);
V_{DM} = the total volume of dredge material removed from the channel between surveys (m^3), and
I_d = the number of days between survey.

9.2.1.5 Estimated channel gross volumetric change within 1×90 m channel slices

Net channel volumetric change between 10/03/99 and 02/06/99 within areas with adjacent water depths in the range 6 m $\leq h \geq$ 9 m are determined by measuring the volumetric change within a 20-metre wide swath centred about the corresponding depth (Figure 9.06). The average net infilling of the 20-m wide swath is used to estimate the net channel infilling within 1-m wide slices perpendicular to the strike of the channel, while the estimated volume removed by maintenance dredging from each of the 1 m wide slice is determined assuming uniform dredging along the length of the channel.

The estimated gross infilling within the 1-m slices between surveys is determined using a time-averaged form of eqn. 9.03, and are used to used to validate the 2-cell numerical model.

9.2.2 Predicted channel infilling rates using the developed formulae

Channel infilling rates resulting from both horizontal and vertical sediment fluxes are predicted using a 2-cell numerical model as schematised in Figure 9.03.

The numerical model predicts channel infilling rates using the developed formulae and results from Chapters 3 to 8; including accounting for the retardation of the entrainment rate due to cohesive bonding of the seabed.

9.2.2.1 Horizontal entrained sediment flux in response to wave forcing

The near-bed horizontal sediment flux is considered to result from the combination of sediment entrainment due to near-bed wave orbital velocities and the lateral movement of the entrained sediment due to mean near-bed currents. As such, the horizontal entrained sediment flux ($\vec{\varphi}$) at elevation 'z' is given by,

$$\vec{\varphi} = C_z \times U_z \quad (9.04)$$

in which C_z is the suspended sediment concentration, and U_z is the mean current velocity at elevation 'z' above the seabed. From Chapter 6, the value of C_z is shown to be well predicted assuming the surficial sediment characteristics are known, while the near-bed wave orbital velocity and mean current velocity can be measured directly.

9.2.2.1.1 Wave and current measurements

Wave and current characteristics were measured using an *InterOcean* S4ADW recording 9-minute bursts of wave and current characteristics at a frequency of 2 Hz, every 1 – 2 hours. The instrument was deployed in approximately 10 m (CD) water depth adjacent to the shipping channel (Figure 9.01). The data provided a comprehensive record of wave and current characteristics during the interval between the hydrographic surveys (i.e. between March 10th and June 2nd of 1999).

Near-bed wave orbital statistics were determined by filtering the data within the range 0.04 to 0.2 Hz. Linear wave theory was used to convert near-bed wave orbital velocity statistics to different depths within the range 6 m $\leq h \geq$ 9 m (CD) on the flanks of the shipping channel and within the channel itself in order to determine channel infilling rates.

While the near-bed orbital velocity is the salient parameter for determining entrainment rates, the mean current velocity controls the horizontal transport of the entrained sediment. It is assumed that the near-bed reference concentration in the 1 cm layer above the roughness length (z_0 - a notional height above the seabed at which the velocity goes to zero) is representative of the sediment entrainment and settling out of suspension. Thus, it is the mean velocity at the mid-point of the 1-cm layer ($z_b = z_0$+0.005 m) that controls the horizontal transport rate of the near-bed reference concentration. Spatial differences in these fluxes will lead to either net erosion or net accretion.

The mean velocity at the elevation z_b above the seabed can be related to the mean velocity at the instrument level assuming some knowledge of the velocity profile. Sternberg (1968) notes that in the inner boundary layer near the seabed the velocity profile is well represented by the logarithmic Karman-Prandtl equation, defined as,

$$U = 5.75U^{*}Log_{10}\left(z/z_0\right) \qquad (9.05)$$

in which the Von Karman's constant (κ = 0.4) is incorporated in the constant 5.75, U^* (m.s^{-1}) is the friction velocity, and z_0 is the hydraulic roughness length. The hydraulic roughness length (z_0) by definition is the elevation above the bed where the near-bed logarithmic velocity profile goes to 0 m.s^{-1}. As such, in order to accurately define z_0 it is necessary to have information on the velocity profile near the bed and extrapolate the profile to 0 m.s^{-1}(Van Rijn, 1984a). The necessary instruments (i.e. high resolution acoustic Doppler velocity profilers) were not available and so some assumptions about the magnitude of z_0 are necessary.

Under rough turbulent flows the hydraulic roughness is often taken as a function of the k_b, and as such will vary depending on grain size, ripple dimensions and saltation (Nielsen, 1992), and so can be expected to have varied over the monitoring period.

The smallest form of the roughness (both k_b and z_0) is that of the sediment grains themselves, called "grain roughness", or "Nikuradse roughness". This is usually not the dominant form of roughness in coastal waters but is used as a lower limit for physical roughness estimates. The apparent roughness due to the sediment grains alone is often defined as using eqn 5.04, while the hydraulic roughness is usually defined as (Nielsen, 1992; Van Rijn, 1984a),

$$z_0 = k_b / 30 \tag{9.06}$$

Given a median grain size within the channel of approximately 104μm (Table 9.01) then, from eqn 9.06, the lower limit of the hydraulic roughness is 3.5×10^{6}.

Wiberg and Rubin (1989) preformed lab experiments and revisited existing relationships to develop an expression that relates saltation roughness to sediment size and bed shear stress. Results suggest that the hydraulic roughness associated with saltation is approximately 0.01. However, the z_0 estimate was based on sandy sediment, and Harris (2003) notes that muddy sediments (such as those of this study) tend not to travel as bedload to the extent of sandy sediment, so the z_0 can be expected to be smaller.

Numerous equations for the apparent roughness due to bedforms area available in the literature, including the Nielson (1983, 1992) relationship of,

$$k_b = 8\eta^2 / \lambda \tag{9.07}$$

while Grant and Madsen (1982) use,

$$k_b = 27.7\eta^2 / \lambda \tag{9.08}$$

Assuming typical ripple dimensions with similar water depths in the study site are applicable (i.e. λ = 0.09-0.13 m and η = 0.01 m., Table 5.01) then the hydraulic roughness due to ripple beds can be expected to be of the order 0.001 m assuming the validity of the Grant and Madsen (1982) relationship, and 0.0003 assuming the Nielson (1983, 1992) relationship. The value of 0.001 is identical to the value used by Black et al. (1997) in their numerical modelling of Poverty Bay, and has been adopted for this study.

Knowing U and z in eqn 9.05 (i.e. the mean velocity from the S4ADW and the instrument elevation respectively), the velocity at the elevation z_b is given by,

$$U_{z_b} = \frac{U_{z_i} Log_{10}\left(z_b / z_0\right)}{Log_{10}\left(z_i / z_0\right)} \tag{9.09}$$

in which z_i is the instrument elevation. This formula does not require knowledge of the friction velocity (U^*).

Assuming that the current directions are consistent within the area of the shipping channel, then the component of the current perpendicular to the shipping channel can be determined using trigonometry. A component of the mean velocity perpendicular to the channel will always be directed into the channel, either from the NW or SE side of the channel. Therefore, by considering the absolute magnitude of the mean velocity perpendicular to the channel reduces the requirements for the model from 3 to 2-cells

In order to account for the mean velocity change due to the contraction and expansion of the flow over differing water depths the near-bed mean velocities for sites in 6, 7, 8, 9 and 10.5 m (U_{z_i}') are derived assuming a linear scaling of the mean near-bed velocity at the instrument site (U_{z_i}) of the form,

$$U_{z_h}' = U_{z_h} \Big/ \left(h_{z_i} \Big/ h_{z_d} \right) \tag{9.10}$$

in which h_{z_i} and h_{z_d} is the water depth at the instrument site and the site of interest respectively.

9.2.2.1.2 Predicted sediment entrainment using developed formulae

Near bed reference concentrations at sites within and adjacent to the shipping channel in water depths (h) of 6, 7, 8, 9 and 10.5 m are predicted using the formulae outlined in Chapter 6.

A modified wave-induced skin friction factor that incorporated the effect of flow enhancement near the crests of the ripple bedforms (eqn 6.09) was used to predict near-bed reference concentrations (C_0), while the retardation of the sediment entrainment rate due to cohesive bonding of the mixed sand/mud seabeds was accounted for by applying the developed formula,

$$\ln(\zeta) = -0.51 - 1.30\chi^3 \tag{9.11}$$

in which ζ is the relative entrainment factor (i.e. ratio of observed to predicted near-bed reference concentration), and χ is the normalised in-situ shear strength of the seabed. The evolution of this formula is discussed in Chapter 6.

Grain size characteristics of the surficial sediment within, and adjacent to the shipping channel are determined from the interpolated grain size distribution grids discussed in Chapter 3, while the corresponding shear strength of the surficial sediment has been determined from the interpolated in-situ shear strength grid discussed in Chapter 4. Table 9.01 summarises the d_{50} and shear-strength parameters for sediment adjacent to (h = 6, 7, 8, 9 m CD) and within the shipping channel

(h = 10.5 m CD) used in predicting the corresponding near-bed reference concentration.

Characteristic vortex ripples with dimensions λ = 0.10 m and η = 0.02 m are used at all sites to determine the predicted near-bed reference concentration. The values of λ = 0.10 m and η = 0.02 m are consistent with the findings of Chapter 7.

In order to determine the suspended sediment concentration at the elevation $z_b = z_0$+0.005 m above the seabed the time-averaged concentration profile equation proposed by Nielsen, (1986), is used to extrapolate the concentration profile upwards from the seabed (i.e. z = 0). Chapter 6 has shown that, for these mixed muddy-sand sedimentary conditions, near the bed the concentration profile and near-bed reference concentration are well predicted by the Nielsen, (1986) form of the time-averaged convection-diffusion equation, defined as,

$$C_{z_b} = C_0 \exp^{(-z_b / l_s)} \tag{9.12}$$

The near bed reference concentrations have been extrapolated to the elevation z_b (m) above the seabed using a near-bed mixing length (l_s) value of 0.06 m. The value of l_s = 0.06 m is consistent with the findings of Chapter 5.

9.2.2.1.3 Net horizontal sediment flux into the shipping channel

The net horizontal sediment flux into the shipping channel ($\vec{\varphi}_T$) is determined by accounting for the sediment flux orientated both into ($\vec{\varphi}_{in}$) and out off ($\vec{\varphi}_{out}$) the channel, such that

$$\vec{\varphi}_T = \vec{\varphi}_{in} - \vec{\varphi}_{out} \tag{9.13}$$

in which $\vec{\varphi}_{in}$ and $\vec{\varphi}_{out}$ are determined from eqn 9.04.

The inward sediment flux is determined assuming sediment entrainment and transport rates are consistent with the seabed, orbital velocity and mean current characteristics experienced on the flanks, and within the shipping channel. Differing seabed sediment characteristics (i.e. grain size and in-situ shear strength) and relevant near-bed orbital velocities between sites result in different magnitudes of $\vec{\varphi}_{in}$ and $\vec{\varphi}_{out}$, and hence a net change in the horizontal sediment flux into the shipping channel.

9.2.2.2 Vertical sediment flux in response to river discharge

Suspended sediment concentration (*SSC*) in the surface water at sites above the 1-metre strips was determined from the relationship relating *SSC* to discharge rates of the Turanganui River. The *SSC* at cast site 7 (Chapter 8, Figure 9.06) is assumed to be representative of the sediment in suspension above the area of channel with adjacent water depths in the range 6 m $\leq h \geq$ 9 m. The equation relating the *SSC* of

the surface water within the Turanganui Rive plume to river discharge rate at site 7 is given as,

$$C_{z(7)} = 0.023 \times \varphi_{river} + 0.10 \tag{9.14}$$

where φ_{river} is the discharge of the Turanganui River.

Assuming that there is no inhibition to the downward movement of sediment and the *SSC* due to river discharging is vertically uniform, then the downward sediment flux ($\varphi\downarrow$) per square meter of seabed per unit time is given by,

$$\varphi_{\downarrow} = C_{z(7)} w_f \tag{9.15}$$

in which w_f is the fall velocity of the relatively fine suspended sediment within the river plume (i.e. medium silt ≈ 0.0002 m.s^{-1}).

Assuming the deposited sediment has a bulk density, $\rho_{(bulk)}$, of 1300 kg.m^{-3}, consistent with the findings of Chapter 4, then the absolute change in water depth (Δh) due to the deposition of the relatively fine sediment from the river plume is given by,

$$\Delta h = \frac{\varphi_{\downarrow}}{\rho_{(bulk)}} \tag{9.16}$$

Gross volumetric change within each of the 1-m strips due to the downward sediment flux was determined for a channel width of 90 m.

9.2.3 Evaluation of the predictive formulae in determining channel infilling

Error analysis between estimated and predicted channel infilling rates is used to evaluate the ability of the developed formulae to predict channel infilling rates. The error (δ) between the estimated gross channel volumetric change and the net predicted channel volumetric change for each of the 1×90 m strips of channel being considered is determined as,

$$\delta = \frac{\left(\Delta Q_e - \Delta Q_p\right)^2}{\Delta Q_e{}^2} \tag{9.17}$$

in which ΔQ_e and ΔQ_p are the estimated and predicted changes in volume respectively. Smaller relative errors indicate a better fit between the estimated and the theory predicted channel infilling rates.

9.3 Results

9.3.1 Estimated gross channel volumetric change

The gross channel volumetric change between 10/03/99 and 02/06/99 is determined using a time-averaged form of eqn 9.03, and considers the sediment removed from the channel during maintenance dredging and the volumetric change between the hydrographic surveys on the 10/03/99 and 02/06/99.

9.3.1.1 Estimated volumetric change due to maintenance dredging

Figure 9.07 illustrates the daily volume of sediment that removed from the channel by maintenance dredging between the March 10th and June 2nd 1999. Dredging operations were sporadic due to being dependant on both the weather and shipping movements.

Based on the maintenance records a total of 28,200 m^3 (± 10%) of sediment has been removed from both the Swinging Basin and the shipping channel. Assuming that the dredging was essentially uniform spread over both the shipping channel and Swinging Basin, then approximately $1.7 \pm 0.17 \times 10^4$ m^3 of sediment was removed from the channel between 10/03/99 and 02/06/99 (Table 9.02). Not considering the horizontal and vertical sediment fluxes, this corresponds to an approximate increase in water depth of 0.124 m (± 0.01 m), or approximately 11.2 m^3 (± 1.2 m^3) within the 1 m × 90 m strip of channel being considered in the 2-cell numerical model.

9.3.1.2 Estimated volumetric change from hydrographic surveys

The shipping channel bathymetry on 10/03/99 and 02/06/99 is illustrated in Figure 9.08. The isobathic contours indicate that changes in the bathymetry of the shipping channel occurred during the survey periods. The change in channel bathymetry between surveys is illustrated in the difference grid (Figure 9.09), which shows channel infilling occurred between the survey periods regardless of dredging. Largest volumetric changes occurred near the flanks of the channel (Figure 9.09).

From Table 9.02, the net change in volume of sediment within the shipping channel, determined as the difference between the consecutive hydrographic surveys on the 10/03/99 and 02/06/99, is approximately $1.1 \pm 2.3 \times 10^4$ m^3. The relatively large error is due to the composite error in the difference grid, as defined in eqn. 9.02.

Six bathymetric profiles perpendicular, and three parallel to the strike of the channel (Figure 9.10) were used to illustrate net channel infilling characteristics. The bathymetric profiles (Figures 9.11, 9.12 and 9.13) illustrate that the largest changes in bathymetry between surveys occurs near either flank of the channel. Further, Profiles A to F illustrate that the seabed on the northwest side of the channel has experienced significant lowering (Figures 9.11 and 9.12).

9.3.1.3 Total estimated gross channel volumetric change

The total gross volumetric change within the port of Gisborne shipping channel in the 84-day period between 10/03/99 and 02/06/99 is 39,449 m^3, corresponding to a daily infilling rate of 470 m^3, or approximately 171,000 m^3 per year. The coordinates of the area used to determine the volumetric change of the shipping channel are given in Table 9.03. The total area of channel, excluding the Swinging Basin, being considered is 137,300 m^2.

9.3.1.4 Estimated gross volumetric change within 1×90 m channel slices

Volumetric analysis suggests that between 10/03/99 and 02/06/99 a net channel volumetric change of approximately $1.1 \pm 2.3 \times 10^4$ m^3 occurred. However, the net volumetric change was not uniformly distributed along the length of the channel.

The net infilling (exclusive of dredging) within the 1×90 m slices of channel with adjacent water depths within the range $6 \text{ m} \leq h \geq 9 \text{ m}$ was found to vary between 6 m^3 to 18 m^3 ± 15.3 m^3 (Table 9.04). Total gross infilling quantities (inclusive of dredging) within each of the 1×90 m channel slices are given in Table 9.04.

9.3.2 Wave and current characteristics between 10/03/99 and 02/06/99

The time-series of significant wave height (H_s), peak spectral period (T_p) and the third moment of the horizontal orbital velocity (U_3) in 10.5 m water depth (CD) between 10/03/99 and 02/06/99 is shown in Figure 9.14. H_s varied from 0.2 to 2.5 m, with a medium of $H_s = 0.63$ m, while T_p ranged from 4-19 s. The U_3 statistic is well correlated with the wave height and period, with maximum velocities occurring during the most persistent and relatively large sea-state that occurred between 01/05/99 and 06/05/99 (Figure 9.14). Linear theory is used to extrapolate the U_3 to water depth of 6 m, 7 m, 8 m and 9 m. The extrapolated U_3 statistics are used to predict sediment entrainment at the corresponding sites.

Figure 9.15 illustrates the time-series of mean current direction and speed between 10/03/99 and 02/06/99 at the site and elevation of the S4ADW. During the survey period mean currents reached 0.37 $m.s^{-1}$, however the average current speed was 0.08 $m.s^{-1}$ (Figure 9.15). The median current direction is towards 142°T.

9.3.3 Predicted channel infilling

As stated in section 9.2.2 the predicted channel infilling resulting from both horizontal and vertical sediment fluxes. The net volumetric change within several 1×90 m channel strips has been predicted using the 2-cell numerical model, and using the variations of the sediment entrainment formulae given in Table 9.05. The 2-cell numerical model considers both horizontal and vertical sediment fluxes using the findings and developed formulae from Chapters 3 to 8, and accounts for the

cohesive bonding of the seabed. The following sections describe the components of the 2-cell numerical model that predict the horizontal and vertical sediment fluxes.

9.3.3.1 Predicted channel volumetric change due to the horizontal sediment flux

Equation 9.04 shows the horizontal sediment flux to be dependant on the volume of sediment entrained by near-bed wave orbital velocities and the speed of the mean current. Channel volumetric changes due to the horizontal sediment flux are determined assuming that the suspended sediment within a 0.01 m layer at an elevation immediately above the roughness length (z_0) is representative of the concentration of sediment settling out of suspension (i.e. $C_{(z_0+0.005)}$). A roughness length (z_0) consistent with the value used in the sediment transport modelling of northern Poverty Bay performed by Black et al., (1997) has been used in the analysis (i.e. $z_0 = 0.001$ m), while eqn 9.12 is used to predict the *SSC* at the elevation $z_b = z_0+0.005$.

Figure 9.16 illustrates the time-series of predicted C_{z_b} within the channel (10.5 m) and in 6 m of water adjacent to the channel. The near-bed reference concentrations at elevation z_b above the seabed have been determined using the formulae outlined in Chapter 6 and include the effect of cohesive bonding on retarding the sediment entrainment rate. The variation in the value of C_{z_b} between sites results from the near-bed orbital velocities, seabed grain sizes and in-situ shear strengths being different at each site.

From equation 9.04 the other component that influences the horizontal sediment flux is the mean velocity at the level being considered (i.e. $z_b = z_0+0.005$). The contraction/expansion of flow over different water depths results in the mean velocity varying between sites. Figure 9.17 illustrates the time-series of the mean velocity component perpendicular to the channel at an elevation of $z_b = z_0+0.005$ in water depths of 10.5 m and 6.0 m.

Table 9.06 gives the total predicted volumetric change due to the horizontal sediment flux within each of the 1×90 m strips of channel being considered. The predicted infilling rates have been determined by accounting for both the inward and outward sediment flux ($\bar{\varphi}_{in}$ and $\bar{\varphi}_{out}$ respectively) using the methods outlined in section 9.2.2.1, and surficial sediment characteristics as defined in Table 9.01. Significantly, the predicted infilling rates are shown to vary between sites and indicate that, within the examples modelled, the greatest channel infilling is predicted to occur when the water depth adjacent to the channel is 8 m (Table 9.06).

Table 9.07 illustrates the hypothetical predicted infilling rates assuming uniform surficial sediment characteristics, and illustrates that if the sediment characteristics are considered to be uniform then the infilling rate of the channel increases with decreased adjacent water depth.

9.3.3.2Predicted channel volumetric change due to the vertical sediment flux

From Chapter 8, a good correlation has been shown to exist between the relatively fine suspended sediment ($w_f = 0.0002$ m.s^{-1}) in the turbid Turanganui River plume and river discharging. The correlation has been used to predict downward sediment fluxes, and the resulting depositional rates within the shipping channel. The depositional rate is determined assuming that the downward movement of sediment is not inhibited or enhanced by density stratification or turbulence respectively. Further, it is assumed that the *SSC* within the turbid river plume is vertically uniform.

The time-series of predicted *SSC* within the surface water of the river plume as predicted using eqn 9.14 is illustrated in Figure 9.18. Figure 9.19 illustrates the time-series of the predicted change in absolute water depth (Δh) based on eqn 9.16.

The cumulative change in absolute water depth (Δh) between the March 10th and the June 2nd 1999 within the shipping channel is 0.11 m, or 9.75 m^3 per 1×90 m slice of channel (i.e. the area considered in the two cell model). The median volume of water discharged into Poverty Bay by the Turanganui River between the 10th of March and the 2nd of June 1999 is 1.23 m^3.s^{-1}.

9.3.3.3Total predicted channel volumetric change

Table 9.06 lists the total predicted channel infilling from the 2-cell numerical model, determined as the sum of both the net horizontal and vertical sediment fluxes into the shipping channel. The magnitude of the total net predicted channel infilling is shown to vary between sites. Within the examples modelled the greatest channel infilling is predicted to occur when the water depth adjacent to the channel is 8 m (Table 9.06).

The different volumetric changes between sites are attributed to the variation in the hydrodynamical processes, and the variation in surficial sediment characteristics, i.e. the grain size (d_{50}) and the shear strength of the surficial sediment.

9.3.4 Comparison between predicted and estimated channel infilling between 10/03/99 and 02/06/99

The estimated gross channel infilling is determined as the sum of the measured volumetric change from the hydrographic survey and the volume removed during maintenance dredging, while the net predicted channel infilling is determined using the 2-cell numerical model and includes the predicted downward sediment fluxes and the net horizontal sediment flux into the channel.

Table 9.08 lists the errors (δ) between the estimated and predicted (using the 2-cell numerical model) volumetric changes for the 1×90 m strips of channel with adjacent water depths (h) within the range 6 m $\geq h \leq$ 9 m. Lowest errors are achieved when the 2-cell numerical model incorporates a flow-enhanced wave induced skin friction

factor (eqn 6.09), and the retardation of the entrainment rate due to cohesive bonding is accounted for using eqn. 9.011 (Table 9.08).

To illustrate the effect the variable grain size and shear strength of the seabed has on the predicted volumetric change within the channel an example has been modelled in which d_{50} and the in-situ shear strength are held constant. Holding the surficial sediment characteristics (i.e. d_{50} and shear strength) constant results in the predicted net volumetric change in the channel increasing as the adjacent water depth decreases (Table 9.07).

9.4 Discussion

If the conditions experienced in the survey period are considered to be representative of the environs, then extrapolation suggests that an estimated annual shipping channel volumetric change of ~171,000 m^3 per year (Table 9.09). The estimate is based on net volumetric change and maintenance dredging records between 10/03/99 and 02/06/99. In order to make practical comparisons between previous estimates the area over which channel infilling is estimated must be considered. Table 9.09 summarises previous daily and annual estimates of the infilling rate of the port of Gisborne shipping channel, and the absolute change in water depth (Δh) normalised by the area being considered. Previous estimates of Δh by Healy et al., (1980), Miller (1981) and Kensington (1990) are significantly smaller than those estimated by this study (Table 9.09). The volumetric changes estimated by Healy et al., (1980), Miller (1981) and Kensington (1990) are based on comparatively low resolution hydrographic surveys, with total errors due to positioning possibly being significant in the determination of infilling. As such, it is likely that the variation shown between estimates is due to advances in positioning, hydrographic sounding and interpolation of the bathymetric data between 1990 (i.e. the date of publication of Kensington) and the present. Advances in data collection and processing since 1990 imply this study provides more accurate estimates of Δh, and hence the infilling rates. Significantly, from Table 9.02 the net volumetric change in the channel was found to be positive, indicating that maintenance dredging did not keep up with the channel infilling rate between 10/03/99 and 02/06/99.

Black et al., (1997) partitions maintenance dredging requirements, and hence infilling rates for the port of Gisborne shipping channel into 'average', 'stormy' and 'sever' years, with Δh of 0.75 m, 1.84 m and 5.32 m respectively (Table 9.09). The estimates of Black et al., (1997) are based on numerical sediment transport modelling.

Based on the ranges of maintenance dredging requirements proposed by Black et al., (1997) the average infilling rate extrapolated from the data spanning the period 10/03/99 to 02/06/99 is representative of conditions between an 'average year' and a 'stormy year'. The salient mechanism determining the near-bed horizontal sediment flux is the near-bed wave orbital velocities and near-bed mean current, while the turbidity of the river plume is the salient parameter determining the downward sediment flux. During the period between surveys the average H_s was 0.73 m, while from Chapter 2 the average offshore H_s from the 20-year hindcast data is 1.34 m, indicating that the wave conditions experienced during the monitoring period were smaller that the long-term average offshore conditions. The median river discharge

between March 10th and June 2nd was 1.23 $m^3.s^{-1}$, which is similar to the long-term median value of 1.35 $m^3.s^{-1}$ (Chapter 8). Therefore, assuming minimal wave height attenuation due to frictional dissipation, the wave and river discharge conditions during the monitoring period are equivalent to average to less than average conditions, suggesting that the maintenance dredging requirement estimates of Black et al., (1997) may be conservative.

Bathymetric profiles of the shipping channel (Figures 9.11, 9.12 and 9.13) illustrate that during the period 10/03/99 to 02/06/99 the largest variability in Δh within the channel (i.e. reduction in absolute water depth) were found on either side of the channel leads (centre line). Hutt, (1997) identified similar infilling characteristics, however did not identify a mechanism for the spatial variability in Δh. In contrast, during the survey period Δh along Profile H (i.e. the channel leads, Figure 9.13) did not vary as significantly as the profiles on either side of the channel leads (Profiles G and I). Similar infilling characteristics are illustrated by the depth profiles orientated perpendicular to the channel (Figures 9.11 and 9.12). The horizontal sediment flux is the likely mechanism for the observed heightened accretion rate on either side of the channel (Figures 9.11, 9.12 and 9.13). The variation in near-bed orbital velocity within and on either flank of the shipping channel (due to differing water depths) results in preferential settlement of the entrained sediment within the channel, with differential settling resulting in the highest rate of settlement near the edge of the channel. Further, accretion on either side of the leads suggests that the diabathic component of the horizontal sediment flux perpendicular to the channel can, at times, be directed either NW or SE. The limited variability in Δh along the channel leads (Profile H) suggests that between 10/03/99 and 02/06/99 maintenance dredging has maintained the channel depth along the leads.

The depth profiles orientated perpendicular to the strike of the shipping channel show the water depth (h) on the NW (towards Waikanae Beach) side of the channel to have increased by up to 1 m, while on the SE (offshore) side of the channel the water depth is shown to be relatively stable (Figures 9.11 and 9.12). The variation in water depth shown on the NW side of the channel is consistent with the seabed being part of a dynamic beach/ebb tidal delta system. Assuming that the parabathic sediment transport is limited, the depth transects and mean current direction (heading towards 146°T) suggest a net offshore (into the channel) diabathic transport of the entrained sediment. Once in the channel, maintenance dredging removes the sediment from the nearshore littoral system, which, if the sediment is disposed of at an offshore disposal ground, results in a loss to the beach sediment budget. This relationship was identified by Black et al., (1997), and a near-shore littoral dredge disposal ground that retained the sediment within the littoral system of the beach was proposed following the 1997 Port Gisborne Ltd. Assessment of Environmental Effects (AEE) study. Healy et al., (2002) notes that the nearshore disposal ground proposed by Black et al., (1997) retains the dredged sediment within the storm wave breaking zone, so that the sediment remains part of the nearshore littoral zone.

From Table 9.04, the estimated net and gross volumetric change as determined from dredging reports and hydrographic surveys vary along the shipping channel, with the largest change occurring approximately 130-150 m from the tip of the breakwater (i.e. water depth adjacent to the channel of 8 m). The relatively high infilling rate 150 m seaward of the breakwater tip is consistent with the findings of Miller (1981), Kensington (1990) and Hutt (1997).. Kensington (1990) attributed the relatively high infilling rates 130-150 m from the tip of the breakwater to the presence of a sub-

tidal bar in the lee of the main breakwater however, hydrographic surveys do not conclusively show the presence of this sub-tidal bar (Figure 9.01).

Infilling of the shipping channel was predicted using a 2-cell numerical model that incorporates the results and formulae developed in Chapters 5, 6, 7, and 8 and the measured surficial sediments characteristics as given in Chapters 3 and 4. Significantly, largest infilling rates are predicted approximately 130-150 m from the tip of the breakwater, in keeping with the estimated channel infilling characteristics. Results from the 2-cell numerical model suggest that the relatively large estimated infilling characteristics at 130-150 m from the tip of the breakwater are due to hydrodynamical and sedimentological variability rather than the presence of an offshore lee-bar. Eliminating the variability of the seabed characteristics (i.e. d_{50} and shear strength) in the model runs result in the predicted infilling rate increasing as the water depth adjacent to the channel decreases. The results highlight the need to account for the variability in seabed characteristics when modelling sediment fluxes, and suggest that the variability in the infilling rate along the channel is due to the variability in seabed characteristics rather than the presence of an offshore lee bar.

Error analysis of the estimated to predicted (using the 2-cell numerical model) infilling rates show that the best agreement is achieved when both the downward flux and net horizontal flux is considered. The downward flux is predicted using the relationship derived in Chapter 8 and assumes the turbid plume is vertically uniform. The net horizontal sediment flux into the channel is determined by accounting for flow enhanced wave induced skin friction (eqn 6.09), and the retardation of the entrainment rate due to cohesive bonding (eqn 9.11, Table 9.05). Not accounting for the cohesive bonding of the seabed results in significantly larger total errors, regardless of whether the standard Shields mobility number (determined using $k_b = 2.5d_{50}$) or flow enhanced Shields mobility number is used in the prediction of the horizontal entrained sediment flux. The results highlight the need to include the effect of cohesiveness in any prediction of sediment entrainment and transport rates over mixed sand/mud seabeds, and substantiate the predictive formulae developed during this study.

Understanding the sediment entrainment and transport characteristics of the mixed sand/mud seabed in northern Poverty Bay has profound implications on the development of future port configurations. If a new port design is implemented at the port of Gisborne that involves re-orientating the shipping channel such as that proposed by Black et al., (2002) a significant reduction in the maintenance dredging requirements, and hence potential cost savings to the port company can be achieved by understanding the sediment characteristics, in particular the cohesive bonding of the surficial sediment. The cohesive bonding of the surficial sediment has been shown both in this study (i.e. Chapter 6) and in numerous other studies (e.g. Kamphuis and Hall, 1983; Kuijper et al., 1989; Mehta et al., 1989; Mitchener and Torfs, 1996; Toorman, 2001) to retard the sediment entrainment rate to increase the critical shear stress of erosion.

9.5 Conclusion

Shipping channel infilling rates between 10/03/99 and 02/06/99 have been estimated using dredging reports and high-resolution hydrographic surveys. Within the area examined a total volumetric change of 11,249 m^3 occurred in the 84-day interval. Extrapolation of the infilling rate to an annual rate suggests that the characteristics of

infilling are consistent with 'average' to 'stormy' conditions as defined by Black et al., (1997). However, during the interval between surveys the two salient parameters controlling horizontal and vertical sediment fluxes (i.e. river discharge and wave characteristics), and hence channel infilling rate, were less than the mean annual conditions, suggesting that the estimates of Black et al., (1997) are conservative.

Volumetric analysis of the difference between the hydrographic surveys on the 10/03/99 and 02/06/99 suggests that maintenance dredging was unable to keep up with the infilling rates.

Examination of the channel infilling characteristics shows the infilling rate to be variable along the length of the channel, with largest infilling rates occurring approximately 120-150 m from the tip of the port breakwater.

Bathymetry transects and contoured difference surfaces illustrate that the largest net volumetric changes occurred near the sides of the channel, while the water depth near the centre of the channel remained relatively consistent, presumably due to maintenance dredging. Further, transects show the water depth on the landward side of the channel (NW) to increase during the survey period, suggesting that the area is part of the dynamic beach/ebb-tidal delta system, and responds to near-shore hydrodynamical processes. Therefore, removal of sediment from the dredged channel, and disposal of the sediment at an offshore site can potentially result in a loss of sediment from the nearshore littoral zone.

A 2-cell numerical model that considers a 1-m wide strip of channel has been developed (as schematised in Figure 9.03) that greatly simplifies infilling predictions, and illustrates that predictions of channel infilling do not necessarily require the implementation of a full 3-dimensional hydrodynamical model. The model considers measured seabed sediment characteristics (d_{50}, shear strength), and the settlement of relatively fine sediment from the turbid plume of the Turanganui River.

The model successfully predicts channel infilling rates, including the variability in estimated infilling along the length of the channel. The variability in estimated infilling along the length of the channel is found to be a function of the seabed grain size and shear strength variation on the flanks of the shipping channel.

Error analysis of predicted-to-observed infilling rates validates the predictive formulae developed during this study, and illustrates that not accounting for grain size and shear strength variability can result in erroneous predictions of the channel infilling rate.

Results from the study significant advance the understanding of channel infilling rate and characteristics at the port of Gisborne, and suggest that the developed formulae and findings can be used to predict sediment fluxes in Northern Poverty Bay.

Table 9.01 Median grain size (d_{50}) and in-situ shear strength of the sediment within and adjacent to the port of Gisborne shipping channel. Values of d_{50} and the in-situ share strength have been obtained from the interpolated grids and measured values in Chapter 3 and 4 respectively.

	Median grain size (μm)	In-situ shear strength (kPa)
Within the shipping channel	130	1.72
At 6 m water depth adjacent to channel	120	1.25
At 7 m water depth adjacent to channel	104	1.22
At 8 m water depth adjacent to channel	89	1.27
At 9 m water depth adjacent to channel	87	1.3

Table 9.02 Estimated net and gross volumetric changes in the shipping channel between 10/02/99 and 02/06/99. The estimated net volumetric change is determined from hydrographic surveys, while the Gross volumetric change includes both the volumetric change as measured from the difference between the hydrographic surveys and the volume estimated to have been dredged from the shipping channel. Also shown are the potential errors based on a survey accuracy estimate of the water depth (0.17 m) in the hydrographic surveys, and a 10% error in the volume estimated to have been removed during maintenance dredging.

Measure	Quantity	Potential error
Area of channel hydrographically surveyed m^2	137,300	
Approximate *NET* Total volumetric change from hydrographic surveys m^3	**1.1**	**$\pm 2.3\times10^4$**
Area of channel and Swinging Basin actively dredged m^2	226,900	
Total volume of sediment removed by maintenance dredging (including Swinging Basin) m^3	2.82×10^4	0.282×10^4
Total volume of sediment removed by maintenance dredging from the Shipping Channel m^3	17,060	1,706
GROSS volumetric change within channel (inclusive of the volume of sediment dredged from the channel) m^3	**2.83×10^4**	**$\pm 2.5\times10^4$**

Table 9.03 Co-ordinates that bound the area used to determine the volumetric changes between the hydrographic surveys on the 10/03/99 and 02/06/99. Co-ordinates are in Poverty Bay Circuit (NZGD49).

Easting (m)	Northing (m)
311646.22	694072.75
311695.00	694002.13
311685.94	693982.06
311544.97	693879.00
311436.91	693795.00
310637.91	693234.00
310579.91	693323.94
311646.22	694072.75

Table 9.04 Estimated net and gross volumetric changes within portions of the channel where the adjacent water depth (h) is within the range 6 m $\leq h \geq$ 9 m between 10/03/99 and 02/06/99. The largest estimated volumetric change (i.e. 29.3 m^3) is shown to occur within the section of the channel in which the adjacent water depth (h) is 8 m, approximately 120-150 m from the tip of the port of Gisborne breakwater (Figure 9.06).

	20 m swath (m^3)	1 m strip (m^3)	Estimated volume removed by dredging (m^3)	Total (m^3)
Volume change at 6 m	122.55	6.13 (± 15.3)	11.18 (± 1.1)	17.31 (± 16.4)
Volume change at 7 m	288.78	14.44 (± 15.3)	11.18 (± 1.1)	25.62 (± 16.4)
Volume change at 8 m	362.66	18.13 (± 15.3)	11.18 (± 1.1)	29.31 (± 16.4)
Volume change at 9 m	277.78	13.89 (± 15.3)	11.18 (± 1.1)	25.07 (± 16.4)

Table 9.05 Variations of the formulae used to predict the wave induced skin friction factor (ψ' or ψ''). The Sediment entrainment rates are predicted using eqn. 6.10. All methods use a bed roughness of $k_b = 2.5d_{50}$, however methods 2 and 3 use a modified wave induced skin friction factor that accounts for the effect flow enhancement near the crest of vortex ripples has on sediment entrainment rates as defined by Du Toit and Sleath, (1981). Further, Method 3 accounts for the effect cohesive bonding of the surficial sediment has on retarding the entrainment rate using the formula developed in Chapter 6.

	Bed roughness	Wave induced skin friction factor	Shear strength accounted for
Method 1	$k_b = 2.5d_{50}$	$\psi' = \frac{f_w U^{*2}}{2sgd_{50}}$	NO
Method 2	$k_b = 2.5d_{50}$	$\psi' = \frac{f_w U^{*2}}{2sgd_{50}}$ $\psi'' = \frac{\psi'}{(1-\pi\eta/\lambda)^2}$	NO
Method 3	$k_b = 2.5d_{50}$	$\psi' = \frac{f_w U^{*2}}{2sgd_{50}}$ $\psi'' = \frac{\psi'}{(1-\pi\eta/\lambda)^2}$	YES

Table 9.06 Predicted channel infilling rates at sites within the channel where the adjacent water depth (h) is within the range 6 m ≤ h ≥ 9m. The predictions have been made using a simplistic two-cell model that considers a 1×90 m section of channel that accounts for both the horizontal and vertical sediment flux. Infilling rates have been determined using the methods outlined in Table 9.05. Sediment characteristics used to determine channel infilling varied between sites and are listed in Table 9.01. Largest channel infilling rates are predicted when the water depth adjacent to the channel is 8 m

		Channel infilling adjacent to 9 m water depth (m^3)	Channel infilling adjacent to 8 m water depth (m^3)	Channel infilling adjacent to 7 m water depth (m^3)	Channel infilling adjacent to 6 m water depth (m^3)
Infilling due to the *horizontal flux*	Method 1 (m^3)	3.53	3.82	2.53	1.55
	Method 2 (m^3)	25.55	27.63	18.32	11.24
	Method 3 (m^3)	13.51	15.52	13.04	8.64
Infilling due to the *downward flux*	RIVER INPUT	12.00	12.00	12.00	12.00
TOTAL INFILLING	Method 1 (m^3)	15.52	15.81	14.53	13.55
	Method 2 (m^3)	37.54	39.62	30.31	23.24
	Method 3 (m^3)	25.51	27.52	25.04	20.63

Table 9.07 Predicted channel infilling rates at sites within the channel where the adjacent water depth (h) is within the range 6 m ≤ h ≥ 9m between 10/03/99 and 02/06/99. The predictions have been made using a simplistic two-cell model that considers a 1×90 m section of channel that accounts for both the horizontal and vertical sediment flux. Sediment characteristics (d_{50} and in-situ share strength) have been held constant in order to highlight the effect the variation of d_{50} and the in-situ shear strength has on channel infilling characteristics. Keeping the seabed characteristics constant results in predicted infilling rates increasing as the water depth adjacent to the channel decrease.

		Channel infilling adjacent to 9 m water depth (m^3)	Channel infilling adjacent to 8 m water depth (m^3)	Channel infilling adjacent to 7 m water depth (m^3)	Channel infilling adjacent to 6 m water depth (m^3)
Infilling due to the *horizontal flux*	Method 1 (m^3)	2.19	2.61	3.28	4.35
	Method 2 (m^3)	15.89	18.89	23.74	31.51
	Method 3 (m^3)	9.34	11.22	14.03	18.30
Infilling due to the *downward flux*	RIVER INPUT	12.00	12.00	12.00	12.00
TOTAL INFILLING	Method 1 (m^3)	14.19	14.60	15.27	16.35
	Method 2 (m^3)	15.89	18.89	23.74	31.51
	Method 3 (m^3)	23.53	25.82	29.31	34.65

Table 9.08 Comparison between the estimated and predicted channel infilling rates between 10/03/99 and 02/06/99. Channel infilling characteristics have been examined within several 1×90 m strips of channel in which the adjacent water depth (h) is within the range 6 m ≤ h ≥ 9m. Error analysis illustrates that the lowest errors between estimated and predicted channel infilling rates (*highlighted*) occur using Method 3 (Table 9.05). Method 3 uses a modified Shields mobility parameter that accounts for the flow enhancement near the crest of the vortex ripples, and accounts for the retardation of the entrainment rate due to cohesive bonding of the surficial sediment is accounted for using the formula developed in Chapter 6. The suitability of Method 3 is in keeping with the findings of Chapters 6 and 7.

		Channel infilling adjacent to 9 m water depth (m^3)	Channel infilling adjacent to 8 m water depth (m^3)	Channel infilling adjacent to 7 m water depth (m^3)	Channel infilling adjacent to 6 m water depth (m^3)
TOTAL PREDICTED INFILLING	Method 1 (m^3)	15.52	15.81	14.53	13.55
	Method 2 (m^3)	37.54	39.62	30.31	23.24
	Method 3 (m^3)	25.51	27.52	25.04	20.63
TOTAL ESTIMATED INFILLING	Inclusive of volume removed by dredging and volumetric change between hydrographic surveys	26.05	29.75	25.85	17.50
ERROR	Method 1	0.1633	0.2195	0.1919	0.0510
	Method 2	0.1946	0.1101	0.0298	0.1075
	Method 3	**0.0004**	**0.0056**	**0.0010**	**0.0320**

Table 9.09 Summary of previous estimated of both the daily and annual channel infilling rates, and the corresponding potential depth change of the channel assuming the sediment remains within the channel. Also given are the estimated channel infilling rates between 10/03/99 and 02/06/99 as determined from this study. Infilling rates from this study are consistent with an 'average' to 'stormy' year under the scheme of Black et al., (1997), and are larger than estimates pre 1990. The variation between the infilling estimates pre 1990 and those of this study are attributed to superior data and analytical methods.

Source		Daily infilling rate ($m^3.day^{-1}$)	Annual infilling rate ($m^3.yr^{-1}$)	Area being considered (m^2)	Absolute change in water depth (Δh)
Healy et al., (1980)		140 to 157	51100 to 57305	80,000	0.64 to 0.72
Miller, (1981)		157	57,305	80,000	0.72
Kensington, (1990)		107	39,055	80,000	0.49
Black et al., (1997)	Average year	282	103,000	137,300	0.75
	Stormy year	690	252,000	137,300	1.84
	Sever year	2,000	730,000	137,300	5.32
This study, between 10/03/99 and 02/06/99		**470**	**171,415**	**137,300**	**1.25**

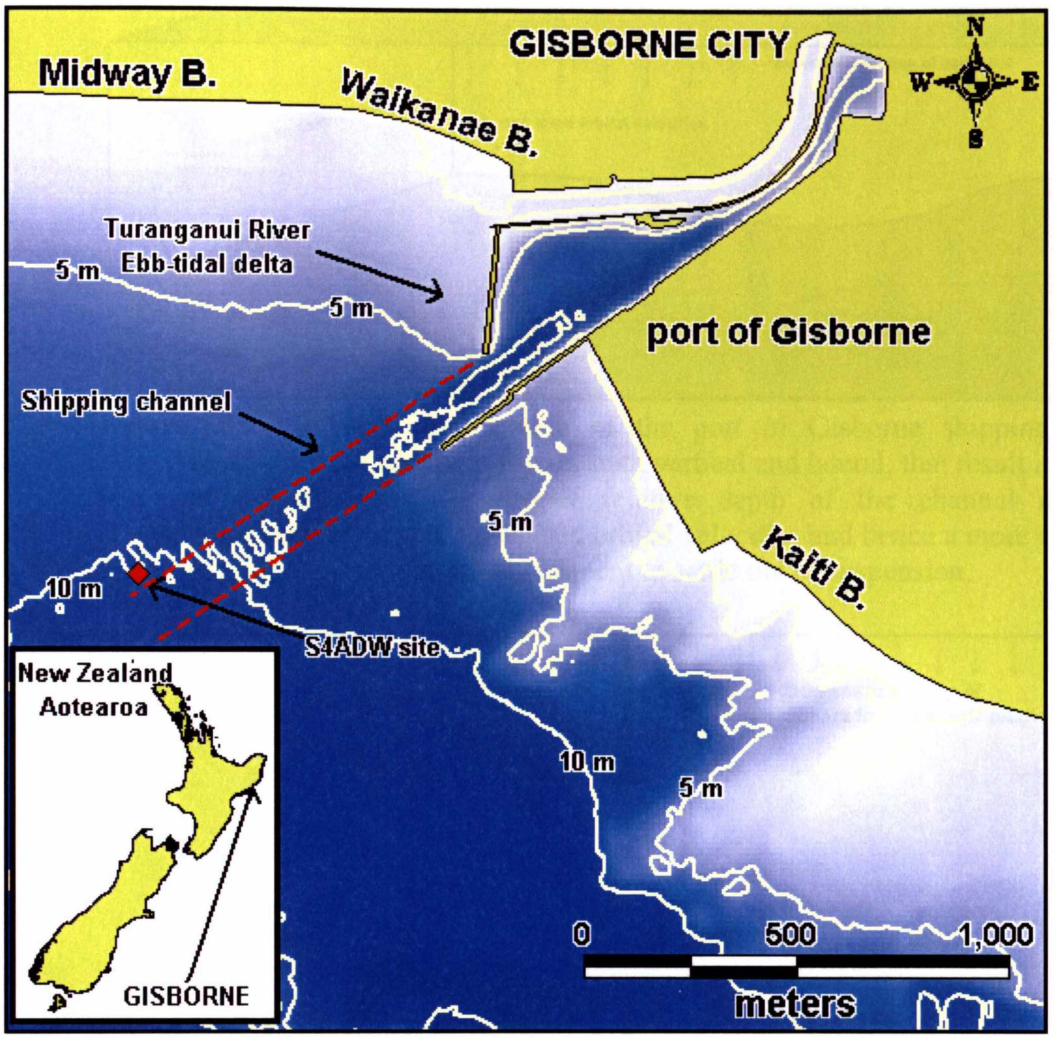

Figure 9.01 The port of Gisborne shipping channel in northern Poverty Bay, on New Zealand's East Coast. The channel is dredged through the ebb-tidal delta of the Turanganui River. Also shown is the location of S4ADW directional wave and current meter that was deployed adjacent to the shipping channel during the river channel survey period 10/03/99 to 02/06/99.

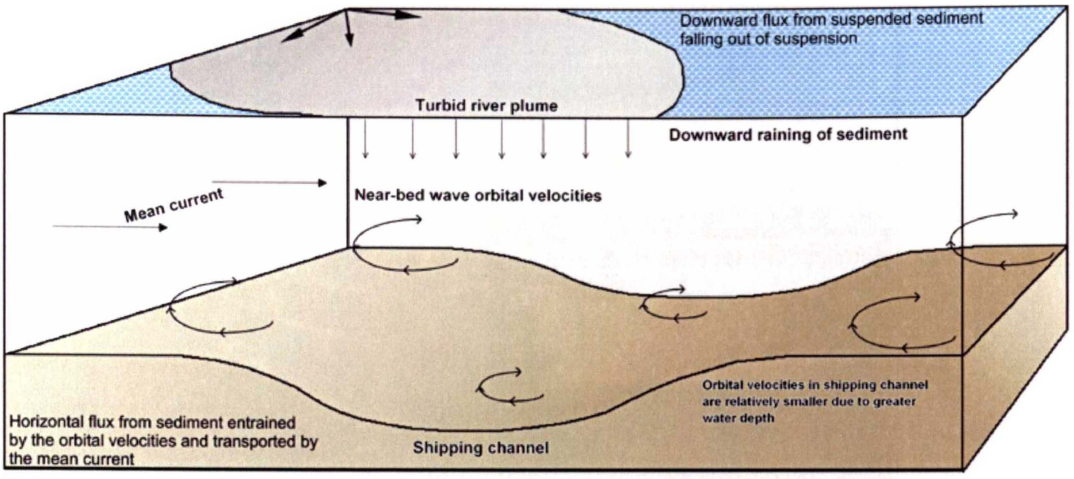

Figure 9.02 Stylised cross-section of the port of Gisborne shipping channel illustrating the sediment fluxes, both vertical and lateral, that result in infilling of the channel. The deeper relative depth of the channel results in comparatively smaller near-bed orbital velocities and hence a more conducive environment for entrained sediment to settle out of suspension.

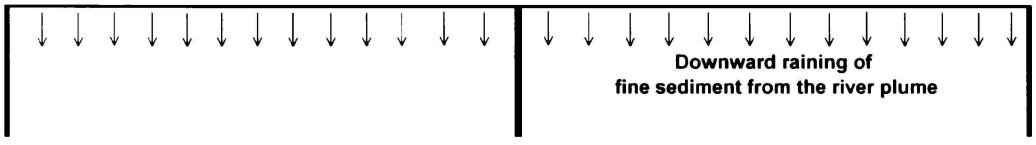

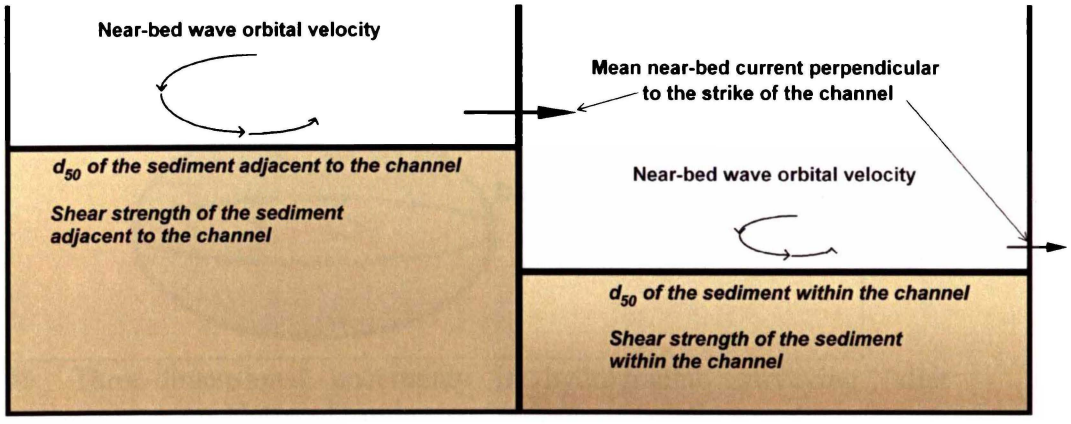

Figure 9.03 Visualisation of the two-cell model used to predict infilling rates of the port of Gisborne shipping channel using the results and formulae developed in Chapters 5, 6, 7 and 8. While being a simplistic representation of the shipping channel, the model considers the complexities associated with both lateral and vertical sediment fluxes and uses measured surficial sediment characteristics to determine entrainment rates. Inward and outward mean near-bed current speeds vary due to contraction/expansion of flow.

Figure 9.04 The cutter-suction dredge the *Pukunui* operated by Adsteam International; the maintenance-dredging contractors. The Pukunui is used to maintain the design depth of the shipping channel.

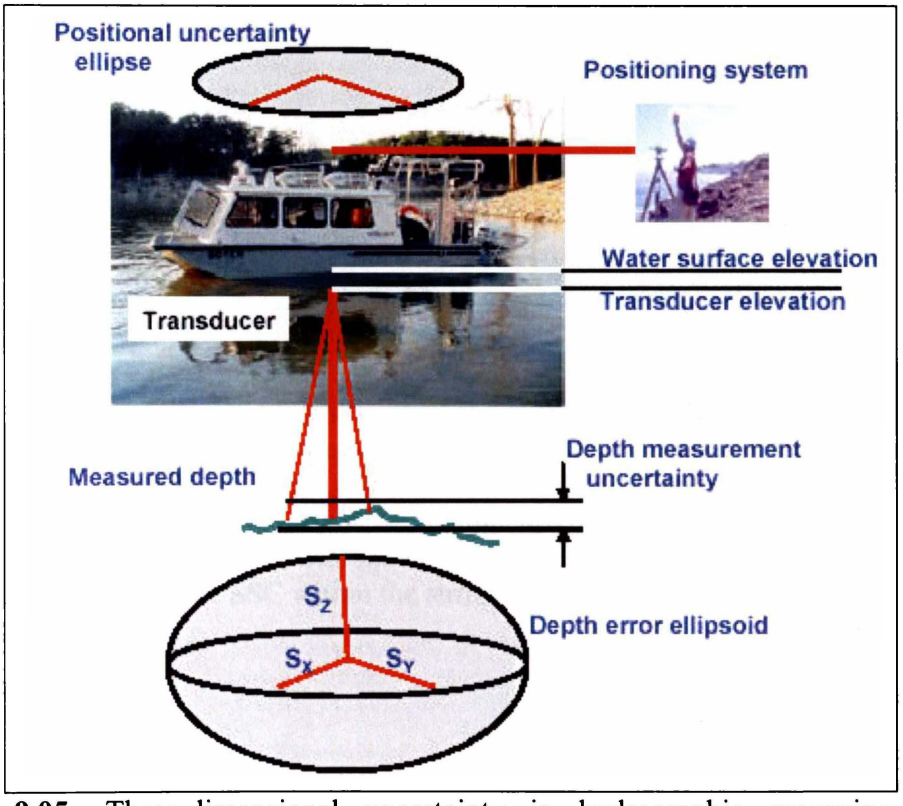

Figure 9.05 Three-dimensional uncertainty in hydrographic surveying (after United States Army Corps of Engineers, 2002b).

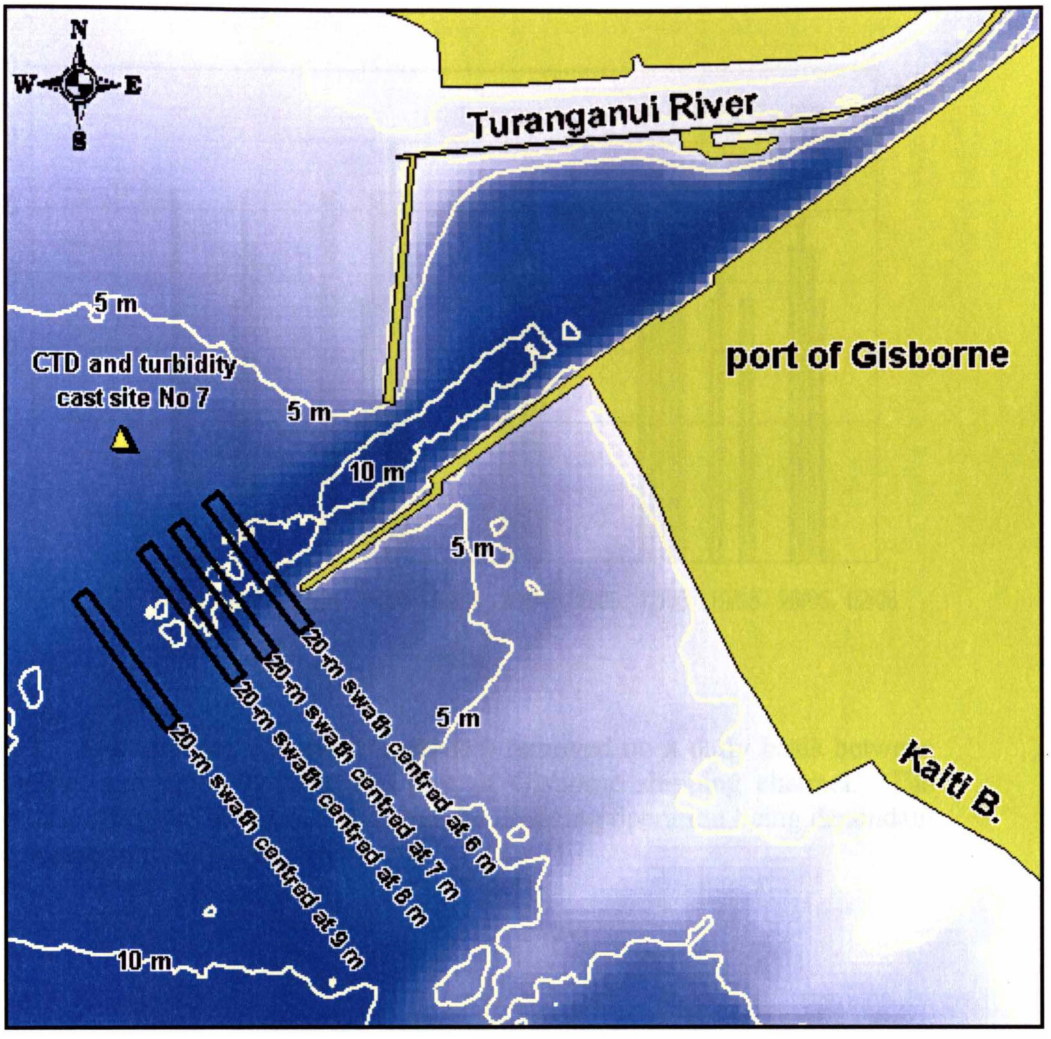

Figure 9.06 Location of the 20-metre wide strips used to determine typical infilling rates within the shipping channel in areas with 9, 8, 7 and 6 m adjacent water depths. The areas are centred about the corresponding depths, and the average infilling rate within a 1-metre strip is used to evaluate the predictive formulae. Volumetric changes in the channel area only are considered. Also shown is the CTD and turbidity cast site location used to evaluate SSC within the surface water due to river discharging.

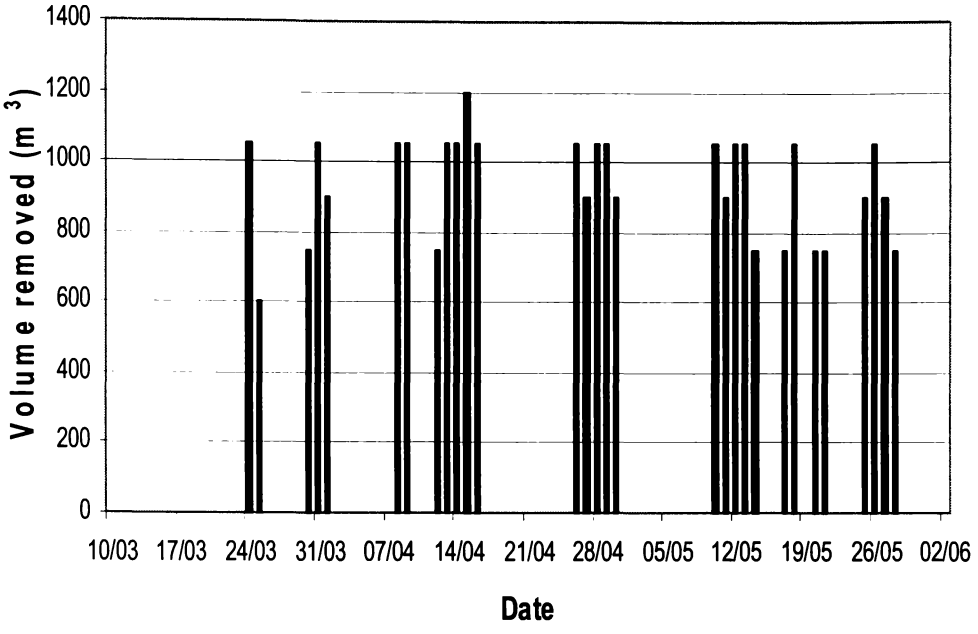

Figure 9.07 Approximate volume of sediment removed on a daily basis between 10/03/99 and 02/06/99 from the port of Gisborne shipping channel. The sporadic nature of the record is due to the dredging operation being dependant on weather and shipping movements.

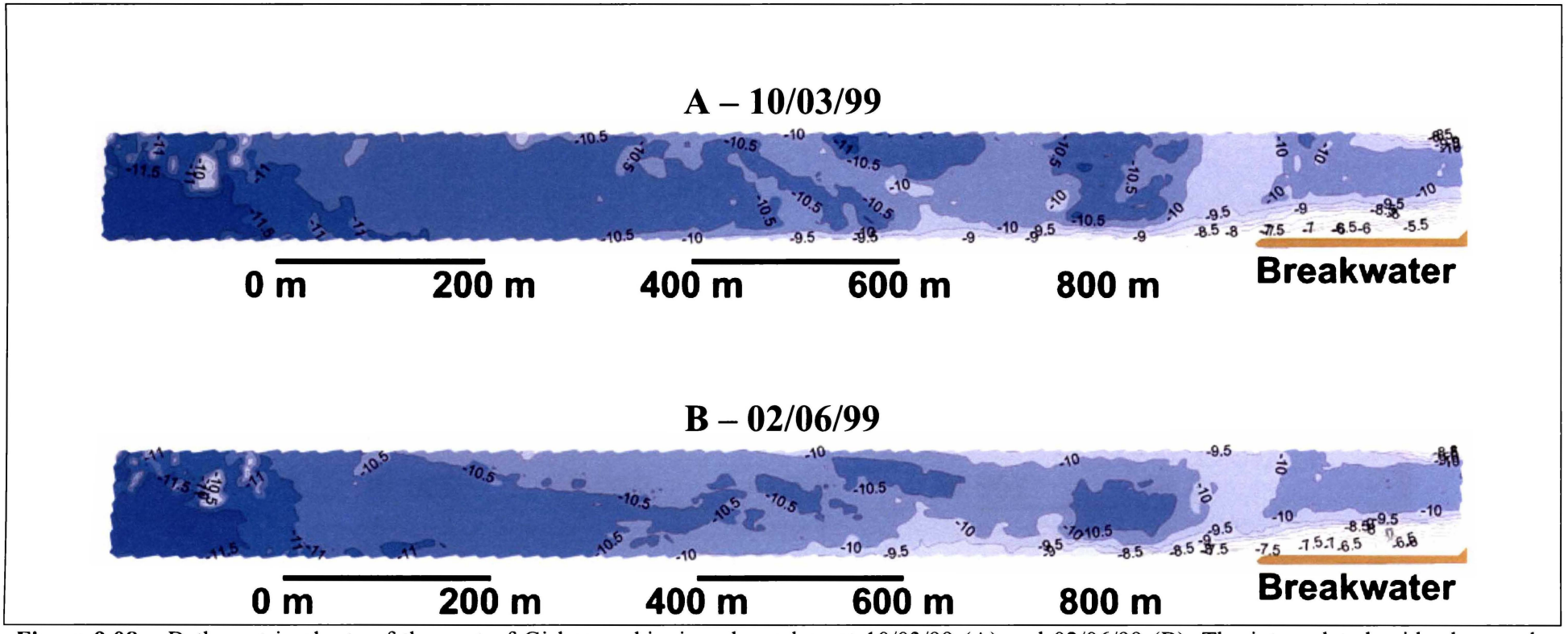

Figure 9.08 Bathymetric charts of the port of Gisborne shipping channel as at 10/03/99 (A) and 02/06/99 (B). The interpolated grids show only small differences in the location of the isobathic contours.

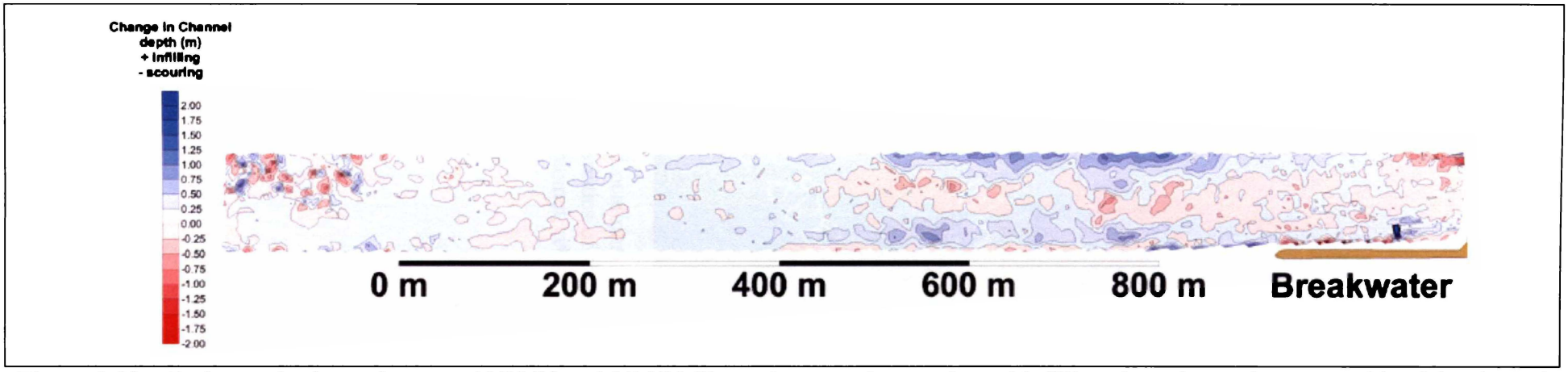

Figure 9.09 Bathymetric change between 10/03/99 and 2/06/99 illustrating conspicuous channel infilling along the north-western side of the channel with up to 0.5 m change in absolute water depths within the channel, and deepening along the channel centre near the breakwater. The negative depth changes (scouring) within the centre of the shipping channel adjacent to the breakwater is attributed to dredging operations.

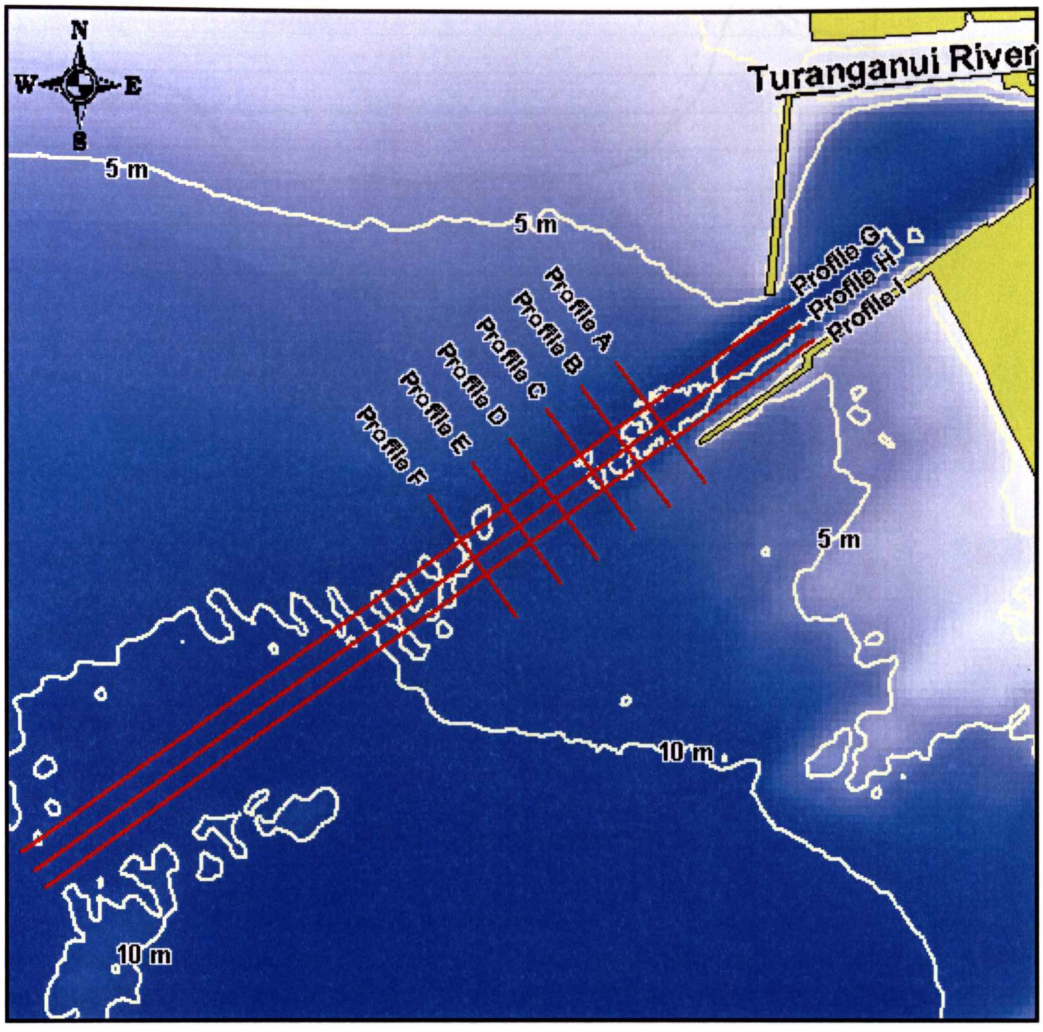

Figure 9.10 Locations of the bathymetric profiles used to investigate the characteristics of the gross channel infilling. Six profiles strike perpendicular to the channel, while three run parallel.

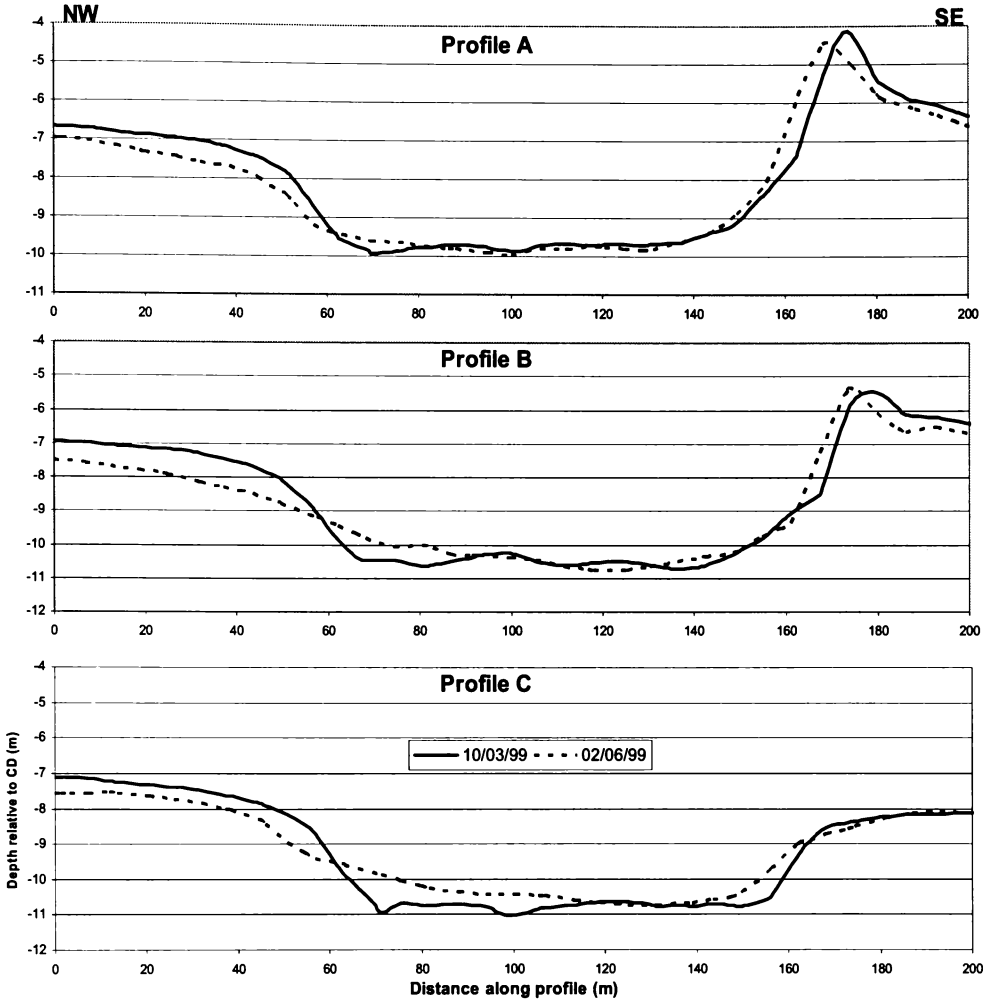

Figure 9.11 Bathymetric profiles A, B and C orientated perpendicular to the channel on the 10th of March and the 2nd of June. Profiles strike from NW on the left to SE on the right and are illustrated in Figure 9.10. The shipping channel is conspicuously located in the centre of the profiles. On all profiles largest variations occur on the either flank of the channel. Significantly, the seabed on the NW side of the channel, towards Waikanae and Midway Beaches, has been lowered by as much as 1 metre, while the NW side of the channel has experienced significant infilling.

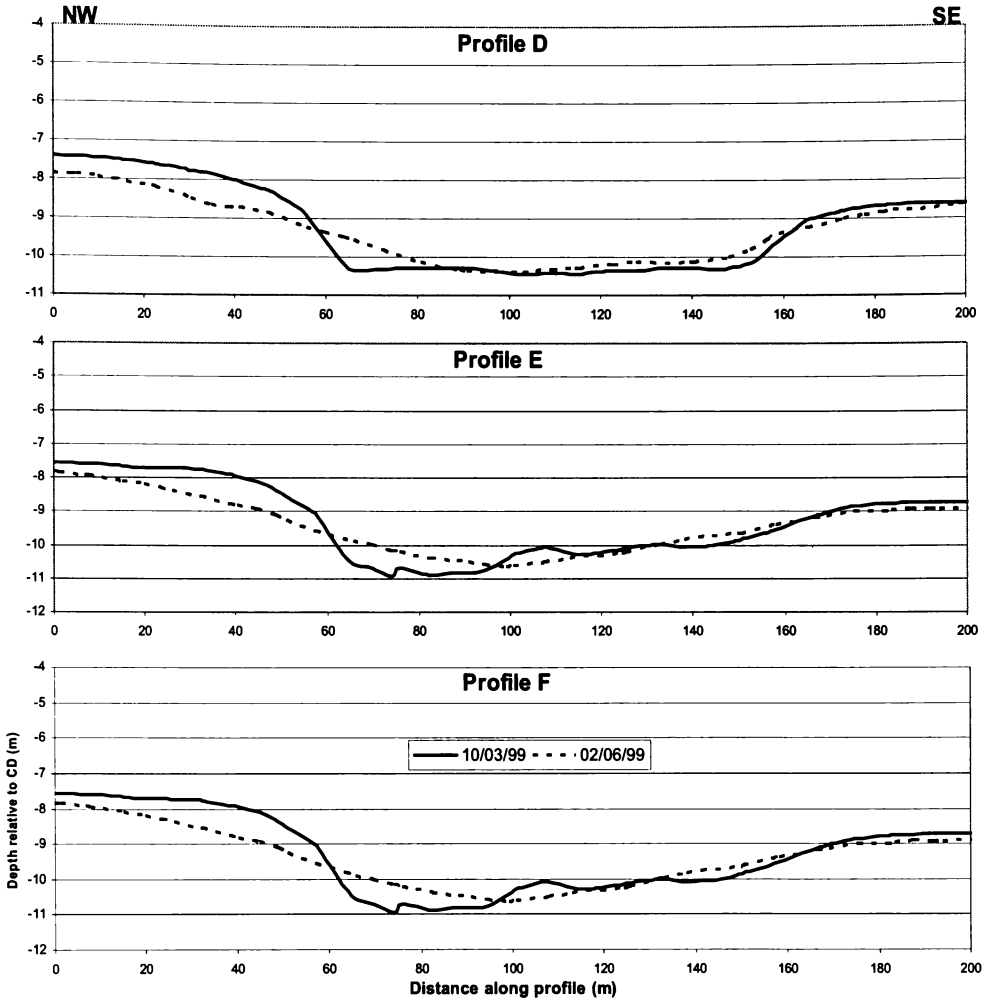

Figure 9.12 Bathymetric profiles D, E and F orientated perpendicular to the channel on the 10th of March and the 2nd of June. Profiles strike from NW on the left to SE on the right and are illustrated in Figure 9.10. The shipping channel is conspicuously located in the centre of the profiles. On all profiles largest variations occur on the either flank of the channel. Significantly, the seabed on the NW side of the channel, towards Waikanae and Midway Beaches, has been lowered by as much as 1 metre, while the NW side of the channel has experienced significant infilling.

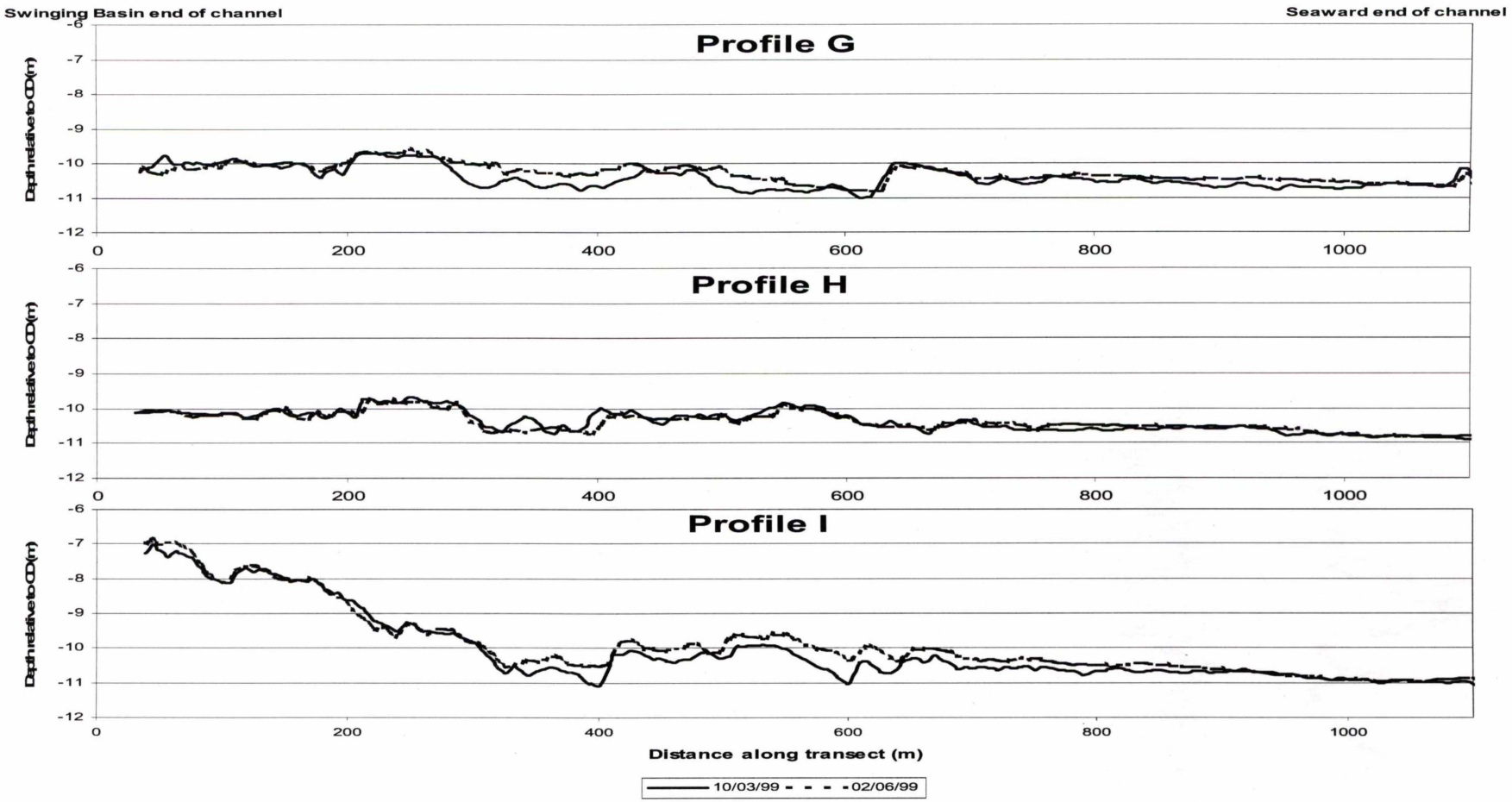

Figure 9.13 Bathymetric profiles orientated parallel to the channel on the 10th of March and the 2nd of June. Figure 9.10 illustrates profile location. The profiles show relatively more variation on either side of the channel (i.e. Profiles G and I).

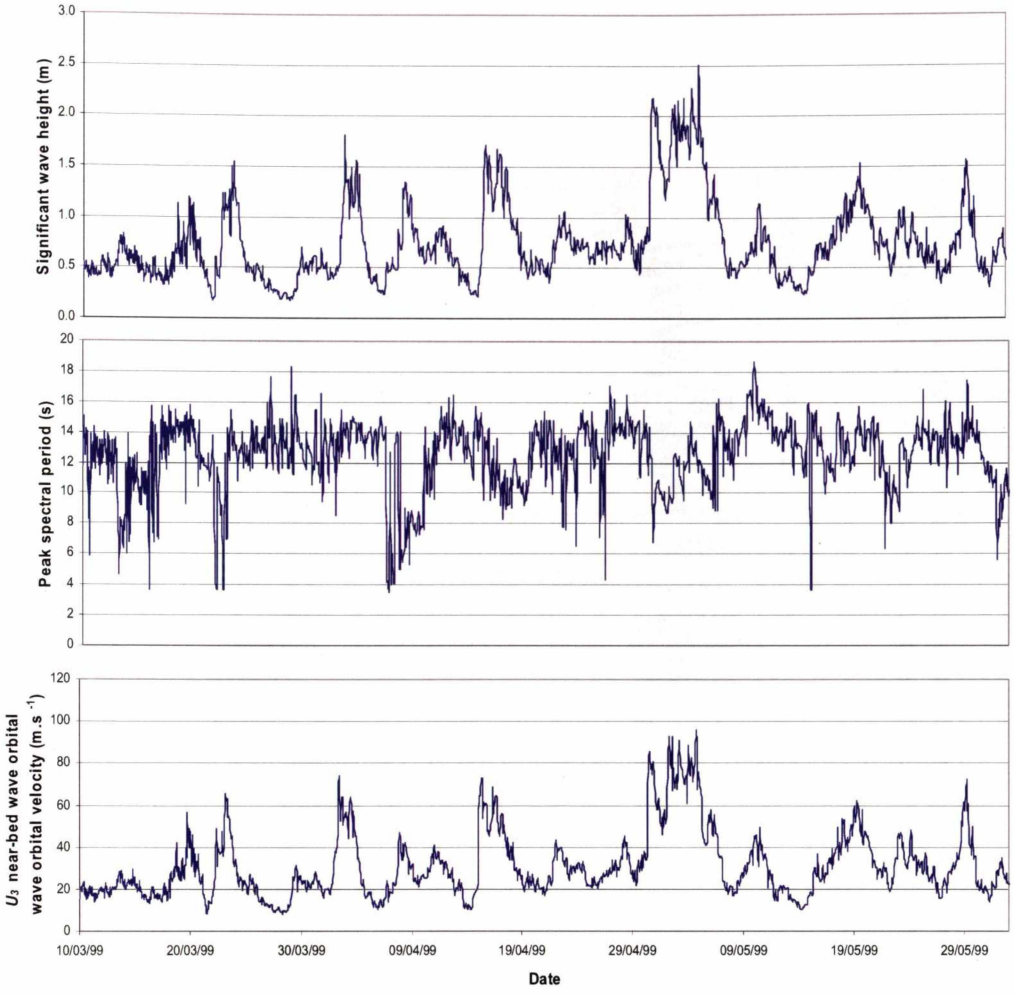

Figure 9.14 Wave and U_3 near-bed orbital velocity statistics between 10/03/99 and 02/06/99 in the vicinity of the port of Gisborne shipping channel. The U_3 statistics correspond to the orbital characteristics for the shipping channel (i.e. 10.5 m water depth)

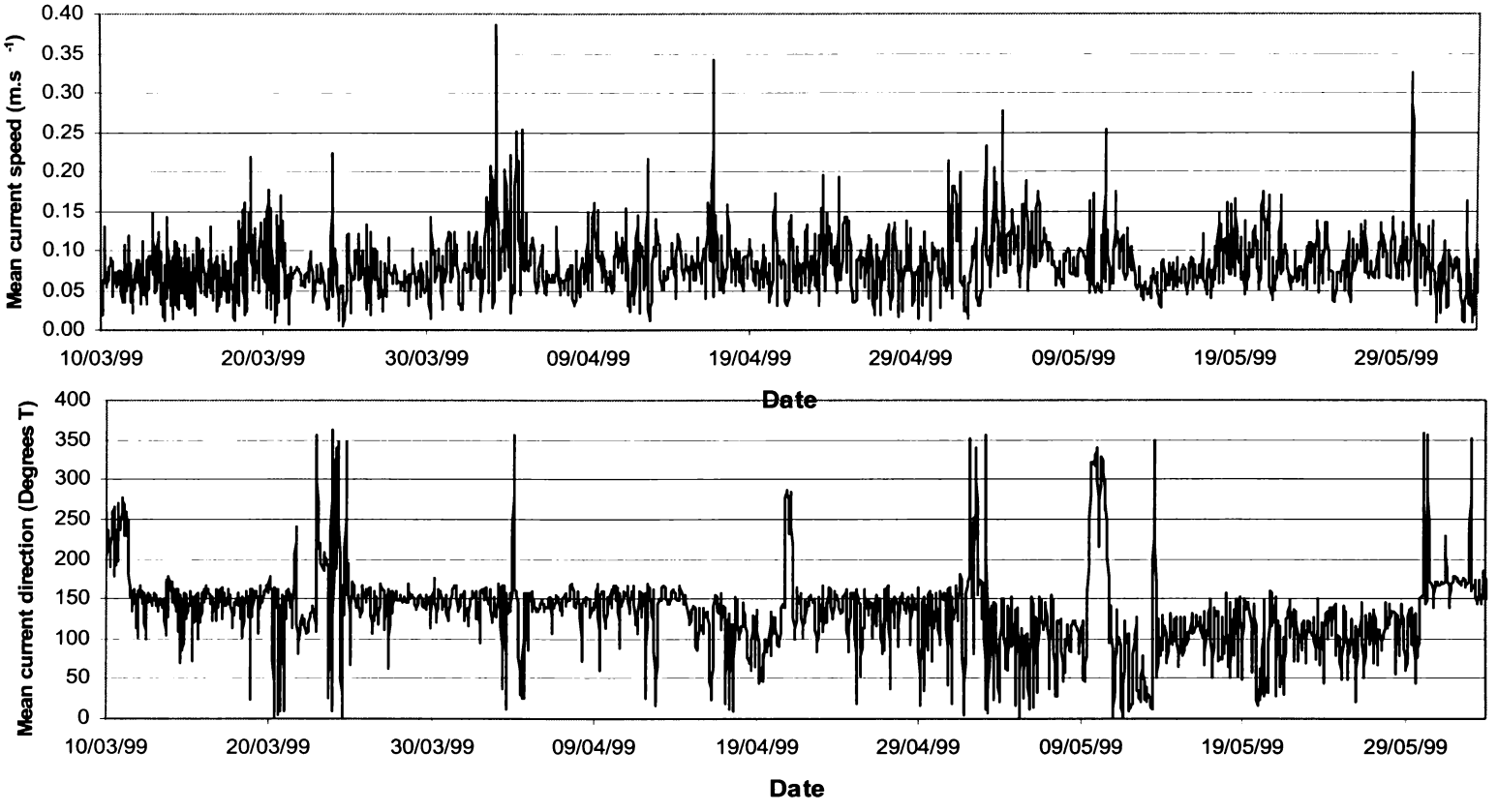

Figure 9.15 Mean current speeds and directions (heading towards) at the instrument elevation above the bed at the S4ADW site. Current velocities are rotated to an orientation perpendicular to the shipping channel in order to determine the relative component of the velocity that is influencing channel infilling.

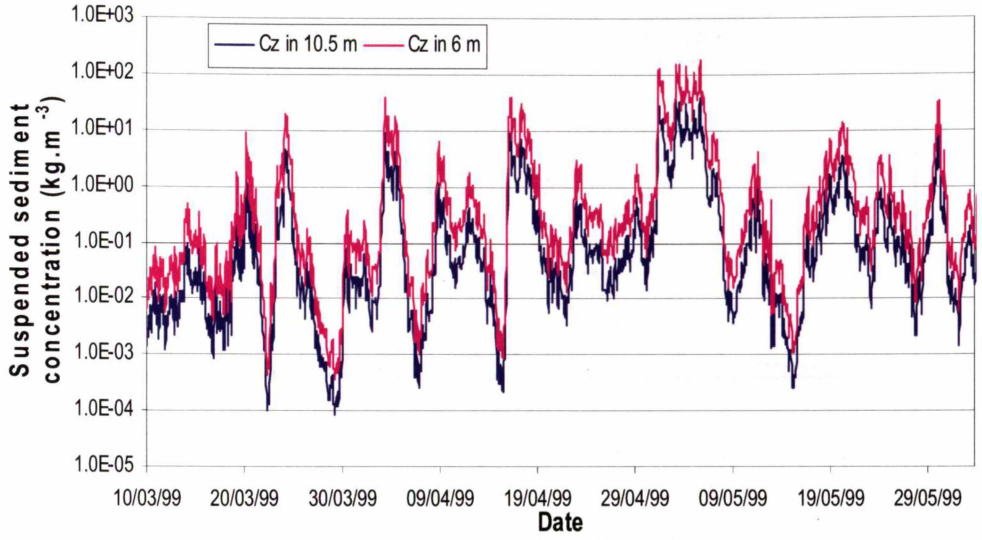

Figure 9.16 Suspended sediment concentrations at an elevation $z_b = z_0$+0.005 within the channel (h = 10.5) and at a site in 6 m water depth adjacent to the shipping channel. The variation is concentration between sites is attributed to the variation in near-bed orbital velocities; surficial sediment d_{50} and in-situ shear strength. Table 9.01 lists the surficial sediment characteristics used in the analysis.

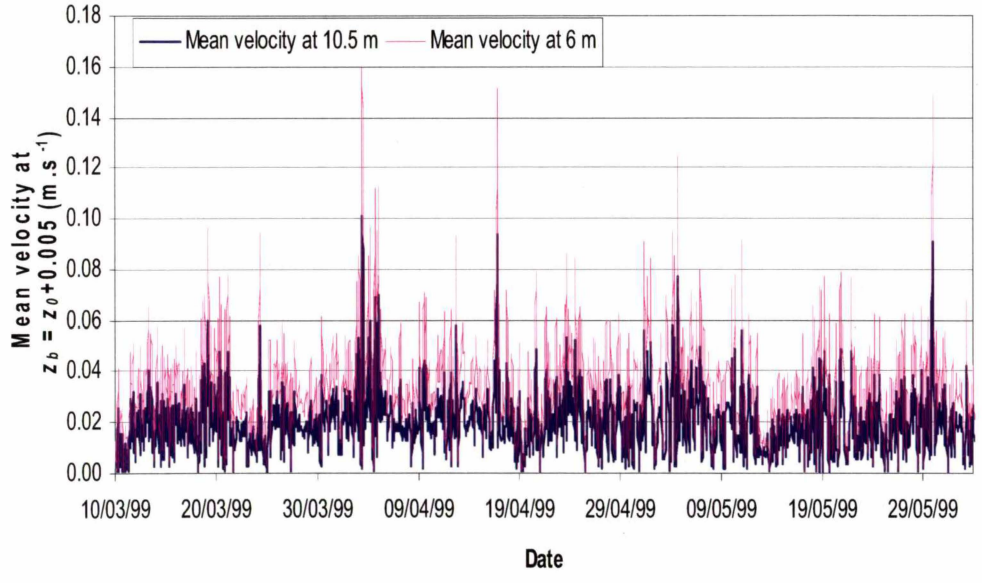

Figure 9.17 Mean current velocity at an elevation $z_b = z_0$+0.005 above the seabed between 10/03/99 and 02/06/99 at 10.5 m and 6 m water depths. Current velocities are orientated perpendicular to the strike of the port of Gisborne shipping channel. The variation in velocities between sites results from the contraction/expansion of flow in different water depths.

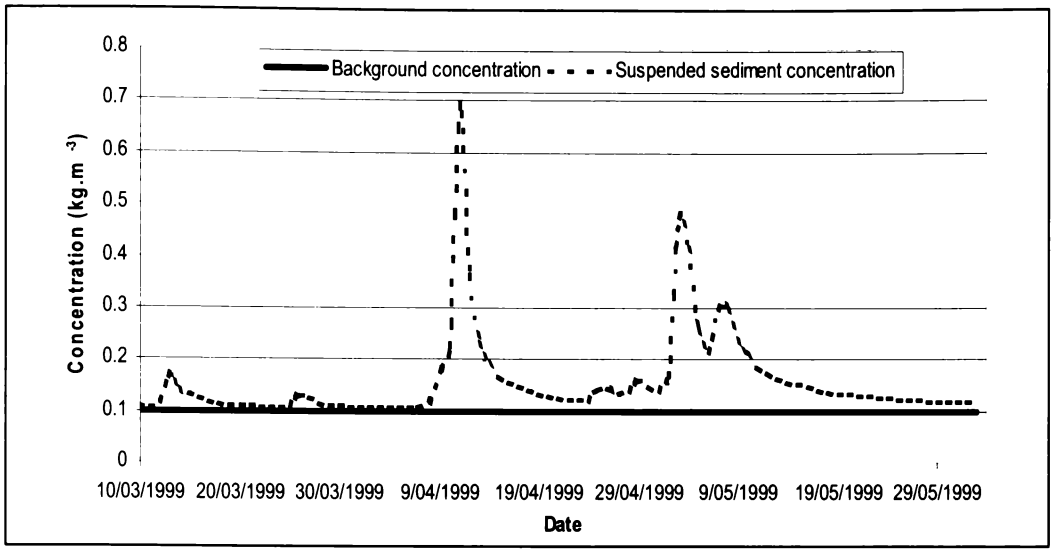

Figure 9.18 Predicted suspended sediment concentration of the surface water in the Turanganui River plume at CTD Site 7 (Figure 9.06) between 10/03/99 and 02/06/99. The predicted SSC is based on the relationship derived in Chapter 7 relating the volume of water discharged from the Turanganui River to the *SSC* of the surface water at the CTD site 7.

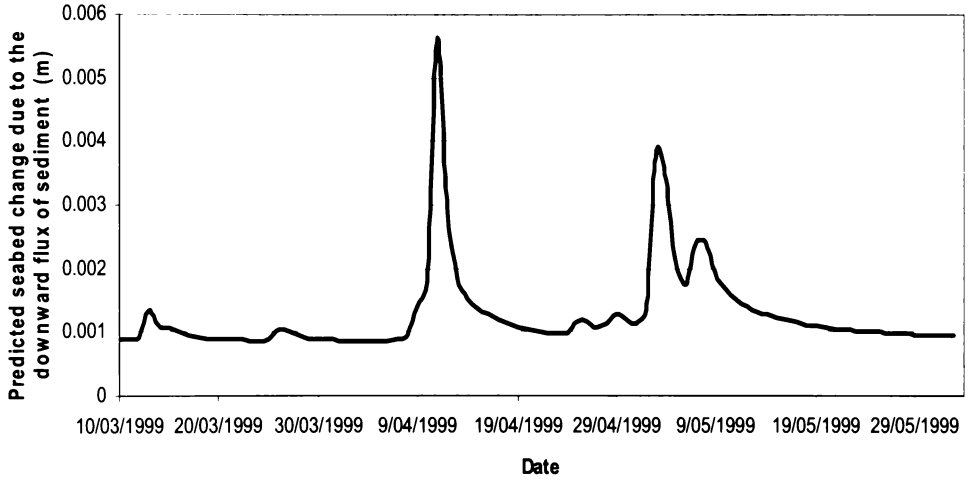

Figure 9.19 Time-series of predicted absolute seabed level change (Δh) between 10/03/99 and 02/06/99 at CTD site 7 (Figure 9.06). The predicted change in the level of the seabed (i.e. Δh) has been determined using a downward flux calculated using an equivalent fall velocity of 0.0002 $m.s^{-1}$ (i.e. medium silt) and assuming vertical uniformity in the *SSC* associated with the turbid river plume of the Turanganui River.

Chapter 10. Conclusions

"*The use of the sea and air is common to all; neither can a title to the ocean belong to any people or private persons, forasmuch as neither nature nor public use and custom permit any possession thereof.*" - Queen Elizabeth I

10.1 Introduction

Northern Poverty Bay has provided a useful environment in which to examine, within one relatively small locality, the hydrodynamic and sedimentological processes that affect much of the world's coastline, including, but not limited to, sediment entrainment due to wave-orbital velocities, horizontal sediment transport, river discharging, density driven circulation, and ocean-atmosphere interactions can be studied. Studying both the horizontal and vertical sediment flux within an environment such as northern Poverty Bay presented the challenge of tackling the complexities associated with a range of interactive hydrodynamical and sedimentological processes.

In terms of the horizontal sediment flux, the field site offered an ideal location in which to examine the complicated relationship between the cohesive bonding of a mixed sand/mud seabed and the retardation of sediment entrainment rates, an area in which only limited previous research has been undertaken (Toorman, 2001). The study has incorporated multi-disciplinary aspects of the sediment and hydrodynamical processes, including seabed and entrained grain size characteristics, sediment geomechanical properties, and near-bed wave orbital statistics. The variability of the relative percentage of sand and mud in the surficial sediment presented the opportunity to examine entrainment rates over a range of seabed conditions.

While entrainment and transport of the mixed sand/mud seabed represented one aspect of the total sediment flux within the environs (i.e. the horizontal sediment flux), the input of fine-grained fluvial sediment, and the associated downward sediment flux is identified as an important contribution to coastal morphological evolution (Wang et al., 2002). As such, the dynamics associated with the mixing of the turbid plume of the Turanganui River with the more saline oceanic water, including the dispersion of the sediment in suspension within the plume, has been examined, and empirical formulae developed that describe the distribution characteristics of the suspended sediment.

Studying the characteristics of the downward and horizontal sediment flux has led to an understanding of the sediment dynamics within northern Poverty Bay, and expanded the existing knowledge on the erosional behaviour of mixed sand/mud cohesively bound sediment. Further, the study is also relevant to the local port industry; as understanding the characteristics of the sediment flux in northern Poverty Bay will allow better management of aspects of the port operations and development as discussed later.

10.2 Advances in scientific knowledge

The following sections describe the knowledge gains arising from the study.

10.2.1 Entrained sediment profiles

In terms of sediment entrainment, this study has examined the characteristics of the near-bed *SSC* profile of the entire dispersed fall velocity (w_f) distribution under unbroken waves, particularly focusing on the variability in the diffusion of different w_f within the profile as described by the ratio of eddy diffusivity (ε_f) to sediment diffusivity (ε_s), i.e. β. A new formulae has been developed from the micro-scale pumped water/sediment measured near-bed *SSC* to describe β, given as,

$$ln(\beta) = -0.95 - \frac{0.4\psi}{ln(\psi)} \tag{5.24}$$

in which $\psi = w_f/U^*$, and U^* is the friction velocity. Although β is defined as the ratio of ε_s to ε_f, it is essentially used as a correction factor for predictive *SSC* profile equations.

Further, over the one-minute sampling period the maximum near-bed orbital velocity statistic (U_{max}) was found to best describe the *SSC* profile. Although, it is likely that over a longer sampling period a different, relatively more stable, statistic of the near-bed orbital velocity distribution will be more suitable in describing the *SSC* profile (i.e. U_3).

10.2.2 Entrained rate over mixed sand/mud seabeds

The retardation in the entrainment rate due to cohesive bonding of the seabed has been investigated by comparing the entrainment rate factor (ζ), defined as the ratio of predicted to observed near-bed reference concentration, to the various sediment textural characteristics and the seabed in-situ shear strength. The best correlation (Adjusted $R^2 = 0.99$) was found by relating ζ to the normalised in-situ shear strength of the sediment (χ) as measured using a hand-held shear vane. As such, a new relationship that defines the retardation of the entrainment rate over mixed sand/mud seabeds based on the geomechanical properties of the surficial sediment has been presented,

$$\ln(\zeta) = -0.51 - 1.30\chi^3 \tag{6.23}$$

The formula is based on a C_0 predicted using the relatively stable third-moment of the horizontal near-bed orbital velocity (U_3).

10.2.3 Reconstitution of a effective fall velocity distribution

A method has been presented for reconstructing the effective fall velocity (w_f) distribution from measured *SSC* profiles. The method involves relating the measured mixing lengths (l_s) from individual dispersed grain size bins within the *SSC* profile to the predicted sediment diffusivity (ε_s). While the reconstructed effective w_f distribution does not necessarily describe the flocculated w_f distribution, it does describe the behaviour of the sediment within the near-bed *SSC* profile.

10.2.4 Horizontal diffusion of fluvial sediment in a river plume

An equation has been tested that describes the diffusion of sediment within the turbid river plume with distance (x) from the mouth of the Turanganui River, and uses a decay rate factor (D_x) that is analogous to the mixing length (l_s) in the time-averaged gradient diffusion equation described by Nielsen (i.e. eqn. 6.12). The tested equation is given as,

$$C_x = C_{ob} e^{(-x/D_x)} \tag{8.13}$$

The decay rate factor has been correlated ($R^2 = 0.92$) with river discharge (φ_{river}), and hence the concentration (due to concentration increasing with increasing river discharging), and shown to be statistically significant. The decay rate factor has been found to exponentially decrease with increasing φ_{river}. The equation describing the relationship is given as,

$$D_x = 591 + 2850 \exp\left(-\varphi_{river} / 2.1\right) \tag{8.14}$$

The decreased D_x at higher discharge rates suggests that the effective fall velocity of the suspended sediment within the river plume increases with increasing *SSC*, presumably due to increased flocculated particle size, consistent with theory.

Additionally, equations 8.13 and 8.14 have been used to predict the annual fluvial input of sediment into northern Poverty Bay from the Turanganui River.

10.2.5 Development of a Two-cell numerical mode

The study has applied the formulae for predicting both horizontal and downward sediment fluxes within a 2-cell numerical model. The model considers the downward flux of fluvial sediment due to river discharging, seabed characteristics (including textural and geomechanical), sediment entrainment due to near-bed wave orbital velocities, and horizontal transport rates.

The 2-cell numerical model has been shown to accurately predict channel infilling rates, and represents an alternative to the implementation of a full 3-dimensional hydrodynamic model.

10.3 Implications and findings relevant to the port of Gisborne

10.3.1 Implication for maintenance dredging operations

Hydrographic surveys between the 10/03/99 and 02/06/99 suggest the dredged navigation channel is part of the Waikanae Beach littoral system, consistent with the findings of Healy et al., (1980). Therefore, disposal of dredged sediment from the shipping channel at an offshore spoil ground will result in a loss of sediment from the Waikanae beach littoral system. As such, the port needs to be aware of the potential impact of maintenance dredging on the beach morphology. While this has been addressed, in part, by the development of a nearshore disposal ground (Black et al., 1997; Healy et al., 2002) in addition to the existing offshore disposal ground, the port operating company should ensure that the sandy proportion of the dredged sediment (dredged from the shipping channel outside the breakwaters) is disposed of within the nearshore disposal ground, and thereby maintained in the beach littoral system.

The hydrographic surveys also indicated that between 10/03/99 and 02/06/99 net channel infilling occurred, suggesting that in that period maintenance dredging did not keep up with the channel infilling rate. While the hydrographic surveys showed water depth to be maintained along the channel leads, significant infilling occurred near the sides of the channel during the period. As such, the port operating company should ensure that maintenance dredging programme is structured to include the full channel width.

The development of the validated 2-cell numerical model provides a useful tool to the port operating company with which to predict channel infilling rates based on both the downward and horizontal sediment fluxes. The ability to predict channel infilling rates will allow the port to estimate maintenance dredging requirements for the existing port, allowing for better financial budgeting. However, as with any model that considers hydrodynamical processes the quality of the predictions will be dependant on the quality of the input data. While the discharge of the Turanganui River can be estimated from the gauging stations on the Waimata and Taraheru Rivers (maintained and operate by Gisborne District Council), there is not instrumentation in northern Poverty Bay dedicated to collecting wave and current data. As such, in order to fully utilize the developed 2-cell numerical model for predicting ongoing maintenance dredging requirements the port operating company needs to obtain data on local wave and current conditions. This can be achieved by deploying a self-contained wave/current meter within the environs, while real-time telemetry of the data back to a base station at the port will allow the port operating company to predict, in real-time, channel infilling characteristics. Additionally, the data would provide both the port pilot and the general public with information on the sea-state within the bay, potentially making boating and shipping activities in the bay safer.

Given that the cost of removing sediment from the shipping channel by maintenance dredging is between \$5 – \$7 per m^3 (pers comms Tahata, 2002), extrapolation of the infilling rate during the monitoring period to an annual rate suggests an estimated cost of maintaining the existing channel of between \$857,000 to \$1,200,000 per year. However the magnitude of the river discharging and significant wave heights

experienced during the monitoring period were smaller than average annual conditions. This suggests that the average cost to the port operating company of maintaining the existing shipping channel will be, on average, in excess of $1,200,000 per annum, and based on the predicted infilling rates of Black, et al. (1997), could be as high as $3,650,000 to $5,110,000 in extreme years.

10.3.2 Implications for future port designs

If the port at Gisborne is to utilise the expected increase in export tonnage over the next few decades (Figure 1.03), the existing port needs to expand, both in the usable storage area and the number of shipping berths capable of handling large (~200 m) ships. Expansion of the port provides the ideal opportunity to address issues such as seiching within the port, and the cost of continual maintenance dredging. While aspects of the seiching within the port are beyond the scope of this study, seiching in the existing port and various proposed port designs have been examined extensively by Black et al, (2002; 1997).

If the configuration of the port is to change such that the navigation channel and port entrance is relocated, then by considering the dynamics of both the downward and horizontal sediment fluxes in northern Poverty Bay the potential channel infilling rate of the proposed channel can be minimised, and therefore the continual cost of maintenance dredging. This can be achieved by,

- Locating the proposed channel further from the entrance of the Turanganui River (limiting downward flux),
- Locating the proposed channel in an area with relatively stronger in-situ shear strength (limiting horizontal flux), and
- Locating the channel and entrance to the port in deeper water (limiting horizontal flux by reducing the relative strength of the near-bed orbital velocity).

In terms of horizontal sediment fluxes, the exponential relationship given in eqn. 8.13 mathematically expresses that the potential downward flux of sediment into the channel will be reduced if the proposed channel is located further from the entrance to the Turanganui River.

The horizontal sediment flux into the proposed channel can be limited by understanding the relationship between the cohesive bonding of the mixed sand/mud seabed and the retardation in the entrainment rate, and locating the proposed channel accordingly. Further, relocating the shipping channel and the entrance to the port into deeper water will reduce the relative strength of the near-bed wave orbital velocities, the salient sediment entrainment parameter, and hence reduce the entrainment rate, and the horizontal sediment flux.

10.3.3 Implications for proposed port reclamation

From Chapter 4, using a mixture of sediment dredged from the shipping channel and cement to create mudcrete will provide a potential source of sediment for use in any reclamation. Further, using the Tertiary mudstone unit that underlies the

unconsolidated sand/mud sediment within the Swinging Basin and the shipping channel in the reclamation will help improve the developed soil structure and increase the structural strength of the final reclamation. The technique of using a mixture of dredged sediment and cement has been used effectively by the Ports of Auckland for construction of strong, stable reclamations (Vazey, 2002).

10.04 Future research

While the processes influencing the sediment flux within northern Poverty Bay have been examined within this study, there are aspects that are worthy of further research, particularly,

- Focused investigation into the flocculation process within the turbid river plume using in-situ measurements of the suspended sediment grain size in order to determine the effect of salinity, temperature and turbulence on the in-situ flocculated particle size.

- Application of the developed formulae into a full 3-dimensional numerical model using multi-year hindcast wave and river discharge data to provide information on the sediment fluxes within northern Poverty Bay, and hence illustrate the variation in the predicted channel infilling rates and likely impact on port finances and operations.

While the formulae developed during this study describe the physical sediment transport processes operation in northern Poverty Bay, a full 3-dimensional coupled hydrodynamic and sediment transport model that uses the developed formulae would provide a valuable tool for predicting variations in sediment fluxes within the region.

References

Aagaard, T., Black, K.P. and Greenwood, B., 2002. Cross-shore suspended sediment transport in the surf zone: a field-based parameterization. Marine Geology, 185: 283-302.

Aagaard, T. and Greenwood, B., 1999. Directionality of cross-shore sediment transport in the surf zone under high-energy conditions, Coastal Sediments '99, pp. 1003-1018.

Allaby, A. and Allaby, M. (Editors), 1999. A dictionary of Earth Sciences. Oxford University Press, Oxford, 512 pp.

Allbrook, R.F., 1980. The Drop-Cone Penetrometer Method for Determining Atterberg Limits. New Zealand Journal of Science, 23: 93-97.

Alvarez-Hernandez, E.M., 1990. The influence of cohesion on sediment movement in channels of circular cross-section. Ph.D. Thesis, University of Newcastle.

Amaryan, L.S., 1993. Soft Soil Properties and Testing Methods. A.A. Balkema Publishers, 180 pp.

Amos, C.L., Sutherland, T.F. and Zevenhuizen, J., 1995. The stability of fine-grained sediments in Manitouk Sound, Hudson Bay, Canada. Sedimentology.

Armanini, A. and Ruol, P., 1988. Non-uniform suspended sediment under waves, Coastal Engineering, pp. 1129-1139.

Augustinus, P., 2002. Biochemical factors influencing deposition and erosion of fine grained sediment. In: T.R. Healy, Y. Wang and J. Healy (Editors), Muddy Coasts of the World: Processes, Deposits and Function. Elsevier publishing, Amsterdam, pp. 542.

Baver, L.D., Gardner, W.H. and Gardner, W.R., 1972. Soil Physics. Wiley, New York, 498 pp.

Beamsley, B.J., 1999. Analysis of Sediment to be Maintenance Dredged, January-March 1999, University of Waikato, Coastal Marine Department, Hamilton.

Beamsley, B.J., Black, K.P. and Healy, T.R., 2001a. Micro-scale pumped measurements of suspended sediment over a mixed sand/mud bed: profiles, grain sized and sediment diffusivity. Journal of Coastal Research Special Issue, 34: 342-356.

Beamsley, B.J., Healy, T.R. and Black, K.P., 1998. Supplementary Report: - Proposed Inshore Sand Spoil Ground Sedimentological Investigation, Centre of Excellence in Coastal Oceanography and Marine Geology, incorporating the Coastal Marine Group, Department of Earth Sciences, The University of Waikato, and the National Institute of Water and Atmospheric Research, Hamilton.

Beamsley, B.J., Healy, T.R. and Black, K.P., 2001b. Textural parameters and in-situ shear strength of bed sediments within an oceanic embayment, The 15th Australasian Coastal and Ocean Engineering Conference & The 8th Australasian Port and Harbour Conference, Gold Coast, Australia, pp. 383-388.

Beamsley, B.J., Stephens, S.A. and R., H.T., 1997. Geotechnical Investigation of Port Environs and Dredge Spoil Dump Grounds Relating to the Port Gisborne Expansion., Centre of Excellence in Coastal Oceanography and Marine Geology, incorporating the Coastal Marine Group, Department of Earth Sciences, The University of Waikato and the National institute for Water and Atmospheric Research, Hamilton.

Beavis, F.C., 1985. Engineering Geology. Blackwell Scientific Publishing, 231 pp.

Bell, D.H. and Pettinga, J.R., 1984. Presentation of geological data. Proceedings from the Symposium Engineering for Dams and Canals, Alesandra, pp. 4.1-4.33.

Bell, R.G., 1985. Coastal current data from Aanderaa current meter deployments 1982-1985., National Institute of Water and Atmospheric Research, Hamilton, New Zealand.

Berlamont, J., Ockenden, M., Toorman, E.A. and Winterwerp, J.C., 1993. The characterisation of cohesive sediment properties. Coastal Engineering, 7: 105-128.

Black, K.P., 1990. Hydrodynamics and Salt Transport in an Esturaine Channel, Part 3 Numerical Model. ISSN-0729-4182, VIMS, Melbourne.

Black, K.P., 1994. Suspended sediment load during an asymmetric wave cycle over a plane bed. Coastal Engineering, 23: 95-114.

Black, K.P. et al., 2002. Port Gisborne Expansion: Outline Design Study, ARS Limited, Hamilton.

Black, K.P. et al., 1997. Numerical Modelling for the Port Gisborne Expansion, A report on behalf of Port Gisborne Ltd., Centre of Excellence in Coastal Oceanography and Marine Geology, incorporating the Coastal Marine Group, Department of Earth Sciences, The University of Waikato, and the National Institute of Water and Atmospheric Research,, Hamilton.

Black, K.P. and Rosenberg, M.A., 1991. Suspended sediment load at three time scales. Coastal sediments, pp. 313-327.

Black, K.P. and Rosenberg, M.A., 1992. Hydrodynamics and sediment dynamics in wave-driven environments. 15, Victorian Institute of Marine Science, Melbourne.

Black, K.P. and Rosenberg, M.A., 1994. Suspended sand measurements in a turbulent environment: field comparison of optical and pump sampling techniques. Coastal Engineering, 24: 137-150.

Black, K.P. and Vincent, C.E., 2001. Sediment suspension under shoaling waves: high-resolution field measurements and numerical models. Coastal Engineering, 42: 173-197.

Bosman, J.J., van der Velden, E.T.J.M. and Hulsbergen, C.H., 1987. Sediment concentration measurement by transverse suction. Coastal Engineering, 11: 353-373.

Boyce, F.M., Hamblin, P.F., Robertson, D.G. and Chiocchio, F., 1990. Evaluation of sediment traps in Lake St. Clair, Lake Ontario and Hamilton Harbour. Journal of Great Lakes Research, 16(3): 366-379.

British Standard, 1986. Code of Practice for Foundations, British Standards Institution, London.

Brook, N., 1985. The Equivalent Core Diameter Method of Size and Shape Correction in Point Load Testing. International Journal of Rock Mech. Min. Sci. Geomech. Abstracts(2): 61-70.

Brown, E.T. (Editor), 1985. International Society for Rock Mechanics. Published for the commission on testing methods, International society for Rock Mechanics. Pergamon Press, 211 pp.

Cameron, W.M. and Pritchard, D.W., 1963. Estuaries. In: M.N. Hill (Editor), The Sea. Wiley, N.Y., pp. 306-324.

Carrier, W.D. and Beckman, J.F., 1984. Correlations Between Index Tests and the Properties of Remoulded Clays. Geotechnique, 34(2): 211-228.

Carstens, M.R., 1952. Accelerated motion of a spherical particle. 33 (5), American Geophysical Union.

Chesher and Ockenden, M., 1997. Numerical modelling of mud sand mixtures. In: N. Burt, R. Parker and J. Watts (Editors), Cohesive Sediments. John Wiley publishers, Chichester, U.K., pp. 197-211.

Chiswell, S.M., 1999a. Temperature, salinity and seafloor topography controls on the re-circulation of the Wairarapa Counter Current near Mahia Peninsula. In: B.J. Beamsley (Editor), Hamilton.

Chiswell, S.M., 1999b. The Wairarapa Counter Current, New Zealand ..... Marine Sciences Conference, Programme and Abstracts. New Zealand Marine Society, Wellington.

Chiswell, S.M. and Roemmich, D., 1998. The East Cape Current and Two Eddies: A Mechanism for Larval Retention? New Zealand Journal of Marine and Fresh Water Research, 32: 385-397.

Claridge, G.G.C., 1960. Clay Minerals, Accelerated Erosion, and Sedimentation in the Waipaoa River Catchment. New Zealand Journal of Geology and Geophysics, 3: 184-191.

Coates, T., 2000. How GPS works. Trimble Navigation Limited, 74 pp.

Coleman, N.L., 1970. Flume studies of the sediment transfer coefficient. Water Resources Research, 6(3): 801-809.

Collins, M.B., 1989. The behaviour of cohesive and non-cohesive sediment, Proceedings of the international seminar on the Environmental Aspects of Dredging Activities, Nantes, France.

Cooley, W.W. and Lohnes, P.R., 1966. Multivariate Procedures for the Behavioural Sciences. John Wiley and Sons, Inc., 211 pp.

Council, G.D., 1994. Waipaoa River at Kanakanaia - Monthly Suspended Sediment Yields, Gisborne District Council, Gisborne.

Craig, R.F., 1994. Soil Mechanics. Chapman and Hall Publishers, London.

Deigaard, R., Fredsoe, J. and Hedegaard, I.B., 1986. Suspended sediment in the surf zone. Journal of Waterway, Port, Coastal and Ocean Engineering, 112(1): 115-127.

Dredge operators, A.I., 1998. Characteristics of the dredged sediment from the port of Gisborne shipping channel and Swinging Basin. In: B.J. Beamsley (Editor), Gisborne.

Du Toit, C.G. and Sleath, J.F.A.G., 1981. Velocity measurements close to rippled beds in oscillatory flow. Journal of Fluid Mechanics, 112: 71-96.

Dyer, K.R., 1986. Coastal and Estuarine Sediment Dynamics. John Wiley and Sons, Chichester.

Dyer, K.R. and Manning, A.J., 1999. Observation of the size, settling velocity and effective density of flocs, and their fractal dimensions. Journal of sea research, 41: 87-95.

Fennessy, M.J. and Dyer, K.R., 1996. Floc population characteristics measured with Inssev during the Elbe Estuary intercalibration experiment. Journal of sea research, 36(1): 55-62.

Fischer, H.B., List, E.J., Koh, R.C.Y. and Brooks, N.H., 1979. Mixing in Inland and Coastal Waters. Academic Press Inc., Jovanovich, 483 pp.

Flint, A.B., 1998. Sediment trapping in the nearshore coastal environment. Master of Science (Technology) Thesis, The University of Waikato, Hamilton, 197 pp.

Folk, R.L., 1968. Petrology of Sedimentary Rocks. The University of Texas, Austin, Texas, Austin, 197 pp.

Foster, G. and Carter, L., 1997. Mud Sedimentation on the Continental Shelf at an Accretionary Margin - Poverty Bay, New Zealand. New Zealand Journal of Geology and Geophysics, 40: 157-173.

Fredsoe, J., Anderson, O.H. and Silberg, S., 1986. Distribution of suspended sediment in large waves. Journal of Waterway, Port, Coastal and Ocean Engineering, 111(6): 1041-1059.
Fredsoe, J. and Deigaard, R., 1992. Mechanics of coastal sediment transport. World Scientific Publishing Co., Singapore, 369 pp.
Friedman, G.M. and Sanders, J.E., 1978. Principles of Sedimentology. John Wiley and Sons, Inc, 792 pp.
Fruchter, B., 1954. Introduction to Factor Analysis. D. Van Nostrand Company, Inc. Princeton, New Jersey, USA, 280 pp.
Gambrell, R.P., Patrick, W.H.J. and Engler, R.M., 1984. A biochemical evaluation of disposal options. In: R.C. Montgomery and J.W. Leach (Editors), Proceedings of the Conference on Dredging. American Society of Civil Engineers, New York., pp. 467-477.
Garvine, R.W., 1987. Estuary plumes and fronts in shelf waters. Journal of Physical Oceanography, 17(11): 1877-1896.
Gibb, J.G., 1978. Rates of Coastal Erosion and Accretion in New Zealand. Journal of Marine and Freshwater Research, 124: 429-456.
Gibbs, R.J., Matthews, M.D. and Link, D.A., 1971. The relationship between sphere size and settling velocity. Journal of Sedimentary Petrology, 41: 7-18.
Gisborne District Council, 1994. Waipaoa River at Kanakanaia - Monthly Suspended Sediment Yields, Gisborne District Council, Gisborne.
Glenn, S.M. and Grant, W.D., 1987. A suspended sediment stratification corrections for the combined wave and current flow. Journal of Geophysical Research, 92: 8244-8264.
Gorman, R.G. et al., 1997. Field data collection programme for the Port Gisborne expansion. The University of Waikato and National Institute of Water an Atmospheric Research, Hamilton.
Green, M.O., Bell, R.G., Dolphin, T.J. and Swales, A., 2000. Silt and sand transport in a deep tidal channel of a large estuary (Manukau Harbour, New Zealand). Marine Geology, 163: 217-240.
Green, M.O. and Black, K.P., 1999. Suspended -sediment reference concentration under waves: field observations and critical analysis of two predictive models. Coastal Engineering, 38: 115-141.
Green, M.O., Dolphin, T.J., Swales, A. and Vincent, C.E., 1999. Transport of mixed-size sediments in a tidal channel. Coastal sediments '99. American Society of Civil Engineers, pp. 644-658.
Griffiths, G.A. and Glasby, G.P., 1985. Input of River-Derived Sediment to the New Zealand Continental Shelf. Coastal and Shelf Science, 21: 73-787.
Grim, R.E., 1962. Applied Clay Mineralogy. McGraw-Hill, New York, 422 pp.
Hamilton, R.M. et al., 1966. Gisborne Earthquake, New Zealand, March 1966. 194, New Zealand Department of Scientific and Industrial Research, Wellington.
Harold, 2001. Personal communication with Harold, Adsteam International.
Harris, T.F.W., Hughes, T.S. and Valentine, E.M., 1983. Deepwater waves off Hicks Bay and the North-East Coast, North Island. 56, National Water and Soil Conservation Organisation, Wellington.
Hatcher, A., Hill, P., Grant, J. and Macpherson, P., 2000. Spectral optical backscatter of sand in suspension: effects of particle size, composition and colour. Marine Geology, 168: 115-128.
Hayter, J.E., 1984. Estuarial sediment bed model. In: A.J. Mehta (Editor), Proceedings of a workshop on cohesive sediment dynamics with special reference to physical processes in Estuaries. Springer-Verlag, Tempa, Florida, pp. 326-359.

Head, K.H., 1984. Manual of Soil Laboratory Testing. Soil Classification and Compaction Tests, 1. ELE International, Plymouth, London, 412 pp.
Head, K.H., 1988. Manual of Soil Laboratory Testing. Shear Strength and Compressibility tests, 2. ELE International, Plymouth, London, 747 pp.
Healy, T.R. et al., 1980. A Volumetric Analysis of Channel Dredging at the Entrance of the Port of Gisborne., The University of Waikato, Hamilton.
Healy, T.R. et al., 2002. Port redesign and planned beach renourishment in a high wave energy sandy-muddy coastal environment, Port Gisborne, New Zealand. Geomorphology, 48: 163-177.
Healy, T.R. et al., 1997. Side-scan sonar investigation of sedimentation relating to the Port Gisborne expansion. Centre of Excellence in Coastal Oceanography and Marine Geology, incorporating the Coastal Marine Group, Department of Earth Sciences, The University of Waikato and the National institute for Water and Atmospheric Research, Hamilton, New Zealand.
Healy, T.R. and Tahata, B., 1993. Environmental Impact Assessment in Support of a Resource Consent for a Maintenance Dredging Programme, The University of Waikato, Hamilton.
Heath, R.A., 1975. Oceanic Circulation off the East Coast of New Zealand. 55, New Zealand Oceanographic Institute, Wellington.
Hessell, J.D.W., 1980. The Climate and Weather of the Gisborne Region, New Zealand Meteorological Service Miscellaneous Publications, pp. 29.
Hunter, P., 1999. Gisborne 1999 - Survey report - Post dredging March 1999. Hunter Hydroigraphics Services, Timaru.
Hutt, J.A., 1997. A Volumetric Sediment Analysis at the Entrance to the Port of Gisborne, Coastal Marine Group, Department of Earth Sciences, University of Waikato and National Institute of Water and Atmospheric Research, Hamilton.
Inman, D.L. and Nordstrom, C., 1971. On the Tectonic and Morphologic Classification of Coasts. Journal of Geology. 79: 1-21.
Kamphuis, W. and Hall, K.R., 1983. Cohesive material erosion by unidirectional currents. American Society of Civil Engineers Journal of Hydraulic Engineering (January): 49-61.
Kanayama, S., Shimisu, T. and Ueki, K., 1992. Settling Properties of Cohesive sediments in a cooling water intake basin. Coastal Engineering: 3106-3120.
Kensington, G.L., 1990. Port Developments and Dredging Spoil Dispersion in Northern Poverty Bay. Unpublished MSc. Thesis, The University of Waikato, Hamilton, 235 pp.
King, L.J., 1969. Statistical Analysis in Geography. Prentice-Hall, Inc., New Jersey, USA., 288 pp.
Kingma, J.T., 1964. Geological Map of New Zealand. D.S.I.R., Wellington.
Kingma, J.T., 1965. Geological Map of New Zealand. D.S.I.R., Wellington.
Kingma, J.T., 1974. The Geological Structure of New Zealand. Wiley & Son., New York, 407 pp.
Kjerfve, B. et al., 2002. Morphodynamics of muddy environments along the Atlantic coasts of North and South America. In: T.R. Healy, Y. Wang and J. Healy (Editors), Muddy Coasts of the World: Processes, Deposits and Function. Elsevier publishing, Amsterdam, pp. 542.
Komar, P.D., 1998. Beach Processes and Sedimentation. Prentice Hall., New Jersey, USA, 544 pp.
Kos'yan, R.D., 1985. Vertical distributions of suspended sediment concentrations seaward of the breaking zone. Coastal Engineering, 9: 171-187.

Kranck, K., 1984. Settling behaviour or cohesive sediment. In: A.J. Mehta (Editor), Proceedings of a workshop on cohesive sediment dynamics with special reference to physical processes in estuaries. Springer-Verlag, Tempa, Florida, pp. 473pp.

Kraus, N.C., 1987. Application of portable traps fro obtaining point measurements of sediment transport rates in the surf zone. Journal of Coastal Research, 3(2): 139-152.

Krone, 1962. Flume studies of the transport of sediment in estuarial processes, Engineering lab, Sanit Engineering Research Laboratory, University of California, Berkeley.

Kuijper, C., Cornelisse, J.M. and Winterwerp, J.C., 1989. Research on Erosive Properties of Cohesive Sediment. Journal of Geophysical Research, 4(C10): 14341-14350.

Kuti, E.O. and Yen, C.L., 1976. Scouring of Cohesive Soils. Journal of Hydraulic Research, 143(3): 195-206.

Lambe, T.W. and Whitman, R.V., 1979. Soil Mechanics, SI version. John Wiley and Sons Publishing, 553 pp.

Leeder, M.R., 1982. Practical Sedimentology. Hutchinson Ross Publishing Company, Stroudsburg, Pennsylvania, USA, 229 pp.

Lewis, K.B., 1985. New Seismic Profiles, Cores, and Dated Rocks from the Hikurangi Margin, New Zealand. 22, New Zealand Oceanographic Institute, Wellington, New Zealand.

Malvern Instruments Ltd., 1996. Mastersizer Reference Manual, 423 pp.

Mantua, N.J., Hare, S.R., Zhang, Y., Wallace, J.M. and Francis, R.C., 1997. A Pacific interdecadal climate oscillation with impacts on salmon production. Bull. Amer. Meteor. Soc, 78: 1069-1079.

McComb, P., 2001. Coastal and sediment dynamics in a high-energy, rocky environment. D.Phill Thesis, The University of Waikato, Hamilton, 286 pp.

Mehta, A.J., 1984. Characterization of cohesive sediment properties and transport processes in estuaries. In: A.J. Mehta (Editor), Proceedings of a workshop on cohesive sediment dynamics with special reference to physical processes in estuaries. Springer-Verlag, Tempa, Florida, pp. 473pp.

Mehta, A.J., Hayter, J.E., Parker, W.R., Krone, R.B. and Teeter, A.M., 1989. Cohesive Sediment Transport I: Process Description. Journal of Hydraulic Engineering, 115(8): 1076-1093.

Miller, K.R., 1981. Surficial Sediments and Sediment Transport in Poverty Bay. Unpublished MSc. Thesis, The University of Waikato, Hamilton, 179 pp.

Milligan, T.G. and Hill, P.S., 1997. A laboratory assessment of the relative importance of turbulence, particle composition, and concentration in limiting maximum floc size and settling behaviour. Journal of sea research, 39: 227-241.

Mitchener, H. and Torfs, H., 1996. Erosion of Mud/Sand mixtures. Coastal Engineering, 29: 1-25.

Mocke, G.P. and Smith, G.G., 1992. Wave breaker turbulence as a mechanism for sediment suspension. International Conference on Coastal Engineering. American Society of Civil Engineering, pp. 1646-1660.

Moore, 1988. Structural divisions of eastern North Island. New Zealand Geological Survey Record, 30: 24.

Mullan, B., 1996. Effects of ENSO on New Zealand and the South Pacific. Prospects and Needs for Climate Forecasting, 34. The Royal Society of New Zealand, Wellington, New Zealand, 23-27 pp.

Murray, W.A., 1977. Erosion of Coarse Sand-Clayey Silt Mixtures. American Society of Civil Engineers Journal of Hydraulic Engineering (October): 1222-1227.

Navy, H.O.o.t.R.N.Z., 1989. Poverty Bay and Approaches to Gisborne. Hydrographic Office of the Royal New Zealand Navy, Auckland.

Nelson, C.S. and Healy, T.R., 1982. Side-scan Sonar survey of the sea floor of northern Poverty Bay in the vicinity of the Port of Gisborne. 9, Department of Earth Sciences, The University of Waikato, Hamilton, New Zealand.

Nicholls, N., 1992. Historical El Niño/Southern Oscillation variability in the Australasian region. El Niño: Historical and paleoclimatic aspects of the Southern Oscillation. Cambridge University Press. Cambridge, United Kingdom., 151-174. pp.

Nielsen, P., 1983. Entrainment and distribution of different sand sizes under water waves. Journal of Sedimentary Petrology, 53(2): 423-428.

Nielsen, P., 1984. Suspended sediment concentrations under waves. Coastal Engineering, 10: 23-31.

Nielsen, P., 1986. Field measurements of time-averaged suspended sediment concentrations under waves. Coastal Engineering, 8: 51-72.

Nielsen, P., 1992. Coastal bottom boundary layers and sediment transport. Advanced Series on Ocean Engineering, 4. World Scientific, Singapore, 324 pp.

Parrels, P.A.J. and Karelse, M., 1982. A Two-dimensional Laterally Averaged Model for Salt Intrusion in Estuaries, Transport Models for Inland and Coastal Waters. Academic Press, Delft Hydraulics Laboratory, pp. 483-535.

Pickrill, R.A. and Mitchell, J.S., 1979. Ocean Wave Characteristics around New Zealand. New Zealand Journal of Marine and Fresh Water Research, 13(4): 501-520.

Pillans, B., 1986. A late Quaternary uplift map for North Island, New Zealand. 24, Royal Society of New Zealand, Wellington.

Power, S. et al., 1998. Australian temperature, Australian rainfall and the Southern Oscillation, 1910-1992: coherent variability and recent changes, *Aust. Met. Magazine.*, pp. 85-101.

Prandle, D. and Mathews, J., 1990. The dynamics of nearshore surface currents generated by tides, wind and horizontal density gradients. Continental Shelf Research, 10(7): 665-681.

Pritchard, D.W., 1955. Estuaries Circulation Patterns. American Society of Civil Engineers, Proceedings, American Society of Civil Engineers, pp. 1-11.

Pullar, W.A., 1962. Soil and Agriculture of Gisborne Plains. 20, New Zealand Soil Bureau. Wellington.

Pullar, W.A. and Penhale, H.R., 1970. Periods of Recent Infilling of the Gisborne Plains Basin: Associated Marker Beds and Changes in Shoreline. New Zealand Journal of Science, 13: 410-434.

Quayle, A.M., 1984. The Climate and Weather of the Bay of Plenty Region, New Zealand Meteorological Service, Ministry of Transport., Wellington.

Reyners, M., 1989. New Zealand Seismicity 1964-87: an Interpretation. New Zealand Journal of Geology and Geophysics, 32: 307-315.

Riddolls, P.M., 1987. New Zealand Geology. Science Information Publishing Centre, Department of Scientific and Industrial Research, Wellington, New Zealand.

Ridgway, N.M., 1960. Surface Water Movement in Hawke Bay, New Zealand. New Zealand Journal of Geology and Geophysics: 253-261.

Roberts, B.M., 1993. Geomechanical Investigation of Dredge Material Relating to confined Land Disposal, Ports of Onehunga and Auckland. Unpublished MSc. Thesis, University of Waikato, Hamilton, 206 pp.

Ryan, S.G., 1989. Investigation of the Sedimentological Impact of Dredge Spoil in the Purakau Channel, Manukau Harbour. Unpublished MSc. Thesis, University of Waikato, Hamilton, 183 pp.

Salinger, M.J. and Mullan, A.B., 1998. New Zealand climate: temperature and precipitation variations 1930-1994. International Journal of Climatology, 19: 1049-1071.

Sander, R.M., 1993. Chemical Investigation into the Effects of Dredge Spoil dumping in Poverty Bay. Unpublished MSc. Thesis, The University of Waikato, Hamilton, 191 pp.

Selby, M.J., 1993. Hillslope Materials and Processes. Oxford University Press, New York, 264 pp.

Singamsetti, S.R., 1966. Diffusion of sediment in a submerged jet. Journal of Hydraulics Division, American Society of Civil Engineers, 92(HY 2): 153-168.

Smith, R.K., 1988. Poverty Bay, New Zealand: A case of Coastal Accretion 1886-1975. New Zealand Journal of Marine and Fresh Water Research, 22: 135-141.

Sorensen, A.H., 1984. Soil Analysis and Dredging. In: R.L. Montgomery and J.W. Leach (Editors), Dredging '84. American Society of Civil Engineers, New York, pp. 334-346.

Standards Association of New Zealand, 1986. Standards Association of New Zealand. NZS 4402, Standards Association of New Zealand, Wellington.

StatSoft, I., 1995. STATISTICA for Windows [Computer program manual]. StatSoft, Inc., Tulsa, OK., USA.

Stephens, S.A., 1999. Personal communication with Scott Stephens, Niwa Hamilton.

Stephens, S.A., 2001. Wind, Shelf-current and Density-Driven Circulation in Poverty Bay, New Zealand. Doctor of Philosophy Thesis, University of Waikato, Hamilton, 330 pp.

Stephens, S.A., Bell, R.G. and Black, K.P., 2000. Complex Circulation in a Coastal Embayment: Shelf-Currents, Wind and Density-Driven Circulation in Poverty Bay, New Zealand. In: T.R. Healy (Editor), International Coastal Symposium (ICS 2000). Waikato Print, The University of Waikato, Rotorua, pp. 45-59.

Stephens, S.A., Black, K.P., Healy, T.R. and Tahata, B., 1999. Circulation in Poverty Bay, New Zealand: A Verification of Numerical Modelling Predictions. Coasts and Ports 1999, Perth, pp. 639- 643.

Sternberg, R.W., 1968. Friction factors in tidal channels with differing bed roughness. Marine Geology, 6: 243-260.

Suggate, R.P., Stevens, G.R. and Te Punga, M.T. (Editors), 1978a. The Geology of New Zealand, 1. New Zealand Government Printer, Wellington, 820 pp.

Suggate, R.P., Stevens, G.R. and Te Punga, M.T. (Editors), 1978b. The Geology of New Zealand, 2. New Zealand Government Printer, Wellington, New Zealand, 820 pp.

Swart, D.H., 1974. Offshore sediment transport and equilibrium beach profiles. 131, Delft Hydraulics laboratory.

Tahata, B., 2002. Personal communication of the cost of removing sediment from the port of Gisborne shipping channel by maintenance dredging. In: B. Beamsley (Editor).

Tompson, L.M. and Troeh, F.R., 1973. Soil and Soil Fertility. McGraw-Hill Publishers.

Tonkin & Taylor Ltd., 1994. Westham Dredging Company Gisborne Harbour Investigation, Tonkin & Taylor Ltd, Auckland.

Toorman, E.A., 2001. Cohesive sediment transport modelling: European perspective. In: W.H. McAnally and A.J. Mehta (Editors), Coastal and Estuarine Fine Sediment Properties. Elsevier publishing, Amsterdam, pp. 506.
Tucker, M. (Editor), 1988. Techniques in Sedimentology. Blackwell Scientific Publications, Blackwell, UK, 393 pp.
United States Army Corps of Engineers, 1991. Tidal Hydraulics. EM1110-2 1607, 1. United States Army Corps of Engineers, 154 pp.
United States Army Corps of Engineers, 2001. Hydrodynamic Analysis and Design Conditions, Coastal Engineering Manual. Coastal Engineering Manual. United States Army Corps of Engineers, Washington, pp. 612.
United States Army Corps of Engineers, 2002a. Hydrodynamic analysis and design conditions. In: U.S.A.C.o. Engineers (Editor), Coastal engineering manual. United States Army Corps of Engineers, pp. 67.
United States Army Corps of Engineers, 2002b. Survey accuracy measurements for dredging and navigation projects. In: U.S.A.C.o. Engineers (Editor), Engineering and Design - Hydrographic surveying. United States Army Corps of Engineers, pp. 22.
Van Rijn, L.C., 1984a. Sediment pickup functions. American Society of Civil Engineers Journal of Hydraulic Engineering, 110(12): 1733-1754.
Van Rijn, L.C., 1984b. Sediment transport, Part II: Suspended load transport. Journal of Hydraulic Engineering, 110(11): 1613-1641.
Van Rijn, L.C., 1993. Principles of sediment transport in rivers, estuaries and coastal seas. Aqua Publications, 629 pp.
Vazey, G., 2002. Ports of Auckland prepare for bigger ships. Port Technology International, 13: 127-131.
Vickers, B., 1978. Laboratory Work in Soil Mechanics. Gramada Publishing, London, 148 pp.
Walpole, B., 1997. Personal communication with Bruce Walpole, Gisborne District Council.
Wang, Y. et al., 2002. Definition, properties, and classification of muddy coasts. In: T.R. Healy, Y. Wang and J. Healy (Editors), Muddy coasts of the world: processes, deposits and Function. Elsevier, Amsterdam, pp. 9-18.
Wards, I. (Editor), 1976. New Zealand Atlas. A. R. Shearer Government Printer, Wellington, New Zealand, 292 pp.
Warren, S.K., 1992. The geomechanics and dispersion of dredge spoil dumped in open water on the inner shelf, Tauranga, New Zealand. Masters of Science Thesis, The University of Waikato, Hamilton, 281 pp.
White, L.D., 1990. The use of sediment traps in high-energy environments. Marine Geophysical Research, 12: 145-152.
Whitehouse, U.G., Jeffrey, L.M. and Debbrecht, J.D., 1960. Differential settling tendencies of clay minerals in saline waters, Proceedings of the 7th Conference on Clays, Clay Mineralogy., pp. 1-79.
Whyte, P., 1984. Gisborne's Battle for a Harbour. Gisborne Harbour Board, Kaiti Beach Road, Gisborne, Gisborne, 152 pp.
Williams, H.C., 1959. The movements and dispersion of seawater in Poverty Bay, Gisborne City Council, unpublished report, Gisborne.
Williams, H.C., 1966. The Gisborne Submarine Sewer Outfall. New Zealand Engineering, 21: 110-120.

Appendix I

Moment statistics formulae

$$mean = \overline{X}_{\phi} = \frac{\sum fm}{n}$$

$$sorting = \sigma_{\phi} = \sqrt{\frac{\sum f\left(m - \overline{x}_{\phi}\right)^2}{100}}$$

$$skewness = Sk_{\phi} = \frac{\sum f\left(m - \overline{x}_{\phi}\right)^3}{100\sigma_{\phi}^3}$$

$$kurtosis = K_{\phi} = \frac{\sum f(m - \overline{x}_{\phi})^4}{100\sigma_{\phi}^4}$$

Graphical statistics formulae

$$mean = \frac{\left(p16 + p50 + p84\right)}{3}$$

$$median = p50$$

$$sorting = \frac{\left(p84 - p16\right)}{4} + \frac{\left(p95 - p1\right)}{6.6}$$

$$skewness = \frac{\left(p84 + p16 - 2 \times p50\right)}{2\left(p84 - p16\right)} + \frac{\left(p95 + p5 - 2 \times p50\right)}{2\left(p95 - p5\right)}$$

$$kurtosis = \frac{\left(p95 - p5\right)}{\left(2.44\left(p75 - p25\right)\right)}$$

where *p(i)* is the *i*th percentile.

Descriptive terms used for statistical measures (Folk, 1968; Pettijohn *et al*, 1975; Leeder, (1982) and McManus, 1988)

Sedimentological size classification (phi)
Udden-Wentworth grain size scale

Boulder	<-8.00
Cobble	-8.00 to -5.00
Pebble	-5.00 to -2.00
Granule	-2.00 to -1.00
Very coarse sand	-1.00 to 0.00
Coarse sand	0.00 to 1.00
Medium sand	1.00 to 2.00
Fine sand	2.00 to 3.00
Very fine sand	3.00 to 4.00
Coarse silt	4.00 to 5.00
Medium silt	5.00 to 6.00
Fine silt	6.00 to 7.00
Very fine silt	7.00 to 8.00
Clay	> 8.00

Sorting classification (phi)

Very well sorted	<0.35
Well sorted	0.35 to 0.50
Moderately well sorted	0.50 to 0.70
Moderately sorted	0.70 to 1.00
Poorly sorted	1.00 to 2.00
Very poorly sorted	2.00 to 4.00
Extremely poorly sorted	>4.00

Skewness classification (phi)

Strongly fine-skewed	>0.30
Fine-skewed	0.10 to 0.30
Near-symmetrical	0.10 to -0.10
Coarse-skewed	-0.10 to -0.3
Strongly coarse-skewed	<-0.30

Kurtosis classification (phi)

Very platykurtic	<0.67
Platykurtic	0.67 to 0.90
Mesokurtic	0.90 to 1.11
Leptokurtic	1.11 to 1.50
Very leptokurtic	1.50 to 3.00
Extremely leptokurtic	>3.00

Plasticity or A-line chart classifications terms

Sample plots above the A-line	
Low plasticity clays	CL
Medium plasticity clays	CI
High plasticity clays	CH
V-High plasticity clays	CV
Extremely high plasticity clays	CE
Sample plots below the A-line	
Low plasticity silts	ML
Medium plasticity silts	MI
High plasticity silts	MH
V-High plasticity silts	MV
Extremely high plasticity silts	ME

(Following the British practice as set out by Head, 1984)

Uniaxial compressive strength classification scheme (Brown, 1985)

Rock Description	Field identification	Approx. range of uniaxial compressive strength (MN/m^2)
Ext. weak	Indented by thumb nail	0.25-1.0
V. weak	Crumbles under firm blows with point of geological hammer, can be pealed by a pocket knife	1.0-5.0
Weak	Can be pealed by a pocket knife with difficulty, shallow indentations made by firm blow with point of geological hammer	5.0-25
Med. strong	Cannot be scraped of pealed with pocket-knife, specimen can be fractured with single firm blow of geological hammer	25-50
Strong	Specimen requires more than one blow from geological hammer to fracture it.	50-100
V. strong	Specimen requires many blows of geological hammer to fracture it	100-250
Ext. strong	Specimen can only be chipped with geological hammer	>250

(Brown, 1985)

Slake-durability classification scheme of Gamble (1971) as cited in Brown, (1985)

I_{d2} (%)	Classification
0-30	Very low
30-60	Low
60-85	Medium
85-95	Medium high
95-98	High
98-100	Very High

Appendix II

Surficial sediment textural characteristics with corresponding descriptive terms for the bed sediment sample sites within the field area (for a explanation of the descriptive terms refer to Appendix I). Positions are given in Northing and Easting Poverty Bay Circuit coordinates.

Sample site			Textural descriptions					
	Poverty Bay circuit (NZGD49)		Numerical value	Description	Numerical value	Description	Numerical value	Description
	Northing (m)	Easting (m)	Mean (Phi)		Sorting	Sorting	Skewness	Skewness
Site 1	692823.43	310209.89	*	*	*	*	*	*
Site 2	692984.11	310427.61	4.67	c. silt	1.85	ps	0.74	sfs
Site 3	693194.61	310745.48	3.42	vf. sand	1.21	ps	0.53	sfs
Site 4	693432.81	311086.63	5.08	m. silt	2.39	vps	0.52	sfs
Site 5	693591.58	311307.26	♦	♦	♦	♦	♦	♦
Site 6	693781.78	311585.99	♦	♦	♦	♦	♦	♦
Site 7	692120.54	310104.59	*	*	*	*	*	*
Site 8	693147.05	310361.09	6.58	f. silt	2.52	vps	-0.12	cs
Site 9	693350.10	310684.78	4.75	c. silt	1.88	ps	0.60	sfs
Site 10	693556.92	311005.53	4.33	c. silt	1.60	ps	0.69	sfs
Site 11	693708.22	311253.74	4.33	c. silt	1.60	ps	0.69	sfs
Site 12	693898.43	311528.12	♦	♦	♦	♦	♦	♦
Site 13	693472.39	310554.42	5.08	m. silt	2.29	vps	0.67	sfs
Site 14	693738.81	310554.78	4.17	c. silt	1.70	ps	0.71	sfs
Site 15	693946.07	310555.05	4.50	c. silt	2.05	vps	0.57	sfs
Site 16	694179.19	310555.36	3.50	vf. sand	1.69	ps	0.66	sfs
Site 17	693885.99	311142.34	3.67	vf. sand	1.32	ps	0.55	sfs
Site 18	694143.20	311142.71	3.25	vf. sand	1.72	ps	0.66	sfs
Site 19	692957.04	309893.96	5.25	m. silt	2.44	vps	0.52	sfs
Site 20	693312.27	309894.40	4.67	c. silt	2.10	vps	0.58	sfs
Site 21	693560.16	309894.71	3.75	vf. Silt	1.55	ps	0.51	sfs
Site 22	693704.47	309894.89	3.42	vf. silt	1.21	ps	0.53	sfs
Site 23	693834.02	309895.05	3.08	vf. silt	1.18	ps	0.47	sfs
Site 24	694004.19	309895.26	2.58	f. sand	1.42	ps	0.42	sfs
Site 25	692428.56	309308.91	5.75	m. silt	2.73	vps	0.40	sfs
Site 26	692728.29	309309.26	4.42	c. silt	2.24	vps	0.66	sfs
Site 27	692989.16	309309.56	4.17	c. silt	1.84	ps	0.47	sfs
Site 28	693314.87	309309.94	4.08	c. silt	1.84	ps	0.58	sfs
Site 29	693510.91	309310.17	3.92	vf. sand	1.90	ps	0.64	sfs
Site 30	693771.78	309310.48	3.25	vf. sand	1.89	ps	0.58	sfs
Site 31	691922.32	308758.76	4.50	c. silt	2.20	vps	0.60	sfs
Site 32	692680.85	308759.59	4.08	c. silt	1.84	ps	0.58	sfs
Site 33	692938.06	308759.88	3.42	vf. sand	1.52	ps	0.48	sfs
Site 34	693180.39	308760.14	3.25	vf. sand	1.46	ps	0.60	sfs
Site 35	693385.76	308760.37	2.92	f. sand	1.32	ps	0.51	sfs
Site 36	693552.27	308760.56	2.75	f. sand	1.57	ps	0.58	sfs
Site 37	692071.69	311948.89	5.75	m. silt	2.69	vps	0.42	sfs
Site 38	692280.51	312091.28	4.58	c. silt	2.14	vps	0.65	sfs
Site 39	692395.19	312165.40	4.33	c. silt	2.09	vps	0.73	sfs
Site 40	692487.57	312223.58	R	R	R	R	R	R
Site 41	692474.38	312349.71	R	R	R	R	R	R
Site 42	692072.38	311481.98	6.08	f. silt	2.69	vps	0.13	fs
Site 43	692349.63	311666.55	5.00	m. silt	2.35	vps	0.63	sfs
Site 44	692549.27	311794.49	5.00	m. silt	2.39	vps	0.60	sfs

Sample site			Textural descriptions					
	Poverty Bay circuit		Numerical value	Description	Numerical value	Description	Numerical value	Description
	Northing (m)	Easting (m)	Mean (Phi)		Sorting	Sorting	Skewness	Skewness
Site 45	692756.33	311925.30	R	R	R	R	R	R
Site 46	692942.96	312057.48	R	R	R	R	R	R
Site 47	693081.59	312140.35	R	R	R	R	R	R
Site 48	692073.07	310989.04	R	R	R	R	R	R
Site 49	692396.62	311186.64	R	R	R	R	R	R
Site 50	692687.57	310786.82	4.42	c. silt	2.24	vps	0.66	sfs
Site 51	692880.85	311499.15	4.42	c. silt	2.09	vps	0.64	sfs
Site 52	693119.31	311635.75	3.92	vf. sand	3.05	vps	0.65	sfs
Site 53	691496.57	311785.62	R	R	R	R	R	R
Site 54	692100.33	309930.56	4.83	c. silt	2.49	vps	0.62	sfs
Site 55	692360.85	310216.52	4.67	c. silt	2.04	vps	0.73	sfs
Site 56	692599.07	310472.09	R	R	R	R	R	R
Site 57	692854.07	310795.75	4.33	c. silt	1.60	ps	0.69	sfs
Site 58	693086.89	311019.42	5.58	m. silt	2.24	vps	0.48	sfs
Site 59	693251.34	311222.64	4.67	c. silt	1.98	ps	0.52	sfs
Site 60	693447.08	311443.41	4.08	c. silt	1.84	ps	0.58	sfs
Site 61	693594.89	311627.75	R	R	R	R	R	R
Beach 1	694394.00	309404.00	2.83	f. sand	0.65	mws	0.16	fs
Beach 2	694508.00	309881.00	2.67	f. sand	0.62	mws	-0.1	ns
Beach 3	694698.00	310377.00	2.33	f. sand	0.85	ms	0.21	fs
Beach 4	694661.00	310910.00	2.25	f. sand	0.72	ms	0.06	fs
Beach 5	694604.00	311559.00	2.33	f. sand	0.65	mws	0.16	fs
D1•	694320.00	311958.00	7.58	vf. Silt	2.49	vps	-0.23	cs
D2•	694190.00	311800.00	7.58	vf. silt	2.45	vps	-0.22	cs
D3•	693740.00	311360.00	4.75	c. silt	2.04	vps	0.63	sfs
D4•	693590.00	311155.00	4.75	c. silt	2.04	vps	0.63	sfs
(EN)∇	693352.57	310835.87	3.75	vf. sand	0.91	mws	0.14	fs
(EM)∇	693373.10	310706.82	3.58	vf. sand	1.12	ps	0.35	sfs
(ES)∇	693678.39	310704.33	3.67	vf. sand	0.91	ms	0.38	sfs
(SN)∇	693897.50	311466.05	2.42	f. sand	0.89	ms	0.01	ns
(SM)∇	694054.84	311421.32	3.83	vf. sand	1.47	ps	0.26	fs
(SS)∇	694115.96	311374.99	3.25	vf. sand	0.79	ms	0.14	fs
(SB)∇	694222.60	311836.37	6.92	f. silt	2.24	vps	-0.01	ns
(OS1)∇	691901.92	310893.35	6.92	f. silt	2.96	vps	0.02	ns

Abbreviations and symbols:

R Rocks observed at site,

* Located in the sewage plume, not dived,

♦ Sample lost or misplaced,

∇ Surficial sediment sample collected as part of the 1996-97 Port Gisborne AEE (after Beamsley et al. 1997), and

• Surficial sediment sample collected as part of the 1999 Westham Dredging Company commissioned sediment analysis (Beamsley, 1999).

Surficial sediment sample site bed textural characteristics (mean grain size, Sand, Silt and Clay % etc.), physical/environmental setting of the site (distance from major sediment source) and the shear strength of the sediment used for multivariate Factor Analysis.

Site Number	Shear Strength	Min distance to sediment supply (river or spoil ground)	Water depth (m)	In channel 1-yes 0-no	Mean (μm)	Bimodal 1-yes 0-no	Clay%	Silt%	Sand%	Organic content	Clay/Sand	Mud/sand
Site 2	81.3	1370	15	0	72.4	0	7.8	29.5	62.7	0.44	0.124	0.594
Site 3	76.8	1450	10	0	105.5	0	4	12.2	83.8	0.57	0.048	0.194
Site 4	72.9	1170	10	0	70.4	0	11.7	39.5	48.8	1.68	0.24	1.049
Site 9	61.7	1480	10.7	1	72.2	0	7.2	34.1	58.7	1.21	0.122	0.702
Site 10	51.4	1110	10	1	73.6	0	6.4	29.9	63.7	0.93	0.1	0.57
Site 11	63.7	850	8.4	1	72.9	0	6.9	31.1	62.1	0.65	0.111	0.611
Site 13	47.4	1480	10.2	0	69.5	0	10.2	36.4	53.4	1.87	0.191	0.874
Site 14	45.5	1330	8.9	0	86.9	0	6.6	23.7	69.7	1.3	0.094	0.434
Site 15	35	1220	7.2	0	88.6	0	8.5	26.6	64.8	0.25	0.131	0.542
Site 16	29.8	1150	5.6	0	133.9	0	5.7	12.5	81.8	1.15	0.07	0.223
Site 17	42.5	770	7	0	89.1	0	5.6	18.5	75.9	1.15	0.074	0.317
Site 18	29.4	610	5.4	0	152	0	5.9	10.9	82.2	1.36	0.071	0.204
Site 19	46.7	1660	14.9	0	62	0	14.6	42.8	42.7	1.36	0.341	1.344
Site 20	68.5	1930	14	0	73.6	0	9.3	32.6	58.1	1.25	0.161	0.722
Site 21	75.2	1990	11.7	0	99.1	0	6	18	76	1.25	0.078	0.315
Site 22	76.5	1930	10.4	0	110.7	0	4.2	11.4	83.7	0.99	0.05	0.186
Site 23	70	1880	8.2	0	135.6	0	4.4	8.2	87.4	1.26	0.05	0.144
Site 24	54.3	1830	5.9	0	200	0	4.1	8	87.9	1.33	0.047	0.137
Site 25	61.7	2870	16.4	0	57.5	1	20.9	43.1	36.1	1.93	0.578	1.771
Site 26	76.2	1980	15.3	0	95.5	0	9.7	26.7	63.7	1.5	0.152	0.57
Site 27	72.2	2130	13.7	0	93.5	0	7.5	27.3	65.2	1.61	0.115	0.534
Site 28	68.3	2330	11.8	0	103.4	0	7.1	21.7	71.2	1.49	0.099	0.405
Site 29	63.8	2460	10.5	0	117.5	0	6.3	14.4	79.3	0.24	0.08	0.261

Site Number	Shear Strength	Min distance to sediment. supply (river or spoil ground)	Water depth (m)	In channel 1-yes 0-no	Mean (µm)	Bimodal 1-yes 0-no	Clay%	Silt%	Sand%	Organic content	Clay/Sand	Mud/sand
Site 30	44	2460	7	0	175.3	0	6.2	11.6	82.3	1.56	0.075	0.216
Site 31	49.9	2310	16.3	0	83.5	0	10.8	31.1	58.1	1.15	0.186	0.72
Site 32	56	2470	14.2	0	103.1	0	7.5	22.1	70.4	1.26	0.106	0.42
Site 33	59.8	2580	12.1	0	115.2	0	5.3	14.6	80.1	1.34	0.066	0.248
Site 34	52.2	2680	10.8	0	123.5	0	5.3	11.8	83	1.51	0.064	0.206
Site 35	39.5	2810	9.1	0	162.7	0	4.5	8.2	87.3	1.08	0.051	0.145
Site 36	44	2900	6.5	0	183.9	0	5.2	9.5	85.3	1.48	0.061	0.172
Site 37	63.4	620	14.1	0	52.3	1	20	44.6	35.4	1.94	0.566	1.826
Site 38	73.2	1140	14	0	79	0	9.9	28.9	61.2	0.99	0.161	0.633
Site 39	44.1	1260	12.9	0	105.7	0	7.5	18.1	74.5	0.98	0.1	0.343
Site 42	30.8	500	17.6	0	50.2	1	21.7	45.4	32.9	2.7	0.658	2.039
Site 43	85	830	16	0	71.2	1	9.9	37.5	52.6	1.63	0.189	0.902
Site 44	81.8	1060	14.5	0	79.1	0	11.6	33.7	54.7	1.59	0.213	0.829
Site 50	60.5	950	15.8	0	92.6	0	9.2	26.7	64.1	1.17	0.144	0.559
Site 51	64.7	1180	11.1	0	100.5	0	8	22	70	1.15	0.114	0.429
Site 54	85.4	1180	17.4	0	82.6	0	11	32.9	56.1	1.21	0.197	0.783
Site 55	87.3	1030	17.2	0	72.1	0	8.7	31.8	59.5	0.9	0.146	0.68
Site 57	96.2	1110	11.4	0	74.8	0	6.3	30.1	63.6	2.49	0.1	0.572
Site 58	83.7	1300	13.3	0	43.4	0	15.1	58	26.9	0.93	0.563	2.722
Site 59	87.2	1280	10.4	0	76	0	7.8	36.8	55.4	0.84	0.141	0.805
Site 60	83.1	1030	9.8	0	101.5	0	6.7	24.1	69.3	0.75	0.096	0.443